



Lecture Notes in Mechanical Engineering

U. Chandrasekhar
Lung-Jieh Yang
S. Gowthaman *Editors*

Innovative Design, Analysis and Development Practices in Aerospace and Automotive Engineering (I-DAD 2018)

Volume 2

 Springer

Lecture Notes in Mechanical Engineering

Lecture Notes in Mechanical Engineering (LNME) publishes the latest developments in Mechanical Engineering—quickly, informally and with high quality. Original research reported in proceedings and post-proceedings represents the core of LNME. Volumes published in LNME embrace all aspects, subfields and new challenges of mechanical engineering. Topics in the series include:

- Engineering Design
- Machinery and Machine Elements
- Mechanical Structures and Stress Analysis
- Automotive Engineering
- Engine Technology
- Aerospace Technology and Astronautics
- Nanotechnology and Microengineering
- Control, Robotics, Mechatronics
- MEMS
- Theoretical and Applied Mechanics
- Dynamical Systems, Control
- Fluid Mechanics
- Engineering Thermodynamics, Heat and Mass Transfer
- Manufacturing
- Precision Engineering, Instrumentation, Measurement
- Materials Engineering
- Tribology and Surface Technology

To submit a proposal or request further information, please contact: Dr. Leontina Di Cecco Leontina.dicecco@springer.com or Li Shen Li.shen@springer.com.

Please check the Springer Tracts in Mechanical Engineering at <http://www.springer.com/series/11693> if you are interested in monographs, textbooks or edited books. To submit a proposal, please contact Leontina.dicecco@springer.com and Li.shen@springer.com.

Indexed by SCOPUS.

More information about this series at <http://www.springer.com/series/11236>

U. Chandrasekhar · Lung-Jieh Yang
S. Gowthaman
Editors

Innovative Design, Analysis and Development Practices in Aerospace and Automotive Engineering (I-DAD 2018)

Volume 2

 Springer

Editors

U. Chandrasekhar
Vel Tech Rangarajan Dr. Sagunthala R&D
Institute of Science and Technology
Avadi, Chennai, India

S. Gowthaman
Vel Tech Rangarajan Dr. Sagunthala R&D
Institute of Science and Technology
Avadi, Chennai, India

Lung-Jieh Yang
Department of Mechanical and
Electromechanical Engineering
Tamkang University
Tamsui District, New Taipei City, Taiwan

ISSN 2195-4356 ISSN 2195-4364 (electronic)
Lecture Notes in Mechanical Engineering
ISBN 978-981-13-2717-9 ISBN 978-981-13-2718-6 (eBook)
<https://doi.org/10.1007/978-981-13-2718-6>

Library of Congress Control Number: 2018955447

© Springer Nature Singapore Pte Ltd. 2019

This work is subject to copyright. All rights are reserved by the Publisher, whether the whole or part of the material is concerned, specifically the rights of translation, reprinting, reuse of illustrations, recitation, broadcasting, reproduction on microfilms or in any other physical way, and transmission or information storage and retrieval, electronic adaptation, computer software, or by similar or dissimilar methodology now known or hereafter developed.

The use of general descriptive names, registered names, trademarks, service marks, etc. in this publication does not imply, even in the absence of a specific statement, that such names are exempt from the relevant protective laws and regulations and therefore free for general use.

The publisher, the authors and the editors are safe to assume that the advice and information in this book are believed to be true and accurate at the date of publication. Neither the publisher nor the authors or the editors give a warranty, express or implied, with respect to the material contained herein or for any errors or omissions that may have been made. The publisher remains neutral with regard to jurisdictional claims in published maps and institutional affiliations.

This Springer imprint is published by the registered company Springer Nature Singapore Pte Ltd. The registered company address is: 152 Beach Road, #21-01/04 Gateway East, Singapore 189721, Singapore

Preface

Designs and developments are the aspirations of tomorrow's technologies for aero and auto industries to be alive in the competitive world, where cost-effective solutions, improvements in a greenhouse environment, longevity/life cycle, eco-friendly materials and manufacturing, certification and government legislation demands are becoming stringent. Whether aerospace or automotive, the pulse and echo are similar in meeting the expected performances in the air or on the road, respectively. Both the industries have come to symbolise the essence of a modern industrial society. Perhaps more than any other single icon, it is associated with a desire for independence and freedom of movement—an expression of economic status. For the next decades, they are marching towards new concept designs, analysis and manufacturing technologies, where more swing is for improved performance through specific and/or multifunctional linguistic design aspect to downsize the system; improve the weight-to-strength ratio, fuel efficiency; make better the operational capability at room and elevated temperatures; reduce wear and tear, NVH aspects while balancing the challenges of beyond Euro IV emission norms, greenhouse effects and recyclable materials. The conference covered the areas such as additive manufacturing, aerodynamics, CAD, CFD, design engineering, environment, finite element method, fuels and energy source, integration of analysis and expected results, life cycle engineering, manufacturing, materials, MDO techniques, modelling of materials, optimisation technologies, propulsion systems, quality, reliability and durability, sensors and health monitoring, simulations, 3D scanning and re-engineering, and 3D printing. The conference aimed at addressing these issues of tomorrow where academia–industry–R&D partnerships and collaborative programs can be shared and implemented. The organisers of the 3rd International Conference on Innovative Design, Analysis and Development Practices in Aerospace and Automotive Engineering (I-DAD 2018) wish to provide

a platform for deliberations on design engineering, numerical methods, analysis/optimisation techniques, life cycle engineering, system engineering, configuration management, advanced materials, novel manufacturing/prototyping, vibration and health monitoring, propulsion system and quality and reliability in the aerospace and automotive fields. The response to the conference was overwhelming on both national and international fronts.

Chennai, India

U. Chandrasekhar
Lung-Jieh Yang
S. Gowthaman

Contents

Modeling and Optimization of SIS Process Using Evolutionary Computational Approach	1
D. Rajamani, E. Balasubramanian, P. Arunkumar, M. Silambarasan, G. Bhuvaneshwaran and R. Manivannan	
Computational Characterization of a CD Nozzle with Variable Geometry Translating Throat	11
S. Apoorva and Suresh Chandra Khandai	
Synthesis and Characterization of Al₂O₃-Cr₂O₃-Based Ceramic Composites for Artificial Hip Joint	21
Chandramani Goswami, Amar Patnaik, I. K. Bhat and Tej Singh	
Experimental Investigation on Tensile and Fracture Behaviour of Glass Fibre-Reinforced Nanoclay/Mg-Al LDH-Based Fibre Metal Laminates	29
K. Logesh, V. K. Bupesh Raja, M. Venkatasudhahar and Hitesh Kumar Rana	
Experimental Study on Micro-deburring of Micro-grooves by Micro-EDM	41
Elumalai Boominathan and S. Gowri	
Influences of Tool Pin Profiles on Mechanical Properties of Friction Stir Welding Process of AA8011 Aluminum Alloy	47
K. Giridharan, V. Jaiganesh and S. Padmanabhan	
Numerical Investigation of the Behaviour of Thin-Walled Metal Tubes Under Axial Impact	55
L. Prince Jeya Lal and S. Ramesh	
Improving Process Performance with World-Class Manufacturing Technique: A Case in Tea Packaging Industry	65
Vishal Naranje, Anand Naranje and Sachin Salunkhe	

Tensile Testing and Evaluation of 3D-Printed PLA Specimens as per ASTM D638 Type IV Standard	79
S. Anand Kumar and Yeole Shivraj Narayan	
Design Optimization and Testing of Structure of a Single Door Refrigerator	97
Nishchay Anand and S. Sivarajan	
Use of Low-Fidelity Codes for Teaching Aircraft Design	107
H. K. Narahari and Deepak Madhyastha	
Drag Reduction for Flow Past a Square Cylinder Using Rotating Control Cylinders—A Numerical Simulation	113
Ghosh Subhankar, S. Senthilkumar and S. Karthikeyan	
Study the Effect of Mill Scale Filler on Mechanical Properties of Bidirectional Carbon Fibre-Reinforced Polymer Composite	121
Aman Soni and Amar Patnaik	
Study on Carbon, Glass, and Flax Hybrid Composites Using Experimental and Computational Techniques	131
M. Dinesh, B. Rubanrajasekar, R. Asokan, S. Vignesh and S. Rajesh	
Design Evaluation of a Mono-tube Magnetorheological (MR) Damper Valve	145
Solomon Seid, Sujatha Chandramohan and S. Sujatha	
Characterization of Soot Microstructure for Diesel and Biodiesel Using Diesel Particulate Filter	153
Indranil Sarkar, Ritwik Raman, K. Jayanth, Aatmesh Jain and K. C. Vora	
Performance of Diesel Particulate Filter Using Metal Foam Combined with Ceramic Honeycomb Substrate	163
Hardik Sarasavadiya, Manthan J. Shah, Indranil Sarkar and Aatmesh Jain	
Dry Machining of Nimonic 263 Alloy Using PVD and CVD Inserts	179
K. Vetri Velmurugan, K. Venkatesan, S. Devendiran and Arun Tom Mathew	
Investigation of Parameters for Machining a Difficult-to-Machine Superalloy: Inconel X-750 and Waspaloy	199
K. Vetri Velmurugan, K. Venkatesan, S. Devendiran and Arun Tom Mathew	
Aerodynamic Characteristics of Semi-spiroid Winglets at Subsonic Speed	217
Karthick Dhileep, S. Arunvinthan and S. Nadaraja Pillai	

Vibrational Analysis of Self-aligning Rolling Contact Bearing Defects	225
T. Narendiranath Babu, Abhinav Giri Goswami, Animesh Srivastava and Rishabh Kumar Tiwari	
Fabrication and Characterization of $\text{Cu}_{2-x}\text{Zn}_{1.3}\text{SnS}_4$ Kesterite Thin Films Synthesized by Solvent Based Process Method for Photovoltaic Solar Energy Applications	241
B. Khadambari, S. S. Bhattacharya and M. S. Ramachandra Rao	
Formula SAE Power Increment	249
Jasjeev Singh, M. V. N. Sankaram, Vishal Naranje and Sachin Salunkhe	
Temperature Behavior-Based Monitoring of Worm Gears Under Different Working Conditions	257
T. Narendiranath Babu, Dhavalkumar Patel, Devansh Tharnari and Akash Bhatt	
Production and Comparison of Fuel Properties for Various Biodiesels	267
D. Ravichandra, Ravi Kumar Puli and V. P. Chandramohan	
Experimental Determination of Fluid Flow Parameters to Study Permeation Process Inside a Porous Channel	277
Hussain Najmi, Eddy El-Tabach, Nicolas Gascoin, Khaled Chetehouna and François Falempin	
Diesel Engine Cylinder Head Port Design for Armored Fighting Vehicles: Compromise and Design Features	285
Hari Viswanath, A. Kumarasamy and P. Sivakumar	
Design Optimization of Advanced Multi-rotor Unmanned Aircraft System Using FSI	299
R. Vijayanandh, M. Senthil Kumar, K. Naveenkumar, G. Raj Kumar and R. Naveen Kumar	
Studies on Carbon Materials-Based Antenna for Space Applications	311
Prasanna Ram, Manoj Aravind Sankar and N. G. Renganathan	
Progress and Issues Related to Designing and 3D Printing of Endodontic Guide	331
Ankit Nayak, Prashant K. Jain and P. K. Kankar	
Physical and Tribological Behaviour of Dual Particles Reinforced Metal Matrix Composites	339
V. Mohanavel, K. Rajan, M. Ravichandran, S. Suresh Kumar, M. Balamurugan and C. Jayasekar	

Parametric Optimization of Friction Welding Parameter of Ferritic Stainless Steel and Copper Material Using Taguchi Approach	349
C. Shanjeevi, S. Velu, J. Thamilarasan and S. Satish Kumar	
Experimental Investigation on the Thermal Performance of the Light-Emitting Diode (LED) Heat Sinks	357
A. S. Praveen, Kaipa Sai Chaithanya, R. Jithin and K. Naveen Kumar	
Numerical Modelling of Spiral Cyclone Flow Field and the Impact Analysis of a Vortex Finder	363
R. Vignesh, D. Balaji, M. Surya, A. Vishnu Pragash and R. Vishnu	
Lattice Boltzmann Simulation of Double-Sided Deep Cavities at Low Reynolds Number	373
Balashankar Kesana, Vikas V. Shetty and D. Arumuga Perumal	
A Study of Thermo-structural Behavior of Annular Fin	381
Rahul Sharma, Lakshman Sondhi, Vivek Kumar Gaba and Shubhankar Bhowmick	
A New Design to Achieve Variable Compression Ratio in a Spark Ignition Engine	389
Aditya Roy, Chetan Mishra, Sarthak Jain and Naveen Solanki	
Experimental Investigation on Energy Saving due to Bubble Disturbance in Boiling Process	397
S. Santhosh Kumar and S. Balaguru	
Highway Traffic Scenario-Based Lane Change Strategy for Autonomous Vehicle	405
Gourish Hiremath, Kiran Wani and Sanjay Patil	
Friction and Wear Analysis of PTFE Composite Materials	415
Sachin Salunkhe and Pavan Chandankar	
Flow Analysis of Catalytic Converter—LCV BS III Applications for Optimising Pressure Drop	427
C. P. Om Ariara Guhan and G. Arthanareeswaran	
Step Toward Computer-Aided Integration of Sheet Metal Applications	437
Ravi Kumar Gupta, H. M. A. Hussein, S. S. Salunkhe, Mukur Gupta and S. Kumar	
Thermodynamic Analysis of Diesel Engine Fuelled with Aqueous Nanofluid Blends	445
S. P. Venkatesan and P. N. Kadiresh	

Investigation of Twin Cylinder Direct Injection CI Engine Characteristics Using Calophyllum Inophyllum Biodiesel Blends 457
 Pathikrit Bhowmick, Dhruv Malhotra, Pranjal Agarwal, Aatmesh Jain and K. C. Vora

A Novel Beetle-Inspired Fuel Injection System for Improved Combustion Efficiency 467
 R. Kuppuraj and S. A. Pasupathy

Effect of Friction Stir Processing on the Dry Sliding Wear Behaviour of AA6082-5TiB₂ Composite 477
 Sreehari Peddavarapu and S. Raghuraman

Optimization of Sliding Wear Performance of Ti Metal Powder Reinforced Al 7075 Alloy Composite Using Taguchi Method 485
 A. Kumar, A. Patnaik and I. K. Bhat

A Comparative Study on Mechanical and Dry Sliding Wear Behaviour of Al 7075-T6 Welded Joints Fabricated by FSW, TIG and MIG 499
 Lalta Prasad, Lalit Mohan, Himanshu Prasad Raturi and Virendra Kumar

Overview of Cryogenics Production and Automation in Cryo-distribution at TIFR, Mumbai 507
 K. V. Srinivasan, A. Manimaran, K. A. Jaison and Vijay A. Arolkar

Analysis of Recast Layer, Wear Rate and Taper Angle in Micro-electrical Discharge Machining Over Ti-6Al-4V 517
 S. Rajamanickam and J. Prasanna

Evaluation of Critical Speed for Aluminum-Boron Carbide Metal Matrix Composite Shaft 527
 Arun C. Dixit, B. K. Sridhara and M. V. Achutha

Smart System for Feature Recognition of Sheet Metal Parts: A Review 535
 Sachin Salunkhe, Soham Teraiya, H. M. A. Hussein and Shailendra Kumar

Author Index 551

About the Editors

Dr. U. Chandrasekhar is Pro Vice Chancellor of Vel Tech Dr. RR & Dr. SR Technical University, Chennai. Previously, he was Director of the Engineering Staff College of India (ESCI), an autonomous organ of the Institution of Engineers (India). Prior to that, he was Additional Director at a Ministry of Defence R&D Organisation called Gas Turbine Research Establishment. For the past 26 years, he has been involved in the design, analysis, prototyping, rapid manufacturing and testing of aero gas turbine engines. He has set up the first-ever rapid prototyping laboratory in the country.

He is currently leading a critical technology development project on high-temperature thin film sensors in collaboration with NRC, Canada, and serves on the Council of the Institution of Engineers and National Design and Research Forum. He was also chosen to represent India at the Young Leaders Convention of World Federation of Engineering Organisations at Geneva.

He holds a B.E. in mechanical engineering from NIT Surathkal; an M.Tech. in design stream from IIT Madras; and a Ph.D. from VTU. For his research efforts, he received a commendation medal from the Scientific Advisor to the Defence Minister, and in recognition of his academic excellence at IIT Madras, he received an award from former President of India, Dr. A. P. J. Abdul Kalam.

Dr. Lung-Jieh Yang received his M.S. from the Tamkang University, Taiwan, in 1991 and his Ph.D. from the Institute of Applied Mechanics, National Taiwan University, Taiwan, in 1997. He was Visiting Associate of electrical engineering at Caltech, USA, from 2000 to 2001, and is currently Professor in the Department of Mechanical and Electromechanical Engineering and Director of the Instrument and Experiment Center, Tamkang University, Taiwan. He is also Member of IEEE and AIAA. His current research interests include flapping micro aerial vehicles (MAVs) and gelatin MEMS technology. His research areas are polymer composites, nano-materials, high-temperature foams, experimental mechanics and sensors for health monitoring and energy harvesting.

Dr. S. Gowthaman is Director of R&D and Associate Professor in the Department of Mechanical Engineering, Vel Tech Dr. RR & Dr. SR University, Chennai. He received his B.E. in mechanical engineering from Bharathidasan University (Shanmugha College of Engineering) and his M.S. and Ph.D. in mechanical engineering from North Carolina A&T State University, USA. His research activities include polymer-based composite materials, experimental mechanics, nanoengineering and advanced materials for various applications. Before joining Vel Tech University in 2013, he worked at Nanyang Technological University (NTU), Singapore, and at the Center for Aviation Safety (CAS) at NC A&T State University, USA. He has worked in research projects sponsored by various agencies like NASA, the United States Army, ONR and Wright Materials Research (all USA), DSTA (Singapore), DST-SERB (India), DRDO-ERIPR (India) and DST-TDT (India). He has collaborated and is collaborating with a number of national and international institutes and research laboratories. He has published more than 30 research papers in international journals and conference proceedings. He is a member of several committees and societies including AIAA Materials Technical Committee, USA, in 2011, serves as a reviewer for a number of journals including *Composites Part A*, *Journal of Reinforced Plastics and Composites*, *AIAA Journal* and *IE Springer Journal*, and is a member of the editorial board for international conferences like I-DAD and ICAM-3D. He has received a number of awards from NC A&T State University, USA, and Bharathidasan University for his academic and research achievements, an NTU (Singapore) Post-Doctorate Fellowship and a DST-SERB (India) Early Career Research Project Award.

Modeling and Optimization of SIS Process Using Evolutionary Computational Approach



D. Rajamani, E. Balasubramanian, P. Arunkumar, M. Silambarasan, G. Bhuvaneshwaran and R. Manivannan

Abstract Due to the existence of diverse selective inhibition sintering (SIS) processing variables and intricate stochastic nature, arriving optimal processing conditions to enhance the product quality is extremely difficult. This paper concentrates on the development of SIS system model to predict the optimal SIS process variables to improve the dimensional accuracy. Response surface methodology (RSM) is employed to design the experiments and develop the mathematical models by considering various SIS process parameters. The developed regression models are further optimized by an evolutionary approach of genetic algorithm (GA) scheme. The proposed approach can be effectively utilized to predict the dimensional accuracy under various process conditions.

Keywords Selective inhibition sintering · Response surface methodology · Simulated annealing · Dimensional accuracy

1 Introduction

Additive manufacturing (AM) is the process of joining the desired materials in layer by layer to manufacture the parts directly from computed-aided design three-dimensional (3D) models [1]. AM has tremendous potential in aerospace, automobile, medical, and toy industrial applications to swiftly realize the parts [2, 3]. Unlike subtractive manufacturing, AM does not necessitate any molds, fixtures, and other work holding devices which lessen the cost of production and it is an effective process to produce complicated profile or shape of the part that makes the system user-friendly [4]. In addition, AM parts are achieved superior

D. Rajamani (✉) · E. Balasubramanian · P. Arunkumar · M. Silambarasan
G. Bhuvaneshwaran · R. Manivannan
Department of Mechanical Engineering, Centre for Autonomous
System Research (CASR), Vel Tech Rangarajan Dr. Sagunthala
R&D Institute of Science and Technology, Chennai 600062, India
e-mail: rajamanitamil1991@gmail.com

© Springer Nature Singapore Pte Ltd. 2019
U. Chandrasekhar et al. (eds.), *Innovative Design, Analysis and Development Practices in Aerospace and Automotive Engineering (I-DAD 2018)*, Lecture Notes in Mechanical Engineering, https://doi.org/10.1007/978-981-13-2718-6_1

dimensional accuracy and experienced less residual stress in comparison to conventional molding and casting [5]. There are more than twenty AM techniques available to produce functional parts for diverse applications and adhesion of layers for each process is varied [6].

Being capable of processing a wide range of materials including polymers and metals and non-usage of support structures, selective laser sintering (SLS) is presently regarded as the most versatile AM process [7]. In the SLS process, CO₂ laser beam is selectively moved as per the desired profile of the part [8]. SLS is extensively used in high-end industries to realize the parts with high strength [9]. However, elimination of laser reduces machine cost and built time, but it necessitates an alternative method for selectively sintering the particles [10].

The selective inhibition sintering (SIS) [11] is considered to be cost-effective AM process, wherein costly laser system is replaced with low-cost ceramic or infrared heaters. In SIS, part profiles are determined through spraying inhibitors, and sintering of powder particles is achieved in the desired surface of powder bed [12]. However, in the case of SLS, laser beam is focused based on the required pattern using prior path planning. The selective region of powder surface is printed with inhibitor that will absorb heat energy; therefore, the powder below the inhibitor will not become sintered and the remaining area will be sintered. Finally, the inhibitor and un-sintered powder are washed and cleaned at the post-processing stage. As in the case of SIS system, there are more than twenty-five parameters that can affect the part quality, and in this study, few process parameters namely thickness of polymer powder layer, heat supply per unit area, delivery of inhibition, and movement of heater along the part bed are considered for its importance. However, arriving optimal solutions of these parameters necessitates a suitable optimization algorithm. Author's earlier work dealt on the investigation of mechanical strength, wear, and polymer characteristics [13–15] using other optimization algorithms. Therefore, in this study, genetic algorithm (GA) is accounted to determine optimal solution for evaluating the shrinkage of HDPE parts.

2 Methodologies

2.1 Response Surface Methodology

The experimental strategy is carried out with an aid of Box–Behnken design (BBD) [16]. It is used to perform non-sequential experiments and all design points are falling in the safe ranges of parameters under consideration [9]. A total number of 29 test specimens are fabricated according to design matrix, as presented in Table 1.

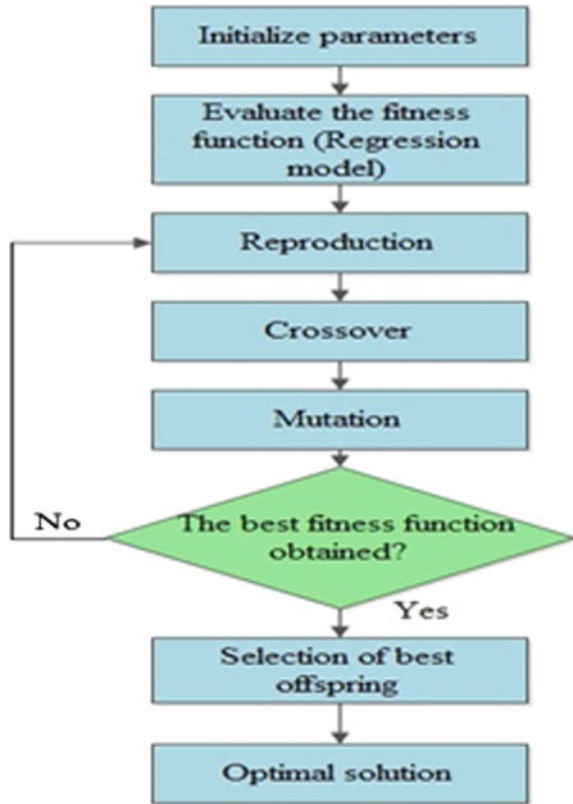
Table 1 Design matrix and measured response values

Run	Layer thickness (mm)	Heater energy (J/mm ²)	Heater feed rate (mm/s)	Printer feed rate (mm/min)	Avg. shrinkage (S) (mm)
1	1	0	1	0	5.2377
2	0	1	-1	0	5.4883
3	-1	0	1	0	7.6974
4	0	0	0	0	4.8634
5	1	0	0	-1	5.674
6	-1	0	0	1	4.0502
7	0	0	1	1	7.3224
8	0	0	-1	1	4.1842
9	0	1	1	0	5.4127
10	0	0	0	0	4.9960
11	0	1	0	-1	4.7922
12	0	-1	0	-1	4.6457
13	1	0	-1	0	7.6864
14	0	-1	0	1	4.5373
15	0	-1	1	0	6.4098
16	1	-1	0	0	4.9551
17	0	0	0	0	4.5302
18	-1	0	-1	0	3.8804
19	0	0	1	-1	5.1980
20	0	0	0	0	4.4074
21	0	0	0	0	4.3545
22	0	0	-1	-1	7.1749
23	0	1	0	1	3.9028
24	-1	0	0	-1	5.2213
25	-1	1	0	0	3.7661
26	-1	-1	0	0	4.9519
27	1	1	0	0	5.4256
28	0	-1	-1	0	5.4756
29	1	0	0	1	4.9536

2.2 Genetic Algorithm

Genetic algorithm (GA) is a population-based meta-heuristic optimization technique and has been used to determine the optimal region when the problem becomes complex and generally does not depend on the initial solution [17]. GA can solve linear and nonlinear problems through investigating all regions of the state space and developing promising areas with a set of possible solutions or chromosomes that are randomly generated from the described set of probabilistic rules to obtain

Fig. 1 Flowchart of genetic algorithm



minimum dimensional shrinkage. The entire set of these chromosomes includes a population. The chromosomes expand during several iterations or generations.

The crossover and mutation formulations are employed for splitting and flipping the chromosomes. After that, the fitness function is used to evaluate the chromosomes. This process is repeated until the best fitness attained by one chromosome and thus taken as the best solution to the problem. Hence, an optimal solution is identified using genetic algorithm and Fig. 1 illustrates the flowchart of GA.

3 Experimental Details

The SIS system consists of five independent movements such as translation along X , Y , Z , deposition of inhibitor and travel of heater. The XY planar motion is achieved through a timing belt and pinion setup actuated by stepper motor. The up-and-down motion of feed and build tanks along Z direction is actuated through a stepper motor in such a way that the desired layer thickness is maintained for sintering of polymer powders. The desired three-dimensional (3D) CATIA model is exported as a

stereolithographic (.STL) file. The STL file is imported into Slic3r software which slices the STL file with specific layer thickness and then it is transformed into G-codes. These G-codes, then, are imported into Pronterface software to create machine tool paths of SIS machine for smearing the inhibitor at the part boundary. As per the machine path generation, HDPE powder is deposited with a desired layer thickness from the storage chamber using a roller mechanism. Inhibition is carried out with reference to required part profile which acts as support material for the part. Sintering phenomenon is achieved through controlling the temperature of ceramic heater with appropriate feed rate. The layer-by-layer deposition of powder, inhibition, and sintering is performed until the required part is fabricated. Post-processing of cleaning of inhibitor from the built part completes the SIS process.

High-density polyethylene (HDPE) with an average grain size ranging of 35–80 μm supplied by JP Polymers, India, is utilized for part fabrication. During the course of experiments, 100% virgin powder is used to avoid irregularities in sintered parts. The test specimens are fabricated for investigation with a dimension of $135 \times 35 \times 8$ mm. The shrinkage is measured using Checkmaster (Model: 216-242, Helmel Inc., USA) benchtop coordinate measuring machine equipped with Geomet[®] 7.00.035 CMM software. The experimental design matrix and measured shrinkage values are presented in Table 1. Based on measured dimensions, shrinkage of a specimen is calculated using [18],

$$\%dX = \frac{|X - X_{CAD}|}{X_{CAD}} \times 100 \quad (1)$$

where X_{CAD} represents the dimension from CAD model, X is the actual size measured using vernier caliper, and $\%dX$ stands for percentage change in dimension along specified direction.

4 Results and Discussion

4.1 Development of Empirical Equations

In the analysis of variance, the coefficient of regression model is obtained through removing the insignificant terms. The formulated regression model is given as:

$$\begin{aligned} \text{Avg. Shrinkage } (S) = & 65.614 + 62.988A + 1.461B - 36.791C - 0.425D \\ & + 1.31AB - 31.329AC - 0.159BC + 0.128CD + 28.716A^2 \\ & - 0.018B^2 + 4.983C^2 + 0.0001D^2 \end{aligned} \quad (2)$$

4.2 Optimization of Dimensional Shrinkage Using Simulated Annealing

In the present investigation, a single-objective optimization for minimizing the shrinkage of SIS processed parts sheet within the prescribed set of bounds is presented. The regression models developed using RSM are as a fitness function in genetic algorithms. The GA algorithm for these optimization studies are performed using MATLAB codes. The standard mathematical format for minimizing shrinkage can be stated as:

$$\text{Minimize} = \text{Shrinkage}(A, B, C, D) \quad (3)$$

Subjected to constrained variables are placed as bounds on the four input parameters such as,

$$\begin{aligned} 1 \text{ mm} &\leq A \leq 3 \text{ mm} \\ 22.16 \text{ J/mm}^2 &\leq B \leq 28.48 \text{ J/mm}^2 \\ 3 \text{ mm/s} &\leq C \leq 4 \text{ mm/s} \\ 80 \text{ mm/min} &\leq D \leq 120 \text{ mm/min} \end{aligned}$$

The regression models developed using RSM are used as the fitness function for both the algorithms. The initial setting for running the GA is mentioned in Table 2. The critical parameters on genetic algorithm are population size, population type, crossover function, mutation function, migration rate, and the direction of migration. In case of simulated annealing algorithm, initial temperature, annealing function, annealing interval, and temperature update function are considered as critical parameters.

Simulation is performed in MATLAB environment using optimization toolbox. Steep curve is observed (Fig. 2) due to maximized search space and then converges in 75th generation to obtain a best possible optimal solution. The optimal process parameters to achieve minimal dimensional shrinkage are observed at 133rd iteration, and the results are shown in Fig. 2.

Table 2 Combination of GA parameters leading to optimal solutions

Type of population	Double vector
Size of population	100
Crossover function	Scattered
Rate of crossover	0.8
Type of mutation	Adaptive feasible
Rate of mutation	0.7
Creation function	Feasible population
Migration rate	0.2
Direction of migration	Forward

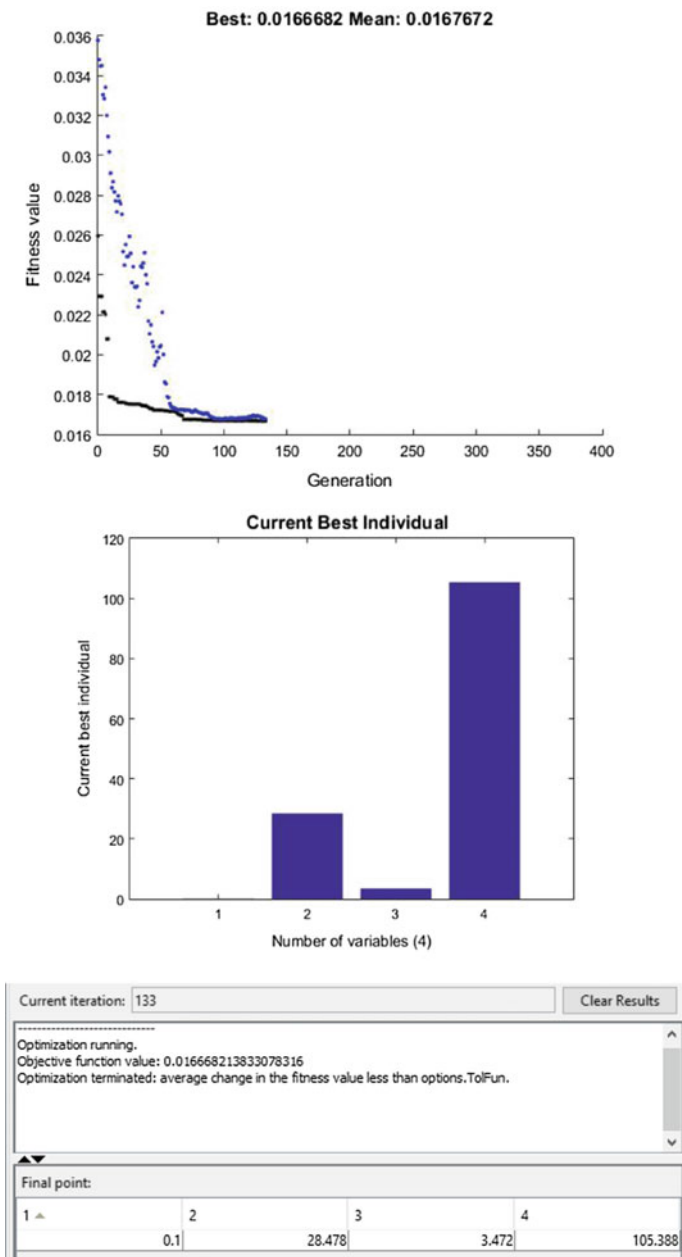


Fig. 2 Genetic algorithm optimal solution fronts

5 Conclusion

The present investigations dealt on the significance of SIS process variables in estimating the shrinkage characteristics of fabricated HDPE parts. The process model is established through using RSM-based BBD method and a global convergence genetic algorithm is then applied for obtaining optimum SIS process parameters. Experimental and optimization results show that the use of this combined RSM Genetic algorithm approach is an effective choice in determining optimal SIS process variables such as thickness of each layer is about 0.1 mm, heat supply of 28.478 J/mm², feed rate of heating system is 3.472 mm/s, and inhibitor feed rate of 105.388 mm/min for production of parts of superior dimensional accuracy.

References

1. ISO/ASTM Standard 52900: Additive Manufacturing-General Principles-Terminology. ISO/ASTM International, Switzerland (2015)
2. Weaver, T.: Made to measure. *Eng. Mag.* 20–21 May 2006
3. Degrange, J.: Paradigm shift from rapid prototyping to direct manufacturing. In: Proceedings from the SLS User Group Meeting, Orlando, FL, Sept 2003
4. Wohlers: Rapid prototyping tooling and manufacture. Annual State of the Industry report. Wohlers Associates. USA (2003)
5. Jauffre's, D., Lame, O., Vigier, G., Dore, F., Douillard, T.: Sintering mechanisms involved in high-velocity compaction of nascent semi crystalline polymer powders. *Acta Materialia* **57**, 2550–2559 (2009)
6. Khalil, Y., Kowalski, A., Hopkinson, N.: Influence of energy density on flexural properties of laser-sintered UHMWPE. *Addit. Manuf.* **10**, 67–75 (2016)
7. Gu, D., Zhang, G.: Selective laser melting of novel nanocomposite parts with enhanced tribological performance. *Virtual Phys. Prototyp.* **8**(1), 11–18 (2013)
8. Calignano, F., Manfredi, D., Ambrosio, E.P., Luliano, L., Fino, P.: Influence of process parameters on surface roughness of aluminium parts produced by DMLS. *Int. J. Adv. Manuf. Technol.* **67**(9), 2743–2751 (2013)
9. Zhang, J., Khoshnevis, B.: Selective separation (SSS) a new layer based additive manufacturing approach for metals and ceramics. In: Proceedings from the 26th SFF Symposium, Austin, TX, pp. 71–79 (2015)
10. Hopkinson, N., Erasenthiran, P.: High speed sintering—early research into a new rapid manufacturing process. In: Proceedings from the 15th SFF Symposium, Austin, Texas, pp. 312–320 (2004)
11. Khoshnevis, B., Asiabanpour, B., Mojdeh, M., Koraihy, B., Palmer, K., Deng, Z.: SIS—A new SFF method based on powder sintering. In: Proceedings from the 13th SFF Symposium, Austin, Texas, pp. 440–447 (2002)
12. Asiabanpour, B., Palmer, K., Khoshnevis, B.: An experimental study of surface quality and dimensional accuracy for selective inhibition of sintering. *Rapid Prototyp. J.* **10**(3), 181–192 (2004)
13. Rajamani, D., Esakki, B., Arunkumar, P., Udayagiri, C., Sachin, S.: Experimental investigation of SHS process variables using NSGA-II and RSM for evaluating mechanical strength characteristics of polyethylene parts. *Int. J. Manuf. Technol. Res.* **10**(1) (2018)

14. Esakki, B., Ponnambalam, A., Rajamani, D.: Modeling and prediction of optimal process parameters in wear behaviour of selective inhibition sintered high density polyethylene parts. *Prog. Addit. Manuf.* 1–13 (2017)
15. Arunachalam, A., Ponnambalam, A., Esakki, B.: Comparative study of high performance polymers in selective inhibition sintering process through finite element analysis. *J. Polym. Polym. Compos.* **25**(3), 199–202 (2017)
16. Evans, M.: *Optimization of Manufacturing Processes: A Response Surface Approach*. Carlton House Terrace, London (2003)
17. Holland, J.: *Adaptation in natural and artificial systems*. The University of Michigan, Ann Arbor (1975)
18. Sood, A.K., Ohdar, R.K., Mahapatra, S.S.: Improving dimensional accuracy of fused deposition modelling processed part using grey Taguchi method. *Mater. Des.* **30**, 4243–4252 (2009)

Computational Characterization of a CD Nozzle with Variable Geometry Translating Throat



S. Apoorva and Suresh Chandra Khandai

Abstract Nozzles constitute the exhaust system of jet engines. They are designed to regulate the flow properties to provide the required thrust force for all flight conditions. In the present work, the simulation of a de Laval nozzle outfitted with a throat shifting mechanism is compassed. The mechanism adds a variation in the throat geometry during the translation of the throat. A convergent–divergent (CD) nozzle is designed for Mach 2 initially. The geometry of the throat is varied by keeping the settling chamber pressure constant. The scope of the effort was to investigate the characteristics over the range of geometries (throat diameters, 10, 9.5, 9, and 8.5 mm) and operating conditions. The simulation of the nozzle flow is carried out using ANSYS CFX. Shear stress transport (SST) turbulence is used for the flow simulation. Grid-independent study is also performed for better mesh results. The simulation is carried out for chamber pressures of 8, 9.5, 11.5, and 14 bar. The Mach number, pressure, velocity, and temperature readings are taken along the nozzle axis and also the important cross sections of the nozzle for all cases. Thrust is calculated for all the cases and compared. Plot comparison of variations in the parameters was done, and optimum results were inferred.

Keywords CD nozzle · Pressure · Temperature · Variable geometry translating throat · Grid · SST

List of Symbols

M	Mach number
V	Nozzle exit velocity (m/s)
A_e	Nozzle exit area (mm ²)
A^*	Nozzle throat area (mm ²)
d^*	Nozzle throat diameter (mm)
d_e	Nozzle exit diameter (mm)

S. Apoorva (✉) · S. C. Khandai
Department of Aeronautical Engineering, Rajalakshmi Engineering College,
Thandalam, Chennai 602105, India
e-mail: apoorva.s.2015.aero@rajalakshmi.edu.in

© Springer Nature Singapore Pte Ltd. 2019
U. Chandrasekhar et al. (eds.), *Innovative Design, Analysis and Development Practices in Aerospace and Automotive Engineering (I-DAD 2018)*, Lecture Notes in Mechanical Engineering, https://doi.org/10.1007/978-981-13-2718-6_2

P_{amb}	Ambient pressure (N/m^2)
P_o	Inlet pressure (N/m^2)
P_e	Exit pressure (N/m^2)
T_o	Inlet temperature (K)
T_e	Exit temperature (K)
L	Nozzle length (mm)
X	Distance from nozzle inlet (mm)

1 Introduction

Nozzles constitute the exhaust system of jet engines. They are designed to regulate the flow properties to provide the required thrust force for all flight conditions. The convergent, convergent–divergent (CD) and divergent nozzles dwell as the three basic types of nozzles used in jet engines. The location in the CD nozzle where the cross-sectional area is at its minimum is labeled as the throat. The throat sees a choked flow ($M = 1$) when the back pressure and the corresponding pressure ratio are in range. Downstream of the throat, the nozzle cross-sectional area increases and the gas begins to expand to supersonic velocities.

The expansion ratio of the nozzle interprets the ratio of exit area to throat area. When the exit pressure is less than the ambient pressure (over-expansion), the external pressure nudges the flow inward, thus reducing the efficiency of the nozzle due to the availability of extra wall not contributing to any additional thrust. Hence, the nozzle should be shorter in length and should have smaller exit area to ensure better efficiency. When exit pressure is equal to ambient pressure, it is an optimum expansion. Optimum expansion of flow always ensures maximum thrust. When exit pressure is greater than ambient pressure (under-expansion), the flow continues to expand outward after leaving the nozzle, not exerting any pressure on the nozzle wall, and thus not contributing to any thrust. Hence, the nozzle should be longer enough and fitted with a larger exit area to ensure better efficiency.

If the engine has to operate over a variety of operating ranges, a fixed geometry nozzle may not really serve the purpose. It might be necessary to increase or decrease the nozzle area which is why the variable area nozzles came into play. Variable area nozzles or adjustable nozzles are thus required for matched operation under all conditions.

An experimental investigation of the throat shift of a family of two-dimensional high-speed civil transport nozzle concepts was conducted on the internal aerodynamic stability by Edwin J. Kawecki and Gregg L. Ribeiro.

Natta et al. [1], Pandey and Singh [2], and Pandey and Yadav [3] numerically investigated and discussed the variation of flow parameters of a rocket nozzle for a design Mach of 3 at various divergence angles keeping the throat and inlet diameter constant. The degree of angle for conical nozzle can be large as 12° – 18° . Pansari

and Jilani [4] conferred the analysis of the performance of flow characteristics of CD nozzles. It was concluded that the shock strength increases with decrease in operating pressure ratio and a shift in shock location toward exit was also observed mutually. An increase in the exit Mach number and the Mach number ahead of the shock was also observed for the decreasing operating pressure ratio. Stark [5] investigated the flow separation in rocket nozzles. Cold and hot flow tests were conducted to investigate the flow separation. Analysis of flow within CD supersonic nozzle for different cross sections like rectangular, square, and circular, keeping the same input conditions, using ANSYS FLUENT 12.0 has been carried out by Satyanarayana et al. [6]; it was found that rectangular nozzle gives higher exit velocity as compared to square and circular nozzles.

The design and CFD analysis of CD tri-nozzle had been carried out by Vinod Kumar et al. [7]. It was optimized to have high expansion coefficient than single nozzle without altering the divergent angle. The variations in mean velocity profiles of the x component along the x -axis of the twin jets at the designed Mach number were discussed by Pandey and Kumar [8]. It was found that the velocity profiles are fairly symmetrical about $y = 0$ and its gradients decay along x -axis. Due to the effect of entrainment in the shear layer, the velocity between two jets and the width of twin jets were found to increase with the x -axis. Lijo [9] explained a numerical investigation of transient flows in an axisymmetric over-expanded thrust optimized contour nozzle to validate results and investigated oscillatory flow characteristics during the start-up processes.

Ali et al. [10] majored the numeric simulation of fluidic modulation of nozzle thrust and identified that secondary injection pressure and size of the injector (added mass flow) regulate the thrust production for a fixed geometry and operating pressure. Increased secondary mass flow ratio increased the modulation of thrust.

2 Nozzle Design

The nozzle initially is tailored for a design Mach number (M) of 2.0 (area ratio (A_e/A^*) = 1.69), assuming the flow to be isentropic. The first case (Fig. 1a) is presumed to have a throat diameter (d^*) of 10 mm and hence an exit area (equal to the inlet area) of $A_e = 132.50 \text{ mm}^2$. Fixing maximum deflection angle as 2° throughout, case 1 sees equal converging and diverging lengths (along nozzle axis) of 42.79 mm. Hence, overall nozzle length is 85.58 mm. In accordance with the fitted mechanism, cases 2, 3, and 4 have throat diameters of 9.5, 9, and 8.5 mm and corresponding converging lengths of 32.63, 28.47, and 21.31 mm, respectively. The overall length and the inlet and exit areas of the nozzle remain the same for all four cases of variation of throat geometry and location.

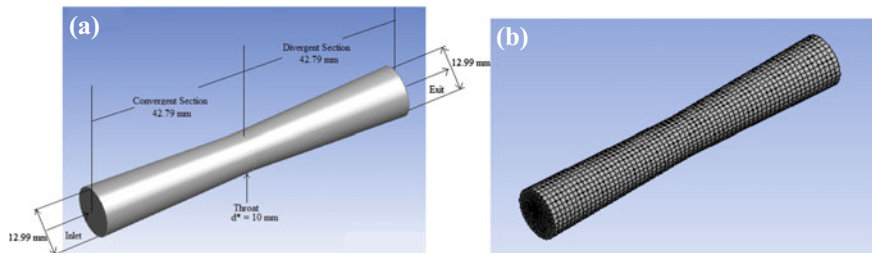


Fig. 1 a Nozzle with throat at initial position and b meshed nozzle

Table 1 Nozzle design parameters

Design parameters	Values
Total nozzle length (mm)	85.58
Inlet diameter (mm)	12.99
Exit diameter (mm)	12.99

3 Computation Procedure

The simulation of nozzles was carried out by ANSYS CFX with the assumption of air as an ideal fluid. The analysis includes modeling, meshing, preprocessing, solving, and post-processing. Three nozzle geometries were created by varying the dimension and location of the throat. Altogether, geometrical contours of four nozzles with throat diameters 10, 9.5, 9, and 8.5 mm were constructed (Table 1).

The grid-independent and domain optimization studies were carried out, and the grid chosen for the simulations had 16,796 elements with 18,216 nodes with unstructured fine meshing (Fig. 1b). The computation was carried out, and the results are analyzed in the results and discussions (Table 2).

4 Results and Discussions

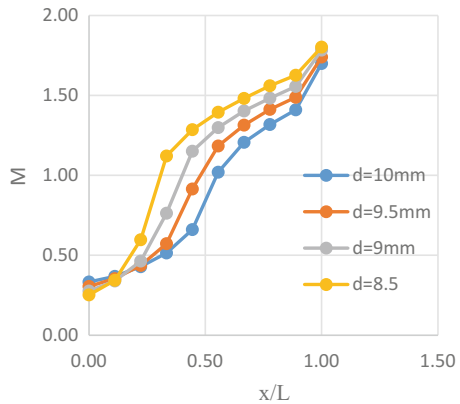
The variation of parameters like static pressure, Mach number, and velocity with change in area ratio and throat location was studied. The chamber pressure is kept constant while varying the geometry of the nozzle. The simulation is carried out for chamber pressures of 8, 9.5, 11.5, and 14 bar.

The Mach number plots (for settling chamber of 8 bar) of the nozzle with throat diameters 10, 9.5, 9, and 8.5 mm along the nozzles are shown in Fig. 2. The Mach number at exit reaches its highest value ($M = 1.8$) for $d^* = 8.5$ mm case and is lowest ($M = 1.7$) for the initial case of $d^* = 10$ mm. The observed Mach numbers were 1.78 and 1.74 for the $d^* = 9$ and 9.5 mm, respectively. Decrease in Mach

Table 2 Boundary conditions

Boundary conditions	Medium of flow = Air ideal gas		
		Inlet total pressure (bar)	Outlet average relative static pressure (bar)
	1	8	0.01075
	2	9.5	0.00625
	3	11.5	0.00775
	4	14	0.00945

Fig. 2 Mach number variation along the nozzle for settling chamber pressure of 8 bar



number was observed with increase in throat diameter for the settling chamber pressure of 8 bar. Similar trends were observed for the nozzles with different chamber pressures as shown in Figs. 5, 8, and 11. Hence, the Mach number seems to increase as the throat shrinks and translates rearward.

The static pressure variation of the conical nozzles with throat diameters 10, 9.5, 9, and 8.5 mm at locations inside the nozzles is shown in Fig. 3. The minimum pressure values reached the exit were 0.54, 0.61, 0.66, and 0.87 bar for throat diameters 10, 9.5, 9, and 8.5 mm, respectively. Similarly, pressure variations for chamber pressures 9.5, 11.5, and 14 bar are shown in Figs. 5, 8, and 11, respectively. The static pressure for all four cases decreases from the inlet to exit in order to mix with the ambient air (Figs. 4, 6, 7, 9, and 10).

Velocity variations inside conical nozzles with throat diameters 10, 9.5, 9, and 8.5 mm for chamber pressures 8, 9.5, 11.5, and 14 bar are shown in Figs. 4, 7, 10, and 13, respectively. The maximum velocity (V_{max}) at the nozzle exit among the four indicated cases was obtained for the minimum throat diameter of 8.5 mm.

Thrust is determined numerically for all the simulated cases, and it is inferred that although the velocity and corresponding Mach number for the minimum throat diameter case ($d^* = 8.5$ mm) have maximum values for a given inlet pressure, thrust for the same happens to be minimum (Table 3). The percentage decrease in

Fig. 3 Pressure variation along the nozzle for settling chamber pressure of 8 bar

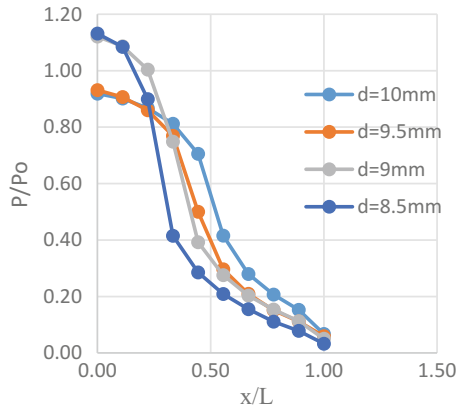


Fig. 4 Velocity variation along nozzle axis for settling chamber pressure of 8 bar

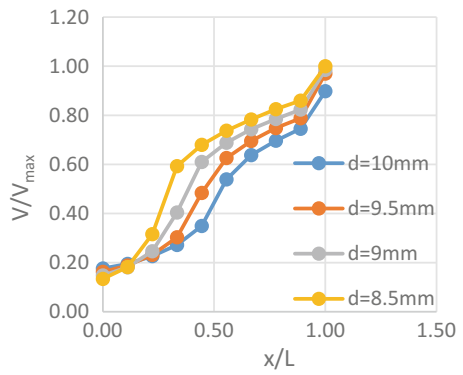


Fig. 5 Mach number variation along nozzle axis for settling chamber pressure of 9.5 bar

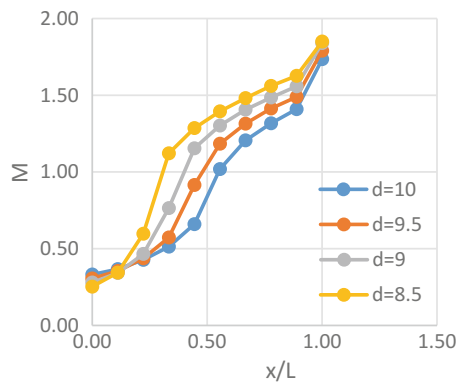


Fig. 6 Pressure variation along nozzle axis for settling chamber pressure of 9.5 bar

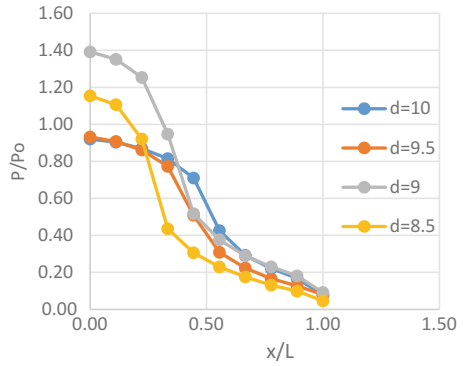


Fig. 7 Velocity variation along nozzle axis for settling chamber pressure of 9.5 bar

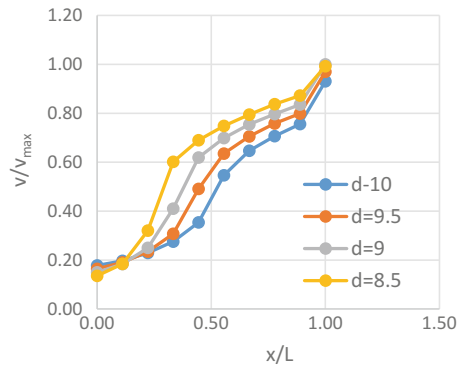
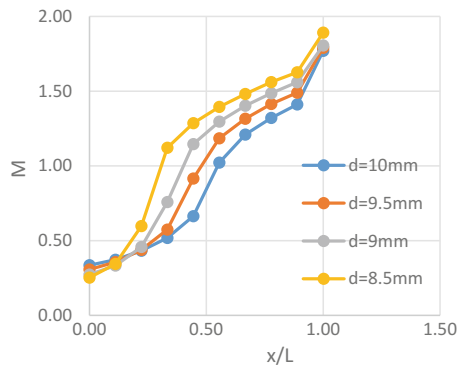


Fig. 8 Mach number variation along nozzle axis for settling chamber pressure of 11.5 bar



thrust observed during the throat shift from $d^* = 10$ mm to $d^* = 8.5$ mm is 30.6% for the first case ($P_o = 8$ bar). The successive cases with chamber pressures 9.5, 11.5, and 14 bar see 29.3, 28.3, and 28.1% decrease in thrust, respectively, during the throat shift (Figs. 6, 9 and 12).

Fig. 9 Pressure variation along nozzle axis for settling chamber pressure of 11.5 bar

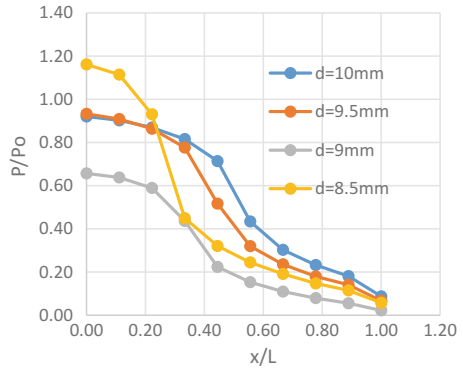


Fig. 10 Velocity variation along nozzle axis for settling chamber pressure of 11.5 bar

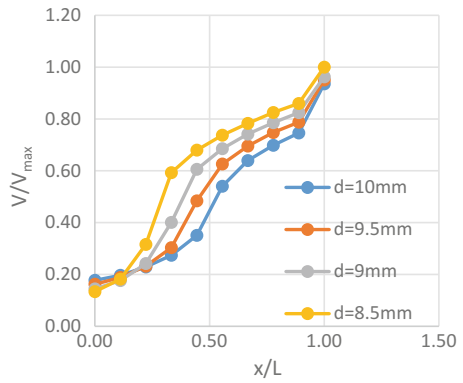
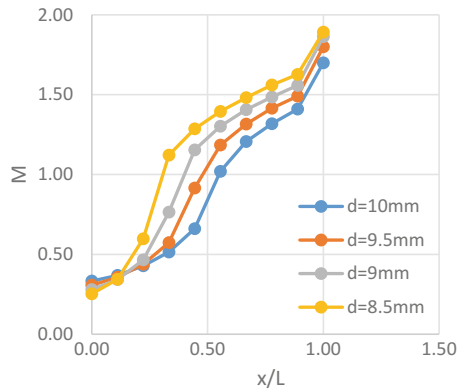


Fig. 11 Mach number variation along nozzle axis for settling chamber pressure of 14 bar



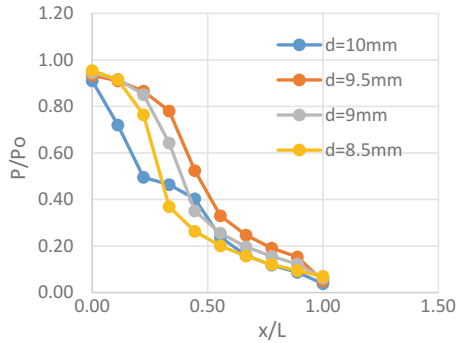


Fig. 12 Pressure variation along the nozzle for settling chamber pressure of 14 bar

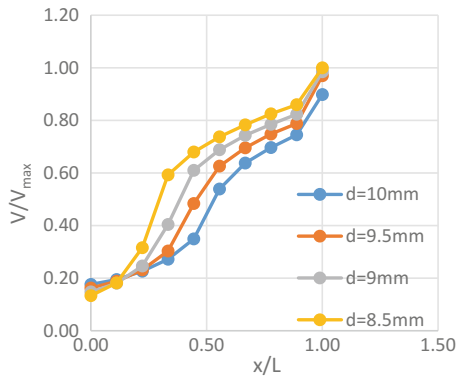


Fig. 13 Velocity variation along the nozzle for settling chamber pressure of 14 bar

Table 3 Nozzle exhaust thrust

	$P_o = 8$ bar	$P_o = 9.5$ bar	$P_o = 11.5$ bar	$P_o = 14$ bar
$d^* = 10$ mm	82.022 N	101.942 N	128.664 N	160.182 N
$d^* = 9.5$ mm	73.035 N	93.233 N	116.245 N	145.872 N
$d^* = 9$ mm	65.438 N	83.936 N	102.028 N	130.069 N
$d^* = 8.5$ mm	56.903 N	72.055 N	92.162 N	115.15 N

5 Conclusions

The simulation of a CD nozzle outfitted with a throat shifting mechanism has been completed, and the Mach number, pressure, and velocity readings were taken along the nozzle axis. The important cross sections of the nozzle over the range of

geometries (throat diameters, 10, 9.5, 9, and 8.5 mm) and operating conditions have been observed for chamber pressures of 8, 9.5, 11.5, and 14 bar using ANSYS CFX. It is inferred that

- Mach number increases as the throat shrinks and translates rearward.
- The maximum velocity magnitude at the nozzle exit among the four indicated cases is obtained for the minimum throat diameter case of 8.5 mm.
- The thrust calculated for each case is tabulated, and it is seen that maximum thrust of 160.18 N is obtained for the maximum throat diameter case ($d^* = 10$ mm) with maximum given settling chamber pressure of 14 bar. The thrust for the minimum throat diameter case ($d^* = 8.5$ mm) has a minimum value for a given inlet pressure.
- The percentage decrease in thrust observed during the throat shift from $d^* = 10$ mm to $d^* = 8.5$ mm is 30.6% for the first case ($P_o = 8$ bar). The successive cases with chamber pressures 9.5, 11.5, and 14 bar see 29.3, 28.3, and 28.1% decrease in thrust, respectively, during the throat shift.

References

1. Natta, P., Ranjith Kumar, V., Hanumantha Rao, Y.V.: Investigation of variation of flow parameters of a rocket nozzle. *IJERA* (2012). ISSN 2248–9622
2. Pandey, K.M., Singh, A.P.: CFD analysis of conical nozzle for mach 3 at various angles of divergence with fluent software. *IJCEA* **1**(2) (2010). ISSN 2010–0221
3. Pandey, K.M., Yadav, S.K.: CFD analysis of a rocket nozzle with four inlets at Mach 2.1. *IJCEA* **1**(4) (2010). ISSN: 2010–0221
4. Pansari, K., Jilani, S.A.K.: Analysis of performance of flow characteristics of convergent-divergent nozzles. *IJAET* (2013). ISSN: 22311961
5. Stark, R.H.: *Flow Separation in Rocket Nozzles*. AIAA, German Aerospace Center, Lampoldshausen, D-74239, Germany (2005)
6. Satyanarayana, G., Varun, C., Naidu, S.S.: CFD analysis of convergent-divergent nozzle. *Acta Technica Corviniensis Bull. Eng. Fascicule 3* (2013). ISSN 2007–3809
7. Vinod Kumar, P., Kishore Kumar, B.: Design and CFD analysis of convergent-divergent nozzle. *Int. J. Prof. Eng. Stud.* **9**(2) (2017)
8. Pandey, K.M., Kumar, V.: CFD analysis of twin jet flow at Mach 1.74 with fluent software. *Int. J. Environ. Sci. Dev.* **1**(5) (2010). ISSN: 2010-0264
9. Lijo, V.: Numerical investigation of transient flows in an axisymmetric over-expanded thrust optimized contour nozzle. *Int. J. Heat Fluid Flow* 409–417 (2010)
10. Ali, A., Neely, A., Young, J., Blake, B., Lim, J.Y.: Numerical simulation of fluidic modulation of nozzle thrust. In: 17th Australian Fluid Mechanics Conference, 5–9 Dec 2010

Synthesis and Characterization of Al₂O₃-Cr₂O₃-Based Ceramic Composites for Artificial Hip Joint



Chandramani Goswami, Amar Patnaik, I. K. Bhat and Tej Singh

Abstract The purpose of the present research work is to study the structural, mechanical and wear properties of artificial hip ceramic composites with varying proportion of aluminum and chromium oxide. The ceramic composites containing fixed amount of zirconium oxide, magnesium oxide, silicon nitride with varying amount of aluminum and chromium oxide were fabricated by using spark plasma sintering process and subsequently evaluated for structural (XRD, X-ray diffraction), elemental (EDS, energy-dispersive spectroscopy), mechanical (fracture toughness, elastic modulus and hardness) and wear properties. The results showed that aluminum and chromium oxide contents have a significant influence on the mechanical and wear properties of the fabricated ceramic composites. In particular, the composites containing 1.5 wt% chromium oxide and 70.5 wt% of aluminum oxide showed better mechanical properties with improved wear resistance. This result clearly indicates that the proposed ceramic materials may be a better alternative for artificial hip material.

Keywords Artificial hip material · Ceramic composites · Mechanical Wear

1 Introduction

Hip joint materials should possess high wear resistance and mechanical properties with good bio-compatibility in order to minimize the production of wear debris for their long-run. However, currently available hip joint materials wear out rapidly and

C. Goswami · A. Patnaik (✉)
Department of Mechanical Engineering, MNIT, Jaipur 302017, India
e-mail: apatnaik.mech@mnit.ac.in

I. K. Bhat
Applied Mechanics Department, MNNIT, Allahabad 211004, India

T. Singh
Department of Mechanical Engineering, Manav Bharti University, Solan 173229, India

© Springer Nature Singapore Pte Ltd. 2019
U. Chandrasekhar et al. (eds.), *Innovative Design, Analysis and Development Practices in Aerospace and Automotive Engineering (I-DAD 2018)*, Lecture Notes in Mechanical Engineering, https://doi.org/10.1007/978-981-13-2718-6_3

cause severe damage to the body [1]. For the few decades, many material combinations have been developed for hip joints, which include ceramic-on-polyethylene, metal-on-polyethylene, ceramic-on-ceramic, metal-on-metal and ceramic-on-metal. Traditional metal and polymer-based implants have been reported to have cancer and osteolysis risk [2]. The lower wear rates and reduced harmful effect on the human body, aluminum oxide-based ceramic composites have gain widespread popularity for hip joint replacement [3–7]. For young patients, alumina-on-alumina composite will be the best preference for a total hip arthroplasty [8]. Hip joints made of alumina and zirconia had shown extremely lower wear properties [9]. With the addition of silicon nitride to alumina–zirconia composite reported to exhibit a very low friction, negligible wear rate, excellent bio-compatibility and can be used as inserts with or without bone cement [10–13]. The beneficial effect of chromium oxide on the mechanical and wear properties of alumina-based composites was also reported in literature [14]. Hence, it is expected that chromium oxide will also affect the performance of alumina–zirconia–magnesium oxide–silicon nitride-based ceramic composites in beneficial way. Therefore, in current research work, chromium oxide was reported to be used as reinforcement in ceramic composites. Hence, ceramic hip implant composites containing magnesium oxide, zirconium oxide, silicon nitride and varying proportion of aluminum oxide and chromium oxide were fabricated by using spark plasma sintering process and evaluated for their mechanical and wear properties.

2 Experimental Details

2.1 *Materials and Fabrication*

Commercially available aluminum oxide (Al_2O_3 , 99.9%), zirconium oxide (ZrO_2 , 99.5%), magnesium oxide (MgO , 99.5%), silicon nitride (Si_3N_4 , 99.8%), chromium oxide (Cr_2O_3 , 99.5%) with an average particle size in the range of 5–10 μm have been used to synthesize the composite for hip implant.

Four series of composites were fabricated with varying weight percentage of ingredients as shown in Table 1. The weighed powder amount was first milled with the help of ball milling machine for 4 h using tungsten grinding media in toluene solution with a ball to powder ratio of 10:1 at 300 rpm. This mixture was separated and oven-dried. Afterward, the dried mixture was spark plasma sintered (SPS Syntex, Japan) at 1400 °C with a uni-axial pressure of 60 MPa, at 300 °C per minute heating rate and under vacuum.

Table 1 Compositional details and designation of the hip implant ceramic composites

Composition (wt%)	Designation			
	CR-1	CR-2	CR-3	CR-4
*Parent composition	28	28	28	28
Al ₂ O ₃	72.0	71.25	70.5	69.75
Cr ₂ O ₃	00.00	00.75	1.5	2.25

*Parent composition = ZrO₂ (20 wt%), Si₃N₄ (5 wt%), MgO (3 wt%)

2.2 Characterization

Identification of phases were carried out by using a X³pert Pro (Panalytical, USA) X-ray diffractometer with a CuK α radiation source over 20–80°. Elemental composition of the fabricated hip implant composites was characterized with the help of energy-dispersive spectroscopy (EDS) on field emission scanning electron microscope (FESEM, Zeiss, SUPRA 40VP). Hysitron TI 750-D Ubi-1 model used for nano-indentation measurements. Indentations were performed at 5000 μ N at loading rate of 500 μ N/s with a holding time of 2 s at maximum load. The Anstis model was [15] selected for the calculation of radial median crack.

$$K_{Ic} = 0.016 \sqrt{\frac{E}{H}} \times \frac{P}{\sqrt[3]{c}} \quad (1)$$

where P is the load; H is the hardness; E is Young's modulus and c is the length of the surface crack length. Indentation was carried out using a micro-hardness tester (1600–1000 indenter, Buehler, Lke Bluff IL). Five indentations were made on each of the diagonal at a load of 20 N and 13 s of dwell time. Indentation-crack technique using Vickers micro-hardness tester employed for measurement of fracture toughness, with a load of 20 N for 13 s of indentation time. Wear tests are carried out as per ISO 6474-1:2010 [16]. Simulated body fluid prepared according to ISO 23317 [17] was used as lubricant medium.

3 Results and Discussion

3.1 Microstructural Characterization

X-ray diffraction (XRD) spectrums of the fabricated ceramic composites are presented in Fig. 1. It was observed from Fig. 1 that, all the samples exhibited the phase purity of initial constituents. Further to note that, Al₂O₃ and ZrO₂ are the major ceramic powders present in the composite, while others, such as, MgO, Si₃N₄ and Cr₂O₃ are present in trace amounts. It is also observed that Cr₂O₃ peaks have

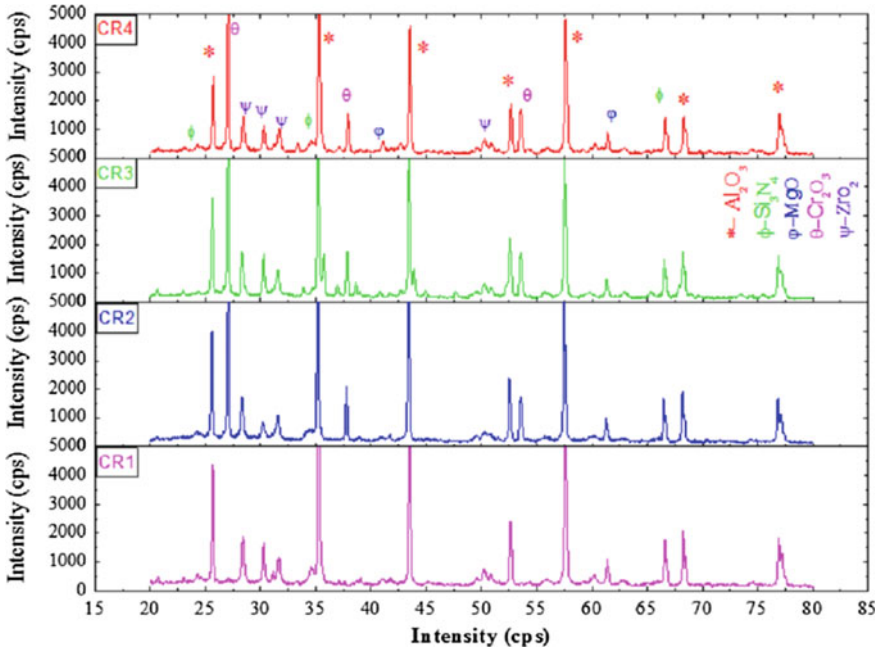


Fig. 1 XRD pattern of the fabricated ceramic composites

broadly lower intensities compared to the alumina due to its lower content. The FESEM image and corresponding EDS spectrum of the sintered sample (CR-3) is depicted in Fig. 2, which clearly revealed the presence of constituent elements such as O, Al, Si, Zr, Mg, Cr and N in the fabricated ceramic composite.

3.2 Mechanical and Wear Characterization

Figures 3 and 4 show the consistent improvement of hardness, elastic modulus, fracture toughness and wear rate when Cr_2O_3 was added to the ceramic composite. All the evaluated properties show a gradual increase from 0 to 1.5 wt% of Cr_2O_3 additions before decreasing with 2.25 wt% addition. The ceramic composite shows a gradual increment in hardness (Fig. 3) from 20.79 GPa (0 wt% Cr_2O_3 , i.e., CR-1) to 24.38 GPa (1.5 wt% Cr_2O_3 , i.e., CR-3). Moreover, the elastic modulus (Fig. 3) for fabricated ceramic composite reveals a regular enhancement from 231.39 GPa (CR-1) to 244.53 GPa (CR-3) which was $\sim 6\%$ increment compared to the pure CR-1, having 0 wt% Cr_2O_3 . The fracture toughness (Fig. 4) behavior mostly follows the similar movement of both hardness and elastic modulus shown in Fig. 3. The ceramic composite added with 1.5 wt% Cr_2O_3 , i.e., CR-3 has the highest fracture toughness among fabricated ceramic composite ($5.21 \text{ MPa m}^{1/2}$), while for

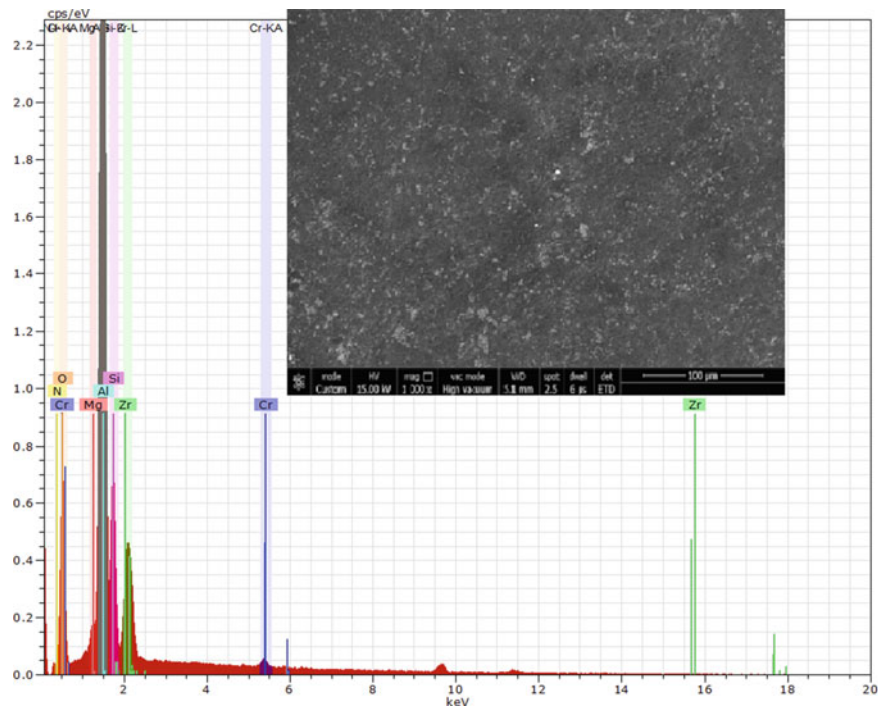


Fig. 2 EDS analysis of CR-3 composite (insert—SEM image of the CR-3 composite)

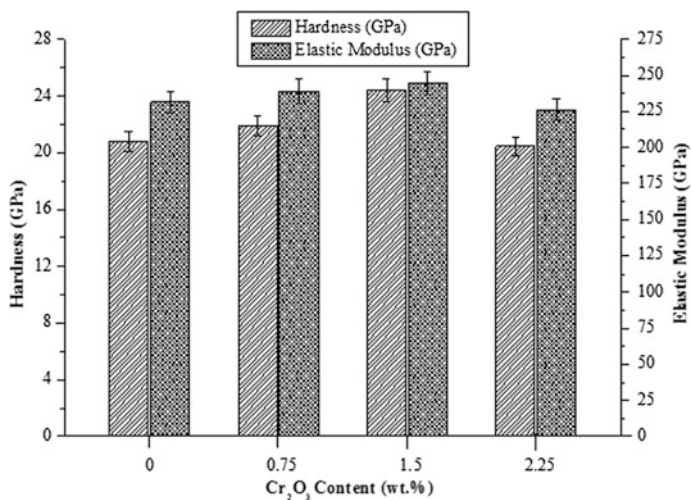


Fig. 3 Effect of Cr₂O₃ content on hardness and elastic modulus of ceramic composite

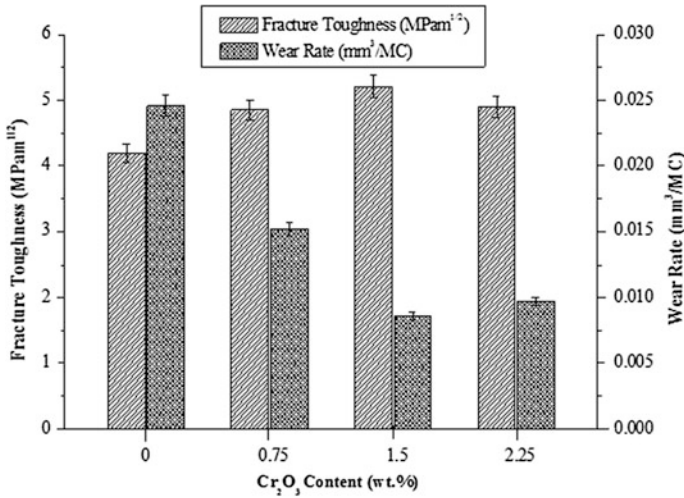


Fig. 4 Effect of Cr₂O₃ content on fracture toughness and wear rate of ceramic composite

the CR-1 having no Cr₂O₃ resulted in 4.19 MPa m^{1/2}. As regards the wear rate (Fig. 4), Cr₂O₃ has positive impact on the improvement of the wear rate of fabricated ceramic composites. The wear rate of ceramic composite also shows a steep decrease (65%) at the beginning from 0.0246 mm³/MC (0 wt% Cr₂O₃) to 0.0086 mm³/MC (1.5 wt% Cr₂O₃); after that, the wear rate of the samples is increased to about 13%; from 0.0086 to 0.0097 mm³/MC (2.25 wt% Cr₂O₃).

4 Conclusion

In this investigation, the evaluation of structural, mechanical and wear properties of aluminum and chromium oxide-filled ceramic composite was carried out. The evaluated mechanical (hardness, elastic modulus and fracture toughness) properties of the ceramic composites increased up to 1.5 wt% chromium oxide and 70.5 wt% aluminum oxide content and then decrease above 1.5 wt% chromium oxide and 70.5 wt% aluminum oxide contents. Conversely, the wear rate was found to decrease up to 1.5 wt% chromium oxide and 70.5 wt% aluminum oxide content and then increase above 1.5 wt% chromium oxide and 70.5 wt% aluminum oxide contents. Finally, it was concluded that the ceramics composite with 1.5 wt% chromium oxide and 70.5 wt% aluminum oxide addition produced composite with best hardness (24.38 GPa), elastic modulus (244.53 GPa), fracture toughness (5.21 MPa m^{1/2}) and lowest wear rate (0.0086 mm³/MC).

References

1. Trindade, M.C.D., Lind, M., Sun, D., Schurman, D.J., Goodman, S.B., Smith, R.L.: In vitro reaction to orthopaedic biomaterials by macrophages and lymphocytes isolated from patients undergoing revision surgery. *Biomaterials* **22**(3), 253–259 (2001)
2. Hu, D., Tie, K., Yang, X., Tan, Y., Alaidaros, M., Chen, L.: Comparison of ceramic-on-ceramic to metal-on-polyethylene bearing surfaces in total hip arthroplasty: a meta-analysis of randomized controlled trials. *J. Orthop. Surg. Res.* **10**, 22 (2015). <https://doi.org/10.1186/s13018-015-0163-2>
3. Mattei, L., Di Puccio, F., Piccigallo, B., Ciulli, E.: Lubrication and wear modelling of artificial hip joints: a review. *Tribol. Int.* **44**, 532–549 (2011)
4. Skinner J.A., Haddad F.S.: Ceramics in total hip arthroplasty: a bearing solution?. *Bone Joint J.* **99-B**(8), 993–995 (2017)
5. Yoshitoshi, H., Yukihar, H., Taisuke, S., Daigo, K., Naoki, I.: Significantly lower wear of ceramic-on-ceramic bearings than metal-on-highly cross-linked polyethylene bearings: A 10- to 14-year follow-up study. *J. Arthroplast.* **31**(6), 1246–1250 (2016)
6. Vendittoli, P.A., Amzica, T., Roy, A.G., Lusignan, D., Girard, J., Lavigne, M.: Metal ion release with large-diameter metal-on-metal hip arthroplasty. *J. Arthroplast.* **26**(2), 282–288 (2011)
7. Smeekes, C., Ongkiehong, B., Van der Wal, B., Wolterbeek, R., Henseler, J.F., Nelissen, R.: Large fixed-size metal-on-metal total hip arthroplasty: higher serum metal ion levels in patients with pain. *Int. Orthop.* **39**(4), 631–638 (2015)
8. Bizot, P., Nizard, R., Lerouge, S., Prudhommeaux, F., Sedel, L.: Ceramic/ceramic total hip arthroplasty. *J. Orthop. Sci.* **5**, 622–627 (2000)
9. Rahman, H.S.A., Choudhury, D., Osman, N.A.A., Shasmin, H.N., Abas, W.A.B.W.: In vivo and in vitro outcomes of alumina, zirconia and their composited ceramic-on-ceramic hip joints. *J. Ceram. Soc. Jpn.* **121**(4), 382–387 (2013)
10. Bahraminasab, M., Sahari, B.B., Edwards, K.L., Farahmand, F., Arumugam, M., Hong, T.S.: Aseptic loosening of femoral components—a review of current and future trends in materials used. *Mater. Des.* **42**, 459–470 (2012)
11. Silva, C.C.G.E., Higa, O.Z., Bressiani, J.C.: Cytotoxic evaluation of silicon nitride-based ceramics. *Mater. Sci. Eng., C* **24**, 643–646 (2004)
12. Bal, B.S., Khandkar, A., Lakshminarayanan, R., Clarke, I., Hoffman, A.A., Rahaman, M.N.: Fabrication and testing of silicon nitride bearings in total hip arthroplasty. *J. Arthroplast.* **24**(1) (2009)
13. Nevelos, J.E., Prudhommeaux, F., Doyle, M., Hamadouche, C., Ingham, E., Meunier, A., Nevelos, A.B., Sedel, L., Fisher, J.: Comparative analysis of two different types of alumina-alumina hip prosthesis retrieved for aseptic loosening. *J. Bone Joint Surg. (Br)* **83-B**, 598–603 (2011)
14. Jenabzadeh, A.R., Pearce, S.J., Walter, W.L.: Total hip replacement: ceramic-on-ceramic. *Semin. Arthroplast.* **23**(4), 232–240 (2012)
15. Anstis, G.R., Chantikul, P., Lawn, B.R., Marshall, D.B.: A critical evaluation of indentation techniques for measuring fracture toughness: I. Direct crack measurements. *J. Am. Ceram. Soc.* **64**(9), 533–538 (1981)
16. International Standards, ISO-6474-2-2012 (en): Implants for surgery Ceramic materials -Part 2: Composite materials based on a high-purity alumina matrix with zirconia reinforcement. 04 (2012)
17. International Standards, ISO-23317: Implants for Surgery-In Vitro Evaluation for Apatite-Forming Ability of Implant Materials, 1st edn (2007)

Experimental Investigation on Tensile and Fracture Behaviour of Glass Fibre-Reinforced Nanoclay/Mg–Al LDH-Based Fibre Metal Laminates



K. Logesh, V. K. Bupesh Raja, M. Venkatasudhahar and Hitesh Kumar Rana

Abstract Nano-sized particulate materials have been influencing their effect in the modern world. In this paper, morphological conduct is been decided by using the sandwich sheets of fibre-metal laminates (FMLs) containing nanoclay Cloisite 30B and Mg–Al layered double hydro-oxide (Mg–Al LDH). Atomic force microscope (AFM) is been utilized to discover the harshness of the nano-particles. Here, the tensile test for 3, 4 and 5 wt% of layered double hydroxide (LDH)/nanoclay added FML sheets was analysed. The EDAX is employed to discover the real structure of the chosen nano-powders along the identification of the chemical composition of the nanofiller. It results that the sandwich sheet with nanoclay had smooth surface for a similar molecule measure than the LDH. The fractured surface is analysed by scanning electron microscopy (SEM) hence indicates ductile nature of fracture for modified epoxy and reinforced with glass fibre metal. Henceforth, nanoclay and LDH-based FMLs can be decided on applications in automotive applications.

Keywords Tensile test · Fibre-metal laminates (FML) · Nanoclay (Closite-30B) LDH (Mg–Al) · Atomic force microscope (AFM) · Scanning electron microscopy (SEM)

K. Logesh (✉) · M. Venkatasudhahar (✉) · H. K. Rana (✉)
Department of Mechanical Engineering, Vel Tech Rangarajan Dr. Sagunthala
R&D Institute of Science and Technology, Chennai, Tamil Nadu, India
e-mail: klogesh7@gmail.com

M. Venkatasudhahar
e-mail: kmrflowers@gmail.com

H. K. Rana
e-mail: hiteshkumarr.rana@gmail.com

V. K. Bupesh Raja (✉)
Department of Automobile Engineering, Sathyabama Institute of Science
and Technology, Chennai, Tamil Nadu, India
e-mail: bupeshvk@gmail.com

1 Introduction

Layered double hydroxides (LDHs) otherwise said to be as anionic clays are a group of layered materials and have been in attention in modern days. Along with it comes the fibre/metal laminates (FML's) based on stacked arrangement of a fibre-reinforced epoxy resin and the aluminium alloy and LDH materials because of its smaller-sized particulates are usually classified under nanofillers. They are used to remove viruses and bacteria in water and the FMLs such as GLARE(glass fibre/aluminium), CALL (carbon-fibre/aluminium) and ARALL(aramide-fibre/aluminium) and have found their application in upper fuselage skin structure in Airbus A380 [1]. LDH is used as the heat stabilizing source and also acid-scavenging mediums in many halogenated polymers [2]. LDH has stable structure due to the presence of hydrogen bond [3].

In this study, the LDH/nanofillers based FMLs is observed using AFM technique and EDAX. Thermal endurance of the powder increases on adding of LDH powder in minute quantity over the metal, due to which its fire retardant property is enhanced [3]. Nanoclay is a cheap naturally found mineral and is applied in preparing nanocomposite due to its good thermal resistivity [4].

The synergetic effect of LDH and glass fibre reinforced epoxy composite materials aids in achieving high strength to weight ratio. Epoxy resin based on diglycidyl ether of biphenyl A (DGEBA), Tri Ethylene Tetra Amine (TETA), Dimethyl Form amide (DMF), and glass fibre were used [5, 6]. The X-ray diffraction (XRD) analysis, tensile strength and flammability analysis had done by using vertical and horizontal burning test [7]. Thus, the result of Epoxy/LDH/glass fibre shows that they are having highest tensile and flexural strength results [8].

The properties of Nano composites with the combination of Epoxy/nanoclay were realized. It was found that increased amounts of fibre-matrix splitting are exhibited by the lower levels of surface treatment. The scanning electron microscopy (SEM), spectroscopy, tensile testing, Fourier transform infrared (FTIR), differential scanning calorimetric (DSC), thermogravimetric analysis (TGA), and chemical resistance test help evaluate the thermomechanical, morphological and resistance to chemical characteristics of jute fibre PE/MMT nanocomposites [8–11]. Investigating of the fracture characteristics of a FML based on a tough glass fibre-reinforced poly-propylene composite is carried out. Following this, the impact properties and quasistatic of these lightweight systems will be investigated.

2 Experimental Procedures

2.1 Material Investigation

In this experiment, the FML nanocomposites employed were made from aluminium alloy AA5052-H32/glass fibre/AA5052-H32 along with epoxy resin added

nanoclay + MgAl layered double hydroxide as matrix. Layered double hydroxides (LDHs) are the new class of layered inorganic crystalline materials attracting interest in the preparation of clay-based nanocomposites. LDH materials as nanofillers have an availability of a wide range chemical compositions. It has a ability of being modified by different organic anionic surfactants [12]. (Gonzales, TX. USA). Nanoclays taken here are the high aspect ratio of layers of organomodified silicate minerals whose platelets can be as thin as 1 nm. These clays have natural occurrence and low cost because of which it can be used in commercial applications [13, 14]. The commercial-grade epoxy resin (type-AV138) and HV998 (hardner) was applied in fabrication. There are various chemical and physical properties of the hardener. The vapour pressure is lesser than 0.01 Pa at 21 °C, and specific gravity must be between 1.5 and 1.2 at 25 °C. The boiling point and the composition temperature must be greater than 200 °C [15]. The glass fibre with woven roving mat of areal of 610 gsm, tensile strength is 1950 MPa, thermal expansion is 4.9–5.1 °C⁻¹ and thermal conductivity is 1.2–1.35 W/m K, was used for the fabrication of specimen. Closite 30B, a commercial product is the nanoclay (NC) selected is supplied by Southern Clay Products the different mechanical properties of the materials E-Glass Fibre and the Aluminium Alloy AA5052-H32-0.5 mm. The properties of the aluminium alloy, tensile strength are 210–260 MPa, thermal expansion is 23.7 °C⁻¹, density is 2.68 kg/m³, and thermal conductivity is 138 W/m K.

2.2 *Manufacturing Method of FML Composites*

By combining composites with the monolithic Al alloys, total mass may be reduced. Meanwhile, material properties like fire tolerance and fatigue over standard monolithic Al alloys may be improved. The composite was fabricated by using hand lay-up method. The dual nanofillers like nanoclay/LDH, i.e. 3, 4, 5 wt%, were stirred separately and used for fabricating the composite structures, and Fig. 1 shows the cross section of the nano-based FML composites. The premixing/stirrer process was done by using ethanol. The aircraft may find a crucial failure, which might come back from a range of sources, like low-velocity (up to 10 m/s) objects of dropped tools throughout maintenance or high velocity (up to 100 m/s) objects as well as aiming bird or shell from tire failure. Also delamination between metal layers and composites, delamination between composite layers, similarly as debonding and fibre breakage [16]. Fibre-metal laminate (FML) is the material made from a compound matrix reinforced with fibres. The fibre consists of usually glass, carbon, basalt or aramid, in spite of availability of different fibres like paper or wood or amphibole. The compound is sometimes an epoxy, vinyl organic compound or polyester thermosetting plastic, marine, and construction industries. The reinforcement used here is glass [17].

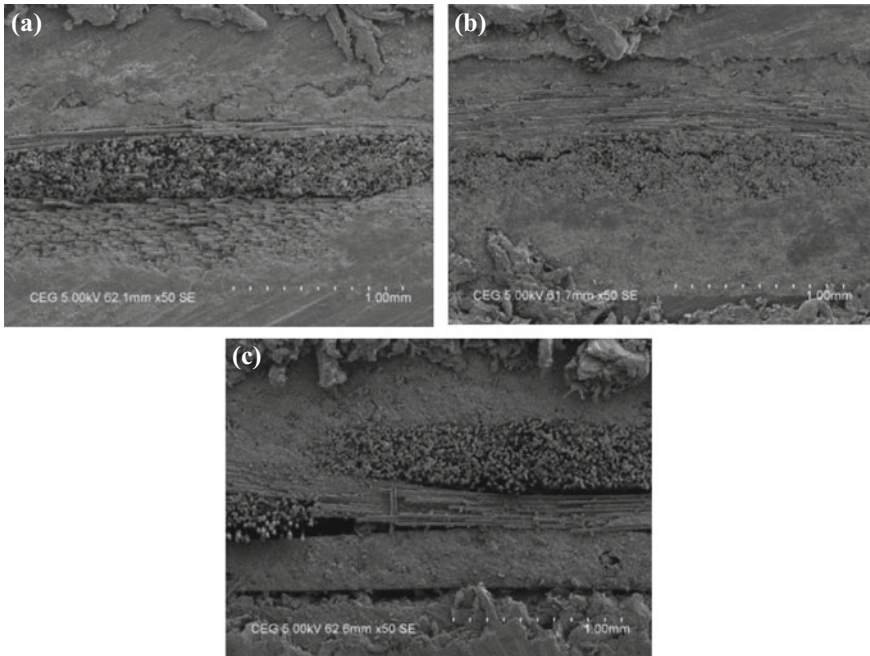


Fig. 1 Cross section of FMLs with different wt% of LDH and nanoclay. **a** FML + 3 wt% of LDH/nanoclay. **b** FML + 4 wt% of LDH/nanoclay. **c** FML + 5 wt% of LDH/nanoclay

2.3 Atomic Force Microscopy

AFM employs a high-resolution SPM. It is indulged with resolution shown in fractions of nanometres that are better than 1000 times the optical diffraction limit. A cantilever beam with sharp-tipped probe is employed by AFM to scan over the surface of the sample [11]. Image formation is one of the typical classifications of the operation modes of AFM also known as colour mapping. The colour mapping is seen as a concern represented by the symbol R. The material pelletized was measured using AFM. Maximum sizes of the pellets were found to be in the range of 11–21 nm.

Pelletization

Pelletization compacts the materials in powder type which is further given a definite shape with the help of the pelletizer instrument, die setup and nanopellet. The pellets can be used to take a look at metal specimen rather than powder. During this method, the compact powder is moulded into a form by mechanical dies and forced to make balls for ball millings [18].

2.4 EDAX Analysis

EDAX is an analysis process which helps in finding the constituents of the powders. EDAX is an X-ray qualitative analysis technique for elemental composition determination. It may be used during imaging in TEM, SE, etc. Once worn out using SEM instrument, a signal is acquired from a spot, an area, a line profile or a second map. Its energy dispersive X-ray system by that energy absorption sites area unit was found within the specimen [19]. The results are plotted in the graph [16]. The graph has peaks. This is due to the electrons that are present in l-shell returns to the k-shell orbit. This is because the excitation due to the X-ray is made to switch off [17].

2.5 Tensile Strength

Tensile strength is carried out using FIE Universal Testing Machine (UTM). The gauge length and cross-head speeds as 5 mm/min are chosen relating to the ASTM D638 standards. The testing process includes applying tension to the specimen until it fractures by placing it in the testing machine. The increase in the gauge length helps record the tensile force. The sample is exposed to a increase in load until fracture with the help of grippers.

3 Results and Discussion

3.1 Tensile Properties

The tensile test results are given in Table 1. The samples which have FMLs are much better, even after fracture. From the experimental results, it is seen that along zero degree rolling direction, the tensile strength which is presented in FML specimen of the Al/fibre is higher than the values seen in the sample 1. This is the

Table 1 Tensile properties of FML + LDH/nanoclay composites

Sample	Break load (kN)	Maximum displacement (mm)	Elongation %	Yield strength, σ_y (MPa)	Ultimate tensile strength, σ_u (MPa)
GLARE + 3 wt% of LDH + nanoclay	2922	7.43	12.38	127.33	163.54
GLARE + 4 wt% of LDH + nanoclay	2769	7.90	13.16	148	170
GLARE + 5 wt% of LDH + nanoclay	3952	6.76	11.27	133.66	180.31

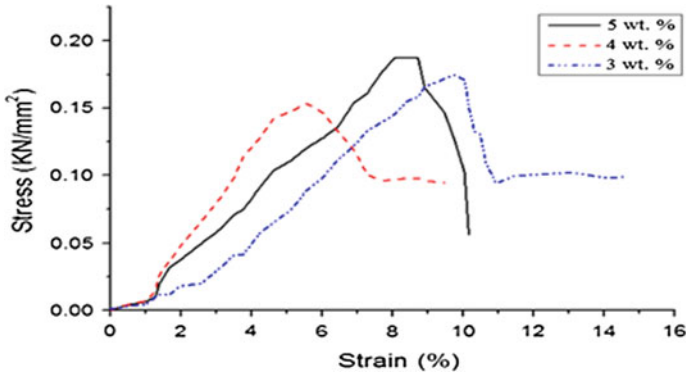


Fig. 2 Tensile stress–strain curves for FML nanocomposites

reason why the aluminium between the reinforcement of fibre-epoxy with 3 wt% of LDH + nanoclay mixed in the matrix-interface is stable in the reinforcement of fibre direction. The maximum tensile strength obtained in the FML samples as 116 MPa. This due to the compatibility with synthetic polymers and the variation in the fabrication process, which can result in the problems with process ability or the lack of dimensional stability [19–21]. Good yield strength is found for the 132 MPa in the nano-FML specimens. The thickness strain is calculated theoretically with the width and length measurements by isochoric assumption [1]. Figure 2 shows the tensile stress–strain curves for FML composites.

3.2 SEM Analysis

SEM images of the surfaces that are fractured are considered to analyse the mode of fracture and failure mechanisms. Testing of the fracture properties of FML based on e-glass fibre-reinforced epoxy matrix composite was done. Also, the fibre pull out which is observed in the 3 wt%, some of the matrix fracture identified in the 4 wt%. The exact delamination occurs, and matrix breakages happen on the 5 wt% as shown in Fig. 3. SEM was used to evaluate the produced composites. The SEM micrograph of FML + LDH/nanoclay composite is shown in Fig. 5. An improvement was observed in the effect of damage based on glass fibre, matrix cracking, pore and dimples due to ultimate tensile stress. The pores present can lead to crack formation that successively causes the debonding of the skin surface from the optical fibre. The fracture was recorded at 100× magnification and scale level is 500×10^6 m.

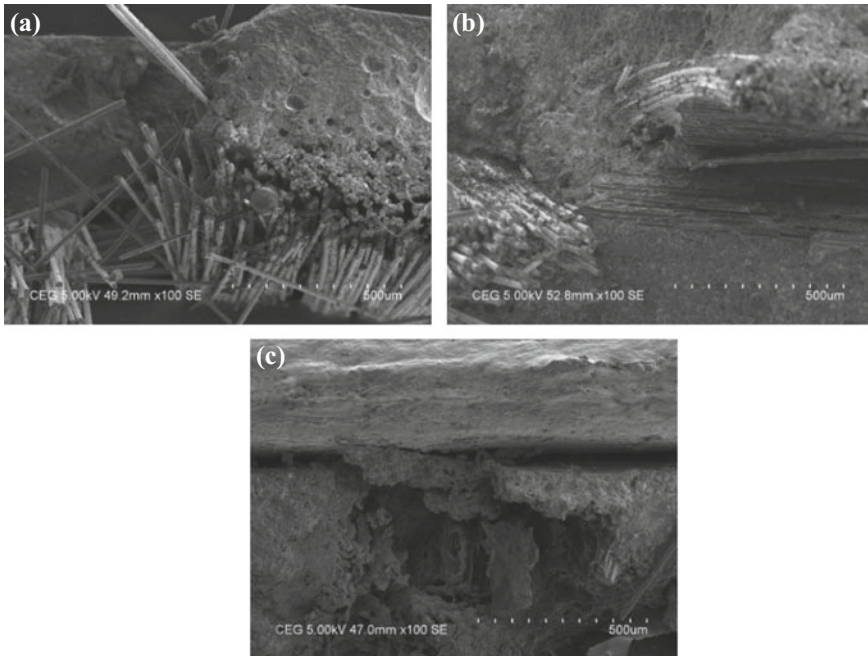


Fig. 3 **a** FML + 3 wt% of LDH/nanoclay, tensile fracture samples. **b** FML + 4 wt% of LDH/nanoclay, tensile fracture samples. **c** FML + 5 wt% of LDH/nanoclay, tensile fracture samples

3.3 AFM Observation

AFM Analysis of Mg–Al LDH and Nanoclay

The most direct way to assess the interphase at a free surface is atomic force microscopy (AFM), a powerful tool with unparalleled lateral resolution for characterizing not only morphology but also local surface mechanical properties. There are several dedicated modes available for distinguishing surface features based on mechanical response [22]. The images of the AFM topographic of LDH are shown in Fig. 4 at 20 \times magnification, and the corresponding parameters, Ra, are derived from the AFM scans. The most commonly used AFM modes are tapping mode (trademark of Bruker Corporation) that excites the cantilever at a single frequency. In addition to surface topography, this single-frequency method provides a phase image showing contrast corresponding to changes in material properties [23]. The AFM topographic images of the nanoclay are represented in Fig. 5, and the corresponding parameters, Ra, are derived from the AFM scans; the roughness analysis are shown in Table 2.

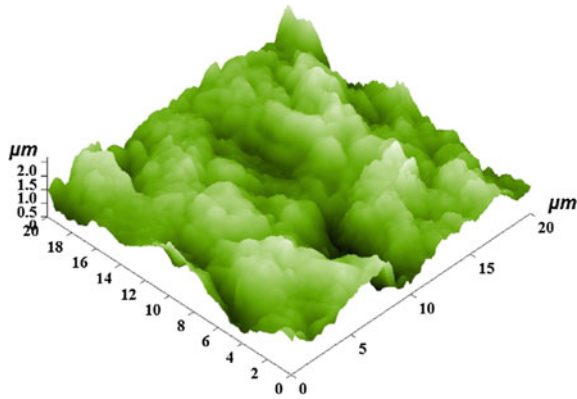


Fig. 4 3D image of MgAl LDH in AFM in 20×10^6 m

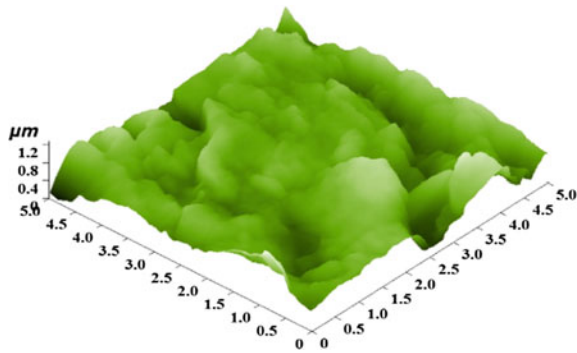


Fig. 5 3D image of nanoclay in AFM

Table 2 Roughness analysis of layered double hydroxide and nanoclay

S. No.	Details	MgAl LDH	Nanoclay
		Parameters	
1	Number of sampling	65,536 no	65,536 no
2	Max	1513.84 nm	556.136 nm
3	Min	0 nm	0 nm
4	Peak-to-peak, Sy	1513.84 nm	556.136 nm
5	Ten point height, Sz	761.419 nm	286.122 nm
6	Average	800.254 nm	307.039 nm
7	Average roughness, Sa	117.855 nm	56.5725 nm
8	Root mean square, Sq	160.574 nm	73.606 nm
9	Second moment	666,191	99,690.6
10	Surface skewness, Ssk	-0.0916793	0.0395785
11	Coefficient of kurtosis, Ska	2.21324	0.752605
12	Entropy	12.516	11.54
13	Redundance	-0.18489	-0.265808

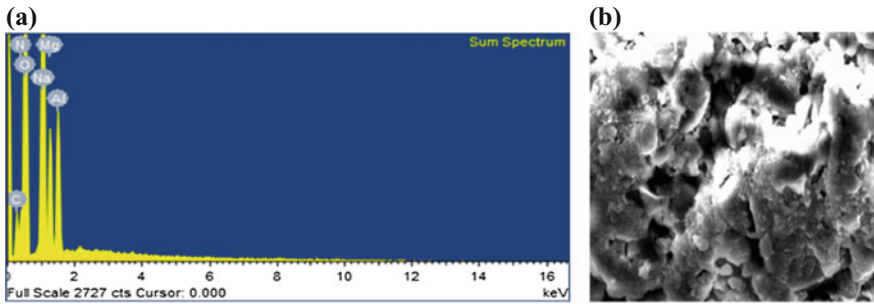


Fig. 6 a EDAX graph for LDH. b SEM image for LDH

Table 3 EDAX results for Mg–Al LDH and nanoclay

EDAX results for Mg–Al LDH			EDAX results for nanoclay		
Element	wt%	at. %	Element	wt%	at. %
CK	7.25	10.28	CK	26.09	38.42
NK	6.87	8.36	OK	32.86	36.32
OK	56.36	60.01	MgK	1.01	0.74
NaK	22.52	16.68	AlK	10.45	6.85
MgK	3.55	2.49	FeK	3.04	0.96
AlK	3.46	2.18	SiK	26.55	16.72
Total	100	100	Matrix	Correction	ZAF

3.4 EDAX Analysis of LDH and Nanoclay

EDAX is the associated analytical technique used for the fundamental chemical properties of a sample. Its properties are due in vast part to the basic principle of electromagnetic emission spectrum (that is the main principle of spectroscopy). The SEM image of layered double hydro-oxide powders is depicted in Fig. 7. The EDAX analysis of LDH and its composition is visible in order in Fig. 6 and Table 3. Surface of the specimen was found with some coarse grains.

Nanoclays are the present nanofiller and belong to a wider cluster of clay minerals. They are not new to mankind, and ceramists are victimizing them within the development of clay product since prehistoric times. For example, many clay products had been made ready using China clay, with the normal name kaoline, and its use is dated to the third-century BC in China. The EDAX of nanoclay and the following composition is shown in Fig. 7 and Table 3 along with that of LDH. Discovery of the composition of the specimen was done by the EDAX analysis.

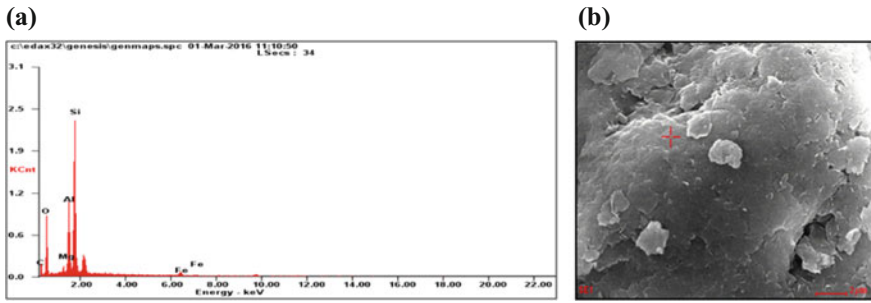


Fig. 7 a EDAX image for nanoclay. b SEM image for LDH

4 Conclusion

Hence from the paper, we can conclude as given below:

- Size of LDH was larger than nanoclay as shown by AFM of LDH and nanoclay.
- LDH powder was found coarser when compared to nano-clay.
- A peak of 0.82 μm particle size at a single point was found in LDH roughness of powders the resulted histogram.
- For nanoclay, the histogram showed that the coarseness of particles has a range over various sizes of particles.
- The line diagram of nano-particulates and LDH resulted that nanoclay was brought to fine-sized particles and hence can be used on different metal as fire resistance coating which needs a better surface finish.

References

1. Logesh, K., Bupesh Raja, V.K.: Evaluation of mechanical properties of Mg-Al layered double hydroxide as a filler in epoxy-based FML composites, pp.1–19. *Int. J. Adv. Manuf. Technol.* (2018). <https://doi.org/10.1007/s00170-018-1692-8>
2. Logesh, K., Bupesh Raja, V.K., Sasidhar, P.: An experiment about morphological structure of Mg-Al layered double hydroxide using field emission scanning electron microscopy with EDAX analysis. *Int. J. ChemTech Res.* **8**(3), 1104–1108 (2015). ISSN: 0974-4290
3. Becker, C.M., Gabbardo, A.D., Wypych, F., Amico, S.C.: Mechanical and flame-retardant properties of epoxy/Mg–Al LDH composites. *Compos. A* **42**, 196–202 (2011)
4. Klemkaite, K., Prosycevas, I., Taraskevicius, R., Khinsky, A., Kareiva, A.: Synthesis and characterization of layered double hydroxides with different cations (Mg Co, Ni, Al), decomposition and reformation of mixed metal oxides to layered structures. *Cent. Eur. J. Chem.* **9**(2), 275–282 (2011)
5. Gabr, M.H., Okumura, W., Ueda, H., Kuriyama, W., Uzawa, K., Kimpara, I.: Mechanical and thermal properties of carbon fiber/polypropylene composite filled with nano-clay. *Compos. B* **69**, 94–100 (2015)

6. da Costa, E.F.R., Skordos, A.A., Partridge, I.K., Rezai, A.: RTM processing and electrical performance of carbon nanotube modified epoxy/fibre composites. *Compos. A. Appl. Sci. Manuf.* **43**(4), 593–602 (Apr 2012)
7. Becker, C.M., Dick, T.A., Wypych, F., Schrekker, H.S., Amico, S.C.: Synergetic effect of LDH and glass fiber on the properties of two- and three-component epoxy composites. *Polym. Test.* **31**, 741–747 (2012)
8. Wang, K., Chen, L., Kotaki, M., He, C.: Preparation, microstructure and thermal mechanical properties of epoxy/crude clay nanocomposites. *Compos. A* **38**, 192–197 (2007)
9. Hossen, Md.F., Hamdan, S., Rahman, Md.R., Islam, Md.S., Liew, F.K., Lai, J.C., Rahman, Md.M.: Effect of clay content on the morphological, thermo-mechanical and chemical resistance properties of propionic anhydride treated jute fiber/polyethylene/nanoclay nanocomposites. *Measurement* **90**, 404–411 (2016)
10. Li, M., Gu, Y., Liu, Y., Li, Y., Zhang, Z.: Interfacial improvement of carbon fiber/epoxy composites using a simple process for depositing commercially functionalized carbon nanotubes on the fibers. *Carbon* **52**, 109–121 (2013)
11. Bogner, A., Jouneau, P.H., Thollet, G., Basset, D., Gauthier, C.: *A History of Scanning Electron Microscopy Developments: Towards “wet-STEM” Imaging*, vol. 38, p. 391. Elsevier Ltd (2007)
12. Ramesh, M., Palanikumar, K., Hemachandra Reddy, K.: Evaluation of mechanical and interfacial properties of sisal/jute/glass hybrid fiber reinforced polymer composites. *Trans. Indian Inst. Met.* <https://doi.org/10.1007/s12666-016-0844-5>
13. Costa, F.R., Wagenknecht, U., Heinrich, G.: LDPE/MgAl layered double hydroxide nanocomposite: thermal and flammability properties. *Polym. Degrad. Stab.* **92**, 1813–1823 (2007)
14. Wypych, F., Satyanarayana, K.G.: Functionalization of single layers and nanofibers: a new strategy to produce polymer nanocomposites with optimized properties. *J. Colloid Interface Sci.* **285**, 532–543 (2005)
15. Hu, P.-Y., Hsieh, Y.-H., Chen, J.-C., Chang, C.-Y.: Characteristics of manganese-coated sand using SEM and EDAX analysis. *J. Colloid Interface Sci.* **272**(2), 308–313 (2004)
16. Deva Kumar, M.L.S., Drakshayani, S., Vijaya Kumar Reddy, K.: Effect of fuel injection pressure on performance of single cylinder diesel engine at different intake manifold inclinations. *Int. J. Eng. Innov. Technol. (IJEIT)* **2**(4) (Oct 2012). ISSN: 2277-3754
17. Zhang, H., Gn, S.W., An, J., Xiang, Y., Yang, J.L.: Impact behaviour of GLAREs with MWCNT modified epoxy resins. *Exp. Mech.* **54**, 83–93 (2014)
18. Lokhande, C.D., Sankapal, B.R., Mane, R.S., Pathan, H.M., Muller, M., Giersig, M., Ganesan, V.: XRD, SEM, AFM, HRTEM, EDAX and RBS studies of chemically deposited Sb₂S₃ and Sb₂Se₃ thin films. *Appl. Surf. Sci.* **193**(1–4), 1–10 (2002)
19. Jezerska, L., Zajonc, O., Rozbroj, J., Vyletělek, J., Zegzulka, J.: Research on effect of spruce sawdust with added starch on flowability and pelletization of the material. *IERI Procedia* **8**, 154–163 (2014)
20. Logesh, K., Bupesh Raja, V.K.: Formability analysis for enhancing forming parameters in AA8011/PP/AA1100 sandwich materials. *Int. J. Adv. Manuf. Technol.* **93**(1-4), 113–120 (2017)
21. Ramesh, M., Nijanthan, S.: Mechanical property analysis of kenaf–glass fibre reinforced polymer composites using finite element analysis. *Bull. Mater. Sci.* **39**(1), 147–157 (2016)
22. Gonzalez-Canche, N.G., Flores-Johnson, E.A., Cortes, P., Carrillo, J.G.: Evaluation of surface treatments on 5052-H32 aluminum alloy for enhancing the interfacial adhesion of thermoplastic-based fiber metal laminates. *Int. J. Adhes. Adhes.* (2018). <https://doi.org/10.1016/j.ijadhadh.2018.01.003>
23. Majzoobi, G.H., Morshedi, H., Farhadi, K.: The effect of aluminum and titanium sequence on ballistic limit of bi-metal 2/1 FMLs. *Thin-Walled Struct.* **122**, 1–7 (2018)

Experimental Study on Micro-deburring of Micro-grooves by Micro-EDM



Elumalai Boominathan and S. Gowri

Abstract Deburring of micro-structures is found to be a tedious job. But it is to be done during machining of micro-channels. This article describes the experiments conducted to remove top burrs in micro-channels produced by micro-milling. The correlation between burr size and feed rate is studied. The burr formation in the down-milling side always tends to be higher than that on the up-milled side. This is correlated with the so-called size effects in tool-based micro-machining. The bottom surfaces of the micro-channels are studied for surface quality. Moderate feed rate ($1.25 \mu\text{m}/\text{tooth}$) produces better surface quality and less top burrs. Micro-EDM is employed to remove the top burrs. Different energy levels were employed in a capacitance-based micro-EDM. It is found that the lesser the energy level better the deburred surface. High energy levels tend to damage the quality of the micro-channels.

Keywords Micro-deburring • Micro-EDM • Micro-milling • Inconel 600

1 Introduction

Burrs are major shortcomings in micro-milling process to create micro-grooves or micro-channels. Removal of the burrs is very much essential for proper functioning of the micro-components or channels. Burrs in micro-channels adversely affect the flow in micro-channels [1]. But deburring is considered as non-value-added and tedious operation in machining especially in case of micro-domain. Various methods have been suggested for deburring the micro-features by researchers in micro-domain [2–4].

E. Boominathan (✉)
Easwari Engineering College, Chennai, India
e-mail: elumalainathan@gmail.com

S. Gowri
College of Engineering, AU, Chennai, India

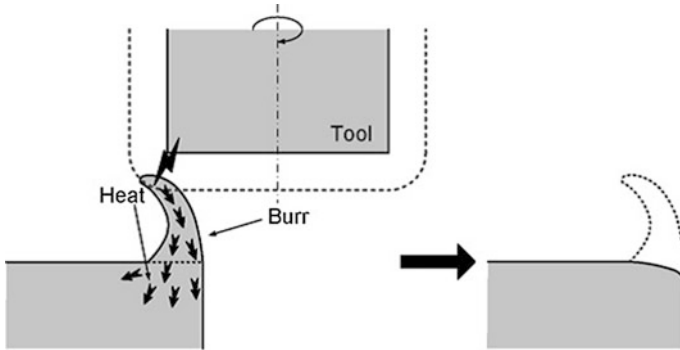


Fig. 1 Concept of EDM deburring [5]

In this study, the feasibility of micro-EDM to remove the top burrs produced by the micro-milling of Inconel 600 is analyzed. Tungsten carbide is used as electrode, and the operations were carried out in EDM oil as electrolyte, and three energy levels are considered. Figure 1 shows the concept of EDM-based deburring process.

2 Experimentation

Experiments were conducted in multipurpose micro-machine DT-110. The DT-110 is capable of performing all tool-based micro-machining activities such as micro-EDM, micro-ECM, micro-milling, micro-wire EDM. Micro-channels were machined in Inconel 600 using flat-faced end mill of 500 μm . The machining parameters such as depth of cut and spindle speed were fixed, and different feed values were used to obtain sample micro-channels for deburring activity.

Image-based measuring system was used to measure the micro-channel dimensions and the thickness of the top burrs. Interferometry-based Talysurf Taylor Hobson non-contact instrument was used to measure the bottom surface quality of the micro-channel. The scanning electron microscope image, in Fig. 2, explains the importance of burr removal in micro-channels machined by micro-milling. The machining parameters are listed in Table 1.

Micro-channels with a width of 400 μm and for a depth of 25 μm were produced in Inconel 600 using uncoated tungsten carbide flat end mill. The machining parameters were fixed based on previous set of optimization experiments conducted.

The machined micro-slots were deburred using micro-EDM. The deburring was done without disturbing the fixture setup so that proper positioning of micro-EDM

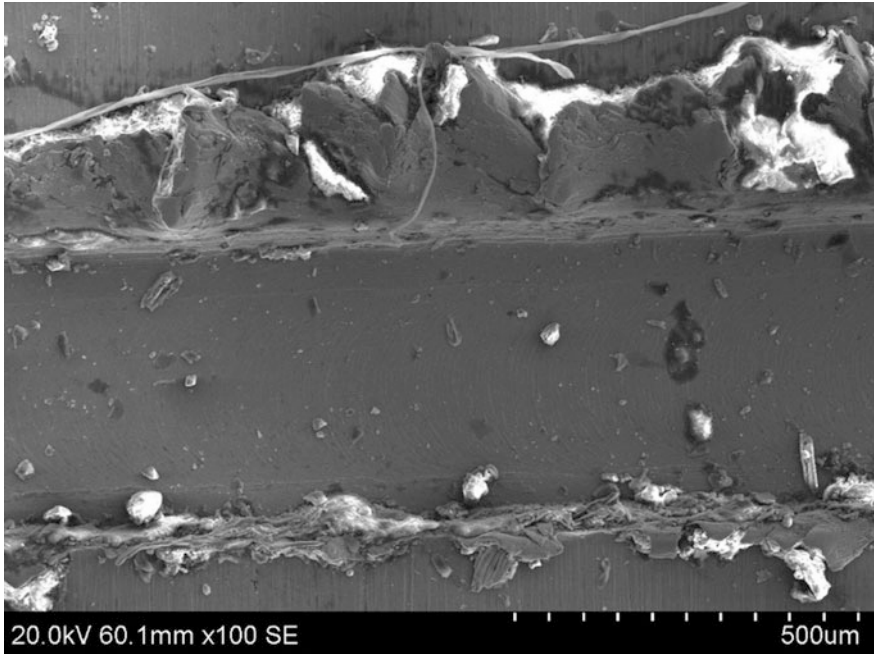


Fig. 2 Burrs in top of micro-channel produced in micro-milling

Table 1 Discharge energies

Capacitance (μF)	Voltage (V)		
	80	100	120
Discharge energy μJ			
0.01	32	40.5	72
0.1	320	405	720
0.4	1280	1620	2880

electrode can be done automatically. For micro-EDM-based deburring, tungsten carbide was used as electrode and EDM oil as dielectric medium. Deburring was done using the top surface of the workpiece as reference surface. Different energy levels, Table 1, were used for deburring, and the electrode was rotating at 500 rpm so that the debris flushed away from the micro-channel. The deburred and fresh slots were analyzed by taking the images in SEM and VMS.

Table 2 Feed rate versus R_a and burr width

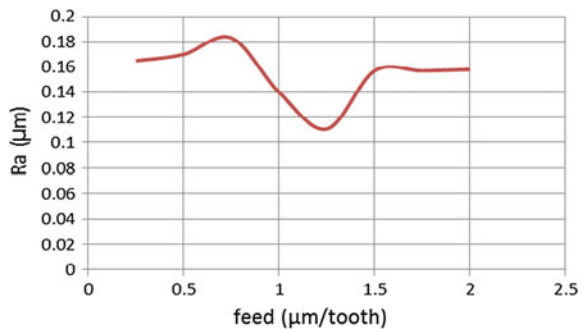
Feed rate ($\mu\text{m}/\text{tooth}$)	Surface roughness R_a (μm)	Burr width (μm)	
		Up-milling side	Down-milling side
0.25	0.165	98	253
0.50	0.170	100	269
0.75	0.183	94	221
1.00	0.140	90	198
1.25	0.111	89	176
1.50	0.157	124	206
1.75	0.157	112	192
2.00	0.158	137	212

3 Results and Discussions

The burr width result, Fig. 2 and Table 2, shows that the burr on the down-milling side is always bigger than the up-milling side. This can be explained by the size effect. In the up-milling side, the uncut chip thickness is minimum at the beginning of the cut and it reaches to the maximum when the edge reaches the middle.

Graph in Fig. 3 illustrates the relationship between feed per tooth and surface roughness. The roughness value decreases to 1.2 $\mu\text{m}/\text{tooth}$ and then increases. For the used machining conditions, the value can be considered as minimum uncut chip thickness.

The micro-deburred micro-slots were studied using SEM images and VMS images, and they were found to be effective in removing burrs in the upper side of the micro-channel. The images in Fig. 4 show the effectiveness of the micro-EDM in burr removal of micro-features.

Fig. 3 Feed versus surface finish

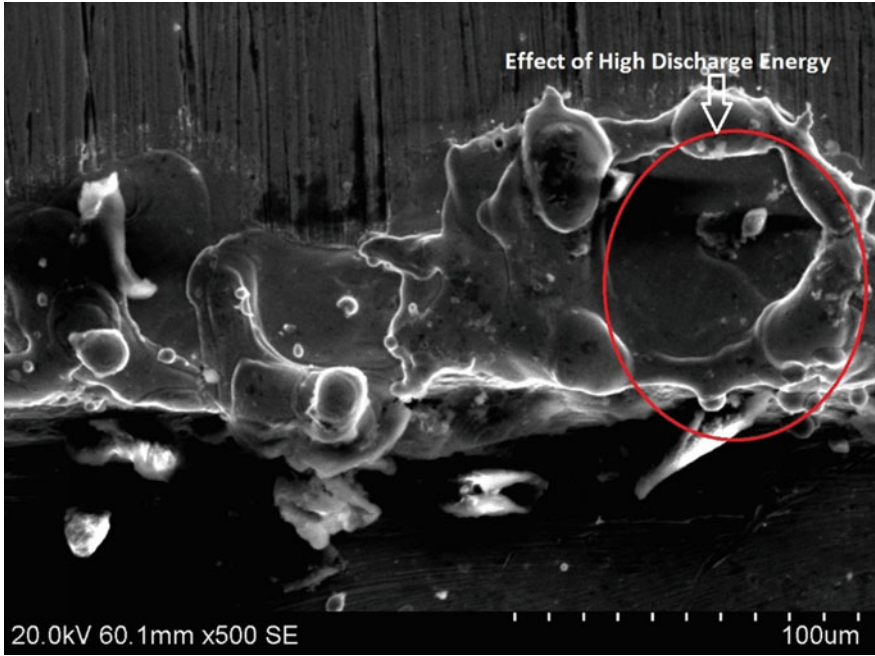


Fig. 4 Effect of high energy

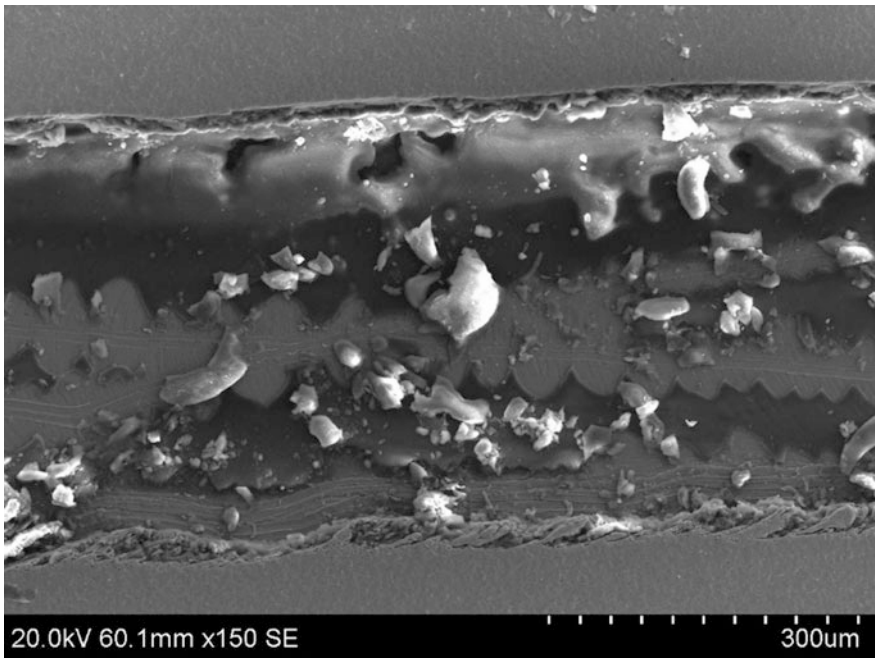


Fig. 5 Overcut during micro-EDM deburring

From the SEM image analysis of the micro-deburred slots, Fig. 4, it is found that the high energy EDM burned the edges of the micro-channel, which is not preferred.

In few cases, the overcut (in addition to deburring, the material under the burr also machined due to non-optimal machining conditions) due to excess EDM machining action is also observed, as shown in Fig. 5, and it is suggested that the proper selection of reference surface and the EDM parameters are necessary to obtain better burr removal.

4 Conclusion

- In slotting operation, the up-milled side experienced small burrs as compared to down-milled side. The information gained can be utilized in tool path planning for micro-machined components. Final passes can be done in up-milling mode.
- The micro-EDM can be successfully used as deburring tool for micro-features machined by micro-milling.
- The energy level of EDM operation decides the effectiveness of deburring action. Mid range of energy level (720 μJ) is suggested for micro-deburring by EDM.

References

1. Ali, M., et al.: Prediction of burr formation in fabricating MEMS components by micro end milling. *Adv. Mater. Res.* **74**, 247–250 (2009)
2. Kienzler, A., et al.: Burr minimization and removal by micro milling strategies or micropeening processes. In: *Proceedings of the CIRP International Conference on Burrs*, pp. 237–243 (2009)
3. Jang, K.-I., et al.: Deburring microparts using a magnetorheological fluid. *Int. J. Mach. Tools Manuf.* **53**, 170–175 (2012)
4. Mathai, G.K., Melkote, S.N.: Deburring of microgrooves by abrasive brushing. In: *Proceedings of the International Conference on Micromanufacturing*, Madison, WI, p. 1979 (1–7) 2010
5. Jeong, Y.H., HanYoo, B., Lee, H.U., Min, B.-K.: Deburring microfeatures using micro-EDM. *J. Mater. Process. Technol.* **14**, 5399–5406 (2009)

Influences of Tool Pin Profiles on Mechanical Properties of Friction Stir Welding Process of AA8011 Aluminum Alloy



K. Giridharan, V. Jaiganesh and S. Padmanabhan

Abstract Friction stir welding (FSW) is a grand new solid-state bonding process is an emerging surface engineering technology based on the principles of friction stir welding (FSW). Friction stir welding is well-matched joining process for non-ferrous metals in the spacious range of various manufacturing applications for joining materials without material losses to get a top priority of defectless welded joints. In this article, a thickness of 5-mm AA8011 series aluminum alloy plate was coupled by butt joint using two dissimilar tool pin shapes of the straight cylindrical probe and taper pin probe with a consistent parameter of tool revolving speed, welding speed, and downward force of 1400 rpm, 35 mm/min, and 6 kN. The tool pin shapes are the important parameter of material joining process to fix the joint properties, characteristics, quality of weld, and joint strength. The friction stir welding effects are determined after completing the joining process under a various ASTM standard testing methods, such as stiffness distribution in the entire welded zone area and material properties as compared to the base metal with testing results. The crucial tool travel feed is achieved with excellence material joints and extraordinary welded joint properties when collating to a straight cylindrical tool probe. It is identified that the taper pin profile tool offers extensive result was obtained both hardness and tensile strength for to enhance productivity, has been discussed along with the future aspects included in the area of FSW process from this experimental investigation.

Keywords Friction stir welding · AA8011 aluminum · Tool pin profiles
Constant process parameters · Heat treatment

K. Giridharan (✉) · S. Padmanabhan
Department of Mechanical Engineering, Easwari Engineering College,
Chennai 600089, India
e-mail: girimech4305@gmail.com

V. Jaiganesh
Department of Mechanical Engineering, SA Engineering College,
Chennai 600077, India

© Springer Nature Singapore Pte Ltd. 2019
U. Chandrasekhar et al. (eds.), *Innovative Design, Analysis and Development
Practices in Aerospace and Automotive Engineering (I-DAD 2018)*, Lecture Notes
in Mechanical Engineering, https://doi.org/10.1007/978-981-13-2718-6_6

1 Introduction

The friction stir welding process is an utmost attractive joining technique of similar or dissimilar materials, which uses heat generated from a non-consumable tool which in a rotation and the tool pin probe stimulating effect. It was started and filed by the welding institute (TWI) in 1991 [1]. The FSW process to fabricate various essential parts and obviously is most significant among them in the effective joining process [2]. In the modern world, the needs for the use of lightweight alloys have developed in various different fields, and particularly in the area of automobiles where the minimization of components weight is the best way in challenging factor for reducing the fuel desolation and the emissions of CO₂ [3]. Basically, the FSW tool is having two main parts, such as tool shoulder and plunging tool pin, and its involves in joining of invariable parts using stir welding process. Therefore, identification of appropriate joint fabrication method involves a necessary function in the specimens in this area of different users [4]. Since less amount of metal melting process of the specimen while welding process, such as the general problems of fusion welding such as the solidification and cracking, porosity, and the material losses are avoided in FSW. These benefits attribute to spread over in a broad variety of commercial success of different applications on soft materials welding. However, welding tool involves heavy stress and huge temperature particularly for joining of massive strength steel materials, stainless steel, and other tough materials. These alloys are used now very less amount through the consideration of huge prize and low life in FSW tools [4]. Because it makes the FSW tool to utilize and to create heat between workpiece and tool shoulder surfaces to produce plastic deformity of welding by changing the potential energy into heat energy at an interact with workpieces without using electrical energy during a tool rotational due to downward force [5] (Fig. 1).

During material joining process, it does not produce the welding defects like oxidation, internal cracks, and toxic gases [6]. FSW process is used to weld massive potency materials for automotive industries, aerospace, and shipbuilding applications. FSW technique produces four various types of region during the weld upon base metal [1–4]. The FSW tool and pin profile give the important responsibility in



Fig. 1 Schematic diagram of FSW machine used in this study

the investigation. In hardened forged steel mostly used marine applications for hull and structures, but the weight and cost of the workpieces are very massive comparing to aluminum alloy commercial grade. The other grade aluminum materials are 5xxx, 6xxx, and 8xxx series that relocates the forged steel [5, 6]. The commercial grade 8xxx aluminum alloy is the suitable materials for this application that has a lightweight material, and a small amount rust properties of aluminum alloy are compared to other marine materials. Compare to marine steel commercial grade alloys has nice decomposition fighting and does not need anodizing, coating when used in ship structuring purpose. So only this type of materials is selected in this present investigation. In previously, a many of the research investigators have completed toward understanding the various efforts of tool shapes, dimensions of tool and FSW parameters on the behavior of material flow, formation and standard material properties, structures in the fabricated joints.

2 Methodology and Experimental Procedure

Since many of the experimental studies in the area of FSW process of the commercial grade, same type of aluminum alloys or metals has been identified by produced but joints between the flat plates by using the straight-line method in using various different tool pin probe geometry by a variety of researchers. It is identified that joints between similar alloys or metals are few more only performed using in the method of friction stir welding. Therefore, the current research has been conducted for friction stir welding of AA8011 aluminum alloy by making of straight but joints by done in stir welding parameters.

3 Experimental Procedure

In the current work, AA8011 aluminum alloy is used to fabricate welded joints. The supposed chemical composition of the plates is given in Table 1. Two aluminum plates of $100 \times 50 \times 5$ mm (length, width, and thickness, respectively) were prepared hydraulic power cutting machine. Before kept the specimens on the machine table, the workpiece edges are properly shaped and prepared with the help

Table 1 Nominal chemical composition (wt%) of the parent metal AA8011 used in the friction stir welding

Elements	Si	Fe	Cu	Mn	Mg	Cr	Zn	Ti
Specified values	0.10–0.80	0.5–1.0	0.10 max	0.10 max	0.10	0.10	0.10 max	0.05
wt%	0.517	0.897	0.059	0.055	0.029	0.011	0.019	0.017

of basic workshop tools. Aluminum plates are located with help of rigid manual top clamp to avoid uneven condition while welding process from the welding route. The welding tool was inserted between two plates against the weld path. The joining process was done by invariable load by controlling the infiltration distance to downward of the tool probe into the combined line. The diameter ratio (D/d) of the FSW tool was maintained and regulates to make required pressure but also avoid the imposition of material while welding process.

3.1 FSW Tool Configuration and Geometry

There are various two FSW tool pin probes used in the similar material joining process to be considered in friction stir welding. These two tools have significant and have to be preferred with care to make sure an unbeaten joint and efficient to do on complete welding process. The connection between the welding speeds and the temperature while welding is difficult but, in common, it can be said that increase the tool rotational motion or reduce the welding speed will consequence in a hotter weld. Two various tool pin shapes are used—one is straight cylindrical pin, and another one is taper pin. Out of different tool like tool steel, high-speed steel, M35 High speed steel, high carbon high chromium steel, carbide, stainless steel, and carbon boron nitride. In this present investigation, M35 grade steel is select as tool material because of its high material hardness, easy to accessibility, easy availability, and minimum cost of tool material. The FSW tool having profiled pin along 7 mm to 4 mm pin diameter, 12 mm shoulder diameter, with the 5 mm length of pin illustrate Fig. 2. FSW tools are manufactured by center lathe by turning operation cutting tool with the help of single point. The tools are oil toughened to gain a rigidity of 60–64 HRC.

3.2 Specimen Preparation

The FSW tools are manufactured as per international standards and maintained material properties like as tensile characteristics, elongation of the material, and effectiveness of the joint strength computed by UTM with the help of centralized computer system. For every welded plate prepared three test specimens and tested in Figs. 3 and 4.

In the hardness test (Brinell), a diamond ball is impressed into the top face of the specimen using a particular force. After tested a ball is removed and measure the intention of ball find using a standard measuring instrument. The applied load and ball diameter are invariable and are chosen to suit the composition of the specimen, hardness, and thickness.

In addition, the hardness of the ball should be at least 1.7 times the test sample to prevent enduring set in a ball.

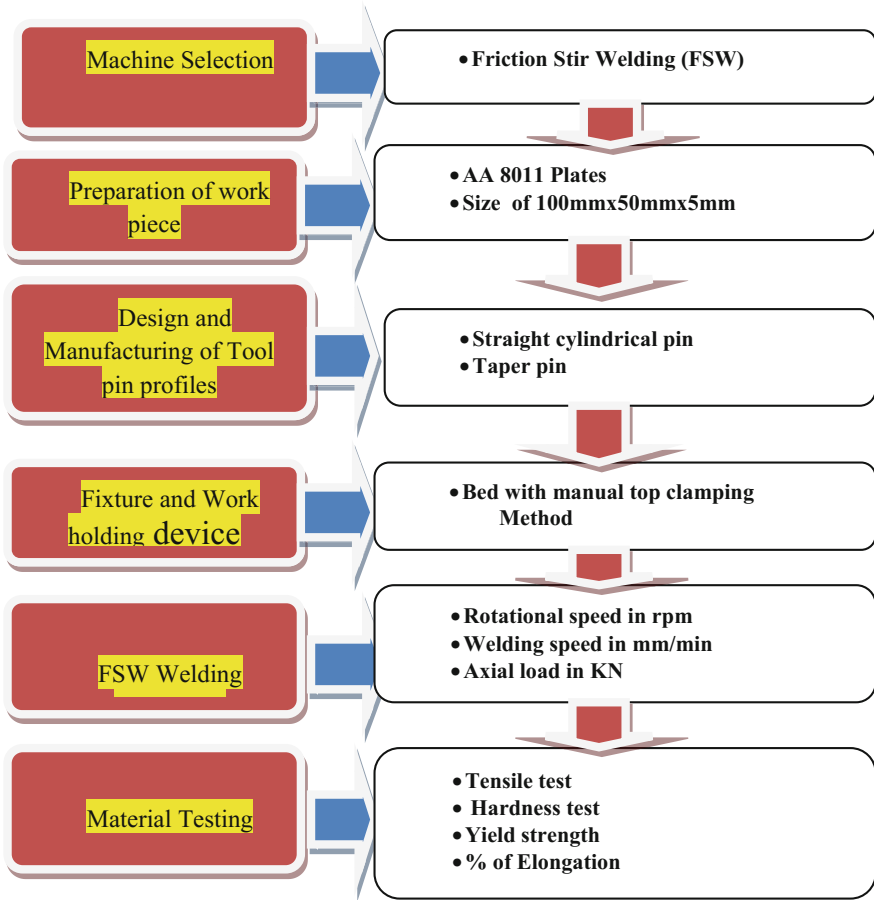


Fig. 2 Methodology of experimental process

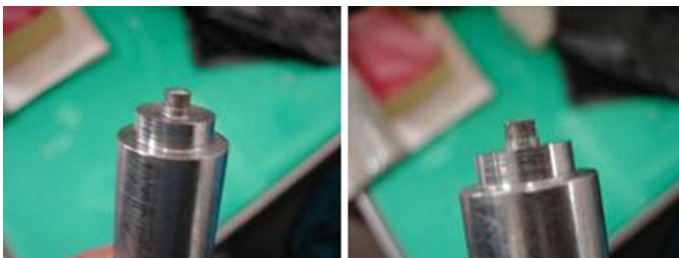


Fig. 3 FSW tools used present work



Fig. 4 Location of weld direction in tensile test specimen

4 Result and Discussion

The initial step to examine the obtained welded specimens is a visual inspection of crowns and roots because the welded surface of the material is exceptionally essential to provide information about the weld quality. The various two FSW tools produced a complete circle nearby the hole. The two various tool pins used in the present research work were taper pin probe and straight cylindrical probe. The taper probe produced massive mixing of friction stir weld and ultimate tensile test reached up to the highest level in the constant parameter. In the weld region area, zinc and iron particles were distributed evenly and also produces largely increase strength. The straight cylindrical tool pin probe produces minimum heat input and spoils the tensile properties. Figure 5 shows that the tapered probe is the huge result of high tensile strength. In this, a constraint reflected that better joint efficiency and shows welded specimens that most excellent performance in the cycle rule. This can considerably reduce the extent of metallurgical conversion taking place while welding process. The taper pin probe (Fig. 6) shows that increased the hardness value. In the FSW process, tool probes contribute to the fabrication of the welded joints. The straight pin probe affects the material properties compared to the taper pin probe, and its substantial softening takes place entire weld region due to the removal of grain hardening effect due to energetic recrystallization (Fig. 7).

Fig. 5 Brinell hardness specimen

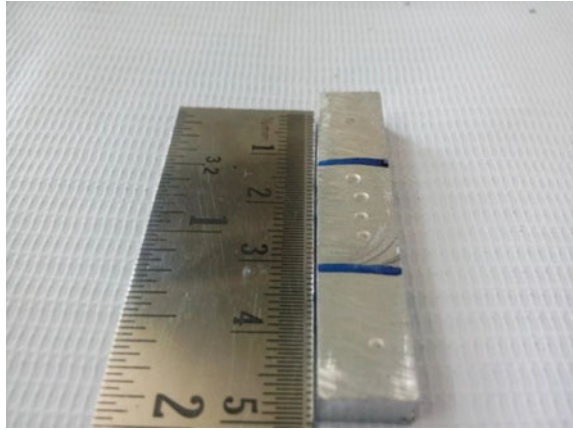


Fig. 6 Tensile strength on axial weld condition

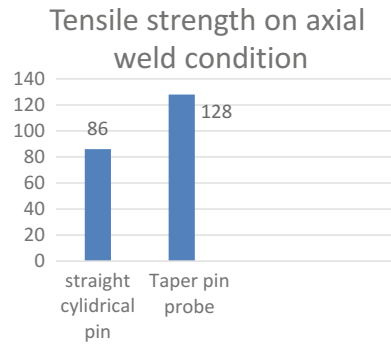
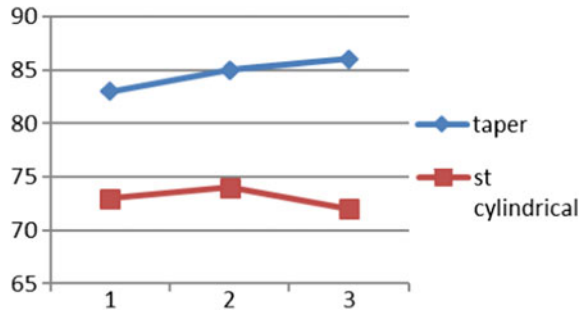


Fig. 7 Hardness versus tool profile



5 Conclusion

After discussed elaborately its helps us to understand that the tool shapes acting in necessary responsibility to find the properties of the weldments during FSW process. Frictions stir welding of AA8011 joints was effectively done for the various

shapes tool probes. The four different FSW constraints involved while the combination of the materials, such as tool rotational speed, welding speed, potential force to be constant, and the weld quality was studied. The different pin profiles are used in FSW such as straight cylindrical probe and taper pin shapes, and the taper tool probe produces sufficient tensile strength and rigidity value when compared to a straight cylindrical tool. In this context investigated in depth and it has identified that increasing the tool faces, it's also increasing the properties of the tested samples. The taper pin probe gives excellent mechanical properties and also achieves superior mixing of material without any defects.

References

1. Cooper, D.R., Allwood, J.M.: The influence of deformation conditions in solid state aluminum welding process on the resulting weld strength. *J. Mater. Process. Technol.* **214**, 2576–2592 (2014)
2. Salih, O.S., Ou, H., Sun, W., McCartney, D.G.: A review of friction stir welding of aluminum matrix composites. *Mater. Des.* **86**, 61–71 (2015)
3. Metha, K.P., Badheka, V.J.: Effects of tool pin design on formation of effects in dissimilar friction stir welding. *Innov. Autom. Mech. Eng. Procedia Technol.* **23**, 513–518 (2016)
4. Reza-E-Rabby, M., Reynolds, A.P.: Effect of tool pin thread forms on friction stir weldability of different aluminum alloys. *Procedia Eng. ICME* **90**, 637–642 (2014)
5. Chen, Y.C., Liu, H., Feng, J.: Friction stir welding characteristics of different heat-treated-state 2219 aluminum alloy plates. *Mater. Sci. Eng.* **420**, 21–25 (2006)
6. Tarannum, H., Satish Kumar, P.: Friction stir welding of aluminum 5086 alloy. *Int. J. Res. Eng. Technol.* (2015)

Numerical Investigation of the Behaviour of Thin-Walled Metal Tubes Under Axial Impact



L. Prince Jeya Lal and S. Ramesh

Abstract Dynamic axial impact of metallic thin-walled tubes of square and circular hollow sections is performed and the impact responses of the lightweight thin tubes along with progressive deformations are simulated. Peak force, crushing modes and force dissipation ability of tubes are determined using a non-linear finite element tool Abaqus CAE. The effectiveness of Abaqus CAE as a tool to model thin tubes and to moderate experimental crash testing is presented. Study shows that concentrically arranged multiple tubes have higher energy absorption properties. Results reveal that for double tubes and steel–aluminium configuration highest energy absorption is recorded. Similarly, for three tubes and aluminium–steel–aluminium configuration highest energy absorption is recorded. Also simulations disclose that the inner tube influences the overall crush behaviour.

Keywords Thin-walled tubes · Dynamic axial impact · Energy absorption

1 Introduction

Automobile sector has a drastic growth in developing countries in the past decade. Likewise, the number of fatal accidents has also been increased rapidly. Hence, safety of occupants is of great concern for an automobile engineer while designing a vehicle without compromising the vehicle efficiency [1]. This demands the use of lightweight high-strength structures to dissipate the high impact forces generated during a collision without sacrificing fuel economy [2]. Research on energy absorbing elements under axial loading started in late 1960s and [3] derived a theory of collapse mechanism ‘concertina’ of thin circular shells. Johnson et al. [4] derived energy mitigating properties and folding mechanisms of box column. There, after many researchers contributed theories to minimize peak load and to increase energy absorption for various hollow sections considering the effects of

L. Prince Jeya Lal (✉) · S. Ramesh
Department of Mechanical Engineering, KCG College of Technology, Chennai 600 097, India
e-mail: prince.mech@kcgcollege.com

© Springer Nature Singapore Pte Ltd. 2019
U. Chandrasekhar et al. (eds.), *Innovative Design, Analysis and Development Practices in Aerospace and Automotive Engineering (I-DAD 2018)*, Lecture Notes in Mechanical Engineering, https://doi.org/10.1007/978-981-13-2718-6_7

friction and inertia load [5–10]. Instead of empty hollow sections, it was filled with wood and foam, and then the experiments were carried out by [11, 12]. Materials like mild steel, aluminium and magnesium alloys were used to manufacture energy absorbing elements in the form of hollow sections and their impact responses were determined [13, 14]. However, the studies were experimental but [15] simulated the axial crushing of tubular structure using FE code Abaqus explicit 5.8–8. Multiple quasi-static experiments were carried out and the same were simulated. Satisfactory agreement was obtained between experiments and simulations. Likewise, [16] used explicit FEM code DYNA3D to simulate the collapse mode and crash strength of cylindrical shaped hat sections. Numerical simulations were effective, accurate and economical with respect to time and cost and this paved way for the development of new material models [17]. New concepts like those that composite tubes and composite frusta were proposed by [12]. Khalid [18] analyzed the effect of introducing triggering mechanisms experimentally and numerically. The technique of using multiple tubes of same material having various diameters arranged concentrically but separated from each other at equal distance gave superior results compared to single tube and altered the deformation mechanisms under axial loading [19]. Literature reveals that behaviour of different metallic tubes under dynamic axial loading is yet to be studied in detail. The objective of this simulation is to predict the peak load, crushing behaviour and force mitigating ability of thin wall lightweight bimetallic tubes for various configurations.

2 Materials and Methods

2.1 Configuration I

Figure 1 and Table 1.

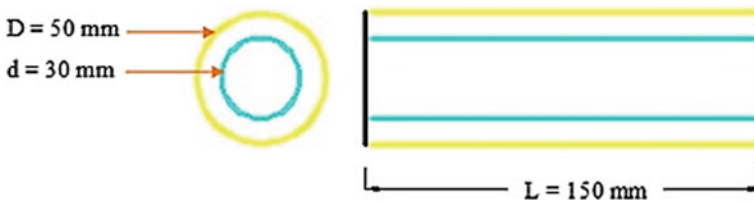


Fig. 1 Tube configuration I

Table 1 Impact sequence for concentric circular tubes separated by 10 mm

Simulation number	Impactor mass and velocity	Tube sequence
Tube 1	60 kg and 10 m/s	Steel–aluminium
Tube 2		Aluminium–magnesium
Tube 3		Steel–magnesium

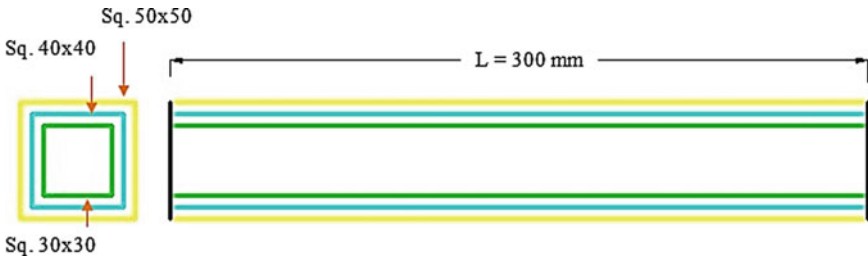


Fig. 2 Tube configuration II

Table 2 Impact sequence for square tubes separated by 10 mm

Simulation number	Impactor mass and velocity	Tube sequence
Tube 4	500 kg and 20 m/s	Magnesium–steel–magnesium
Tube 5		Aluminium–steel–aluminium
Tube 6		Aluminium–magnesium–aluminium
Tube 7		Magnesium–aluminium–magnesium

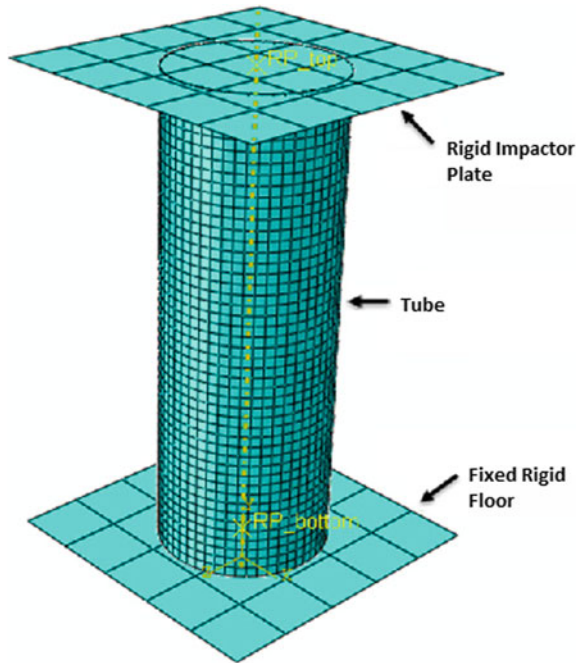
2.2 Configuration II

Figure 2 and Table 2.

3 FEA Model

Element type, mesh size and material model influence the accuracy of simulations to great extent. The tubes are modelled as double and multiple tubes using section manager. Thickness of each tube and number of intermediate integration points are specified in property module. Tubes are assigned with hourglass control and reduced integration 4 node thin shell S4R element. The overall accuracy of the simulations can be improved by doing a mesh sensitivity analysis. A fine mesh is applied to the model and effort is taken to maintain aspect ratio close to one. The tube is crushed between two rigid plates. Lower plate is modelled as a discrete rigid part and all the degrees of freedom are constrained. In order to avoid slipping of the tube during impact, tie constraint is used to hold the tube in its place along with the lower plate. Upper plate termed as impactor is also modelled as a discrete rigid part with mass and is constrained in such a way that it moves only in vertical downward direction. During impact, upper plate comes in contact with the tube and this interaction is defined by mechanical contact. A field output request is created to

Fig. 3 FEA model



compute reaction forces and spatial displacements and from this total energy absorbed is determined. Only two levels of headings should be numbered. Lower-level headings remain unnumbered; they are formatted as run-in headings (Fig. 3).

4 Results and Discussion

4.1 Configuration I Simulations

Figures 4, 5, 6 and 7.

4.2 Configuration II Simulations

Figures 8, 9, 10, 11, 12 and Tables 3, 4.

The results of configuration I are compared with [19]. It is clearly visible from the deformation images of tubes 1 and 3 that the outer steel tube deforms in concertina mode with deformation starting from top region and moving downward with the folds getting pressed into each other, thus resulting in rise in resistance to

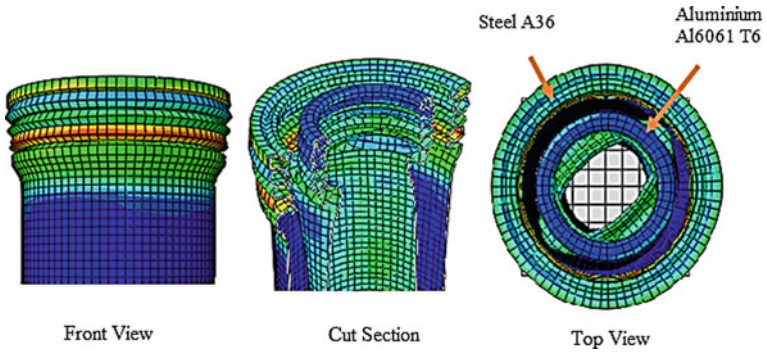


Fig. 4 Simulated image of deformation for tube 1

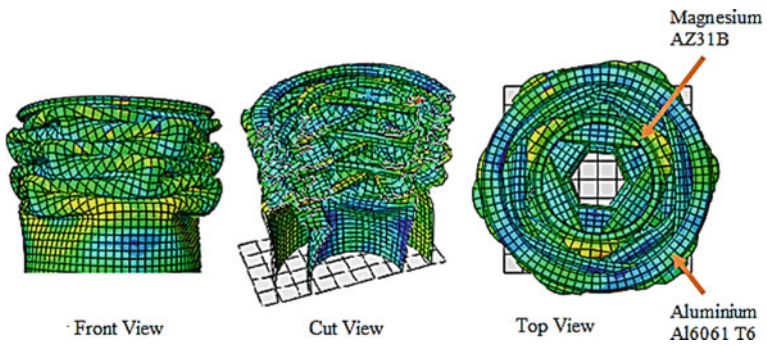


Fig. 5 Simulated image of deformation for tube 2

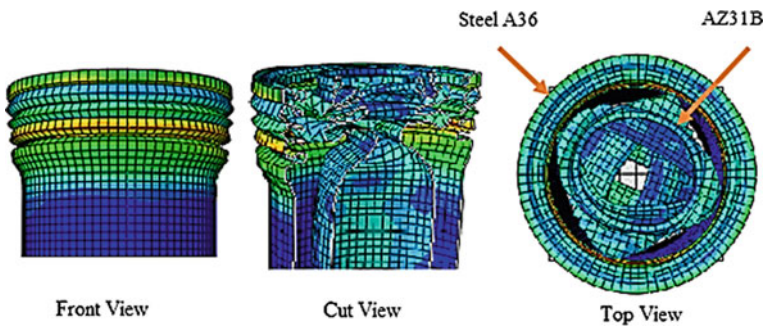


Fig. 6 Simulated image of deformation for tube 3

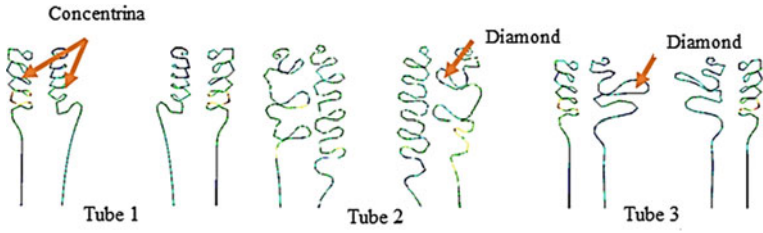


Fig. 7 Collapse modes for configuration I

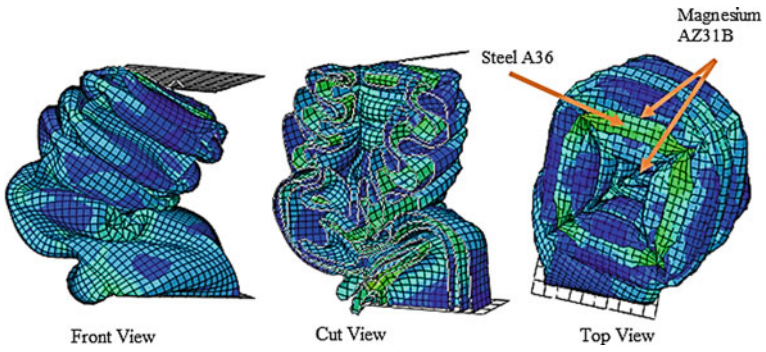


Fig. 8 Simulated image of deformation for tube 4

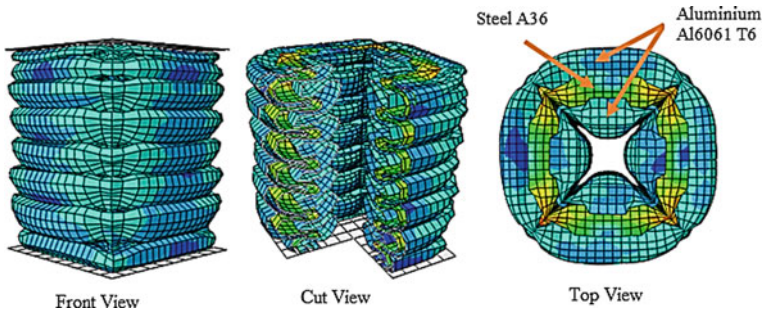


Fig. 9 Simulated image of deformation for tube 5

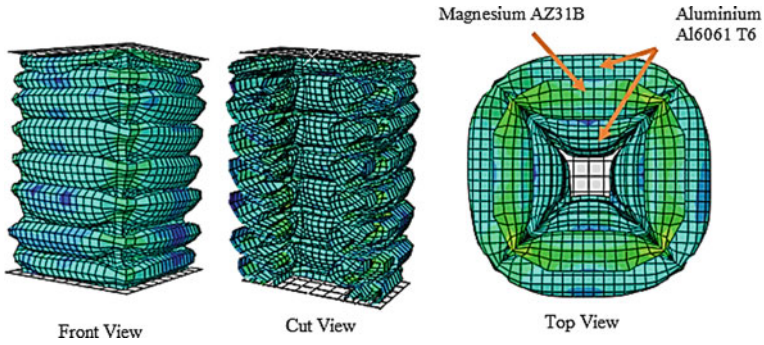


Fig. 10 Simulated image of deformation for tube 6

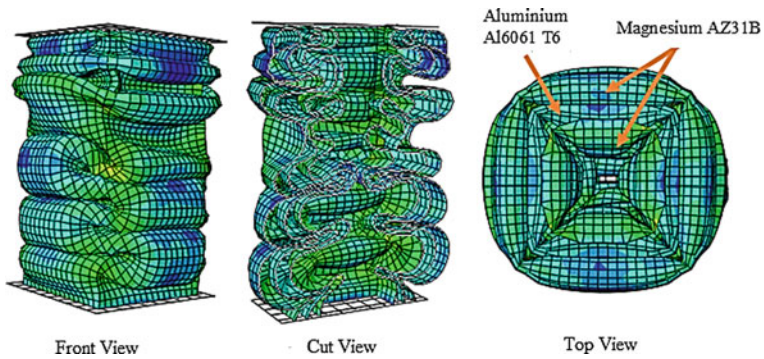


Fig. 11 Simulated image of deformation for tube 7

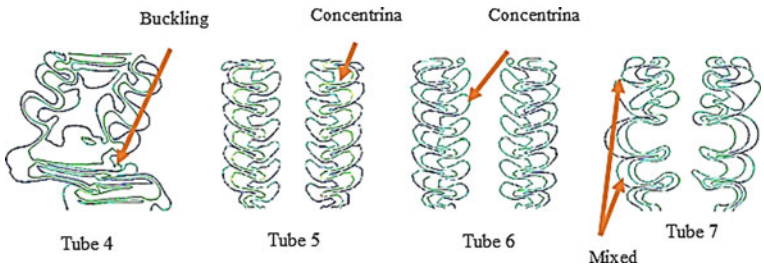


Fig. 12 Collapse modes for configuration II

deformation. It is to be noted that aluminium collapsed with concentrina mode when it was inner tube but its collapse mode changed to diamond mode when it was placed as outer tube. It is to be noted that the first fold propagates outwards, which results in increase in diameter. 1 mm thick Al 6061 T6 and AZ31B tubes crushed

Table 3 Energy absorption and peak load for configuration I

Tube	Material		Peak load (kN)	Energy absorbed (kJ) (deformation for $L_d = 60$ mm)
	Outer tube	Inner tube	Numerical	Numerical
1	A36	Al6061	60.83	2.08
2	Al6061	AZ31B	43.10	1.66
3	A36	AZ31B	56.0	2.04

Table 4 Energy absorption and peak load for configuration II

Tube	Crushing mode	Peak load (kN)	Energy absorbed (kJ) (Deformation up to 60 mm)	
			Numerical	Literature
4	Euler buckling mode	315.11	10.14	1.073 [21]
5	Concentrina	411.65	10.62	
6	Concentrina	239.085	8.5	
7	Mixed	249.23	9.37	

under diamond mode but energy absorption per unit mass compared with the other materials were poor [20].

The results of configuration II are compared with [21]. In numerical simulations, steel tubes collapsed with symmetric or concentrina mode and in experimental also the mode was same. Likewise, aluminium tubes collapsed with diamond mode in numerical analysis and literature also reveals the same. Tube no. 4 for the configuration of aluminium–steel–aluminium has higher energy absorption, peak load than all the other tubes, and undergo concentrina collapse mode. Tube no. 6 for the configuration of aluminium–magnesium–aluminium has the lowest peak load and energy absorption. Likewise, in tube no. 7, the energy absorption is lesser than tubes 4, 5.

5 Conclusion

Crash response of double and multiple thin-walled bare tubes of circular and square profiles with no trigger mechanisms are simulated. Seven simulations have been carried out in order to moderate the experimental tests. Collapse modes, peak force and energy absorption properties are studied. The collapse modes were predicted using numerical simulations and compared with literature. It is to be noted that steel and aluminium tubes collapsed with concentrina or symmetric mode. It is found that the peak load and energy absorption are lesser in the tubes having magnesium tubes in the inner side. In this investigation, metallic tubes of circular and square

profile are arranged concentrically and it is presented that the energy absorption properties of tubes can be modified. Numerical simulations predict that for double tubes and steel–aluminium configuration highest energy absorption is recorded. Similarly, for three tubes and aluminium–steel–aluminium configuration highest energy absorption is recorded. Collapse mechanisms illustrate that magnesium tubes as combined with steel or aluminium tubes bring down the peak load. Also from this numerical investigation, it can be concluded that the inner tube influences the overall crush behaviour.

References

1. Guoxing, L., Tongxi, Y.: *Energy Absorption of Structures and Materials*, pp. 1–23. Woodhead Publishing Limited (2003)
2. Alghamdi, A.: Collapsible impact energy absorbers: an overview. *Thin Wall. Struct.* **239**, 189–213 (2001)
3. Alexander, J.M.: An approximate analysis of the collapse of thin cylindrical shells under axial load. *Q. J. Mech. Appl. Math.* **13**, 10–15 (1969)
4. Johnson, W., Soden, P.D., Al-Hassani, S.T.S.: In extensional collapse of thin-walled tubes under axial compression. *J. Strain Anal.* **12**, 317–330 (1977)
5. Al Hassani, S.T.S., Johnson, W., Lowe, W.T.: Characteristics of inversion tubes under axial loading. *J. Mech. Eng. Sci.* **14**, 370–381 (1972)
6. Wierzbicki, T.: *Crushing analysis of metal honeycombs*. MIT Report 83-1 (1983)
7. Abramowicz, W., Jones, N.: Dynamic axial crushing of square tubes. *Int. J. Impact Eng.* **2**(2), 179–208 (1984)
8. Abramowicz, W., Jones, N.: Dynamic progressive buckling of circular and square tubes. *Int. J. Impact Eng.* **4**(4), 243–270 (1986)
9. Mamalis, A.G., Manolacos, D.E., Viegelah, G.L., Vaxevanidis, N.M., Johnson, W.: On the in-extensional axial collapse of thin PVC conical shells. *Int. J. Mech. Sci.* **28**, 323–335 (1986)
10. Karagiozova, D., Jones, N.: Inertia effects in axi-symmetrically deformed cylindrical shells under axial impact. *Int. J. Impact Eng.* **24**, 1083–1115 (2000)
11. Abramowicz, W., Wierzbicki, T.: Axial crushing of foam-filled columns. *Int. J. Mech. Sci.* **30**, 263–271 (1988)
12. Gupta, N.K., Velmurugan, R.: Axial compression of empty and foam filled composite conical shells. *J. Compos. Mater.* **33**, 567–591 (1999)
13. Tarlochan, F.: Design of thin wall structures for energy absorption applications: enhancement of crashworthiness due to axial and oblique impact forces. *Thin Wall. Struct.* **71**, 7–17 (2013)
14. Steglich, D., Tian, X., Bohlen, J., Riekehr, S., Kashaev, N., Kainer, K.U., Huber, N.: Experimental and numerical crushing analyses of thin-walled magnesium profiles. *Int. J. Crashworthiness* **20**, 177–190 (2015)
15. Aljawi, A.A.N.: Finite element and experimental analysis of axially compressed plastic tubes. *Belgium Soc. Mech. Environ. Eng.* **45**, 3–10 (2000)
16. Yamashita, M., Gotoh, M., Sawairi, Y.: A numerical simulation of axial crushing of tubular strengthening structures with various hat-shaped cross-sections of various materials. *Key Eng. Mater.* **193**, 233–236 (2003)
17. Feng, F.: A constitutive and fracture model for AZ31B magnesium alloy in the tensile state. *Mater. Sci. Eng., A* **594**, 334–343 (2014)

18. Khalid, K.S.: Examine bi-metallic rectangular thin walled tube under different trigger mechanisms. *Adv. Mater. Sci.* **1**, 4–8 (2016)
19. Goel, M.D.: Deformation energy absorption and crushing behavior of single, double and multi-wall foam filled square and circular tubes. *Thin Wall. Struct.* **90**, 1–11 (2015)
20. Beggs, P.D.: Failure modes during uniaxial deformation of magnesium alloy AZ31B tubes. *Int. J. Mech. Sci.* **52**, 1634–1645 (2010)
21. Goel, M.D.: Numerical investigation of the axial impact loading behavior of single, double and stiffened circular tubes. *Int. J. Crashworthiness* 1–10 (2015)

Improving Process Performance with World-Class Manufacturing Technique: A Case in Tea Packaging Industry



Vishal Naranje, Anand Naranje and Sachin Salunkhe

Abstract There is no doubt that the world-class manufacturing offers a vast variety of economic development opportunities and plays a vital role in rapid economic changes, productivity improvement, and international competitiveness enhancement for developing countries. In this paper, a WCM methodology has been applied to tea packing process to minimize the defects occurred in the current process. It consists of various quality control tools such as Pareto analysis, 5W + 1H analysis, brainstorming, why-why analysis. After implementation of this methodology, a better control over the process has been obtained. Detailed analysis of root cause results into the permanent solution to the problem which reduces defects and improves profit of the company.

Keywords World-class manufacturing · Quality control tools · Productivity improvement

V. Naranje (✉)
Department of Mechanical Engineering, Amity University
Dubai Campus, Dubai, UAE
e-mail: varanje@amityuniversity.ae

A. Naranje
Adarsha Science, J.B. Arts and Birla Commerce Mahavidyalaya,
Dhamangaon, Rly. Amravati, India
e-mail: proanand@rediffmail.com

S. Salunkhe
Department of Mechanical Engineering, Vel Tech-Technical University,
Chennai, Tamil Nadu, India
e-mail: kashid32@gmail.com

1 Introduction

Manufacturing has evolved considerably since the advent of industrial revolution. In current global and competitive age, it is very important for organization to have manufacturing practice which is lean, efficient, cost-effective, and flexible. To be competitive in the market, the process industries must have various kind of flexibility in terms of production, volume, and schedule so that it will fulfill maximum number of customer requirements. In the year 1986, Japanese professional Schonberger introduced the term “World Class Manufacturing” which consist of many techniques and technologies designed to enable a company to match its best competitors. World-class manufacturing sets standard for production and manufacturing for another organization to follow, which helps to increased competitiveness, development of new and improved technology and innovation, increased flexibility, increased communication between management and production employees, and an increase in work quality and workforce, etc. Many industries such as automobile, electronics and steel, cement industries successfully implemented the WCM practice to perform at a best-on-class in all levels. A considerable research work has been carried out in process improvement through applying WCM standards. A brief review of some selected references on this topic is presented here. These main impetuses have lead people and associations to welcome the significance of world-class manufacturing WCM [1]. Since the worldwide contenders working in worldwide markets quite often tend to have world-class execution [2], nonstop change has turned into a need for the survival of organizations in a much-focused condition on the planet. Nearby rivalry bit by bit loses its legitimacy, on the grounds that even the most distant organizations are compelled to contend. For every one of the reasons, it is insufficient to create at required quality for organizations; they ought to likewise have a sorted-out structure suitable to the generation framework created [3]. Many organizations are going to the acknowledgment that their survival relies on upon the ability to deal with the creation as a chief key capacity [4]. In this unique situation, WCM is a guide for organizations. Truth be told, just like the case with numerous other new ideas in administration, there is no predictable meaning of WCM. The expression “world class” was began by Hayes and Wheelwright [5] to portray the abilities which had been created by some Japanese and German organizations, and in addition the US firms, which had contended similarly with the Japanese and German firms. The expression “world class assembling” was utilized in light of the fact that these organizations have accomplished a remarkable execution in their worldwide rivalry, bringing about their being portrayed as “World Class” [6]. World-class fabricating (WCM) was characterized at first by Hayes and Wheelwright [5] and Schonberger [7] as a focused methodology utilizing the accepted procedures in quality, lean creation, and simultaneous designing [8]. Schonberger [7], building up the idea of WCM, concentrated on persistent change, including the advancement of provider connections, item out-line and JIT. Gunn [9] gives a solid accentuation on the part of innovation in world-class producing, while Hall [10] stresses that world-class assembling is an in a general sense distinctive method for working an association, as opposed to an

arrangement of systems see quality and the client as the essential concentration of world-class producing, upheld by a blend of assembling system and capacities, administration approaches, authoritative elements, human resources, innovation and execution estimation [11]. Hanson and Voss [12] see world-class producing regarding practice and execution. They characterize world class as having best practice in complete quality, simultaneous designing, lean generation, producing frameworks, coordination's and association and practice. Moreover, it is having operational execution measuring up to or outperforming best worldwide organizations [13]. In spite of the fact that the words might be revised and show up in an unexpected way, the message is essentially the same—WCM is worried with the opposition between the best producers on the planet [14]. As a typical theory concentrating on generation right off the bat, WCM incorporates more auxiliary changes, for example, new creation advancements, and both just-in-time—JIT and total quality management—TQM. WCM, changing states of mind and convictions, gives a mix between reacting quickly to client requests and a high level of client center [15]. WCM figures out which set of exercises should be embraced by distinguishing what is required by the organizations keeping in mind the end goal to contend all inclusive. Additionally, WCM itself includes many elements efficiently identified with advancement, for example, crude materials, vitality, apparatus, work and administration. Besides, world-class organizations streamline the critical thinking capacities of their representatives in applying both current strategies and conventional building process [16]. Being the best on the planet at assembling, an out-of-date item does not make an association world class. Progressively turbulent undertaking situations, portrayed by truncated item life cycles and divided buyer markets, require world-class producers to be sufficiently adaptable to fulfill changing business sector requests [17]. WCM organizations are those organizations which persistently beat the business' worldwide accepted procedures, and personally know their clients and providers and in addition knowing their rivals' exhibitions and knowing their own particular qualities and shortcomings. The greater part of the qualities above frames the premise of—consistently changing—aggressive procedures and execution destinations [18]. Receiving compelling administration rehearses, equipped for keeping pace with the changing mechanical condition, is especially essential to achievement in worldwide markets. WCM requires consistent change since world principles always show signs of change [17]. Organizations occupied with WCM rehearses concentrate on enhancing operations, end of waste, overseeing client connections, making lean associations and executing green practices, among others [19]. World-class undertakings incorporate both aggregate quality and attributes of learning associations [20]. Such upgrades cannot be accomplished with customary techniques. They require on a very basic-level re-examining and drastically upgrading business procedures and practices. This is the substance of world-class execution [21]. Thus, banding together with an association with world-class capacities can offer access to innovation, devices, and systems that the association may not as of now have; more organized philosophies, strategies, and documentation; and an upper hand through extended aptitudes [22]. Successfully overseeing and measuring the item improvement process is generally observed as a method for guaranteeing business survival through

diminished time to advertise, expanded quality, and decreased expenses. There is generally next to no data accessible to directors to guide them on acquainting execution measures with help with item improvement [23]. An issue which is basic to endeavors to characterize the idea of world-class manufacturing is the manner by which to decipher the measures inside the working setting of the firm [24]. Writing on the execution measures of world-class assembling is extremely constrained. The main purpose behind this could be the way that no single best practice structure exists for the usage of world-class fabricating standards, as every system will require the formation of various execution measures. The main basic components that could be recognized from the writing are cost, quality, and unwavering quality/throughput. The principle point of world-class assembling is the quest for most extreme proficiency for the creation framework to amplify the association's benefit [25].

The aim of this work is to present establishments of the basic model of world-class manufacturing (WCM) quality management for the improving process performance in tea packing industry in order to make products of the highest quality eliminating losses in all the factory fields an improvement of work standards. The topics covered in the paper are detailed analysis of the upper transport wheel to improve the quality of product (quality control), elimination of non-value-added activities (NVAA), etc. The work covers various departments such as focused improvement, professional maintenance, and quality control. The activities observed in the production area are classified as NVAA, SVAA or VAA. Analysis and elimination of MURI, MURA and MUDA focuses over the operation of work and have the objective to describe all movements that can generate negative impact over the quality, the cost, the safety, and health of people.

2 Statement of the Problem and Methodology

The aim of the project is to reduce the losses that occurred when the upper transportation wheel is not picked up by the bag removal and it continues its journey; this results in overlapping of tea bag with another tea bag; this error is known as bag overrun. This is occurred because of tea bag top not formed correctly, bag not stapled correctly, or threads are not cut properly.

2.1 Research Objectives

Regarding the above problem, the objectives of this study are as follows:

- Determine the significant factors that are responsible for tea bag overrun. This may lead to reduce process cycle time and operation cost. In addition to the throughput or productivity of the system can be increased.

- Develop new design of upper transportation wheel and find the appropriate setting for input data that give the highest productivity within the assumption and limitation of the company.

2.2 Methodology

A methodology is formulated to accomplish the objectives. This will form the guideline, and it will result into the minimization of defects occurring with current tea packaging process. The methodology is as follows.

The first step is to map the current tea packaging process using suitable tool. In the proposed work, blender software and high-speed videos are used to model and record the complete process. The various stages of the of tea making processes such as withering, crushing, drying, milling, blending, measuring, tea bag assembly has been modeled and animated to get the clearer understanding of a process. This process mapping helps to identify bottlenecks, repetition, and delays in tea packing process; also it helps to visualize and gain complete understanding of the process. The next step is to carry out defect analysis to identify major defects those are contributing in major rejection percentage. For this, Pareto chart and 5W + 1H analysis has been used. This analysis will help to find out 20% of defects that will generate 80% of loss. Based on the Pareto principle of 80/20 rule, in tea bag packing process, it is found that minor stoppage is the rank first defects causes the loss as 13.00% of total loss, then contamination source in rank second cause causing loss of 10.00% of total loss, then non-value added activity (NVAA) ranked as third and responsible for loss of another 10% of total loss. The other factors such as maintenance time, no production orders, bank holidays, energy breakdown, quality defect, indirect planned stoppage time are also responsible for losses. These are the “vital few” factors that cause 81% of total loss to revenue in the tea packing process. Figure 1 shows the Pareto chart for losses versus defects responsible for losses.

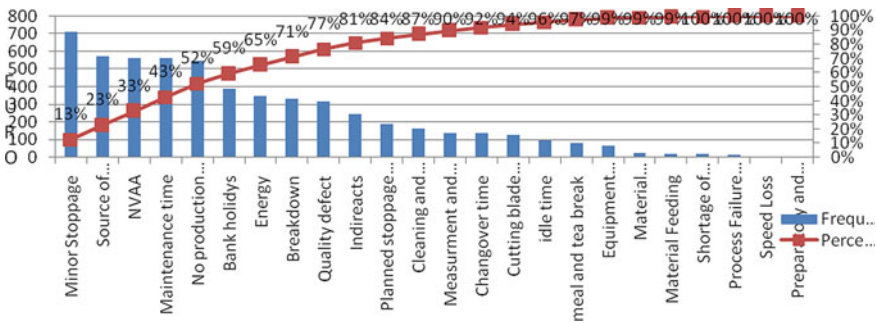


Fig. 1 Overall loss due to various quality defects in the process

5W (what, which, who, when, and where) + 1H (how) analysis: 5W + 1H (who, what, where, when, why, how) is a method of asking questions about a process or a problem taken up for improvement. Four of the W's (who, what, where, when) and the one H is used to comprehend for details, analyze inferences and judgment to get to the fundamental facts and guide statements to get to the abstraction. The last W (why) is often asked five times so that one can drill down to get to the core of a problem. 5W1H of six sigma explains the approach to be followed by exactly understanding and analyzing the process, project or a problem for improvement. Figure 2 shows the analysis has been carried out using 5W + 1H techniques.

The defects caused due to Bag overrun in tea packaging process were analyzed using a simulation software. When the tea bag in the upper transport wheel is not picked up by the bag removal and it continues its journey up the upper transport wheel, it causes an error known as bag overrun. Figure 3 shows a tea bag overlapping another tea bag, in the upper transport wheel, caused by a bag overrun.

To understand and solve quality defects associated with bag overrun problem, it was decided to study the working of upper transportation wheel (Fig. 4) and identify the causes for bag overrun problem. In UTW, five tasks will be completed. First in the paper tube folding station (1) the filter paper with the heap of tea is folded to form a tube and the seam is crimped. The tube is transferred by transport rollers to the paper tube knife station (2) to cut the tea bag of specified length. The ten lower knives of the upper transport wheel function as supports for the paper tube knife. The upper transport wheel (3) also has the following functions: (a) The cut tube sections are taken over by the right flap and transported under the cover (4). (b) In the functional unit with the bottom folder subassembly, the bottom fold in the tea bag is made on the folding wedge (5). (c) As the other stations move, the head fold pusher on the left flap changes its position and holds the top of the tea bag in position. The movements of the flaps, bottom folding wedge, and head fold pusher are controlled by cams. The transport wheel is driven continuously by gears.

The complete process of UTW has been modeled using CATIA software. The model has been simulated to see the working of the upper transportation wheel. It was found that during the operation of UTW, tea bag was not picked up by the bag removal unit and it continues up its journey up the UTW, which results in tea bag overlapping another tea bag. This problem contributes around 70% of total quality defects. It is found that it occurs mainly because of three reasons (1) top fold not formed correctly (2) bag not stapled correctly (3) thread not cut. Out of the above-mentioned problems, the problem related to top fold not formed correctly has been solved successfully. To completely eliminate the remaining two problems, i.e., bag not stapled correctly and thread not cut, point process analysis (PPA) has been carried out for staple wire guiding assembly. The details of this analysis are shown in Table 1.

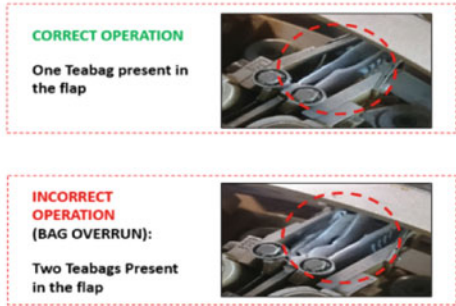
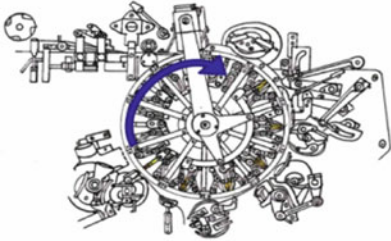
After analysis, it was found that the above two problems occur because the frictional force is inhibiting the movement of the aluminum wire causing buildup of shavings at the wire guide plate. We analyze the amount of shavings generated at various time periods. Figure 5 shows the buildup of aluminum shavings at the entry and exit point of the wire guide plate. Further calculation has also been carried out

(a)

What : Bag overrun in UTW

When the tea bag in the Upper Transport Wheel is not picked up by the bag removal and it continues its journey up the upper transport wheel, it causes an error known as bag overrun.

We see a tea bag overlapping another tea bag, in the upper transport wheel, caused by a Bag overrun



(b)

When : Relation between frequency of the minor stop to factors such as Cleaning and Professional Maintenance

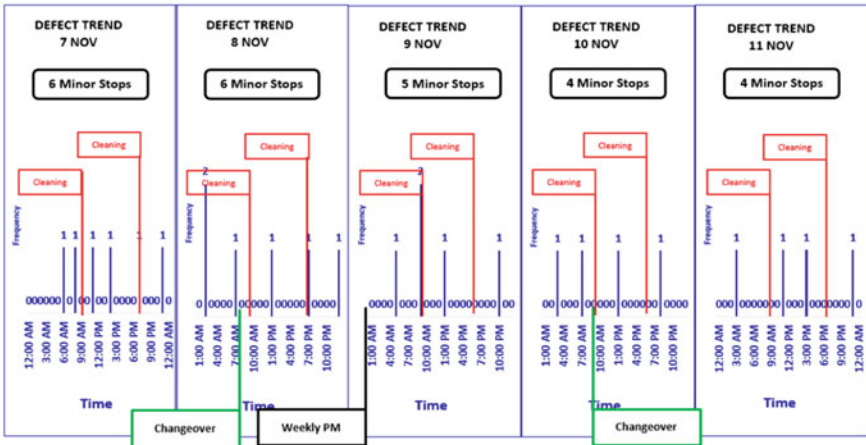
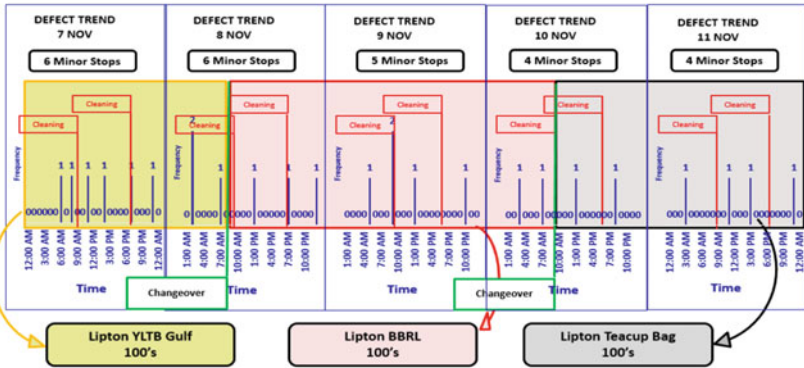


Fig. 2 a Analysis using 5W + 1H technique (what), b analysis using 5W + 1H technique (when), c analysis using 5W + 1H technique (which), d analysis using 5W + 1H technique (who), e analysis using 5W + 1H techniques (where), f analysis using 5W + 1H technique (how)

(c)

Which : Relation between the frequency of the minor stop and the SKU in production



(d)

Who : Relation between the frequency of the minor stop and the skill of the machine operator

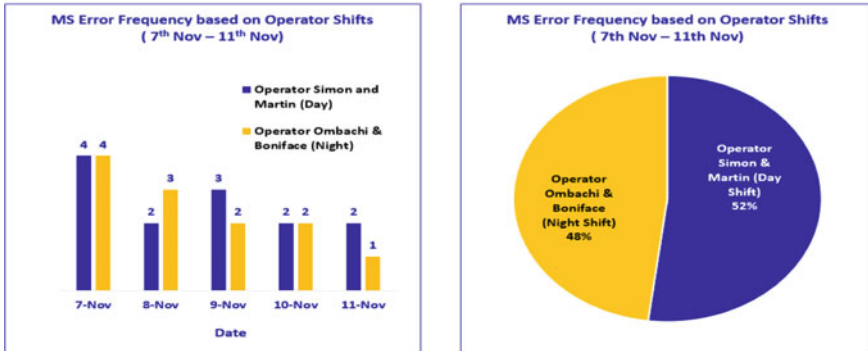
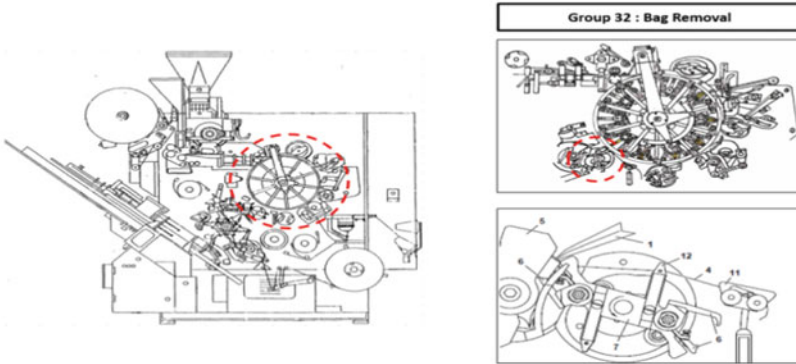


Fig. 2 (continued)

(e)

Where : The region within the machine where the minor stop is detected




(f)

How : Symptoms associated with the Minor Stop error Bag Overrun in the Upper Transport Wheel


3 different phenomena observed

- Top fold not formed correctly
- Bag not stapled correctly
- Thread not cut

Phenomena 1 (already attacked) :
Top fold not formed correctly



Phenomena 2:
Bag not stapled correctly



Phenomena 3:
Thread not cut




Fig. 2 (continued)



Fig. 3 A tea bag overlapping another tea bag

Fig. 4 Upper transport wheel

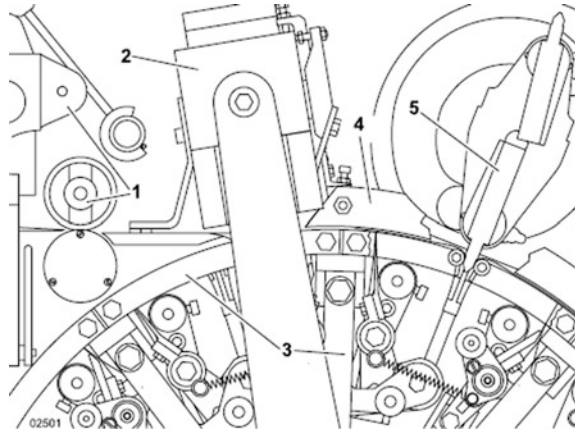


Table 1 Analysis of process point for staple wire guiding assembly

Sr. no.	Particulars	Details
1	Purpose	To guide staple wire toward the guide plate where it is pushed toward the anvil
2	Components	Wire guide plate, insert, angle, guide block, bending die, guide plate
3	Principle	A canal of 0.75 mm width accommodates the wire of 0.5 mm diameter into the guide block where it is cut and bent to form the staple
4	Operating standards	For the correct wire length, the start of the wire must be approx. 1–2 mm inside the guide plate. Wire diameter must be in range of 0.5 ± 0.2 mm and material to be use is AIMg ₃

to know the amount of draw force and friction coefficient on the surface of wire guide plate. The details of calculation are given below.

Draw force calculations for the wire guide plate

Entry and exit points: The point where the wire enters and exits the wire guide plate.

To calculate the draw force, we use the equation

$$\sigma_z f / Y = [(1 + B) * (1 - (1 - r)B)] / B$$

$\sigma_z f$ Forward tension

Y Yield stress

r Reduction in cross-sectional area

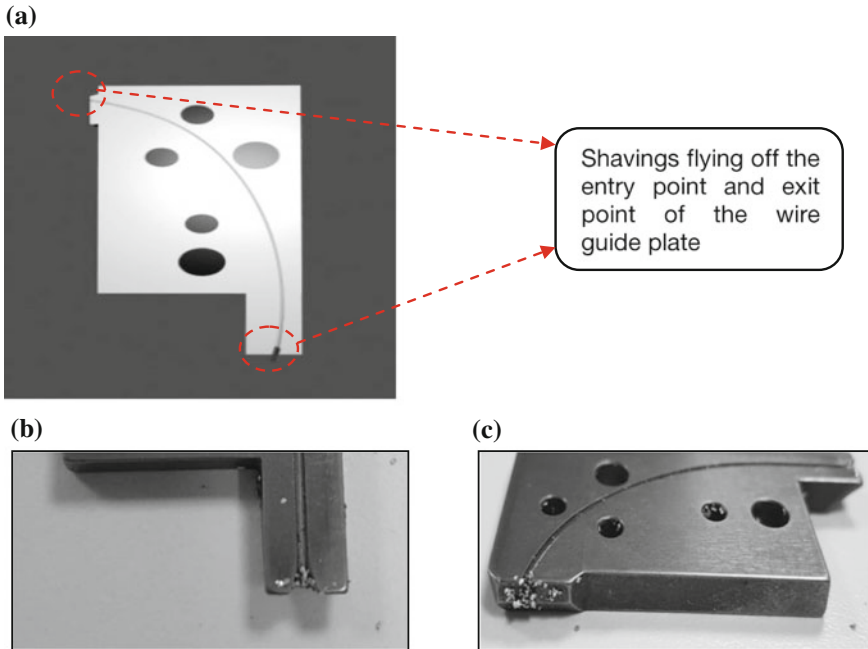


Fig. 5 **a** Buildup of aluminum shavings of wire guide plate, **b** deposition of Al shaving entry wire point guide plate, **c** deposition of Al shaving of exit point of wire guide plate

$$\begin{aligned}
 r &= 1 - (Df^2 - Di^2) \\
 &= 1 - (5^2 - 4.9^2) \\
 &= 0.0396
 \end{aligned}$$

$$\begin{aligned}
 B &= \mu \cot \alpha \\
 &= (0.6) * \cot(5^\circ) \\
 &= 6.85
 \end{aligned}$$

Using the above equation in this case,

$$\begin{aligned}
 \sigma_z f / Y &= [(1 + B) * (1 - (1 - r)B)] / B \\
 &= [(1 + 6.85) * (1 - (1 - 0.0396)6.85)] / 6.85 \\
 &= [7.85 * (1 - 0.758)] / 6.85 \\
 &= [7.85 * (0.241)] / 6.85 \\
 \sigma_z f / Y &= 0.277
 \end{aligned}$$

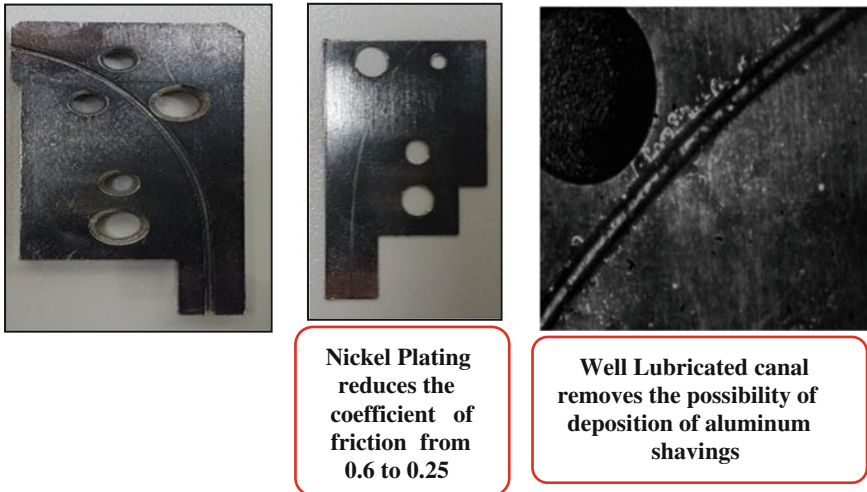


Fig. 6 Improving the lubrication by electroplating the wire guide plate

$$\sigma_z f / Y = F_f / Y * A_f$$

(F_f —draw force, Y —yield stress, A_f —cross-sectional area)

$$F_f = 0.277 * 2.8 * 107 * 5$$

$F_f = 39 \text{ N/mm}^2$ (tensile strength— 340 N/mm^2)

The wire is subject to a pulling force (F_f) of 39 N/mm^2

Frictional coefficient (μ) between dry aluminum and steel surfaces = 0.6

Frictional force (μF_f) = 23.4 N/mm^2

To reduce this frictional force which inhibiting the movement of the aluminum wire, it was decided to properly lubricate canal on wire guide plate that will removes the possibility of deposition of aluminum shavings and to reduce the friction coefficient wire guide plate by doing nickel electroplating of wire guide plate (Fig. 6).

3 Improvements

After implementing above solution, the data were collected to check the chronic and sporadic errors were eliminated or not. It is found that the error bag overrun in upper transportation wheel has been eradicated completely. Figure 7 shows not a single error reported due to bag overrun problem.



Fig. 7 Data collection after improvement

4 Conclusion

A WCM methodology has been used to identify the problem in tea packing industry. The design of upper transportation wheel has been modified to resolve the problem of tea bag overrun in UTW. Using point process analysis modification was also done to the tea bag stapling station. Due to this, greater efficiency has been achieved and losses due to the minor stop phenomena have been completely eliminated. Further, NVAA analysis was applied to minimize the NVAA losses. Future developments include the extension of the WCM methodology to the entire plant.

References

1. Digalwar, A., Sangwan, K.S.: Development and validation of performance measures for world class manufacturing practices in India. *J. Adv. Manuf. Syst.* **6**(1), 21–38 (2007)
2. Saxena, K.B.C., Sahay, B.S.: Managing IT for world-class manufacturing: the Indian scenario. *Int. J. Inf. Manage.* **20**(1), 29–57 (2000)
3. Ipekgil, D.: The impact on the operational performance of world class manufacturing strategies: a company application. *Int. J. Bus. Human. Technol.* **3**(8), 141–149 (2013)
4. Kasul, R.A., Motwani, J.G.: Performance measurements in world-class operations: a strategic model. *Benchmarking Qual. Manage. Technol.* **2**(2), 20–36 (1995)
5. Hayes, R.H., Wheelwright, S.C.: *Restoring Our Competitive Edge: Competing Through Manufacturing*. Wiley, New York (1984)
6. Eid, R.: Factors affecting the success of world class manufacturing implementation in less developed countries the case of Egypt. *J. Manuf. Technol. Manage.* **20**(7), 989–1008 (2009)
7. Schonberger, R.J.: *World Class Manufacturing*. Free Press, New York (1986)
8. Fullerton, R., McWatters, C.S.: An examination of the relationship among world-class manufacturing practices, non-financial performance measures, and firm profitability. Available at SSRN: <https://ssrn.com/abstract=449880>
9. Gunn, T.: *21st Century Manufacturing: Creating Winning Business Performance*. OMNEO, Essex Junction (1992)
10. Hall, R.W.: *Zero Inventories*. Dow Jones-Irwin, Homewood, IL (1983)
11. Flynn, B.B., Schoroeder, R.G., Flynn, E.G.: World class manufacturing: an investigation of Hayes and Wheelwright's foundation. *J. Oper. Manage.* **17**, 249–269 (1999)
12. Hanson, P., Voss, C.A.: Benchmarking best practice in European manufacturing sites. *Bus. Process Re-Eng. Mgmt. J.* **1**(1), 60–74 (1995).
13. Voss, C.A.: Alternative paradigms for manufacturing strategy. *Int. J. Oper. Prod. Manage.* **15**(4), 5–16 (1995)

14. Falah Al, K., Zairi, M., Ahmed, A.: The role of supply-chain management in world-class manufacturing: an empirical study in the Saudi context. *Int. J. Phys. Distrib. Logist. Manage.* **33**(5), 396–407 (2003)
15. Lind, J.: Control in world class manufacturing—a longitudinal case study. *Manage. Account. Res.* **12**(1), 41–74 (2001)
16. Salaheldin, I.S., Eid, R.: The implementation of world class manufacturing techniques in Egyptian manufacturing firms: an empirical study. *J. Ind. Manage. Data Syst.* **107**(4), 551–566 (2007)
17. Cook, J.S., Cook, L.L.: Achieving competitive advantages of advanced manufacturing technology. *Benchmarking Qual. Manage. Technol.* **1**(2), 42–63 (1994)
18. Greene, A.: Plant-wide systems: a world class perspective. *Prod. Inventory Manage.* **11**(7), 14–15 (1991)
19. Haleem, A., Sushil, Qadri, M.A., Kumar, S.: Analysis of critical success factors of world class manufacturing practices: an application of interpretative structural modeling and interpretative ranking process. *Prod. Plan. Control Manage. Oper.* **21**(2), 1–13 (2012)
20. Hogetts, R.M., Luthans, F., Lee, S.M.: New paradigm organisations: from total quality to learning to world class. *J. Org. Dyn.* **22**(3), 4–20 (1994)
21. Kearney, W.T.: A proven recipe for success: the seven elements of world-class manufacturing. *Natl. Prod. Rev.* **16**, 67–76 (1997)
22. Ghodeswar, B., Vaidyanathan, J.: Business process outsourcing: an approach to gain access to world-class capabilities. *Bus. Process Manage. J.* **14**(1), 23–38 (2008)
23. Driva, H., Pawar, K.S., Menon, U.: Measuring product development performance in manufacturing organizations. *Int. J. Prod. Econ.* **63**, 147–159 (2000)
24. Harrison, A.: Manufacturing strategy and the concept of world class manufacturing. *Int. J. Oper. Prod. Manage.* **18**(4), 397–408 (1998)
25. Mey, J.H.P.: The impact of implementing world class manufacturing on company performance: a case study of the Arcelor Mittal South Africa Saldanha Works Business Unit. Research report presented in partial fulfillment of the requirements for the degree of Masters of Business Administration at the University of Stellenbosch (2011)

Tensile Testing and Evaluation of 3D-Printed PLA Specimens as per ASTM D638 Type IV Standard



S. Anand Kumar and Yeole Shivraj Narayan 

Abstract Additive Manufacturing is playing a major role in the manufacturing of parts by providing an alternative to the existing processes. However, strength of such 3D-printed parts using specific materials is still an area of current research. Polylactic acid, a biodegradable material, is one of the compatible materials in fused deposition modelling-based 3D printing process. Researchers have primarily focused on testing of PLA material as per ASTM D638 Type I standard. In this research ASTM D638 type IV specimens printed on FDM printer using PLA material are subjected to tensile testing and then compared relatively with the simulated results. Process involves preparation of ASTM specimens in Solidworks software followed by printing using PLA material in a Makerbot 3D printer, conditioning the printed specimens and then subjecting it to tensile testing in AutoGraph AG 15 universal testing machine. CAD model of the test specimens is then subjected to tensile loads in ANSYS software to obtain simulated tensile strength and maximum deformation.

Keywords Tensile testing · Polylactic acid · ASTM D638 Type IV 3D printing

1 Introduction

FDM is one of the most popular additive layer-by-layer manufacturing technologies capable to deliver or duplicate unsupported modern structures in one piece [1]. Additive manufacturing permits programmed creation of complex shapes with a critical decrease in assembling cost, contrasted with conventional subtractive manufacturing methods [2]. In the most recent years, the utilizing additive manufacturing has developed generously equally in volume and extension [3, 4]. Independent of the particular strategy, additive manufacturing producing brings

S. Anand Kumar · Y. Shivraj Narayan (✉)
VNR Vignana Jyothi Institute of Engineering and Technology,
Hyderabad TS 500090, India
e-mail: shivrajyeole@vnrvjiet.in

© Springer Nature Singapore Pte Ltd. 2019
U. Chandrasekhar et al. (eds.), *Innovative Design, Analysis and Development Practices in Aerospace and Automotive Engineering (I-DAD 2018)*, Lecture Notes in Mechanical Engineering, https://doi.org/10.1007/978-981-13-2718-6_9

about segments with a layer of microstructure; inside each of the layers, the direction of layers in 3D-printed parts effects the mechanical properties [5, 6]. Main principle of FDM technology is to produce parts directly from three-dimensional computer-aided design (CAD) data by using material extrusion process [7]. Three-dimensional CAD model is saved as *.stl* file configuration and later exported to a 3D printer. The plan is then printed by the FDM printer layer-by-layer structuring a genuine product. 3D printing enables creators and designers to go from level screen to correct part [8]. FDM is an unpredictable procedure with number of parameters that impact material properties and quality of the product, and also, the mix of these parameters is frequently hard to understand [9, 10]. Printing parameters like layer thickness, feed rate, infill pattern and density, raster width and angle, orientation of the part show a substantial effect on performance and quality of the FDM-printed parts [10–15].

2 Polylactic Acid

Polylactic acid (PLA) is a thermoplastic polyester which can be produced from renewable resources. It is presently considered a substitute for synthetic plastic materials in food packing marketplace as its cost is moderately low and possesses superior process-ability. PLA is likely to reduce the impact on the environment due to the production and use of petrochemical polymers [16]. PLA has a larger strength and lower ductility than the traditional acrylonitrile butadiene styrene (ABS) material. PLA is a sustainable thermoplastic alternative which addresses the problem of added waste from end-users manufacturing components at home and has similar characteristics as ABS. PLA parts produced via FDM have also been of high interest to the medical field, due to its biocompatibility in applications such as tissue engineering and custom-made patient-specific implants [17]. PLA may be

Table 1 Material properties of PLA [23–28]

Property	Unit	Value
Elongation at break	%	7.0
Melting temperature, T_m	°C	130–230
Shear modulus, G	MPa	1287
Elastic modulus, E	MPa	3500
Rockwell hardness	Hr	88
Yield strength, σ_y	MPa	70
Flexural strength, σ_x	MPa	106
Poisson's ratio, ν		0.360
Ultimate tensile strength, σ_{usd}	MPa	73
Tensile modulus	GPa	2.7–16
Crystallinity	%	37
Unnotched Izod impact	J/m	195

stronger over ABS, yet more fragile. PLA has a lower effect of warping due to its lower coefficient of thermal expansion, which increases the adhesion of part to the printed surface and reduces cracking of the part while printing [18]. Table 1 shows the material properties of PLA material.

3 Specimen Design

ASTM D638 standard procedure is adopted for evaluating the tensile behaviour of 3D-printed PLA test specimens. Solidworks software is used for modelling the geometry of the specimens as per the dimensions specified in ASTM D638 standard as shown in Fig. 1 and Table 2, respectively. Models are then saved in .stl file format as shown in Fig. 2 and then imported to the 3D printing software [19].

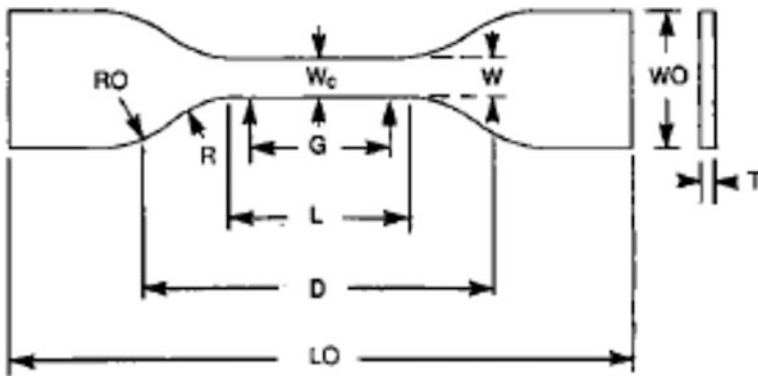


Fig. 1 ASTM D638 Type IV specimen [22]

Table 2 ASTM D638 Type IV specimen dimensions [22]

Dimensions	Type IV (mm)
<i>L</i> —Length of narrow section	33
<i>W</i> —Width of narrow section	6
<i>LO</i> —Length overall	115
<i>WO</i> —Width overall	19
<i>R</i> —Fillet radius	14
<i>RO</i> —Outer radius	25
<i>D</i> —Distance between grips	65
<i>G</i> —Gage length	25

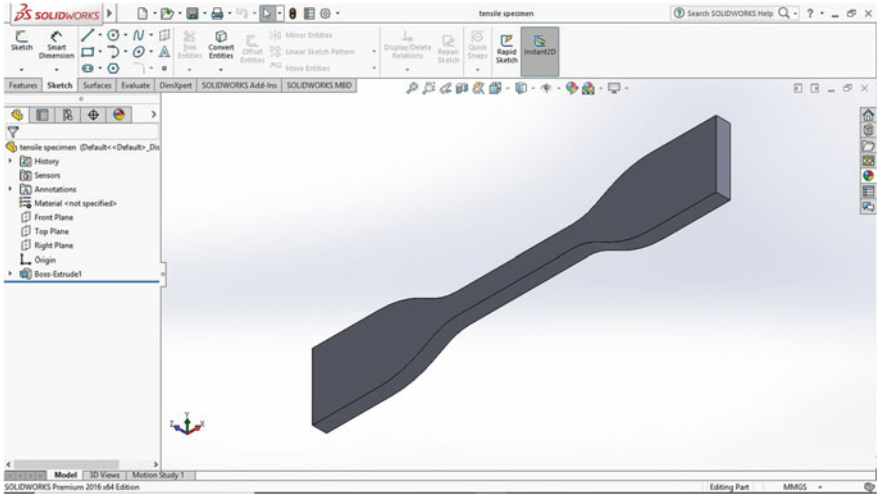


Fig. 2 Modelled tensile specimens

3.1 Tensile Specimen with Detailed Dimension

Figure 3 displays a schematic of tensile specimen with detailed dimensions based on the ASTM standard. A tensile specimen has augmented finishes or shoulders for grasping. The critical piece of the example is the gage area. The cross section of the gage area is reduced so deformation and distress will be restricted in this area. The gage length is the area over which estimations are made and is focused inside the decreased segment. Separations amongst finishes of the gage area and shoulders must be sufficiently extraordinary so that bigger closures do not oblige deformity within the gage length, and the gage length ought to be perfect with respect to its distance. Rather, the anxiety state will be more mind-boggling than straightforward pressure. Portrayals of standard example shapes are given in detail on malleable testing of particular materials.

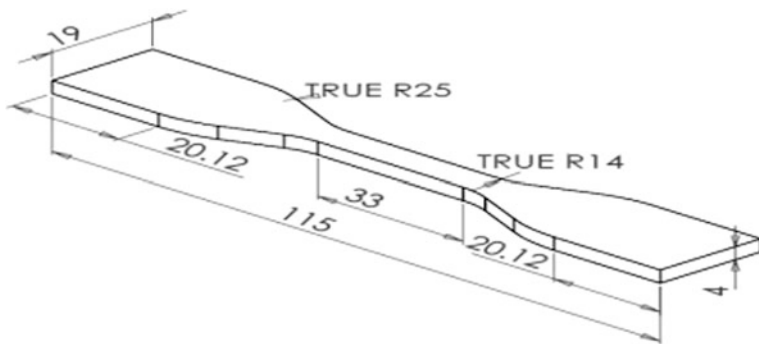


Fig. 3 Tensile specimen with detailed dimension

There are different methods for holding. For example, screwing the samples into a grasp handle, it can be stuck, butt closures can also be utilized, or the hold segment may be held amid wedges. Determination of a grasping approach is made by assuring the greatest load of the specimen that is held without any slippage in the hold area, and the twisting has to be limited.

3.2 STL File of Tensile Specimen

The created 3D model using Solidworks software is saved in .stl format. Figure 4 shows the .stl file of tensile specimens. As depicted in Fig. 5, this format is

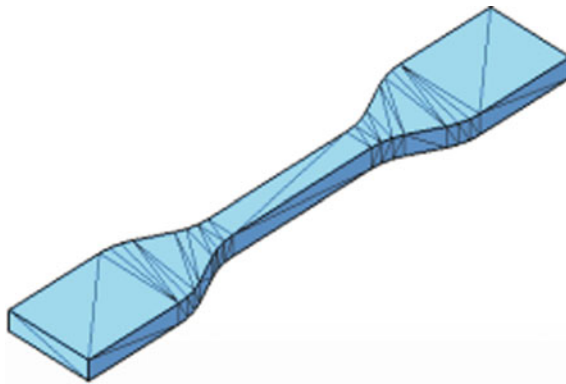


Fig. 4 .stl file of tensile specimens

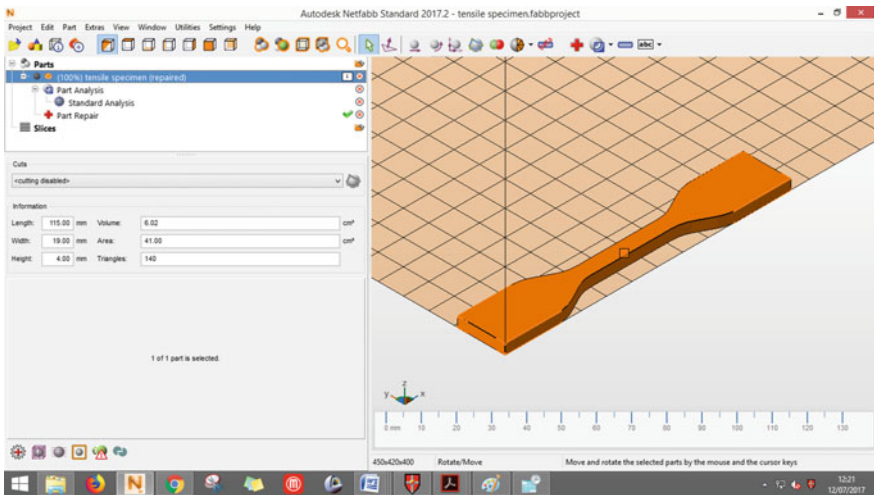


Fig. 5 .stl file of tensile specimens imported to Netfabb

imported into software called Netfabb, which sorts out any errors that are present in the sliced layers of the 3D model. The output is the new *.stl* file with minimum or no errors in the model.

4 Fabrication of Specimen

4.1 *Makerbot Replicator Z18*

Makerbot Industries has an online platform “Thingiverse”, where clients can transfer 3D printable records, report plans, and team up with 3D printing ventures. The site is a synergistic storehouse for configuration documents utilized as a part of 3D printing, laser cutting and other DIY producing forms.

Additive Manufacturing (AM) makes a 3D model in which the filament is combined in a layer form using codes generated by the software to make a part, with material being included, (e.g. fluid particles or powder grains) being intertwined. Different geometry or profile can be delivered utilizing computerized data from a 3D display source, for example additive manufacturing file (AMF) file (typically in successive layers). Stereolithography (*.stl*) is a standout amongst the most well-known document sorts that is utilized for 3D printing. Most of the fifth-generation Makerbot 3D printers use a document type of *.makerbot* to send the guidelines to printer for model to be built. Makerbot desktop software naturally changes any type of 3D printable format to *.makerbot* file for its convenience, which contains the guidelines for the print like extruder path, rasters and temperature. *.stl* and *.obj* are file sorts utilized for 3D printable models in Makerbot 3D printers. *.thing* documents are a method for sparing courses of action and settings for 3D models (Figs. 6 and 7).

4.2 *STL*

A standard tessellation language (STL) is a generally utilized 3D model file format. It comprises of surfaces which are composed of triangles. Every triangle has an inward side and an external side. External side is known as ‘normal’. In an all-around framed stl, everyone of the normal’s confronting outward and the surface is nonstop, without any gaps. At the point when these guidelines are met by a model, it is alluded to as complex *.stl*’s containing normal’s that face inwards (modified normals) might be able to print; however, complex models are commonly viewed as obligatory for 3D printing.

.stl is now compatible with most of the 3D modelling software’s and became a standard for 3D printing models. Table 3 shows the parameter values that are used in 3D printing and Fig. 8 shows the 3D printed specimens.



Fig. 6 Makerbot Replicator Z18

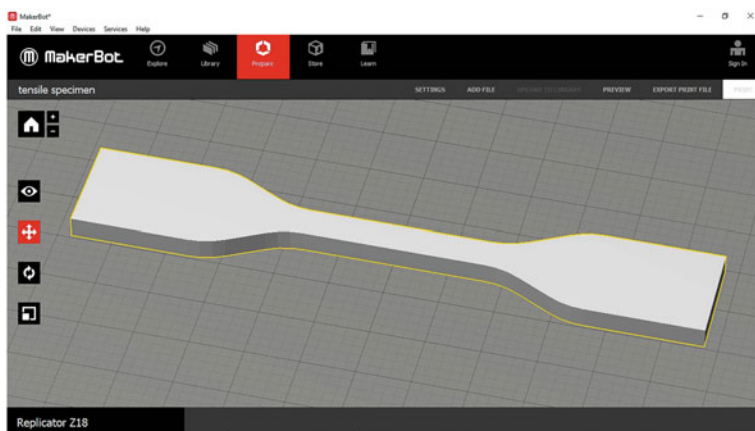


Fig. 7 .stl file imported to makerware software

Table 3 3D printing parameter values

Parameters	Values
Layer height (mm)	0.3
Feed rate (mm/s)	150
Extruder temperature (°C)	230
Bed temperature (°C)	110
Number of shells	2
Infill density (%)	100

**Fig. 8** 3D-printed tensile specimen

Makerbot Replicator Z18 3D printer with Makerbot PLA material is used to print the specimens for conducting tensile tests.

5 Experimental Procedure

3D-printed PLA specimens conditioned as per ASTM D618-13 [29] are tested experimentally for tensile strength on a universal testing machine (UTM) in specimen preparation laboratory at Central Institute of Plastic Engineering and Technology, Hyderabad. Figure 9 depicts UTM used for testing specimens. Tensile properties measurement is carried out on Shimadzu Japan make UTM machine whose specifications are given in Table 4.

AutoGraph AG 15 UTM has a grip attachment distance of 33 mm. A load of 5.0 kN at a constant speed of 5 mm/min is applied. Test specimens are prepared in compliance with ASTM D638 Type IV standard. Sample width and thickness are measured for individual specimens [20].

Specimens are placed in the UTM with the help of grippers, and a gradual load is applied on the specimens until failure, and the resultant loads are noted down for every single specimen thus obtaining the tensile loads for every specimen.



Fig. 9 Universal testing machine. *Source* CIPET, Hyderabad

Table 4 Specifications of UTM

Identification	CHYD/PTC/UTM/3
Model no.	AutoGraph AG 14
Range	0–50 kN
Accuracy	0.01 N
Location	Specimen preparation laboratory
Make	Shimadzu Japan
Applicable test	Tensile, compressive, flexural, tear, shear, elongation and modulus

6 Analysis of Specimens

Simulations are carried out in static structural analysis mode with one end fixed in ANSYS 16.2 software.

6.1 Stress Analysis of Tensile Specimen

Stress analysis is carried out on the tensile test specimen with different loads acting on the specimen as shown in Fig. 10.

The stress is induced in the specimen after the application of tensile load. Minimum and maximum values are obtained. Gauge length has high stress values when compared to the other regions of the specimen due to plastic flow or slippage

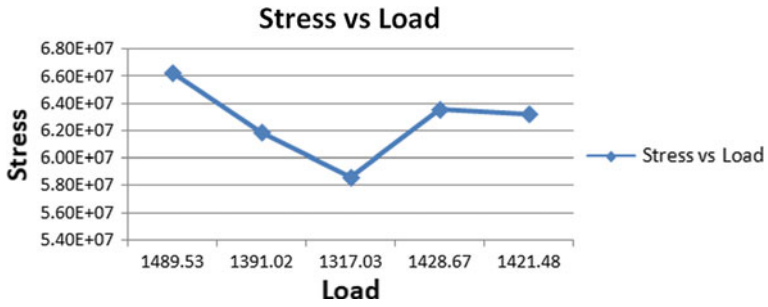


Fig. 10 Stress versus load graph of the analyzed tensile specimens

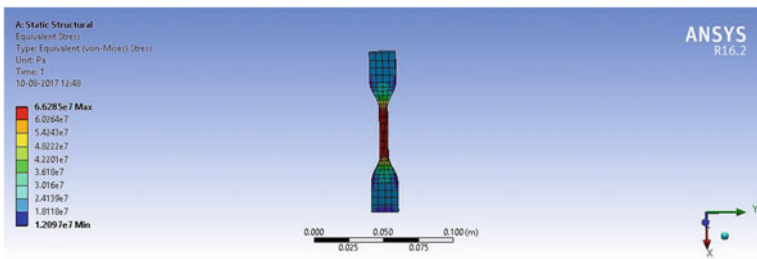


Fig. 11 Maximum stress obtained in the tested tensile specimens

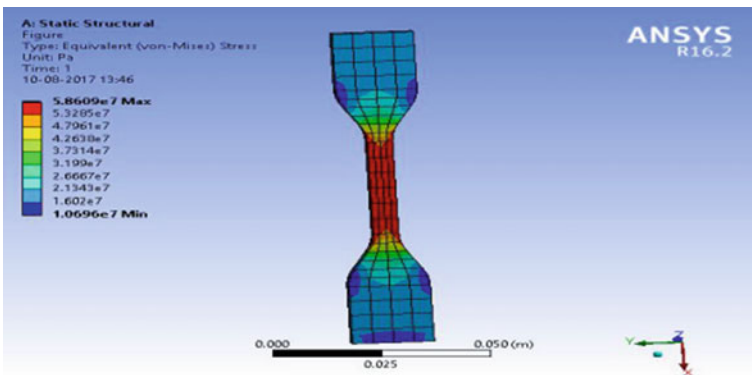


Fig. 12 Minimum stress obtained in the tested tensile specimens

along molecular slip planes when load is applied beyond elastic limit shown in Figs. 11 and 12, respectively. Table 5 shows the maximum and minimum equivalent stress obtained when the relevant load is applied on the specimen.

Table 5 Results of stress analysis of tensile specimens

Load (N)	Minimum equivalent stress (N/mm ²)	Maximum equivalent stress (N/mm ²)
1489.53	1.2097e ⁷	6.6285e ⁷
1391.02	1.1297e ⁷	6.1901e ⁷
1317.03	1.0696e ⁷	5.8609e ⁷
1428.67	1.1603e ⁷	6.3577e ⁷
1421.48	1.1544e ⁷	6.3257e ⁷

The minimum equivalent stress is observed for the load of 1317.03 N, and maximum equivalent load is observed for load of 1428.67 N.

The von-misses stress values of tensile specimen at various loads are as shown in Fig. 10. As different loads are applied on the specimen, different behaviour is observed. The graph gives a clear variation of stress versus load behaviour for particular loads acting on the specimen.

6.2 Deformation Analysis of Tensile Specimen

Deformation analysis is carried out on the tensile test specimen with different loads acting on the specimen as shown in Fig. 13.

The deformation is induced on the specimen after the application of tensile load. Minimum and maximum values are obtained. Table 6 shows various maximum and minimum deformation values for different loads acting on the specimen. Due to the applied load and work done by external forces acting on the specimen, large deformation is observed as shown and is indicated in red colour shown in Figs. 14 and 15, respectively. Maximum deformation is observed for the load of 1428.67 N. The deformation values of tensile specimen at different loads are as shown in Fig. 13.

Fig. 13 Deformation versus load graph of the analyzed tensile specimens

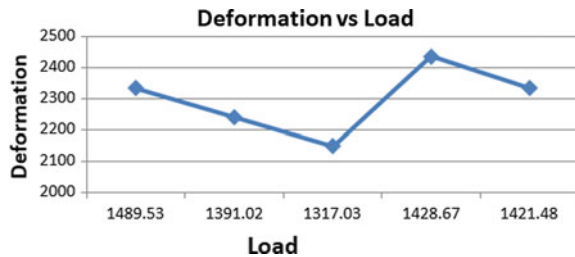


Table 6 Result of deformation analysis of tensile specimens

Load (N)	Minimum deformation (mm)	Maximum deformation (mm)
1489.53	0	2336.2
1391.02	0	2241.1
1317.03	0	2149.5
1428.67	0	2438
1421.48	0	2282.6

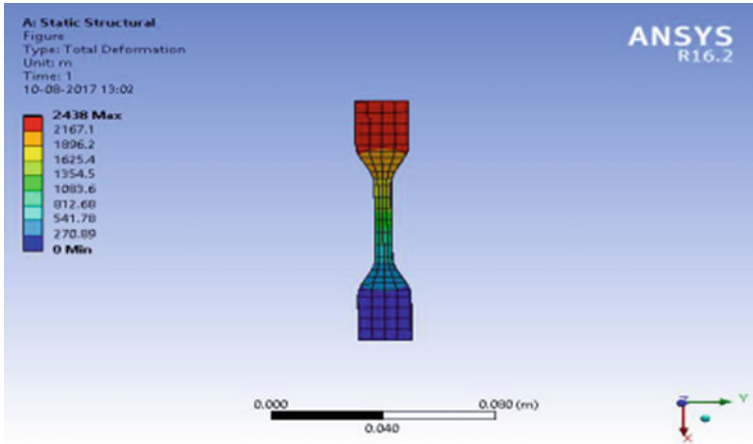


Fig. 14 Maximum deformation obtained from the tested tensile specimens

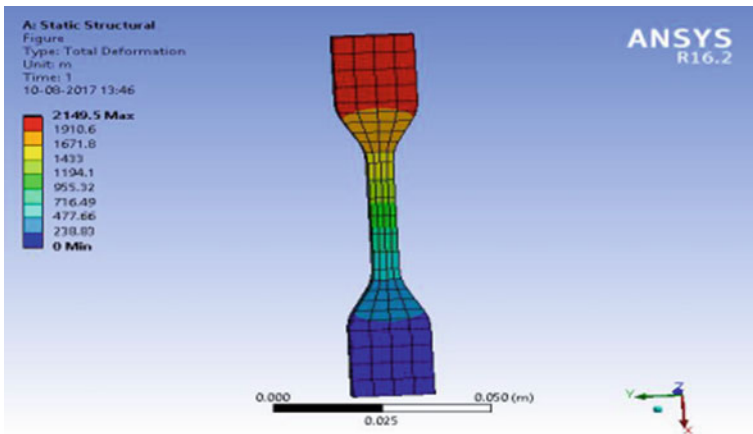


Fig. 15 Minimum deformation obtained from the tested tensile specimens

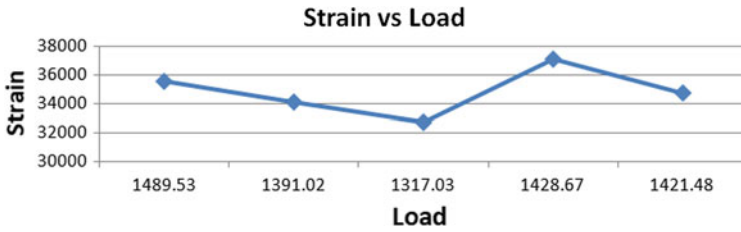


Fig. 16 Strain versus load graph of the analyzed tensile specimens

Table 7 Result of strain analysis of tensile specimens

Load (N)	Minimum elastic strain	Maximum elastic strain
1489.53	6641.5	35,534
1391.02	6371.1	34,087
1317.03	6110.6	32,693
1428.67	6930.9	37,082
1421.48	6489	34,718

6.3 Strain Analysis of Tensile Specimen

Strain analysis is carried out on the tensile test specimen with different loads acting on the specimen as shown in Fig. 16.

The strain is induced in the specimen after the application of tensile load. Minimum and maximum values obtained of the specimen at different loads are shown in Table 7. Strain at 1428.67 N is high in gauge length when compared to the other regions of the specimen due to reason that there is an increment in the length of specimen and decrease in the cross-sectional area of the specimen as shown in Figs. 17 and 18. Minimum elastic strain is seen for load of 1317.03 N, and maximum elastic strain is observed for load of 1428.67 N.

7 Results

As seen in Fig. 19, the behaviour of specimens under different loading conditions on the universal testing machine is depicted. It is observed that all the specimens except specimen 3 followed a similar pattern. Specimen 3, when subjected to a load of 1317.03 N, failed abruptly due to the fragility of the material. Figure 20 shows the failure of tensile specimens when subjected to different on AutoGraph AG 15 Universal Testing Machine.

Maximum displacement, maximum stress, maximum strain and modulus obtained under tensile testing are illustrated in Table 8.

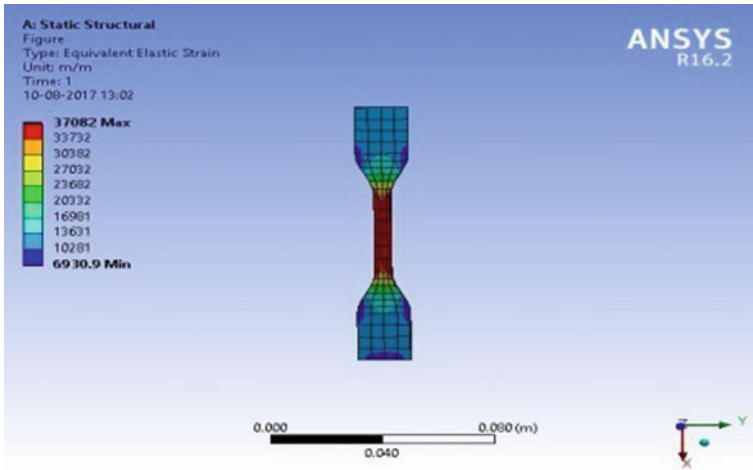


Fig. 17 Maximum strain obtained from the tested tensile specimens

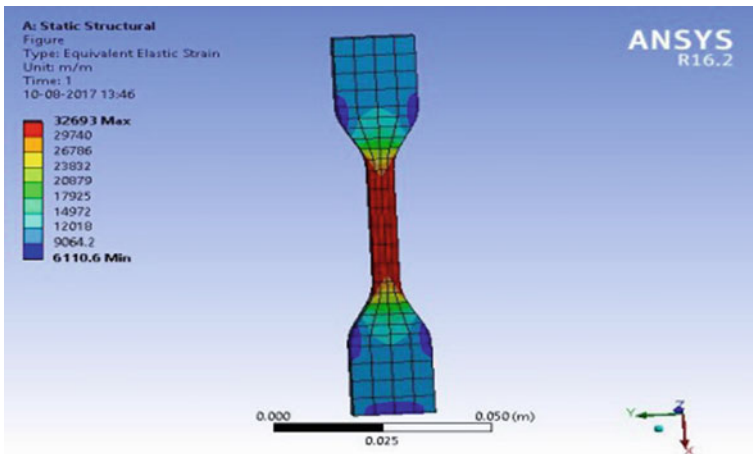
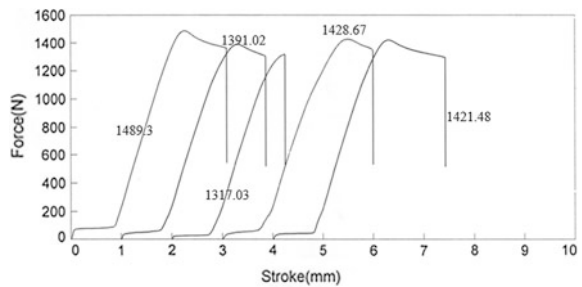


Fig. 18 Minimum strain obtained from the tested tensile specimens

Fig. 19 Force versus stroke graph of the tested tensile specimens



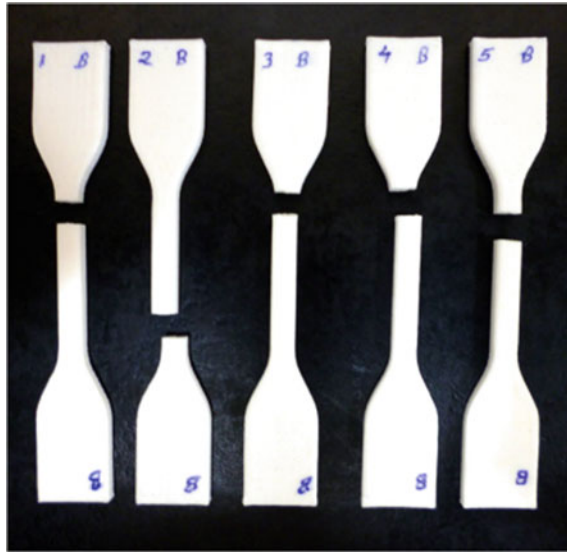


Fig. 20 Tested tensile specimens

Table 8 Tensile test values

Parameters	Max force	Max displacement	Max stress	Max strain	Modulus
Units	(N)	(mm)	(N/mm ²)	(%)	(N/mm ²)
1	1489.53	2.2600	54.4634	5.6500	1865.52
2	1391.02	2.3100	51.5430	5.7750	1816.07
3	1317.03	2.2430	48.7638	5.6075	1792.79
4	1428.67	2.49400	52.6486	6.2350	1714.58
5	1421.48	2.3050	52.7970	5.7625	1822.14
Mean	1409.55	2.3224	52.0432	5.8060	1802.22

8 Conclusion

This paper presents the evaluation of tensile strength of ASTM D638 Type IV specimens of PLA material additively manufactured using FDM-based Makerbot desktop 3D printer and its simulation in ANSYS software. Following results are observed:

- Maximum stress of 63.577 and 54.46 N/mm² is observed for a load of 1489.53 N under simulated and UTM testing, respectively.
- Maximum deformation of 2.336 and 2.4940 mm is attained for a load of 1428.67 N under simulated and UTM testing, respectively.

- Maximum elastic strain of 4.06 and 6.23% is observed for load of 1428.67 under simulated and UTM testing, respectively.
- The obtained tensile strength of 54.46 N/mm² is similar to that of the results obtained by other researchers reported in [18] and [21].
- Behaviour of specimen 3 is found to be different with respect to other specimens due to the fragility of the material which caused it to fail before reaching yield point, failing at a load of 1317.03 N.

As the strength of the 3D-printed PLA specimens are almost similar to the conventionally used ones, they can be used in almost all applications ranging from packaging, agricultural, sanitary, consumer products like trays, boxes, packaging, seeding pots, boxes, containers, dinnerware, dairy containers, meat trays and many more.

References

1. Ramya, A., Vanapalli, S.L.: 3D printing technologies in various applications. *Int. J. Mech. Eng. Technol.* **7**(3), 396–409 (2016)
2. Dimitrov, D., van Wijck, W., Schreve, K., de Beer, N.: Investigating the achievable accuracy of three dimensional printing. *Rapid Prototyp. J.* **12**(1), 42–52 (2006)
3. McLoughlin, L., Fryazinov, O., Moseley, M., Sanchez, M., Adzhiev, V., Comminos, P., et al.: Virtual sculpting and 3D printing for young people with disabilities. *IEEE Comput. Graph. Appl.* **36**(1), 22–28 (2016)
4. Joshi, S.C., Sheikh, A.A.: 3D printing in aerospace and its long-term sustainability. *Virtual Phys. Prototyp.* **10**(4), 175–185 (2015)
5. Shaffer, S., Yang, K., Vargas, J., Di Prima, M.A., Voit, W.: On reducing anisotropy in 3D printed polymers via ionizing radiation. *Polymer.* **55**(23), 5969–5979 (2014)
6. Es-Said, O., Foyos, J., Noorani, R., Mendelson, M., Marloth, R., Pregger, B.A.: Effect of layer orientation on mechanical properties of rapid prototyped samples. *Mater. Manuf. Process.* **15**(1), 107–122 (2000)
7. Hossain, M.S., et al.: Improving tensile mechanical properties of FDM-manufactured specimens via modifying build parameters. In: 24 Annual International Solid Freeform Fabrication Symposium, vol. 1, pp. 380–392. Austin (2013)
8. More, M.P.: 3D printing making the digital real. *Int. J. Eng. Sci. Res. Technol.* **2**(7) (2013)
9. Casavola, C., Cazzato, A., Moramarco, V., Pappalettere, C.: Orthotropic mechanical properties of fused deposition modelling parts described by classical laminate theory. *Mater. Des.* **90**, 453–458 (2016)
10. Mohamed, O.A., Masood, S.H., Bhowmik, J.L.: Optimization of fused deposition modeling process parameters: a review of current research and future prospects. *Adv. Manuf.* **3**, 42–53 (2015)
11. Tymrak, B.M., Kreiger, M., Pearce, J.M.: Mechanical properties of components fabricated with open-source 3D printers under realistic environmental conditions. *Mater. Des.* **58**, 242–246 (2014)
12. Domingo, M., Puigriol, J.M., Garcia, A.A., Lluma, J., Borros, S., Reyes, G.: Mechanical property characterization and simulation of fused deposition modeling polycarbonate parts. *Mater. Des.* **83**, 670–677 (2015)
13. Ning, F., Cong, W., Hu, Y., Wang, H.: Additive manufacturing of carbon fiber-reinforced plastic composites using fused deposition modeling: effects of process parameters on tensile properties. *J. Compos. Mater.* **51**(4), 451–462 (2016)

14. Lanzotti, A., Grasso, M., Staiano, G., Martorelli, M.: The impact of process parameters on mechanical properties of parts fabricated in PLA with an open-source 3D printer. *Rapid Prototyp. J.* **21**(5), 604–617 (2015)
15. Ullu, E., Korkmaz, E., Yay, K., Ozdoganlar, O.B., Kara, L.B.: Enhancing the structural performance of additively manufactured objects through build orientation. *J. Mech. Des.* **137** (11), 111410–111418 (2015)
16. Fehri, S.M.K.: Thermal properties of plasticized poly (lactic acid) (PLA) containing nucleating agent. *Int. J. Chem. Eng. Appl.* **7**(2), 85–88 (2016)
17. Gordon, A.P.: An approach for mechanical property optimization of fused deposition modeling with polylactic acid via design of experiments. *Rapid Prototyp. J.* **22**(2), 387–404 (2016)
18. Letcher, T.: Material property testing of 3D-printed specimen in PLA on an entry-level 3D printer. In: *International Mechanical Engineering Congress and Exposition 2014, IMECE*, vol. 2, pp. 1–8. Montreal (2014)
19. Chacón, J.M., Caminero, M.A., García-Plaza, E., Núñez, P.J.: Additive manufacturing of PLA structures using fused deposition modelling: effect of process parameters on mechanical properties and their optimal selection (2017)
20. Eng, C.C.: Enhancement of mechanical and dynamic mechanical properties of hydrophilic nanoclay reinforced polylactic acid/polycaprolactone/oil palm mesocarp fiber hybrid composites. *Int. J. Polym. Sci.* **2014**, 1–8 (2014)
21. GiitaSilverajah, V.S., Ibrahim, N.A., Zainuddin, N., Yunus, W.M.Z.W., Hassan, H.A.: Mechanical, thermal and morphological properties of poly(lactic acid)/epoxidized palm olein blend. *Molecules* 11729–11747 (2012)
22. ASTM Designation: D638—14 Standard Test Method for Tensile Properties of Plastics
23. Jamshidian, M., Tehrani, E.A., Imran, M., Jacquot, M., Desobry, S.: Poly-lactic acid: production, applications, nanocomposites, and release studies. *Compr. Rev. Food Sci.* **9**(5), 552–571 (2010)
24. Bijarimi, M., Ahmad, S., Rasid, R.: Mechanical, thermal and morphological properties of PLA/PP melt blends. In: *International Conference on Agriculture, Chemical and Environmental Sciences 2012, ICACES*, pp. 115–117. Dubai (2012)
25. Clarinval, A., Halleux, J.: Classification of biodegradable polymers. In: Smith, R. (ed.) *Biodegradable Polymers for Industrial Applications*, 1st edn. Taylor & Francis, Boca Raton, FL (2005)
26. Ashby, M.F., Johnson, K.: *Materials and Design: The Art and Science of Material Selection in Product Design*, 3rd edn. Butterworth-Heinemann, Oxford, UK (2013)
27. Henton, D.E., Gruber, P., Lunt, J., Randall, J.: Polylactic acid technology. In: Mohanty, A., Misra, M., Drzal, L. (eds.) *Natural Fibers, Biopolymers, and Biocomposites*. Taylor & Francis, Boca Raton, FL (2005)
28. Subhani, A.: Influence of the processes parameters on the properties of the poly(lactides) based bio and eco-biomaterials. PhD thesis, National Polytechnic Institute of Toulouse (2011)
29. ASTM Designation: D618—13 Standard Practice for Conditioning Plastics for Testing

Design Optimization and Testing of Structure of a Single Door Refrigerator



Nishchay Anand and S. Sivarajan

Abstract With growing demand of refrigerators, more and more raw material is required which usually leads to natural resources exploitation and increased cost of manufacturing. For a manufacturing company to remain efficient, research and development becomes necessary to maintain the cost, quality, and features of the product. The aim of this work is to design optimization and testing for cost opportunity (material or process time reduction) and for increased ease of mass manufacturing which indirectly also benefits in reduction of carbon footprint. To achieve this, first the process knowledge was acquired so that the change in design could be met with the existing machinery. Next, the design study of the existing product was done to understand the purpose of the part and its structural features. Next, process involves brainstorming to generate ideas and design conceptualization, followed by design modeling and assembly in CREO/Solidworks. Design analysis of each concept generated was done in ANSYS to study them and compared with the existing design. Final design is chosen from the generated concepts on the basis of benefits it offers in terms of structural strength, cost, and ease of manufacturing.

Keywords Refrigerator · Structure · Deck reinforcement · Optimization

1 Introduction

A refrigerator is a popular household appliance that consists of a thermally insulated compartment and a refrigeration system that cools the compartment space. The refrigerator cabinet in this study is from a 260 L refrigerator. It is a mature design having been in production for over ten years. Many cost reductions have been implemented over the years but never had there been a comprehensive attempt to optimize the deck reinforcement and top hinge cover. Typically, cost reductions of

N. Anand · S. Sivarajan (✉)

School of Mechanical & Building Sciences, Vellore Institute of Technology, Chennai, India
e-mail: sivarajan.s@vit.ac.in

© Springer Nature Singapore Pte Ltd. 2019

U. Chandrasekhar et al. (eds.), *Innovative Design, Analysis and Development Practices in Aerospace and Automotive Engineering (I-DAD 2018)*, Lecture Notes in Mechanical Engineering, https://doi.org/10.1007/978-981-13-2718-6_10

97

the cabinet's structural components have been accomplished as follows. Several concepts of deck reinforcement are built implementing the proposed changes. These products are then stiffness tested, and the results are compared to current reinforcements. If the change is small or not discernible, then the change is approved.

The primary structure is a sandwich of steel on the outer surface, a foam core, and plastic inner liners. The outer steel is comprised of a wrapper with roll-formed front and rear flanges, corner bracket reinforcements, a back panel, and a deck. The bottom support structure is made from six formed sheet metal parts: front rail, back rail, two s-channels, and glider rails (left and right). The cabinet sits on four rollers that are attached to the front and back rails. The main function of the cabinet is to maintain the food in a sealed refrigerated compartment. In order to do this, the deflection must be small enough that the door seal is retained. Several attempts were made by various researchers around the globe to analyze the structures of refrigerator cabinet parts [1–5]. Deck reinforcement and pedestal assembly are analyzed in this article.

Deck reinforcement purpose is to provide structural strength to avoid damage during drop, drag, etc., in various stages of the life cycle of the product (Fig. 1). It provides mounting points for CMP, pedestal, drier holder, power cord, and earthing.



Fig. 1 Image of deck reinforcement

2 Methodology

The strength is important for the refrigerator cabinet. Critical parts are assembled, and their FEA is completed by using ANSYS. Initially, meshes of each part are created according to the structure. Force and boundary scenarios are determined on each part with FEM simulations. The total deformation and von Mises stresses were found for refrigerator cabinet parts.

In the first concept, the following design changes are made. Deck reinforcement plate was removed. Rib was introduced to increase structural strength. Flaring was performed for increased surface contact with screw. In the second concept, the following design changes were made. Deck reinforcement plate was removed. Flaring was done for increased surface contact with screw, and sheet thickness was kept as 0.7 mm. In the third concept, removal of deck reinforcement plate, introduction of rib to increase structural strength, and flaring for increased surface contact with screw were made. In the fourth concept, the following design changes were made. Deck reinforcement plate was removed. Flaring was done for increased surface contact with screw, mounting point for wire harness was provided for improved feasibility and sheet thickness was kept as 0.7 mm.

3 Results

The deformation and von Mises stress of Concepts 1 and 2 are shown in Figs. 2, 3, 4, and 5. The results of static structural analysis of the four concepts are given in Table 1. The FEM simulation of drop test analysis is shown in Figs. 6, 7 and 8.

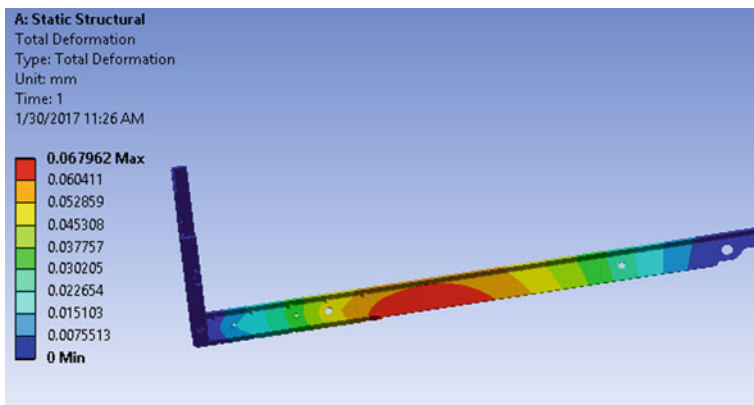


Fig. 2 Total deformation—Concept 1

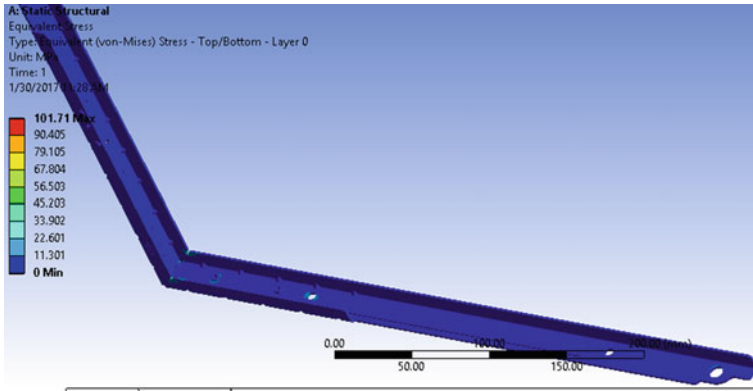


Fig. 3 Equivalent stress—Concept 1

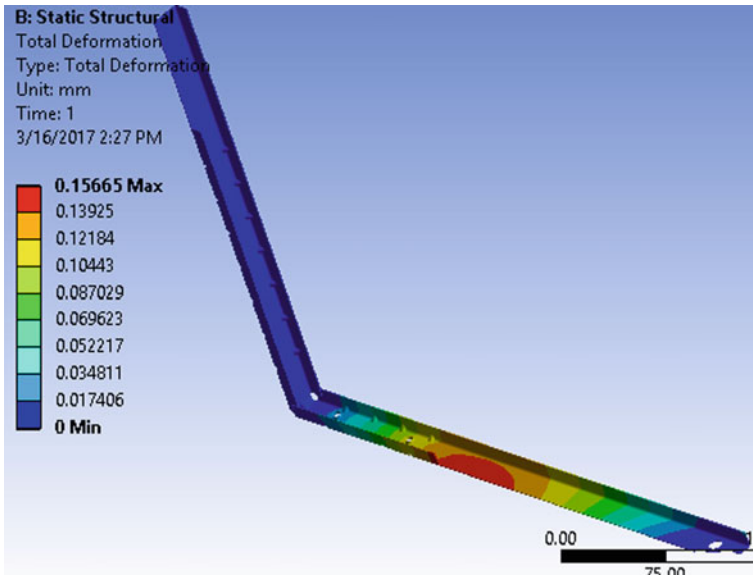


Fig. 4 Total deformation—Concept 2

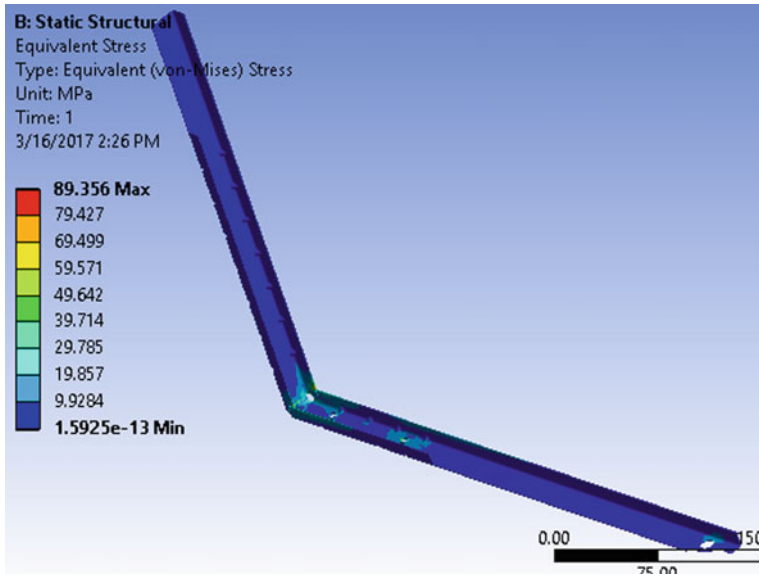


Fig. 5 Equivalent stress—Concept 2

Table 1 Results of static structural analysis

Model	Sheet thickness (mm)	Rib (Y/N)	Equivalent stress (MPa)	Deformation (mm)	FOS
Existing	0.9	N	82.923	.097	2.17
Concept 1	0.9	Y	101.71	.068	1.77
Concept 2	0.7	N	115.43	.136	1.56
Concept 3	0.7	Y	133.99	.082	1.343
Concept 4	0.7	N	89.356	.156	2.01

Figures 9 and 10 show the FEM simulation of the proposed design concept. The results of DFA analysis, proposed concept analysis, and drop test analysis are shown in Tables 2, 3 and 4.

4 Discussion

In Concept 1, with the presence of rib, the stress gets localized; thus, the maximum equivalent stress increases and the FOS reduces below the specified limit. In Concept 2, due to the reduction of sheet thickness, the moment of inertia decreases; thus, the equivalent stress and deformation increase. The FOS is less than specified limited; thus, the model cannot be implemented. Concept 3, with the reduction in

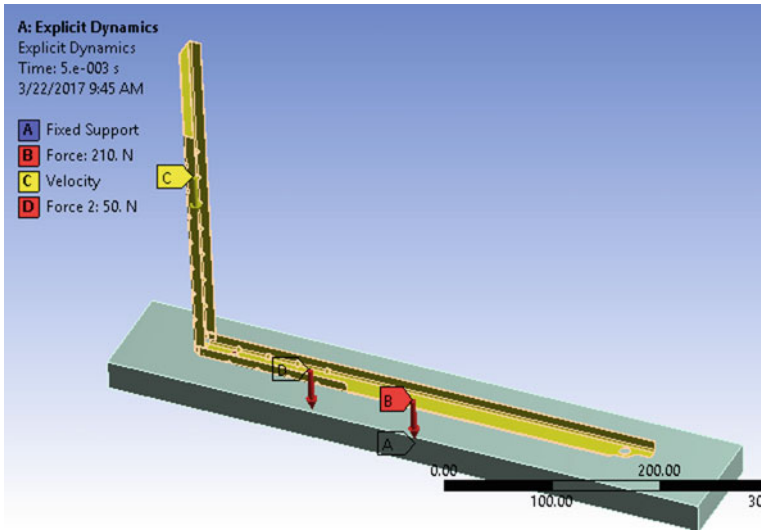


Fig. 6 Boundary conditions—drop test—Concept 4

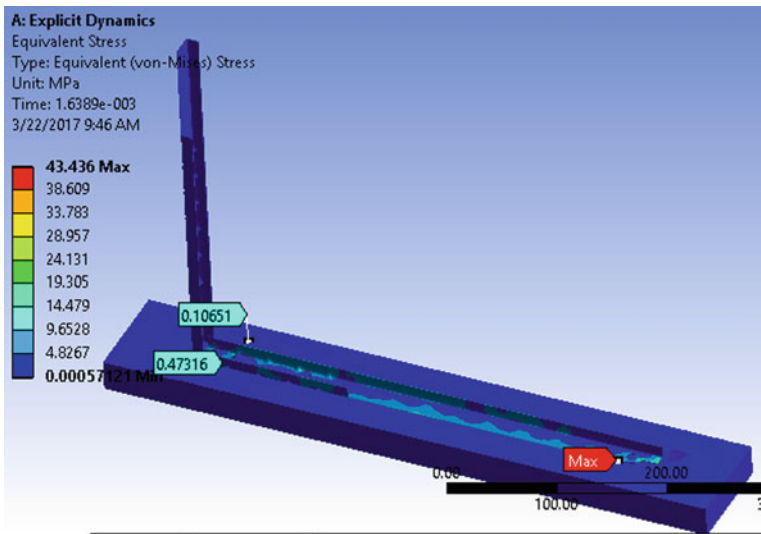


Fig. 7 Equivalent stress—drop test analysis

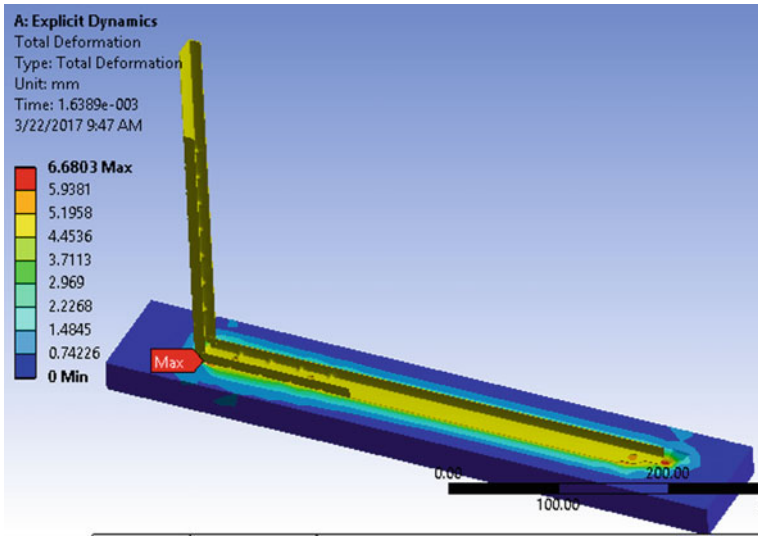


Fig. 8 Deformation—drop test analysis

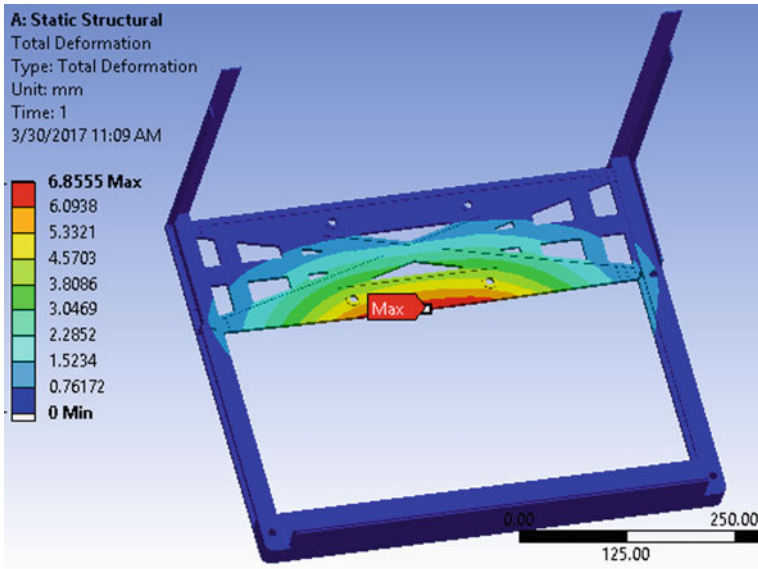


Fig. 9 Conceptual design change in pedestal—deformation

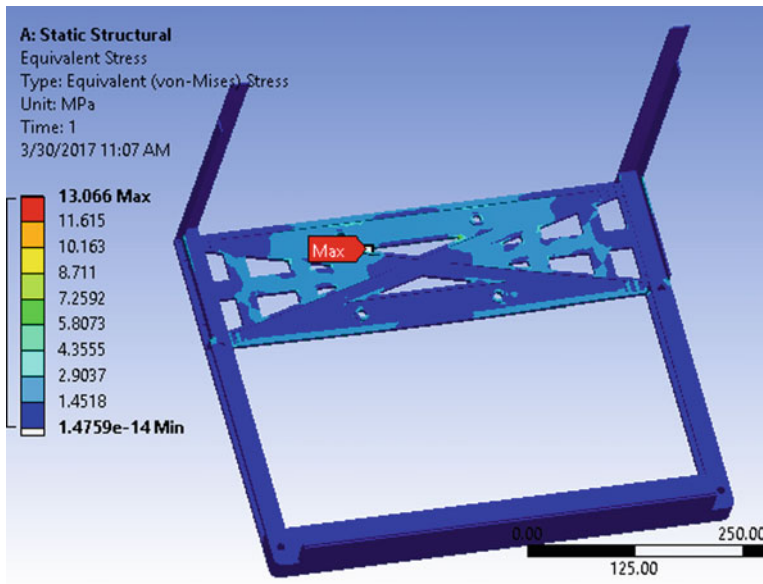


Fig. 10 Conceptual design change in pedestal—equivalent stress

Table 2 DFA complexity factor

	DFA complexity factor
Existing design	11.489
Proposed design	4.24
Target	3.464

Table 3 Static structural analysis—conceptual design

Model	Equivalent stress (MPa)	Deformation (mm)	Ultimate strength (MPa)	FOS
Conceptual design	13.066	6.855	33	2.53

Table 4 Drop test analysis

Model	Equivalent stress (MPa)	Deformation (mm)	FOS
Concept 4	43.436	6.68	4.14

sheet thickness and addition of rib, the deformation changes marginally, but the equivalent stress increases due to stress localization. The FOS is less than specified limited; thus, the model cannot be implemented. In Concept 4, due to increase in

contact area at the junction, the stress localization is reduced; thus, the equivalent stress is low. The FOS is above the specified limit. Thus, this model is acceptable. Introduction of rib will reduce the quality of spot weld between the deck reinforcement and the wrapper in the cabinet assembly; thus, to add rib in the reinforcement, a similar rib needs to be added in the wrapper. Addition of rib increases the moment of inertia thus reduces the bending stress, but from the above data, we can observe that if we add rib in the design, the maximum deformation reduces but the maximum equivalent stress increases. This is due to stress localization.

Conceptual Model—Deck Reinforcement Incorporation of deck reinforcement, front cross-reinforcement, compressor mounting plate into a single part resulting in process time reduction.

The DFA complexity factor is decreasing as the number of parts and process time reduces.

As the FOS is under specified limit, the model is acceptable. The conceptual design illustrates that the deck reinforcement can even be totally eliminated by incorporating the features of CMP, deck reinforcement, front cross-reinforcement into a single part which will further benefit in production and cost. But conceptual design cannot be implemented straight away as a drastic change of the product is not easily implementable. Thus, only Concept 4 is suitable.

As in static structural analysis, the FOS of Concept 4 lies in the specified limit, drop test analysis was done to analyze the part during drop. The EPS base acts as a cushion while impact; thus, the equivalent stress is low. The FOS is within specified limit, i.e., 2. Thus, the model is acceptable.

5 Conclusions

The design optimization and study of the deck reinforcement was done in which four concepts were made and the final concept selection was done on the basis of cost saving, structural strength, ease of manufacturing, and quality. The final design is flexible in terms of joining methods as spot welding and clinching both can be implemented. The benefits the new design offers are reduction in sheet thickness, removal of reinforcement sheet which will reduce the process time, improvement in quality offered by increased surface area, and ease of mass manufacturing. The conceptual design illustrates that the deck reinforcement can even be totally eliminated for future development by incorporating the features of CMP, deck reinforcement, front cross-reinforcement into a single part which will further benefit in production and cost. But conceptual design cannot be implemented straight away as a drastic change of the product is not easily implementable.

References

1. Curtis, R.N.: Structural optimization of a refrigerator cabinet. In: International ANSYS Conference (2002)
2. Jeong, G.-E., Kang, P., Youn, S.-K., Yeo, I., Song, T.-H., Kim, J.O., Kim, D.W., Kuk, K.: Study of structural stiffness of refrigerator cabinet using the topology optimization of a vacuum insulated panel (VIP). *J. Korean Soc. Precis. Eng.* **32**(8), 727–734 (2015)
3. Yuan, H., Fan, G.: Refrigerator cabinet foaming mold accurate design and manufacture based on the vacuum Deformation mechanism. In: 2nd International Conference on Electronic & Mechanical Engineering and Information Technology (2012)
4. Emes, M.R., Hepburn, I.D., Ray, R.J., Worth, L.B.C.: Structural analysis of a cryogen-free refrigerator for space. *Cryogenics* **41**, 771–779 (2002)
5. Youn, S.-J., Noh, Y.: Reliability-based design optimization of refrigerator door hinges using PIDO technology. *Int. J. Precis. Eng. Manuf.* **16**(4), 715 (2015)

Use of Low-Fidelity Codes for Teaching Aircraft Design



H. K. Narahari and Deepak Madhyastha

Abstract The concept of using unmanned aerial vehicles (UAVs) for aerial surveillance is acquiring lot of importance in military as well as public sectors. The use of rotary wing UAVs for surveillance has gained popularity due to the hovering capabilities. The endurance and range for the rotary wing are considerably less compared to fixed-wing UAVs. The range and time span of surveillance can be remarkably improved with use of fixed-wing UAVs for aerial surveillance. The present work concentrates on developing a conceptual design procedure for the fixed-wing UAVs using low-fidelity codes and applying the constraint diagram approach. The performance requirements of the proposed UAV were used, in current design procedure, to generate constraint diagram from which design drivers like power loading, wing loading and maximum lift coefficient were obtained. The procedure is applied for the design of a fixed-wing (wingspan < 3 m) conventional configuration UAV with electric propulsion system.

Keywords Aircraft design · Constraint diagram · UAV

1 Introduction

The concept of using unmanned aerial vehicles (UAVs) for aerial surveillance is acquiring lot of importance in military as well as public sectors. The use of rotary wing UAVs for surveillance has gained popularity due to their hovering capabilities. The endurance and range of the rotary wing are considerably less compared to the fixed-wing UAVs. The range and time span of surveillance can be remarkably improved with the use of fixed-wing UAVs for aerial surveillance. Aircraft design, as in the case of any design activity, is iterative in nature where several parameter combinations need to be tried before freezing of external shape. Low-fidelity

H. K. Narahari (✉) · D. Madhyastha

Department of Automotive and Aeronautical Engineering, Faculty of Engineering and Technology, M. S. Ramaiah University of Applied Sciences, Bengaluru 560058, India
e-mail: narahari.aae.et@msruas.ac.in

© Springer Nature Singapore Pte Ltd. 2019

U. Chandrasekhar et al. (eds.), *Innovative Design, Analysis and Development Practices in Aerospace and Automotive Engineering (I-DAD 2018)*, Lecture Notes in Mechanical Engineering, https://doi.org/10.1007/978-981-13-2718-6_11

107

computer codes like XFOIL and NASA's OpenVSP are available in open domain and can be used during the initial conceptual design. The present work concentrates on developing a conceptual design procedure for the fixed-wing UAVs, using open domain low-fidelity codes and applying the constraint diagram approach. The performance requirements of the UAV developed in current design procedure were used to generate constraint diagram from which UAV design drivers like power loading, wing loading and maximum lift coefficient were obtained. The wing alone and the whole UAV were analysed in low and high fidelity CFD codes to confirm the performance achieved.

2 Design Procedure

A survey was conducted on the UAVs with wingspan less than three metres and also on those which fall under mini category of UAV classification. With the survey data as foundation, design charts were generated. Some of the useful charts developed were maximum take-off mass versus wingspan, aspect ratio of wing versus endurance of the aircraft, etc. The charts were used to relate the performance variables to the geometric characteristics, through which the values of design variables were established. Based on the performance requirements of the mini UAV, the design procedure was initiated through the constraint diagram generation as put forward in [1, 2]. The design drivers such as wing and power loading and maximum lift coefficient of the wing were obtained as outcomes of the constraint diagram. A wing geometry was generated based on the wing loading and maximum take-off mass, while the electric propulsion system components were selected based on the power loading value and sturdiness in the build quality. The selected wing aerofoil and designed wing were analysed in low and high fidelity CFD codes to validate the design performance.

The aerofoils were analysed in XFLR5, software based on XFOIL code and later in ANSYS FLUENT, the commercial finite volume method-based solver of RANS equations. Based on the drag polar and maximum lift coefficient, an aerofoil was selected for the wing. The wing was analysed using three low-fidelity codes (a) panel code (b) OpenVSP + VSAERO and (c) XFLR5 software and verified by ANSYS FLUENT software (high fidelity CFD code). These results were verified by using a commercial CFD package FLUENT. The Navier–Stokes equations were solved using pressure-based solver available in ANSYS FLUENT software. The Spalart–Allmaras turbulence model was chosen to model the turbulent flow based on agreement of the numerical analysis results and the experimental ones. The Reynolds number was calculated as 217,143 based on the cruise flight conditions, which fell under turbulent flow regime.

The propulsion system components were analysed in eCalc and MotoCalc, codes which are meant for analysis of the electric motor propulsion system. CAD models of the UAV subsystems, payloads and avionics were generated along with the mass properties of the corresponding components in CATIA to extract the location of

centre of gravity of the assembled UAV and to calculate the mass moments of inertia of the same. The fuselage design was performed by placing the constituents in a compact arrangement and later wrapping with surfaces, keeping easy facilitation of fabrication in mind.

The empennage design was performed based on the procedure available in [3] and the ratios available in [4]. The horizontal tail incidence angle was set by iterations performed in XFLR5 software by changing the tail setting angle to make the total moment coefficient zero. The extract of the CAD model was used in creating a model of the whole aircraft in XFLR5 software for stability analysis. The stability of the aircraft was analysed analytically in a MATLAB code developed based on procedure available in [5]. The UAV was analysed for static and dynamic stability in XFLR5 software. After confirmation of the stability, the whole UAV was numerically analysed in ANSYS FLUENT software to confirm the performance of the UAV under cruise conditions. The boundary conditions used were similar to that used in wing analysis. The grid used for UAV analysis was unstructured grid with 2.268 million cells.

3 Results

Two iterations of design were performed based on the constraint diagram approach. From the design drivers obtained from constraint diagram, wing specifications were calculated. The results are presented in Table 1.

The taper ratio for the wing was changed to improve the wing-fuselage compatibility in the second iteration. The dihedral angle was incorporated in second design to improve roll stability of the UAV. The fuselage was developed entirely in CATIA, and to improve the aerodynamics, a circular boom was used to connect the

Table 1 Wing geometry obtained for design iterations

Iteration	1st	2nd	Units
Area of wing S	0.7213	1.2263	m ²
Aspect ratio AR	7	7	–
Span of wing b	2.2471	2.9298	m
Mean aerodynamic chord c	0.3210	0.4185	m
Taper ratio	0.5	1	–
Root chord C_r	0.4280	0.4185	m
Tip chord C_t	0.2140	0.4185	m
Dihedral angle	0	2	°
Cruise velocity	10	9	
Reynolds number	185,045.9	217,143	–
C_L required from wing at cruise	1.3158	0.9555	–

empennage section. The empennage section specifications given in Table 2 were obtained based on the wing characteristics and stability requirements.

To facilitate easy hand launch and deep stall landing, the S1223 aerofoil was chosen for wing design as it had C_l max value of 2.1, and it provided the lift coefficient required at cruise conditions. The aerofoil analysis results obtained from XFOIL and ANSYS FLUENT software at 185,129 Reynolds number (first iteration) agree with experimental results. The aerofoil was carried on to next iteration for the previously mentioned reasons.

The results obtained from OpenVSP for wing + empennage are as shown in Fig. 1. Figure 2 is a comparison between results for wing alone. Agreement between the experimental and analysis results can be observed at low values of absolute angles of attack while the same is lost at high angles of attack. The disagreement in the lift coefficient values might be caused due to the use of velocity inlet and shear wall boundary conditions. Velocity contours were observed on the domain surfaces which indicate the failure of the boundary conditions to mimic the actual environment.

Table 2 Empennage section geometry obtained in second iteration of design

Horizontal tail volume ratio V_H	0.5	Vertical tail volume ratio V_V	0.04
Optimum horizontal tail arm length l_{opt}	1.5 m	Vertical tail area S_{VT}	0.0958 m ²
Horizontal tail area S_{HT}	0.17 m ²	Vertical tail aspect ratio AR_{VT}	1.5
Horizontal tail aspect ratio AR_{HT}	4.6667	Vertical tail span b_{vt}	0.3791 m
Horizontal tail span b_{ht}	0.895 m	Vertical tail chord C_{vt}	0.2527 m
Horizontal tail C_{ht}	0.191 m	Taper ratio	0.5
Horizontal tail incidence angle	5°	Vertical tail root chord C_{vtr}	0.3370 m
Aerofoil used for empennage	NACA0008	Vertical tail tip chord C_{vtt}	0.1685 m

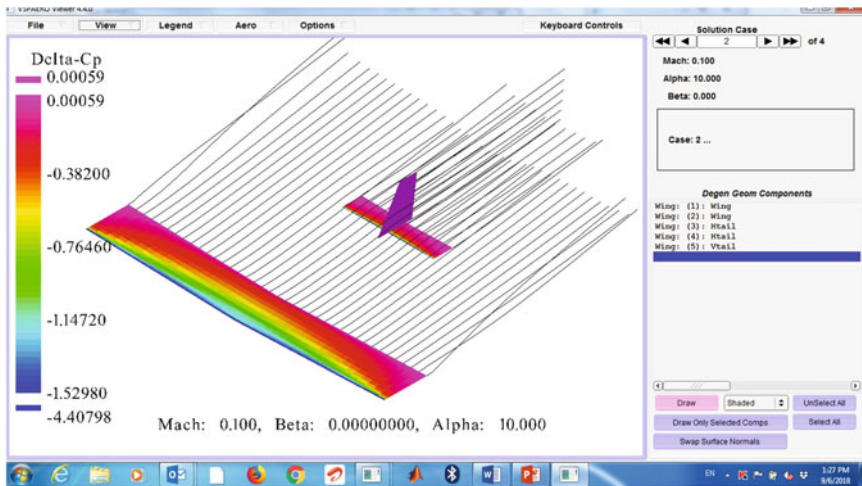


Fig. 1 Delta Cp and trailing wake for wing + empennage at AOA = 10

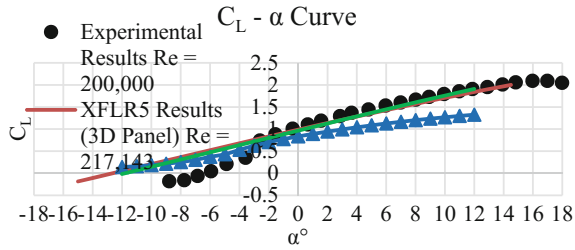


Fig. 2 Lift curve comparison for wing analysis results and experimental aerofoil results

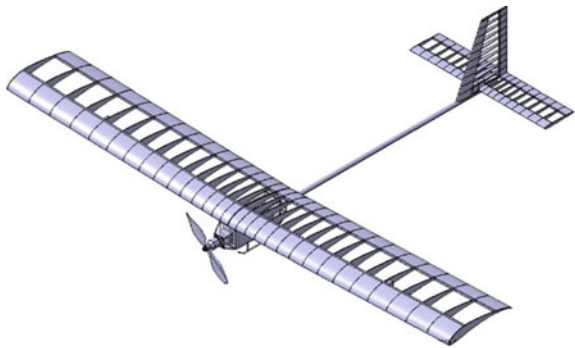


Fig. 3 CAD model of UAV created in CATIA

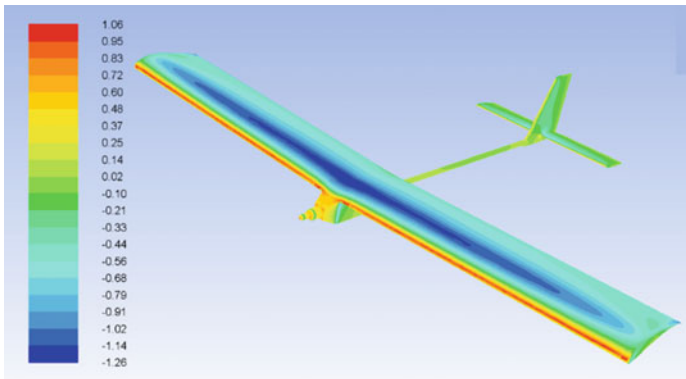


Fig. 4 Pressure coefficient distribution over UAV surfaces obtained from ANSYS FLUENT software

The CAD model developed in CATIA software as shown in Fig. 3 was used to extract the location of centre of gravity and mass moment of inertia.

The pressure distribution over the UAV surfaces, as shown in Fig. 4, was obtained from the UAV analysis in ANSYS FLUENT software with cruise

conditions, i.e. at $Re = 265,397$ and $\alpha = 0^\circ$ as boundary conditions. The UAV generates the required lift coefficient at cruise conditions with minimum moment coefficient. Using the results of analysis, constraint diagram for third iteration of design was generated.

4 Conclusions

The variations in the design drivers converge in 5–6 iterations. The present work is encapsulated in a self-explanatory Excel spreadsheet and OpenVSP scripts, which can be used to conceptually design UAVs propelled by electric propulsion system based on the requirements. The design procedure for the mini category of UAVs was generated by applying the design rules available for commercial airplanes. It can be concluded that the constraint diagram approach can be used for the UAV design procedure without any modifications.

Acknowledgements The second author Mr. Deepak Madhyastha would like to thank MSRSAS for all the support and permission to publish.

References

1. Loftin, L.K.: Subsonic aircraft: Evolution and matching of size to performance. NASA RP 1060 (Aug 1980)
2. Mattingly, J.D., Heiser, W.H., Pratt, D.T.: Aircraft Engine Design. AIAA Education Series, vol. 200, 2nd edn, p. 19
3. Sadraey, M.H.: Aircraft Design: A Systems Engineering Approach. Wiley, West Sussex (2012)
4. Aircraft Aerodynamics and Design Group: Tail Design and Sizing [Online]. Available: <http://adg.stanford.edu/aa241/stability/taildesign.html> (1999). Accessed: 10-June-2015
5. Nelson, R.C.: Flight Stability and Automatic Control. McGraw-Hill International Editions, Singapore (1998)

Drag Reduction for Flow Past a Square Cylinder Using Rotating Control Cylinders—A Numerical Simulation



Ghosh Subhankar, S. Senthilkumar and S. Karthikeyan

Abstract This paper investigates the effect of two control cylinders of same circular cross section on reduction of drag caused by vortex shedding phenomenon at the downstream of the flow past a square cylinder. Numerical computations are performed for a Reynolds number of 100 as this is well below the transitional flow regime where the effect of vortex shedding phenomenon is more significant. Simulations are carried out using a Finite Volume CFD solver for five different positions along with three different rotational speeds (5, 10, 20 rad/s) and directions (clockwise, anticlockwise) of control cylinders. Validation of the base case (i.e., without any control cylinder) shows a good agreement with the available literature data. The transient variations of lift and drag coefficients are monitored for each case and compared with those of the base case. The vortex shedding phenomenon and the physics behind the drag reduction are explained with the help of streamlines and drag coefficient plots. The most effective case with 4% drag reduction is identified when $x_c = 0.65$, $y_c = 0.45$ with the top cylinder rotating in the clockwise direction and the bottom cylinder rotating in the anticlockwise direction with a rotational speed of 20 rad/s.

Keywords Square cylinder · Rotating control cylinder · Drag reduction
Rotational speed

1 Introduction

Bluff body aerodynamics has always been one of the most interesting subjects of research and has got an utmost importance in our current era due to the long range of implicational scope in various hydrodynamics problems like flow past airplanes, ships and civil structures, and combustion flame holder. The phenomenon of vortex

G. Subhankar · S. Senthilkumar (✉) · S. Karthikeyan
Department of Aeronautical Engineering, Vel Tech Rangarajan Dr. Sagunthala
R&D Institute of Science and Technology, Chennai 600062, India
e-mail: s.senthilms@gmail.com

© Springer Nature Singapore Pte Ltd. 2019
U. Chandrasekhar et al. (eds.), *Innovative Design, Analysis and Development Practices in Aerospace and Automotive Engineering (I-DAD 2018)*, Lecture Notes in Mechanical Engineering, https://doi.org/10.1007/978-981-13-2718-6_12

shedding and drag is one of the major issue engineers faces when working with these bluff bodies. Several researchers carried out study on flow over circular cylinder to analyses the wake structures; drag reduction and vortex shedding control by using the various active and passive control techniques. Some examples of passive and active methods are the end plate, splitter plate, base bleed, oscillation in line with the incident flow, rotating oscillation, span-wise waviness to front stagnation face of a rectangular cylinder, rotary, transverse oscillations, or stream-wise. Various vortex control methods can be found in the review paper by Choi et al. [1]. Among which the effect of rotating control cylinders have got a major importance in the list of recent active methodology research about flow past bluff bodies. Hence the current study emphasizes on drag reduction over square cylinder using contra-rotating control cylinder pair.

Saha et al. [2] have investigated the effect of blowing in the form of jet on the vortex shedding at the Reynolds number of 100. They did it for different number of jets, jet velocity profiles, and different blowing velocities. They have observed that parabolic velocity profile is more effective in suppression of vortex shedding compared to the uniform velocity profile. They have mentioned that the vortex shedding has reduced because of the lowered interaction of separated shear layers leading to weak shear layers due to vorticity diffusion. Islam et al. [3] have studied flow over a square cylinder of diameter (D) in presence of multiple small control cylinders at low Reynolds numbers ($Re = 100$ and 160). They have placed the control cylinders at a specific distance (s) and angle of attack (Θ). They have defined a parameter (g) = s/D . They have found that the drag is reduced 99.8 and 97.6% for $(\Theta, g) = (30^\circ, 3)$ at $Re = 100$ and 160 , respectively. The vortex shedding completely disappeared in $Re = 100$ at $(\Theta, g) = (45^\circ, 0.5)$, $(45^\circ, 0.75)$, $(45^\circ, 1)$, and $(45^\circ, 1.5)$, but at $Re = 160$, vortex shedding disappeared at $(\Theta, g) = (30^\circ, 0.5)$. Ali et al. [4] have investigated the interaction of a square cylinder wake and a detached flat plate of length equal to one cylinder height (D) at various downstream locations (G) at the Reynolds number 150. They have observed two modes of wake plate interaction. For short gaps ($G \leq 2D$), a shear layer plate interaction is observed with the first type of flow regime. They have found out that the optimum position of the flat plate will be $G \approx 2D$ for maximum reduction in the fundamental vortex shedding frequency, root mean square lift, and mean drag of the cylinder. They have noticed a new wake plate interaction with sudden jump in the Strouhal number between $2D \leq G \leq 2.5D$. They have concluded that the critical gap lies between $2D \leq G \leq 2.5D$. Zhang et al. [5] have investigated the effect of blowing and suction from the channel walls on the flow past a square cylinder placed inside of that channel numerically. They carried out their study with two different Reynolds numbers of 175 and 250 for both the cases of wall blowing velocity ratios of 0.05, 0.1 and suction ratios of 0.1, 0.25, and 0.3. They have concluded that blowing has a stabilizing effect on the flow past a confined cylinder and critical Reynolds number increases with the increase in blow speed. They have mentioned about a steady asymmetric solution, exist in a certain range of parameters in the case of suction through channel walls. Pantokratoras et al. [6] investigated the laminar flow behavior around the square cylinder by blowing or suction in the theoretical rear

and forward stagnation points at different Re number from 0.001 to 40. And they found that for the case windward injection and leeward suction followed by the windward blowing can suppress the natural vortex shedding behind the cylinder than all other combination of suction and blowing.

2 Computational Methodology

Commercially available CFD code, ANSYS Fluent™ is used for the flow simulations and the laminar flow mathematical equations are solved under incompressible pressure-based SIMPLE algorithm. A second-order upwind scheme is used for the convective flux with the convergence threshold residuals of 10^{-4} . Quad-type meshing elements are preferred. Figure 1b shows the zoomed view of grid structure of the computational domain. The velocity inlet and pressure outlet boundary conditions are used for inlet, outlet, as shown in Fig. 1a. The no-slip boundary condition is used on the wall of the main and control cylinder surface.

3 Results and Discussion

Initially, a grid independent study has performed to make sure that the solution is independent of grid size. In the present investigation, Reynolds number of 100 is fixed based on main square cylinder of side L . The domain sizes in the upstream and downstream are $X_U = 7L$, $X_D = 20L$, respectively and in the Y direction, $Y_U = 10L$, $Y_D = 10L$, respectively as shown in Fig. 1. The origin axis coincides with the center of the main square cylinder and all the dimensions measured with respect to this origin. The computation is performed for flow over square cylinder without control circular cylinders with three different grid sizes as mentioned in Table 1. This is named as baseline case. From the grid independent study the grid size, G2 is

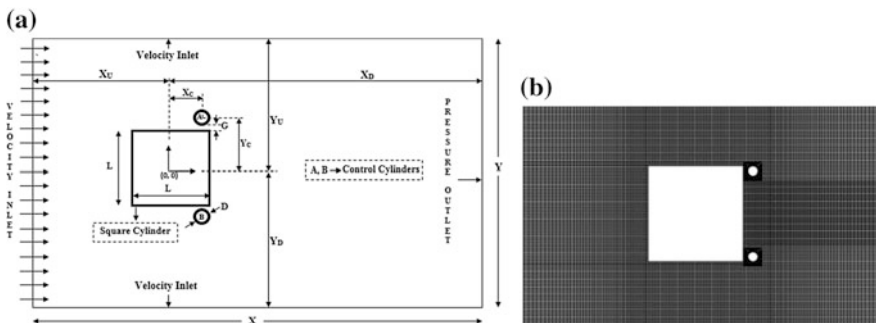


Fig. 1 a Domain specification. b Enlarged mesh structure near the square cylinder

Table 1 Grid independence study

Grid name	No of elements	$\overline{C_D}$	Strouhal number	Reference value [1]	Error (%)
				$\overline{C_D}$	$\overline{C_D}$
G1	37,931	1.467	0.139	1.524	3.74
G2	75,339	1.465	0.139		4.19
G3	150,331	1.465	0.134		3.87

Table 2 Case name based on position of control cylinders

S. No.	Control cylinder position				Case name
	Top		Bottom		
	X_c	Y_c	X_c	Y_c	
1	0.45	0.6	0.45	-0.60	Case 1
2	0.60	0.45	0.60	-0.45	Case 2
3	0.60	0.25	0.60	-0.25	Case 3
4	0.65	0.45	0.65	-0.45	Case 4
5	0.65	0.25	0.65	-0.25	Case 5

chosen for further numerical computations. In the present study, the variation of the drag value is analyzed closely after placing a pair of circular control cylinders of diameter $D = 0.1L$ at five different positions with respect to the main square cylinder.

The simulations have been carried out for two different rotational directions for each of the five cases. The name conventions used in the current discussion for two different cases of rotational directions are T-ACW/B-CW for top control cylinder rotating anticlockwise and bottom control cylinder rotating clockwise rotation and T-CW/B-ACW for the opposite case of rotation, i.e., top control cylinder rotating clockwise and bottom control cylinder rotating anticlockwise rotation. The position of counter-rotating control cylinder pair for different positional case are mentioned with the different values of X_C and Y_C as indicated in Fig. 1. Five different locations of the control cylinder pair are shown in Table 2.

3.1 Effect of Rotational Direction and Speed on Drag

In case 1, it was observed that there is a 12.01% increase of C_D value at 5 rad/s for the rotational condition of T-ACW/B-CW (Tables 2 and 3). For the same case, the C_D is increasing with the speed by 12.69 and 14.10% at 10 rad/s and at 20 rad/s, respectively as compared to the baseline. For the same position of control cylinders with a change in rotational direction i.e., T-CW/B-ACW, it is observed that the drag is still greater than the base value by 11.09% at 5 rad/s. With further increase in the

Table 3 Comparison of CD for T-ACW/B-CW and T-CW/B-ACW case at different speed

Rotation direction and speed of control cylinders						
Rotational speed	T-ACW/B-CW			T-CW/B-ACW		
	5 rad/s	10 rad/s	20 rad/s	5 rad/s	10 rad/s	20 rad/s
Case name	$\overline{C_D}$					
Case 1	1.641	1.651	1.672	1.628	1.617	1.597
Case 2	1.451	1.457	1.469	1.439	1.433	1.421
Case 3	1.437	1.439	1.442	1.436	1.435	1.432
Case 4	1.423	1.427	1.435	1.417	1.413	1.405
Case 5	1.439	1.440	1.444	1.437	1.435	1.432

speed, the drag starts to decrease but the value is still higher than that of the base value. The C_D values are 10.39 and 8.98 for 10 and 20 rad/s, respectively.

In case 2, there is a 0.97% decrease in drag value at 5 rad/s with T-ACW/B-CW. With the increase of speed, there is an increase in drag from the base value. Though the drag is observed to be increased with the speed, the estimated drag value for 10 rad/s is 0.55% lesser than the baseline value, But for 20 rad/s the drag value becomes 0.30% greater compared to the base value. For the same position with T-CW/B-ACW at 5 rad/s, it is found that 1.80% of decrease of drag from the baseline value and further increase in speed reduced the drag by 2.20 and 3.01% at 10 rad/s and at 20 rad/s, respectively.

The case 3 shows 1.92% of drag reduction at 5 rad/s with T-ACW/B-CW condition and drag keeps on increasing with the speed but still remains 1.81% less at 10 rad/s and 1.58% less at 20 rad/s compared to the base value. For T-CW/B-ACW, there is a 1.96% reduction in drag for 5 rad/s. With the increase in speed, the drag value starts to drop and acquire a 2.06 and 2.2% reduction in drag from the base value for 10 and 20 rad/s, respectively. The Case 4 with T-ACW/B-CW, it is observed that as compared to the base value, the drag reductions by 2.87, 2.61, and 2.06% at 5, 10, and 20 rad/s, respectively, while for Case 4 with T-CW/B-ACW, further drag reduction is found and the values are 3.29, 3.57, and 4.10% at 5, 10, and 20 rad/s, respectively. In case 5 with T-ACW/B-CW condition, the reduction in drag is decreased as compared with the previous cases but these values are still lower than those of baseline and about 1.8, 1.69, and 1.47% at 5, 10, and 20 rad/s, respectively. As we alternate the rotational direction as T-CW/B-ACW, the similar trend is found with different reduction values as 1.93, 2.04, and 2.25% at 5, 10, and 20 rad/s, respectively.

3.2 Time History of C_L and C_D Values

The C_L and C_D time history has been monitored for all the cases, here only the base and optimum drag reduction cases have shown for better understanding. And the

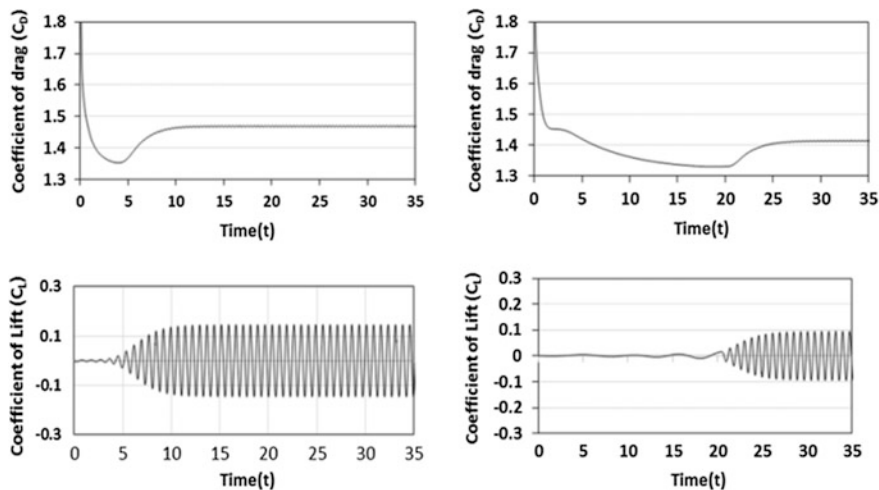


Fig. 2 Time histories of C_L and C_D : Left: Baseline and Right: Case 4 (T-CW/B-ACW)

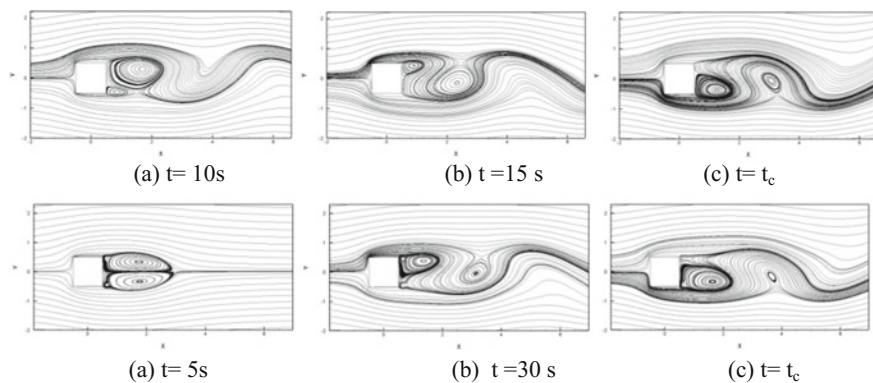


Fig. 3 Streamline evolution at different time instants: Top: Base and Bottom: Case 4 (T-CW/B-ACW)

plot infers that there is a reasonable drag reduction with the case 4 with T-CW/B-ACW, as shown in Fig. 2. This may be due to the presence of rotating control cylinders positioned downstream in the wake region which induces an additional momentum (Fig. 3) to the near wake flow hence alters the flow behaviors behind the square cylinder leads to the reduction in drag, as evident from Fig. 2. There is a significant difference found on the peak value of the C_L history and delay in shedding process is also seen (see Fig. 2) since the flow downstream of the cylinder still has shedding nature as can be seen clearly in the streamlines plot Fig. 3. However, the shedding time remains almost the same for both the cases.

4 Conclusion

Active drag reduction for flow over a square cylinder has been investigated with two rotating circular control cylinders of same circular placed at the downstream of the flow. When the top control cylinder rotates in clockwise direction and bottom control cylinder rotates in anticlockwise, the drag decreases with the increase in speed. When the top control cylinder rotates in anticlockwise and bottom control cylinder rotates in clockwise the drag increases with the increase in speed. However, the drag reduction in comparison with baseline was found for all the cases except the case 1. It shows that the position of the control cylinder at near wake region plays a major role in drag reduction. And highest percentage of drag reduction was found for case 4 (T-CW/B-ACW) at 20 rad/s which is around 4%.

References

1. Choi, H., Jeon, W.P., Kim, J.: Control of flow over a bluff body. *Annu. Rev. Fluid Mech.* **40**, 113–139 (2008)
2. Saha, A.K., Shrivastava, A.: Suppression of vortex shedding around a square cylinder using blowing. *Sadhana* **40**(3), 769–785 (2015)
3. Islam, S.U., Manzoor, R., Islam, Z.U., Kalsoom, S., Ying, Z.C.: A computational study of drag reduction and vortex shedding suppression of flow past a square cylinder in presence of small control cylinders. *AIP Adv.* **7**(4), 045119 (2017). <https://doi.org/10.1063/1.4982696>
4. Ali, M.S.M., Doolan, C.J., Wheatley, V.: Flow around a square cylinder with a detached downstream flat plate at a low Reynolds number. In: 17th Australasian Fluid Mechanics Conference, New Zealand (2010)
5. Zhang, W., Jiang, Y., Li, L., Chen, G.: Effects of wall suction/blowing on two-dimensional flow past a confined square cylinder. *SpringerPlus* **5**(1), 985 (2016). <https://doi.org/10.1186/s40064-016-2666-7>
6. Pantokratoras, A.: Laminar flow across an unbounded square cylinder with suction or injection. *Z. Angew. Math. Phys.* **68**(1) (2017)

Study the Effect of Mill Scale Filler on Mechanical Properties of Bidirectional Carbon Fibre-Reinforced Polymer Composite



Aman Soni and Amar Patnaik

Abstract In this study, the effect of mill scale as the filler with different weight percentage in carbon fibre reinforced polymer composites is investigated. The composites are fabricated with 0, 5 and 10 wt% of mill scale, respectively, using hand lay-up method. The mechanical performance of the composites is evaluated by tensile test, flexural test, inter-laminar shear stress and micro-Vickers hardness test. It is observed that incorporation of mill scale in composite increases the tensile strength by 2.40% (5 wt%) and 4.73% (10 wt%); flexural strength by 35.34% (5 wt%) and by 17.78% (10 wt%); ILSS by 44.40% (5 wt%) and 41.45% (10 wt%); hardness by 14.70% (5 wt%) and by 25.49% (10 wt%). The results reveal that mill scale as filler in composite significantly affects the mechanical properties. This work may provide a meaningful way to modify the conventional manufacturing methods in various industrial applications of CFRPs.

Keywords Carbon fibre-reinforced composites · Mill scale · Epoxy resin

1 Introduction

Conventional carbon fibre epoxy-reinforced composites are widely used in aerospace, automotive, civil engineering, sports goods and an increasing number of other applications due to their versatile properties, wherein matrix plays a significant role in determining the mechanical behaviour of the composite. Epoxy resin is the most suitable bonding agent for carbon fibre composites meant for high-strength applications. Extensive research has been conducted to enhance the strength properties of carbon fibre-reinforced composites. In order to achieve this, methods like hydrogen-plasma treatment, high-pressure hydrogen treatment, heat treatment have been adopted [1–4].

A. Soni · A. Patnaik (✉)

Department of Mechanical Engineering, Malaviya National Institute of Technology, Jaipur 302017, India
e-mail: patnaik.amar@gmail.com

© Springer Nature Singapore Pte Ltd. 2019

U. Chandrasekhar et al. (eds.), *Innovative Design, Analysis and Development Practices in Aerospace and Automotive Engineering (I-DAD 2018)*, Lecture Notes in Mechanical Engineering, https://doi.org/10.1007/978-981-13-2718-6_13

121

Surface modification of carbon fibre is also possible with deposition of certain strengthening agents over the surface of carbon fibre [5–8]. However, the interfacial strength between CFs and the matrix tends to be weak due to poor wettability and adsorption between CFs and the matrix caused by the smooth and chemically inert surfaces of CFs [9–17]. Apart from this, a wide range of techniques has been developed to enhance the mechanical behaviour through modification of resin matrix. Several research teams have explored the modification of the properties of epoxy resins by introducing various toughening agents such as reactive liquid rubber [18], thermoplastics [19, 20], micron-scale rubber particles, nano-rubber particles and nano-scale fillers [21–25].

In recent years, mill scale has attracted tremendous attention because of its excellent mechanical, electrical and thermal properties. Considering the versatile nature of its properties, enhancement of mechanical properties of carbon fabric/epoxy composites is possible through mill scale as filler. But since not much work has been done on investigating the effect of adding mill scale as filler on the mechanical properties of carbon fibre epoxy reinforced composites, this study aims to observe the same.

2 Experimental

2.1 Materials

PAN-based bidirectional plain woven carbon fabrics, 1000 mm in width, with a dry weight of 200 g/m² per layer, are supplied by Hindoostan Composite Solutions, Mumbai, India. Industrial-grade epoxy resin and hardener are bought from Ares Chemical Works, Jodhpur, India. The modifier of the matrices is mill scale, diameter 53–75 µm collected from a local rolling mill, Jaipur, India. To evaluate the mechanical properties of the carbon fibre composites, tensile tests, flexural tests and ILSS tests are performed on Universal Testing Machine (Heico Corporation). The hardness of the samples is tested on micro-Vickers hardness testing machine (UHL VMHT).

2.2 Fabrication of Composites

The four-layered carbon fibre-reinforced composites are fabricated using the hand lay-up method. Firstly, mill scale is magnetically separated out so that any unwanted non-ferrous particles are removed. Thereafter, maintaining 10:1 ratio of epoxy-hardener, a composite is created with 0 wt% of mill scale filler in its matrix. Similarly, two more composites are fabricated with 5 and 10 wt% of filler in the matrix, rest all parameters remaining the same. Each composite is allowed to

solidify for a span of 24 h in dry conditions. The three prepared composites are named as C-0, C-5 and C-10 on the basis of wt% of filler present in them. Samples shall be referred to by the same names now on.

2.3 Characterization Techniques

Tensile Test The tensile strength of the composites is observed using Universal Testing Machine, driven by a hydraulic mechanism. Samples were prepared in accordance with ASTM D3039/D3039 M. Samples of gauge length 70 mm are tested fixing the cross-head speed at 0.1 mm/s. The sample dimensions are 140 mm × 10 mm × 1.8 mm (70 mm being the total tab length). The final tensile strength is the average of the three readings obtained for each composite sample. The tensile strength is calculated by the following expression:

$$E = \frac{P}{A} \quad (1)$$

where

E = Tensile strength (or peak stress) (N/sqmm);

P = Peak load (N);

A = Area of cross section (sqmm).

Flexural test The samples for flexural testing (3 point loading) are prepared in accordance with ASTM D790. The span length is 57.6 mm, which is in exactly 32:1 ratio with the sample thickness. The overall sample dimensions being 57.6 mm × 10 mm × 1.8 mm. The speed of testing is 1 mm/min maintained throughout the testing. The stress may be calculated for any point on the load-deflection curve by the following equation:

$$\sigma = \frac{3PL}{2bh^2} \quad (2)$$

where

σ = stress at the outer surface in the load span region, MPa,

P = applied force, N,

L = support span, mm,

b = width of the beam, mm, and

h = thickness of beam, mm.

The flexural strength of a sample is equal to the maximum stress at the outer surface corresponding to the peak applied force prior to the failure. It is calculated in accordance with Eq. 2 by letting P equal the peak applied force. The final strength is taken to be the average of three readings obtained for each composite.

Inter-Laminar Shear Stress Test The span length for inter-laminar shear stress is 24 mm, which was in accordance with ASTM D 2344/D 2344M. The dimensions of the sample were 24 mm × 10 mm × 1.8 mm. The speed of testing is set to be 1 mm/min; readings of load are recorded at a fixed interval of 0.1 s. The short beam strength can be calculated as

$$F^{\text{sbs}} = \frac{0.75P_m}{bh} \quad (3)$$

where

F^{sbs} = short beam strength, MPa;

P_m = maximum load observed during the test, N;

b = measured specimen width, mm, and

h = measured specimen thickness, mm.

The test is performed on three samples out of each composite, and strength values are noted. The final strength of each composite is taken to be the average of these three readings obtained.

Micro-Vickers Hardness Test The hardness of composites was measured at a load of 200 gm. The HV number is determined by the ratio F/A , where F is the force applied to the diamond in kilograms-force and A is the surface area of the resulting indentation in square millimetres. A can be determined by the formula.

$$A = \frac{d^2}{\sin\left(\frac{136^\circ}{2}\right)} \quad (4)$$

This can be approximated by evaluating the sine term to give

$$A = \frac{d^2}{1.8544} \quad (5)$$

where d is the average length of the diagonal left by the indenter in millimetres. Hence,

$$\text{HV} = \frac{F}{A} = \frac{1.8544F}{d^2} \quad (6)$$

where F is in kgf and d is in millimetres.

The corresponding units of HV are then kilograms-force per square millimetre (kgf/mm^2). To calculate Vickers hardness number using SI units, one needs to convert the force applied from Newton to kilogram-force by dividing by 9.80665 (standard gravity). This leads to the following equation:

$$HV = \frac{0.1891F}{d^2} \quad (7)$$

where F is in N and d is in millimetres.

The final hardness value for each composite is taken to be the average of five test readings obtained for every composite.

3 Results and Discussion

3.1 Analysis of Data in Tensile Test

Observation The tensile strength values and the corresponding peak loads of the three carbon fibre reinforced composites—C-1, C-5 and C-10 are as shown in Fig. 1.

Comparison of Tensile strength The average tensile strength of composite C-0, C-5 and C-10 using UTM is 282.573, 289.33 and 295.90 MPa, respectively. Therefore, it is clearly identified that the tensile strength level of carbon fibre epoxy-reinforced composite has increased by 2.40% for C-5 and 4.73% for C-10. This indicates that mill scale nanoparticles have a strong interface with epoxy resin. While the crack initiates under load in the matrix, as they propagate, they are blocked by particles. The mill scale particles cause branching by blocking the crack tip and deflections in the crack directions, which create significant toughness mechanisms.

Fig. 1 Tensile Strength behaviour variation with wt% of mill scale

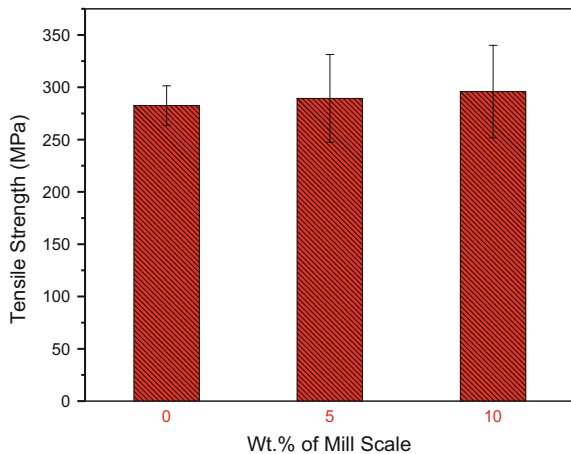
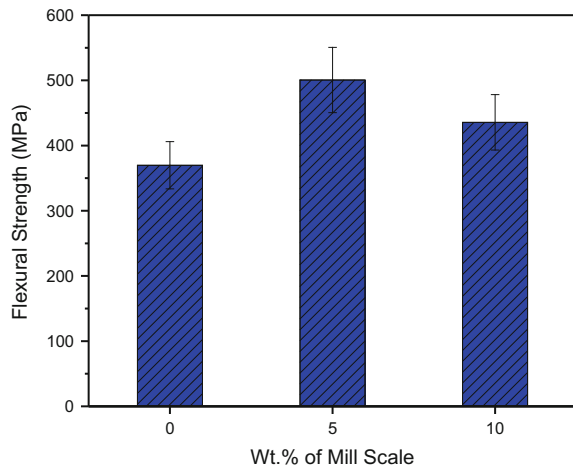


Fig. 2 Flexural Strength behaviour variation with wt% of mill scale



3.2 Analysis of Data in Flexure Test

Observation The flexural strength and the corresponding peak loads of the three respective composites are as shown in Fig. 2.

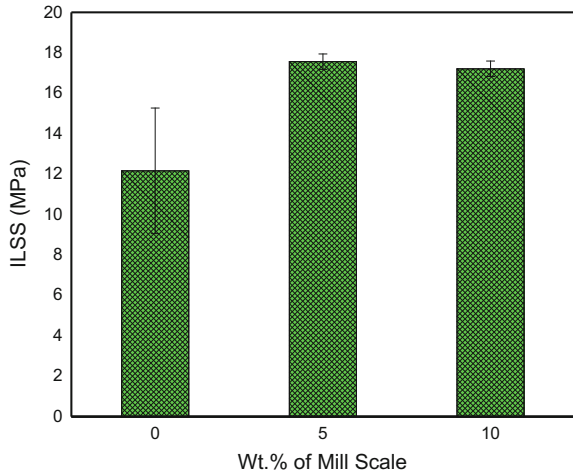
Comparison of Flexural strength Average flexural strengths of composites C-0, C-5 and C-10 are 369.824, 500.507 and 435.610 MPa, respectively. Therefore, the flexural strength of carbon fibre epoxy-reinforced composite increases by 35.34% for C-5 and 17.78% for C-10 as compared to C-0. It can be noticed that increase in strength is more for C-5 than C-10. It is established that the inclusion of mill scale nanoparticles improves the flexural toughness of composites due to strong interface with epoxy. The nanoparticles in the matrix also undergo branching which prevents the growth of cracks and hence improves strength. However, with the concentration of nanoparticles, the strength undergoes a slight reduction. This happens because of abundance of filler nanoparticles in the vicinity in the matrix form clusters, which in turn serves as stress-concentrated zones when subjected to loading, resulting in premature cracking.

3.3 Analysis of Data in Inter-laminar Shear Stress Test

Observation The inter-laminar shear stress values and the corresponding peak loads of the three carbon fibre-reinforced composites—C-1, C-5 and C-10 are as shown in Fig. 3.

Comparison The average values of inter-laminar shear stress as observed for the three respective composites C-0, C-5 and C-10 are 12.16, 17.56 and 17.20 MPa. The percentage rise of inter-laminar shear stress for C-5 and C-10 as compared to

Fig. 3 ILSS behaviour variation with wt% of mill scale

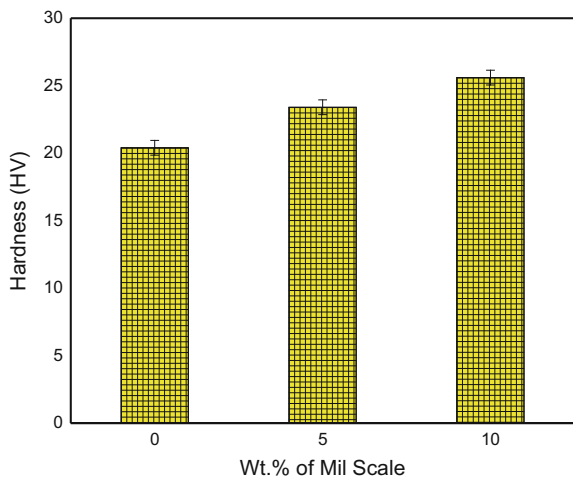


C-0 is 44.4% and 41.45%, respectively. The incrementing pattern of ILSS with the rise in filler amount is similar to the increment pattern of flexural strength; i.e., the rise in ILSS for C-5 is more than that of C-10, both as compared to C-0. The reasons for this pattern in ILSS results are similar to those of flexural test.

3.4 Analysis of Data in Micro-Vickers Hardness Test

Observation The hardness values of C-1, C-5 and C-10 as obtained in micro-Vickers hardness test are as shown in Fig. 4.

Fig. 4 Hardness variation with wt% of mill scale



Comparison The average hardness values of composites C-0, C-5 and C-10 using micro-Vickers hardness test are 20.4 HV, 23.4 HV and 25.6 HV, respectively. It is clearly identified that hardness has increased by 14.70% for C-5 and 25.49% for C-10 as compared to C-0. Clearly, the surface hardness of composites is increasing with increase in wt% of filler in its matrix. Mill scale nanoparticles are well dispersed in the matrix and along with epoxy; they also resist the force of indenter. More the number of nanoparticles, more is the resistance to external force. Therefore, the hardness of the composite increases with increase in the concentration of mill scale in the matrix.

4 Conclusions

For the purpose of improving mechanical properties of carbon fibre epoxy-reinforced composites, mill scale is used as filler in the matrix. The effect of different proportions of mill scale on mechanical properties of composites is examined. Composites consisting of 0%, 5% and 10% mill scale filler in matrices were fabricated using hand lay-up method. The experimental results suggest that mill scale can significantly improve the mechanical behaviour of carbon fibre composites. Tensile strength improvements for 5 and 10 wt% of mill scale are 2.40 and 4.73%. The flexural strength of composite increases by 35.34% for 5 wt% and 17.78% for 10 wt% addition of mill scale filler. Following the same pattern, ILSS increases by 44.40% and 41.45%. Hardness increase is rather regular, i.e. 14.70% for 5 wt% and 25.49% for 10 wt%.

Acknowledgements This project was supported by Advanced Research Laboratory for Tribology, Department of Mechanical Engineering, Malaviya National Institute of Technology, Jaipur, India. The authors also extend thanks to Research Laboratory, Department of Metallurgy Engineering, Malaviya National Institute of Technology, Jaipur, India.

References

1. Lee, E.S., Lee, C.H., Chun, Y.S., Han, C.J., Lim, D.S.: Effect of hydrogen plasma-mediated surface modification of carbon fibers on the mechanical properties of carbon-fiber-reinforced polyetherimide composites. *Compos. Part B* (2016). <https://doi.org/10.1016/j.compositesb.2016.10.088>
2. Jeon, S.K., Kwon, O.H., Jang, H.S., Ryu, K.S., Nahm, S.N.: Effect of high pressure hydrogen on the mechanical characteristics of single carbon fiber. *Appl. Surf. Sci.* (2017). <https://doi.org/10.1016/j.apsusc.2017.07.005>
3. Baklanova, N.I., Lozanov, V.V., Morozova, N.B., Titov, A.T.: The effect of heat treatment on tensile strength of iridium-coated carbon fiber. *Thin Solid Films* (2015). <https://doi.org/10.1016/j.tsf.2015.02.042>

4. Fan, W., Wang, Y., Wang, C., Chen, J., Wang, Q., Yuan, Y., Niu, F.: High efficient preparation of carbon nanotube-grafted carbon fibers with the improved tensile strength, *Appl. Surf. Sci.* <https://doi.org/10.1016/j.apsusc.2015.12.189>
5. Sun, J., Zhao, F., Yao, Y., Jin, Z., Liu, X., Huang, Y.: High efficient and continuous surface modification of carbon fibers with improved tensile strength and interfacial adhesion. *Appl. Surf. Sci.* (2017). <https://doi.org/10.1016/j.apsusc.2017.03.279>
6. Hung, P.Y., Lau, K.T., Fox, B., Hameed, N., Lee, J.H., Hui, D.: Surface modification of carbon fibre using graphene-related materials for multifunctional composites. *Compos. B* (2017). <https://doi.org/10.1016/j.compositesb.2017.09.010>
7. Sun, J., Li, H., Feng, L., Jia, Y., Song, Q., Li, K.: A novel treatment of carbon fibers with improving tensile strength to synthesize evenly distributed carbon nanotubes on their surface. *Appl. Surf. Sci.* (2017). <https://doi.org/10.1016/j.apsusc.2017.01.165>
8. Dong, J., Jia, C., Wang, M., Fang, X., Wei, H., Xie, H., Zhang, T., He, J., Jiang, Z., Huang, Y.: Improved mechanical properties of carbon fiber-reinforced epoxy composites by growing carbon black on carbon fiber surface. *Compos. Sci. Technol.* (2017). <https://doi.org/10.1016/j.compscitech.2017.06.002>
9. Wang, C., Li, J., Yu, J., Sun, S., Li, X., Xie, F., Jiang, B., Wu, G., Yu, F., Huang, Y.: Grafting of size-controlled graphene oxide sheets onto carbon fiber for reinforcement of carbon fiber/epoxy composite interfacial strength. *Compos.: Part A*. <https://doi.org/10.1016/j.compositesa.2017.07.015>
10. Sun, J., Zhao, F., Yao, Y., Liu, X., Jin, Z., Huang, Y.: A two-step method for high efficient and continuous carbon fiber treatment with enhanced fiber strength and interfacial adhesion. *Mater. Lett.* (2017). <https://doi.org/10.1016/j.matlet.2017.03.007>
11. Jiang, J., Yao, X., Xu, C., Su, Y., Zhou, L., Deng, C.: Influence of electrochemical oxidation of carbon fiber on the mechanical properties of carbon fiber/graphene oxide/epoxy composites. *Compos.: Part A* (2017). <https://doi.org/10.1016/j.compositesa.2017.02.004>
12. Ma, Q., Gu, Y., Li, M., Wang, S., Zhang, Z.: Effects of surface treating methods of high-strength carbon fibers on interfacial properties of epoxy resin matrix composite. *Appl. Surf. Sci.* (2016). <https://doi.org/10.1016/j.apsusc.2016.04.075>
13. Cole, D.P., Henry, T.C., Gardea, F., Haynes, R.A.: Interphase mechanical behavior of carbon fiber reinforced polymer exposed to cyclic loading. *Compos. Sci. Technol.* (2017). <https://doi.org/10.1016/j.compscitech.2017.08.012>
14. Wang, C., Chen, L., Li, J., Sun, S., Ma, L., Wu, G., Zhao, F., Jiang, B., Huang, Y.: Enhancing the interfacial strength of carbon fiber reinforced epoxy composites by green grafting of Poly (oxypropylene) Diamines. *Compos. Part: A* (2017). <https://doi.org/10.1016/j.compositesa.2017.04.003>
15. Zhang, R.L., Gao, B., Ma, Q.H., Zhang, J., Cui, H.Z., Liu, L.: Directly grafting graphene oxide onto carbon fiber and the effect on the mechanical properties of carbon fiber composites. *Mater. Des.* (2016). <https://doi.org/10.1016/j.matdes.2016.01.003>
16. Song, S.A., Lee, C.K., Bang, Y.H., Kim, S.S.: A novel coating method using zinc oxide nanorods to improve the interfacial shear strength between carbon fiber and a thermoplastic matrix. *Compos. Sci. Technol.* (2016). <https://doi.org/10.1016/j.compscitech.2016.08.012>
17. Feng, L., Li, K., Xue, B., Fu, Q., Zhang, L.: Optimizing matrix and fiber/matrix interface to achieve combination of strength, ductility and toughness in carbon nanotube-reinforced carbon/carbon composites (2017)
18. Ozdemir, N.G., Zhang, T., Aspin, I., Scarpa, F., Hadavinia, H., Song, Y.: Toughening of carbon fibre reinforced polymer composites with rubber nanoparticles for advanced industrial applications. *eXPRESS Polym. Lett.* **10** (2016). <https://doi.org/10.3144/expresspolymlett.2016.37>
19. Yamamoto, T., Makino, Y., Uematsu, K.: Improved mechanical properties of PMMA composites: dispersion, diffusion and surface adhesion of recycled carbon fiber fillers from CFRP with adsorbed particulate PMMA. *Adv. Powder Technol.* (2017). <https://doi.org/10.1016/j.apt.2017.08.003>

20. Gonçalves, V., Barcia, F.L., Soares, B.G.: Composite materials based on modified epoxy resin and carbon fiber. *J. Braz. Chem. Soc.* **17**(6), 1117–1123 (2006)
21. Danni, N., Sasikumar, T., Karthikeyan, M., Vimal, S.: Mechanical properties of CFRP composite with carbon nano fiber inclusion. *Int. J. Adv. Res. Manage. Architect. Technol. Eng. (IJARMATE)*
22. Li, Y., Zhang, H., Huang, Z., Bilotti, E., Peijs, T.: Graphite nanoplatelet modified epoxy resin for carbon fibre reinforced plastics with enhanced properties. *Hindawi J. Nanomater.* (2017). <https://doi.org/10.1155/2017/5194872>
23. Liu, F., Deng, S., Zhang, J.: Mechanical properties of epoxy and its carbon fiber composites modified by nanoparticles. *Hindawi J. Nanomater.* (2017). <https://doi.org/10.1155/2017/8146248>
24. Gemi, L., Yazman, S., Uludağ, M., Dispinar, D., Tiryakioğlu, M.: The effect of 0.5 wt% additions of carbon nanotubes and ceramic nanoparticles on tensile properties of epoxy-matrix composites: a comparative study. *Mater. Sci Nanotechnol.*
25. Carolan, D., Ivankovic, A., Kinloch, A.J., Sprenger, S., Taylor, A.C.: Toughened carbon fibre-reinforced polymer composites with nanoparticle-modified epoxy matrices. Springer (2016). <https://doi.org/10.1007/s10853-016-0468-5>

Study on Carbon, Glass, and Flax Hybrid Composites Using Experimental and Computational Techniques



M. Dinesh, B. Rubanrajasekar, R. Asokan, S. Vignesh and S. Rajesh

Abstract Composites have already proven their worth as weight-saving material; the present scenario is to make them cost-effective. Employment of natural fibers as reinforcement along with carbon and glass fibers is an effective method for achieving it. In this paper, various properties of artificial and natural fibers are discussed and the fibers are selected on the basis of static efficiency. Composite laminates were made using different combinations of carbon, glass, and flax using epoxy resin. The mechanical properties of these laminates were studied experimentally using tensile tests and three-point bending tests. The results from experimental tests are validated computationally using Ansys 16 software.

Keywords Hybrid composites · Mechanical properties · Finite element analysis (FEA)

1 Introduction

With a rapid increase in the usage of composite materials, especially in the aerospace industry, there arises a need for the development of a new composite material which gives good properties with relatively low cost. The advantages of natural

M. Dinesh (✉) · B. Rubanrajasekar · R. Asokan · S. Vignesh · S. Rajesh
School of Aeronautical Science, Hindustan Institute of Technology and Science,
Chennai, India
e-mail: dineshf22@gmail.com

B. Rubanrajasekar
e-mail: ruban.r.s.aero@gmail.com

R. Asokan
e-mail: rgasokan@gmail.com

S. Vignesh
e-mail: vignesh04@live.com

S. Rajesh
e-mail: rajeshankar7@gmail.com

fibers like high strength-to-weight ratio, readily available, low density, high stiffness, low cost, renewability, and biodegradability have led to the shift in research from traditional synthetic fibers to natural fibers [1, 2]. Tensile and compressive properties of flax, bamboo, and coir fibers were evaluated, and it was found that flax fiber has better properties overall. Hence, the properties, characteristics, and performance of flax fibers were studied in detail and the results proved that flax fibers can be a potential reinforcement for composite materials [3–6]. The mechanical properties of composite materials are greatly affected by various factors such as fiber loading, fiber length, fiber surface modification, and fiber orientation. Any changes to the above-mentioned factors will lead to a considerable change in mechanical properties such as tensile strength, flexural strength [7–9]. In the case of hybrid composites, apart from the above parameters, the properties are predominantly affected by the variation in fiber volume/weight fraction, variation in stacking sequence of fiber layers, fiber treatment, and environmental conditions [10–12]. Similar to all the composites, the physical properties, like bonding, moisture absorption, chemical reactivity, and mechanical properties, like tensile strength, flexural strength, of the flax fiber-reinforced composites can be improved with suitable chemical treatments, processing methods, weave architecture, fiber configurations, and manufacturing techniques [13]. The experimental test results are validated computationally by finite element analysis using Ansys software [14, 15].

2 Experimental Procedures

2.1 Material Selection

After numerous hours of work on literature survey and considering various factors such as physical properties, mechanical properties prior application in the aerospace industry, processing techniques, ease of manufacture, and also keeping in mind the cost and availability, a conclusion was made to use the following materials:

E-glass fiber—Woven type (200 GSM);

Carbon fiber—Woven type (200 GSM);

Flax fiber—Woven type (200 GSM);

Matrix—Epoxy resin (LY556);

Hardener—HY972;

Volume fractions of the fibers—0.7.

Five sets of laminates were fabricated by arranging the layers of fibers in ($\pm 0/900$) orientation using compression molding. The different sets of laminate combinations are given below,

- Set 1—Glass/Flax/Flax/Flax/Glass/Epoxy;
- Set 2—Flax/Glass/Flax/Glass/Flax/Epoxy;
- Set 3—Carbon/Flax/Flax/Flax/Carbon/Epoxy;

- Set 4—Flax/Carbon/Flax/Carbon/Flax/Epoxy; and
- Set 5—Carbon/Flax/Glass/Flax/Carbon/Epoxy.

2.2 Fabrication of Laminates

The flax, carbon, and E-glass fiber cloths are cut into specific dimensions and with proper orientation as shown in Fig. 1. The required number of layers for obtaining the total thickness can be determined by taking into account the mat density and the fiber-to-resin ratio by weight. The fibers were weighed, and the resin is taken as 30:70 ratio by the weight of the fiber. Then, hardener is added by 10% of the weight of the resin. The resin and hardener are completely mixed which forms the matrix.

Initially, the lower part of the mold is coated with wax or gel. This ensures the laminate does not stick to the mold and also to give a good surface finish. A layer of resin is applied with a brush on the wax or gel coat. For the first combination, the cut glass fiber mat is placed over the resin. By a stippling action using a resin-wetted brush, the resin is squeezed to the top surface. Using a metal roller, the layer is consolidated and all the air entrapped between gel coat and first layer of mat is removed to prevent blisters. Then a cut flax fiber mat is placed over the first layer, and the above steps are repeated. Subsequent layers are laid up in a similar manner according to the ply material and orientation. Thus, procedure has been repeated till the required thickness has been built up. The upper mold is screwed tight to the lower mold after the required thickness is obtained. This compresses the laminate layup and pushes out any excess resin through a hole. Then, the mold is kept in a curing oven at 120 °C and cured for over 2–3 h. Finally, the mold is taken out from the oven and the cured laminate is removed from the mold for further processing. Similarly, the above-mentioned procedure is carried out for fabricating all the remaining laminate sets as shown in Fig. 2.

Specimens are cut from the laminate according to ASTM D3039 for tensile test (250 × 25 × 3 mm) [9] and ASTM D790 for three-point bending test (150 × 25 × 3 mm) [10]. Tabbing for tensile specimen has been done with aluminum tabs of dimensions (50 × 25 × 1.5 mm) as shown in Fig. 3.



Fig. 1 Flax, carbon, and E-glass fiber mats

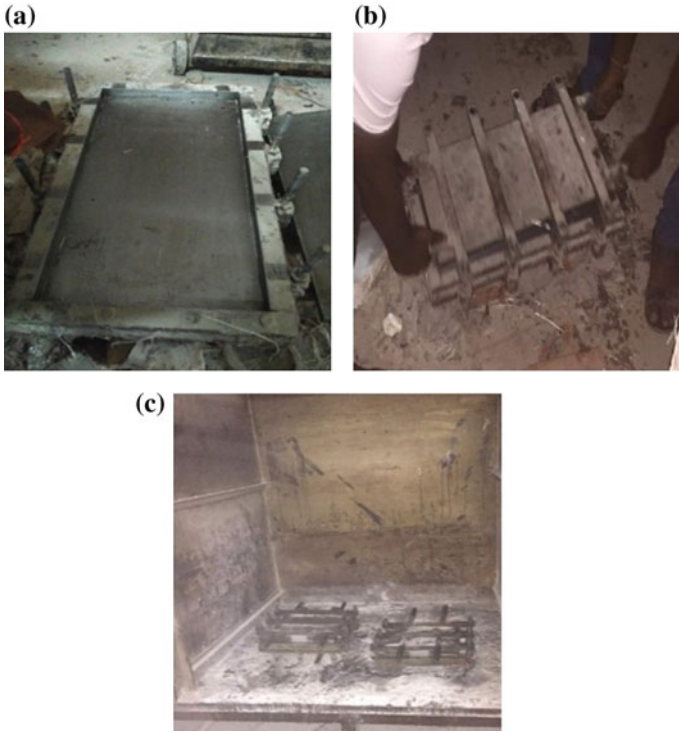


Fig. 2 Fabrication process of laminates **a** lower mold **b** molding process **c** curing oven



Fig. 3 Tensile and bending specimens before testing

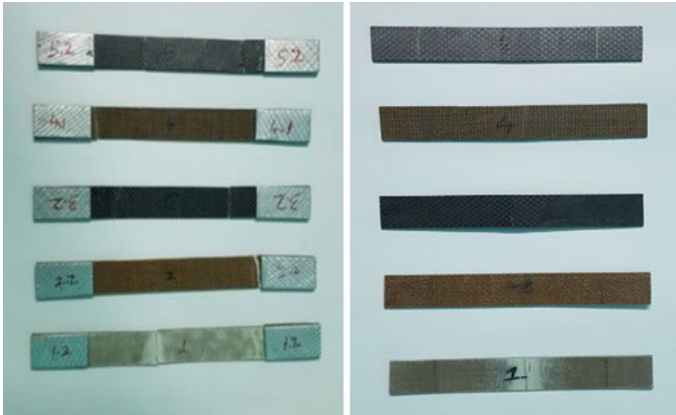


Fig. 4 Tensile and bending specimens after testing

2.3 Mechanical Testing

The tensile test and bending test were carried out using FSA M100 Universal Testing Machine equipped with a digital data acquisition system. The specimens after tests have been shown in Fig. 4.

3 Results and Discussion

All the tests are carried out using standard procedures, and the results were recorded digitally using digital data acquisition system. These results are studied to determine the laminate having the best mechanical properties. The tensile and flexural properties of different sets are shown in Tables 1 and 2.

From the above results, it can be concluded that the set 5 fiber combination has superior tensile properties and bending properties when compared to all the other sets. The maximum tensile strength and the maximum Young's modulus recorded are 272 MPa and 6.41 GPa, respectively, and the maximum flexural strength and the maximum flexural modulus recorded are 449 MPa and 35 GPa, respectively. From the tests carried out on all the laminate sets and studying these test results, it is clearly evident that set 5 composite laminate exhibits high mechanical properties compared to other composite laminate sets as shown in Figs. 5, 6, 7, and 8. All the specimens are further analyzed using Ansys software to validate the experimental results.

Table 1 Tensile properties of different sets of laminates

Set	Ultimate load (KN)	Deformation (mm)	Stress (MPa)	Strain	Young's modulus (GPa)
1	8.828	6.333	121.7	0.042	2.88
	10.664	6.799	147.0	0.045	3.25
2	10.153	6.341	140.0	0.042	3.31
	7.914	5.349	109.1	0.035	3.05
3	8.68	4.664	118.8	0.035	3.32
	11.182	6.135	154.2	0.040	3.77
4	6.673	4.613	92.04	0.030	3.01
	10.449	5.937	144.1	0.039	3.64
5	19.721	8.371	272.0	0.055	4.87
	18.29	5.913	252.3	0.039	6.41

Table 2 Flexural properties of different sets of laminates

Set	Ultimate load (KN)	Deformation (mm)	Stress (MPa)	Slope (N/mm)	Flexural modulus (GPa)
1	0.182	18.14	129.8	37.73	15.469
	0.177	14.77	126.8	44.84	18.638
2	0.216	21.242	159.0	25.38	10.405
	0.22	23.108	158.3	24.06	9.8646
3	0.353	7.882	239.9	47.84	19.614
	0.319	7.305	227.5	4.807	19.708
4	0.288	12.25	205.4	30.21	12.386
	0.285	12.916	203.3	27.77	11.388
5	0.632	9.3	449.4	85.67	35.124
	0.564	7.593	402.3	84.03	34.452

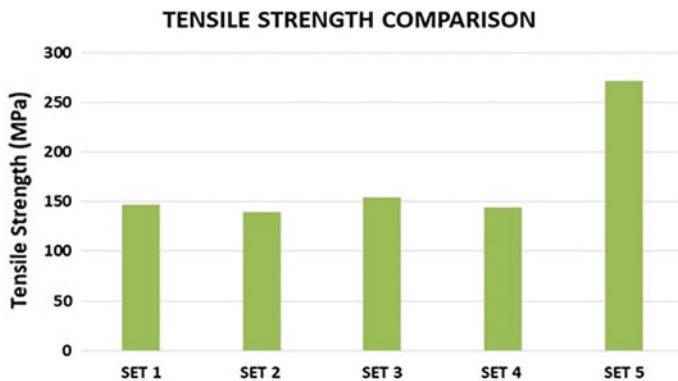


Fig. 5 Comparison on tensile strength

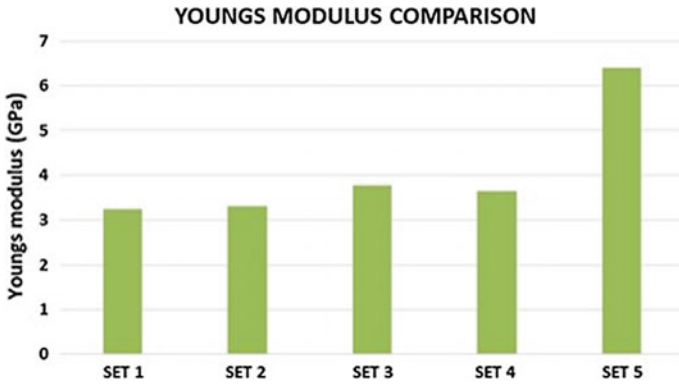


Fig. 6 Comparison on Young's modulus

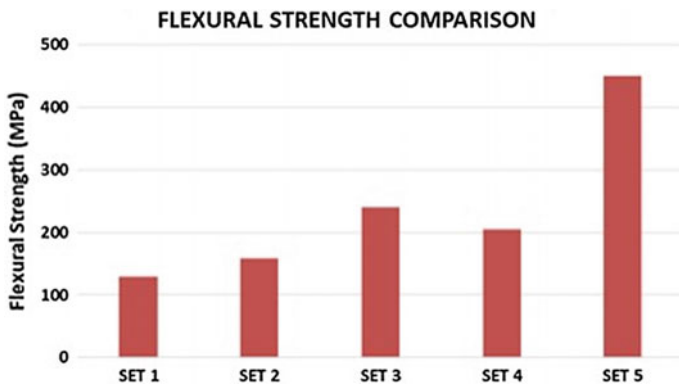


Fig. 7 Comparison on flexural strength

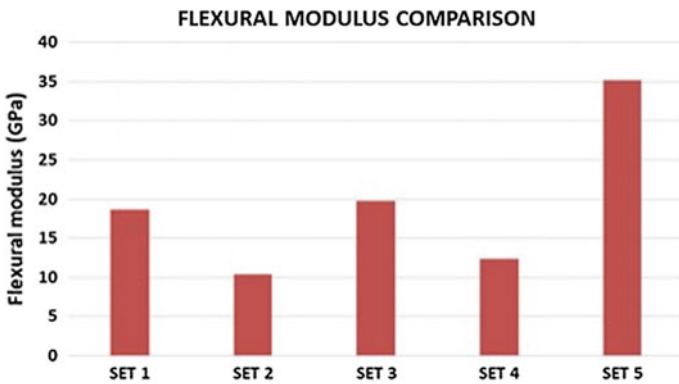


Fig. 8 Comparison on flexural modulus

4 Computational Analysis

4.1 Finite Element Model

The geometry of the composite layer for modeling is already discussed. The dimension of model for tensile test is $250 \times 25 \times 3$ mm, and for bending test, it is $150 \times 25 \times 3$ mm. The material properties for the woven glass fiber-reinforced epoxy laminate, woven carbon fiber-reinforced epoxy laminate, and woven flax fiber-reinforced epoxy laminate are considered as per test results based on individual laminas. Resin epoxy is given as a global drop-off material in the ACP Pre. The models are shown in Fig. 9.

After creating the model, meshing has to be made on the model for creating nodes and elements. For good and accurate results, fine mesh is to be carried out on the geometry as shown in Fig. 10.

The boundary condition for different analysis should be specified as shown in Fig. 11.

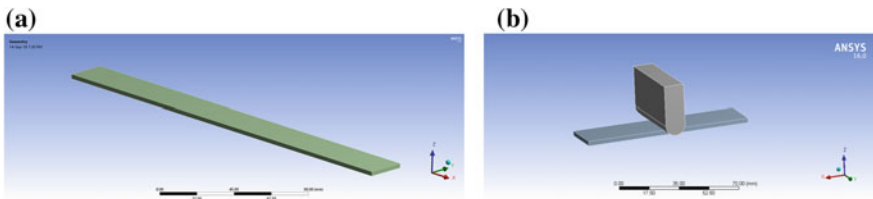


Fig. 9 a Tensile test and b bending test model in ANSYS

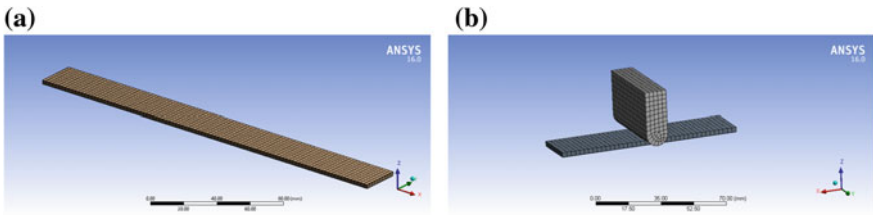


Fig. 10 a Tensile test model and b bending test model after meshing

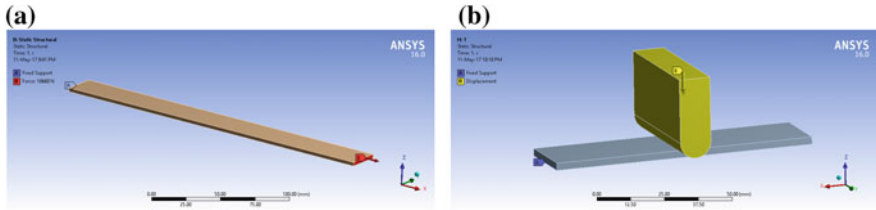


Fig. 11 Boundary conditions for **a** tensile test and **b** bending test

4.2 Finite Element Analysis

For the given model and boundary condition, the analysis process is done using Ansys Multiphysics Solver and this process is time-consuming because of the repeated iteration and based on the configuration of the computer, solving time may vary accordingly. The results can be obtained in post-processing where the various parameters like deformation, equivalent stress, and equivalent strain have been determined for both tensile and bending tests as shown in Figs. 12 and 13.

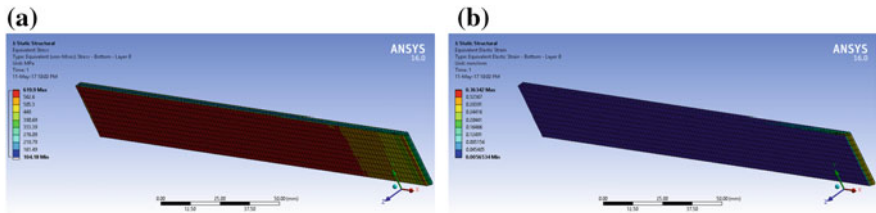


Fig. 12 Tensile test results for the set 5 (C/F/G/F/C) combination **a** equivalent stress **b** equivalent strain

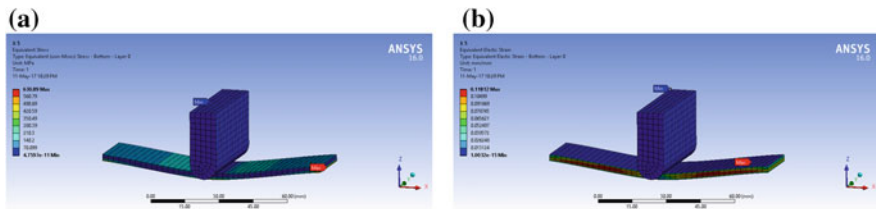


Fig. 13 Bending test results for the set 5 (C/F/G/F/C) combination **a** equivalent stress **b** equivalent strain

4.3 Comparison of Results

After the computational analysis has been completed, the results obtained from computational and experimental analysis are compared for both tensile and bending tests as shown in Tables 3, 4, 5, and 6.

The comparison of test results shows us that the computationally obtained results are very close to that of experimentally obtained results for both tensile and bending tests. Thus, the experimentally obtained results are validated.

Table 3 Comparison of experimental tensile test results

Experimental result			
Set	Deformation (mm)	Equivalent stress (MPa)	Equivalent strain
1	6.33	147.089	0.0422
2	5.349	140.041	0.0356
3	5.664	154.234	0.0358
4	5.937	144.124	0.0307
5	5.913	272.013	0.0394

Table 4 Comparison of computational tensile test results

Computational result			
Set	Deformation (mm)	Equivalent stress (MPa)	Equivalent strain
1	6.827	150.18	0.0452
2	5.534	141.86	0.0371
3	5.823	161.47	0.0395
4	5.965	148.11	0.0381
5	6.048	293.39	0.0425

Table 5 Comparison of experimental bending test results

Set	Deformation (mm)	Equivalent stress (MPa)
1	18.14	129.80
2	21.24	159.09
3	7.882	239.90
4	12.25	205.40
5	9.323	449.40

Table 6 Comparison of computational bending test results

Set	Deformation (mm)	Equivalent stress (MPa)
1	18.13	135.73
2	21.25	175.15
3	7.884	249.59
4	12.25	233.23
5	9.355	490.14

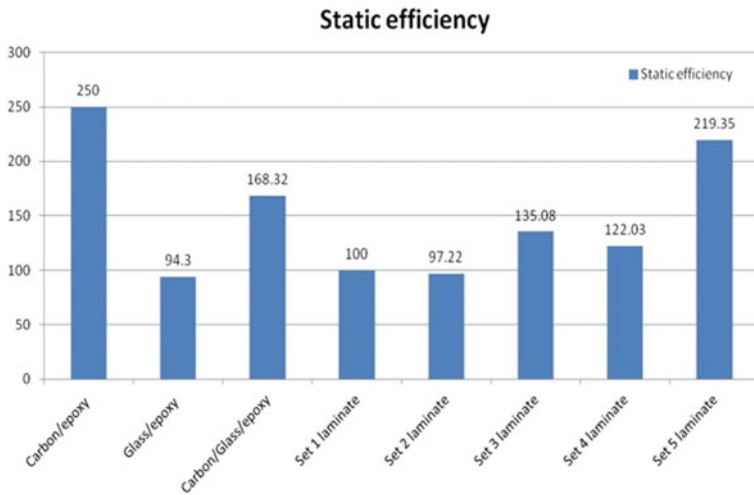


Fig. 14 Static efficiency comparison

5 Comparison of Static Efficiency

From Fig. 14, it is noted that the static efficiency of the set 5 laminate comes very close to that of a carbon/epoxy laminate and even surpasses the carbon/glass/epoxy hybrid. The static efficiencies of the remaining laminate sets also come close to that of the carbon/glass/epoxy hybrid. The set 5 laminate was able to achieve 87.74% of the carbon/epoxy laminate’s static efficiency (Table 7).

Table 7 Static efficiencies or specific strength of different laminates

Material	Tensile strength (MPa)	Young's modulus (GPa)	Static efficiency
Carbon/epoxy	400	9.70	250
Glass/epoxy	179.2	6.450	94.3
Carbon/glass/epoxy	291.2	3.40	168.32
Set 1 laminate	147	3.25	100
Set 2 laminate	140	3.31	97.22
Set 3 laminate	154	3.77	135.08
Set 4 laminate	144	3.64	122.03
Set 5 laminate	272	6.41	219.35

6 Conclusion

The primary goal of this paper is to identify new composite material for application in the aerospace industry. A new hybrid composite is designed using artificial and natural fibers. Various tests like tensile and bending are carried out. From analyzing the results experimentally and computationally, the following conclusions were drawn:

- Composite with fiber combination carbon/flax/glass/flax/carbon (set 5) shows better mechanical properties compared to other sets.
- Set 5 laminate has better properties than carbon/glass hybrid composite in terms of both static efficiency and cost.
- The CFGFC laminate was able to reach 87% of static efficiency of carbon/epoxy composite.

References

1. Sanjay, M.R., Arpitha, G.R., Laxmana Naik, L., Gopalakrishna, K., Yogesha, B.: Applications of natural fibers and its composites: an overview. *Nat. Resour.* 7(3) (2016)
2. Saravana Bavan, D., Mohan Kumar, G.C.: Potential use of natural fiber composite materials in India. *J. Reinf. Plast. Compos.* 29(24), 3600–3613
3. van Vuure, A.W., Baets, J., Wouters, K., Hendrickx, K.: Compressive properties of natural fibre composites. In: 20th International Conference on Composite Materials
4. Bos, H.L.: The potential of flax fibres as reinforcement for composite materials. Technische Universiteit Eindhoven. Proefschrift. ISBN 90-386-3005-0, NUR 913 (2004)
5. Andersons, J., Joffe, R., Sparniš, E.: Stiffness and strength of flax fiber/polymer matrix composites. *Polym. Compos.* 27(2), 221–229 (2006)
6. Yan, L., Chouw, N., Jayaraman, K.: Flax fibre and its composites—a review. *Compos. B* 56, 296–317 (2014)
7. Uma Devi, L., Bhagawan, S., Thomas, S.: Mechanical properties of pineapple leaf fiber-reinforced polyester composites. *Polym. Compos.* (2011)
8. Pothan, L.A., Thomas, S., Neelakantan, N.R.: Short banana fiber reinforced polyester composites: mechanical, failure and aging characteristics. *Reinf. Plast. Compos.* (1997)

9. Sandeep, M.B., Choudhary, D., Inamdar, Md. N., Rahaman, Md. Q.: Experimental study of effect of fiber orientation on the flexural strength of glass/epoxy composite material. *Int. J. Res. Eng. Technol.*
10. Nunna, S., Ravi Chandra, P., Shrivastava, S., Jalan, A.K.: A review on mechanical behavior of natural fiber based hybrid composites. *J. Reinf. Plast. Compos.* (2014)
11. Sandesh, K.J., Umashankar, K.S., Madappady, C., Mohan Kumar, N.M., Thejesh, C.K.: Effect of stacking sequence on mechanical/vibration characteristics of kevlar/glass hybrid reinforced polymer composites. *Int. Adv. Res. J. Sci. Eng. Technol.* (2016)
12. Uleiwi, J.K., Dr.: Experimental study of flexural strength of laminate composite material. *Eng. Technol.* 25 (2007)
13. Zhu, J., Zhu, H., Njuguna, J., Abhyankar, H.: Recent development of flax fibres and their reinforced composites based on different polymeric matrices. *Materials* 6(11), 5171–5198. <https://doi.org/10.3390/ma6115171> (2013)
14. Khan, Z., Patil, R.J.: Composite fiber-resin lamina, compared by finite element analysis and analytical solution. *Int. J. Res. Aeronaut. Mech. Eng.* (2014)
15. Nurhaniza1, M., Ariffin, M.K.A., Ali, A., Mustapha, F., Noraini, A.W.: Finite element analysis of composites materials for aerospace applications. In: 9th National Symposium on Polymeric Materials (NSPM 2009)

Design Evaluation of a Mono-tube Magnetorheological (MR) Damper Valve



Solomon Seid, Sujatha Chandramohan and S. Sujatha

Abstract The primary purpose of this paper is to identify performance indices and evaluate a design of a mono-tube MR damper valve, as a result of which relations among performance indices and possible design approaches are explored. To achieve this, initial design of a mono-tube MR damper valve is considered. Common MR damper valve configuration is adopted to which initial design parameters are specified. Performance indices that need to be considered while evaluating the design of a mono-tube magnetorheological (MR) damper valve are identified, and mathematical models are developed. The performance indices of the damper valve depend upon the magnetic circuit design of the valve; hence, for the adopted MR damper valve configuration, finite element model is built to analyze and investigate the performance indices of a 2-D axisymmetric MR damper valve. All performance indices of the damper valve are simulated within given range of input current and number of turns of coil. The simulation results show that the design of the MR dampers is highly dependent on the performance indices, and hence, the MR damper design should be application oriented. The results obtained in this work provide an insight for designers to create more efficient and reliable MR dampers.

Keywords Magnetorheological (MR) damper valve • Performance indices
Damping force • Magnetic flux density • Magnetic field intensity

S. Seid (✉)

College of Engineering, Defence University, Bishoftu, Ethiopia
e-mail: solomonseid@gmail.com

S. Chandramohan · S. Sujatha

Machine Design Section, Department of Mechanical Engineering,
Indian Institute of Technology Madras, Chennai, India
e-mail: sujatha@iitm.ac.in

S. Sujatha

e-mail: sujsree@iitm.ac.in

© Springer Nature Singapore Pte Ltd. 2019

U. Chandrasekhar et al. (eds.), *Innovative Design, Analysis and Development Practices in Aerospace and Automotive Engineering (I-DAD 2018)*, Lecture Notes in Mechanical Engineering, https://doi.org/10.1007/978-981-13-2718-6_15

1 Introduction

A magnetorheological (MR) damper is a smart material device used in a semi-active control system to mitigate unwanted vibration. For its advantages in terms of compactness, high forces, low power consumption, smoothness, and safety of operation, it can be used in a wide variety of fields ranging from automotive to rehabilitation. It has been applied in the domain of automobile, armed vehicle, civil engineering as well as aerospace, and other fields.

In the last decade, many researchers have carried out studies on semi-active control systems. Researchers have shown that designs that make use of MR fluids and devices are potentially simpler, more reliable, and consistent than conventional electromechanical devices. Nguyen and Choi [1] designed a vehicle MR damper considering damping force and dynamic range. Gudmundsson et al. [2] developed an MR rotary valve for prosthetic knee application considering weight and torque produced. Solomon et al. [3, 4], authors' previous work, designed and evaluated effectively an MR damper for prosthetic knee application in normal level-ground walk.

From the available literature, it is apparent that the study of performance indices for MR damper valve and their impact on the damper design have been unexplored. In this study, the authors have considered an ideal configuration of a mono-tube MR damper valve to study the impact of the performance indices on the damper. The damper performance indices are evaluated, and the results show that in effective design approach of MR damper, one can improve particular aspects of the performance indices of the damper for intended applications.

2 Performance Indices and Mathematical Models

Performance indices of the MR damper are identified to be damping force, dynamic range, valve ratio, inductive time constant, on-state pressure drop, mass of the MR damper valve, and electric power consumption. They are developed based on the quasi-static model of MR damper valves, where the equations are derived based on the assumption that the MR fluid exhibits Bingham plastic behavior, and the flow is fully developed in the ducts [5]. Schematic representation of a single-coil valve with annular duct is shown in Fig. 1, and the Bingham's plastic flow model is given by equation [5]:

$$\tau = \eta \dot{\gamma} + \tau_y (H_{MR}) \text{sgn}(\dot{\gamma}), |\tau| \geq \tau_y \quad \text{and} \quad \tau = G\gamma, |\tau| < \tau_y \quad (1)$$

where τ is fluid shear stress, τ_y is yield stress developed as a result of the applied field, $\dot{\gamma}$ is the fluid shear strain rate, γ is fluid shear strain, and G is complex shear modulus. Equation (1) is used to design a device which works on the basis of MR

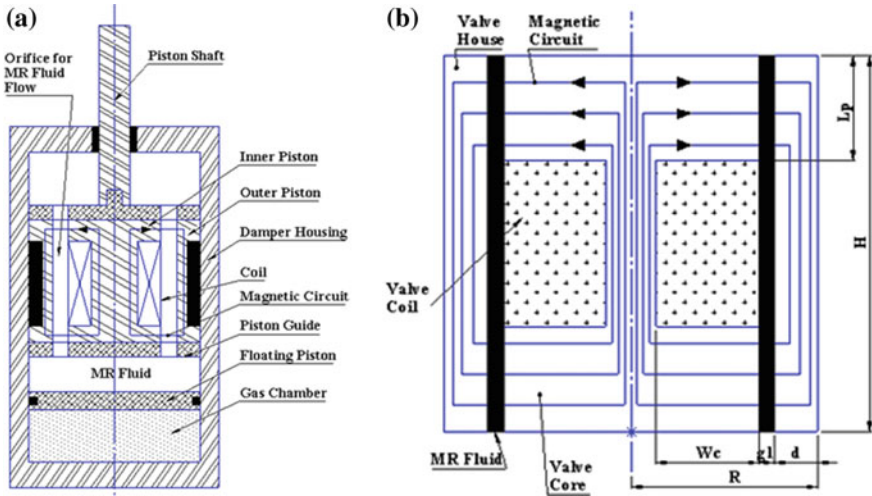


Fig. 1 Schematic configuration of a single-coil. a MR damper, b MR valve

fluid. The total pressure drop in the damper is evaluated by summing the viscous component and yield stress component, which is approximated as follows [6]:

$$\Delta P = \Delta P_{\eta} + \Delta P_{\tau} = 6\eta HQ / (\pi g^3 R_1) + 2cLp\tau_y / g_1 \tag{2}$$

In which ΔP is the pressure drop of the MR fluid flow through the orifice gap of the valve, ΔP_{τ} is the applied field dependent pressure drop, ΔP_{η} is the applied field independent pressure drop, η is the plastic viscosity of MR fluid without applied magnetic field, and Q is volumetric rate of flow. The parameter c is a coefficient which depends on the flow velocity profile, and it has a value varying from 2.07 to 3.07. The coefficient c can be approximately estimated as follows [1, 6]: $c = 2.07 + \frac{12Q\eta}{12Q\eta + 0.8\pi R_1 d^2 \tau_y}$. R_1 is the average radius of the duct given as a distance between the axis of the valve and the centroid of the duct. For the rectangular annular duct, R_1 is given by: $R_1 = R - d - 0.5g_1$. Upon fitting a polynomial to the MR fluid (MRF132-DG) data from Lord Corporation, the induced yield stress of the MR fluid as a function of the applied magnetic field intensity of MR fluid along the pole length, H_{MR} , can be approximately expressed as [5]:

$$\tau_y = C_0 + C_1 H_{MR} + C_2 H_{MR}^2 + C_3 H_{MR}^3 \tag{3}$$

In Eq. (3), the unit of the yield stress is in kPa while that of the magnetic field intensity is in kA/m. The coefficients C_0 , C_1 , C_2 , and C_3 determined from experimental results by applying the least squares curve fitting method are, respectively, identified as 0.3, 0.42, -0.00116 , and 1.05×10^{-6} . Damping force is given by [1, 6],

$$F_d = P_a A_s + C_{vis} \dot{x}_p + F_{MR} \text{sgn}(\dot{x}_p) \quad (4)$$

where $P_a = P_o \left(\frac{V_o}{V_o + A_s x_p} \right)^k$, $C_{vis} = \frac{6\eta H}{\pi R_1 g_1^3} (A_p - A_s)$ and $F_{MR} = (A_p - A_s) \frac{2cL_p}{g_1} \tau_y$, C_{vis} is the damping coefficient, F_{MR} is the frictional force, which is related to the fluid yield stress, P_a is pressure in the gas chamber, P_o is the initial pressure in the gas chamber, V_o is the initial volume of the gas chamber, A_s is the effective cross-sectional area of the shaft, and x_p is the displacement of the piston. The parameter k represents the coefficient of thermal expansion, which varies between 1.4 and 1.7. A_p is the effective cross-sectional area of the piston. \dot{x}_p is velocity of the piston. Therefore, the followings are derived mathematical models of the performance indices:

Dynamic range [6],

$$\lambda_d = \frac{F_o + C_{vis} \dot{x}_p + F_{MR} \text{sgn}(\dot{x}_p)}{F_o + C_{vis} \dot{x}_p} \quad (5)$$

Valve ratio [6],

$$\lambda = \frac{\Delta P_\eta}{\Delta P_\tau} = \frac{3\eta H Q}{\pi g_1^2 R_1 c L_p \tau_y} \quad (6)$$

On-state pressure drop [6],

$$\Delta P_\tau = \frac{2cL_p \tau_y}{g_1} \quad (7)$$

Inductive time constant of the valve [1, 6],

$$T = \frac{2R_1 A_w \int_0^{L_p} B_{MR}(s) ds}{r d I L_p} \quad (8)$$

Electrical power consumption [6],

$$N = I^2 R_w \quad (9)$$

where B_{MR} is the magnetic flux density of the MR fluid along the pole length, A_w is the cross-sectional area of the coil wire, r represents the resistivity of the coil wire, $0.01726 \times 10^{-6} \Omega \text{ m}$ for copper wire, I is the electrical current applied to the valve, and \bar{d} is the average diameter of the coil, which can be given as $\bar{d} = R - d - g_1 - \frac{w_c}{2}$, $R_w = N_c \pi \bar{d} \frac{r}{A_w}$, and $N_c = \frac{A_s}{A_w}$. R_w is the resistance of the coil wire, and N_c is the number of coil turns.

3 Finite Element Model of MR Damper Valve

The MR damper valves consist of a piston over which the coil is wound, and a gap is maintained between the inner and outer pistons. The piston is made up of low carbon cold rolled steel SAE 1020 due to its high relative permeability; materials adopted are shown in Table 1. Figure 2a shows the 2-D axisymmetric MR damper piston and its components. Number of elements per line is used for specifying meshing size. Several simulations with different mesh size have been conducted in order to find optimum mesh size, which generates accurate results efficiently. The number of elements on the lines across the MR fluid orifice is specified as a parameter called a basic meshing number. The number of elements of other lines in the model is selected as a product of the basic meshing number and an appropriate scalar. This method of meshing has also been adopted in previous work [1]. For this work, it has been found that the basic meshing number 23 is sufficiently accurate to ensure the convergence of the finite element solution. The 2-D axisymmetric finite element model of the adopted configuration of the damper valve is also shown in Fig. 2b. The model is analyzed and computed for the variation of magnetic field intensity and magnetic flux density along the active length of the pole, path-AA in Fig. 2c, in ANSYS 2014, with PLANE53 elements; they are computed as follows

$$[1]: B_{MR} = \frac{\int_0^{L_p} B_{MR}(s) ds}{L_p} \text{ and } H_{MR} = \frac{\int_0^{L_p} H_{MR}(s) ds}{L_p}. B_{MR}(s) \text{ and } H_{MR}(s) \text{ are the magnetic}$$

Table 1 Materials adopted

Valve components	Material and density	Relative permeability	Saturation flux (T)
Valve core	SAE1020 (7870 kg/m ³)	B-H curve	2.390
Valve housing	SAE1020 (7870 kg/m ³)	B-H curve	2.390
MR fluid	MRF 132 DG (2950 kg/m ³)	B-H curve	1.65
Coil	Copper (24-Guage) (8900 kg/m ³)	1	–

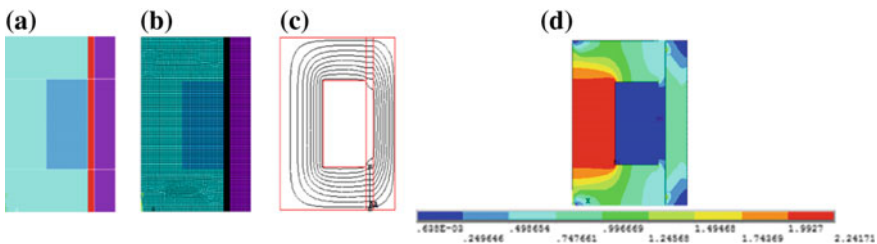


Fig. 2 a 2-D axisymmetric MR damper valve, b finite element model of the valve, c flux lines around the electrical coil and the path-AA for computing H_{MR} and B_{MR} , d magnetic flux density (Tesla) of the initial model at 2 A

flux density and magnetic field intensity, respectively, at each nodal point located on the defined path-AA, Fig. 2c. The variation of magnetic flux density at 2 A is shown in Fig. 2d.

4 Simulation Results and Analysis for Initial Design

The aforementioned performance indices of the valve are computed for the configuration of the piston valve, and the results are shown in Fig. 3. For the initial design of desired MR damper, the dimensions of the valve and parameters adopted are: active pole length, $L_p = 5$ mm, initial volume of the gas chamber, $V_o = 6371.15$ mm³, coil width, $W_c = 6$ mm, displacement of the piston, $x_p = 28.13$ mm, outer piston thickness, $d = 3$ mm, radius of piston shaft, $R_s = 5$ mm, duct gap length, $g_1 = 1$ mm, range of applied current, $I = 0.1\text{--}2$ A, radius of the valve, $R = 16$ mm, number of turn of coil, $N_c = 294$, height of the valve, $H = 20$ mm, copper wire diameter (for 24-gauge), $d_c = 0.51$ mm, and initial pressure of the gas chamber, $P_o = 5.45$ N/mm². The simulation results depicted in Fig. 3 show the performance indices of the initial model within the range of 0.1–2.0 A.

5 Discussion

From Fig. 3, it can be observed that variations in performance indices have been significantly affected by the input current variation. As the input current increases, magnetic field intensity, magnetic flux density, damping force, dynamic range, and

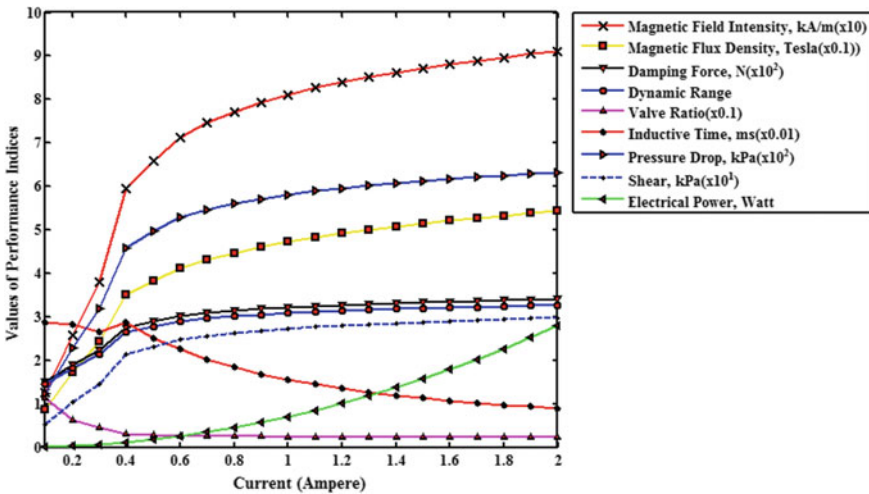


Fig. 3 MR damper performance indices for initial design

shear stress increase, but valve ratio and inductive time constant decrease. However, the increase or decrease in respective performance indices is not uniform before and after about 0.5 A. This is because of the fact that as the current increases, the system tends toward the saturation limit of the MR fluid, where any increase in input current cannot change the performance indices, 1.65 T. It should also be noted that the increase in current is directly related to the increase of electrical power consumption. In designing an MR damper valve, high damping force, high dynamic range, low inductive time constant, low electric power consumption, high on-state pressure drop due to yield stress, low valve ratio, and low weight are generally desired. From the result depicted, the MR fluid magnetic flux density along path-AA is 0.55 T. Therefore, as long as the magnetic flux density of MR fluid is below its saturation limit, one can have varieties of possible design approach to optimally design the MR damper valve by making trade-off among the performance indices, depending upon the application.

6 Conclusions

In this work, performance indices of the MR damper that need to be considered while designing a mono-tube MR damper have been presented. The MR damper valve, constrained in a specific volume, was designed through finite element method with the objective of evaluating the performance indices at 2 A. The developed methodology can also be adopted for other types of MR damper valve such as twin tube and rotary MR damper valves. Future work includes application oriented optimal design and performance evaluation of an MR damper valve.

References

1. Nguyen, Q.H., Choi, S.B.: Optimal design of a vehicle magnetorheological damper considering the damping force and dynamic range. *Smart Mater. Struct.* **18**(1), 015013–015022 (2008)
2. Gudmundsson, K., Jonsdottir, F., Thorsteinsson, F.: A geometrical optimization of a magneto-rheological rotary brake in a prosthetic knee. *Smart Mater. Struct.* **19**(3), 035023–035033 (2010)
3. Solomon, S., Sujatha, S., Sujatha, C.: Design of controller for single-axis knee using MR damper. In: *Proceedings of ECCOMAS Thematic Conference on Multibody Dynamics*, pp. 989–998, International Center for Numerical Methods in Engineering (CIMNE), Barcelona, Catalonia, Spain (2015)
4. Solomon, S., Sujatha, S., Chandramohan, S.: Performance evaluation of magnetorheological damper valve configurations using finite element method. *Int. J. Eng. (IJE), Trans. B: Appl.* **30**(2), 303–310 (2017)
5. Jolly, M.R., Bender, J.W., Carlson, J.D.: Properties and applications of commercial magnetorheological fluids. *J. Intell. Mater. Syst. Struct.* **10**(1), 5–13 (1999)
6. Nguyen, Q., Choi, S., Lee, Y., Han, M.: An analytical method for optimal design of MR valve structures. *Smart Mater. Struct.* **18**(9), 095032–095044 (2009)

Characterization of Soot Microstructure for Diesel and Biodiesel Using Diesel Particulate Filter



Indranil Sarkar, Ritwik Raman, K. Jayanth,
Aatmesh Jain and K. C. Vora

Abstract Diesel fuel exhaust, produced in an internal combustion engine, also contains particulate matter. Its composition differs based on the type of fuel, its consumption rate, and the mode of engine operation. International Agency for Research on Cancer (IARC) has classified diesel exhaust as a carcinogenic, inhaling which can cause lung cancer. A standard wall-flow filtration device like diesel particulate filter (DPF) is used to remove particulate matter or soot from diesel exhaust. With BS-VI emission norms, the emission standards have become stricter and thus an attempt is made to compare the microstructure and amount of soot produced by diesel and a biodiesel blend. The use of biodiesel is increasing continuously since it has lower net CO₂ emission, and the EU demands the use of renewable sources in the transport sector. It has been found, by weighing the respective DPFs, that engine running with biodiesel blends is producing less soot. Size of soot particles affects its reactivity during filter regeneration. Soot trapped is analyzed under a scanning electron microscope (SEM) to observe its structure and density. EDX analysis revealed the presence of zinc in low concentration in biodiesel soot. This also indicates uniform blending of biodiesel.

Keywords Soot microstructure · DPF · Biodiesel · SEM · EDX

1 Introduction

India is in the transition toward the Bharat VI which imposes stringent emission norms on the automobile sector. Heavy-duty vehicles and diesel cars will need the diesel particulate filters (DPFs) which are one of the aftertreatment devices used to meet the norms [1]. The BS-VI norms specify that the PM should be limited to 6×10^{11} [2]. These soot particles, a by-product of the combustion of fuel, are released into the atmosphere [3, 4]. Even though the concentration of these particles

I. Sarkar (✉) · R. Raman · K. Jayanth · A. Jain · K. C. Vora
ARAI Academy, Pune, India
e-mail: sarkarindranil639@gmail.com

© Springer Nature Singapore Pte Ltd. 2019
U. Chandrasekhar et al. (eds.), *Innovative Design, Analysis and Development Practices in Aerospace and Automotive Engineering (I-DAD 2018)*, Lecture Notes in Mechanical Engineering, https://doi.org/10.1007/978-981-13-2718-6_16

are very less, its presence in the atmosphere causes serious health issues and also affects global warming by absorbing solar radiations [5]. Thus, reduction of these soot particles must be filtered out before they reach the atmosphere.

DPFs are the standard wall-flow filtration devices used to filter the particulate matter effectively. These DPFs are honeycomb structures made of ceramics like cordierite and silicon carbide. These have a series of parallel flow paths that are plugged alternatively to force the gases to pass through the filter. The porosity, mean diameter of pore, and wall thickness determine the efficiency of the wall-flow DPFs [6–8]. The percentage of soot particles that are trapped by the DPF depends on the pore diameter. Trapping efficiency of DPF decreases as the pore size decreases. After certain duration, it will clog the filter and thus regeneration is required. Filter regeneration burns the soot into harmless ash thus clearing the pathways for continuous filtration.

In recent research, the use of biofuels has been dedicated to improve the performance of the engines and also to counter the fast depletion of fossil fuels. The biofuels also have effects on the soot particles. The biodiesel produces less CO₂ and particulate matter than diesel, but it produces more NO_x emission. Thus in this paper, the effects of the biodiesel on soot particles is studied and compared with that of the diesel.

Recent research involving scanning electron microscope (SEM) and transmission electron microscopy (TEM) analysis of soot particles of diesel and biodiesel blends showed that B100 have less soot deposition and contains more ashes than B20 and diesel [9–13].

2 Experimental Setup

A cylindrical casing is mounted between the calorimeter and exhaust pipe. The DPF is fixed inside the casing. Two valves are provided on either side of the DPF to connect the manometer that is used to measure the pressure drop across the DPF. The two DPFs were operated on the same engine (Fig. 1).

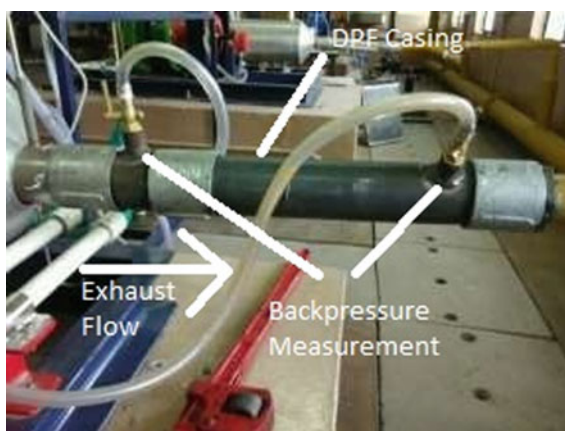
The characteristics of the engine are summarized in Table 1.

Two DPFs made of cordierite, 30 mm diameter, 60 mm long, wall thickness of 0.12 mm, and volume weight of 550 g/L, have been used in this study.

2.1 Fuels Used

Commercially available diesel fuel (2-D) was used in this experimentation which was obtained from gas station.

Pongamia oil is extracted from the seeds of the *Millettia pinnata* tree. In this investigation, B20 blend was used. Pongamia is an oilseed-bearing tree, which is non-edible and does not find any suitable application with only 6% being utilized

Fig. 1 Casing of DPF**Table 1** Specification of engine

Engine parameter	Unit	Value
No. of cylinder		1
Cubic capacity	L	0.553
Rated speed	Rpm	1500

out of 200 million tons per annum [14]. Under optimal condition, pongamia oil can yield maximum amount of methyl ester (97–98%) which is basically the main reason behind the use of pongamia oil in this research [15]. Also, it can grow on debased and minimal land, not at all like numerous edible yields.

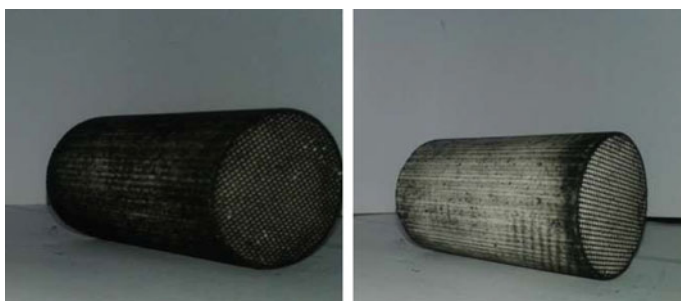
2.2 Transesterification of Pongamia Oil

Transesterification of pongamia oil using base catalysts (NaOH and KOH):

Pongamia oil is transesterified by warming them with a vast overabundance of dehydrated methanol and a catalyst. The dehydrated unrefined oil was collected in two different beakers and warmed up to 60 °C. Methanol with measured amounts of momentum broke up, in it by vivid mixing was individually added to the measuring glasses containing the oil. The response blend was mixed at 300 rpm for 45 min at 60 °C. Cooling of transesterified oil was done and in this way permitted to settle overnight in an isolating pipe. The transesterification procedure brings about two fluid stages: ester and unrefined glycerin. Rough glycerin, the heavier part is isolated after total settling in an isolating channel. The rest of the ester (biodiesel) is washed a few times with water until the ester layer turns out to be clear. The resultant biodiesel is collected and put away for further studies [16].

Table 2 Property of oil after esterification [17]

Property	Karanja	Diesel	IS for biodiesel
Density (kg/m ³)	88.5	836	860–900
Kinematic viscosity (stokes)	5.60	3.8	2.5–6
Flash point (°C)	217	56	120
Fire point (°C)	223	63	130
Heating value (kJ/kg)	36,120	42,800	37,270
Specific gravity	0.876	0.85	0.86–0.90

**Fig. 2** Diesel DPF (left) and biodiesel DPF (right)

The properties of diesel and biodiesel are given in Table 2.

Substantial difference in the amount of soot deposition is seen in the state of DPF after running the engine for 100 min (Fig. 2).

3 Results and Conclusions

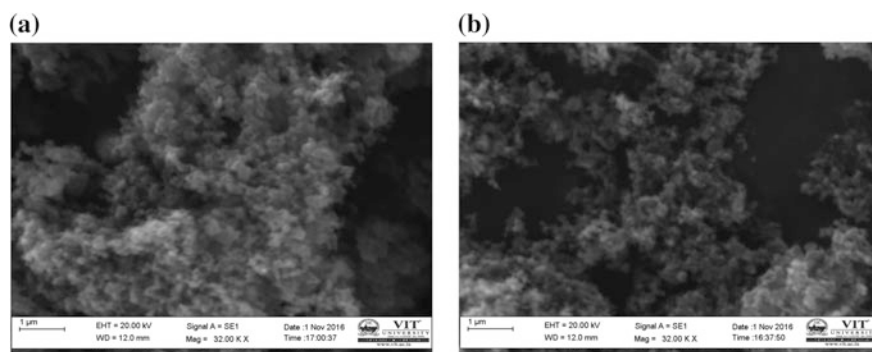
Percentage increase in weight of DPF directly corresponds to weight of soot collected. Engine running on diesel produced almost 32% more soot compared to that on B20 blend (Table 3).

3.1 SEM Results

Distribution of soot particles is seen in Fig. 3a. There is no cluster formation as such because of its inherent stability. Rather than spherical, the soot particles are ellipsoidal in shape. The average particle size along minor axis is about 100 nm and around 200 nm about the major axis.

Table 3 Weight of DPF before and after experimentation

Weight	Diesel (g)	B20 (g)
Initial	60.0304	60.5060
Final	60.098	60.558
% Increase	0.112	0.085

**Fig. 3** a SEM result of diesel soot, b SEM results of B20 soot

Shape and size of the soot for both fuels are found to be approximately same. Figure 3b shows the results of SEM analysis on soot from biodiesel. Agglomeration of individual soot particles is observed leading to big cluster formations and a non-uniform distribution.

The instability could be attributed to the highly reactive zinc present in the biodiesel soot as discovered in the EDX analysis.

3.2 EDX Analysis

The EDX analysis of diesel soot gives the composition of the soot: 73% by weight is carbon white and 27% oxygen (Table 4).

Table 4 Diesel and biodiesel soot composition

Element	Diesel		Biodiesel	
	Weight %	Atomic %	Weight %	Atomic %
C K	73.16	78.40	73.11	78.62
O K	26.84	21.60	26.34	21.27
Zn K	0	0	0.55	0.11
Total	100	100	100	100

Biodiesel soot, as observed from the EDX analysis, contains trace amounts of highly reactive elements like Zn. This causes the individual soot particles to form clusters as observed in the SEM analysis. Formation of such globular structure can be attributed to reactive elements like Zn, Ca, and P. Since a 20% blend is used, only trace quantity of Zn is observed in the EDX (Figs. 4, 5, 6, and 7).

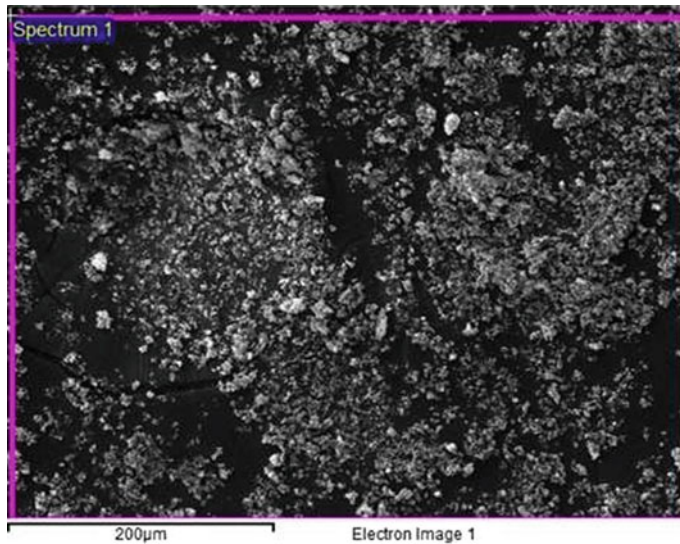


Fig. 4 Spectrum: diesel soot particles

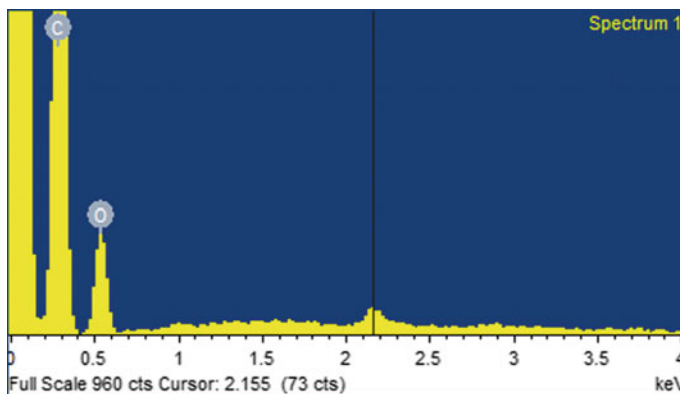


Fig. 5 EDX spectrum diesel soot

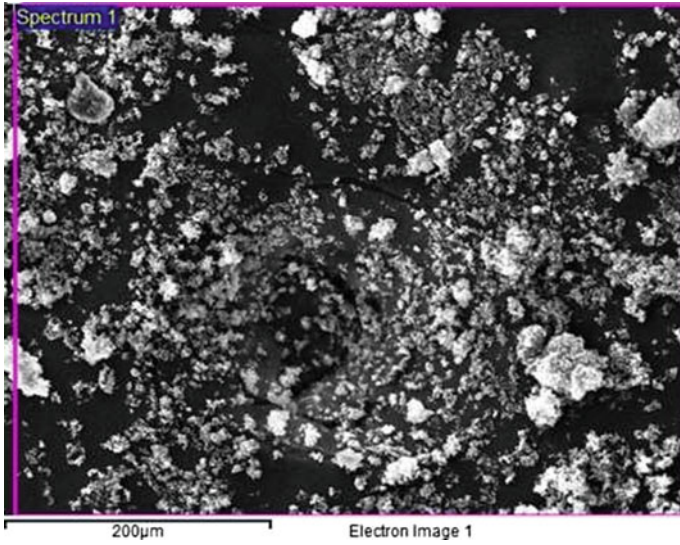


Fig. 6 Spectrum: B20 soot particles

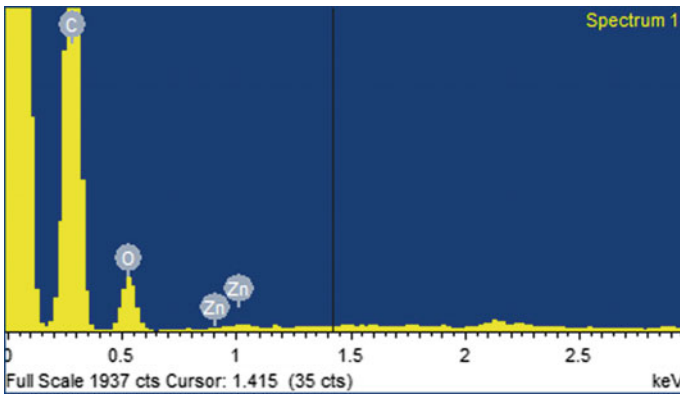


Fig. 7 EDX spectrum biodiesel soot

4 Conclusion

On the basis of macroscopic and microscopic investigation of particulate matter collected in the DPFs operating with the same engine, the following conclusions can be drawn:

The soot formation in the case of the B20 blend is less than that of the diesel. Engine running on diesel produced 32% more soot compared to the one running on B20 blend.

1. Average particle size of soot particles is same around 100–200 nm depending on the axis as the particles are ellipsoidal in shape.
2. Diesel soot is distributed, stable, and does not contain any trace elements.
3. B20 blend soot is highly unstable due to the presence of reactive elements like Zn and other elements in trace amounts. Cluster formation takes place because of the use of 20% blend.
4. More accurate conclusions can be drawn if SEM and TEM analyses are conducted for a range of biodiesel blends.

Acknowledgements We would like to thank Automotive Research Association of India (ARAI) and Vellore Institute of Technology (VIT) for giving us the opportunity to take up this project. To Mr. Aatmesh Jain and Dr. K. C. Vora, we wish to express our gratitude for guiding and helping us when we needed. We want to acknowledge the staff at the SEM analysis laboratory who found time in their busy schedule to help us complete our project. Finally, we want to mention the staff at engine laboratory who were patient enough to teach us how to operate the engine safely and helped us when we needed, thank you.

References

1. Adler, J.: Ceramic diesel particulate filters. *Int. J. Appl. Ceram. Technol.* **2**(6), 429–439 (2005)
2. Regulation (EC) No 715/2007 of European Parliament and of the Council of 20 June 2007
3. Patricia Sierra-Vargas, M., Teran, L.M.: Air pollution: impact and prevention. *Respirology* **17**, 1031–1038 (2012)
4. Heal, M.R., Kumar, P., Harrison, R.M.: Particles, air quality, policy and health. *Chem. Soc. Rev.* **41**, 6606–6630 (2012)
5. McEnally, C.S., Pfefferle, L.D., Atakan, B., Kohse-Höinghaus, K.: Studies of aromatic hydrocarbon formation mechanisms in flames: Progress towards closing the fuel gap. *Prog. Energy Combust. Sci.* **32**, 247–294 (2006)
6. Nova, I., Bounechada, D., Maestri, R., Tronconi, E., Heibel, A.K., Collins, T.A., Boger, T.: Influence of the substrate properties on the performances of NH₃-SCR monolithic catalysts for the after treatment of diesel exhaust: an experimental and modeling study. *Ind. Eng. Chem. Res.* **50**(1), 299–309 (2011)
7. Neyertz, C.A., et al.: K/CeO₂ catalyst supported on cordite monoliths: diesel soot combustion study. *Chem. Eng. J.* **181–182**, 93–102 (2012)
8. Pidria, M.F., et al.: Mapping of diesel soot regeneration behavior in catalyzed silicon carbide filters. *Appl. Catalyst B: Environ.* **70**(1–4), 241–246 (2007)
9. Liati, A., Eggenschwiler, P.D., et al.: Comparative studies of particles deposited in diesel particulate filters operating with biofuel, diesel fuel and fuel blends. In: SAE International (2011)
10. Mokhri, M.A., Abdulla, N.R., et al.: Soot filtration in recent simulation analysis in Diesel Particulate Filter (DPF). *Procedia Eng.* **41** (2012)
11. Ess, M.N., Bladt, H., et al.: Reactivity and structure of soot generated at varying biofuel content and engine operating parameters. *Combust. Flame* **163** (2016)
12. Lamharess, N., Millet, C.-N., et al.: Catalyzed diesel particulate filter: study of the reactivity of soot arising from biodiesel combustion. *Catal. Today* **176** (2011)
13. Popovicheva, O., Engling, G., et al.: Diesel/biofuel exhaust particles from modern internal combustion engines: microstructure, composition and hygroscopicity. *Fuel* **157** (2015)

14. Biswas, D.: Parivesh, Biodiesel as Automobile Fuel. Central Pollution Control Board, Ministry of Environment and Forests. Available from: <http://www.cpcb.delhi.nic.in/diesel/ch70902.htm> (2002)
15. Meher, L.C., Dharmagadda, V.S.S., Naik, S.N.: Optimization of alkali-catalyzed transesterification of *Pongamia pinnata* oil for production of biodiesel
16. Vuppaladiyam, A.K., Sangeetha, C.J., Sowmya, V.: Transesterification of *Pongamia pinnata* oil using base catalysts: a laboratory scale study. *Univers. J. Environ. Res. Technol.* **3** (1), 113–118 (2013)
17. Mamilla, V.R., Mallikarjun, M.V., et al.: Preparation of biodiesel from Karanja oil. *Int. J. Energy Eng. IJEE0102008*

Performance of Diesel Particulate Filter Using Metal Foam Combined with Ceramic Honeycomb Substrate



Hardik Sarasavadiya, Manthan J. Shah, Indranil Sarkar
and Aatmesh Jain

Abstract Although diesel engines have higher thermal and volumetric efficiencies, sufficiently large amount of particulate matter (PM) including soot is emitted during its exhaust stage. Thus, a need is raised for implementation of the diesel particulate filters (DPFs) in diesel engines as it has become the customary technology for the control of soot aerosol emissions. An analytical study of the performance of a circular ceramic honeycomb substrate (cordierite) diesel particulate filter with and without the use of metal foam filter at both ends as well as variation in channel length of ceramic substrate is reported to observe the change in the amount of soot particles trapped and pressure drop along its axis. The drop in pressure and filtration process depends on the filter pore structure properties such as permeability, porosity (40%) as well as channel length (60 and 100 mm). For each case, the depositions of soot through the filter were calculated by weighing approach, optimum drop in pressure using water U-tube manometer, and permeability of material by adopting graphical approach. However, after certain time, it is observed that due to increase in the accumulation of soot inside the diesel particulate filter there is a rise in pressure loss.

Keywords Diesel engines · After treatments · Diesel particulate filter
Ceramic honeycomb substrate · Metal foam filter · Pressure drop
Permeability

Definition, Acronyms, Abbreviations

a honeycomb filter cell size
 A coefficient in linear fit
 A_{filt} filtration area
 B coefficient in linear fit

H. Sarasavadiya (✉) · M. J. Shah · I. Sarkar
Department of Automotive Engineering, VIT University, Vellore, India
e-mail: hardiksvadiya22@gmail.com

A. Jain
ARAI Academy, Pune, India

© Springer Nature Singapore Pte Ltd. 2019
U. Chandrasekhar et al. (eds.), *Innovative Design, Analysis and Development Practices in Aerospace and Automotive Engineering (I-DAD 2018)*, Lecture Notes in Mechanical Engineering, https://doi.org/10.1007/978-981-13-2718-6_17

d_{pore}	pore diameter
D	filter outer diameter
F_w	factor equal to 28.454
K_w	filter wall permeability
L	filter outer length
Q	exhaust volumetric flow rate
V_{mon}	effective filter volume
w_w	filter wall thickness
K_w	permeability of wall
T	temperature of exhaust gas
HC	hydrocarbon
NO_x	nitrogen oxide
PM	particulate matter
SFC	specific fuel consumption
DPF	diesel particulate filter
CPSI	cells per square inch
PPM	part per million
CHS	ceramic honeycomb substrate
mA	Sample-A with metal foam
mB	Sample-B with metal foam

Greek Letters

β_F	Forchheimer's coefficient
ΔP	pressure drop across the filter
ξ	contraction/expansion inertial losses coefficient
μ	exhaust dynamic viscosity
σ	honeycomb filter cell density or standard deviation

1 Introduction

In comparison with equivalent gasoline engines, diesel engines have comparatively higher thermal and volumetric efficiency, lesser fuel consumption and CO_2 emissions [1]. At the same time, it emits higher NO_x and particulate matter (PM) including soot particles (solid) in the exhaust gas. The reason behind the formation of complex multi-component particulate matter is due to the improper mixing of sprayed fuel droplets with the abundant oxygen at a molecular level during its combustion process. There is a sequence of pathways leading to the formation of polycyclic structures, which are the source for generation of soot particles. The composition of diesel PM is uneven, depending on where in the engine they are formed and how they are trapped [2]. These fine particles (i.e., $<2.5 \mu\text{m}$, referred to as $\text{PM}_{2.5}$) cause environmental effluence and are potentially

dangerous to human health [3]. India is implementing emission norms: Bharat Stage-6 (BS-6) (0.08 g/km NO_x , $0.17 \text{ g/km HC} + \text{NO}_x$, 0.0045 g/km PM) by the end of 2020 which sets the new corridor for both engine and exhaust gas aftertreatment development for diesel vehicles. For effective reduction of NO_x and PM to achieve BS-6 emission norms, either engine modifications [4] or the aftertreatment of exhaust gas or both could be used such as upgrading of the fuel injection with the common rail [5, 6] as well as exhaust gas recirculation [7, 8], implementing oxidation catalysts [9], adopting diesel particulate filter (DPF) [10] and use of NO_x reduction catalyst [11]. Presently, as regards to the particulate matter, the wall-flow particulate filter is the most efficient aftertreatment device, attaining filtration efficiency of over 90%, with low pressure drop and good regeneration characteristics [12, 13]. The performance of wall-flow filters depends on the filter microstructure (i.e., pore size distribution, porosity) and geometric properties (i.e., DPF diameter and length, cell density, wall thickness) as well as the flow pattern and temperature conditions.

Figure 1 shows a schematic pattern of the wall-flow DPF which possess monolithic wall-flow structure made of ceramic (cordierite $2\text{MgO}-2\text{Al}_2\text{O}_3-5\text{SiO}_2$) with bundle of flow channels called as cells, typically of square cross section and the porous ceramic walls which act as a filter. Flow channels are alternatively plugged at every end; as a result, the gas in open channels at inlet monolith cross section is forced to flow diagonally through the porous wall of the ceramic substrate. At last, the flow goes into the outlet channels and leaves the monolith. Particulate matters are removed from the exhaust gas when they flow through the porous wall. The filtration process involves the loading of the porous wall, and at the same instance, the pressure drop increases due to the formation of the soot layer [14, 15] as the inner structure of the DPF is changed due to the accumulation of soot which in turn changes the flow pattern of exhaust gas [16, 17]. This process means as the time progresses, there is increase in pressure drop of DPF due to the

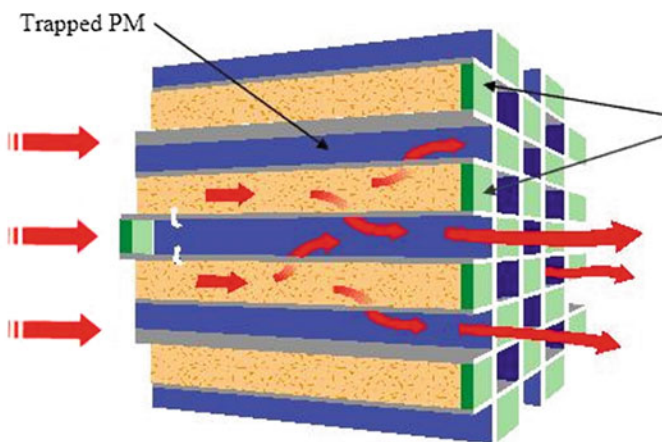


Fig. 1 Flow pattern through particulate filter

accumulation of higher amount of soot particles and increase of specific fuel consumption (SFC) due to increase in engine back pressure.

Thus for ideal DPF, utmost performance, lower pressure loss, higher filtration efficiency, and regeneration at low temperature [18] are demanded and the capacity for soot depositions inside the DPF can be enhanced by increasing the aperture ratio of inlet cell to outlet cell. The pressure drop during soot loading is low, because the soot layer is thinner [19, 20].

The advancement of DPF has comprised of the investigation of different systems defined by the amalgamation of materials and flow path-lines: ceramic honeycomb wall-flow monoliths, ceramic foams, ceramic fibers, sintered or metal fiber filters [21]. In this context, this paper presents a comparative study of ceramic honeycomb wall-flow DPF model with and without the use of metal foam filter at both its end to analyze the intensity and amount of soot particles trapped (for constant time duration) in addition with engine's back pressure under full load condition and specific fuel consumption as the time progresses for fixed cycle duration.

2 Experimental Setup and Methodology

2.1 Experimental Setup

One of the most important factors affecting the accuracy of drop in pressure is the experimental setup and its measurement procedure (Table 1).

Apart from basic experimental study, a good practical guideline such as accurate flow rate, pressure head, temperature measurement, and rate at which amount of fuel is consumed are the important features that require extra attention. An experimental setup comprises constant speed single-cylinder four-stroke water-cooled AV1 Kirloskar diesel engine coupled with eddy current dynamometer, water U-tube manometer, a DPF casing with particulate filter, and metal foam filter asides (Fig. 2).

Table 1 Engine specification

AV1 Kirloskar single-cylinder water-cooled engine		
Sr. no.	Parameter	Value
1	Rated power (kW)	3.7
2	Constant speed (rpm)	1500
3	Displacement (cc)	662
4	Bore diameter (mm)	87.5
5	Stroke length (mm)	110
6	Compression ratio	17.5
7	SFC (g/kWh)	245
8	Maximum permissible back pressure in exhaust system (kPa)	2.50
9	Maximum permissible intake depression (kPa)	1.00

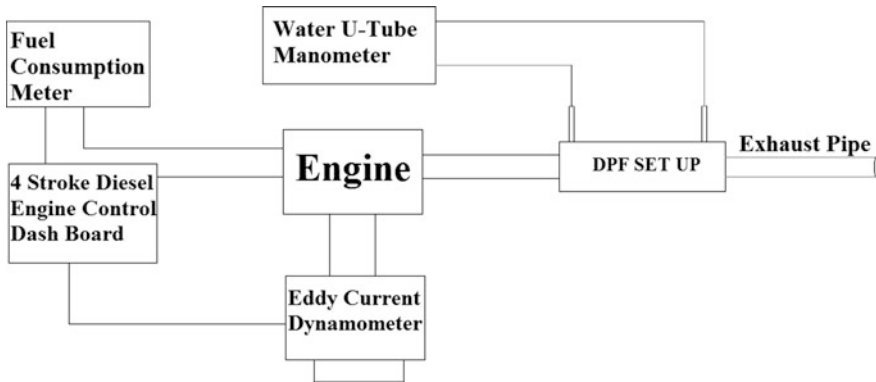


Fig. 2 Block diagram of an active diesel particulate filter control system installed in diesel engine

Table 2 Properties of diesel [22]

Flash point (°C)	45–110
Distillation range (°C)	140–400
Density at 15 °C (g/cm ³)	0.80–0.087
Sulfur content (ppm)	<10

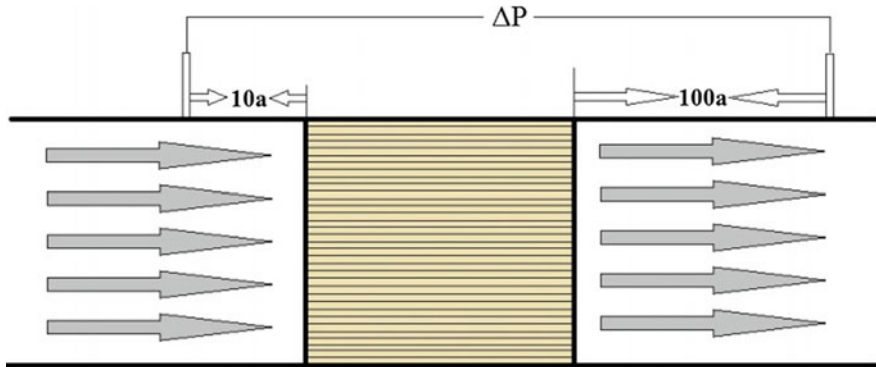


Fig. 3 Location of particulate filter

Following values mentioned in Table 2 are the properties of the diesel which was used to carry out the experimental analysis of amount of particulate matter generation during running the diesel engine for fixed cycle duration.

With regard to flow of an exhaust gas through DPF, a more appropriate setup is shown in Fig. 3, where the flow approaches the filter uniformly with no variation in cross section. The upstream pressure taps are placed at a distance of more than 10

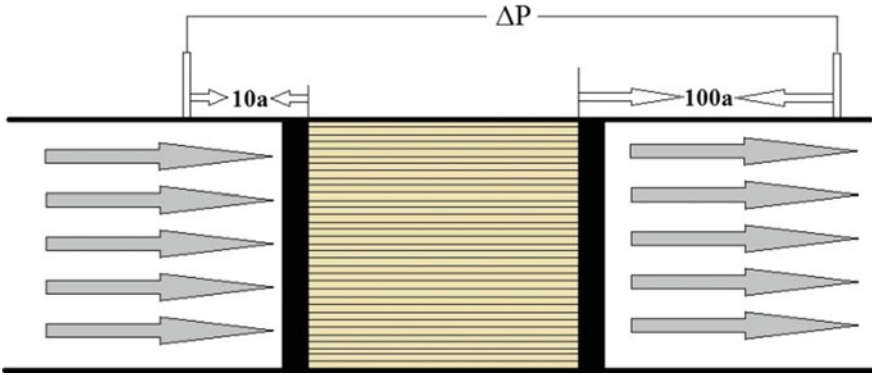


Fig. 4 Location of particulate filter along with metal foam filter

times a channel width ($10 \cdot a$) and the downstream pressure taps at a distance more than 100 times a channel width ($100 \cdot a$) which in turn gives the complex flow field observed in [23].

In addition to above, a metal foam filter (stainless steel scrubber) is placed at both the ends of particulate filter with same position arrangement as above with reference to pressure taps for analyzing the flow characteristic in addition with accumulation of soot particles on the expense of drop in pressure as shown in Fig. 4.

2.2 Methodology

The projected methodology quantifies the permeability of the clean porous honeycomb substrate wall-flow DPF and characterizes the pressure drop through it. But the experimental information regarding the drop in pressure produced by the filter is required (Fig. 5).

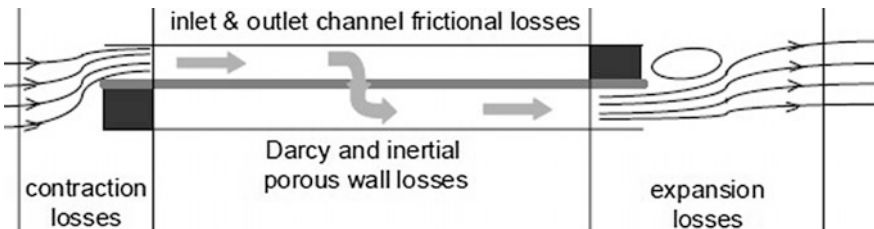


Fig. 5 Schematic of local value of pressure in wall-flow filter

Table 3 Viscosity correlation constants for various gases at $T_0 = 293$ K [23]

Gas	μ_0 (kg/ms)	ν
Air	$1.82 * 10^{-5}$	0.717
Nitrogen	$1.76 * 10^{-5}$	0.710
Exhaust gas (10% O ₂)	$1.72 * 10^{-5}$	0.740

The pressure drop through the porous wall depends on Darcy’s law [24, 25]. The calculation can be performed accurately starting from the local form of Darcy’s law for the filter wall as follows

$$\frac{dp}{dx} = - \frac{\mu}{k_w} \frac{Q}{A_{\text{filt}}} \tag{1}$$

The estimation of permeability of filter from also depends on the value of the dynamic viscosity (μ) of exhaust gas. The gases engaged are air, nitrogen, or engine exhaust gases, depending on the experimental setup. Estimation of the viscosity is achieved with the following power law equation:

$$\mu = \mu_0 \left(\frac{T^{\nu}}{T_0^{\nu}} \right) \tag{2}$$

The constants used in above equation are listed in Table 3 where subscript 0 denotes ambient condition.

Konstandopoulos [23] projected a lumped parameter model for the drop in pressure calculation in honeycomb wall-flow monoliths on the basis of incompressible flow approach. The drop in pressure for an isolated clean monolith is given by

$$\Delta P_{\text{dpf}} = \frac{\mu Q}{2V_{\text{mon}}} (a + w_w)^2 \left(\frac{w_w}{k_w a} + \frac{8F_w L^2}{3a^4} \right) + \frac{\rho Q^2}{V_{\text{mon}}^2 \alpha^2} (a + w_w)^4 \left(\frac{\beta_F w_w}{4} + 2\xi \frac{L^2}{a^2} \right) \tag{3}$$

The friction process is controlled by the permeability of porous walls (k_w). The pressure drop due to friction in square porous channels also depends on the coefficient of momentum transfer (F_w), which is considered constant and equal to 28.454 [26]. On the other hand, the inertial terms are proportional to the squared volumetric flow rate which results in the following contributions:

- (1) Drop in pressure across the porous wall by means of Forchheimer’s coefficient (β_F).
- (2) Drop in pressure at the entry to the inlet channels due to the local contraction.
- (3) Drop in pressure at the exit of the outlet channels due to the local expansion.

The ratio between the drop in pressure and the volumetric flow rate can be uttered by a linear function of the volumetric flow rate as,

$$\frac{P_{\text{dpf}}}{Q} = A + BQ \quad (4)$$

where coefficients A and B are, respectively,

$$A = \frac{\mu}{2V_{\text{mon}}} (a + w_w)^2 \left(\frac{w_w}{k_w \alpha} + \frac{8F_w L^2}{3a^4} \right) \quad (5)$$

$$B = \frac{\rho Q}{V_{\text{mon}}^2 \alpha^2} (a + w_w)^4 \left(\frac{\beta_F w_w}{4} + 2\xi_{\text{mon}} \frac{L^2}{a^2} \right) \quad (6)$$

Thus, the experimental data provides the drop in pressure and the volumetric flow rate to get the value of coefficient 'A'. As a result, by knowing the coefficient 'A' and the geometry of the DPF, the permeability of the porous wall can be obtained by Eq. (7)

$$k_w = \frac{\frac{w_w}{a}}{\left(\frac{2V_{\text{mon}} A}{\mu(a + w_w)^2} - \frac{8F_w L^2}{3a^4} \right)} \quad (7)$$

After running the engine for certain fixed duration (i.e., 120 min), particulate matter gets accumulated at the porous walls of particulate filter as well as in metal foam filter placed at its end in the form of soot layer which can be measured by highly sensitive weighing machine with accuracy in range of ± 0.001 .

3 Filter Geometry and Characteristic of Filter

The permeability and the inertial losses term of a wall-flow filter depend on geometrical features of filters, i.e., external diameter, length, plug length and plug ring (to provide structural strengthening and heat insulation), wall thickness, and cell density. These properties and geometrical parameters values of filter are the nominal values and not exact ones quoted by filter manufacturers (Fig. 6).

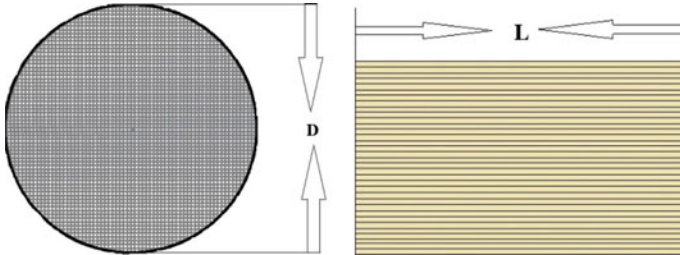


Fig. 6 Schematic of wall-flow DPF, depicting geometrical parameters

Table 4 Properties of filter (sample specifications)

Sr. no.	Properties	Value	
		Material-A	Material-B
1	Material type	Cordierite	Cordierite
2	Length (mm)	100	60
3	Diameter (mm)	45	40
4	Weight (gm)	90	60
5	Cells density (CPSI)	300	300
6	Wall thickness (mm)	0.12 (4.72 mil)	0.12 (4.72 mil)
7	Channel width (mm)	1.3	1.3
8	Porosity (%)	40	40
9	Density (kg/mm ³)	0.7 * 10 ⁻³	0.7 * 10 ⁻³
10	Volume weight (gm/L)	510	510
11	Volume (mm ³) (by dimensions)	159,043.5	75,398.4

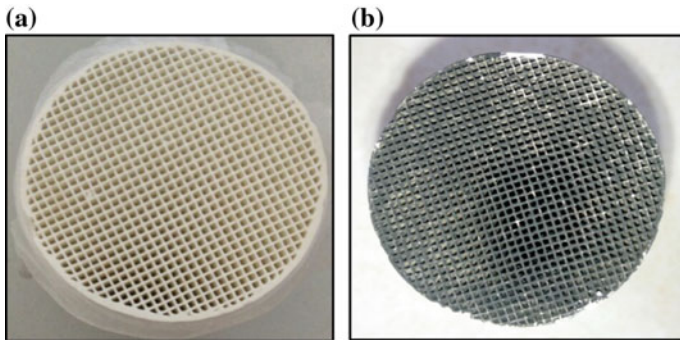


Fig. 7 Appearance of **a** new square cell DPF and **b** used square cell DPF

The correlation based on given dimensions by manufacturer is as follow:

$$\text{Channel width, } a = \frac{1}{\sqrt{\sigma}} - w_w \text{ [23]} \tag{8}$$

DPFs are made of ‘honeycomb’ structures. They consist of numerous ‘segments’ cemented together as shown in figure. Each segment is made of several square parallel channels (square tubes) with the opposite ends of adjacent channels being plugged as shown in figure. These DPFs trap particles with a filtration efficiency of 95–99% as per manufacturer consideration. Engines ran with commercial fuels of low sulfur content (<10 ppm). Commercial lubricating oils (SAE 15W-40) with 4000 ppm sulfur have been used. Two ceramic (cordierite) DPF samples of square cells with verified length and diameter were used in this study. The sample specifications are shown in Table 4. The cell structure of square cell bare DPF is shown in Figs. 7 and 8.

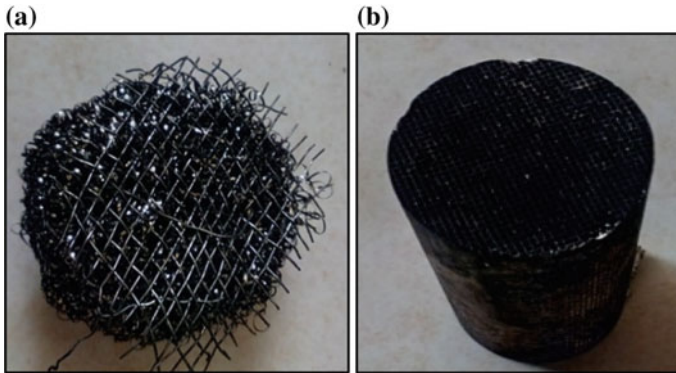


Fig. 8 a Metal foam filter and b ceramic honeycomb DPF substrate

Each sample has the same cell density 300 CPSI, and the wall thickness is 0.12 mm. The inlet aperture ratio of the square cell DPF is 72.30%. The porosity of SQ bare was approximately 40%.

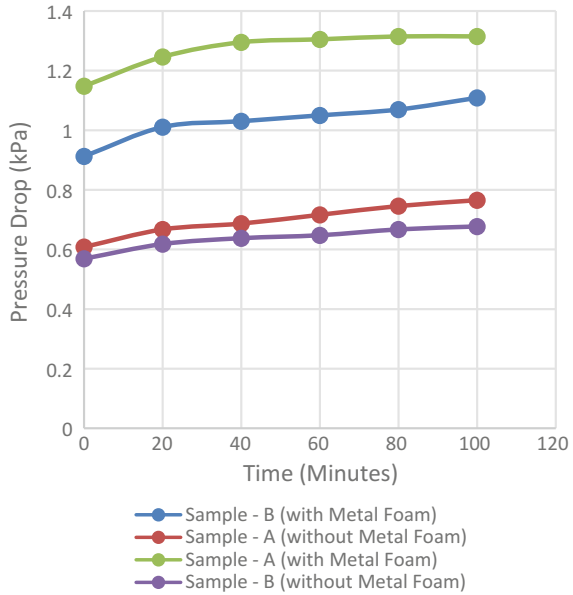
4 Result and Discussion

The current study puts forward different outcomes of particulate filter by adopting experimental approach. We performed the experiments with two different samples having distinguished properties as well as implementation of metal foam material with ceramic honeycomb substrate for comparative study on different cases. We also analyzed the accumulation of soot particles for each case using weighing method as well as permeability of filter (cordierite) using graphical and analytical approach.

4.1 Pressure Drop—Time

The pressure drop in DPF increases with increase in time (engine running duration). Rise in pressure drop is influenced by factors such as deposition of soot particle in filter and decrease in permeability property of filter material. Based on the experimental results, the pressure drop will be highest in Sample-A with metal foam among all samples as shown in Fig. 9.

Fig. 9 Measured drop in pressure of particulate filter with time



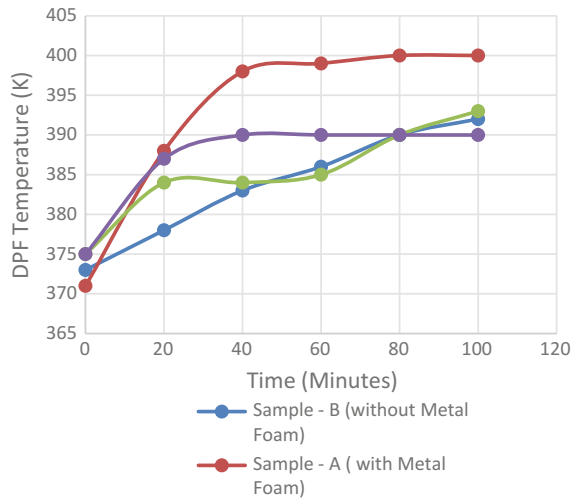
4.2 Pressure Drop—Flow Rate

Flow rate of exhaust gas is the function of exit pressure head. As pressure head increases with increase in engine running time, flow rate keeps on increasing continuously. The increase in flow rate affects the increase in pressure drop linearly. On comparison with different filter materials, we found that pressure drop will be more in Sample-A with metal foam.

4.3 DPF Temperature—Time

As we know that engine temperature is the function of in-cylinder pressure and time factor thus, temperature will increase as the time progresses. These results in rise of exhaust temperature with time and corresponding rise in temperature of ceramic honeycomb substrate. But the ceramic filter material can resist such high temperature due to its wide range of operating properties; i.e., thermal coefficient of expansion and thermal shock resistance temperature of substrate are $1.6 * 10^{-6}/K$ and $500\text{ }^{\circ}C$, respectively. During the experiments, we found the maximum temperature of filter material was nearly about $130\text{ }^{\circ}C$ (Fig. 10).

Fig. 10 Rise in exhaust temperature with time (experimentally)



4.4 Fuel Consumption—Pressure Drop

Performance of any engine depends on its fuel consumption. Experimental results show that with increase in pressure drop, the amount of fuel consumed by engine increases slightly; as a result, the condition of engine becomes worse. But particulate filter enables to accumulate soot particles in the expense of slightly higher fuel consumption.

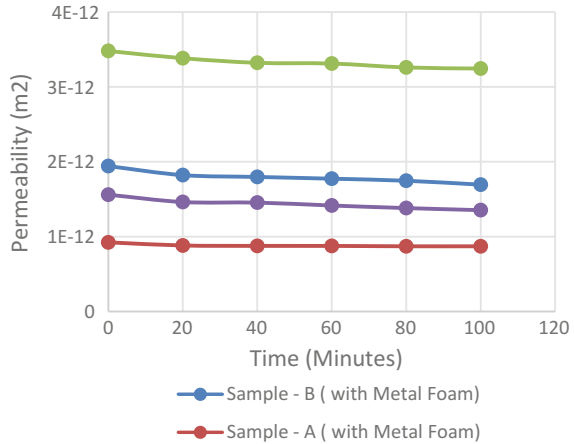
4.5 Permeability—Time

Permeability of any material is the measure of its ability to permit the fluid throughout. The tendency of permeability of ceramic honeycomb substrate decreases with respect to time due to the deposition of soot particles; as a result, resistance to fluid flow increases which results in drop in pressure. From our experimental study, we found the different values of permeability at each stage as shown in Fig. 11.

4.6 Pressure Drop/Flow Rate—Flow Rate

The graph between (pressure drop/flow rate) and flow rate gives the straight line which resembles the linear equation: $\Delta P = a + bQ^2$ by Konstandopoulos [23]. From experiment, it was seen that all the results were approximately linear to satisfy theoretical considerations.

Fig. 11 Deviation in permeability of filter material



In short, above graphical results can be summarized as follows

1. Highest and lowest pressure drop has been noted in Sample-mA (with metal foam) and Sample-B filter (without metal foam), respectively.
2. Similarly, highest and lowest amount of soot accumulation has been noted in Sample-mA and Sample-B filter, respectively.
3. Fuel consumption while using Sample-A with metal foam and Sample-B without metal foam filter is highest and lowest, respectively.

On the other hand, permeability of Sample-B is highest among all samples because of lower drop in pressure and smaller geometrical specification which implies that the more exhaust gas is allowed to be permitted, while sample-mA with metal foam has the lowest permeability due to higher drop in pressure.

5 Conclusion

In this study, flow behavior in terms of drop in pressure and permeability of diesel particulate filter with and without metal foam material is described with the total accumulation of soot particles for same filter material with varying dimensions. Thus, comparative study is presented for their reliable assessment from experimental data. So by considering overall factors affecting the performance of particulate filter, we came to know that Sample-mB with metal foam is the most favorable particulate filter among all others in use.

Since maximum permissible back pressure (as mentioned in Table 1) is 2.50 kPa for Kirloskar engine, under experimental condition we got the maximum drop in pressure 1.3 kPa. Hence, we have succeeded in the achieving the desired performance of DPF through experimental approach.

References

1. Currier, W.N., Yezerets, A., Kim, H.D., Epling, S.W., Eadler, A.H., Peden, H.F.C.: Differential kinetic analysis of diesel particulate matter (soot) oxidation by oxygen using a step-response technique. *Appl. Catal. B Environ.* **61**, 120–129 (2005)
2. Kittelson, D.B.: Engines and nanoparticles: a review. *J. Aerosol Sci.* **29**, 575–588 (1998)
3. Kennedy, I.M.: The health effects of combustion generated aerosols. *Proc. Combust. Inst.* **31**, 2757–2770 (2007)
4. Mari, K., Fukano, I., Sugakawa, K., Kawatani, T., Koyama, T.: SAE Paper No. 932654 (1993)
5. Knecht, W.: Diesel engine development in view of reduced emission standards. *Energy* **33**(2), 264–271 (2008)
6. Novella, R., Torregrosa, A.J., Mónico, L.F., Broatch, A.: Suitability analysis of advanced diesel combustion concepts for emissions and noise control. *Energy* **36**(2), 825–838 (2011)
7. Maiboom, A., Hézet, J.F., Tauzia, X.: Experimental study of various effects of exhaust gas recirculation (EGR) on combustion and emissions of an automotive direct injection diesel engine. *Energy* **33**(1), 22–34 (2008)
8. Bermúdez, V., Pla, B., Lujan, J.M., Linares, W.G.: Effects of low pressure exhaust gas recirculation on regulated and unregulated gaseous emissions during NEDC in a light-duty diesel engine. *Energy* **36**(9), 5655–5665 (2011)
9. Clerc, J.C.: Catalytic diesel exhaust after treatment. *Appl. Catal. B Environ.* **10**, 99–115 (1996)
10. Fino, D.: Diesel emission control: catalytic filters for particulate removal. *Sci. Technol. Adv. Mater.* **8**, 93 (2007)
11. Twigg, M.V.: Roles of catalytic oxidation in control of vehicle exhaust emissions. *Catal. Today* **117**, 407–418 (2006)
12. Khair, M. A review of diesel particulate filter technologies. SAE Technical Paper 2003-01-2303 (2003). <https://doi.org/10.4271/2003-01-2303>
13. Van Setten, B.A.A.L., Moulijn, J.A., Makkee, M.: Science and technology of catalytic particulate filters. *Catal. Rev.* **43**(4), 489–564 (2001)
14. Lapuerta, M., Oliva, F., Fernández, J.R.: Effect of soot accumulation in a diesel particle filter on the combustion process and gaseous emissions. *Energy* **47**(1), 543–552 (2012)
15. Piscaglia, F., Ferrari, G.: A novel 1D approach for the simulation of unsteady reacting flows in diesel exhaust after-treatment systems. *Energy* **34**, 2051–2062 (2009)
16. Wirojsakunchai, E., Kolodziej, C., Schroeder, E., Foster, D.E., Root, T., Schmidt, N., et al.: Detailed diesel exhaust particulate characterization and real-time DPF filtration efficiency measurements during PM filling process. SAE Technical Paper 2007-01-0320 (2007)
17. Yamamoto, K., Yamashita, H., Oohori, S., Daido, S.: Simulation on soot deposition and combustion in diesel particulate filter. *Proc. Combust. Inst.* **32**, 1965–1972 (2009)
18. Torregrosa, A.J., Arnau, F.J., Serrano, J.R., Piqueras, P.: A fluid dynamic model for unsteady compressive flow in wall-flow diesel particulate filters. *Energy* **36**, 671–684 (2011)
19. Ogyu, K., Hong, S., Ohno, K., Komori, T.: Ash storage capacity enhancement of diesel particulate filter. SAE Technical Paper 2004-01-0949 (2004)
20. Ogyu, K., Oya, T., Konstandopolous, G.A., Ohno, K.: Improving of the filtration and regeneration performance by the SiC-DPF with the layer coating of PM oxidation catalyst. SAE Technical Paper 2008-01-0621 (2008)
21. Murtagh, M.: Diesel Particulate Filters (DPF): A Short Course in Diesel Particulate and NO_x Emissions Course. University of Leeds, Ann Arbor, MI (2002)
22. Indian Standards for Properties of Diesel Fuel: IS 1460: Automotive Diesel Fuel (2005)

23. Konstandopoulos, A.G., Masoudi, M., Skaperdas, E.: Inertial contributions to the pressure drop of diesel particulate filters. SAE Technical Paper 2001-01-0909 (2001)
24. Miyairi, Y., Abe, F., Miwa, S., Xu, Z., Nakasuji, Y.: Numerical study on forced regeneration of wall-flow diesel particulate filters. SAE Technical Paper 2001-01-0912 (2001)
25. Versaevel, P., Rigaudeau, C., Noirot, R., Koltsakis, G.C., Colas, H., Stamatelos, A.M.: Some empirical observations on diesel particulate filter modeling and comparison between simulations and experiments. SAE Technical Paper 2000-01-0477
26. Bisset, E.J.: Mathematical model of the thermal regeneration of a wall-flow monolith diesel particulate filter. Chem. Eng. Sci. **39**(7–8), 1233–1244 (1984)

Dry Machining of Nimonic 263 Alloy Using PVD and CVD Inserts



K. Vetri Velmurugan, K. Venkatesan, S. Devendiran
and Arun Tom Mathew

Abstract Nickel-based alloys are used in critical components where superior mechanical strength, corrosion and oxidation resistance at high operating temperatures are a prerequisite. Of the nickel-based alloys, one that has excellent resistance to thermal fatigue and creep characteristics suitable for use in the combustion chamber of aircraft engines is Nimonic C-263. This is a difficult to turn material owing to its superior properties, and the proper selection of a cutting tool along with cutting parameters plays major role is required in order to enhance its machinability. This paper presents a comparative analysis of force, roughness and tool wear during the dry machining Nimonic 263 alloy using coated carbide inserts. Machinability experiments based on Taguchi's L16 orthogonal array are carried out. From the experimental results, the cutting force could not be improved, although a remarkable reduction in roughness and tool wear is observed for the AlTiN PVD coated insert under different cutting condition compared to TiN/Al₂O₃/TiCN.

Keywords Tuning responses · Coated carbide inserts · Dry machining

1 Introduction

Superalloys, also known as heat resistant super alloys, are nickel (Ni)-based alloys which possess outstanding mechanical and creep strengths at elevated temperatures. Due to these properties, these alloys are found in advanced aircraft engines and currently comprise over 50% of their weight [1]. This grade of alloys has 52.49% Ni with the remaining elements being cobalt (Co), chromium (Cr), and molybdenum (Mo). Hastelloy, Inconel, Nimonic and Waspaloy are few common examples

K. Vetri Velmurugan

Department of Mechanical Engineering, Sri Sairam Engineering College, Chennai, India

K. Venkatesan (✉) · S. Devendiran · A. T. Mathew

School of Mechanical Engineering, Vellore Institute of Technology, Vellore, India

e-mail: venkatesan.kannan@vit.ac.in

© Springer Nature Singapore Pte Ltd. 2019

U. Chandrasekhar et al. (eds.), *Innovative Design, Analysis and Development Practices in Aerospace and Automotive Engineering (I-DAD 2018)*, Lecture Notes in Mechanical Engineering, https://doi.org/10.1007/978-981-13-2718-6_18

179

of Ni-based alloys. Nimonic C-263 is found in the combustion chamber of aircraft engines due to its unique resistance to thermal fatigue and creep characteristics. In this alloy, the presence of Cr (19–21%) and Mo (5.6–6.1%) strengthens the grain boundaries by solution hardening with the formation of MC, M₆C and M₂₃C₆ metallic carbides. Furthermore, the high cobalt content (19–21%) induces higher plastic deformation and considered as difficult to turn material than that of Inconel 718 [2]. Other major phases in Nimonic C-263 are γ' (Ni,Co)₃(Ti,Al), η -(Ni,Co)₃Ti, MC-(Ti,Mo)C, M₂₃C₆-(Cr,Mo)₂₃C₆ and M₆C-(Co, Ni)₃Mo₃C [3]. However, this alloy suffers from poor machinability owing to its low thermal diffusivity, high strength at higher temperature, propensity to harden, the presence of coarse and stiff particles in its microstructure and a chemical affinity towards cutting tool materials. Cutting force, power consumption, surface roughness, tool wear, cutting temperature and chip morphology are the quality characteristics that define the machining performance of nickel-based alloys [4]. These machinability characteristics are greatly influenced by the selection of cutting tool materials and cutting parameters. Carbide inserts (both coated and uncoated) are employed, for economic and productivity reasons in the machining of different grades of nickel-based alloys, to study the effect of different coating on the tool cutting edge for given cutting parameters that of ceramic tools. It is reported that CVD TiN/Al₂O₃/TiCN lowers the cutting force compared to PVD TiN/TiAlN due to its high thermal stability layer of Al₂O₃ and its resistance to wear layer of TiCN [5]. However, a lower cutting force was also reported with a similar PVD coated tool when compared to its CVD TiCN/Al₂O₃ coated tool counterpart [6]. Due to the ability of CVD (TiN/TiCN/Al₂O₃/ZrCN) coated tools to withstand high cutting temperatures compared to an uncoated tool, the tool life of an uncoated carbide tool is found to be lower than that of CVD with a multi-coating layer during machining of Nimonic C-263, and the roughness of the coated tool is less [4].

In other work by the author [5] looking at the application of the desirability function approach (DFA), the optimal parameters were determined as follows when ceramic tools are used: a speed of 210 m/min, a feed of 0.05 mm/rev and a cutting depth of 0.5. Regression models were developed to forecast machinability attributes in order to correlate the process parameters of force [5], roughness [5, 7, 8] and flank wear [5, 8] using response surface analysis (RSA) with the same cutting tool. With the use of a statistical approach (3D finite element analysis), the author [2] found an error of about 6% when predicting cutting force, cutting temperature, stress and strain at the tool-workpiece interface compared with experimental values during machining of C-263 Nimonic alloy using a PVD coated tool. Cutting speed is found to be most influential factor instead of cutting depth while turning on alloy with PVD coated insert as reported by Ezugwu and Okeke [9, 10]. Feed rate was more important than speed for a whisker-reinforced ceramic cutting tool operating at between 125 and 250 m/min when cutting force and flank wear were considered during machining of C-263 Nimonic alloy [5, 8]. It was also reported by the author [11] that a PVD multilayer coated tool is outperformed at 50–90 m/min even though a CVD tool should not exceed 60 m/min during the turning of C-263 Nimonic alloy. Micro-hardness and residual stress are increased when the feed is

increased from 0.102 to 0.143 mm/rev under a high turning speed of 250 m/min during the dry turning of C-263 alloy [12].

The application of cutting fluids can be removed experimentally by utilizing the specific range of machining parameters from the turning of Inconel 725 in combination with coated tools [13]. Although cryo-machining reduces the conventional cutting temperature, it prompts surface work-hardening of the workpiece [14, 15]. The cutting force is higher during cryo-machining that of dry and wet environments [14, 16]. However, interestingly, a TiN/TiAlN PVD tool reduced turning force by 40 and 16% in a dry environment compared with flood and MQL cutting conditons [1]. High pressure cooling (HPC) decreased flank wear and cutting forces by more than 30 and 10% respectively. In contrast, compared to dry machining, notch wear is higher and becomes a significant problem in HPC [17]. Recent reports reveal that machining costs associated with the use of cutting fluid contribute to a maximum of about 20% compared with the tool cost which is estimated to be approximately 4% [14]. Therefore, in the current study, dry machining is chosen as the primary objective for C-263 Nimonic alloy in order to minimize or eliminate the use of cutting fluid.

It is evident that conclusive data regarding the varying of cutting parameters along the cutting tool is relatively scarce for the machining of C-263 Nimonic alloy. Moreover, there are no available data on the comparative effectiveness of physical vapor disposition (PVD) and chemical vapor deposition (CVD) coatings during the turning of C-263 Nimonic alloy. As a result, the objective of the present study is to investigate the capability of single layer PVD (AlTiN) along with the influence of turning speed, rate of feed and cutting depth on the physical characteristics of machinability in comparison with a multilayer coated CVD (TiN/TiCN/Al₂O₃) insert.

2 Experimental Section

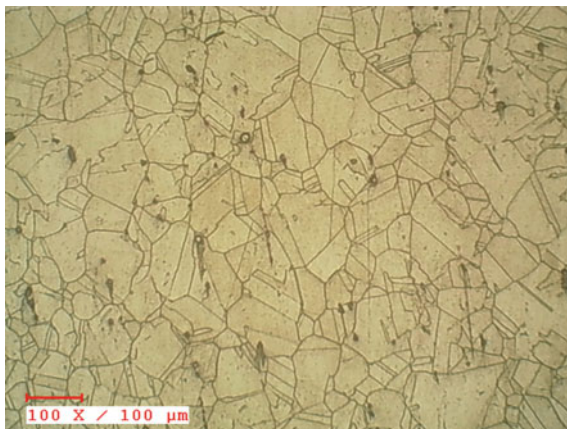
2.1 Experimentation on Nimonic C-263 Superalloy

Nimonic 263 alloy in rod forms of 300 mm length and with a diameter of 36 mm were procured with an average hardness of 32 HRC. The chemical composition of the alloy was 51.49% Ni, 0.17% Si, 0.44% Mn, 19.5% Cr, 6.18% Mo, 0.06% Cu, 1.1% Fe, 16.6% Co, 1.9% Ti, 0.4% Al and 0.2% W. It can be seen from Table 1 that iron (Fe), nickel (Ni) and chromium (Cr) were the major constituents in the

Table 1 Cutting parameters

Parameter, symbol	Unit	Level 1	Level 2	Level 3	Level 4
Speed (<i>v</i>)	m/min	60	90	120	150
Feed (<i>f</i>)	mm/rev	0.05	0.12	0.18	0.25
Cutting depth (<i>ap</i>)	mm	0.2	0.3	0.4	0.5

Fig. 1 The microstructure of the as-received Nimonic 263 alloy



as-received material. The received sample was initially cleaned with acetone before being chemically etched with Keller's reagent to get optical micrograph image. The etchant is a Keller's solution (5 ml HCl, 3 ml acetic acid, 3 ml of HNO_3 and 2–3 drops of glycerol). An image analyzer was used to observe the optical microstructure of the as-received Nimonic 263 alloy and this is shown in Fig. 1. It can be seen that grains are uniformly distributed. The microstructure of Nimonic 263 consists of an austenite face-centered cubic (FCC) matrix known as gamma (γ) and can be held together by solid solution firming up (Mo and Cr) in nickel together with other secondary phases and through precipitation toughening (Ti, Nb, Al) by establishing intermetallic phases.

The high-speed lathe turning experiments were carried out without cutting fluid (in a waterless environment). A turning center was used with a top turning speed of 3500 rpm and an input power of 1.25 kW as shown in Fig. 2. In this research, parameters such as speed (V_c), rate of feed (f) and cutting depth (a_p) were considered for experimentation. The force (F_z), roughness (R_a) and tool wear (V_{ba}) were regarded as the target functions. It was assumed that the effects of turning parameters on target functions are composite and nonlinear and as a result the trial was set up with three levels of design. Three turning parameters were chosen, and for every factor, four levels were presumed. Based on the carefully chosen turning parameters and their attitudes, a design matrix was created in accordance with the standard L_{16} orthogonal arrangement. Different sets of speed, feed and cutting depth were used in the test and are potted in Table 1. The design conditions comprised of 16 rows conforming to the total amount of experimentation trials.

The cutting tools used for the turning experiments are PVD coated (AlTiN) and CVD coated ($\text{TiN}/\text{Al}_2\text{O}_3/\text{TiCN}$) carbide inserts. Cutting tools having carbide tips with a code according to ISO (CNMG 120408-MP, KCU 25) and (CNMG 120408-MP, KCM25) with -6 orthogonal rake angles were employed. The specification of the cutting tool holder is PCLNR 2020K12. Cutting forces

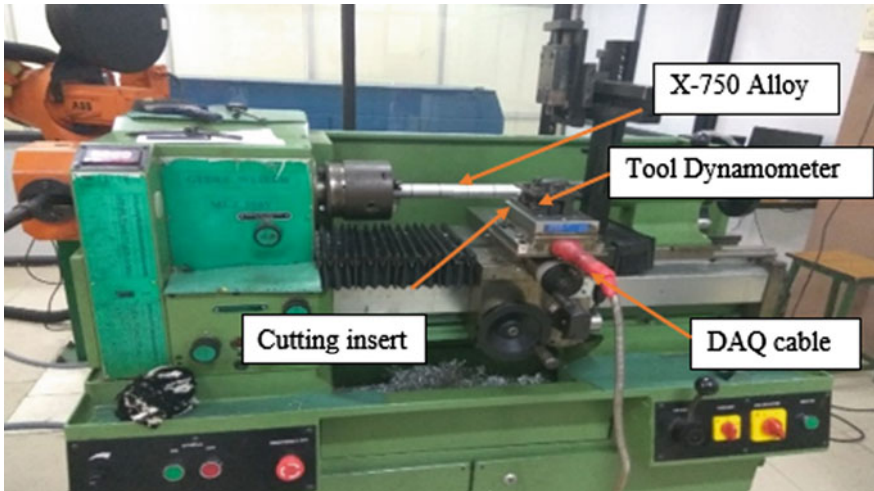


Fig. 2 Experimental setup for the machining experiments

were measured by a piezoelectric Kistler dynamometer (Model 9257B), and the surface finish was measured using a surface profilometer (Marsurf GD120) to the ISO 4287 standard. The experimental results for a machining length of 40 mm are as shown in Table 2 for the PVD coated carbide insert and Table 3 for the CVD coated carbide insert.

3 Results and Discussion

3.1 Analysis of Variance

ANOVA results for the output responses are shown in Table 4 for the PVD insert and Table 6 for CVD insert respectively. Statistical model accuracy estimator values are provided in Table 5 for the PVD insert and Table 7 for the CVD insert respectively. The *F*-value for the PVD and CVD inserts having a *P*-value lower than 0.001 in Tables 4 and 6 implies that the model is statistically significant. The interaction of cutting speed and feed rate along with cutting speed and cutting depth is a substantial factor for PVD inserts, while cutting depth and both turning speed and feed are an significant term for CVD inserts. From the results, variation in feed rate is the most influential factor for the PVD insert and cutting depth is the most influential factor for the CVD insert. The corresponding regression coefficient of the R2 values of each response of FZ, Ra and Vba is >85% for both inserts as shown in Tables 5 and 7 respectively. This implies that the developed models could help to predict the responses for the function of selected input-independent turning parameters.

Table 2 Experimental results for PVD inserts

Trial no.	Control factors			Mean response values			
	Vc (m/min)	f (mm/rev)	ap (mm)	Fz (N)	Ra (μ m)	Flank (mm)	Crater (mm)
1	60	0.1	0.2	55.43	0.66	0.043	0.174
2	60	0.15	0.3	79.50	0.74	0.048	0.214
3	60	0.2	0.4	123.4	0.898	0.063	0.249
4	60	0.25	0.5	197.6	1.679	0.077	0.272
5	90	0.1	0.3	46.86	0.561	0.076	0.203
6	90	0.15	0.2	76.39	1.298	0.053	0.228
7	90	0.2	0.5	129.0	1.536	0.087	0.239
8	90	0.25	0.4	113.4	3.283	0.068	0.254
9	120	0.1	0.4	70.66	0.613	0.078	0.218
10	120	0.15	0.5	82.79	1.05	0.066	0.223
11	120	0.2	0.2	93.40	1.996	0.069	0.218
12	120	0.25	0.3	70.86	2.171	0.082	0.213
13	150	0.1	0.5	95.62	0.539	0.038	0.234
14	150	0.15	0.4	91.61	1.089	0.053	0.198
15	150	0.2	0.3	116.7	1.47	0.073	0.172
16	150	0.25	0.2	70.23	2.967	0.111	0.161

Table 3 Experimental results for CVD inserts

Trial no.	Control factors			Mean response values			
	V (m/min)	f (mm/rev)	ap (mm)	Fz (N)	Ra (μ m)	Flank (mm)	Crater (mm)
1	60	0.1	0.2	31.9	0.747	0.079	0.124
2	60	0.15	0.3	72.76	1.391	0.092	0.186
3	60	0.2	0.4	106.11	2.443	0.096	0.249
4	60	0.25	0.5	146.7	3.928	0.106	0.276
5	90	0.1	0.3	65.34	1.301	0.096	0.169
6	90	0.15	0.2	50.11	1.627	0.105	0.183
7	90	0.2	0.5	149.9	1.944	0.073	0.225
8	90	0.25	0.4	110.1	2.505	0.102	0.248
9	120	0.1	0.4	75.56	1.015	0.078	0.175
10	120	0.15	0.5	122.5	1.242	0.058	0.200
11	120	0.2	0.2	50.24	2.012	0.083	0.198
12	120	0.25	0.3	76.12	2.175	0.071	0.196
13	150	0.1	0.5	80.62	0.788	0.048	0.156
14	150	0.15	0.4	89.65	1.296	0.053	0.154
15	150	0.2	0.3	73.44	1.515	0.073	0.167
16	150	0.25	0.2	36.16	2.593	0.072	0.171

Table 4 ANOVA results for PVD inserts

Source	Fz		Ra		Vba	
	F-value	p-value	F-value	p-value	F-value	p-value (Pr)
Model	18.52	0.001	18.71	0.001	44.62	0.000
A: Vc	2.54	0.517	2.38	0.174	2.96	0.136
B: F	0.47	0.050	75.95	0.000	5.62	0.050
C: ap	5.89	0.303	1.23	0.310	24.19	0.003
AB	16.86	0.006	0.29	0.612	49.48	0.000
AC	5.07	0.050	5.66	0.050	138.52	0.000
BC	9.71	0.021	0.00	0.995	1.53	0.263
A ²	11.78	0.014	9.02	0.024	26.95	0.002
B ²	2.85	0.142	8.62	0.026	19.19	0.005
C ²	4.19	0.087	0.04	0.857	1.08	0.902
Error	685.1		0.4613		0.00075	
Total	19718.2		12.10		0.0051	

Table 5 Statistical model accuracy estimator for PVD inserts

	Standard deviation	R-squared	Adj R-squared	Pred R-squared
Fz	10.68	0.9653	0.9131	0.6581
Ra	0.263	0.9656	0.9140	0.6386
Vba	0.0035	0.9853	0.9632	0.9046

Table 6 ANOVA results for CVD inserts

Source	Fz		Ra		Vba	
	F-value	p-value	F-value	p-value	F-value	p-value
Model	282.08	0.000	34.94	0.001	6.42	0.000
A: Vc	2.46	0.168	6.03	0.174	9.18	0.025
B: F	46.85	0.000	26.53	0.000	0.15	0.715
C: ap	794.56	0.000	2.87	0.310	10.62	0.017
AB	4.82	0.070	14.40	0.612	6.27	0.046
AC	10.99	0.016	24.24	0.050	4.24	0.085
BC	43.76	0.001	0.37	0.995	0.53	0.574
A ²	32.77	0.002	1.53	0.024	1.70	0.240
B ²	71.26	0.000	4.96	0.026	0.33	0.585
C ²	4.19	0.934	3.05	0.857	1.09	0.338
Error	44.7		0.189		0.00075	
Total	18977.2		10.11		0.0051	

Table 7 Statistical model accuracy estimator for CVD inserts

	Standard deviation	R-squared	Adj R-squared	Pred R-squared
Fz	2.73	0.99761	0.9941	0.9763
Ra	0.177	0.9813	0.9532	0.8248
Vba	0.008	0.9062	0.7654	0.6481

3.2 Force Results of PVD and CVD

The effects of the different process parameters for both coated carbide inserts are drawn on the target function of 263 Nimonic alloys, which are predicted from the developed mathematical model by varying two parameter values from their minimum to maximum level while holding the values of a third factor at a constant level. The hold values for speed, feed and cutting depth are 105 m/min, 0.175 mm/rev and 0.35 mm respectively. The experimental results are plotted and presented in Fig. 3. For turning with PVD inserts, from plot 1 of Fig. 3, the lowest force of <50 N is seen at low speed (60 m/min) and feed (0.1 mm/rev). A reduction in force is observed for increasing speed up to 100 m/min for given values of feed rate, and a magnitude of 110–130 N is found at a higher feed rate value. This is due to its low

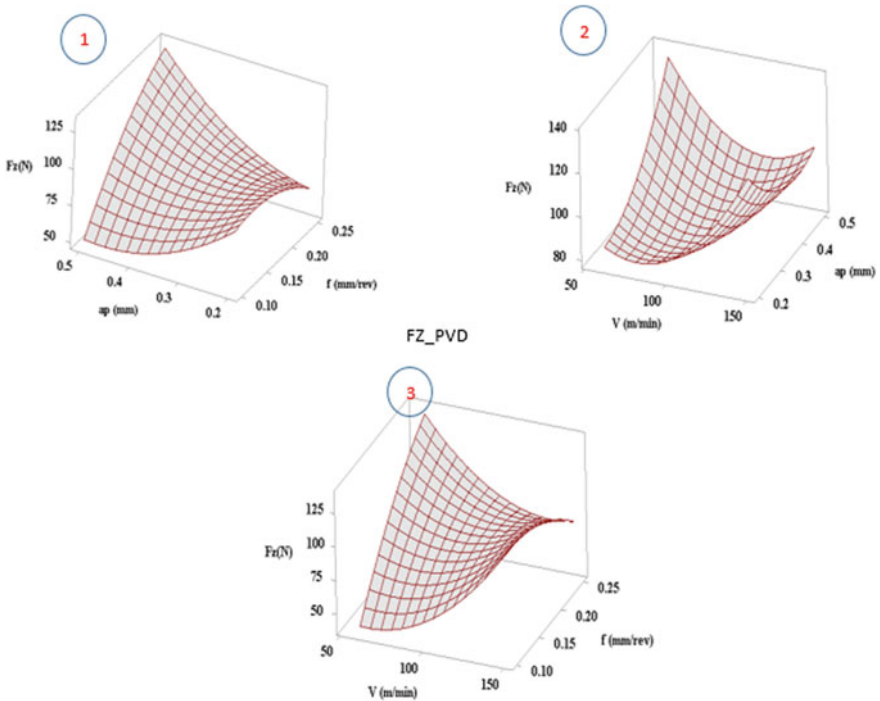


Fig. 3 Surface plots of cutting forces for PVD coated carbide inserts

heat transfer coefficient and the fact that heat remains on the cutting surface for a given feed rate. This results in a softening of material and elastic deformation behavior occurs on the surface of the workpiece. Thus a reduction in force is observed. Further increases in cutting speed resulted in an increase in cutting force and this was attributed to the formation of a built-up edge (BUE) [3]. Increasing feed increased the forces at a lower rate due to a noticeable increase in load on the tool tip. It was also recognized that a reduction in cutting force at a higher rate was due to the formation of separate segmented chips under very high feed conditions (0.15 and 0.25 mm/rev) as reported by Ezilarasan et al. (2013b). From plot 2 of Fig. 3, the highest force (>128 N) was obtained at low speed (60 m/min) and high cutting depth (0.5 mm). The decrease in force (<80 N) with an increase in speed from 60 to 120 m/min occurred under the condition of low (0.2 mm) to moderate (0.35 mm) cutting depth. From plot 3 of Fig. 3, the smallest force (<60 N) was observed at level feed (0.1 mm/rev) and higher cutting depth (0.5 mm) before it increased (>120 N) with an increase in feed rate and extent of cut. With an increase in either feed or cutting depth, the volume of the chip produced increased or the amount of material created server workpiece-tool interface friction [18]. Accelerated flank wear, burr formation, notching and plowing phenomenon may lead to a sharp increase in forces and subsequently deteriorate the finish of the surface [19]. This results in an increasing of forces. Therefore, at low feed and higher cutting depth, force reduction occurs.

For turning with CVD inserts, from plot 4 of Fig. 4 the magnitude of cutting force (<60 N) is lower at higher speeds and low feed rates than for low speeds and higher feed rates. The cutting force values are increased while the increase of feed rate at higher speeds is due to the high coefficient of friction between the workpiece material and the cutting tool. Moreover, the magnitude is low at higher levels of speed and feed and this is due to the fact that minimum shear energy for plastic deformation is achieved. From plot 5, the cutting force is increased (>140 N) with increased speed and cutting depth compared to a high speed and a low depth cut (<40 N). This may be the retain of thermal stability of the tool cutting edge or an increase in the cross-sectional area of the uncut chip. Thus force decreases at high speeds and low cutting depths. From plot 6, cutting forces are found to be higher (>150 N) at a high feed rate and cutting depth compared to a low cutting depth and feed rate. From the experimental plots it can be seen that low speed, feed rate and higher cutting depth for PVD carbide inserts, along with a higher top speed, low feed and cutting depth for CVD carbide inserts, are required to minimize the cutting force. The higher speed for CVD carbide inserts may be because the functional top layer of Al_2O_3 protects the cutting edge from transferring heat to the substrate. It is stated in [3] that the lower temperature is observed when using a CVD TiN/ Al_2O_3 /TiCN coated tool rather than a PVD TiN/TiAlN coated tool. It could be attributed to the higher thermal conductivity of the coating layer (Al_2O_3 /TiCN) of the CVD coated tool along the upper edge radius. As a result, plowing became a more dominant mechanism of cutting than shearing, leading to a decrease in cutting zone temperature.

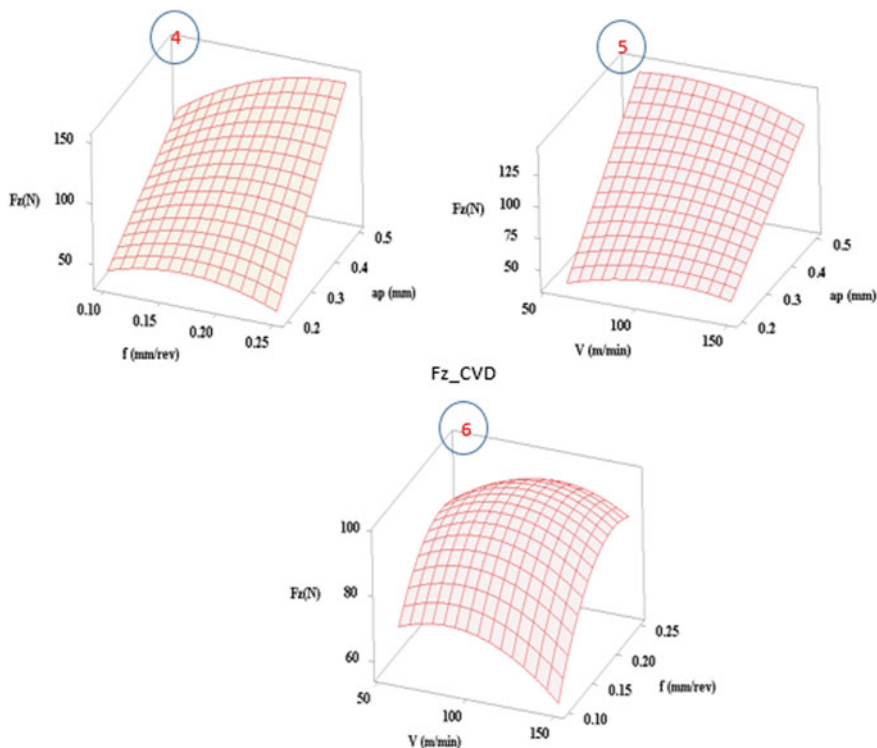


Fig. 4 Surface plots of cutting forces for CVD coated carbide inserts

The comparison of results of the coated carbide inserts is shown in Fig. 5. From the results obtained and shown in Fig. 3b, it can be seen that there is a greater increase in cutting force with the CVD tool than with its PVD counterparts. On the other hand, a significant reduction in cutting force for the PVD tool of about 48% is observed compared to the CVD tool. Similar results were also noted by [3]. This may be due to higher thermal stability, resistance to wear and spalling of Al_2O_3 , while TiCN layers in the CVD coated tool might have played a significant role in lowering the cutting force.

3.3 Surface Roughness Results for PVD and CVD

The surface roughness is the measured value on the turned surface. This has an impact on the functional end use part by governing frictional and wear behavior at the interfaces of bodies in contact, lubrication efficacy, tension corrosion and the progress of fatigue cracks, etc. [18, 19]. Figure 6 shows the variation in the

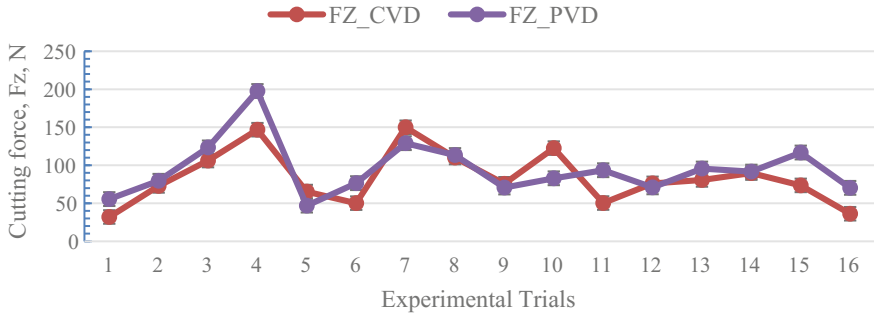


Fig. 5 Process benefits of cutting forces for coated carbide inserts

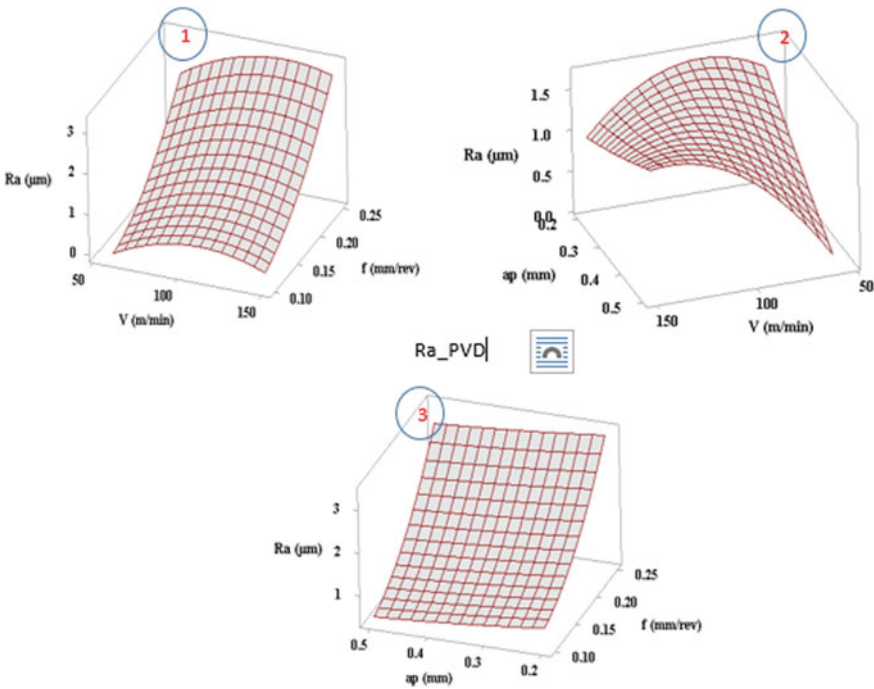


Fig. 6 Surface plots of cutting forces for PVD coated carbide inserts

roughness of Nimonic C-263 with various turning factors for both PVD and CVD tools. For turning with PVD inserts, from plot 1 of Fig. 6 it can be seen that the higher value of roughness of about $>3 \mu\text{m}$ is at a moderate speed and higher feed of 0.25 mm/rev while the lowest value of approximately $<0.5 \mu\text{m}$ is at a higher top speed and a lower feed. This shows that a decrease in surface roughness occurs with

increasing cutting speed for machining the various grades of nickel-based superalloys [3, 20]. This is further explained as the lessening in the BUE, reduced machine vibration [21]. It can also be seen that an increase in roughness occurs with increasing speed at high cutting depth, while a decrease in roughness occurs at a low cutting depth. An increase in surface roughness with speed may result in increased tool flank wear [22, 23]. The results are, however, contradictory to those reported by [3]. From plot 2 it can be seen that the highest roughness occurs at a speed of 60 m/min and a cutting depth of 0.2 mm, while the lowest roughness occurs at a lower speed and higher cutting depth. Plot 3 shows that the highest value of roughness is obtained at a feed of 0.25 mm/rev and a cutting depth of 0.5 mm, while the lowest occurs at a lower feed and cutting depth. With an increase in feed rate, the surface roughness is increased at all levels of cutting depth. This may be due to the presence of the hard carbide part of the workpiece material. At a higher feed rate the roughness is increased and this is attributed to increasing the amount of friction between the work material and the turning tool. This is clarified by either amplified feed marks or a high cutting load generated at the cutting edge leading to higher plastic deformation and resultant higher roughness [20]. Increasing value of surface roughness with feed rate and decreasing values of surface roughness with cutting speed were also observed and examined by [24]. An increase in reducing the depth of cut can markedly increase cutting forces and surface roughness.

For the turning of CVD coated tools, from plot 4 of Fig. 7 it can be seen that the surface roughness is found to be high at low speed and high feed rate that with a high speed and a low feed rate. Furthermore, the effect of speed on surface roughness is found to be insignificant at a low feed rate. It can also be seen that roughness decreases for all given values of feed rate and cutting speed. From plot 5, the observed value of roughness is lower at high speed with a higher cutting depth than with a low speed and higher cutting depth. At low cutting speed an increase in cutting depth leads to an increase in roughness while roughness decreases at higher cutting depth and increasing cutting speed. Plot 6 shows the magnitude of surface roughness is increased with the increase of feed rate and cutting depth up to 2.5 μm . From the experimental results it can be seen that feed rate and cutting depth are the principal factors affecting the roughness values rather than cutting speed.

The comparison results of roughness between the coated carbide inserts are shown in Fig. 8. It is apparent that across the entire range of cutting conditions, the PVD tool produces a better surface finish than its PVD counterpart. A similar observation was also noted during machining of other grades of nickel-based superalloys [22, 23, 25]. A significant reduction in the surface roughness of the work material is observed up to a maximum of 87% with the PVD tool compared with the CVD tool at low cutting speeds. This can be attributed to the better resistance to abrasion of the PVD tool premature coating removal on CVD tool occurred because of high frictional drag force at low cutting speed.

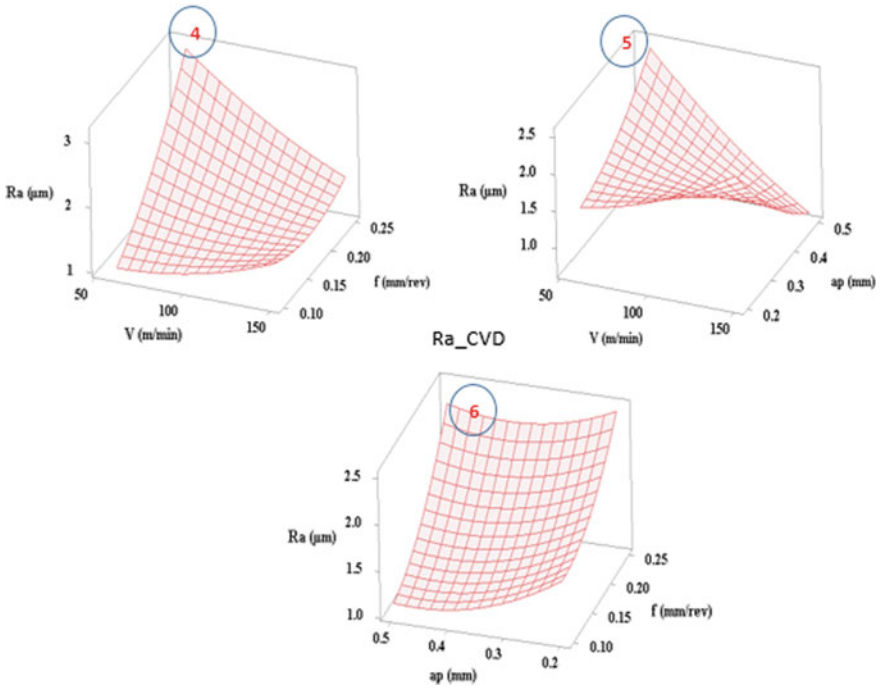


Fig. 7 Surface plots of cutting forces for CVD coated carbide inserts

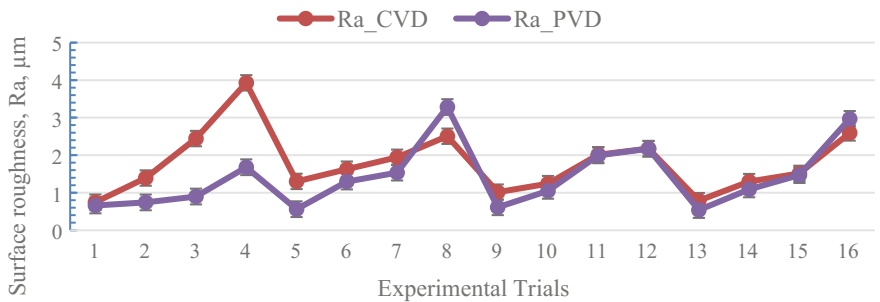


Fig. 8 Process benefits of surface roughness for coated carbide inserts

3.4 Tool Wear

Tool wear is one of the most important machinability characteristics as it affects many performance measures either directly or indirectly. The wear mechanism in a tool is directly influenced by V_c and f in particular. This has a visible influence on cutting zone temperature. Tool wear—characterized as flank wear and crater wear—was studied using optical microscopy after dry machining of the Nimonic C-263

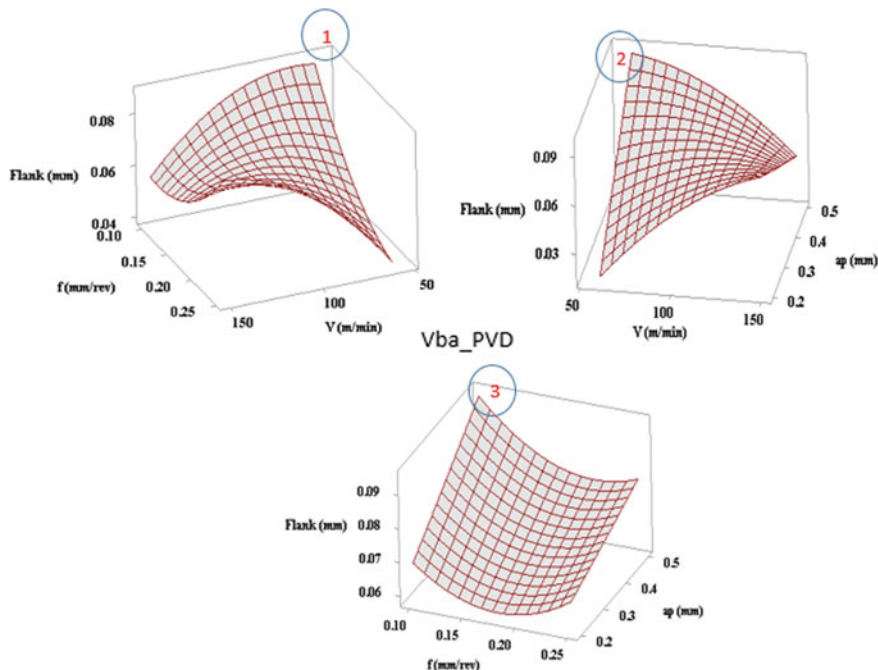


Fig. 9 Surface plots of flank wear for CVD coated carbide inserts

alloy with PVD and CVD coated carbide tools. Figure 9 shows the variation in flank wear of the alloy with variable cutting parameters using PVD and CVD coated tools respectively. From plot 1 of Fig. 9 it can be seen that the width of flank wear at the tooltip increased with an increasing speed at both moderate and higher levels of feed rate. The increase in feed rate resulted in a decrease in conventional cutting temperature at given cutting speed using carbide tools. From plot 2 it can be seen that flank wear is higher at low speed and cutting depth than with high cutting speed and moderate cutting depth. With an increase in cutting speed at a higher depth of cut, the temperature increased causing the flank wear to increase. Plot 3 shows that the amount of flank wear at the tooltip decreased with an increase in feed rate up to 0.15 mm/rev and then increased.

As shown in Fig. 9 of Plot 3, flank wear is observed at different cutting depth and feed rate respectively. Accordingly, flank wear increases with increasing cutting depth and feed rate while other input parameters are constant. Additionally, the chipping, mechanical fracture and thermal cracking (in that order) of the tool happened with an increase in cutting depth. The damage to the front flank face of the tool is a standard wear mechanism observed in the turning of superalloys on account of edge chipping, particularly with a high depth of cut. A high cutting temperature resulting from the low thermal conductivity of the workpiece materials leads to mechanical fracture and thermal cracking at the rake face and flank face,

and is corroborated by Devillez et al. [26]. However, this is reduced using speed at a critical level and with a moderate cutting depth rather than increasing the depth of cut which causes chipping of the carbide inserts.

Regarding turning with a CVD coated insert, from plot 4 of Fig. 10 it can be seen that the width of flank wear decreases with an increase in speed at higher levels of feed rate. From plot 5 the observed flank wear is higher with a high cutting speed and low cutting depth than with a high cutting speed and high cutting depth. Scheme 6 shows that the width of flank wear decreases with an increase in feed rate for all levels of cutting depth.

The comparison results of flank and crater wear between the coated carbide inserts are shown in Fig. 11. A significant reduction in tool flank wear is observed at low cutting speed, up to a maximum of 47% with the PVD tool compared with the CVD tool. This can be attributed to the better resistance to abrasion of the PVD tool whereas premature coating removal occurred in the CVD tool because of the high frictional drag force at low cutting speed.

From the 3D plots in Figs. 3 and 4, a lower force is produced at a speed of 66 m/min for PVD and CVD inserts. When considering the feed and cutting depth, the forces generated are smaller at a feed of 0.05 mm/rev and a cutting depth of 0.4 mm for the PVD insert and at a feed of 0.15 mm/rev and a cutting depth of 0.2 mm for the CVD

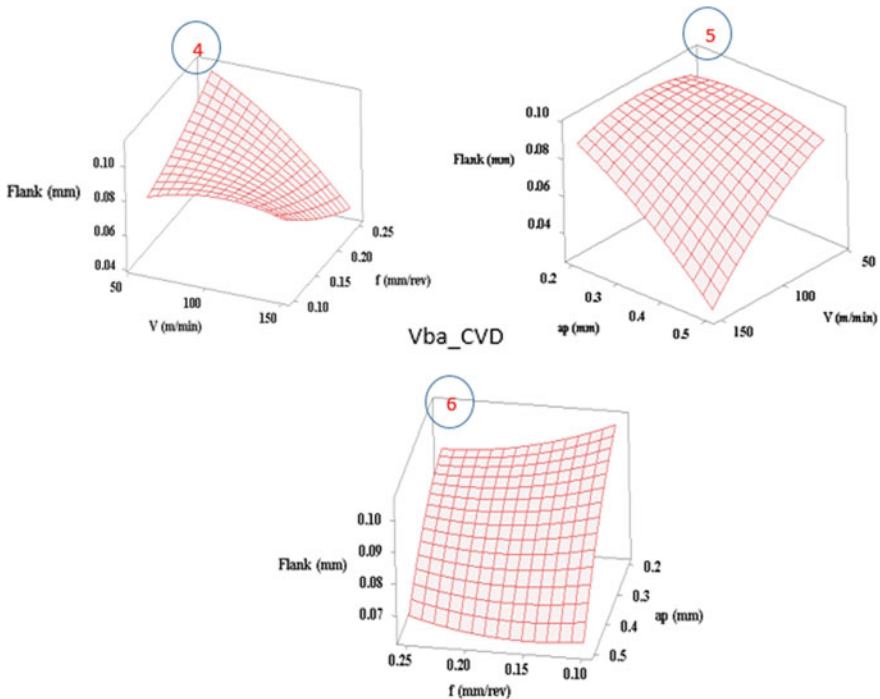


Fig. 10 Surface plots of flank wear for CVD coated carbide inserts

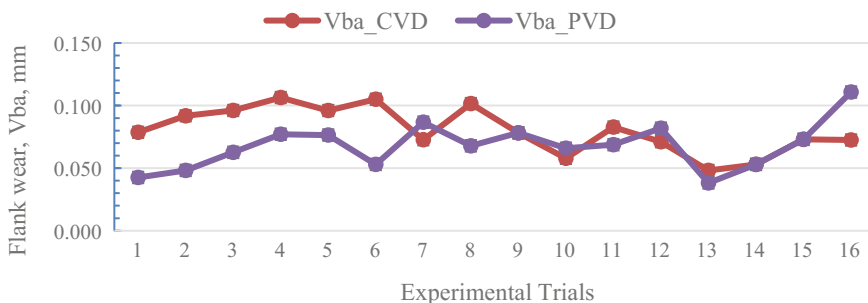


Fig. 11 Process benefits of flank wear for coated carbide inserts

insert. Higher magnitude forces are obtained at a speed of 60–90 m/min and 0.5 mm of depth using both inserts. On machining the material with PVD and CVD inserts, there is a continuous decrease in force when speeds are increased up to 120 m/min, and a slight increase is also observed subsequently. From Figs. 6 and 7, a low roughness value is seen at a speed of 60 m/min and a feed of 0.10 mm/rev for the PVD insert and at 150 m/min with a feed of 0.17 mm/rev for the CVD insert. When considering the cutting depth, higher values of roughness are obtained at a depth of cut of 0.5 mm for both CVD and PVD inserts. On machining the material with PVD inserts, there is an increase in roughness when the speed is increased from 60 to 90 m/min and then a decrease with speeds up to 150 m/min, while in the case of CVD inserts there is a continuous decrease up to 150 m/min. The increase in feed rate from 0.17 to 0.25 mm/rev increased the surface roughness linearly for both PVD and CVD inserts. From Figs. 9 and 10, the generated flank wear is found to increase with an increase of speed to 90 m/min for PVD inserts and 150 m/min for CVD inserts. When feed rate is considered, minimum flank wear is obtained at a feed rate of 0.25 mm/rev for both PVD inserts and CVD inserts. The depth of cut of 0.3 mm is the input at which minimum flank wear is obtained for both supplements.

Finally, given the discussion above, it can be established that for PVD inserts low cutting speed, feed rate and cutting depth result in minimum cutting force, surface roughness and flank wear using response surface desirability function multi-response optimization. Similarly for CVD inserts, a higher cutting speed, low feed rate and high cutting depth lower the responses while turning of Nimonic c-263 alloy. These sets of parameters produce cutting forces of $F_z = 78.33$ N for CVD inserts and $F_z = 57.9$ N for PVD inserts, a surface roughness of $R_a = 0.72$ μm for PVD inserts and $R_a = 0.80$ μm for CVD inserts and surface flank wear of $V_{ba} = 0.038$ mm for PVD inserts and $V_{ba} = 0.048$ mm for CVD inserts. With these optimized cutting conditions, process benefits of a maximum decrease in cutting force of around 36%, surface roughness of about 41% and flank wear of about 88% were evident while using PVD inserts compared to CVD inserts.

3.5 Morphology of Chip

During turning, an understanding of the different forms of chip morphology is necessary for newly formed surface in machining point of view. An attempt is made here to study chip characteristics along with machinability characteristics. Washer-type snarled helical shaped chips are found at lower cutting conditions. The possible reason for this may be rubbing and abrasive actions are stronger at lower cutting conditions than with accurate machining, hence an unevenly shaped chip is produced. However, with a simultaneous increase in depth of cut and feed rate, the type of chip obtained changed from snarled helical to long helical as shown in Fig. 12.

The increase of feed rate and cutting speed at a low depth of cut of 0.4 mm changed the chips from snarled helical to extended helical and then to short helical in the case of both inserts. At the higher cutting speed of 150 m/min, an increase in feed rate from 0.05 to 0.25 mm/rev change the chips from snarled helical to short helical with both inserts, but long helical type chips are obtained at medium feed rates with CVD inserts. At a feed rate of 0.25 mm/rev most of the chips produced are of the long helical type except at a low depth of cut where small helical chips are produced. At a low feed rate of 0.05 mm/rev snarled helical chips are obtained for all inputs of cutting speed and all depths of cut. From these results it is significant that snarled chips are mostly obtained at lower feed rates. At medium cutting speeds of 90 and 120 m/min, long helical chips are collected at all feed rates except at a low feed rate of 0.05 mm/rev.

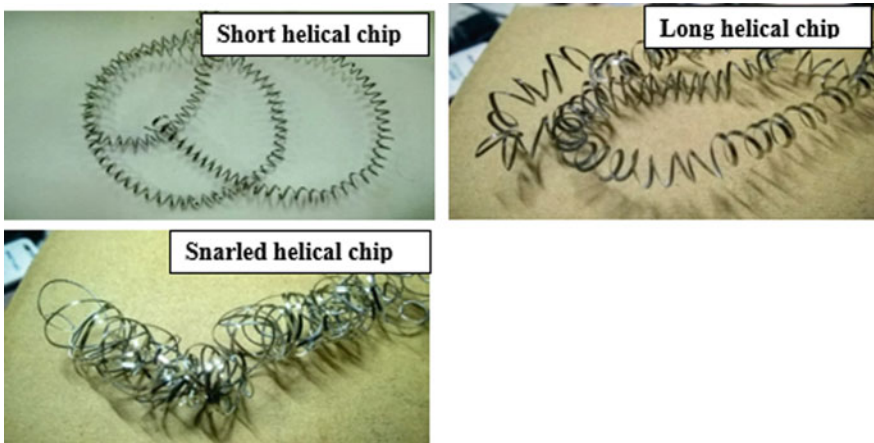


Fig. 12 Chip morphology

4 Conclusion

In this study, the comparative benefits of PVD coated and CVD coated carbide inserts based on an orthogonal design was carried out and the optimal machining parameters were identified using desirability function-based multi-response optimization. A variance test was used to assess the effect of turning parameters on the planned responses in the machining of Nimonic C-263 alloy using coated carbide tools. The following conclusions can be drawn for both inserts:

1. A higher magnitude of cutting force is obtained when increasing both rate of feed and cutting depth. This is attributed to a greater amount of friction produced between the tool and work material. However, the observed cutting force started to decline when increasing the cutting speed due to thermal softening. On the other hand, a significant reduction in cutting force for the PVD inserts of about 48% is observed compared to CVD inserts.
2. Excellent surface roughness and lower flank wear are obtained at a lower cutting speed for the PVD tool, while the higher amount for CVD, a smaller amount of feed rate and a moderate amount of depth of cut. A significant reduction in work material surface roughness and flank wear is observed up to a maximum of 87 and 47% respectively for the PVD tool compared to the CVD tool.
3. ANOVA models are developed and the corresponding correlation coefficients were >85% for cutting force, surface roughness and flank wear. From the ANOVA results, the highest influences on all the responses for PVD and CVD are from feed rate and cutting depth followed by speed.
4. The optimum turning parameters for machining Nimonic C-263 superalloy are identified as 150 m/min of cutting speed, 0.10 mm/rev of feed rate and 0.5 mm of depth of cut for the CVD inserts. For PVD inserts, these parameters are 60 m/min of cutting speed, 0.10 mm/rev of feed rate and 0.2 mm depth of cut for the PVD inserts. These cutting parameters produce a decrease in turning forces and flank wear along with an acceptable surface roughness. With these optimized cutting conditions the process benefits from a maximum decrease in cutting force of around 36%, surface roughness of about 41% and flank wear of about 88% while using a PVD coated insert rather than a CVD coated insert.

References

1. Thakur, A., Gangopadhyay, S.: State-of-the-art in surface integrity in machining of nickel-based super alloys. *Int. J. Mach. Tools Manuf.* **100**, 25–54 (2016)
2. Ezilarasan, C., Senthil Kumar, V.S., Velayudham, A.: Theoretical predictions and experimental validation on machining the Nimonic C-263 super alloy. *Simul. Model. Pract. Theory* **40**, 192–207 (2014)
3. Ezilarasan, C., Velayudham, A.: An experimental analysis and measurement of process performances in machining of Nimonic C-263 super alloy. *Measurement* **46**(1), 185–199 (2013)

4. Thakur, A., Gangopadhyay, S., Mohanty, A., Maity, K.: Experimental assessment on performance of TiN/TiCN/Al₂O₃/ZrCN coated tool during dry machining of Nimonic C-263. *Int. J. Mach. Mater.* **18**(5–6), 452–465 (2016)
5. Thakur, D.G., Ramamoorthy, B., Vijayaraghavan, L.: Some investigations on high-speed dry machining of aerospace material Inconel 718 using multicoated carbide inserts. *Mater. Manuf. Processes* **27**(10), 1066–1072 (2012)
6. Thakur, A., Gangopadhyay, S., Maity, K.P., Sahoo, S.K.: Evaluation on effectiveness of CVD and PVD coated tools during dry machining of Incoloy 825. *Tribol. Trans.* **59**(6), 1048–1058 (2016)
7. Ezilarasan, C., Senthil Kumar, V.S., Velayudham, A., Palanikumar, K.: Modelling and analysis of surface roughness on machining of Nimonic C-263 alloy by PVD coated carbide insert. *Trans. Nonferrous Met. Soc. China* **21**(9), 1986–1996 (2011)
8. Ezilarasan, C., Zhu, K., Velayudham, A., Palanikumar, K.: Assessment of factors influencing tool wear on the machining of Nimonic C-263 alloy with PVD coated carbide inserts. *Adv. Mater. Res.* **291**, 794–799 (2011)
9. Ezugwu, E.O., Okeke, C.I.: Effects of coating materials on the machinability of a nickel base, C-263, alloy. *Tribol. Trans.* **43**(3), 549–553 (2000)
10. Ezugwu, E.O., Okeke, C.I.: Behavior of coated carbide tools in high-speed machining of a nickel base alloy. *Tribol. Trans.* **45**(1), 122–126 (2002)
11. Koyilada, B., Gangopadhyay, S., Thakur, A.: Comparative evaluation of machinability characteristics of Nimonic C-263 using CVD and PVD coated tools. *Measurement* **85**, 152–163 (2016)
12. Ezilarasan, C., Velayudham, A.: Effect of machining parameters on surface integrity in machining Nimonic C-263 super alloy using whisker-reinforced ceramic insert. *J. Mater. Eng. Perform.* **22**(6), 1619–1628 (2013)
13. Tazehkandi, A.H., Pilehvarian, F., Davoodi, B.: Experimental investigation on removing cutting fluid from turning of Inconel 725 with coated carbide tools. *J. Clean. Prod.* **80**, 271–281 (2014)
14. Pusavec, F., Hamdi, H., Kopac, J., Jawahir, I.S.: Surface integrity in cryogenic machining of nickel based alloy—Inconel 718. *J. Mater. Process. Technol.* **211**(4), 773–783 (2012)
15. Dhokia, V., Newman, S.T., Imani-Asrai, R.: An initial study of the effect of using liquid nitrogen coolant on the surface roughness of Inconel 718 nickel-based alloy in CNC milling. *Procedia CIRP* **3**, 121–125 (2012)
16. Yildiz, Y., Nalbant, M.: A review of cryogenic cooling in machining processes. *Int. J. Mach. Tools Manuf.* **48**(9), 947–964 (2008)
17. Suárez, A., López de Lacalle, L.N., Polvorosa, R., Veiga, F., Wretland, A.: Effects of high-pressure cooling on the wear patterns on turning inserts used on alloy IN718. *Mater. Manuf. Processes* **32**(6), 678–686 (2017)
18. Ulutan, D., Ozel, T.: Machining induced surface integrity in titanium and nickel alloys: a review. *Int. J. Mach. Tools Manuf.* **51**(3), 250–280 (2011)
19. Pervaiz, S., Rashid, A., Deiab, I., Nicolescu, M.: Influence of tool materials on machinability of titanium-and nickel-based alloys: a review. *Mater. Manuf. Processes* **29**(3), 219–252 (2014)
20. Umbrello, D.: Investigation of surface integrity in dry machining of Inconel 718. *Int. J. Adv. Manuf. Technol.* **69**(9–12), 2183–2190 (2013)
21. Fan, Y., Hao, Z., Zheng, M., Sun, F., Yang, S.: Study of surface quality in machining nickel-based alloy Inconel 718. *Int. J. Adv. Manuf. Technol.* **69**(9–12), 2659–2667 (2013)
22. Thakur, A., Gangopadhyay, S., Maity, K.P.: Effect of cutting speed and CVD multilayer coating on machinability of Inconel 825. *Surf. Eng.* **30**(7), 516–523 (2014)
23. Thakur, A., Mohanty, A., Gangopadhyay, S.: Comparative study of surface integrity aspects of Incoloy 825 during machining with uncoated and CVD multilayer coated inserts. *Appl. Surf. Sci.* **320**, 829–837 (2014)

24. Nalbant, M., Altın, A., Gokkaya, H.: The effect of cutting speed and cutting tool geometry on machinability properties of nickel-based Inconel 718 super alloys. *Mater. Des.* **28**, 1334–1338 (2007)
25. Bushlya, V., Zhou, J., Ståhl, J.-E.: Effect of cutting conditions on machinability of superalloy Inconel 718 during high speed turning with coated and uncoated PCBN tools. *Procedia CIRP* **3**, 370–375 (2012)
26. Devillez, A., Le Coz, G., Dominiak, S., Dudzinski, D.: Dry machining of Inconel 718, workpiece surface integrity. *J. Mater. Process. Technol.* **211**(10), 1590–1598 (2011)

Investigation of Parameters for Machining a Difficult-to-Machine Superalloy: Inconel X-750 and Waspaloy



K. Vetri Velmurugan, K. Venkatesan, S. Devendiran and Arun Tom Mathew

Abstract Nickel based super alloys has high mechanical strength, resistance to corrosion and oxidation and high temperature strength. Research work on Alloy X-750 and Waspaloy has been infrequent due to difficulties in machining. The present investigation aims to analyze the tool wear, turning forces, and roughness in dry turning of Inconel X-750 and Waspaloy. The experiments are designed using the following parameters: speed = 50, 75, 100 m/min; rate of feed = 0.05, 0.075, 0.125 mm/rev. The depth of cut was kept at a constant value of 0.5 mm. PVD-coated carbide inserts are used for the turning operation, and the coating material was AlTiN. The cutting forces and surface roughness were measured post the tool wore out. The microstructures and Vickers' hardness of the superalloys were also studied. Finally, the range of cutting conditions is recommended for machining this alloy in an industrial environment.

Keywords Tuning responses · Coated carbide inserts · Dry machining

1 Introduction

Superalloy mainly nickel alloy has massive high strength, resistance to strong corrosion along with oxidation and more in temperature stability. Due to this excellent properties, nickel-based found about 50 wt% as components includes turbine disks, compressor disks. [1, 2]. Conversion of this alloy into a required element would need machining process. However, the cutting tool suffers thermal and mechanical loads owing to its lower thermal conductivity, the occurrence of

K. Vetri Velmurugan
Mechanical Engineering, Sri Sairam Engineering College, Chennai, India

K. Venkatesan (✉) · S. Devendiran · A. T. Mathew
School of Mechanical Engineering, Vellore Institute of Technology, Vellore, India
e-mail: venkatesan.kannan@vit.ac.in

abrasive carbide particles, and more work hardening [3, 4]. While Inconel alloys are studied the most, investigations on Waspaloy are sporadic in spite of having 70% composition of the primary metal [5, 6]. Selection of the right process parameters in machining difficult-to-machine materials is imperative to ensure tool safety. The cutting speed has the highest impact on tool life, followed by the depth of cut and feed rate [7]. It is inferred that low feed rate and depth of cut along with high cutting speed resulted in the lowest cutting force while machining Nimonic C-263 [8]. The lowest surface roughness is obtained at high values of cutting speed and depth of cut, and little value of feed rate. Additionally, high wear on the flank surface was observed at high values of cutting speed compared to feed rate [9]. Furthermore, the surface integrity of nickel superalloys, in particular, is influenced by feed rate and cutting time. The performance of PVD-coated carbide tools in turning Nimonic C-263 was deemed suitable for obtaining good surface roughness with the cutting speed as 54 m/min, feed rate as 0.051 mm/rev, and depth of cut as 1 mm [10]. Further performed turning of Inconel X-750 with supercritical CO₂-based minimum quantity lubrication to conclude an increase in tool life compared to operations performed using aqueous coolants [11]. A comparison of tool wear in machining Waspaloy and Alloy 718 revealed that the flank wear was lower in case of the former for all sets of operations [12]. The tool is said to be worn out once the flank wear reaches 0.3 mm. Additionally, the tool wear was subjected to notch wear and its controlling factor for tool life. Significant notch wear was recorded while turning Inconel 718 due to the high rate of work hardening [13].

Much research has been concentrated on multi-component coatings such as TiAlN, TiCrN, TiVN; conventional hard coatings such as TiN, TiC, TiCN; and superhard coatings such as diamond and CBN. The materials used for coating the cutting tools are also of vital importance in determining the tool life and cutting forces. The effectiveness of multilayer (TiN/TiCN/TiN) coated tool compared to single layer (TiAlN) tool in lowering cutting force. This was explained by higher abrasive wear and burr formation for the single layer tool, owing to its insufficient edge support [14, 15]. Also, it was observed that multilayer TiN/TiCN/TiN coated tool affected less cutting force due to its sharper cutting edge than a single layer TiN-coated tool with a honed edge [14]. Comparative performance study on different hard metal coating on WC-6 wt% Co in the dry turning of Inconel 718 has been studied and found that the multilayer component of TiAlN outperformed that of TiAlN-monolayer and TiN/TiCN/TiAlN inserts. It is also reported that abrasive and plastic deformation of the edge of the cutting tool is the wear mechanism occurred during turning [15]. Work hardening occurs quickly in both these materials, and a smooth, continuous cutting action must be maintained to avoid it [16]. It is concluded that PVD-coated tools resulted in a reduction of surface roughness up to 74.3% (maximum) when compared to its CVD counterpart under a low cutting speed of 51 m/min [17]. A maximum reduction of 13.4% was measured in the cutting temperature and 6.3% in cutting forces for the same cutting speed [18]. The compressive strength of PVD-coated tools is superior to the tools coated by CVD [19]. Among the various coatings applied on the inserts through PVD, the best metal cutting performance was observed in the case of TiAlN-coated tools [20, 21].

This was attributed to the coating's higher resistance to abrasive wear and crater wear, even at high cutting speeds of 75 m/min [3]. Further, it is found that TiAlN-based coatings exhibited good performance in the cutting speed range of 60–80 m/min [22]. Recent research in the fields of materials science and manufacturing has proved that usage of cutting fluids can increase the total manufacturing cost by 17% [23]. Hence for economic considerations, the focus is now shifting toward dry machining [24]. In recent times, the benefits of using cutting fluids for machining operations are actively debated as they are known to affect the environment and the health of the workers using them [25, 26]. This project is thus an effort to bolster the sustainability of the machining process by ensuring a balance between manufacturability and environment-friendliness. Dry turning is recommended for sustainable manufacturing by the author [26].

Based on the above facts, a detailed study of machinability characteristics in the dry turning of Inconel X-750 and Waspaloy is reported few. The aim of the study is to investigate the tool wear mechanisms when both materials are turned under the same set of operating conditions and machining environment. Post the tools wear out, resultant cutting forces and surface roughness are measured. The microstructures of the workpiece materials are analyzed followed by measurement of Vickers' hardness. Finally, the range of machining parameters for industrial serial production is recommended.

2 Experimental Section

2.1 *Experimentation on Inconel X-750 and Waspaloy Alloy Superalloy*

Inconel X-750 is a Ni–Cr super alloy which is precipitation strengthened by add-ons of Al and Ti. Typical applications of Incoloy X-750 are heat-exchanging components in conventional power and petrochemical plants, steam generator tubes in nuclear power plants. Also, it is used in hot ducts, re-heaters in power plants, superheaters, pressure vessels, and fuel cladding where the operating temperature often ranges from 550 to 700 °C. Chemical composition for this Inconel X-750 alloy is 71.80% Ni, 0.50% Si, 0.70% Mn, 14.72% Cr, 0.20% Mo, 6.67% Fe, 0.75% Co, 2.4% Ti, 0.8% Al, 0.8% Cb. Waspaloy is an age hardenable alloy with a face-centered cubic structure that has excellent strength temperature up to 700 °C. Its other beneficial properties are in common with the family of nickel superalloys include corrosion resistance, creep strength, and low thermal conductivity that make it suitable for extreme conditions. The chemical composition of the workpiece material is as follows: Cr (19.50%), Co (13.00%), Fe (1.00%), Mo (4.30%), Ti (3.00%), Al (1.40%), B (0.001%) C (0.05%), Zr (0.70%), and Ni (57% Bal.) which evidently described that cobalt (Co), chromium (Cr), and Nickel (Ni) are the most important elements in the as-received material. Both the workpiece material in rod

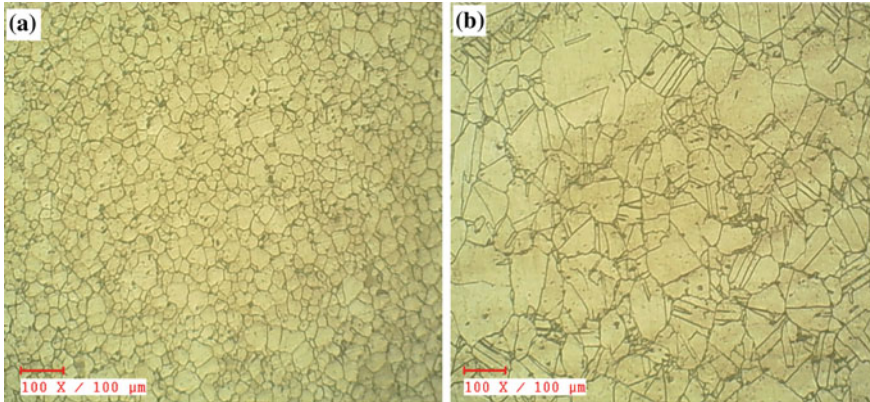


Fig. 1 Microstructure of the **a** Inconel X-750 **b** Waspaloy alloy for the received state

form of 32 mm diameter and 300 mm length is procured an optical image as received workpiece material is shown in Fig. 1. The etchant used for Waspaloy is 10% Oxalic acid, and Inconel X-750 was Glyceregia (Composition: 15 cc HCl + 10 cc Glycerol + 5 cc HNO₃). The images are obtained from the metalurgical microscope “METSCOPE-1A.”

The microstructure of the X-750 sample revealed fine grains of austenite throughout the matrix. Austenite imparts excellent corrosion resistance to the alloy and hence is significant in the applications of such alloys under extreme conditions. The microstructure of the Waspaloy sample revealed grains of austenite throughout the matrix. Also, some twinned grains were also observed in this particular matrix. Mechanical twinning imparts considerable strength to the material using plastic deformation. The strength of the material is increased as the twin boundaries interfere with the slip process. It occurs in certain metals or alloys either during mechanical deformation or as the result of annealing following plastic deformation. It is facilitated majorly by low temperatures and high strain rates.

The high-speed lathe turning experiments are carried out to avoid of cutting fluid (the workpiece is rotated without cutting liquid) while it is clamped on a high-speed machine with a maximum spindle speed of 3600 rpm and power of 1.25 kW. Figure 2 shows macro-flowchart of experimental setup in the high-speed device and its research methodology adopted in the current study. The flow diagram shown above is a systematic representation of the project execution stages. The first stage of the project involves the dry turning operation of Waspaloy and Inconel X-750 for the decided range of cutting speed, feed rate, and depth of cut. The wear of the tool is then measured using a DinoLite Digital Microscope, and the variation of the tool wear is plotted against the machining length of each pass kept at 50 mm for Inconel X-750 and 30 mm for Waspaloy. Obtaining SEM images of the cutting tool after the tool wore out to further understand tool wear mechanisms. Post the tool wear, the cutting forces and surface roughness are measured followed by the work

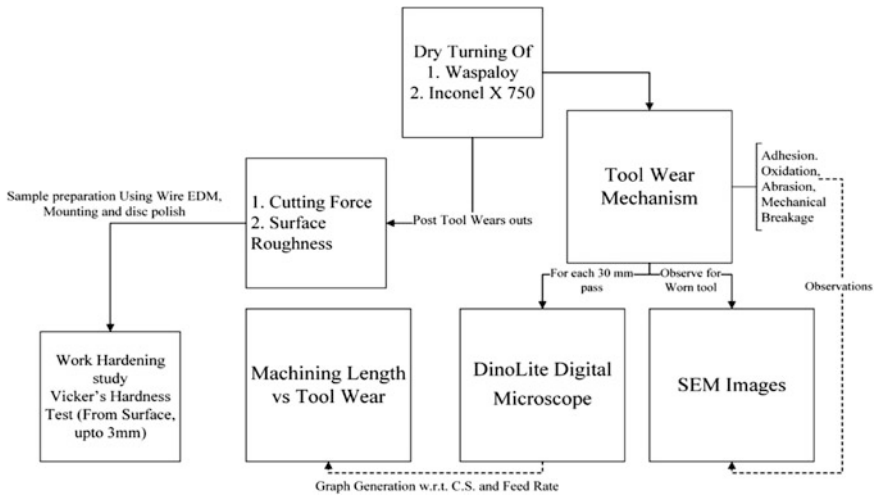


Fig. 2 Flowchart of the work carried

hardening study in which the Vickers’ hardness test is performed on the workpiece materials from the surface up to 3 mm.

The turning parameter used in this research work is turning speed (V_c), the rate of feed (f), and cutting depth (a_p). Different sets of speed, feed, and cutting depth used in the test are potted in Table 1. The target functions are a resultant force, roughness, and tool wear. The cutting tool used for the turning experiments is PVD-coated (AlTiN) carbide inserts. The used cutting tools are the carbide tips with a code according to ISO (CNMG 120408-MP, KCU 25) with -6 orthogonal rake angles. The specification of cutting tool holder is PCLNR 2020 K12, respectively. The tool wear was measured using a “DinoLite Digital Microscope” and the software “DinoCapture 2.0.” The cutting forces were measured using a “KISTLER” Dynamometer, and the surface roughness values were obtained using a TalySyrf “MAHR MarSurf GD 120.” A CNC Wire Cut EDM was used to prepare samples to study the microstructures of Inconel X-750 and Waspaloy.

3 Results and Discussion

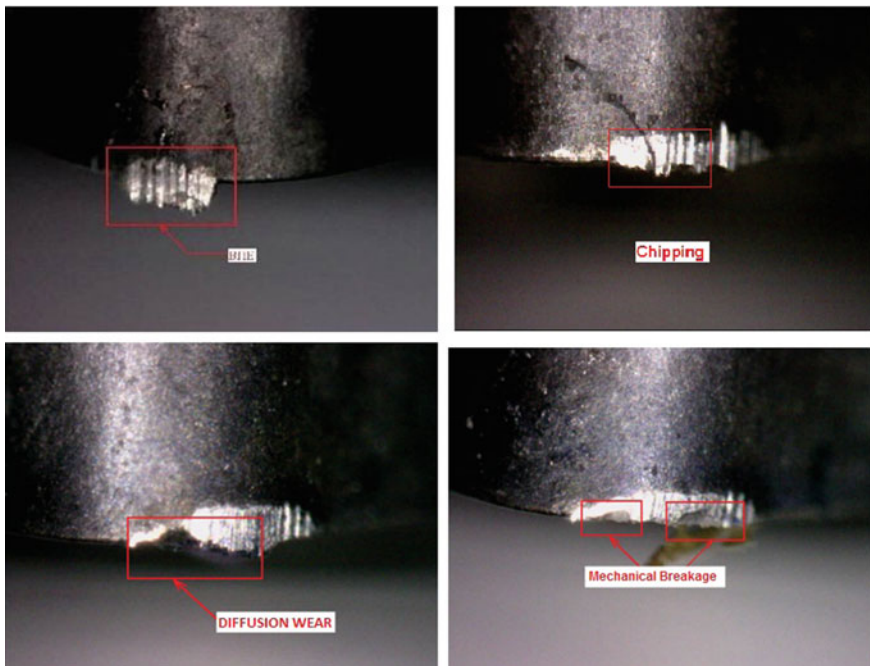
3.1 Tool Wear Study

Tool wear refers to the degradation of cutting or clearance surface, reduction in some of the mechanical properties of the tool and its fracture. The most important and widely used machinability characteristics are tool life for any cutting tool. Much research attention has been directed toward enhancing tool life which can be improved by proper selection of machining parameters, tool material, use of

Table 1 Cutting parameters

Trial. No.	Speed (m/min)	Feed rate (mm/rev)	Cutting depth, a_p (mm)
1	50	0.05	0.5
2	75	0.05	0.5
3	100	0.05	0.5
4	50	0.075	0.5
5	75	0.075	0.5
6	100	0.075	0.5
7	50	0.125	0.5
8	75	0.125	0.5
9	100	0.125	0.5

coolant, tool coating, etc. From the first set of experiments performed for Inconel X-750 at low feed, the propagation of tool wear mechanism occurs in the following order (from start to finish): built-up edge formation, chipping, mechanical breakage, diffusion wear as shown in Fig. 3, whereas the propagation of wear mechanism in Waspaloy occurs from built-up edge formation to diffusion wear without any visible chipping or mechanical breakage shown as Fig. 4.

**Fig. 3** (Clockwise from top). Propagation of wear in Inconel X-750

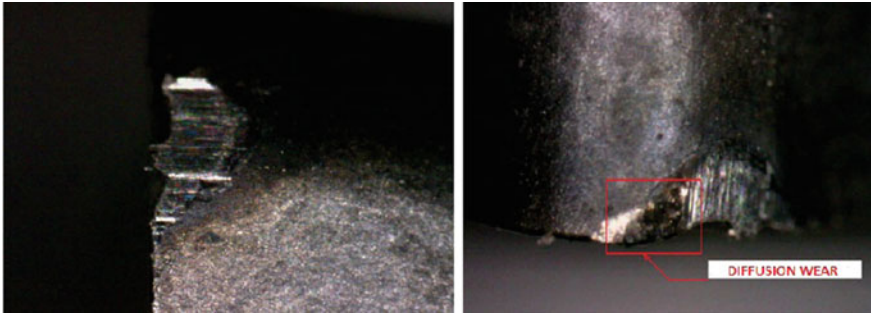


Fig. 4 (Clockwise from top). Propagation of wear in Waspaloy

Figure 5 represents the variation of flank wear with machining length for experiments 1, 2, 3 for Inconel X-750. The maximum machining length is 950 mm for a cutting speed of 75 m/min. The tool wears are also the highest for this case. The images of the cutting tool for the different experiments after wear (both flank and nose) have been shown. The tool life is most extended for the cutting speed of 75 m/min. This is attributed to the formation of a stable thermal layer of Al_2O_3 [3].

From Fig. 6 shows the variation of flank wear and nose wear with machining length for experiments 4, 6 for Inconel X-750. The maximum machining length is 800 mm. The highest machining length and tool wear occur for a cutting speed of 75 m/min. Figure 7 represents the variation of flank wear and nose wear with machining length for Experiments 7, 8, 9 for Inconel X-750. The maximum machining length is 1500 mm, and it is observed for a cutting speed of 75 m/min. The tool wears are highest at 100 m/min speed.

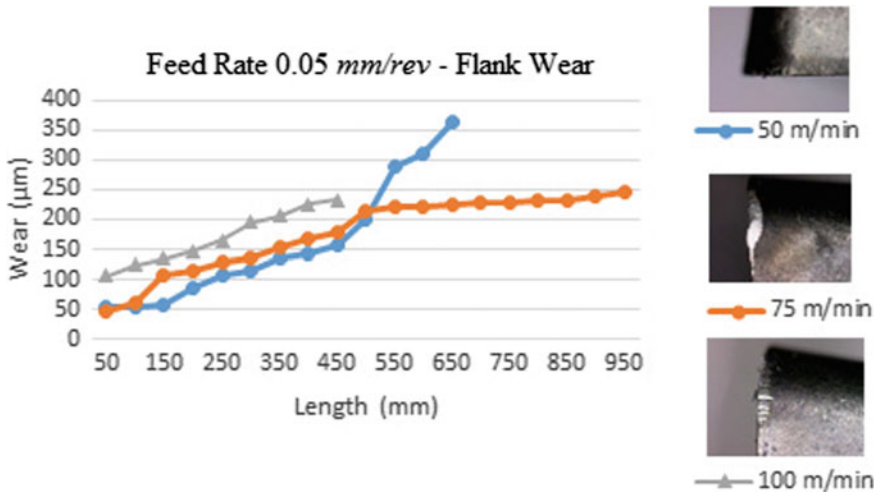


Fig. 5 Flank wear for experiments 1, 2, and 3 for Inconel X-750

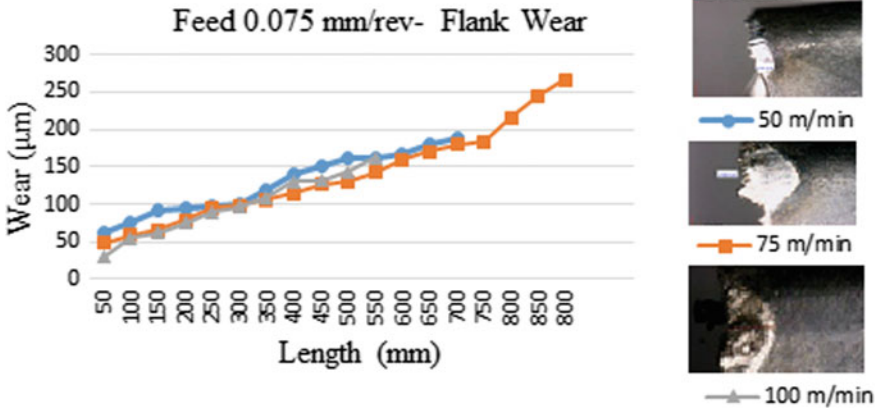


Fig. 6 Flank wear for experiments 4, 5, and 6 for Inconel X-750

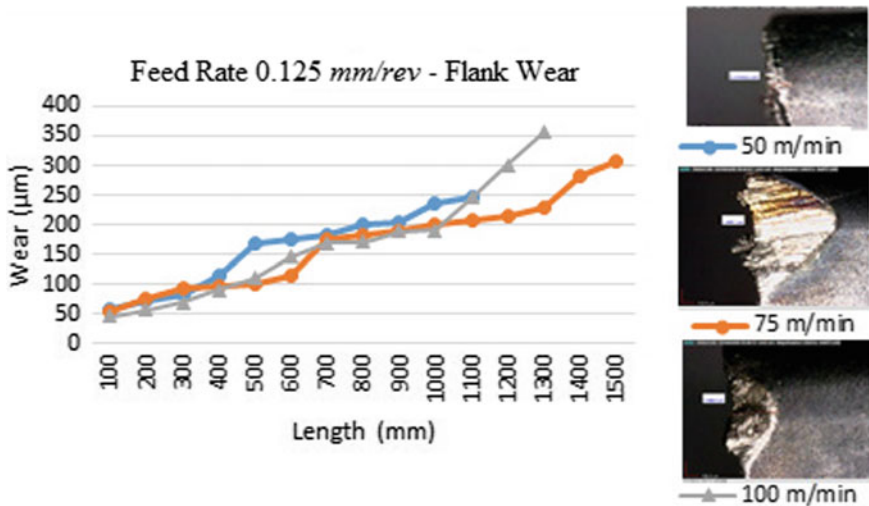


Fig. 7 Flank wear for experiments 7, 8, and 9 for Inconel X-750

Figure 8 represents the variation of flank wear and nose wear with machining length for Experiments 1, 2, 3 for Waspaloy. The wears are highest for a high cutting speed of 100 m/min, followed by the medium cutting speed of 75 m/min and then a cutting speed of 50 m/min. The maximum machining length is 120 mm and is observed when the speed is 50 m/min. The images of the cutting tool for the different experiments after wear (both flank and nose) have been shown. The tool life is higher for low speed of 50 m/min when the feed is set as 0.05 mm/rev.

Figure 9 represents the variation of flank wear and nose wear with machining length for Experiments 4, 5, 6 for Waspaloy. The maximum machining length is

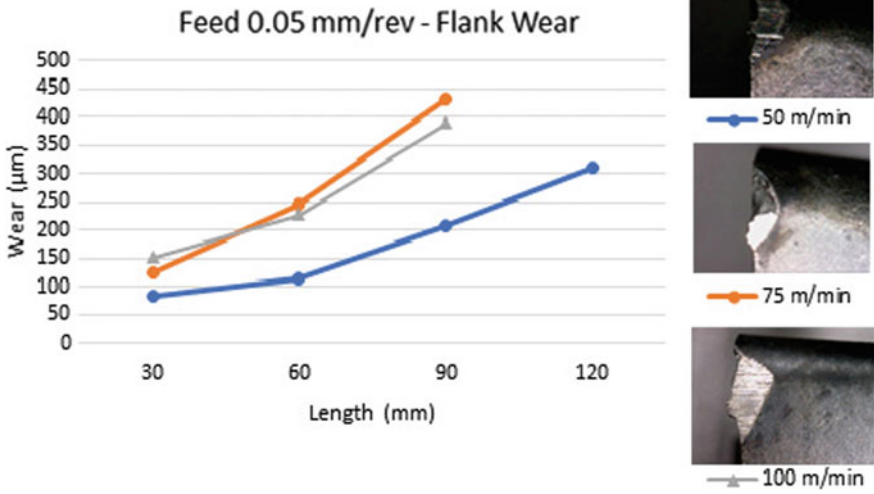


Fig. 8 Flank wear for experiments 1, 2, and 3 for Waspaloy

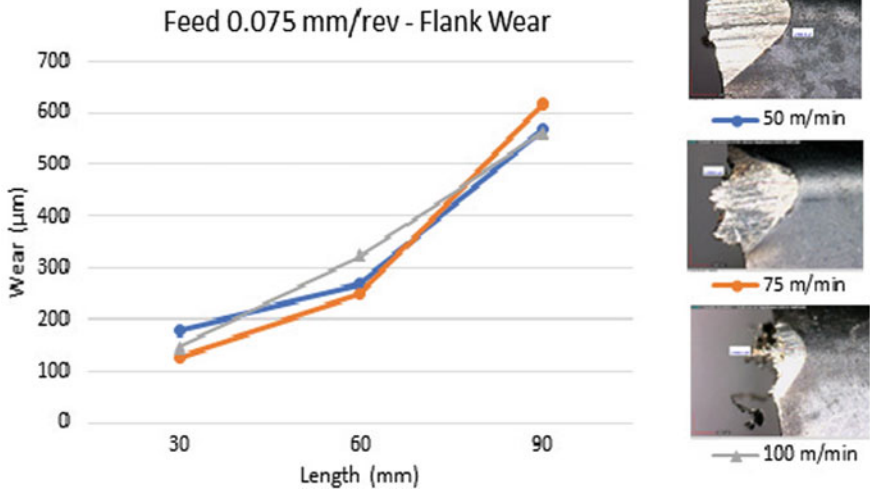


Fig. 9 Flank wear for experiments 4, 5, and 6 for Waspaloy

90 mm. The tool wears are highest for a cutting speed of 75 m/min. Figure 10 represents the variation of flank wear and nose wear with machining length for Experiments 7, 8, 9 for Waspaloy. The maximum machining length is 90 mm.

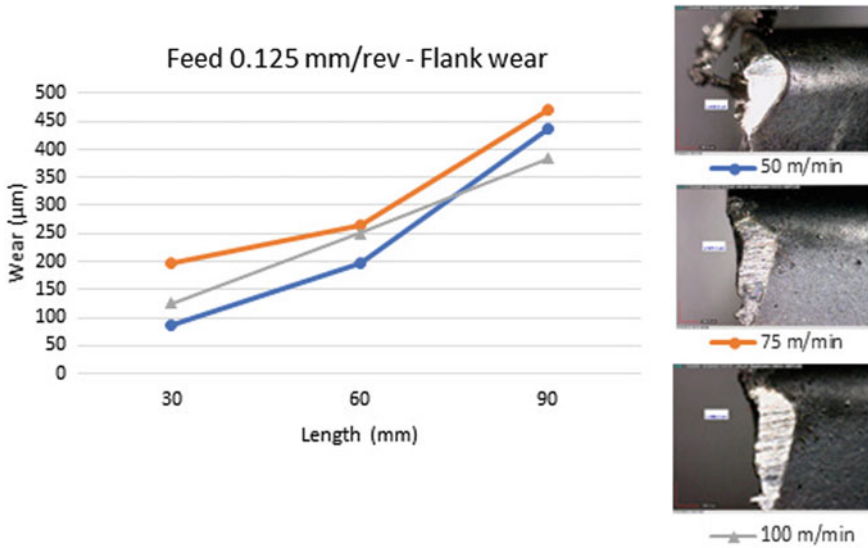


Fig. 10 Flank wear for experiments 7, 8, and 9 for Waspaloy

The tool wears are highest for a low cutting speed of 50 m/min due to the generation of high forces that accelerate the wear rate.

The SEM images were collected post the completion of Experiments 1, 2, and 3 for both Inconel X-750 and Waspaloy is shown in Fig. 11. The tool wear discussion is as follows: In Inconel X-750, Experiment 1, flaking or delamination of the cutting tool takes place during the turning operation. Flaking signifies the loss of material from a large area of the tool face. This type of tool wear is caused by sudden impact between tool and workpiece or when the device is suddenly disengaged during massive duty cut involving large cutting force. In Inconel X-750, Experiment 2, abrasive wear can be seen apparently as a result of frictional rubbing between machined surface and flank face of the tool. Presence of hard abrasive particles in work material is responsible for such wear mechanism. As a result, deep and multiple scratches/scores are perceived on the flank face of the tool. For Inconel X-750, Experiment 3, mechanical breakage can be seen as a portion of the tool surface which is completely removed. In case of Waspaloy, Experiment 1, the formation of built-up edge/adhesive wear is observed on the tool surface. This is primarily promoted under low cutting speed owing to high chip–tool interface friction. Under the action of machining forces, such BUE gets dislodged from the cutting edge or rake face taking a small chunk of tool material and thus leaves a crater or results in edge chipping.

In Waspaloy, Experiment 2, diffusion wear begins to appear on the tool surface. Machining under very high cutting temperature leads to diffusion wear in which the atoms from harder (either from workpiece or tool materials) diffuse into the softer material. Owing to intimate sliding contact between chips and rake face,

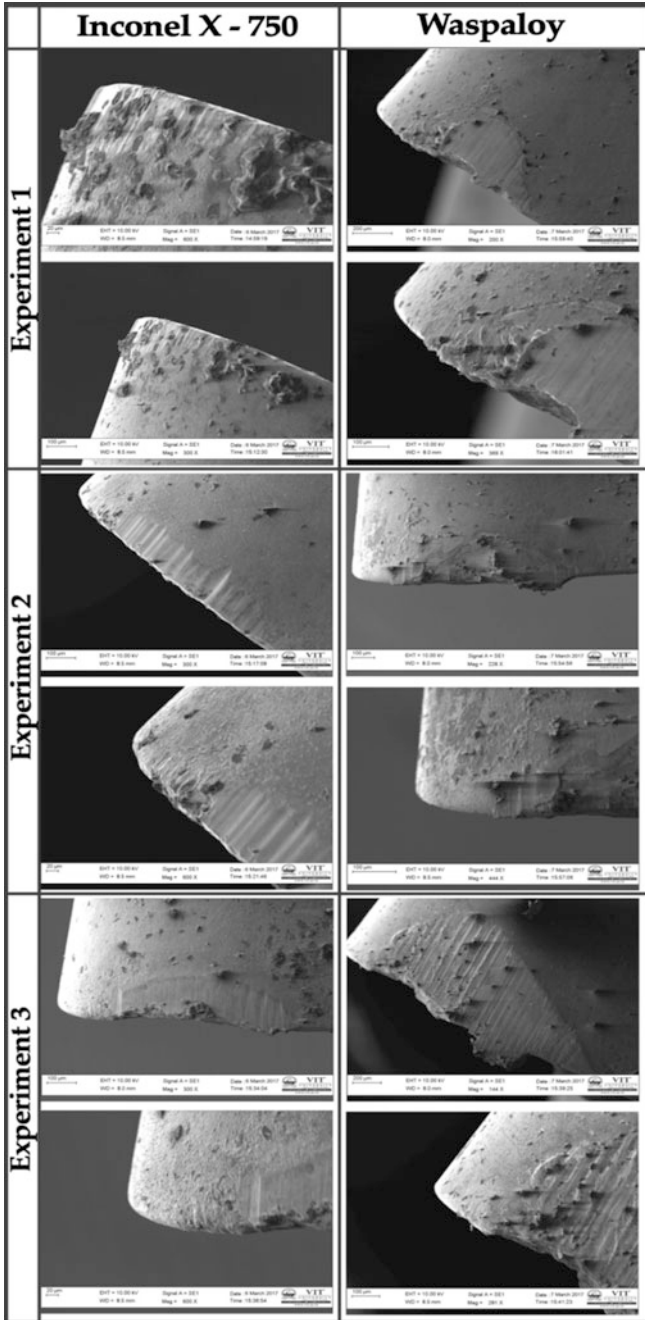


Fig. 11 SEM images of cutting edges for the experiments 1, 2, 3

the temperature at their interface is high. This causes diffusion of metal atoms from harder tool material into softer work material. In Waspaloy, Experiment 3, diffusion wear leaves a crater on the surface of the tool as represented in the image.

3.2 *Effect of Turning Parameters on Force for Inconel X-750 and Waspaloy*

The forces were measured for a pass length of 10 mm for each designed experiment. The measurement of radial forces, cutting forces, and feed forces was done using a KISTLER dynamometer. The resultant calculated force for X-750 and Waspaloy was provided in Table 2. For machining with PVD insert, from Table 1, the value of cutting force tends to increase when the amount of feed rate is raised for both workpieces. This can be concluded from the fact that the rise of material removal rates due to increases of tool–work contact length and strain-hardening effect occurred between workpiece material and cutting tool during turning. Further, these increased turning forces with the function of feed are attributed to higher friction between the work–tool and increase of flank wear. The rise in flank wear at a higher amount of feed rate is due to server load on the cutting tool, and correspondingly, the abrasion takes place between the cutting edge and workpiece surface. Further, it is noticed that the higher amount of force is generated at a higher level of rate of feed for the given value of cutting speed. The strength drops when the cutting speed is raised due to higher temperature produced which induce thermal softening of the workpiece material. Based on the comparison result in Fig. 12, the higher amount of force is obtained for Waspaloy that of Inconel X-750 for all the cutting conditions due to its higher tensile strength. It is noticed for the workpieces high amount of cutting force is obtained at a lower value of reducing the speed of 50 m/min and higher value of feed rate 0.125 mm/rev at constant cutting depth 0.5 mm.

Table 2 Resultant cutting force values for Inconel X-750 and Waspaloy

Trial No.	Speed (m/min)	Feed rate (mm/rev)	X-750 resultant force (N)	Waspaloy resultant force (N)
1	50	0.05	190.32	314.68
2	75	0.05	173.67	254.45
3	100	0.05	132.04	141.70
4	50	0.075	267.50	396.70
5	75	0.075	246.19	330.76
6	100	0.075	218.86	283.47
7	50	0.125	374.12	453.20
8	75	0.125	281.61	419.27
9	100	0.125	295.68	364.73

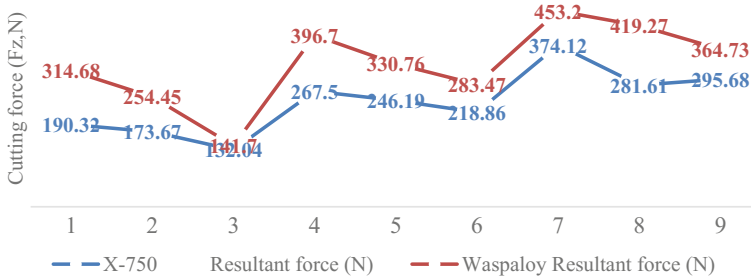


Fig. 12 Process benefits of cutting forces for coated carbide inserts

3.3 Effect of Turning Parameters on Surface Roughness Results for Inconel X-750 and Waspaloy

The surface roughness of the machined component is of vital importance due to its purpose of indicating surface quality or integrity of the same. The measurements were taken at three locations, each being 90° apart around the circumference of the workpiece and their mean was calculated. The tabulation of the obtained surface roughness values post each experiment for Waspaloy, and Alloy X-750 is presented in Table 3. As it can be inferred from the received values for both Waspaloy (9 trials) and Inconel X-750 (8 trials), the surface roughness is inversely proportional to cutting speed and directly proportional to feed rate. The corresponding values of surface roughness are greater for Alloy X-750 compared to Waspaloy due to the formation of grooves on the surface of the material during the turning operation. Severe frictional rubbing combined with the creation of BUE within the specified cutting range was responsible for worsening surface finish. This implied a poor surface finish resulting in higher values as a result of interrupted machining.

Table 3 Surface roughness values for Inconel X-750 and Waspaloy

Trial No.	Speed (m/min)	Feed rate (mm/rev)	X-750 surface roughness, Ra (µm)	Waspaloy surface roughness, Ra (µm)
1	50	0.05	0.7611	0.565
2	75	0.05	0.4574	0.538
3	100	0.05	0.3133	0.298
4	50	0.075	1.2548	0.983
5	75	0.075	1.1136	0.776
6	100	0.075	1.0032	0.571
7	50	0.125	1.8524	1.479
8	75	0.125	1.7687	1.132
9	100	0.125	1.5697	1.010

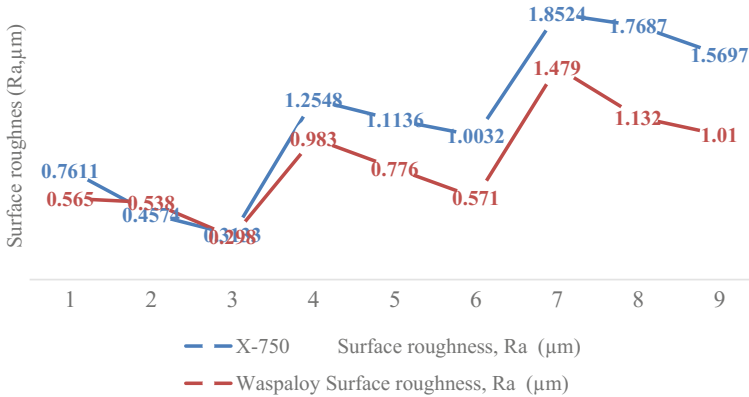


Fig. 13 Comparative advantages of surface roughness for coated carbide inserts

No such grooves were observed while machining Waspaloy as the cutting was smooth and uninterrupted.

For both workpiece materials, it can be noticed that the value of surface roughness tends to increase with increment in feed rate for all levels of cutting speed. The increment in magnitude may be attributed to increasing the amount of friction between work materials and turning tool. Also, it was noticed that surface roughness value drops as the increment in cutting speed due to thermal softening of materials. An increase of feed rate contributed to a higher unevenness on surface and it increase the height of ridges resulted to higher surface roughness. The lower value of surface roughness is observed at higher level speed and low feed rate that of the high level of speed and feed rate for both materials. It is identified that feed rate is found to be an influence factor that of cutting speed. The observed value of surface roughness ranges is 076–1.56 μm for X-750 alloy, whereas 0.56–1.01 μm (Fig. 13). Increasing the amount of surface roughness with feed rate and decreasing the amount of surface roughness with cutting speed are also observed and examined by another researcher [10].

3.4 Micro-hardness Study of X-750 Alloy and Waspaloy

Post the analysis of the microstructures; the workpiece samples for experiments 1 and 9 (low speed–low feed, and high speed–high feed, respectively) for Inconel X-750 and Waspaloy were subjected to a Vickers' hardness test to study the influence of work hardening. The samples were cut from the rods using Wire EDM. This was followed by mounting and polishing them (using a Double Disk Variable Speed Grinder Polisher). The applied load was 500 gf. Six readings were taken for each experiment beginning with a depth equal to 0.05 mm up to 3 mm. Hence, the total number of readings obtained from the Vickers' micro-hardness tester was 24.

The variation of the hardness (HRC) with the depth from the surface has been plotted in Figs. 14 and 15, respectively. The graph represented above shows an increase in the hardness value for the condition of high speed–high feed (Experiment 9) compared to each corresponding data point for the status of low speed–low feed (Experiment 1). The hardness values remain nearly the same after reaching a depth of 0.15 mm for both experiments. Hence, this shows that the strain-hardening effect after the dry turning of Inconel X-750 is not severe as no appreciable change in the hardness is observed with an increase in depth from the surface. In the graph shown for Waspaloy, the hardness value increases up to a depth of 0.15 mm and then decreases till 0.3 mm in experiment 1. However, in the case of trial 9, the hardness rises up to 0.1 mm post which it declines to 0.3 mm. The corresponding data points for the latter remain higher than the former. Compared to Inconel X-750, there is the visible effect of strain hardening in Waspaloy as the hardness changes up to a specific depth post which it falls to a level where no significant or appreciable difference can be observed if the depth is increased further.

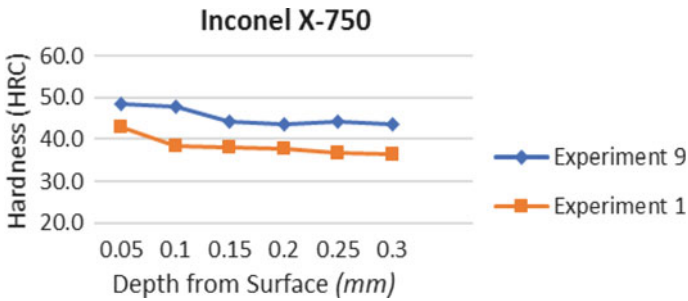


Fig. 14 Hardness values for Inconel X-750

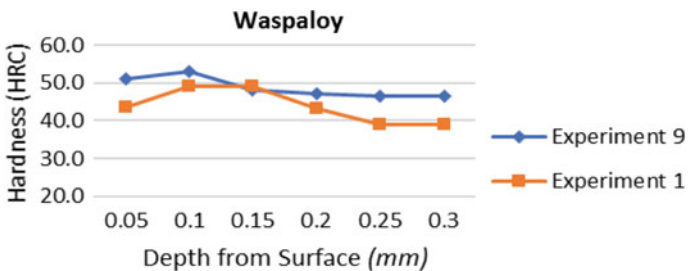


Fig. 15 Hardness values for Waspaloy

4 Conclusion

In the present research, the effect of turning parameters on Inconel X-750 and Waspaloy using PVD-coated carbide insert and identified the optimal turning parameters. The findings obtained from work done for the project are as follows:

1. The propagation of tool wear mechanism for low feed condition ranges from built-up edge formation to chipping, to mechanical breakage to diffusion wear in Inconel X-750. Diffusion wear occurs after built-up edge formation without any visible chipping, or mechanical damage happens in Waspaloy.
2. In the dry turning of Inconel X-750, the highest machining length until tool wore out was observed for a cutting speed of 75 m/min. This occurred due to the formation of a stable thermal layer of Al_2O_3 . Hence, the recommended cutting condition for maximum tool life in dry turning of Inconel X-750 is $V_c = 75$ m/min, $f = 0.125$ mm/rev, $a_p = 0.5$ mm.
3. In the dry turning of Waspaloy, the highest machining length until the tool wore out was observed for a cutting speed of 50 m/min. Hence, a low speed–low feed condition is best suited for the dry turning of Waspaloy. The cutting parameters are $V_c = 50$ m/min, $f = 0.05$ mm/rev, $a_p = 0.5$ mm.
4. Machinability of Inconel X-750 is higher than that of Waspaloy as it resulted in lesser cutting force, implying the cutting force while machining Waspaloy is much higher. This occurs due to the presence of twin boundaries in Waspaloy.
5. The surface roughness in the case of Inconel X-750 is higher than corresponding values of Waspaloy due to interrupted machining caused by the formation of grooves on the surface.
6. There is visible strain-hardening effect in Waspaloy compared to Inconel X-750.

References

1. Venkatesan, K., Ramanujam, R., Kuppan, P.: Parametric modeling and optimization of laser scanning parameters during laser-assisted machining of Inconel 718. *Opt. Laser Technol.* **78**, 10–18 (2016)
2. Ulutan, D., Ozel, T.: Machining induced surface integrity in titanium and nickel alloys: a review. *Int. J. Mach. Tools Manuf.* **51**(3), 250–280 (2011)
3. Bhatt, A., Attia, H., Vargas, R., Thomson, V.: Wear mechanisms of WC coated and uncoated tools in finish turning of Inconel 718. *Tribol. Int.* **43**(5), 1113–1121 (2010)
4. Thakur, A., Gangopadhyay, S.: State-of-the-art in surface integrity in machining of nickel-based super alloys. *Int. J. Mach. Tools Manuf.* **100**, 25–54 (2016)
5. Ezentaş, R.: The investigation of the machinability of Inconel 718 and Waspaloy superalloys in CNC milling machines. Uludağ University Scientific Research Projects, Project 2008/74 (2010)
6. Ha, J.W., Seong, B.S., Jeong, H.W., Choi, Y.S., Kang, N.: Effects of the aging temperature and stress relaxation conditions on γ' precipitation in Inconel X-750. *J. Nucl. Mater.* **457**, 362–368 (2015)

7. Thakur, A., Gangopadhyay, S.: Dry machining of the nickel-based superalloy as a sustainable alternative using TiN/TiAlN coated tool. *J. Clean. Prod.* **129**, 256–268 (2016)
8. Ezilarasan, C., Senthil kumar, V.S., Velayudham, A.: An experimental analysis and measurement of process performances in machining of Nimonic C-263 superalloy. *Measurement* **46**, 185–199 (2013)
9. Swain, N., Venkatesh, V., Kumar, P., Srinivas, G., Ravi Shankar, S., Barshilia, H.C.: An experimental investigation on the machining characteristics of Nimonic 75 using uncoated and TiAlN coated tungsten carbide micro-end mills. *CIRP J. Manuf. Sci. Technol.* **16**, 34–42 (2017)
10. Ezilarasan, C., Senthil Kumar, V.S., Velayudham, A., Palanikumar, K.: Assessment of factors influencing tool wear on machining of Nimonic C-263 alloy with PVD coated carbide inserts. *Adv. Mater. Res.* **291–294**, 794–799 (2011)
11. Stephenson, D.A., Skerlos, S.J., King, A.S., Supekar, S.D.: Rough turning Inconel 750 with supercritical CO₂-based minimum quantity lubrication. *J. Mater. Process. Technol.* **214**(3), 673–680 (2014)
12. Olovsjö, S., Nyborg, L.: Influence of microstructure on wear behavior of uncoated WC tools in turning of alloy 718 and Waspaloy. *Wear* **282–283**, 12–21 (2012)
13. Cantero, J.L., Díaz-Álvarez, J., Miguélez, M.H., Marín, N.C.: Analysis of tool wear patterns in finishing turning of Inconel 718. *Wear* **297**(1–2), 885–894 (2013)
14. Ezugwu, E.O., Okeke, C.I.: Effects of coating materials on the machinability of a nickel base, C-263, alloy. *Tribol. Trans.* **43**(3), 549–553 (2000)
15. Ezugwu, E.O., Okeke, C.I.: Behavior of coated carbide tools in high-speed machining of a nickel-based alloy. *Tribol. Trans.* **45**(1), 122–126 (2002)
16. Prengel, H.G., Jindal, P.C., Wendt, K.H., Santhanam, A.T., Hegde, P.L., Penich, R.M.: A new class of high-performance PVD coatings for carbide cutting tools. *Surf. Coat. Technol.* **139**(1), 25–34 (2001)
17. Podder, B., Paul, S.: Improvement of machinability in end milling of Nimonic C-263 by application of high-pressure coolant. *Int. J. Mach. Mach. Mater.* **11**(4), 418–433 (2012)
18. Koyilada, B., Gangopadhyay, S., Thakur, A.: Comparative evaluation of machinability characteristics of Nimonic C-263 using CVD and PVD coated tools. *Measurement* **85**, 152–163 (2016)
19. Hsieh, J.H., Liang, C., Yu, C.H., Wu, W.: Deposition and characterization of TiAlN and multi-layered TiN/TiAlN coatings using unbalanced magnetron sputtering. *Surf. Coat. Technol.* **108**, 132–137 (1998)
20. Thakur, A., Gangopadhyay, S.: Dry machining of the nickel-based superalloy as a sustainable alternative using TiN/TiAlN coated tool. *J. Clean. Prod.* **129**, 256–268 (2016)
21. Thakur, A., Gangopadhyay, S., Maity, K.P., Sahoo, S.K.: Evaluation on effectiveness of CVD and PVD coated tools during dry machining of Incoloy 825. *Tribol. Trans.* **59**(6), 1048–1058 (2016)
22. Settineri, L.: Surface properties and performance of multilayer coated tools in turning Inconel. *CIRP Ann. Manuf. Technol.* **54**(1), 515–518 (2005)
23. Nalbant, M., Altin, M., Gokkaya, H.: The effect of cutting speed and cutting tool geometry on machinability properties of nickel-base Inconel 718 superalloys. *Mater. Des.* **28**, 1334–1338 (2007)
24. Klocke, F., Settineri, L., Lung, D., Priarone, P.C., Arft, M.: High-performance cutting of gamma titanium aluminides: influence of lubricoolant strategy on tool wear and surface integrity. *Wear* **302**, 1136–1144 (2013)
25. Diniz, A.E., de Oliveira, A.J.: Optimizing the use of dry cutting in rough turning steel operations. *Int. J. Mach. Tools Manuf.* **44**(10), 1061–1067 (2004)
26. Wang, X., An, L.: Experimental study on the surface roughness of superalloy GH169 by dry turning with CBN cutting tools. In: *Innovative Design and Manufacturing (ICIDM), Proceedings of the 2014 International Conference on IEEE* (2014)

Aerodynamic Characteristics of Semi-spiroid Winglets at Subsonic Speed



Karthick Dhileep, S. Arunvinthan and S. Nadaraja Pillai

Abstract In recent years, owing to the improving global socio-economic conditions, the number of air passengers grows rapidly. Despite the phenomenal increase in the passenger growth, the airline fuel cost continues to dominate with 27% of the total airline operating cost. Induced drag due to the pressure differential induced between the wings being the major contributor accounts for 25% of total drag at cruise to around 60% during take-off. With a view to overcome this, end plates were introduced in the 1980s to reduce the wingtip vortices. Several studies have been performed by researchers over various configurations and found that the angle at which the winglets are inclined greatly influences the strength of the wingtip vortices shed away from the winglets. In order to understand the effect of eccentricity on aerodynamic performance, a baseline swept wing with vertical winglets and seven different modified models featuring curved winglets with different eccentricities were computationally investigated for various angles of attack at $Re = 4.0 \times 10^6$. Results reveal that the curved semi-spiroid winglet with eccentricity e (0.2) outperforms clean wing showing a 9.85% increment in the aerodynamic efficiency over the pre-stall regions.

Keywords Spiroid winglets · Eccentricity · Induced drag · CFD

1 Introduction

In recent years, air travel has eventually become a preferred mode of transport owing to various factors like globalization and improving global economic conditions. IATA forecast states that the air passenger numbers will double to seven billion annually by 2034. Despite this tremendous growth, the airline fuel cost continues to hold its first position among the total operating cost of an aircraft.

K. Dhileep · S. Arunvinthan · S. Nadaraja Pillai (✉)
School of Mechanical Engineering, SASTRA Deemed to be University,
Tirumalaisamudram, Thanjavur 613401, Tamil Nadu, India
e-mail: nadarajapillai@mech.sastra.edu

© Springer Nature Singapore Pte Ltd. 2019
U. Chandrasekhar et al. (eds.), *Innovative Design, Analysis and Development Practices in Aerospace and Automotive Engineering (I-DAD 2018)*, Lecture Notes in Mechanical Engineering, https://doi.org/10.1007/978-981-13-2718-6_20

Similarly, the rapid growth of air travel in recent years contributes to an increase in the total pollution. Being threatened by the depletion of fossil fuels and rising pollution which causes environmental issues [1], judicious use of fuel is deemed necessary. As it is known that the fuel consumption is directly influenced by the accompanied drag of an aircraft, aerodynamicists started exploring several ways to reduce the drag. Studies reveal that the drag can be categorized into skin friction drag and pressure drag. Pressure drag can further be classified into wake drag and induced drag. The induced drag which is greatly due to the pressure differential induced between the top and bottom surfaces over the wings, thus forming a vortex accounts for 25% of total drag at cruise and around 60% during take-off [2]. Following that several researchers started focusing on reducing the induced drag by limiting the strength of the vortex formed at the wing tip using different techniques as shown in Fig. 1. One such is the use of endplates to reduce the wingtip vortices which dates back to the 1890s, introduced by F. W Lancaster, a British aerospace engineer [3]. In 1976, R. T Whitcomb of NASA Langley Research Centre came up with the idea of winglets that reduced the strength of the trailing vortex inspired from bird flight [3, 4]. Whitcomb also suggested that a properly cambered/angled vertical surface placed above or below the tip could reduce the strength of the trailing vortex, and thereby reducing the lift-induced drag. Over the past years, different configurations of winglets at various cant angles [5–7] have been studied by various researchers to identify the most efficient one.

Even though winglets have become standard equipment on almost all the civil and military aircraft, the knowledge on the spiroid winglets is less known and is little explored because of its intricacies in design. The preliminary numerical and experimental investigations were performed on spiroid winglets by Soltani et al. [7], and Guerrero et al. [8] demonstrated that the total pressure in the wake is influenced by the type of winglet adopted and reported that the spiroidal winglets have a

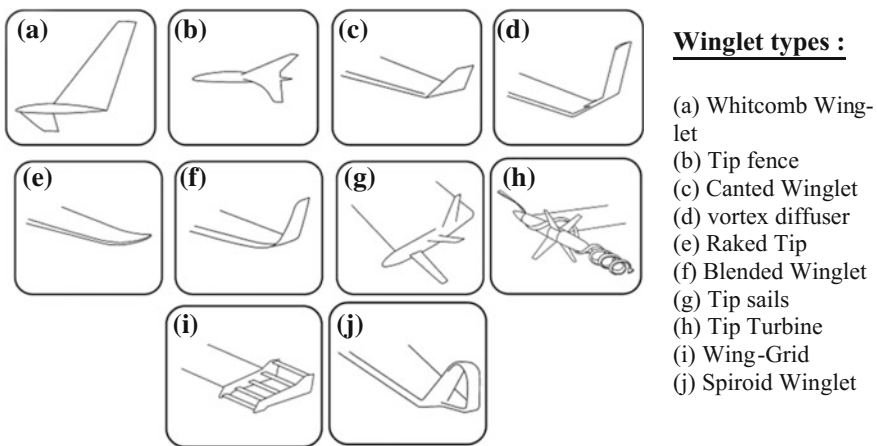


Fig. 1 Typical configurations of winglets currently in use [8]

greater tendency to effectively dissipate vortex faster compared to other winglets. Researchers claimed that the winglets are capable of reducing fuel consumption and increasing the operating range of an aircraft [4] along with numerous benefits like improved flight handling characteristics on and off ground along with reduced noise and engine emissions [9]. Previously published works on similar configuration is limited only to the parametric investigation of multiple winglet shapes and configurations. To the author's knowledge, no study on the aerodynamic characteristics of the effect of the curvature of a curved semi-spiroidal winglet has been done. Therefore, the present paper aims at studying the aerodynamic characteristics of semi-spiroid winglets as a function of eccentricity of the ellipse. It is expected that adopting semi-spiroid winglets over the normal spiroid winglet the induced/parasite drag can be reduced.

2 Computational Details

Table 1 represents the dimensions of the clean wing (CW) model used in this research which is loosely based on Boeing 747-400 wing [2, 10] and is shown in Fig. 2. With a view to understand the influence of the winglet eccentricity, a CW model and seven different models with different eccentricities were considered as the test cases. The major axis of the spiroid winglet, i.e., height was taken to be 10% of the span. The eccentricity was varied by varying the length of the semi-minor axis of the spiroidal winglet as in Table 2. A semi-spiroid winglet with wing model is shown in Fig. 3. The computational test arrangement is shown in Fig. 4. A standard rectangular domain is chosen to reduce the disturbance of the boundary.

All the models were subjected to eleven different angles of attack ranging from -25° to 25° in an increment of 5° . The CFD simulations were conducted using 3D steady-state solver. The computational analysis for all the models was conducted at a free stream velocity of 60 m/s. The flow over the models are considered to be turbulent, so Reynolds averaged Navier–Stokes equations (RANS) $k-\epsilon$ turbulence model is used since the computational analysis is in the outer region of the boundary layer and in free shear flows [11–13] rather than RANS $k-\omega$ SST turbulence model by Menter [11]. A convergence criterion of 10^{-6} was used for all the residuals.

Table 1 Model dimensions

Clean wing	
Parameters	Dimensions
Semi span	32.22 m
Root chord	14.63 m
Tip chord	4.06 m
Sweep angle	37°

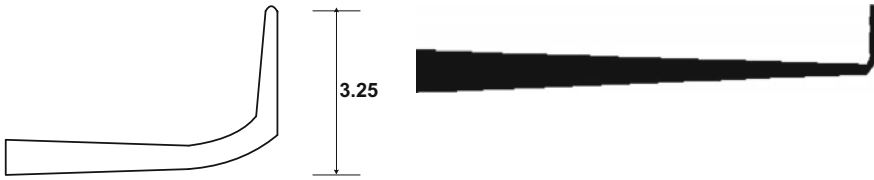


Fig. 2 Plan view of clean wing model with vertical winglets

Table 2 Configuration of various spiroid chosen for testing

Model label	Semi-minor axis length, b (m)
e (0.1)	1.617
e (0.2)	1.592
e (0.3)	1.550
e (0.4)	1.489
e (0.5)	1.407
e (0.6)	1.300
e (0.7)	1.160

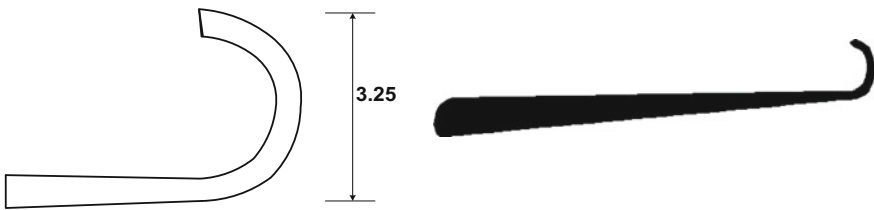


Fig. 3 Plan view of wing model with semi-spiroidal winglet

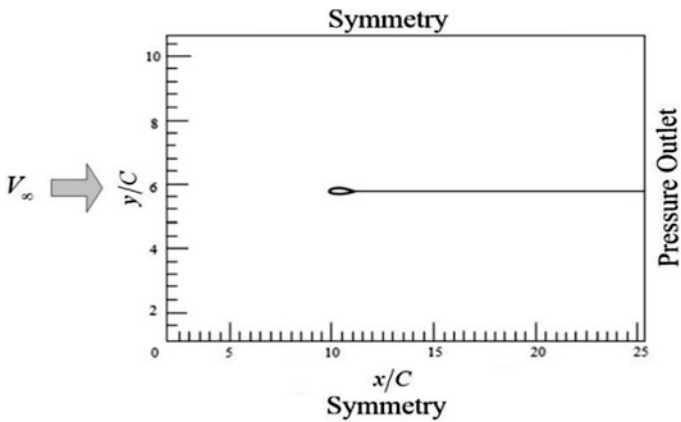
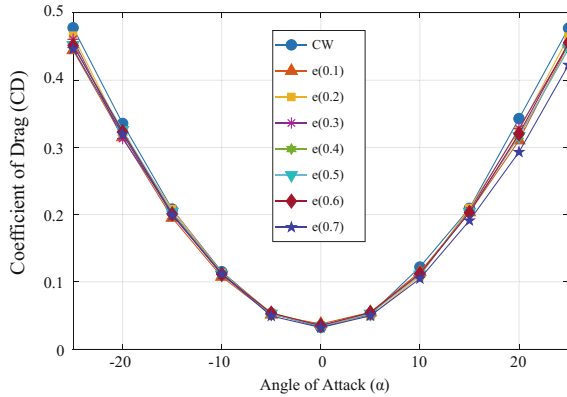


Fig. 4 Computational test arrangement

Fig. 6 Variation of Coefficient of drag (C_D) versus Angle of Attack (α)



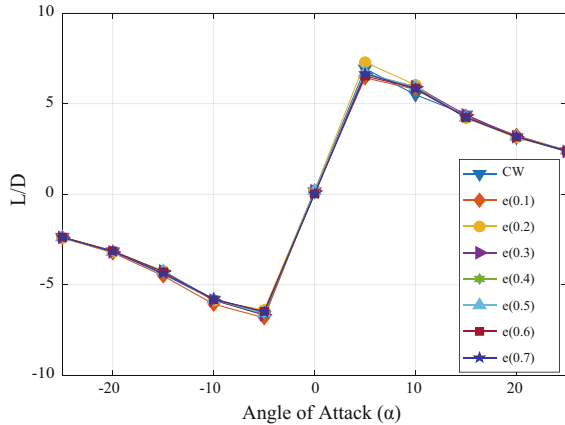
other modified models. Therefore, it can be inferred that the eccentricity influences drag in consideration with the baseline CW model. In the increasing direction of angles of attack, modified semi-spiroidal winglets with different eccentricities is 14.08% better than the clean wing configuration.

3.3 Aerodynamic Performance

The lift-to-drag ratio which signifies the aerodynamic performance is shown in Fig. 7. The figure clearly shows that the L/D ratio increases linearly with respect to angle of attack till 5° . At $\alpha = 5^\circ$, with respect to the clean wing in the $e(0.2)$ winglet case there is a 5.2% increase in aerodynamic performance. Similarly, at $\alpha = 10^\circ$, there is an increase of 9.85% in aerodynamic performance with respect to the clean wing. Post 5° AOA, the L/D ratio gradually starts decreasing with respect to angle of attack. In the case, $\alpha = 15^\circ$, the aerodynamic performance of the $e(0.7)$ winglet case drops by 4.38% compared to the CW. However, $e(0.2)$ winglet performs better than the rest of the winglets.

It can be clearly seen from Fig. 7 that $e(0.2)$ winglet provides relatively good aerodynamic performance from $\alpha = 0^\circ$ to 15° . It indicates that an optimum eccentricity is thus required to increase the aerodynamic performance without compromising the lift production. Although the modified models with eccentricities exhibit low C_L values, their corresponding drag reduction capabilities results in good overall aerodynamic performance. In other words, it can be expressed that the winglets featuring eccentricity have the tendency to optimize the aerodynamic performance in the pre-stall region. Even though all the eccentricity-featured winglets provide good performance characteristics, the optimum value of eccentricity needs to be identified. The reason for the same needs to be identified and working mechanism needs to be studied in detail. Therefore, it necessitates the

Fig. 7 Aerodynamic performance (L/D) versus Angle of Attack (α)



importance of understanding the underlying flow phenomenon to utilize its benefit to the fullest.

4 Conclusion

In this paper, the influence of eccentricity on the winglets has been studied extensively on a baseline clean wing and a modified wing featuring different winglets. Based on the above study, the following conclusions are made.

- Winglets featuring eccentricity exhibits optimum aerodynamic performance in the pre-stall region.
- Semi-spiroidal winglets shows 9.85% increase in the overall aerodynamic performance relative to the conventional CW Wing.
- Semi-spiroidal winglet greatly influences the drag characteristics and shows reduced drag over the baseline configuration.

Even though the semi-spiroidal winglets featuring different eccentricities can provide significant aerodynamic performance increment, the optimum value of eccentricity needs to be identified along with its underlying flow mechanism.

Acknowledgements Funding: This work was supported by “Research and Modernization fund, SASTRA University” grant number R&M/0035/SoME-008/2015-16. The authors thank SASTRA University for their financial assistance.

References

1. IATA: Annual review (2016)
2. Anderson, J.D.: *Fundamentals of Aerodynamics*. McGraw-Hill, New York (2011)
3. Whitcomb, R.T.: A design approach and selected wind-tunnel results at high subsonic speeds for wing-tip mounted winglets. NASA Technical Note, NASA TN D-8260, July 1976
4. Chambers, J.R.: *Concept to Reality: Contributions of the NASA Langley Research Center to US Civil Aircraft of the 1990s*. NASA SP-2003-4539 (2003)
5. Panagiotou, P., Kaparos, P., Yakinthos, K.: Winglet design and optimization for a MALE UAV using CFD. *Aerosp. Sci. Technol.* **39**, 190–205 (2014)
6. Falcão, L., Gomes, A., Suleman, A.: Design and analysis of an adaptive wingtip. In: 19th AIAA/ASME/AHS Adaptive Structures Conference, Denver, CO, USA, pp. 1–13 (2011)
7. Soltani, M.R., Ghorbanian, K., Nazarinia, M.: Experimental investigation of the effect of various winglet shapes on the total pressure distribution behind a wing. In: *Proceeding of the 24th International Council of the Aeronautical Sciences*, Yokohama, Japan (2004)
8. Guerrero, J.E., Maestro, D., Bottaro, A.: Biomimetic spiroid winglets for lift and drag control. *C.R. Mec.* **340**(1–2), 67–80 (2012)
9. Air Force Studies Board Division on Engineering and Physical Sciences: *Assessment of Wingtip Modifications to Increase the Fuel Efficiency of Air Force Aircraft*. Committee on Assessment of Aircraft Winglets for Large Aircraft Fuel Efficiency. The National Academies Press (2007)
10. Jackson, P., et al.: *Jane's all the World's Aircraft*. Jane's Information Group (2004)
11. Menter, F.R.: Two-equation eddy-viscosity turbulence models for engineering applications. *AIAA J.* **32**(8), 1598–1605 (1994)
12. Launder, B.E., Sharma, B.I.: Application of the energy dissipation model of turbulence to the calculation of flow near a spinning disc. *Lett. Heat Mass Trans.* **1**(2), 131–138 (1974)
13. Bardina, J.E., Huang, P.G., Coakley, T.J.: *Turbulence modeling validation, testing, and development*. NASA Technical Memorandum 11044 (1997)

Vibrational Analysis of Self-aligning Rolling Contact Bearing Defects



T. Narendiranath Babu, Abhinav Giri Goswami, Animesh Srivastava and Rishabh Kumar Tiwari

Abstract Rolling contact bearings are widely used in various classes of machines and have a lifespan related to their specific use. The occurrence of small defects within the bearings can lead to failure of the bearings over time and may lead to a major breakdown requiring a significant maintenance period. Major causes of damage to a bearing are excessive load, false brinelling, true brinelling, overheating, failure due to fatigue, contamination, reverse loading, misalignment, loose or tight fits and corrosion, etc. A vibrational analysis technique is used in order to determine the various faults and the extent of any damage sustained. Vibrational analysis includes the use of a Fast Fourier Transform (FFT) algorithm to convert time domain data to frequency domain data along with filtering techniques using the help of MATLAB software. In the current project, vibrational data was collected from self-aligning rolling contact bearings under six different fault conditions, namely a bearing with an inner race fault, a bearing with a cage fault, a bearing with one ball removed, a bearing with two balls removed, a bearing with three balls removed and a bearing with an outer race fault, i.e., a fault on the inner surface of the outer race of the bearing. In addition, healthy bearing conditions and a rotation at speed of 1100 rpm were applied. Methods like FFT and filtering techniques such as a Type 1 Chebyshev filter are proposed in this research for the analysis of faults. Furthermore, the classification of faults includes the use of an artificial neural network (ANN).

Keywords Bearing faults · Filtering techniques · Fast Fourier Transform (FFT) Fault classification · Artificial neural network (ANN)

T. Narendiranath Babu (✉) · A. G. Goswami · A. Srivastava · R. K. Tiwari
Department of Mechanical Engineering, Vellore Institute of Technology, Vellore 632014,
Tamil Nadu, India
e-mail: narendiranathbabu.t@vit.ac.in

© Springer Nature Singapore Pte Ltd. 2019
U. Chandrasekhar et al. (eds.), *Innovative Design, Analysis and Development Practices in Aerospace and Automotive Engineering (I-DAD 2018)*, Lecture Notes in Mechanical Engineering, https://doi.org/10.1007/978-981-13-2718-6_21

1 Introduction

1.1 Literature Survey

A robust signal processing technique has been the focus of experimental investigations of outer race and inner race faults of tapered roller bearings. The technique used is an undecimated wavelet transform, in which for further time-frequency analysis, a continuous wavelet transform is used to show signal approximation [1]. This vibrational analysis technique is effective and reliable in the detection of rolling element bearing faults. The defects induced were an outer raceway defect, an inner raceway defect and a combination of bearing element defects. The experimental investigation was carried out at different running speeds and at two load levels [2]. Vibration analysis of the bearing faults using a discrete wavelet transform assisted by a sym5 wavelet was employed to decompose the vibration signal. Experiments were conducted on deep groove ball bearings with various sizes of bearing defects on the outer race [3]. A vibration monitoring technique for rolling bearings was used to review different dynamic models in the presence and absence of local and distributed defects. Signal processing techniques such as wavelet transform and a high frequency resonance technique (HFRT) have been proposed [4]. In bearings, the statistical features such as kurtosis, skewness, mean, root mean square are measured from frequency and amplitude of vibration. The bearing fault diagnosis is investigated with the help of time domain, frequency domain and discrete wavelet transform. Feature ranking methods like chi-square and ReliefF are employed in the selection of the most informative feature and the subsequent reduction in the size of the feature vector. Comparison between feature ranking methods and classifiers enables the diagnosis result to be obtained [5]. A feature learning model approach based on convolutional neural networks allows a comparison between a feature learning-based approach and a feature engineering-based approach, the results of which indicate that a feature learning-based approach outperforms a feature engineering-based approach using manually engineered features and a random forest classifier [6]. Envelope detection has been used in the detection of faults in rolling element bearings through the extraction of a band-passed vibration signal and its subsequent Fourier Transform. The extraction of envelopes of band-passed signals was made with the help of a Hilbert Transform. The paper employed particle swarm optimization (PSO) for the selection of the optimum envelope window of band-passed vibration signals emanating from rotating drivelines [7]. The classification of ball bearings using vibration signals was made using a hybrid intelligent model consisting of a fuzzy min-max (FMM) neural network and a random forest model. For classification, features such as power spectrum and sample entropy are used [8]. Detection of bearing faults in induction machines involved the use of motor current signature analysis (MCSA). Monitoring of the stator current occurred through frequency spectral subtraction using various wavelet transforms. Discrete wavelet transform (DWT), stationary wavelet transform (SWT) and wavelet packet decomposition (WPD) were used for

spectral subtraction and the comparative analysis of fault by means of various fault indexing parameters [9]. A reliable deep learning approach based on a convolutional neural network (CNN) was investigated in order to reduce the information loss which could then reduce computation requirements in the temporal dimensions through the application of convolution computation, rectified linear units and sub-sampling for weight replication of the number of parameters to be learned for the improvement of general feed-forward back propagation training which occurred subsequent to the use of the top classifier in fault classification [10].

1.2 Theoretical Background

Analog Filter Design Using MATLAB The signal processing toolbox of MATLAB includes a number of M-files to directly develop analog transfer functions for the Chebyshev approximation technique.

Type 1 Chebyshev Filter The M-files for the design of analog Type 1 Chebyshev filters are as follows:

```
[z, p, k] = cheblap (N, Rp)
[num, den] = cheby1 (N, Rp, Wn, 's')
[num, den] = cheby1 (N, Rp, Wn, 'type', 's')
[N, Wn] = cheblord (Wp, Ws, Rp, Rs, 's')
```

where,

```
Rp  passband ripple (dB)
Wn  normalized frequency (Hz)
Wp  passband frequency (Hz)
```

Artificial Neural Network (ANN) This is an efficient computing system whose basic premise is analogous to biological neural networks. ANNs are also known as “artificial neural systems,” or “parallel distributed processing systems,” or “connectionist systems.” ANN acquires a large collection of units that are interconnected in a pattern that allows communication between the units. These units are also referred to as nodes or neurons and are simple processors which operate in parallel.

2 Methodology

The experimental setup used in the fault diagnosis of the rolling contact bearings is used to calculate the critical speed of whirling shaft. Self-aligning rolling contact bearings are chosen such that their dimensions are in accordance to the experimental setup, i.e., the inner diameter, $d = 25$ mm, the outer diameter, $D = 52$ mm and the radial thickness = 18 mm. The type of bearing used is a self-aligning bearing (SKF-2205). The following faults were induced on the bearings: (a) Outer race fault, inner race fault and cage fault on the self-aligning bearings with the help of stone grinder. (b) Ball fault such as the removal of one, two or three balls. (c) A normal bearing (in a healthy condition) is also taken into consideration. Circlips, circlip pliers and circlip collars were bought for the mounting and dismounting of the bearings within the head attachments. The experimental setup is connected to the data acquisition system (DAS) where the vibration readings will be taken at a speed of 1100 rpm with the help of DEWESoft 7.1.1 data acquisition software. The data collected were amplitude versus time data in three different directions with a sampling frequency of 12,800 Hz. The x -axis data were then imported into MATLAB and a FFT was applied along with the use of a Type 1 Chebyshev low-pass filter. Generally, the band pass frequency is included in the low frequency band (<1 kHz) and natural frequencies are indicated by the high frequency band (1–10 kHz). Furthermore, the classification of faults was achieved with the help of ANNs and curves such as best validation performance, training state, error histogram, and regression were obtained.

2.1 Experimental Setup

The experimental setup used to determine the critical speed of the whirling shaft was customized according to our requirements in order to obtain amplitude-time data. The experimental setup consists of two self-aligning rolling contact bearings (with cylindrical bore number SKF-2205) along with their respective head attachments. The magnetic sensor (accelerometer) is placed just above the left-side bearing at its head attachments in order to obtain the amplitude-time data with the help of the software. The data is obtained at 1100 rpm (Fig. 1).

The different faults occurring in the rolling contact bearings can be classified according to their damaged elements: outer raceway fault, inner raceway fault, ball fault and cage fault. Depending upon the mechanical dimension of the bearings, the characteristic fault frequency of the rolling contact bearings can be determined. The product of multipliers with the shaft rotational speed gives the defect frequency of a bearing running at a given shaft speed.

To calculate these frequency multipliers for the rolling contact bearing in which the inner race rotates and the outer race is stationary, the following Eqs. (1)–(3) are used:



Fig. 1 a Experimental setup for the vibrational analysis of the rolling contact bearings. **b** Left-hand side faulty bearing with the accelerometer placed at its head attachment

$$BPFO = \left(\frac{N}{2}\right) \left(1 - \left(\frac{B}{P}\right) (\cos \varphi)\right) \tag{1}$$

$$BPFI = \left(\frac{N}{2}\right) \left(1 + \left(\frac{B}{P}\right) (\cos \varphi)\right) \tag{2}$$

$$BSF = \left(\frac{1}{2}\right) \left(\frac{P}{B}\right) \left(1 - \left(\frac{B}{P}\right)^2 (\cos \varphi)^2\right) \tag{3}$$

where,

- N Number of balls = 13,
- B Ball diameter = 7.13 mm,
- P Pitch diameter = 38.98 mm,
- Φ Contact angle = 15°.

Generally the low frequency band (<1 kHz) includes the bearing pass frequencies and the high frequency band (1–10 kHz) indicates the natural frequencies.

In this study, different test cases (using seven bearings of varying health condition) are examined at 1100 rpm.

3 Results and Discussion

3.1 Mathematical Calculation

For Rotational Speed = 1100 rpm

1. Natural Frequency of Vibration, $S = \text{Rotational Speed}/60 \text{ Hz} = 1100/60 = 18.33 \text{ Hz}$ (Table 1)
2. Fundamental Train Frequency = $\left(\frac{S}{2}\right) \left(1 - \left(\frac{B}{P}\right) (\cos \varphi)\right)$
 $= \left(\frac{18.33}{2}\right) \left(1 - \left(\frac{7.13}{38.98}\right) (\cos 15^\circ)\right) = 7.545 \text{ Hz}$
3. Roller Pass Frequency of Inner Race = $\left(\frac{N}{2}\right) (S) \left(1 + \left(\frac{B}{P}\right) (\cos \varphi)\right)$
 $= \left(\frac{13}{2}\right) (18.33) \left(1 + \left(\frac{7.13}{38.98}\right) (\cos 15^\circ)\right) = 140.195 \text{ Hz}$
4. Roller Pass Frequency of Outer Race = $\left(\frac{N}{2}\right) (S) \left(1 - \left(\frac{B}{P}\right) (\cos \varphi)\right)$
 $= \left(\frac{13}{2}\right) (18.33) \left(1 - \left(\frac{7.13}{38.98}\right) (\cos 15^\circ)\right) = 98.094 \text{ Hz}$
5. Ball Spin Frequency = $\left(\frac{P}{2 \times B}\right) (S) \left(1 - \left(\frac{B}{P}\right)^2 (\cos \varphi)^2\right)$
 $= \left(\frac{38.98}{2 \times 7.13}\right) (18.33) \left(1 - \left(\frac{7.13}{38.98}\right)^2 (\cos 15^\circ)^2\right) = 48.541 \text{ Hz}$

3.2 Fault Diagnosis Plots for Self-aligning Bearings

3.2.1 Fault—Cage Fault in Combination with Inner Race Fault and Three Balls Fault (with the Help of a Stone Grinder)

The plots are made for a sampling frequency $f_s = 12,800 \text{ Hz}$, cut-off frequency = 255 Hz and passband ripple, $R_p = 1 \text{ dB}$. The maximum amplitude is 2.423 at a time of 8.827 s as can be seen in the first subplot. After applying the FFT to the amplitude data, a maximum magnitude of 2.702 occurs corresponding to a frequency of 276.8 Hz. With the use of a Type 1 Chebyshev low-pass filter, a filtered amplitude versus time subplot is obtained with a maximum amplitude value of 0.003925 corresponding to a time value of 8.034 s. After applying the FFT to the filtered amplitude data, a maximum magnitude value of 0.004341 occurs corresponding to a frequency of 276.8 Hz. The cage fault is modulated when in

Table 1 Bearing defect characteristic frequency (in Hz)

Characteristic frequency	Frequency (Hz)
Natural frequency of vibration	18.33
Fundamental train frequency	7.545
Roller pass frequency of inner race	140.195
Roller pass frequency of outer race	98.094
Ball spin frequency	48.541

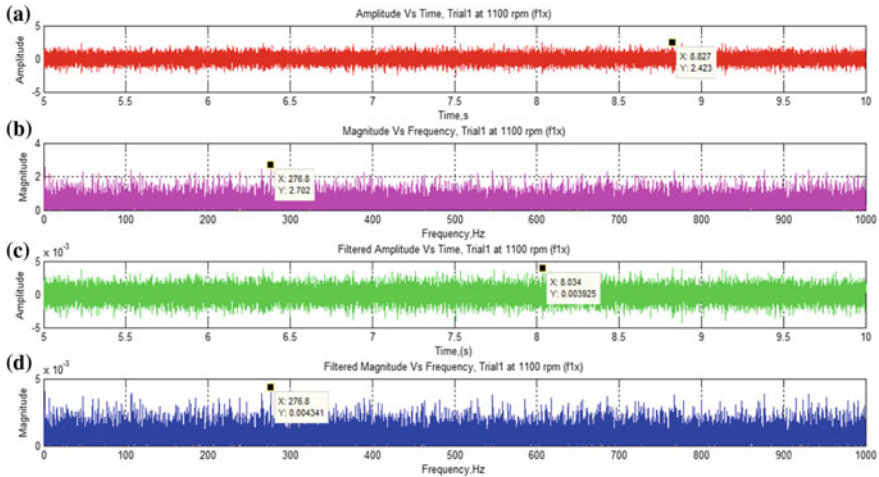


Fig. 2 a Time domain plot, b frequency domain plot after applying the FFT to time domain data, c time domain plot filtered through a Type 1 Chebyshev filter, d frequency spectrum obtained after applying FFT and a Type 1 Chebyshev filter

combination with other faults, hence the maximum amplitude is obtained at the high value of 276.8 Hz in the frequency spectrum (Fig. 2).

3.2.2 Fault—Inner Race Fault (with the Help of a Stone Grinder)

The plots are made for a sampling frequency $f_s = 12,800$ Hz, cut-off frequency = 255 Hz and passband ripple, $R_p = 1$ dB. The maximum amplitude is 4.359 at a time of 3.202 s as can be seen in the first subplot. After applying the FFT to the amplitude data input, a maximum magnitude value of 4.359 occurs corresponding to a frequency of 140.5 Hz. With the use of a Type 1 Chebyshev low-pass filter, a filtered amplitude versus time subplot is obtained with a maximum amplitude of 0.006951 corresponding to a time value of 3.203 s. After applying the FFT to the filtered amplitude data obtained, a maximum magnitude value of 0.006951 occurs corresponding to a frequency of 140.5 Hz. The characteristic defect frequency, i.e., ball spin frequency = 140.195 Hz from the mathematical formulation. Since the frequency values obtained from both the formulation and the frequency spectrum plots are in close agreement with little variation, the result is valid (Fig. 3).

3.2.3 Fault—Single Ball Removed

The plots are made for a sampling frequency $f_s = 12,800$ Hz, cut-off frequency = 255 Hz and passband ripple, $R_p = 1$ dB. The maximum amplitude

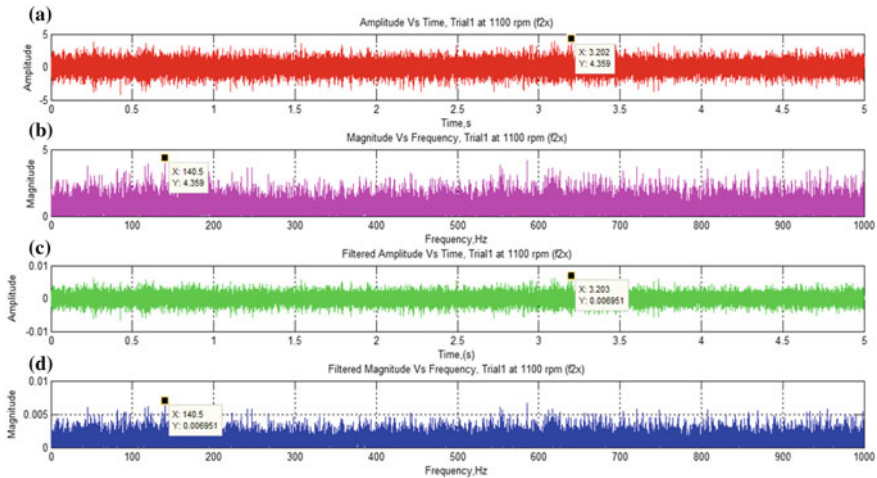


Fig. 3 a Time domain plot, b frequency domain plot after applying the FFT to time domain data, c time domain plot filtered through a Type 1 Chebyshev filter, d frequency spectrum obtained after applying the FFT and the Type 1 Chebyshev filter

is 12.13 at a time of 2.273 s as can be seen in the first subplot. After applying the FFT to the amplitude data input, a maximum magnitude value of 13.11 occurs corresponding to a frequency of 72.7 Hz. With the use of a Type 1 Chebyshev low-pass filter, a filtered amplitude versus time subplot is obtained with a maximum amplitude value of 0.01916 corresponding to a time value of 2.273 s. After applying the FFT to the filtered amplitude data obtained, a maximum magnitude value of 0.02112 occurs corresponding to a frequency of 72.72 Hz. The characteristic defect frequency, i.e., ball spin frequency = 48.541 Hz from the mathematical formulation and hence the over-rolling frequency of one point on the rolling element is equal to $(2 \times 48.541) = 97.082$ Hz. Since the frequency values obtained from both the formulation and the frequency spectrum plots are in close agreement with little variation, the result is valid (Fig. 4).

3.2.4 Fault—Two Balls Removed

The plots are made for a sampling frequency $f_s = 12,800$ Hz, cut-off frequency = 255 Hz and passband ripple, $R_p = 1$ dB. The maximum amplitude is 1.983 at a time of 8.325 s as can be seen in the first subplot. After applying the FFT to the amplitude data input, a maximum magnitude value of 1.983 occurs corresponding to a frequency of 165 Hz. With the use of a Type 1 Chebyshev low-pass filter, a filtered amplitude versus time subplot is obtained with a maximum amplitude of 0.003163 corresponding to the a time of 8.325 s. After applying the FFT to the filtered amplitude data obtained, a maximum magnitude of 0.003163 occurs corresponding to a frequency of 165.1 Hz. The characteristic defect

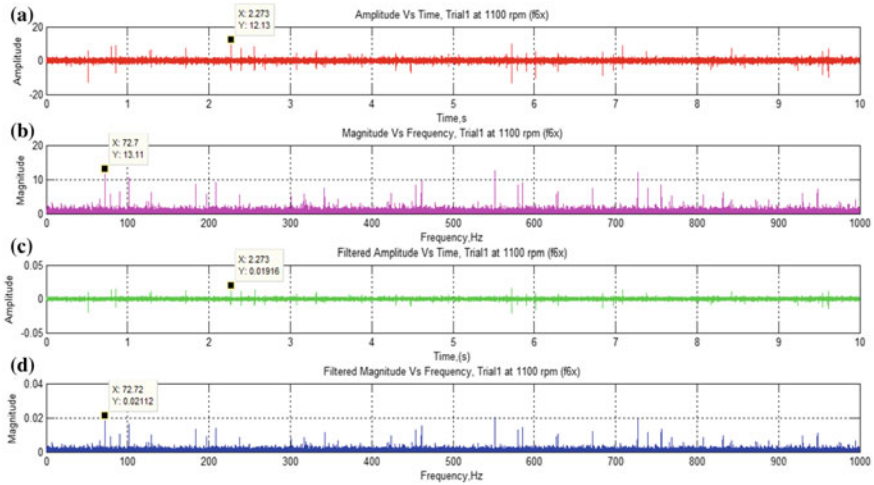


Fig. 4 **a** Time domain plot, **b** frequency domain plot after applying the FFT to time domain data, **c** time domain plot filtered through a Type 1 Chebyshev filter, **d** frequency spectrum obtained after applying the FFT and the Type 1 Chebyshev filter

frequency, i.e., ball spin frequency = 48.541 Hz from the mathematical formulation and hence the over-rolling frequency of one point on the rolling element is equal to $(2 \times 48.541) = 97.082$ Hz. As two balls are removed, the maximum amplitude is obtained at a frequency value greater than that for a single ball. Since the frequency values obtained from both the formulation and the frequency spectrum plots are in close agreement with little variation, the result is valid (Fig. 5).

3.2.5 Fault—Three Balls Removed

The plots are made for a sampling frequency $f_s = 12,800$ Hz, cut-off frequency = 255 Hz and passband ripple, $R_p = 1$ dB. The maximum amplitude is 1.822 at a time of 8.646 s as can be seen in the first subplot. After applying the FFT to the amplitude data input, a maximum magnitude value of 2.201 occurs corresponding to a frequency of 229.1 Hz. With the use of a Type 1 Chebyshev low-pass filter, a filtered amplitude versus time subplot is obtained with a maximum amplitude of 0.002875 corresponding to a time of 8.646 s. After applying the FFT to the filtered amplitude data obtained, a maximum magnitude of 0.003558 occurs corresponding to a frequency of 229.2 Hz. The characteristic defect frequency, i.e., ball spin frequency = 48.541 Hz from the mathematical formulation and hence the

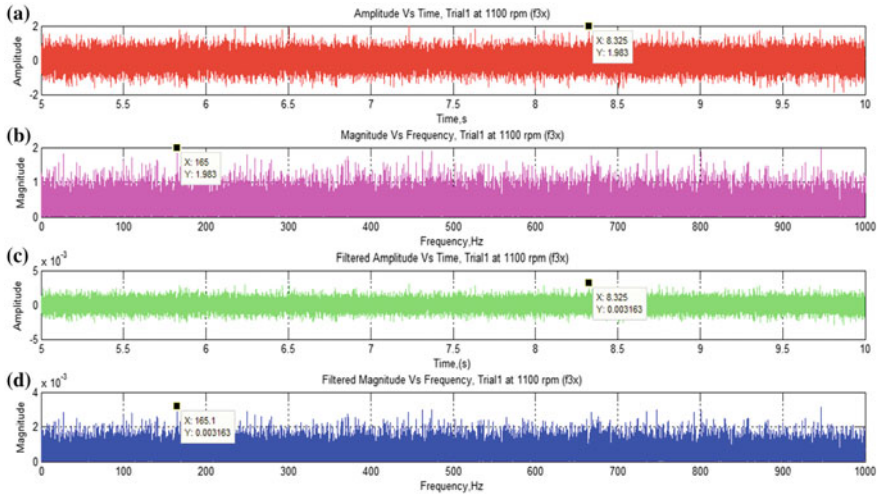


Fig. 5 **a** Time domain plot, **b** frequency domain plot after applying the FFT to time domain data, **c** time domain plot filtered through the Type 1 Chebyshev filter, **d** frequency spectrum obtained after applying the FFT and the Type 1 Chebyshev filter

over-rolling frequency of one point on the rolling element is equal to $(2 \times 48.541) = 97.082$ Hz. As two balls are removed, the maximum amplitude is obtained at a frequency value greater than that for removal of both a single ball and two balls. Since the frequency values obtained from both the formulation and the frequency spectrum plots are in close agreement with little variation, the result is valid (Fig. 6).

3.2.6 Fault—Outer Race Fault (Inner Surface of the Outer Race of the Bearing)

The plots are made for a sampling frequency, $f_s = 12,800$ Hz, cut-off frequency = 255 Hz and passband ripple, $R_p = 1$ dB. The maximum amplitude is 3.777 at a time equal to 6.044 s as can be seen in the first subplot. After applying the FFT to the amplitude data input, a maximum magnitude of 3.777 occurs corresponding to a frequency of 104.4 Hz. With the use of a Type 1 Chebyshev low-pass filter, a filtered amplitude versus time subplot is obtained with a maximum amplitude of 0.005985 corresponding to a time of 6.044 s. After applying the FFT to the filtered amplitude data obtained, a maximum magnitude of 0.005985 occurs corresponding to a frequency of 104.4 Hz. The characteristic defect frequency, i.e., outer race ball pass frequency = 98.094 Hz from the mathematical formulation. Since the frequency values obtained from both the formulation and the frequency spectrum plots are in close agreement with little variation, the result is valid (Fig. 7).

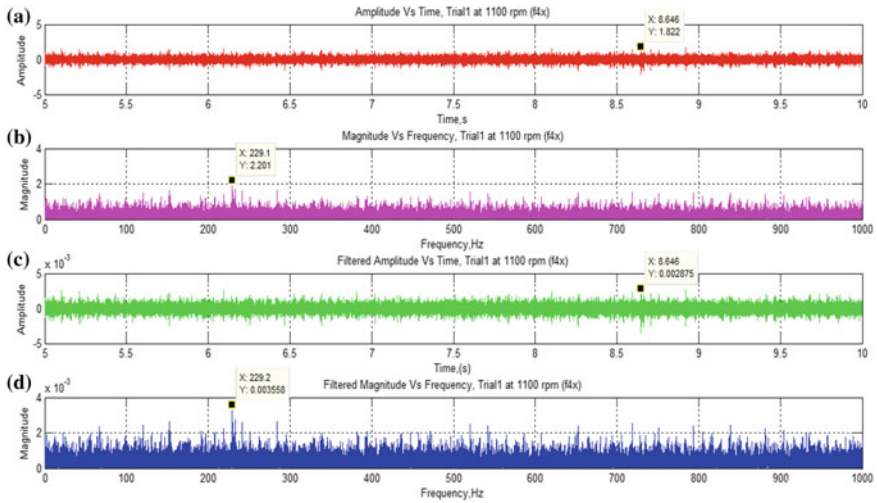


Fig. 6 a Time domain plot, b frequency domain plot after applying the FFT to time domain data, c time domain plot filtered through a Type 1 Chebyshev filter, d frequency spectrum obtained after applying the FFT and the Type 1 Chebyshev filter

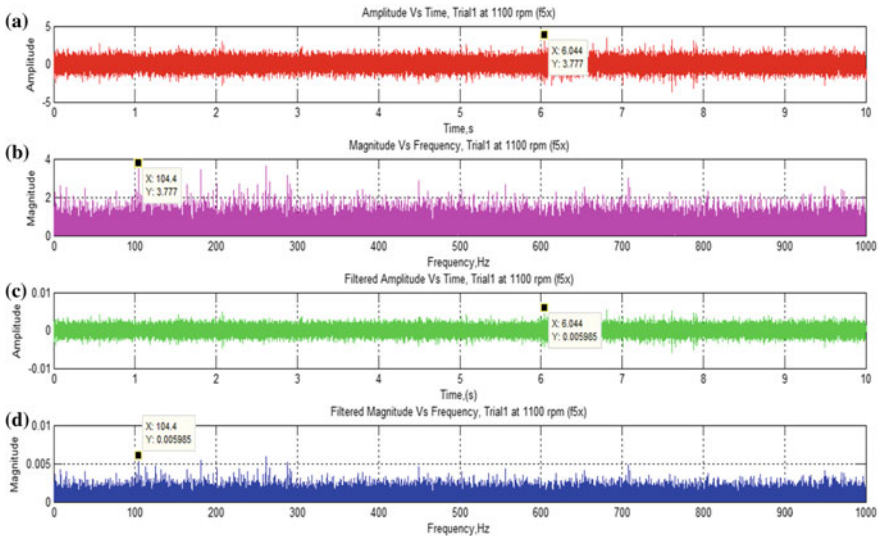


Fig. 7 a Time domain plot, b frequency domain plot after applying the FFT to time domain data, c time domain plot filtered through a Type 1 Chebyshev filter, d frequency spectrum obtained after applying the FFT and the Type 1 Chebyshev filter

3.3 Fault Classification Curves Obtained with the Help of an Artificial Neural Network (ANN)

3.3.1 Best Validation Performance Curves

The minimum value of the mean squared error (mse) is 0.11888. This implies the error value is $\sqrt{0.11888} = 0.34478$. The Minimum value is obtained at epoch 3. Hence the validation is $\left(\frac{1-0.34478}{1}\right) \times 100 = 65.52\%$ (Fig. 8).

3.3.2 Training State

The Gradient reached a value of 1.4379×10^{-7} at epoch 9. The Mu value is 1×10^{-14} at epoch 9. The Validation Checks = 6 at epoch 9 (Fig. 9).

3.3.3 Error Histogram

The validation test occurred for instances of a value between 40 and 50 at a mean error value of -0.01428 , for instances of a value from 0 to 15 at a mean error value of -0.1758 , -0.122 and -0.06813 respectively, and for instances of a value from 0 to 5 at a mean error value of 0.8472 within the error histogram with 20 bins. The training occurred for instances of a value from 0 to 5 at a mean error value of -0.1758 , -0.122 and -0.06813 respectively, for instances of a value from 0 to 45 at

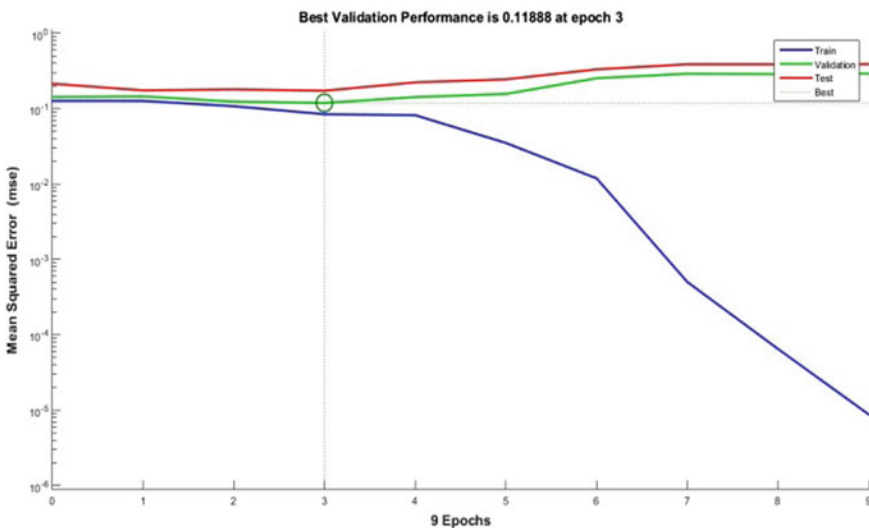


Fig. 8 Best validation performance curve

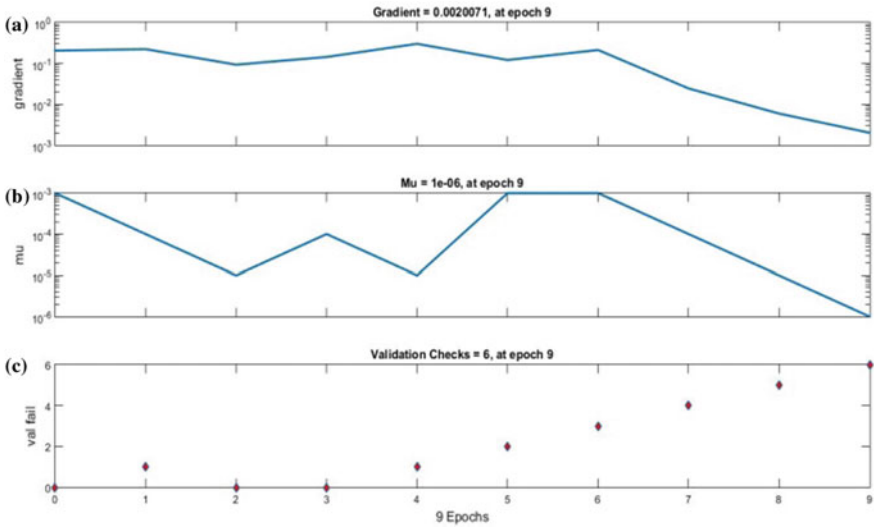


Fig. 9 Training state curve, a gradient, b Mu, c validation checks

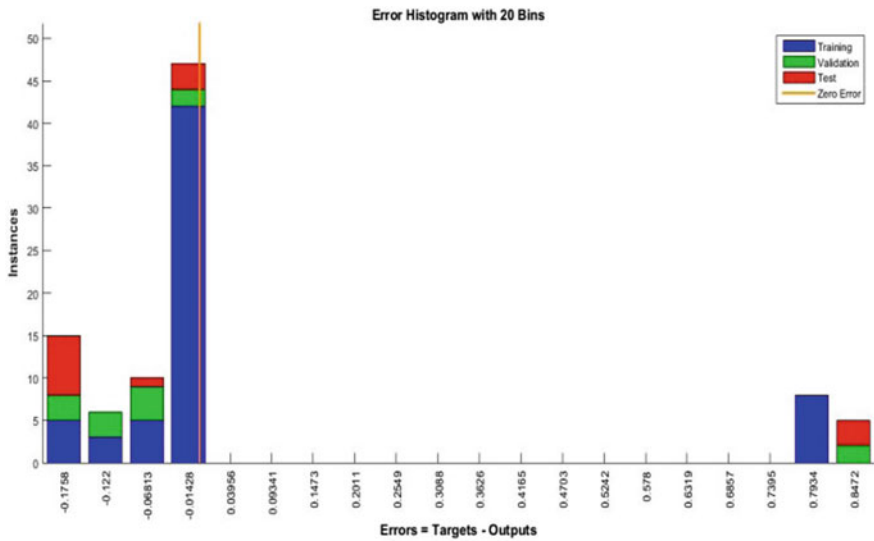


Fig. 10 Error histogram curve

a mean error value of -0.01428 , and for instances of a value from 0 to 10 at a mean error value of 0.7934 . The zero error line passes between -0.01428 and 0.03956 and is close to -0.01428 , slightly cutting through the histogram at that point (Fig. 10).

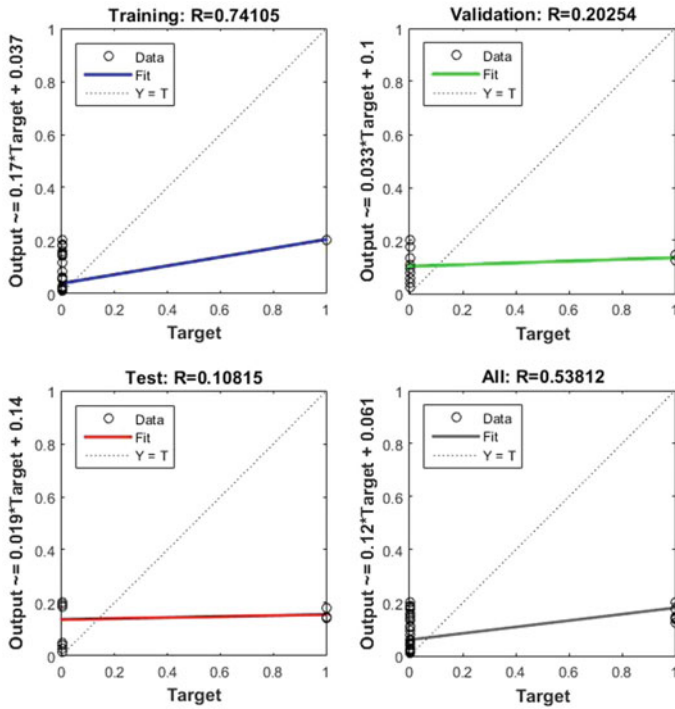


Fig. 11 Regression curves

3.3.4 Regression

The regression plots, i.e., Output versus Target for Training, Validation, Test and All are of order 1. The regression value for Training that is shown in the top-left subplot is 0.74105. The regression value for Validation that is shown in the top-right subplot is 0.20254. The regression value for Test that is shown in the bottom-left subplot is 0.10815. The regression value for All that is shown in the bottom-right subplot is 0.53812 (Fig. 11).

4 Conclusion

The plot results for the vibrational analysis of self-aligning rolling contact bearings are obtained for the above-mentioned different fault conditions and also for bearings in a healthy condition with the use of amplitude and time signals data for each of the conditions at 1100 rpm. The sampling frequency for the signals, $f_s = 12,800$ Hz. The cutoff frequency for the signals, $f_c = 255$ Hz and the passband ripple, $R_p = 1$ dB.

There are many instances where the calculated bearing frequencies don't match exactly with the bearing defect frequencies that appear in the vibration spectra. This is due to the variable loads exerted on the bearings and it leads to change in contact angle and misalignment in the rotor system. Also, the number of rolling elements for a particular bearing size varies and depends on the manufacturer. The fault classification curves show the performance, training state, error histogram and regression (for training, validation, test and all). The fault classification curves shows that best validation performance is 65.52%.

Better results can be obtained through the use of further diagnosis and classification techniques and also by varying the plot interval to a number of epochs.

References

1. Jena, D.P., Panigrahi, S.N.: Precise measurement of defect width in tapered roller bearing using vibration signal. *Measurement* **55**, 39–50 (2014)
2. Saruhan, H., Sandemir, S., Çiçek, A., Uygur, I.: Vibrational analysis of rolling element bearing defects. *J. Appl. Res. Technol.* 384–395 (2014)
3. Khanam, S., Tandon, N., Dutt, J.K.: Fault size estimation in the outer race of ball bearing using discrete wavelet transform of the vibration signal. In: 2nd International Conference on Innovations in Automation and Mechatronics Engineering, ICIAME 2014. *Procedia Technol.* **14**, 12–19 (2014)
4. Shah, D.S., Patel, V.N.: A review of dynamic modeling and fault identifications methods for rolling element bearing. In: 2nd International Conference on Innovations in Automation and Mechatronics Engineering, ICIAME 2014. *Procedia Technol.* **14**, 447–456 (2014)
5. Vakharia, V., Gupta, V.K., Kankar, P.K.: Bearing fault diagnosis using feature ranking methods and fault identification algorithms. In: 12th International Conference on Vibration Problems, ICOVP 2015. *Procedia Eng.* **144**, 343–350 (2014)
6. Janssens, O., Slavkovikj, V., Vervisch, B., Stockman, K., Loccufer, M., Verstockt, S., Van de Walle, R., Van Hoecke, S.: Convolutional neural network based fault detection for rotating machinery. *J. Sound Vib.* **377**, 331–345 (2016)
7. Tyagi, S., Panigrahi, S.K.: An improved envelope detection method using particle swarm optimization for rolling element bearing fault diagnosis. *J. Comput. Des. Eng.* **4**, 305–317 (2017)
8. Seera, M., Wong, M.L.D., Nandi, A.K.: Classification of ball bearing faults using a hybrid intelligent model. *Appl. Soft Comput.* **57**, 427–435 (2017)
9. Kompella, K.C.D., Mannam, V.G.R., Rayapudi, S.R.: Bearing fault detection in a 3 phase induction motor using stator current frequency spectral subtraction with various wavelet decomposition techniques. *Ain Shams Eng. J.* **13**, 143–159 (2017)
10. Lu, C., Wang, Z., Zhou, B.: Intelligent fault diagnosis of rolling bearing using hierarchical convolutional network based health state classification. *Adv. Eng. Inform.* **32**, 139–151 (2017)

Fabrication and Characterization of $\text{Cu}_{2-x}\text{Zn}_{1.3}\text{SnS}_4$ Kesterite Thin Films Synthesized by Solvent Based Process Method for Photovoltaic Solar Energy Applications



B. Khadambari, S. S. Bhattacharya and M. S. Ramachandra Rao

Abstract Solar has become one of the fastest growing renewable energy sources. With the push towards sustainability, it is an excellent solution to resolve the issue of our diminishing finite resources. Alternative photovoltaic systems are of much importance to utilize solar energy efficiently. The Cu-chalcopyrite compounds CuInS_2 and CuInSe_2 and their alloys provide absorber material of high absorption coefficients of the order of 10^5 cm^{-1} . $\text{Cu}_2\text{ZnSnS}_4$ (CZTS) is more promising material for photovoltaic applications as Zn and Sn are abundant materials of earth's crust. Further, the preparation of CZTS-ink facilitates the production of flexible solar cells. The device can be designed with Al doped ZnO as the front contact, n-type window layer (e.g. intrinsic ZnO); an n-type thin film buffer layer (e.g. CdS) and a p-type CZTS absorber layer with molybdenum (Mo) substrate as back contact. In this study, CZTS films were synthesized by a non-vacuum solvent based process technique from a molecular-ink using a non-toxic eco-friendly solvent dimethyl sulfoxide (DMSO). The deposited CZTS films were optimized and characterized by XRD, UV-visible spectroscopy and SEM.

Keywords CZTS-ink · Kesterite · Photovoltaic

B. Khadambari (✉) · S. S. Bhattacharya
Department of Metallurgical & Materials Engineering, Nano Functional Materials
Technology Centre, Indian Institute of Technology Madras, Chennai 600036, India
e-mail: khadam392@gmail.com

M. S. Ramachandra Rao
Department of Physics, Nano Functional Materials Technology Centre and Materials Science
Research Centre, Indian Institute of Technology Madras, Chennai 600036, India

© Springer Nature Singapore Pte Ltd. 2019
U. Chandrasekhar et al. (eds.), *Innovative Design, Analysis and Development
Practices in Aerospace and Automotive Engineering (I-DAD 2018)*, Lecture Notes
in Mechanical Engineering, https://doi.org/10.1007/978-981-13-2718-6_22

1 Introduction

Photovoltaic systems have been gaining in importance in order to utilize solar energy efficiently. The copper chalcopyrite compounds, CuInS_2 and CuInSe_2 , and their alloys can be used as absorber materials with high-absorption coefficients of the order of 10^5 cm^{-1} . CZTS is a promising thin film p-type absorber material for solar cell fabrication, owing to its earth's abundance and environment compatible nature. CZTS results by replacing indium and gallium by less expensive, earth-abundant zinc and tin, from CIGS (copper indium gallium selenide), to make it a less expensive p-type absorber material for solar cell fabrication [1]. CZTS is an $\text{I}_2\text{-II-IV-VI}_4$ quaternary compound. There are various different types of methods developed for fabricating kesterite thin films. Some of the versatile methods are vacuum-based deposition technique, chemical vapour deposition, electrodeposition technique and chemical route sol-gel technique. Guo et al. [2] reported the first synthesis of $\text{Cu}_2\text{ZnSnS}_4$ nanocrystals using hot-injection method and demonstrated its use for the fabrication of solar cells, but the efficiency was less than 1%. With slight changes in the amount of precursors (at non-stoichiometric conditions of CZTS nanocrystals) [3] achieved 7.2% efficiency. CZTS material based solar cells have reached a power conversion efficiency up to 9.2% till date [4]. Kumar Samji et al. [5] predicted that basic defect physics of the material and its influence on phonon spectrum to transport properties may reveal the mechanism behind surge in efficiency under non-stoichiometric conditions. Solvent-based process technique can be sub-divided into two categories: (i) based on the formation of CZTS kesterite crystalline structure before the deposition of the nanocrystalline ink on the soda-lime glass substrate (ii) based on the surface precursor reactions on annealing the CZTS-ink deposited substrate. The solvent based process method of synthesizing CZTS-ink involves the formation of p-type absorber layer thin films with reduced secondary phases, directly from the as synthesized molecular-ink which are non-toxic true solutions whereas are not slurries as in the case of hydrazine-based hot-injection technique [6, 7].

2 Experimental Details

The CZTS films were synthesized and deposited from a molecular-ink using solvent-based process method which uses an eco-friendly non-toxic solvent, dimethyl sulfoxide (DMSO) to fabricate efficient polycrystalline solar cells. The true solution was synthesized by dissolving the precursors of copper, zinc and tin one by one in DMSO solvent for optimized time based on its solubility. At the last, the final chemical of sulphur precursor was added to the solution, resulting in the formation of CZTS-ink. The precursor solution was synthesized by the simultaneous addition of metal precursors into the DMSO solvent, kept under stirring at constant rpm. Initially, 8 mL of DMSO was added to a 25 mL beaker having

copper precursor, 6 mM of copper acetate monohydrate at ambient temperature. This results in the formation of a deep blue coloured solution because of the limited solubility of copper acetate monohydrate in DMSO solvent. This was followed by the addition of tin precursor, 5.5 mM of tin chloride monohydrate into the deep blue coloured solution which was kept under stirring at a constant rpm at ambient temperature. Gradually the deep blue colour solution changed to transparent light green colour solution after 20 h of constant stirring due to the reduction of Cu^{2+} to Cu^+ followed by the stabilization of chloride ions and DMSO ions. This was followed by the addition of zinc precursor, 5.6 mM of zinc nitrate into the transparent light green solution. After a constant stirring of 6 h, the transparent green colour of the metal precursors solution changed to pale greenish yellow. At last, the final chemical of sulphur precursor, i.e., 14.3 mM of thiourea was added. Finally, a clear colourless solution was obtained due to the following two major reasons: (1) The sulphur precursor getting completely dissolved. (2) Due to the presence of a small amount of Cu^{2+} cations in the final solution. The final solution was diluted to 40% with the non-toxic environment friendly solvent DMSO resulting to the formation of non-stoichiometric $\text{Cu}_{2-x}\text{Zn}_{1.3}\text{SnS}_4$ dispersed molecular-ink. The synthesized CZTS molecular-ink was characterized to confirm its kesterite structure. The CZTS thin films were deposited by spin-coating the molecular-ink on to a soda-lime glass substrate to form CZTS p-type absorber layer film. Further, the CZTS films that were fabricated by spin-coating technique was annealed at 500°C with elemental sulphur vapour (sulphurization) in order to enhance and promote crystallinity of the thin film by partial replacement of sulphur atoms.

3 Results and Discussion

In Fig. 1, the X-ray diffractogram of annealed CZTS film shows the formation of pure kesterite phase, which is commonly observed for realizing efficient CZTS solar cells. Peak positions (112), (220) and (312) are indexed in the diffraction pattern which is well in agreement with the literature [5]. The lattice parameters for the CZTS nanocrystals are $a = 5.427 \text{ \AA}$, $b = 5.427 \text{ \AA}$ and $c = 10.848 \text{ \AA}$ [6].

From the Tauc plot of CZTS thin film in Fig. 2, it is inferred that the energy bandgap (E_g) of the annealed kesterite CZTS thin films is 1.4 eV.

The SEM images show that the film is very uniform with thickness $\sim 1 \mu\text{m}$. The surface morphology in the following Fig. 3a, b shows the dense and crack-free films. Films prepared under Cu-poor and Zn-rich conditions adhere well to the glass substrate.

Raman studies on $\text{Cu}_{2-x}\text{Zn}_{1.3}\text{SnS}_4$ ($x = 0, 0.3, 0.5$ and 0.7) thin films were done by changing the incident laser beam intensity. From Fig. 4, it is observed that both copper stoichiometry and incident laser beam intensity induce a disorder in CZTS. In the case of CZTS, it is reported that defect density influences phonon density of states which in turn affects carrier concentration. Therefore, it becomes important to correlate basic defect physics of materials and its influence on phonon spectrum to

Fig. 1 XRD pattern of CZTS thin film

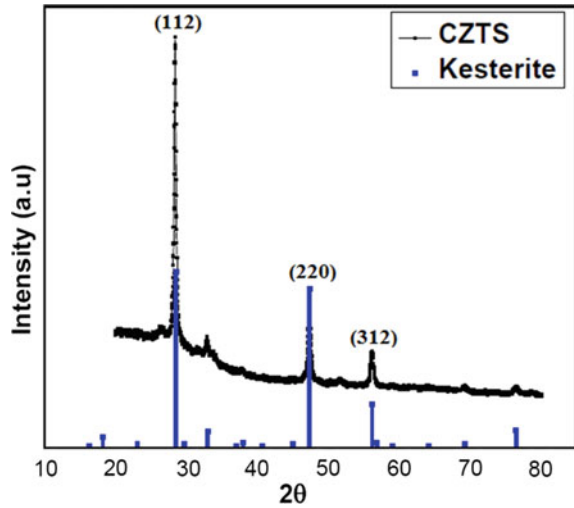
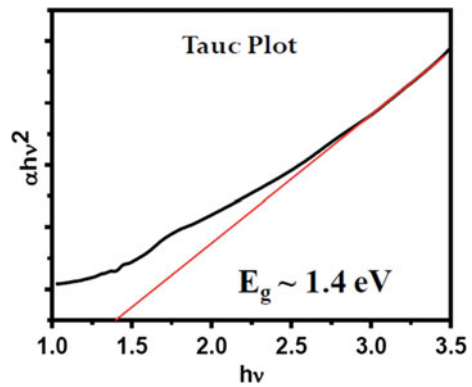


Fig. 2 Tauc plot for CZTS thin film



transport properties; which may reveal the mechanism behind surge in efficiency under non-stoichiometric conditions [5].

After optimizing the p-type (CZTS) and n-type (CdS) layers, a p-n junction have been created in order to analyse the diode characteristics. Figure 5 shows the I–V characteristics (dark) of CZTS/CdS p-n junction.

The CZTS solar cell preparation involved the deposition of Mo, p-CZTS, n-CdS, i-ZnO and Al:ZnO layers in a sequential manner on a soda-lime glass substrate in the form of a stack, as shown in Fig. 6.

The CZTS solar cell is then tested using a solar simulator (incident power 1000 W/m^2) for I–V characteristics and quantum efficiency studies. Figure 7 shows the device characteristics of the fabricated kesterite phase CZTS solar cell. For the

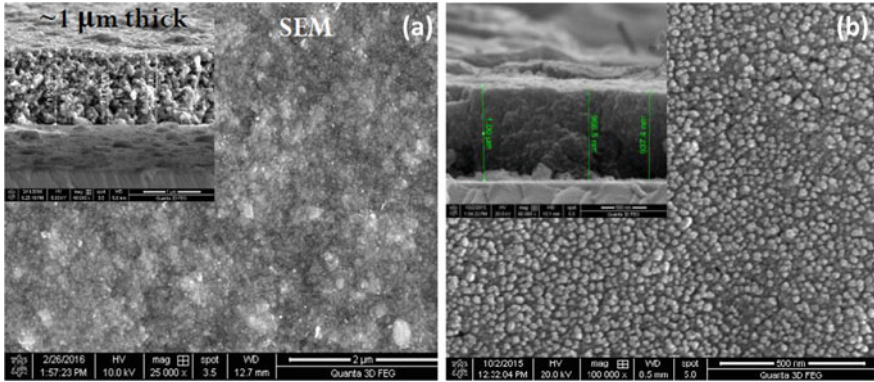


Fig. 3 a and b: SEM image of annealed CZTS thin film

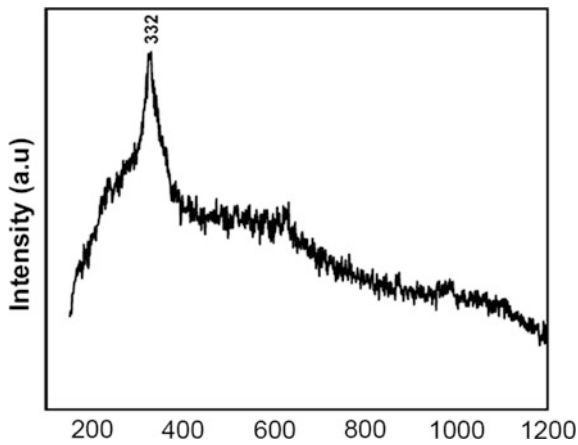


Fig. 4 Raman spectra of CZTS thin film

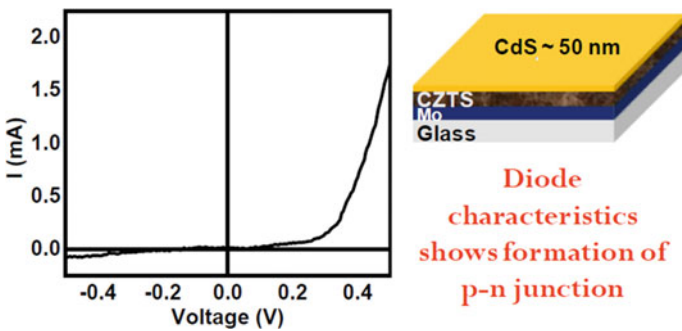


Fig. 5 I-V Characteristics of p-type CZTS/n-type CdS layer

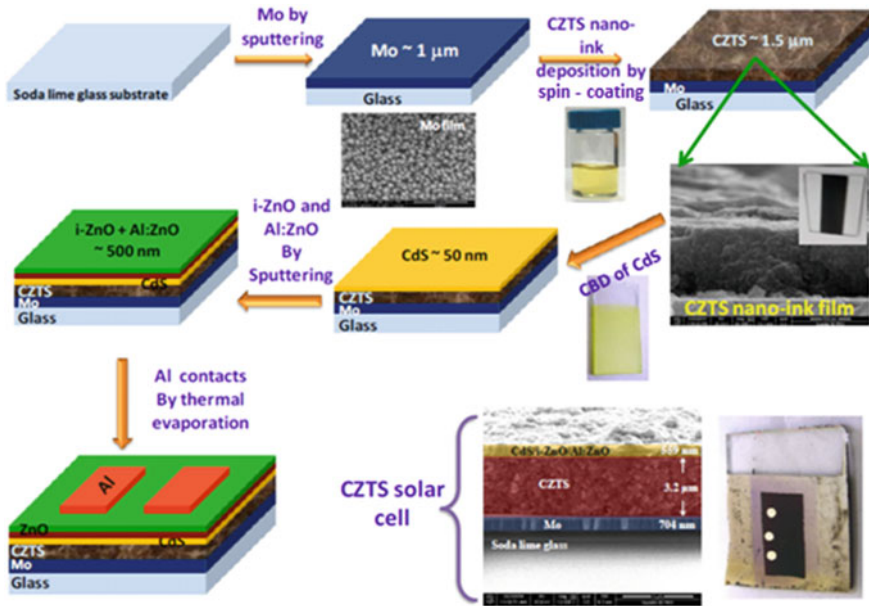
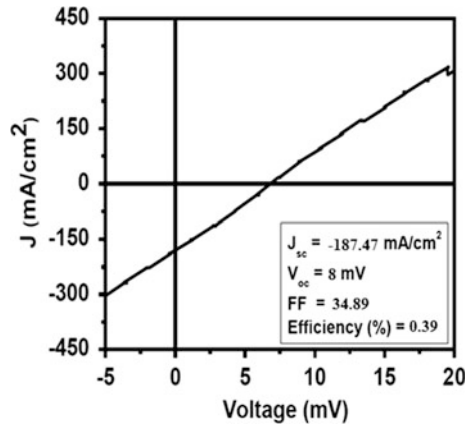


Fig. 6 CZTS solar cell preparation

Fig. 7 CZTS solar cell: device characteristics



initial device, a quantum efficiency of $\sim 0.39\%$ was achieved. Currently, the focus of work is to modify the processing conditions in order to get good interfaces between the materials, which will in turn enhance better efficiency of the solar cell.

4 Conclusion

The CZTS films prepared by solvent-based process technique from its molecular-ink using a non-toxic and ambient friendly solvent dimethyl sulfoxide (DMSO) were very uniform. They adhere to the soda-lime glass substrate and shows Kesterite CZTS phase with the bandgap 1.4 eV. CZTS solar cells show better efficiency in copper poor and zinc rich non-stoichiometric conditions. The solvent based process method of fabricating Kesterite CZTS thin films comparatively reduces the formation of secondary phases which are responsible to reduce the performance of the solar cell. In the case of CZTS, it is reported that defect density influences phonon density of states which in turn affects carrier concentration. Therefore, it becomes important to correlate basic defect physics of materials and its influence on phonon spectrum to transport properties; which may reveal the mechanism behind surge in efficiency under non-stoichiometric conditions [5, 7].

References

1. Nelson, J.: The Physics of Solar Cells. Imperial College Press, UK (2003)
2. Guo, Q., Hillhouse, H.W., Agarwal, R.: Synthesis of $\text{Cu}_2\text{ZnSnS}_4$ nanocrystal ink and its use for solar cells. *J. Am. Chem. Soc.* **131**, 11672–11673 (2009)
3. Guo, Q., Ford, G.M., Yang, W.C., Walker, B.C., Stach, E.A., Hillhouse, H.W., Agarwal, R.: Fabrication of 7.2% efficient CZTSSe solar cells using CZTS nanocrystals. *J. Am. Chem. Soc.* **132**, 17384–17386 (2010)
4. Miskin, C.K., Yang, W.-C., Hages, C.J., Carter, N.J., Joglekar, C.S., Stach, E.A., Agarwal, R.: 9.0% efficient $\text{Cu}_2\text{ZnSn}(\text{S},\text{Se})_4$ solar cells from selenized nanoparticle inks. *Prog. Photovolt Res. Appl.* 2472 (2014)
5. Kumar Samji, S., Tiwari, B., Krishna Surendra, M., Ramachandra Rao, M.S., Light induced phase change in $\text{Cu}_{2-x}\text{Zn}_{1.3}\text{SnS}_4$ thin films. *Appl. Phys. Lett.* **104**, 152106 (2014)
6. Xin, H., Katahara, J.K., Braly, I.L., Hillhouse, H.W.: 8% efficient $\text{Cu}_2\text{ZnSn}(\text{S}, \text{Se})_4$ solar cells from redox equilibrated simple precursors in DMSO. *Adv. Energy Mater.* 1301823 (2014)
7. Singh, S., Kumar Samji, S., Ramachandra Rao, M.S.: Synthesis and characterisation of CuInGaS_2 nano-ink for photovoltaic applications. *J. Exp. Nanosci* **8**, 320–325 (2012)

Formula SAE Power Increment



Jasjeev Singh, M. V. N. Sankaram, Vishal Naranje
and Sachin Salunkhe

Abstract In today’s world, every automobile enthusiast and someone who is passionate about motorsports can’t fulfill their dreams but with the introduction to this project every enthusiast can be a part of the motorsports world and experience it at budget cost. This Project helps to understand the designing of an air intake for a single-cylinder Kawasaki KX450F and improve the power-related factors for better performance and efficiency.

Keywords Automobile · Motorsports · Power · Design

1 Introduction

Formula SAE (FSAE) is a student collegiate design series committed to the configuration and development of open-wheeled race cars. We are going to be looking into specific areas. Although lot of teams use four-cylinder engines from a motorcycle limited to a four-stroke not exceeding a displacement 610 cc. These engines will have high power output and reliability but more complex in terms of intake and exhaust design, unnecessary maintenance, and servicing. The preferred choice would be a single-cylinder four-stroke with fewer injectors, spark plugs,

J. Singh · M. V. N. Sankaram
Department of Mechanical Engineering Dubai Campus UAE,
Birla Institute of Technology, Pilani, India
e-mail: sankaram@dubai.bits-pilani.ac.in

S. Salunkhe
Department of Mechanical Engineering, Vel Tech-Technical University,
Chennai, Tamil Nadu, India
e-mail: kashid32@gmail.com

V. Naranje (✉)
Department of Mechanical Engineering, Amity University Dubai Campus,
Dubai, United Arab Emirates
e-mail: vnaranje@gmail.com

overall less maintenance. It turns out to be more efficient. According to the rules, a restrictor of 19 or 20 mm has to be used based on the fuel type of the engine [1]. With single-cylinder Formula SAE engines, the shape, format, size, and orientation of intake manifolds change. Every group utilizes diverse runner lengths, plenum volumes, and restrictor outlines, and so on for their intake manifold alongside distinctive exhaust setups, which don't take into consideration direct correlations. While the ideas of intake manifolds shift, the restrictor execution is a critical thought for any intake setup. Every diffuser angle and intake design was reenacted utilizing industry standard motor reproduction programming given by Ricardo. Ricardo WAVE was initially used to show the intake system in a full engine replica. The WAVE recreations displayed a 450 cc single-cylinder Kawasaki KX450F engine over the whole RPM range, while the coupled models were kept running at one or a couple RPM points, because of the much higher computational expense.

The coupled model recreates the intake system using the computational fluid dynamics (CFD) code coupled to whatever remains of engine model simulated with ANSYS. In this manner, in the coupled model, the intake system is spoken to in 3-D, rather than 1-D. An IC motor requires appropriate air-fuel ratio to fill in according to its outline [2]. Factory outlined intake of 43 mm has been confined to 20 mm. At the point when engine is running at low rpm of around 3000 rpm, the required mass stream rate is remunerated by expansion in speed of air through the pressure. Be that as it may, FSAE engines need to rev most extreme time at high rpm of around 7000–11,000 rpm [3]. At such high speeds, engine requires considerably more air for burning and in this manner mass flow rate ought to increment, yet because of restrictor region being less air need to go with high speed to compensate or fill the engine with required mass of air. Along these lines, air tries to accomplish most extreme speed through restrictor which offers ascend to basic

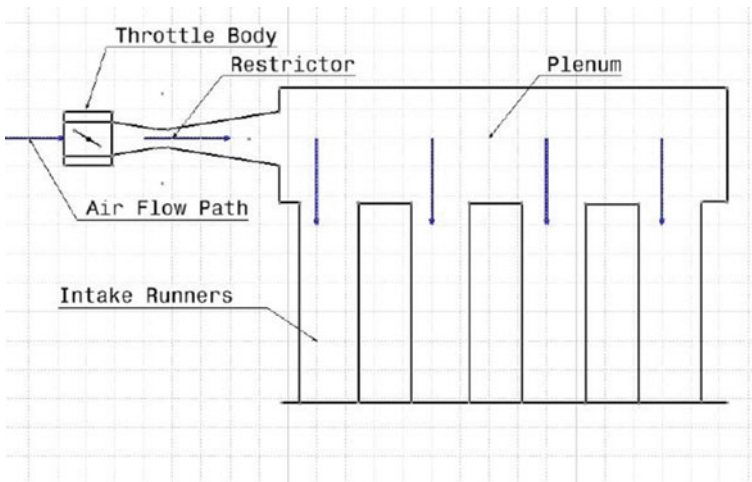


Fig. 1 Complete setup

stream conditions, where in air achieves its greatest velocity of Mach 1 at the restrictor [4]. Along these lines, mass flow rate is altered parameter for 20 mm restrictor, which is used for designing further for improvement of pressure. Presently as indicated by expressed goal to permit most extreme conceivable mass stream from pressure with least weight distinction, we work here onwards with diminishing pressure drop and making engine adequately breathe in air with least pull. The complete setup of of the intek system is shown in Fig. 1.

2 Design Considerations

Conform to FSAE regulations: The main restrictions on the air intake manifold are that it has to have a 20 mm restrictor and no throttling downstream of the restrictor.

- Fits into the current chassis of the car: The air intake manifold must fit into the current chassis without obstructing other main components of the car. If any fuel lines extend beyond the current shield, there must be an addition of extra shielding per FSAE regulations.
- Improve the performance: Custom intake should give the desired for the performance and as well as the efficiency ratio to get the best optimum result for the dynamic events.
- Reduce the weight of the car: This is accomplished by material selection and the size and geometry of the air intake manifold.

3 Restrictor Selection

There are two ways in which the restrictor can be designed either airflow through an orifice or converging, diverging nozzle. The coefficient of discharge is found to be 0.60 for orifice compared to 0.975 for nozzle. Figure 2 shows the orifice plate and venturi meter used for measurement of discharge of fluid.

Clearly, the best choice is nozzle as we require high efficiency. This device will have throat diameter of 20 mm as per rules of the competition. As per basic calculation of throttle body for a single-cylinder 450 cc engine, it is found to be 43 mm.

3.1 *Cylinders and Block Heads*

Intake valves help in the compression of the gasoline and air as a blend when the rich air runs through the entire custom intake. The airflow is terminated at the cylinder during the intake stroke [5]. The cylinder pressure increases during the

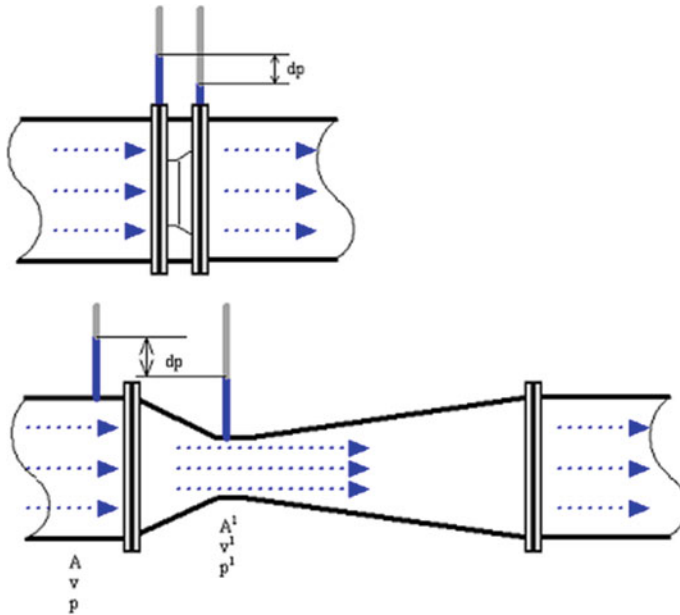


Fig. 2 Orifice and nozzle [7]

compression stroke and when the air-fuel mixture reaches maximum pressure, spark is introduced.

In this section, scrutinizing the design of the Kawasaki KX450F engine is being done, engine dimensions are recorded including bore size, stroke, and connecting rod length. Using this data, a working model of the engine is created in Ricardo is shown in Fig. 3. Ricardo helps replicate the working of the engine. Table 1 shows the dimensions of different parts of intake, using Ricardo software, We can also perform various engine simulations and analysis of the intake system.

3.2 Valve Lifts

The KX450F engine is designed with a double overhead camshaft (DOHC), which gives four valves per cylinder where two of them are divided for intake and exhaust. The valves are placed far apart from each other because of the size of the cylinder bore, this requires a rocker design to open a set of valves. Also, the cylinder incorporates a total of four valves, two for the intake, and two for the exhaust [6]. The two intake valves square measure considerably larger, for the explanation that the oxygen-bearing air has to enter the cylinder quicker, as compared to removing the exhaust gases. Within the exhaust stroke, the exhaust gases within the cylinder, pressurized once the combustion method creates an outsized pressure gradient

across the exhaust valves, permitting a quicker flow [7]. Relatively, the pressure distinction across the intake valves is lower, between the air pressure within the manifold, and therefore the suction pressure of the falling cylinder. To compensate, the valve has got to be larger, serving to in up the volumetric efficiency of the engine.

4 Plenum Selection

4.1 Spherical

The restrictor is set in line with the round plenum; the runner is additionally put inline which is helpful to the performance of the restrictor. This gives uniform pressure pulses at the throat and even VOLEF (volumetric efficiency). Having a taper angle of more than 7° at the restrictor influences VOLEF at high RPM. The shape, angle, length, and situating of the plenum all effect the VOLEF curve of the engine. The unimportant necessity of physically bundling a restrictor likewise largely affects the intake manifold shape and design [8]. On account of a restricted engine, the geometry of the diffuser after the restrictor throat and the geometry of the plenum are viewed as vital for pressure restoration. Restricting the adjustment in plenum volume is vital as that will have some impact on the intake manifold performance and the overall engine VOLEF. When all is said and done, an expansion in volume after the restrictor throat will frequently tend to increment VOLEF high in the RPM band. Restricting the adjustment in plenum volume is vital as that will have some impact on the intake system performance and the overall engine VOLEF.

Orif1 represents the restrictor which diverges into 65 mm (duct2) maintaining taper angle below 7° . Yjun1 shows the spherical plenum of diameter 150 mm. Many sizes were tried (250, 200 mm), the best possible airflow resulted through 150 mm. Runner length of 100 mm and diameter of 40 mm with taper of 6.840 is shown in Fig. 4. Results showing when plenum is spherical shape.

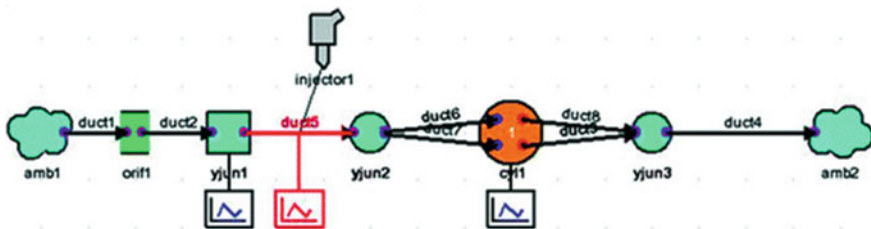


Fig. 3 Ricardo canvas showing entire engine model

Table 1 Dimensions of different parts of intake

SR	Left diameter (mm)	Right diameter (mm)	Length (mm)
Duct1	43	20	100
Duct2	20	65	200
Yjun1	175		
Duct5	175	175	125
Yjun2	40		
Duct6, duct7	40	40	10

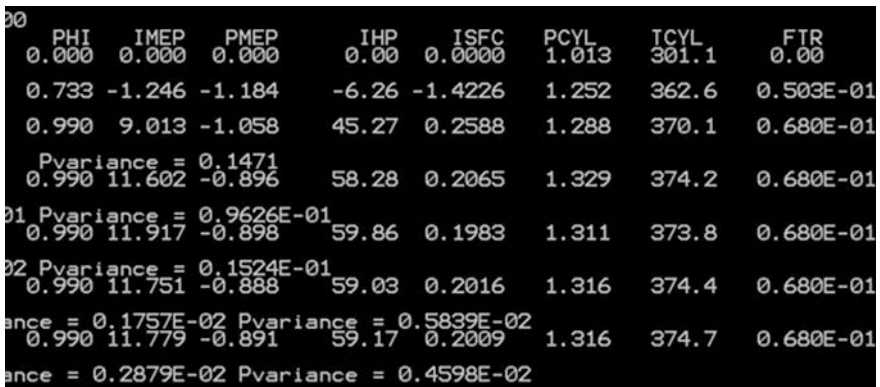


Fig. 4 Results showing when plenum is spherical shape

4.2 Cylindrical

We have changed the plenum shape from spherical to cylinder style to further understand the parameters such as plenum length and plenum volume. The cylinder shape has constant cross-sectional area throughout its length. A cylinder of 175 mm diameter has been used with a length of 200 mm which is approximately the same volume as the sphere, it has been found volumetric efficiency as well as mass flow rate into the engine cylinder has increased, thereby increasing the output of the engine which is shown in Fig. 5.

Choosing a cylindrical shape for the plenum is the best choice showing the maximum mass airflow rate (142.5 kg/h) and peak power (64.57 hp).

	PHI	IMEP	PMEP	IHP	ISFC	PCYL	TCYL	FTR
000	0.000	0.000	0.000	0.00	0.0000	1.013	301.1	0.00
007	0.667	-1.252	-1.146	-6.29	-1.4448	1.457	376.7	0.458E-01
040	0.990	9.254	-1.152	46.49	0.2750	1.441	378.6	0.680E-01
050	Pvariance = 0.1561							
050	0.990	12.652	-1.008	63.55	0.2029	1.452	380.7	0.680E-01
070	Pvariance = 0.9372E-01							
070	0.990	12.760	-0.984	64.09	0.2024	1.460	380.9	0.680E-01
020	Pvariance = 0.2874E-01							
020	0.990	12.832	-0.992	64.46	0.2017	1.464	381.1	0.680E-01
050	Pvariance = 0.2922E-01							
050	0.990	12.855	-0.999	64.57	0.2010	1.461	381.0	0.680E-01
0130	Pvariance = 0.6695E-02							
0130	0.990	12.840	-0.994	64.50	0.2008	1.459	380.9	0.680E-01

Fig. 5 Results showing when plenum is cylindrical shape

5 Conclusion

With the help of Ricardo and SolidWorks, we are able to study the flow of air through an intake and optimize the volume of plenum and intake runners. Using Ricardo, we found the optimum solution to achieve peak horsepower and maximum volumetric efficiency is to keep laminar airflow and serve enough time for fuel/air mixture to atomize. From various simulations, it can be observed that optimum solution showed up for plenum volume of 0.019 m² having a cylindrical shape and runner length of 0.125 m. These dimensions gave the intake the best result to maximize the charge of air and fuel into the engine, satisfying one of the primary design objectives. Later, tools that are used to analyze and verify the design, specifically the SolidWorks Flow Simulation computational fluid dynamics software showed us the airflow through the restrictor. The goal was to minimize pressure loss through the restrictor device.

References

1. Claywell, M., Horkheimer, D., Stockburger, G.: Investigation of intake concepts for a formula SAE four cylinder engine Using 1D/3D (Ricardo WAVE-VECTIS) coupled modeling techniques. (2006). <https://doi.org/10.4271/2006-01-3652>
2. <http://www.hotrod.com/how-to/engine/hrdp-0704-pitstop-fuel-injector-location/>
3. <https://software.ricardo.com/products/wave>, Wave Help File: Ricardo Wave 8.0
4. Applications of the Bernoulli Equation, <http://www.efm.leeds.ac.uk/CIVE/CIVE1400/Section3/bernoulli-apps.htm>
5. Gasser, J.: Capstone Design Project Final Report Semester 2, D1 SAE Intake

6. Andre, O.Y.: Design and analysis of the intake system of a formula sae car, Master of Engineering Thesis National University of Singapore, (2012)
7. Shinde, P.A.: Research and optimization of intake restrictor for Formula SAE car engine. Int. J. Sci. Res. Publ.
8. Singhal, A., Mallika, P.: Air flow optimization via a venturi type air restrictor. WCE, London, UK (2013)

Temperature Behavior-Based Monitoring of Worm Gears Under Different Working Conditions



T. Narendiranath Babu, Dhavalkumar Patel, Devansh Tharnari and Akash Bhatt

Abstract Worm gears have a wide range of applications. Monitoring the gears is highly essential to maintain sustainable operation. Vibration, wear and sound signal analysis have been implemented in several research studies. However, it is many a times difficult to implement these techniques in practical working environments. This research aims to address the analysis on worm gears under different loading and oil level conditions using temperature signals acquired during the experimental studies. An experimental setup was developed which consists of a worm gearbox coupled with a DC motor using flange coupling and rigidly mounted on test bed. Multiple experiments were conducted for varying speeds, loads and oil levels. Temperature signals were collected for the healthy and faulty gearbox setup using J-type thermocouple. The temperature variation observed has been presented for all experimental studies. The technique can further be applied for online fault detection of worm gearbox where incorporation of other techniques solely proves unbeneficial.

Keywords Thermal analysis · Worm gears · Temperature behavior
Fault detection

1 Introduction

1.1 Literature Survey

Technological innovations are growing at an exponential rate that has never been seen before. Using thermocouples, the temperature is determined in the rotating machineries such as gears, bearings and belts. Different combinations of speed and torque require different amount of power, and transmission of power becomes

T. Narendiranath Babu (✉) · D. Patel · D. Tharnari · A. Bhatt
School of Mechanical Engineering, Vellore Institute of Technology,
Vellore 632014, Tamil Nadu, India
e-mail: narendiranathbabu.t@vit.ac.in

© Springer Nature Singapore Pte Ltd. 2019
U. Chandrasekhar et al. (eds.), *Innovative Design, Analysis and Development Practices in Aerospace and Automotive Engineering (I-DAD 2018)*, Lecture Notes in Mechanical Engineering, https://doi.org/10.1007/978-981-13-2718-6_24

crucial at this stage. Gearbox forms the base of power transmission by providing a source of rotational energy to another device. Its capabilities of speed and torque conversions and different gear ratios make it the most suitable component for transmitting power. Worm gearbox constitutes of a worm wheel and worm shaft. Its self-locking capability and high gear reduction ratio make it the most-favored device for a wide range of industrial applications like conveyer belts. Performing fault diagnosis can help the customers to save valuable time and money by detecting any faults in the gearbox at initial stages of crack development. There have been several researches done on condition monitoring of gears which includes sound and vibrational analysis. However, the application of the same in the industrial applications finds immense difficulties [1]. The implementation of temperature signals for online condition monitoring can be used easily and can be highly cost-effective [2]. There are two major types of temperature-based studies. One which uses contact type thermocouple and second which uses infrared thermography. Thermal parameters along with qualitative simulation method were used for the fault diagnosis of centrifugal compressors [3]. Friction losses, other factors with add up to energy losses, increase the temperature of the machines. Thermal energy developed in the operation of several machineries can be measured using infrared thermography (IRT), an ideal non-destructive testing (NDT) technique to highlight the temperature distribution on surfaces. In this paper, they discussed an application of this technique for condition monitoring of blower bearings, shaft and the motors in ventilation systems [4]. There are multiple gear failures including scuffing, pitting and micro pitting. They all are influenced by the change in oil temperature [5]. Thus, the measurement of oil temperatures does help in understanding the condition and behavioral aspects of worm gears.

1.2 Theoretical Background

Worm Gear. Worm gears play a major role in many applications including conveyor belts, lifts, operation of several other gears, automobile. It has many uses because of high reduction ratios that it provides. The study has selected such a gearbox, and the major application of the utilized gearbox for the research purpose is in pumping operations.

Worm gears contact points operate under sliding conditions. Thus, under high load conditions, the probability of taking faults is high including pitting, scoring, development of crack on roots and abrasive wear [5–8].

Thermocouple temperature measurement. The J-type thermocouple is utilized to measure the temperature of the oil in the gearbox. The range of the thermocouple is up to 500 °C and well above the experimental temperature range.

2 Methodology

2.1 Experimental Setup

The experimental setup was developed for the collection of temperature data for different working conditions. The setup consists of the following components. Worm gearbox with a reduction ratio of 50 and the number of worm gear teeth of 50, brushless DC motor with the specifications of 48 V, 3000 rpm, torque: 4.8–14.4 Nm, Potentiometer (Rotary, 10 K Ω) to vary the speed of the motor, contact type tachometer (Systems HTM-590) to measure the speed of the motor, contact type thermocouple to measure the oil temperature of the gearbox. The complete setup was mounted on the test bed.

The test setup was prepared, keeping in mind the research purpose. The bottom of the test bed was provided with rubber attachments to further dampen the vibrations and reduce the overall motion during the experiments. Batteries were used to run the DC motor (Fig. 1).

2.2 Experimental Procedure

The purpose of the study was to analyze the thermal behavior of the worm gearbox under different speeds, loads and oil conditions. The experiments were performed for two oil levels including the half oil level and full oil level and three load conditions including no load, 350 g load and 700 g loading condition. The speed of the motor was set at four different rpm including 1000, 1300, 1800 and 2300 rpm.

The temperature signals were noted with the help of J-type thermocouple. The temperature data collected from different experiments was exported to EXCEL and analyzed for the various working conditions.

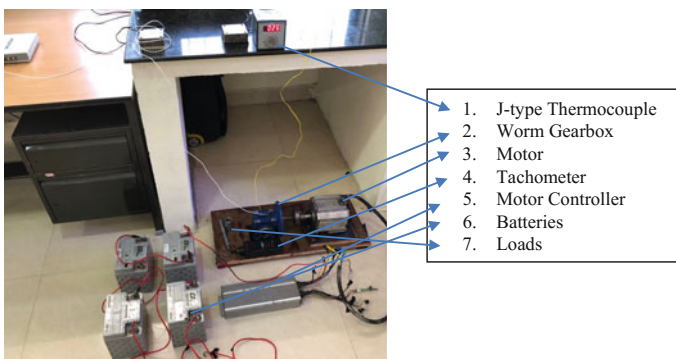


Fig. 1 Experimental setup along with marked components

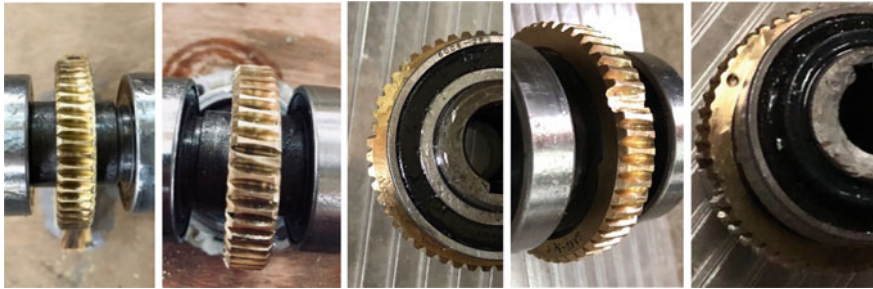


Fig. 2 Gear teeth conditions: healthy gear, material removal on one teeth, removal of half teeth, complete removal of one teeth, multiple faults with a hole

Table 1 Different working conditions

Speed variation	Full oil level	Half oil level
Set speed: 1000, 1300, 1800, 2300 rpm	Load 1: 0 g	Load 1: 0 g
	Load 2: 350 g	Load 2: 350 g
	Load 3: 700 g	Load 3: 700 g

The different working conditions analyzed are presented in the table below. There are a total of 120 sets of temperature readings. The experiments were performed multiple times. The maximum temperature observed for that set was noted. The gearbox oil temperature was allowed to reach room temperature before taking another set of readings. The longer the experiment is run the higher the temperature was noted. The time duration for running the experiment was 5 min each to obtain proper temperature readings.

The data was collected for five different states of the worm wheel including healthy gear, small material removal for one teeth, almost half gear teeth removal, complete teeth removal and hole near the hub of wheel (Fig. 2; Table 1).

3 Results and Discussion

The data collected from different experiments was analyzed using EXCEL. The graphs were generated to process the data. The different working conditions analyzed are as presented in the topics below.

3.1 Experiment 1: Healthy Gearbox

The healthy gearbox was selected for the study. The range of input speed selected was 1000, 1300, 1800 and 2300 rpm. The load conditions are no load, 350 g load

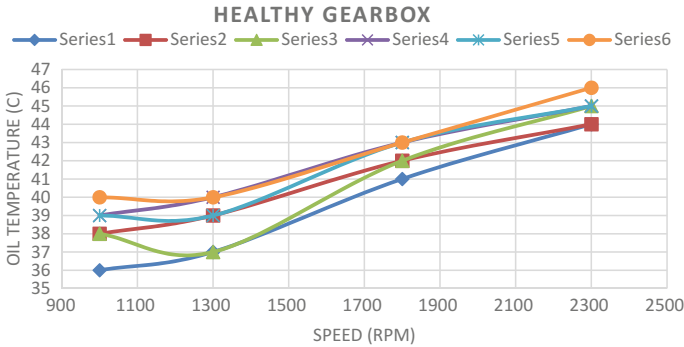


Fig. 3 Temperature variation for healthy gearbox

and 700 g load. The oil conditions for each set were varied for full oil level and half oil level.

The temperature data collected during the experiment was further utilized to understand the behavior of the worm gearbox. The graph plotted using the data is presented below. The graph presents the variation of temperature with respect to speed for six different experimental conditions. The series presented include two oil conditions and three load conditions (Fig. 3).

The series one represents the no load, full oil condition. The series two represents no load, half oil condition. The series three represents full oil level, 350 g load condition. The series four represents half oil level, 350 g load condition. The series five represents full oil level, 700 g load condition. The last series represents half oil level, 700 g load conditions.

The inference laid out from the graph is that as the speed increases the oil temperature increases roughly for most of the cases. The temperature level also increases for half oil level operating condition for all the loads. Lastly, as the load increases, so does the temperature. The variation of oil level for first series as seen from the graph is from 36 to 44 °C. Similarly, there is an increase in temperature for all other cases. The maximum temperature observed is 46 °C for the experimental condition of: 700 g, half oil level. As the load increases the temperature also increases which further reduces the viscosity of the oil and leads to an additional increase in gearbox temperature and vibration.

3.2 Experiment 2: Fault 1, Removal of Some Material of Gear Teeth

This experiment followed the same procedure as followed in the experiment one. The temperature variation observed matches to the one inferred above. The plot is presented in the graph below. The variation is, however, unique for the faulty gearbox.

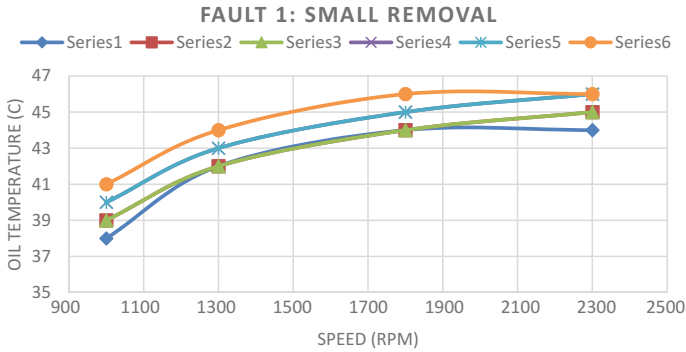


Fig. 4 Temperature variation for Fault 1

The series shown follows the same sequence as explained in the first experiment. The inference laid out from the graph is similar to the first plot. As the speed increases from 1000 to 2300 rpm, the temperature increases.

Further, the load and oil level conditions also significantly affect the thermal footprint as presented in the above graph. The fault imposed in the gear led to an increase in the oil temperature. However, the maximum temperature observed is the same but was noted at the load condition of 350 g and half oil level which is more when compared to the healthy gearbox experiment (Fig. 4).

3.3 Experiment 3: Fault 2, Removal of Half Gear Teeth

The removal of half gear teeth represents the working condition of highly stressed supplication. The operating temperature along with the vibration levels increased due to the fault induced. The variation is presented in the plot below.

The temperature increases from the base of 40 °C to the maximum of 47 °C. The increase is highly significant can mostly due to the fault induced which further creates high friction and energy losses and that leads to the increase in the oil temperature.

3.4 Experiment 4: Fault 3, One Complete Gear Teeth Removal

The fourth experiment was conducted with the removal of one complete gear teeth. The temperature variation was plotted for all the load and oil level condition. The increase in the temperature is drastic when compared to the initial experiments.

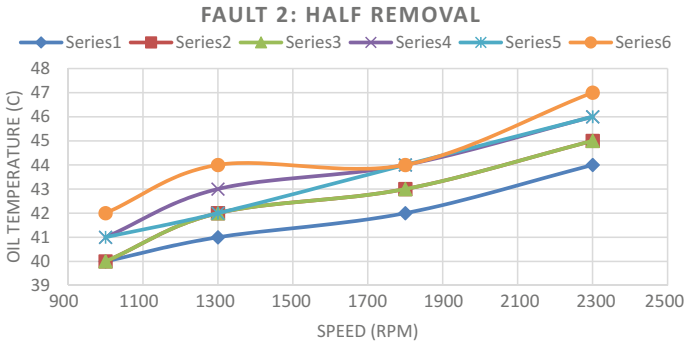


Fig. 5 Temperature variation for Fault 2

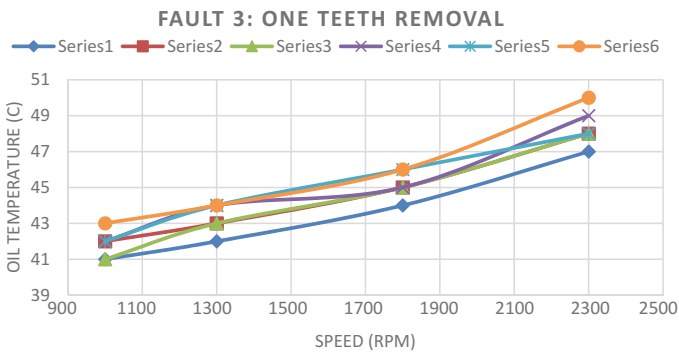


Fig. 6 Temperature variation for Fault 3

This is due to the faulty gear teeth. The vibrations for these experiments increased drastically along with the temperature signals (Figs. 5 and 6).

The maximum temperature observed was 50 °C for the final experimental condition. The temperature varies from 41 °C for no load, full oil level condition to 50° for 700 g, half oil level condition. This rise in temperature highlights the thermal behavior of the gear with condition of the gear teeth.

3.5 Experiment 5: Fault 4: Multiple Faults

This experiment includes the gearbox with multiple gear teeth faults. The temperature variation presented below shows the increase in temperature with increase in speed and other load conditions. The maximum temperature observed for this case is 51 °C. The temperature increase clearly accounts for the frictional losses due to faulty gear teeth operation (Fig. 7).

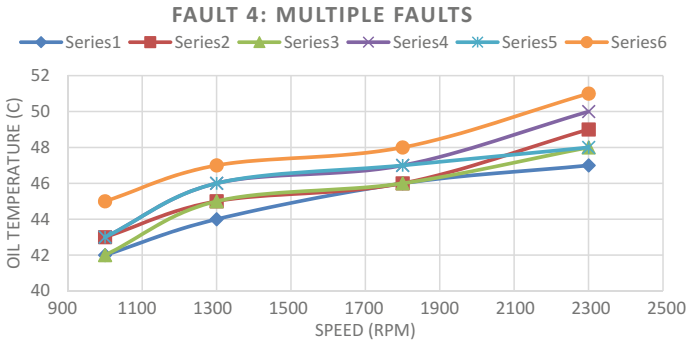


Fig. 7 Temperature behavior for Fault 4

4 Conclusion

An approach for live condition monitoring and analysis of worm gears has been presented in this study. The research tries to analyze the thermal behavior of the gearbox under different loads, speeds and oil level conditions. The experimental setup was specially developed for the research study. Various experiments were conducted with healthy and faulty gear teeth. Temperature signals were noted and plotted to understand the variation with respect to different health conditions. The results inferred from the plots presented were: Firstly, with the increase in the speed the temperature of the gearbox oil increases. Secondly, as the load increases the temperature also increases. This presents the directly proportional relation. As the load increases, the gears get more stressed and the oil thickness at mesh reduces which leads to increase in oil temperature due to contact between gears. Thirdly, as the oil level reduces the temperature increases significantly, due to low lubricating medium. And finally, as the faults increases the smooth operation of the gears diminishes and this leads to more energy being wasted as frictional losses. This further increases the oil temperature of the gearbox. This study tries to present the parameters affecting the thermal behavior of the worm gears. Due to the simplicity of this technique, it can be successfully employed for the fault diagnosis of worm gearbox under non-stationary conditions.

References

1. Touret, T., Changenet, C., Ville, F., Lalmi, M., Becquerelle, S.: On the use of temperature for online condition monitoring of geared systems—a review. *Mech. Syst. Signal Process.* **101**, 197–210 (2018)
2. Bagavathiappan, S., Lahiri, B.B., Saravanan, T., Philip, J., Jayakumar, T.: Infrared thermography for condition monitoring—a review. *Infrared Phys. Technol.* **60**, 35–55 (2013)

3. Lu, Y., Wang, F., Jia, M., Qi, Y.: Centrifugal compressor fault diagnosis based on qualitative simulation and thermal parameters. *Mech. Syst. Signal Process.* **81**, 259–273 (2016)
4. Bagavathiappan, S., Saravanan, T., George, N.P., Philip, J., Jayakumar, T., Raj, B.: Condition monitoring of exhaust system blowers using infrared thermography. *Insight-Non-Destr. Test. Cond. Monit.* **50**(9), 512–515 (2008)
5. Höhn, B.R., Michaelis, K.: Influence of oil temperature on gear failures. *Tribol. Int.* **37**(2), 103–109 (2004)
6. Elasha, F., Ruiz-Cárcel, C., Mba, D., Kiat, G., Nze, I., Yebra, G.: Pitting detection in worm gearboxes with vibration analysis. *Eng. Fail. Anal.* **42**, 366–376 (2014)
7. Waqar, T., Demetgul, M.: Thermal analysis MLP neural network based fault diagnosis on worm gears. *Measurement* **86**, 56–66 (2016)
8. Smith, J.D.: *Gears and Their Vibration: A Basic Approach to Understanding Gear Noise*. Marcel Dekker, Inc, 270 Madison Ave, New York, N. Y. 10016, 1983 170 (1983)

Production and Comparison of Fuel Properties for Various Biodiesels



D. Ravichandra, Ravi Kumar Puli and V. P. Chandramohan

Abstract The improvement of an automobile industry, growth in population and development of the world causes energy demand. At the same time, depletion of fossil fuels and increased environmental issues like the greenhouse effect and emissions from automated vehicles create a major demand for the search of alternative fuels. So, it is important to select an alternative fuel that can be obtained from vegetable oils, biodiesel, alcohol, etc., as renewable resources. Production of biodiesel from edible oil is a very good alternate, but in future food, shortage problems may occur. Due to this, non-edible vegetable oils are considered potential substitutes of edible food crops for biodiesel production. *Azadirachta indica* (neem), cottonseed, *Calophyllum inophyllum* (polanga), *Jatropha curcas* (jatropha), *Linum usitatissimum* (linseed), *Madhuca indica* (mahua), *Nicotianna tabacum* (tobacco) and *Pongamia pinnata* (karanja) are few non-edible oils. Thermophysical properties, production and characteristics of *A. indica* (neem), cottonseed and sesame oils are studied in detail in this paper. The real difficulty with an alternate fuel is that its higher viscosity value which increments concerning time, thus prompts cylinder stalling, gum formation and fuel atomization issues. Mainly this problem is resolved with the help of transesterification process. So, initially, the basic properties are estimated and tabulated in this paper. From the three different fuels such as neem oil, cottonseed feedstock and sesame oil, properties are estimated, and it is found that the values are very close to base diesel fuel.

Keywords Biodiesel · Thermophysical properties · Viscosity · Neem oil
Cottonseed oil · Sesame oil

D. Ravichandra · R. K. Puli · V. P. Chandramohan (✉)
Department of Mechanical Engineering, National Institute of Technology Warangal,
Warangal 506004, Telangana, India
e-mail: vpcm80@nitw.ac.in

© Springer Nature Singapore Pte Ltd. 2019
U. Chandrasekhar et al. (eds.), *Innovative Design, Analysis and Development
Practices in Aerospace and Automotive Engineering (I-DAD 2018)*, Lecture Notes
in Mechanical Engineering, https://doi.org/10.1007/978-981-13-2718-6_25

1 Introduction

The consumption of fossil fuel reserves and increased environmental effects have motivated the researchers for finding the alternative ways of fuels. Because of some compact and notable properties like very high cetane number, flash point and lower kinematic viscosity, pour point of biodiesel fuels (fatty acid methyl ester) from bio-oil is considered as one of the best alternative sources for the diesel and petrol fuels substitute. Indeed, the future of energy mainly depends on the sustainability and clean environment. So, many of the researchers are more concentrating on various sources of natural fuels and pure renewable sources to search for the alternate fuel. From this extensive search, it was found that biodiesels are the main alternative fuels which are used in frequent research articles for diesel engines. There are number of bio-oils used worldwide for internal combustion engines [1–6]. The production of biodiesel is categorized into lipid and alcohol feedstock. Lipid feedstock includes palm oil, rice bran oil, jatropha oil, mahua oil, cottonseed oil, rubber seed oil, rapeseed oil, sunflower oil, linseed oil, sesame oil, neem oil, etc. Especially in India, majority of the development depends on agricultural production potentials [7]. This vegetable oil production capability gives assurance alternate for petroleum (diesel oil) fuel. The selection of biodiesel depends on different variables such as the oil yield of plant seeds, availability, extraction procedures, cost per litre and local administration's support [8, 9].

Vallinayagam et al. [1] conducted the experiment with pine oil as biodiesel with different blends. The results showed that at full load condition, the virgin pine oil decreased exhaust gas emissions such as smoke emissions by 70%, HC (hydrocarbon) by 30%, CO (carbon monoxide) by 65%. It was found that the brake thermal efficiency increases by 5% and heat release rate by 27%, respectively. Mukherjee et al. [2] have analysed palm oil biodiesel in South Asian countries—Thailand, Malaysia and Indonesia. They discussed the advantages of palm oil as bio-oils and investigated about its sustainability in tough weather conditions. They also analysed the origin of palm oil and recent technologies to extract the oil with high yield. Hebbal et al. [3] investigated that performance parameters and emission characteristics of deccan hemp oil with different blends at various loads. The results concluded that 25% blend can be added without further heating and 50% blend can be added with preheating without further engine modifications. Milazzo et al. [4] reviewed the performance and prospects of soy biodiesel production on a global basis. They mentioned the new techniques which are used to increase the life cycle of biofuels. Agarwal and Das [5] have studied some of the problems associated with virgin vegetable oils in CI engine. As a result, the mixture of vegetable oil blends with diesel fuel produced better performances without substantial hardware modification. From the above literature, it was clear that before using the alternate fuel, the properties should be estimated and compared with the base mineral fuel of petroleum fuels. Therefore, the main objective of this paper is to select suitable alternate fuel based on their estimation of properties for a turbocharged diesel engine.

2 Procedure for Flash and Fire Point Estimation

Figure 1 shows the Pensky–Martens apparatus which is used to find flash and fire points of neem oil, cottonseed oil, sesame oil, etc. The first sample of oil was poured into the oil cup up to the specified marking level. Then, the thermometer and stirrer were placed on the top of the oil cup. The thermometer was used to measure the flash and fire point temperatures of sample oil. The stirrer was used to maintain the uniform temperature of the sample of oil. At a certain temperature above 60 °C, every 5–10 °C the temperature of a sample of oil was checked with fire to obtain bluish colour on the surface of the oil. If the sample of oil was continuously burning at least 5 s after ignition, then it was the fire point of the oil sample. By using the Pensky–Martens apparatus, the flash and fire points of neem oil, cottonseed oil, sesame oil were estimated, and the values are shown in Table 1.

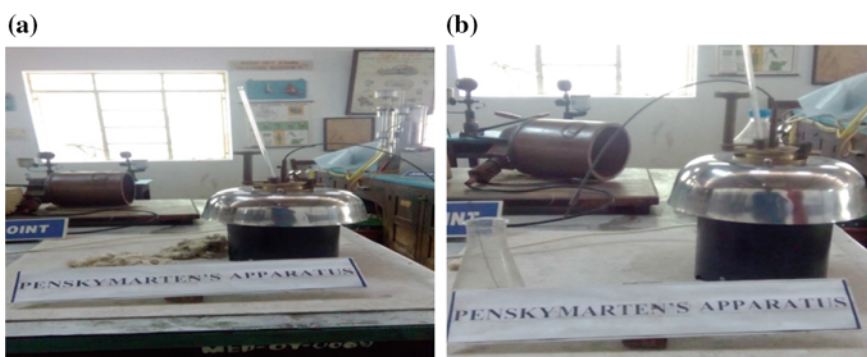


Fig. 1 a and b Pensky–Marten's apparatus

Table 1 Flash and fire points of different oils

S. No	Sample name of oil	Closed cup		Open cup	
		Flash point (°C)	Fire point (°C)	Flash point (°C)	Fire point (°C)
1	Neem oil	185	193	196	204
2	Cottonseed oil	202	215	214	221
3	Sesame oil	195	212	203	217

3 Procedure for Evaluation of Kinematic Viscosity

Measurement of a fluid's resistance to flow is called viscosity. As the temperature of a sample oil increases, the viscosity decreases because viscosity is a dominant function of temperature. Generally, biodiesel consists of higher viscous when compared to diesel fuel. Based on feedstock and oxidation amount, biodiesel viscosity varies from 4.0 and 6.2 cSt. But diesel fuel's viscosity varies from 2.4 to 2.6 cSt. Kinematic viscosity is one of the main properties of a biodiesel. The working principle is explained; initially, the cylindrical oil cup orifice was closed with a ball valve as shown in Fig. 2. The 50-ml-flask was kept below the orifice opening to collect the sample of oil, and water bath was filled with water to the specified mark. Then, pour a sample of oil in the cylindrical oil cup to the specified mark. In the setup, two thermometers were placed one in the sample of oil and another one in the water bath to measure the temperature. By using the heater, the temperature of the water bath was increased. The water bath was stirred and maintained the uniform temperature. At a particular temperature, the ball valve was lifted and collected the oil in the 50-ml-flask. Time taken to collect 50 ml sample of oil was noticed. The temperature of the sample was increased, and repeat the procedure. The estimated values for the different oils are tabulated in Table 2 at 40 °C.

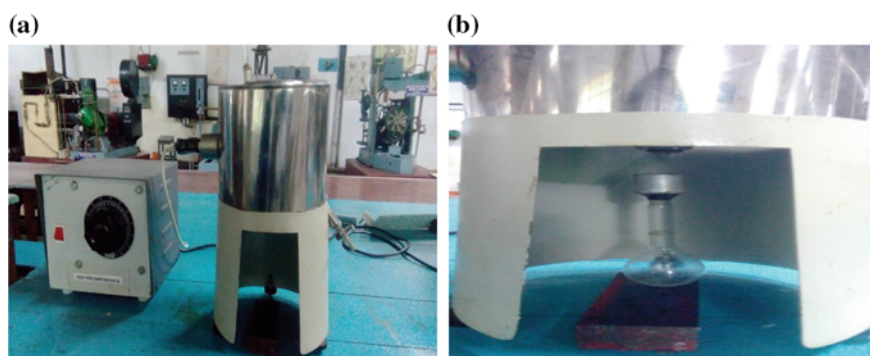


Fig. 2 a and b Redwood viscometer

Table 2 Kinematic viscosity values for different oils

S. No	Sample name of oil	Kinematic viscosity (cSt) at 40 °C
1	Neem oil	37.4
2	Cottonseed oil	44.6
3	Sesame oil	42.7

4 Operating Procedure of Bomb Calorimeter

A bomb calorimeter (Fig. 3) was used to determine the heat of combustion in oxygen in which the heat obtained from the sample of oil is contrasted, and the heat acquired from ignition of a comparable measure of benzoic corrosive whose calorific worth is known. The following procedures were used to determine the heat of combustion. Two litre distilled water was poured into a bucket up to the specified mark in the calorimeter. At this point, the calorimeter basin was placed to such an extent that the spaces on the base of the calorimeter container adjusted to the plastic pegs on the base of the calorimeter [10]. By using the weighing balance (Ohauz PAG 413, 410 g, accuracy ± 0.001 g), 1 g of sample oil was measured. After that, fuse wire of 10 cm length was taken and twisted around the bomb head through the eyelet holes. Then the sample of oil was placed into a small crucible cup. This crucible cup was placed that it should not be touched the fuse wire. The bomb head thumb screw was tightly closed. A thermometer was placed on the top surface of the bomb head to measure temperature. Bomb head was placed in cylinder, and stirrer was attached for maintaining a uniform temperature. Based on the above procedure, calorific value of sample oil was observed. The estimated values are shown in Table 3.

Table 3 Calorific values for different oils

S. No	Sample name of oil	Calorific value (MJ/kg)
1	Neem oil	41.5
2	Cottonseed oil	39.029
3	Sesame oil	35.37

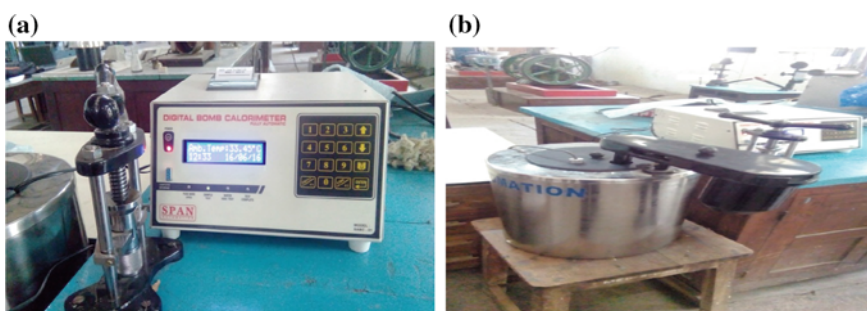


Fig. 3 Bomb calorimeter

Table 4 Density values for different oils

S. No	Sample name of oil	Density (g/cm ³)
1	Neem oil	0.912
2	Cottonseed oil	0.926
3	Sesame oil	0.947

5 Working Principle of Hydrometer

The hydrometer is used to find the density of different fuels. The hydrometer is working with the concept of Archimedes' principle that a solid suspended in a fluid due to buoyancy force. A hydrometer was inserted into the sample of oil jar slowly. After some fluctuations in the jar, the hydrometer reached to rest. The plane of the liquid surface was observed. The point at which the line cuts the hydrometer scale is the required reading. By repeating the same procedure at different temperatures for the sample of oil, the values were obtained from different oils, and it is shown in Table 4. The specific gravity was also measured with respect to the density of a substance.

6 Procedure of PH Analysis

Initially, the calibration test was performed with the water and reference solutions by using digital Elico L1 120 pH meter (Figs. 4 and 5). The 50 ml sample of oil was taken in a small flask, and an electrode was dipped into the flask. By pressing the read button, after some time, the pH meter showed the pH value (Table 5). Figures 5, 6 and 7 show the pH values of neem oil, sesame oil and cottonseed oil, respectively.

If the pH value of oil is <7 , then it is acid; if the pH value of oil is $= 7$, then it is neutral; if the pH value of oil is >7 , then it is base.

Fig. 4 pH value of water

Fig. 5 pH value of neem oil**Table 5** pH values for different oils

S. No	Sample name of oil	pH value of oil	Acid/base
1	Neem oil	4.77	Acid
2	Cottonseed oil	5.30	Acid
3	Sesame oil	3.03	Acid

Fig. 6 pH value of sesame oil**Fig. 7** pH value of cottonseed oil

7 Estimation of Acid Value of Oil

A 5 g of sample oil was taken using the weighing balance and was poured into the conical flask. 50 ml of neutralized methanol solution was added to the sample oil. The mixture of sample oil and methanol was stirred thoroughly and heated for 10 min by using the heater (Fig. 8 for neem oil and Fig. 10 for cottonseed oil). This solution was taken after 10 min and two drops of phenolphthalein indicator was added. NaOH solution of 0.1 normality in the burette was used to titrate the solution mixture and waited for the appearance of pink colour (Fig. 9 for neem oil and Fig. 11 for cottonseed oil). Based on the quantity of NaOH consumption, the free fatty acid (FFA) value of sample oil was estimated.

Fig. 8 Neem oil in heating process



Fig. 9 Titrate solution of neem oil



Fig. 10 Cottonseed oil in heating process

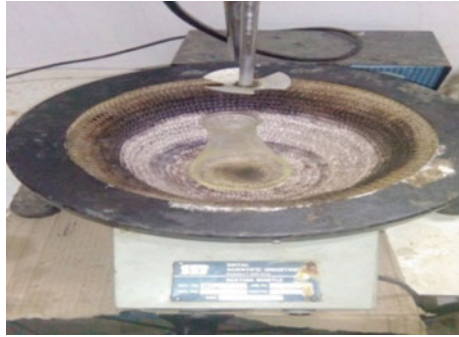
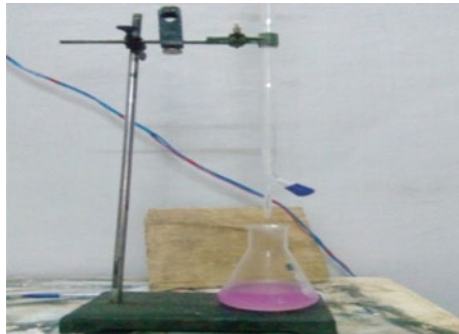


Fig. 11 Titrate solution of cottonseed oil



8 Conclusions from Different Fuel Properties

This paper studied the three different alternate fuels such as neem oil, cottonseed oil and sesame oil characteristics. Based on the above results, the following conclusions were noticed.

- The flash and fire point of biodiesel cannot be less than 93 °C and not too high. Among the three oils selected for this work, neem oil had medium flash fire points. The fuel has higher flash fire point values, then it can be stored safely and transport easily.
- As per the ASTM standards of biodiesel, the kinematic viscosity should be as low as possible. It was observed that the neem oil had less kinematic viscosity compared to other biodiesels. So, the flow of fuel atomization is proper and complete combustion may occur.
- As per the ASTM standards of biodiesel, the calorific should be high. It was noticed that the calorific values of neem oil were higher than the other two oils (cottonseed and sesame oil). Higher calorific value leads to greater brake thermal efficiency.

- The density of the diesel is 0.845 g/cm^3 , so the biodiesel value is around the diesel value.
- Cottonseed and sesame oils are having higher basic properties such as flash and fire point, kinematic viscosity, calorific value, density and pH values when compared to neem oil.
- By considering the above fuel properties, neem oil provides better properties when compared to other fuels, therefore it can be selected as an alternate fuel for better system performance and reduction of exhaust emissions.

References

1. Vallinayagam, R., Vedharaj, S., Yang, W.M., Lee, P.S., Chua, K.J.E., Chou, S.K.: Combustion performance and emission characteristics study of pine oil in a diesel engine. *Energy* **57**, 344–351 (2013)
2. Mukherjee, I., Sovacool, B.K.: Palm oil-based bio fuels and sustainability in Southeast Asia: a review of Indonesia, Malaysia and Thailand. *Renew. Sustain. Energy* **37**, 1–12 (2014)
3. Hebbal, O.D., Vijayakumar, R.K., Rajagopal, K.: Performance characteristics of a diesel engine with Deccan hemp oil. *Fuel* **85**, 2187–2194 (2006)
4. Milazzo, M.F., Spina, F., Primerano, P., Bart, J.C.J.: Soy biodiesel pathways: Global prospects. *Renew. Sustain. Energy* **26**, 579–624 (2013)
5. Agarwal, A.K., Das, L.M.: Biodiesel development and characterization for use as a fuel in compression ignition engines. *J. Eng. Gas Turbines Power* **123**, 441 (2001)
6. Agarwal, A.K.: Biofuels (alcohols and biodiesel) applications as fuels for internal combustion. *Prog. Energy Combust. Sci.* **33**, 233–271 (2007)
7. Agarwal, A.K., Dhar, A.: Comparative performance, emission, and combustion characteristics of rice-bran oil and its biodiesel in a transportation diesel engine. *J. Eng. Gas Turbines Power ASME* **132**, 064503-1 (2010)
8. Issariyakul, T., Dalai, A.K.: Biodiesel from vegetable oils. *Renew. Sustain. Energy Rev.* **31**, 446–471 (2014)
9. Igbokwe, J.O., Nwafor, O.M.I.: Performance characteristics of palm kernel biodiesel and its blend in a CI engine. *Int. J. Ambient Energy* **37**(1), 103–106 (2016)
10. Ravichandra D., Ravikumar P., Chandramohan V. P., Geo E.V.: Experimental analysis of Deccan hemp oil as a new energy feedstock for compression ignition engine. *Int. J. Ambient Energy*, 1–12. <https://doi.org/10.1080/01430750.2017.1421572> (2018)

Experimental Determination of Fluid Flow Parameters to Study Permeation Process Inside a Porous Channel



Hussain Najmi, Eddy El-Tabach, Nicolas Gascoïn,
Khaled Chetehouna and François Falempin

Abstract Porous channels are actively used in the field of transpiration cooling and fuel cell applications. Therefore, it is important to study the fluid flow inside the porous channel and different factors affecting it. In this study, fluid flow analysis is performed using four different gases such as nitrogen, carbon dioxide, methane, and helium. The effects of different inlet flowrates and feed pressures are investigated on the fluid properties. It is found that the viscous sublayer thickness is not the only parameter which governs the permeation inside the porous stainless steel tube. There are also some more parameters which should be taken into account while studying the permeation in a porous tube in addition to the boundary layer. These parameters are the velocity of the main flow, V_z (i.e., axial flow), momentum in the main flow, M_z (i.e., in axial direction), momentum in radial direction, M_y , density, ρ , and viscosity, μ .

Keywords Permeation · Regenerative cooling · Separation process
Fuel cell · Porous tube

1 Introduction

In the literature, different technologies for gas separation can be found [1, 2]. Out of all these methods, the selective permeation through a porous media has an advantage of low operational cost, small impact on environment, easy maintenance, and fast separation time compared to the others. The porous media used for selective permeation can be integrated with the fuel cell with ease; this can solve the

H. Najmi (✉) · N. Gascoïn · K. Chetehouna
INSA-CVL, University of Orléans, PRISME EA 4229, Bourges F-18022, France
e-mail: hussain.najmi@insa-cvl.fr

E. El-Tabach
University of Orléans, IUT Bourges, PRISME EA 4229, Bourges F-18020, France

F. Falempin
MBDA, 1 Avenue Réaumur, 92358 Le Plessis-Robinson Cedex, France

problem of hydrogen storage and result in the onboard hydrogen production and utilization in order to generate power. Different types of porous media are available depending upon the application.

It is found that the porous tube is used in few experimental works to study gas separation [3]. The experimental configuration used in these studies is slightly different than the one used in industrial application. In the literature study (case a), the inlet and permeate flow occur in the radial direction whereas in the industrial application (case b), the permeate flow occurs in a radial direction and the inlet flow takes place in the axial direction [1].

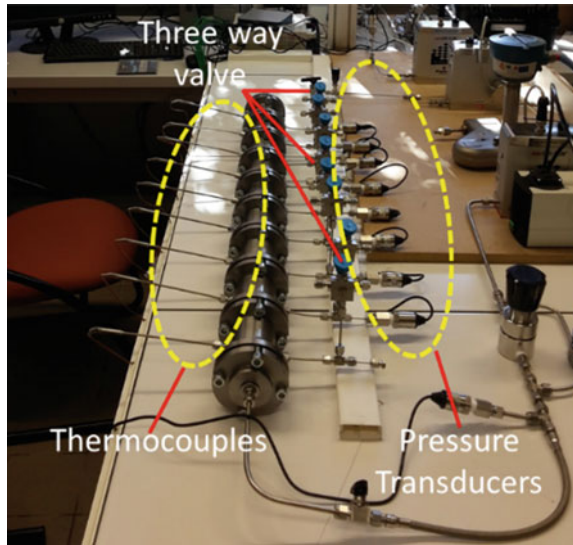
In case a, there is no change in any fluid properties when fluid flows from inlet to outlet and even the boundary layer remains absent whereas in case b, as the fluid flows toward the outlet, the density, viscosity, boundary layer thickness, and temperature vary along the length of the channel due to a decrease in the pressure and mass flowrate along the length because of continuous filtration from the porous surface. This may have a significant effect on the gas separation and should be investigated. To study the variation in fluid properties mass flowrate, pressure and temperature should be monitored along the length of the porous channel. Therefore, a new experimental test bench is developed. It can be used to study the permeability, fluid flow, and selectivity at the same time which makes it very unique. To achieve that, detailed literature study has been performed in which different types of existing experimental benches in the area of permeability [4–7], gas separation or selectivity, and filtration [8–13] have been studied.

2 Materials and Methods

The aim of the developed test bench (Fig. 1) is to determine the axial distribution of different fluid parameters inside the porous channel and the factors affecting permeation. The test bench is composed of a porous stainless steel tube (316L SS). This tube has one inlet and two outlets (one primary outlet which is divided into eight cells and one secondary outlet which is at the end of the tube). When the fluid enters the tube from one end (inlet), some amount of fluid continues into the channel and goes out through the main outlet (secondary outlet), and the rest can filtrate through porous media and go into the respective permeation cell along the length. All the eight cells are isolated from each other. Each cell has two outlets (holes), the first one for the thermocouple and the second for pressure measurement and gas sampling.

In this study, N_2 , CO_2 , CH_4 , and He are used as fluid, supplied by Air Liquide with a purity of 99.99%. The real-time monitoring of all the input parameters (mass flowrate, pressure, and temperature) and their control during the experiments is facilitated by the LabVIEW program. Three Coriolis mass flow meters are used to monitor the outflow. In addition, two mass flow controllers are placed at the inlet. Moreover, pressure transducers and thermocouples are connected to a NI data

Fig. 1 A photograph of the developed test bench



acquisition system to measure the transient variation of parameters at the inlet and outlets. More details regarding the test bench can be obtained from the previous work [1, 14].

The density is computed on the basis of measured pressure and temperature, thanks to the modified perfect gas law with the compressibility factor Z which depends notably on the critical coordinates and on Pitzer's acentric factor [5]. The dynamic viscosity is computed by Chung's method [15]. Reynolds number is determined using the relationship between density, velocity, tube diameter, and viscosity whereas velocity is calculated using a relation based on mass flowrate, density, and area [1]. The viscous sublayer thickness is determined based on the relation between velocity and kinematic viscosity [6]. Momentum of the gas particles inside the flow is calculated using the relation between density and velocity [16].

3 Results and Discussion

Using the measured experimental data (such as mass flowrate, pressure, and temperature), various fluid properties such as density, Reynolds number, viscosity are calculated for all the four gases using the equations as described in the above section. All the calculated and measured properties for nitrogen, carbon dioxide, methane, and helium are compared and tabulated in a single table in an increasing order (Table 1). This will facilitate in understanding which parameter should be considered while studying the gas separation or permeation using a particular fluid.

Table 1 Comparison of different gases on the basis of different fluid properties

<i>Measured parameters</i>	
Inlet pressure (bar)	He > CH ₄ > N ₂ > CO ₂
Pressure at primary outlet (bar)	He > CH ₄ > N ₂ > CO ₂
Total porous mass flowrate (g/s)	CH ₄ > N ₂ > CO ₂ > He
Secondary mass flowrate (g/s)	He > CO ₂ > N ₂ > CH ₄
<i>Calculated parameters</i>	
Pressure drop (inlet to secondary outlet) (bar)	CH ₄ > He > N ₂ > CO ₂
Pressure (inside the tube) (bar)	He > CH ₄ > N ₂ > CO ₂
Density in tube (kg/m ³)	CO ₂ > N ₂ > CH ₄ > He
Density of porous mass flow at primary outlets (kg/m ³)	CO ₂ > N ₂ > CH ₄ > He
Viscosity, μ (Pa·s)	He > N ₂ > CO ₂ > CH ₄
Reynolds number	CH ₄ > CO ₂ > N ₂ > He
Viscous sublayer thickness (m)	He > N ₂ > CO ₂ > CH ₄
Momentum in axial direction, M_z (kg/m·s ²)	He > CH ₄ > N ₂ > CO ₂
Momentum in radial direction, M_y (kg/m·s ²)	He > CH ₄ > N ₂ > CO ₂
Axial velocity or main flow velocity (V_z) (m/s)	He > CH ₄ > N ₂ > CO ₂

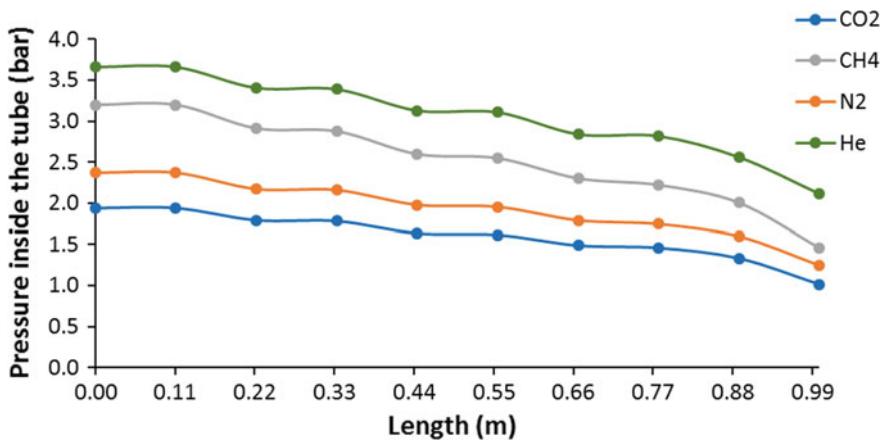


Fig. 2 Pressure profile along the axial direction for different gases

The comparison between different gases for all the fluid properties (measured or calculated) is carried out at the same inlet mass flowrate (1 g/s). It can be seen from Table 1 that viscosity is greatest for helium and smallest for methane for same inlet mass flowrates whereas Reynolds number is greatest for methane and smallest for helium because the Reynolds number is inversely proportional to the viscosity. Hence, it can be concluded that even the Reynolds number is directly proportional to the density and velocity, but it is mostly governed by viscosity in case of a

porous stainless steel tube. The viscous sublayer thickness follows the same trend as of viscosity. It can also be seen from Table 1 that pressure is not the only the factor which governs the filtration or permeation through the porous media because pressure inside the main flow is the highest in case of helium (Fig. 2), but the porous flow is the smallest (Fig. 3).

The viscous sublayer thickness is the smallest in case of methane (Fig. 4) and the corresponding porous flowrate is maximum. It is basically due to the momentum in radial direction (M_y) (Fig. 5) which is almost five times higher compared to the nitrogen and carbon dioxide cases.

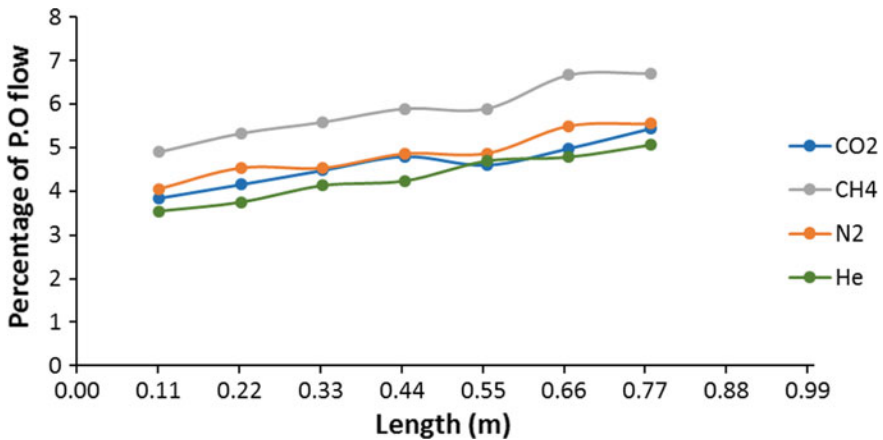


Fig. 3 Percentage of primary outlet flow along the porous tube for different gases

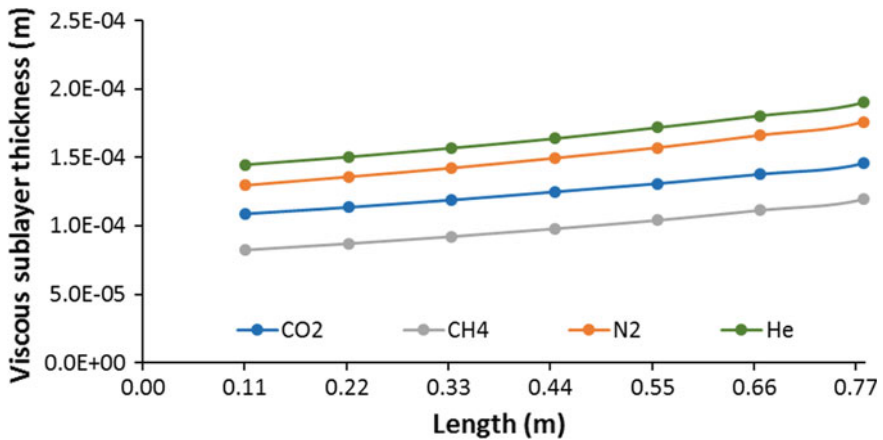


Fig. 4 Evolution of viscous sublayer along the axial direction for different gases

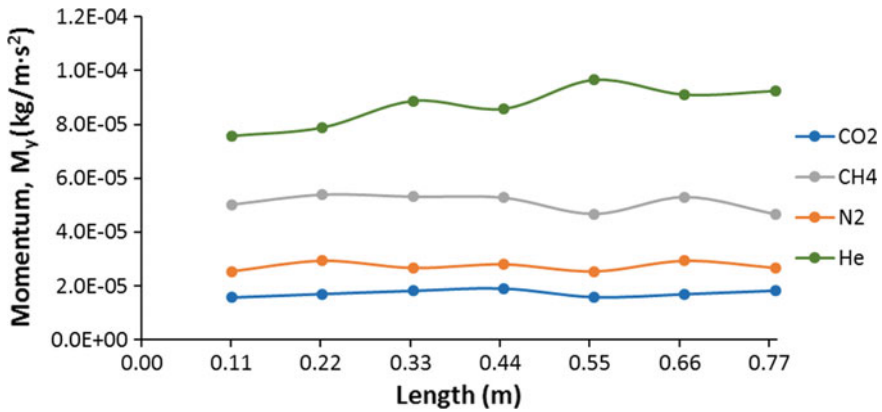


Fig. 5 Momentum of gas particles in radial direction (M_y) for different gases

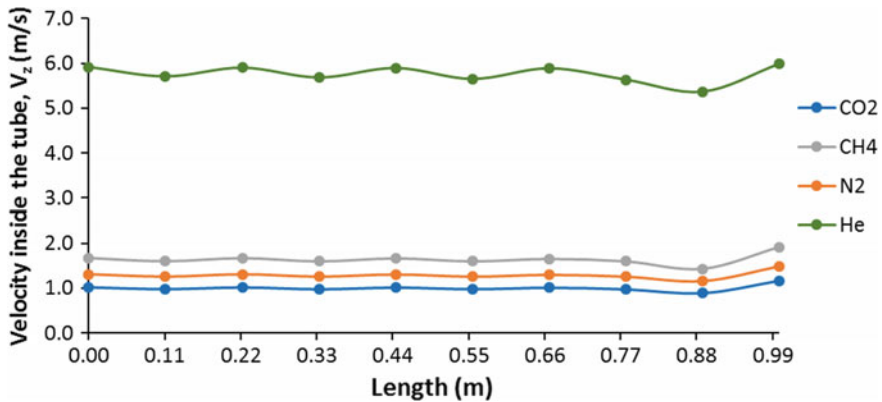


Fig. 6 Velocity profile along the axial direction for different gases

In case of helium, momentum in radial direction (M_y), viscous sublayer thickness, and pressure inside the tube (P_z) all are higher compared to all other gases, but still the permeate flow is the least. It is due to the velocity in axial direction which is very high and almost five times higher than that of nitrogen, carbon dioxide, and methane for the same inlet mass flowrate (Fig. 6). This does not allow the gas particles enough time to permeate and results in a lesser permeate flow. The velocity is inversely proportional to the density. As density of helium is very small due to the small molecular mass compared to other gases, it results in very high velocity.

Therefore, it cannot be said that one parameter is responsible for the permeate flow. It is an interaction between a number of fluid parameters that govern the fluid flow inside the porous tube. However, the increase in permeate flow along the axial

direction is definitely due to the viscous sublayer thickness [1]. It can also be concluded from Figs. 3 and 6 that there is a balance between the porous flow and the main flow. If the main flow speed is high, then the throughflow is more limited. Again, this can be seen as a “flow resistance” which is higher in the radial direction than in the axial and consequently the permeation is limited.

The fluid flow analysis for different fluids helps in identifying the fluid parameters that should be looked upon while studying the fluid flow inside the porous channel. It should be noted that the fluid flow is governed by a number of parameters which are acting together and driving the flow.

4 Conclusion

Fluid flow analysis is performed using nitrogen, carbon dioxide, methane, and helium, and various fluid properties are determined using the measured experimental data. The comparisons have been made between all the studied gases. The potential parameters that can affect the permeation process inside the porous stainless steel tube are velocity of the main flow, V_z (i.e. axial flow), momentum in the main flow, M_z (i.e., in axial direction), momentum in the radial direction, M_y , density, ρ , and viscosity, μ . The permeation process inside the porous tube does not only depend upon the inlet pressure. The variation in fluid properties changes the physics of permeation and can be used for gas separation purpose if implied effectively. In the future work, different types of mixtures such as He/CH₄ and CH₄/CO₂ will be considered for the fluid flow analysis inside the porous tube.

References

1. Najmi, H., El-Tabach, E., Gascoïn, N., Chetehouna, K., Lamoot, L.: Falempin, F: Fluid flow analysis to describe the permeation process along the length of the porous tube. *Int. J. Hydrogen Energy* **42**, 25531–25543 (2017)
2. Wang, M., Lawal, A., Stephenson, P., Sidders, J.: Ramshaw, C: Post-combustion CO₂ capture with chemical absorption: a state-of-the-art review. *Chem. Eng. Res. Des.* **89**, 1609–1624 (2011)
3. Pangrle, B., Alexandrou, N., Dixon, G., Dibiasio, D.: An analysis of laminar fluid flow in porous tube and shell systems. *Chem. Eng. Sci.* **46**, 2847–2855 (1991)
4. Gascoïn, N., Fau, G., Gillard, P., Kuhn, M., Bouchez, M., Steelant, J.: Comparison of two permeation test benches and of two determination methods for Darcy’s and Forchheimer’s permeabilities. *J. Porous Media* **15**, 705–720 (2012)
5. Gascoïn, N.: High temperature and pressure reactive flows through porous media. *Int. J. Multiph. Flow* **37**, 24–35 (2011)
6. Najmi, H., El-Tabach, E., Chetehouna, K., Gascoïn, N., Akridiss, S., Falempin, F.: Flow Configuration Influence on Darcian and Forchheimer Permeabilities Determination. *Springer Lecture Notes Mech. Eng. ‘IDAD’*, pp. 87–94 (2017)

7. Najmi, H., El-Tabach, E., Chetehouna, K., Gascoin, N., Falempin, F.: Effect of flow configuration on Darcian and Forchheimer permeabilities determination in a porous composite tube. *Int. J. Hydrogen Energy* **41**, 316–323 (2015)
8. Barreiro, M., Maroño, M., Sánchez, J.: Hydrogen permeation through a Pd-based membrane and RWGS conversion in H_2/CO_2 , $H_2/N_2/CO_2$ and $H_2/H_2O/CO_2$ mixtures. *Int. J. Hydrogen Energy* **39**, 4710–4716 (2014)
9. Miyajima, K., Eda, T., Nair, B., Iwamoto, Y.: Organic–inorganic layered membrane for selective hydrogen permeation together with dehydration. *J. Memb. Sci.* **421**, 124–130 (2012)
10. Chen, W., Hsu, P.: Hydrogen permeation measurements of Pd and Pd-Cu membranes using dynamic pressure difference method. *Int. J. Hydrogen Energy* **36**, 9355–9366 (2011)
11. Shamsabadi, A., Kargari, A., Babaheidari, M., Laki, S., Ajami, H.: Role of critical concentration of PEI in NMP solutions on gas permeation characteristics of PEI gas. *J. Ind. Eng. Chem.* **19**, 677–685 (2013)
12. Chi, Y., Yen, P., Jeng, M., Ko, S., Lee, T.: Preparation of thin Pd membrane on porous stainless steel tubes modified by a two-step method. *Int. J. Hydrogen Energy* **35**, 6303–6310 (2010)
13. Chen, W., Chi, I.: Transient dynamic of hydrogen permeation through a palladium membrane. *Int. J. Hydrogen Energy* **34**, 2440–2448 (2009)
14. Najmi, H., El-Tabach, E., Gascoin, N., Chetehouna, K., Lamoot L., Falempin, F.: Permselectivity bench to study permation along porous tube. In: 21st AIAA International Space Planes and Hypersonics Technologies Conference, Xiamen, China (2017)
15. Poling, B., Prausnitz, J., O’Connell, S.: The properties of gases and liquids. McGraw-Hill Prof (2001). ISBN-13: 063-9785322160
16. Arakeri, J.: Bernoulli’s equation, *Resonance*. **5**, 54–71 (2000)

Diesel Engine Cylinder Head Port Design for Armored Fighting Vehicles: Compromise and Design Features



Hari Viswanath, A. Kumarasamy and P. Sivakumar

Abstract The cylinder head of diesel engines for armored fighting vehicles (AFVs) should be compact and lightweight and has to operate under severe loading conditions. The cylinder head of a direct-injection (DI) diesel engine has to admit charge to the cylinder and expel the exhaust gas with minimum pumping losses, with required swirl and other properties of charge motion. It must also provide features like mounting of injector, sealing of combustion gases, and maintaining acceptable temperature of the components. The cylinder head is therefore a critical and a complex component in AFV diesel engines. This paper discusses the layout options of intake port and design features that can be applied to the cylinder head of four-stroke direct-injection diesel engines for AFVs. The head layouts followed here can provide more opportunities in positioning of ports and enhance other attributes of the design. The optimized configuration results in improved swirl characteristics, reduced volume and weight along with better cooling with the intake port-generating swirl in two modes, i.e., the directed mode and the helical mode.

Keywords Helical intake port · Swirl number · Paddle wheel test rig

Abbreviations

a	Sonic velocity at inlet manifold conditions (m/s)
A	Area of valve inner seat (m^2)
B	Cylinder bore (mm)
C_D	Discharge coefficient
C_F	Flow coefficient
CFD	Computational fluid dynamics
D	Valve inner seat diameter (mm)
L	Valve lift (mm)
MFC	Mean flow coefficient
MRSR	Mean rig swirl ratio

H. Viswanath (✉) · A. Kumarasamy · P. Sivakumar
CVRDE, Defence Research & Development Organisation, Chennai, India
e-mail: hariviswanath@cvrde.drdo.in

© Springer Nature Singapore Pte Ltd. 2019
U. Chandrasekhar et al. (eds.), *Innovative Design, Analysis and Development Practices in Aerospace and Automotive Engineering (I-DAD 2018)*, Lecture Notes in Mechanical Engineering, https://doi.org/10.1007/978-981-13-2718-6_27

N_R	Non-dimensional rig swirl
Q	Volume flow at port entry conditions (m^3/s)
S	Engine stroke (mm)
V_O	Velocity (m/s)
W_C	Charge swirl speed at IVC (rpm)
W_E	Engine crank shaft speed (rpm)
W_R	Swirl meter vane speed (rpm)
Z	Gulp factor
α_1	Crank angle, IVC (degree CA)
α_2	Crank angle, IVC (degree CA)
∂p	Total pressure drop over port
ρ	Air density (kg/m^3)

1 Introduction

This paper gives an overview of cylinder head configuration and port development for a direct-injection diesel engine for AFVs through parametric port design. The specifications of the engine are given in Table 1.

After designing the cylinder head with an expected swirl and flow parameters, a metallic flow box was prepared. Swirl number is evaluated in steady-state swirl test rig (paddle wheel) for MRSR, MFC, and Z .

Before considering the port layout, it is first necessary to estimate the swirl requirement of the engine under consideration. For the development of 1500-hp diesel engine for AFVs, the above targets were fixed as MRSR—1.5, MFC—0.3, and $Z < 0.6$. By this route, development time, cost, and number of iterative trials are reduced to a greater extent.

Swirl is an organized rotation of charge about the cylinder axis. It is created by the charge with initial angular momentum. Usually, decay in swirl occurs due to

Table 1 Engine specifications

Parameter	Description
Type	Four stroke, V 90, direct injection, turbocharged, charge air cooled, diesel engine
Rated power	1500 hp @ 2600 rpm
Bore \times Stroke(mm \times mm)	138 \times 145
Displacement (liters)	26
No of intake valves per cylinder	2
No of exhaust valves per cylinder	2
Connecting rod length (mm)	261
Max valve lift, intake (mm)	13
Max valve lift, exhaust (mm)	13
Compression ratio	14:1

friction during the engine cycle, but with intake-generated swirl it persists through the compression and combustion processes. Swirl promotes rapid and intimate mixing between inducted air charge and the injected fuel. In developing swirl-supported DI diesel engines for AFVs, it has been a general experience that difference in performance parameters like power and fuel consumption may be obtained using different intake port designs with identical swirl numbers on stationary flow test rig where the MFC and Z do vary and influence overall engine performance.

Application of CFD techniques can give global as well as local information on intake port design; this approach has proved to be efficient and is now applied widely [1].

2 Engine Breathing Demands and the Effect of Swirl

The flow capacity of inlet ports and valves is a key factor in determining volumetric efficiency of the engine. The size of inlet valve determines whether the gas speed will achieve optimum performance up to the desired output speed. Studies were carried out and established that inlet valve position and port layout are major aspects of the design schemes and therefore need to be considered during the concept design. Care must be taken to meet the conflicting requirements of various functions of the cylinder head [2]. Research on port shows that development of successful inlet port configuration remains an iterative process, and the final design is often a compromise between performance and packaging [2]. In general, there are two basic port designs in use, helical port and tangential port. The difference between helical port and tangential port is that the swirl generated above the inlet valve within the port for helical port while with tangential port the swirl is formed by directing the entering airstream against the cylinder wall. Helical ports offer some advantages which may be decisive for the overall performance of DI engines [3]. The swirl generation process in helical intake ports is shown in Fig. 1. Normally helical ports offer higher mass flow coefficient than tangential ports for the same swirl number. But there are practical limitations for the same, like during the casting of cylinder head, core shift or slight port displacement is often a problem. Because of this, combustion quality deteriorates due to changes in swirl level. However, helical ports should be designed in such a way that they are less sensitive to port displacement. Optimum matching of injection system over a wide speed range is generally easier with helical ports. However, for optimum engine performance, the combination of tangential and helical port is preferred. Hence, in this engine development, combination of tangential and helical port is considered. Prediction of swirl level in the design stage within $\pm 10\%$ is possible. An overview of the intake port development process is shown in Fig. 2.

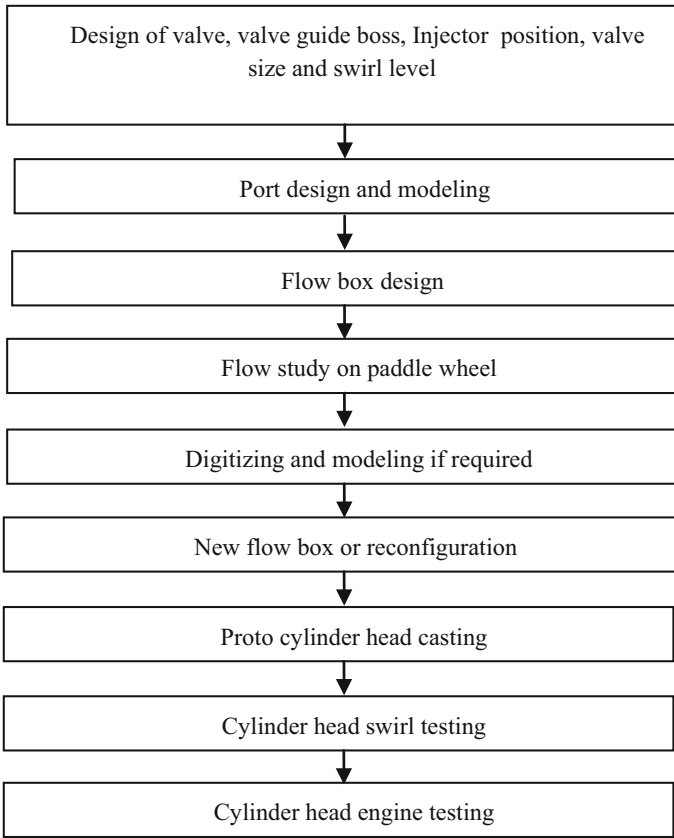
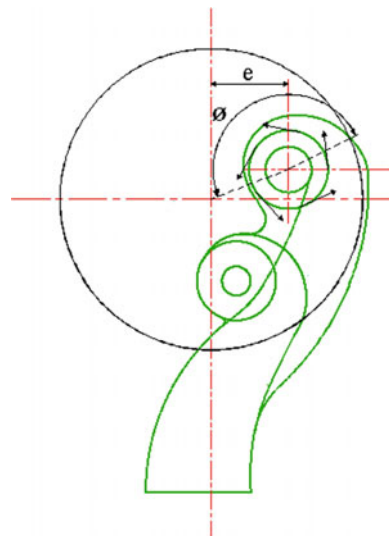


Fig. 1 Swirl generation in helical intake ports

Fig. 2 Intake port development process



3 Layout Study

One of the important constraints in the design of the cylinder head is the location of bolt pattern. This has an important implication for port and camshaft positions, as well as cooling passages and structural integrity of the cylinder head. Here, four-bolt pattern is chosen which has given great scope in port design. With four bolts per cylinder, the bolt loads are distributed uniformly into the cylinder head bottom deck. This is realized by internal ribs and making cylinder head structure sufficiently stiffer to avoid excessive distortion.

Port layout is shown in Fig. 3. Skewed valve arrangement is chosen so that it can provide large room for port configuration and at the same time will occupy lesser volume and weight, which is the driving factor in AFV diesel engine design.

The basic port is defined to describe the overall port geometry. Port design parameters are selected from the literature survey and refined through 3D design. A large inner seat diameter together with average port quality provides good breathing characteristics. The port design is constrained by the boundary condition such as cylinder head bolts, injector, water jackets and without flow separation of the charge air. This was achieved by reducing the cross-sectional areas of the port along the main flow direction and radii of curvature. A cylinder head assembly with the helical intake and exhaust ports is shown in Fig. 4. A detailed layout study is carried out by positioning the valve, injector, and coolant area around the injector and valve as shown in Figs. 4 and 5.

Care was taken during port design to reduce pressure drop in the valve ports and also to achieve a suitable intake port shape to produce intake swirl. The transitional cone between valve seat and bottom of the cylinder head forms a short diffuser after the smallest flow area and exit; port should be made wider in this area. For the

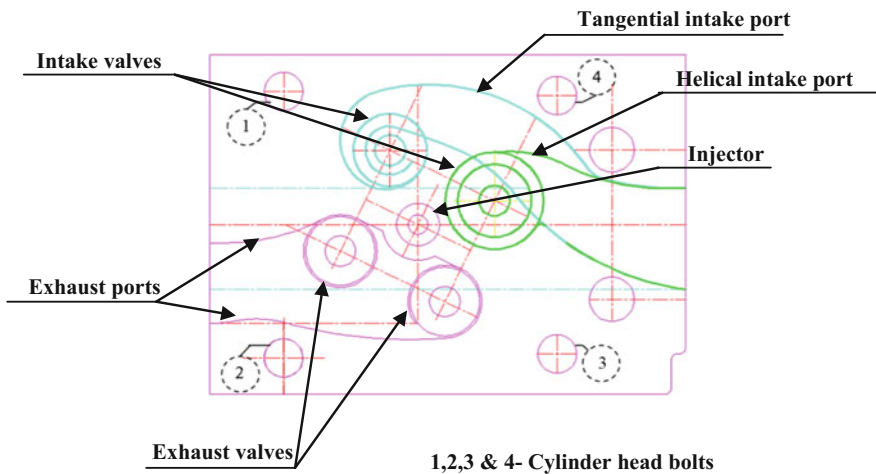


Fig. 3 Cylinder head with ports

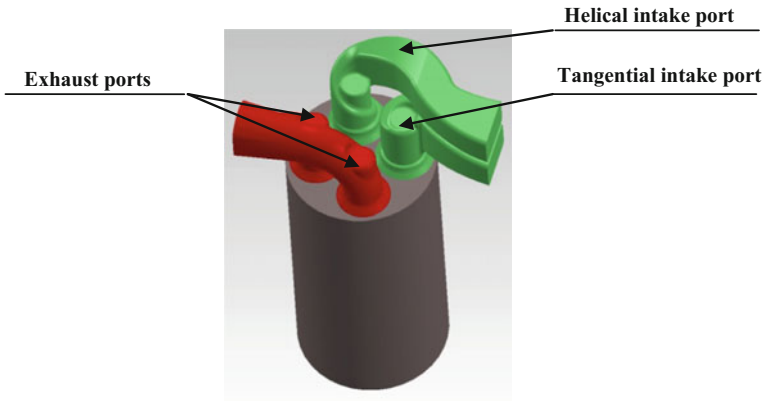


Fig. 4 3D port layout

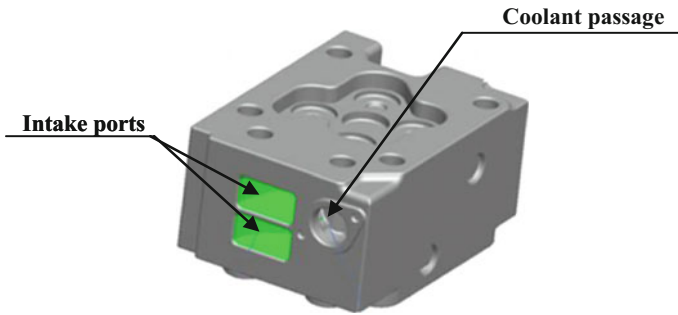


Fig. 5 Port layout

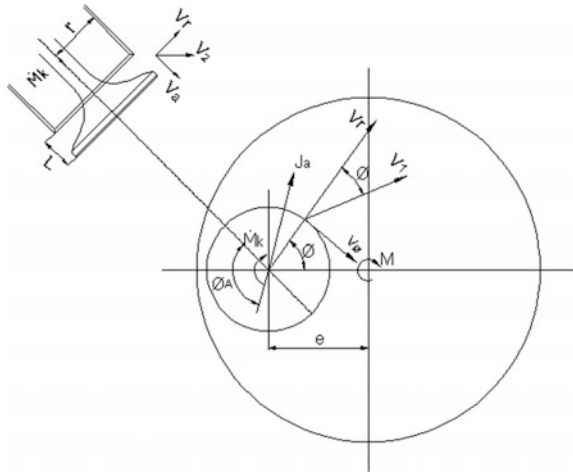
curved portion of the port, the inner radius of curvature has to exhibit a favorable relation to valve seat inner diameter.

4 Helical Intake Port Design

MRSR can be achieved by varying the angle ϕ to the line connecting valve and cylinder centerlines and eccentricity 'e' of a port, as shown in Fig. 6. Rotation of the cylinder charge depends on the discharge angular momentum or the moment of the discharge impulse. For this,

$$\frac{(\text{Valve seat inner diameter})^2}{(\text{Bore Diameter})^2} = \lambda$$

Fig. 6 Velocity of charge for helical intake ports



should be high as possible. $MFC * \lambda$ gives the mean flow capacity, which is an important parameter to decide the port quality.

The moment of momentum \dot{M} in relation to the cylinder axis per unit time of the air charge flowing into the cylinder is composed of exit moment of momentum \dot{M}_k of the port flow which is

$$\dot{M}_k = \gamma/gLr^2 \int_0^{2\pi} V_r V_\theta d\theta \text{ and}$$

the moment of the exit momentum \dot{M}_A ,

$$\begin{aligned} \dot{M}_A &= j_A e \sin \phi_A \\ &= \gamma/gLr e \int_0^{2\pi} V_r V_1 \sin(\theta - \psi) d\theta \\ \dot{M} &= \dot{M}_k + \dot{M}_A \end{aligned}$$

where $g=9.8 \text{ m/s}^2$, L —lift (mm), r —radius vector (mm), and V_r , V_1 , and V_ϕ are the velocity components. j_A is the component of exit momentum perpendicular to the valve axis. This relation gives an idea that rotation of the cylinder charge is produced by rotational port flow as well as unsymmetrical outflow from the valve. For the moment of momentum inside the cylinder produced by the exit momentum, the eccentricity ‘ e ’ and the direction of this momentum (angle ψ_A) are important as shown in Fig. 6. Also the performance of the helical port is based on the high exit moment of momentum \dot{M}_k . Depending on the shape of the helix, the component of

the exit momentum j_A may vanish totally. Ideally for helical port, the cross-sectional area follows

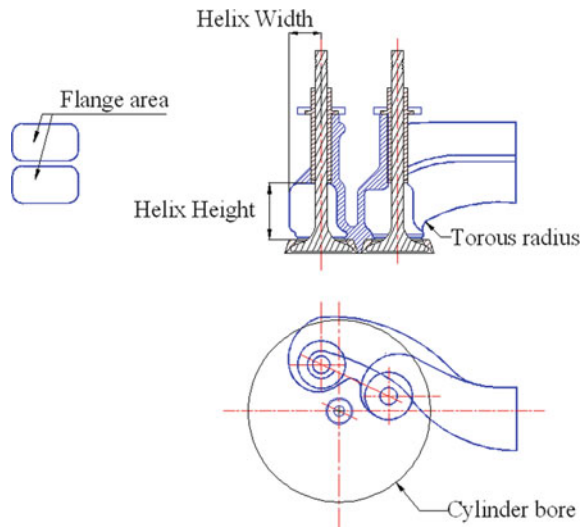
$$V_\varphi \cdot r = K = \text{const.}$$

To favor the condition, a large flange area at the port entrance, which is larger than valve seat area, is preferred. The cross section, in order to achieve the expected swirl, has to be in such a way that it decreases gradually at the start and rapidly afterward.

5 Three-Dimensional Modeling of Helical Intake Port

The design parameters and the port performance relations were studied. The approach is successfully proved in previous studies [4, 5]. Six variables were selected for the port design. The plan is randomized to have a final test matrix. Also several repeated trials are performed to confirm the repeatability. Critical features of port design that influences the swirl characteristics are shown in Fig. 7. The 3D port designed is shown in Fig. 8. In addition to key dimensions for effective port design, blending of surfaces and gradual change were done. After modeling, the metallic flow box is made. The flow box is designed taking care of realistic manufacturing features, including machining throat and all radii are made compatible with casting requirements. Attention was given to ensure that port geometry modification is done for driving parameters. The solid port model is made as shown in Fig. 8.

Fig. 7 Design parameters of intake ports



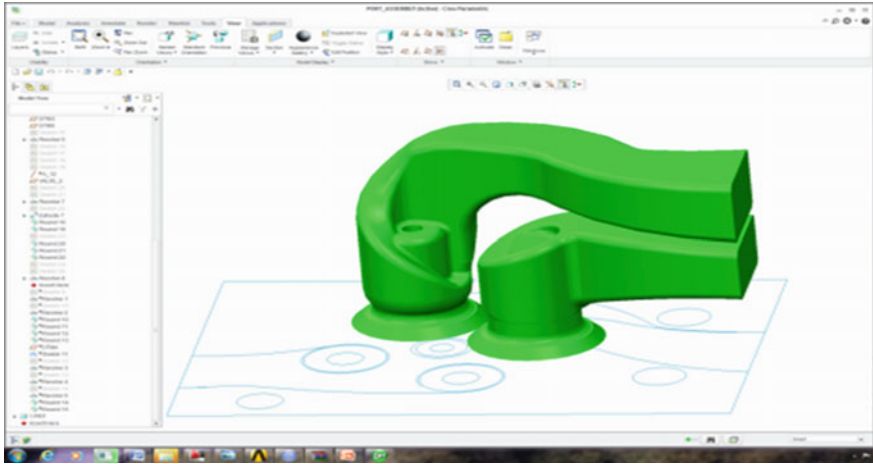


Fig. 8 Model of helical and tangential intake ports

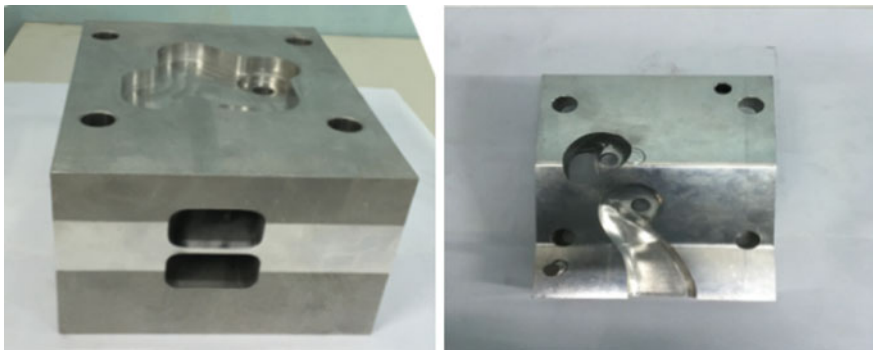


Fig. 9 Manufactured flow box

The metallic flow box is manufactured in CNC machine, and an accuracy check is carried out with original CAD data. Certain extent of error on physical flow box is accepted without compromising important parameters. The manufactured flow box is shown in Fig. 9.

6 CFD Analysis of the Helical Intake Port

A detailed CFD analysis was carried out using commercial software AVL—FIRE. Four configurations of the intake port were analyzed using the software. The details of the calculated swirl are given in Table 2.

Table 2 CFD analysis results

Design	Swirl computed (-)
BE1	1.55
BE2	1.64
BE3	1.76
BE4	1.85

BE4 configuration is considered for flow box testing

7 Port Testing

The stationary flow tests proved to be very useful for the development work on the valve ports. Through the application of modeling techniques, it is possible to arrive at proper port dimensions. However, test bench results remain practically useful. The steady-state swirl rig test results presented as ratios are very useful for determining performance of the engine. The experimental setup of the swirl test rig is as shown in Fig. 10.

The static test rig consists of a blower which will suck air through the port, which is connected to the tank. A constant pressure drop is maintained between the atmosphere and the cylinder liner. In between the tank and the blower, an orifice plate is mounted which gives the pressure difference for every lift of the valve considered for measurement. The tank has a provision at its top for cylinder liner mounting and above which the flow box (port) is mounted. The paddle wheel installed inside the liner measures the air rotation. The air rotation is picked up by magnetic pickup and displayed in electronic rpm meter as (W). The pressure drop across the orifice plate, W , temperature during the test, and the atmospheric pressure are taken as readings for all 13 different lifts according to L/D .

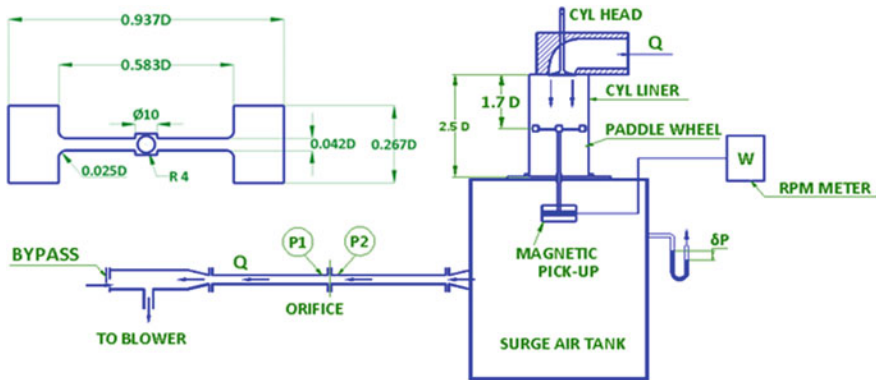


Fig. 10 Experimental setup

8 Estimation of Flow Parameters

At various valve lifts, the values of Q , C_F , C_D , and N_R lifts are calculated, and by their summation, the values of MFC, MRSR, and Z are calculated.

$$V_O = \sqrt{\frac{2\delta p}{\rho}}$$

$$C_F = \frac{Q}{AV_o}$$

$$N = \frac{W_R B}{V_O}$$

$$\text{MFC} = \frac{\int_{\alpha_1}^{\alpha_2} C_F \cdot d\alpha}{\alpha_2 - \alpha_1}$$

$$Z = \left(\frac{B}{D}\right)^2 \frac{2 \cdot S \cdot W_E}{a \cdot C_{F(\text{mean})}}$$

The charge rotation is measured by measuring the speed of the vane through a magnetic pickup connected to rpm meter. Then, swirl ratio is calculated by taking the ratio of anemometer speed to the crank shaft speed. The MRSR is calculated by the summation throughout the valve lift curve.

$$\text{MRSR} = \frac{W_C}{W_E} = \frac{BS}{D^2} \cdot \frac{\int_{\alpha_1}^{\alpha_2} C_F \cdot N_R \cdot d\alpha}{\left(\int_{\alpha_1}^{\alpha_2} C_F \cdot d\alpha\right)^2}$$

Z is calculated from mean gas velocity and velocity of sound. It is a summary coefficient.

Discharge coefficient,

$$C_D = \frac{Q}{A_{\text{act}} \cdot V_O}$$

Assumptions made for calculation

- Flow is considered as incompressible and adiabatic throughout the port on the flow rig as well as on the engine.
- The port retains the same characteristics under the transient condition of the engine as in steady flow rig.
- The pressure drop across the port is constant during induction.

- The angular momentum is conserved, and the skin friction is ignored.
- Flow into the engine was considered independent of the piston motion between IVO and IVC.
- Volumetric efficiency is taken as 100%.

9 Results and Discussions

The results obtained from paddle wheel for different parameters are plotted against ratio of valve lift (L) to valve inner seat diameter (D) shown in Figs. 11, 12, and 13. It is observed in Figs. 11 and 12 that flow coefficient is adequate throughout the valve lift for intake; the exhaust flow coefficient is sufficiently high at high L/D ratios giving an indication on performance of the ports. Figure 13 shows the

Fig. 11 C_F versus valve lift

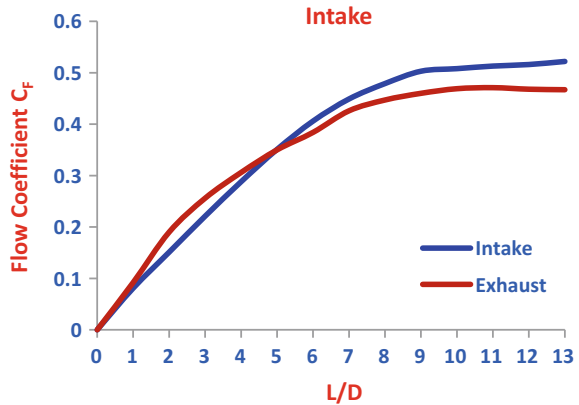


Fig. 12 C_F versus L/D

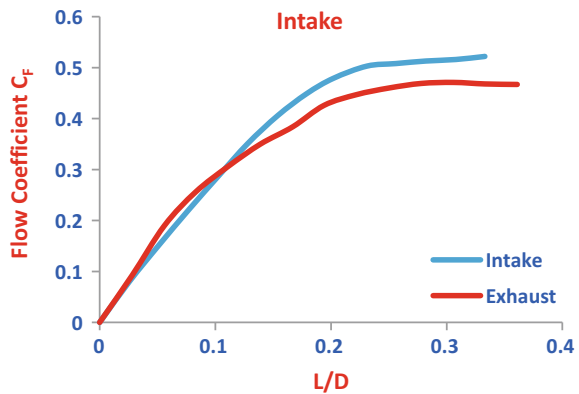


Fig. 13 N_R versus L/D

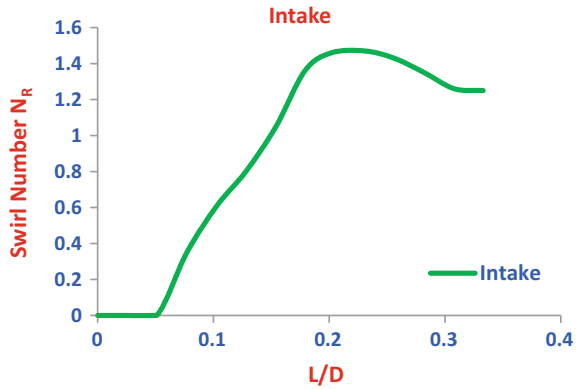


Table 3 Comparison of test results with target values

Parameter	Test result	Target value
MFC	0.342	0.3
MRSR	1.66	1.5
Z	0.58	<0.6

characteristics of swirl that it gives the proper swirl which is stable throughout the valve lift. This gives an indication that stable swirl can be prolonged from intake stroke up to compression stroke and then to combustion which will result in proper mixing of charge with fuel.

10 Summary of Test Results

Table 3 provides the test results of MFC, MRSR, and Z. The measured values are more than the target values with reasonable margin for production.

11 Conclusion

- The port model is designed considering major design parameters of helical port.
- The port is fully optimized within the practical constraints.
- The swirl characteristics are uniform with valve lift.
- Cylinder head meeting the targeted MRSR, MFC, and Z is successfully developed for the AFV diesel engine and was evaluated in test rig.

- From the above work, an optimized cylinder head configuration with improved swirl characteristics, reduced volume and weight along with better cooling with the intake port-generating swirl in the directed mode and the helical mode, was achieved.

References

1. Godrie, P., Zellat, M.: Simulation of Flow Field Generated by Intake Port-Valve Cylinder Configuration-Comparisons With Measurements and Applications. SAE-940521 (1994)
2. Gale, N.F.: Diesel Engine Cylinder Head Design: The Compromises and the Techniques. SAE-900133 (1990)
3. Brandl, F., Reverencic, I., Cartellier, W., Den, J.C.: Turbulent Air Flow in The Combustion Bowl of a D.I. Diesel Engine & its Effect on Engine Performance. SAE-79004C (1979)
4. Brignall, A., Jin, Z.M.: Investigation of inlet port design on engine swirl using orthogonal array experimentation and computational fluid dynamics. In: ImechE Conference on Fluid Mechanics and Dynamics of Multi-valve Engines, London (1999)
5. Lilly, L.C.R.: Diesel Engine Reference Book. Butterworth-Heinemann Publications, Oxford, United Kingdom (1984)

Design Optimization of Advanced Multi-rotor Unmanned Aircraft System Using FSI



R. Vijayanandh, M. Senthil Kumar, K. Naveenkumar, G. Raj Kumar
and R. Naveen Kumar

Abstract At the moment, multi-rotor MAV is being proposed for many critical applications so the engineer must provide an MAV, which have good specifications such as the high lifetime, high operational speed, more secure on-flight, and low maintenance cost in order to survive at critical applications. This work deals with the conceptual design and its optimization of the hybrid multi-rotor MAV for high-speed applications by using FSI simulation. The proposed MAV has characterized by the use of two counter-rotating propellers for vertical operation, and two propellers are located in the rear part of the MAV for forward force and yawing control. The airframe and propellers of the MAV are preferred to be of Kevlar composite, which allows for propeller flexibility without sacrificing durability. High lifetime and low probability of failures in terms of FSI analysis are to be achieved by the implementation of Kevlar composite, which has good impact load withstanding capability. The present work aims at performing a numerical simulation to be used for investigating the design behavior of the MAV by simulating the displacement and principal stress in order to withstand at high-speed operation. The design process entailed the overall system design, component selection, and placement in CATIA. FSI simulation of stress and displacement throughout the Kevlar MAV has been analyzed by Ansys 16.2, and thereby, the design optimization has been carried out in the MAV.

Keywords Aeroelastic · Composite material · Coupled approach
Numerical simulation · MAV

R. Vijayanandh (✉) · M. Senthil Kumar · K. Naveenkumar · G. Raj Kumar
R. Naveen Kumar
Department of Aeronautical Engineering, Kumaraguru College of Technology,
Coimbatore 641049, Tamil Nadu, India
e-mail: vijayanandh.raja@gmail.com

© Springer Nature Singapore Pte Ltd. 2019
U. Chandrasekhar et al. (eds.), *Innovative Design, Analysis and Development Practices in Aerospace and Automotive Engineering (I-DAD 2018)*, Lecture Notes in Mechanical Engineering, https://doi.org/10.1007/978-981-13-2718-6_28

1 Introduction

1.1 Objective

The main objective of this paper is to design a safe and secure MAV in order to provide surveillance with high forward speed by using fluid–solid interaction (FSI) simulation, in which the MAV’s design behavior has planned to monitor in terms of its displacement and resisting force generation while undergoing high-speed boundary conditions.

1.2 Studies on MAV and Its Application

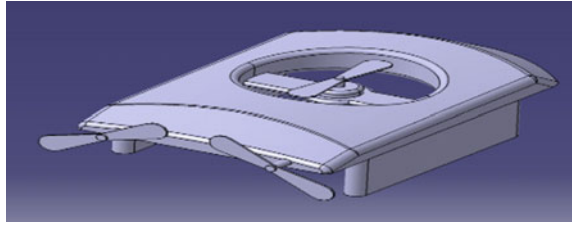
A MAV is an advanced unmanned aircraft, which can able to complete the mission without the onboard crew members’ support, and it has to be modeled/manufactured within 15 cm. The process to design a MAV is completely different from designing a conventional aircraft, which is due to its small size and low airspeed, and the MAV has different aerodynamic characteristics, propulsion, power source, flight stability, and control system [1]. From the literature studies, it is learnt that most of the MAVs flew in the speed of maximum of 15 m/s or 30 mph and most of the MAVs were took off with hand launches. Safe landing and self-landing is critical in MAV because of its design, so this paper deals with the hand launch avoidance by means of self-vertical takeoff and landing (VTOL) and also increasing the speed greater than 15 m/s by changing the overall body of the hybrid MAV with streamline shape. Fabricating the model directly is not the suitable decision because of cost wastage if failure occurs, so this paper analyzes the use of FSI numerical simulation [2]. By using FSI analysis, the model can be optimized and the model which is efficient for fabrication with high probability of success confidently for critical application can be made [3].

2 Design of MAV and Its Optimization

2.1 Design Methodologies Involved in MAV

The design of a MAV and its parameters’ determination are derived from two major processes, which are decision-making process and a selection technique. An optimized MAV, with a minimum of undesirable side effects, requires the application of an integrated life-cycle-oriented “system” approach. The design criteria are determined through the definition of system operational requirements, which in turn evolved from the MAV’s mission [4]. (1) Conceptual design, (2) preliminary design, (3) detail design are the major phases which help to provide the step-by-step

Fig. 1 Preliminary design of the MAV



construction of the MAV in an efficient manner. Figure 1 shows the preliminary design of a MAV, which is modeled by CATIA. The overall dimensions of the MAV are within 145-mm square box, and then, the components' dimensions are evaluated from the theoretical approach.

2.2 Design Optimization—Modification—1

Design is the creation of a plan or convention for the construction of an object or a system. In this paper, design plays a vital role and also creates a new perspective in the MAV design concept. In MAV, propeller, mainframe, and location of components may create criticality in design, so normal designing software could not be able to complete the design process of MAV. Hence, CATIA is able to compute the critical design because of its unique features. The design yields an increase in the weight with the components like safety stand and duct. Hence, another design considering the structural stress and increase in the weight of the duct is made using CATIA [5]. One of the most effective techniques in trade-off studies is multi-disciplinary design optimization, which deals with more complexity because of the inclusion of all disciplines simultaneously. Based on the identified problems from the preliminary design, also increasing the efficiency in the cruise of the MAV, the preliminary design is modified with the duct surface and safety stand in CATIA. Figure 2 shows the typical isometric view of MAV with modification in airframe [6].

Fig. 2 Typical views of MAV—version_1

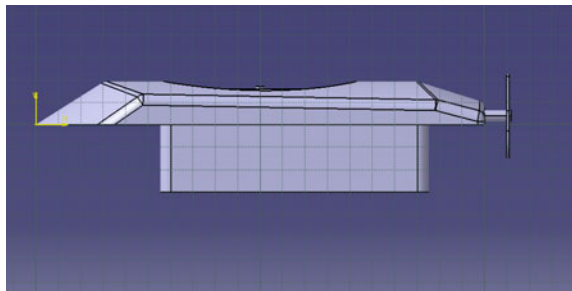
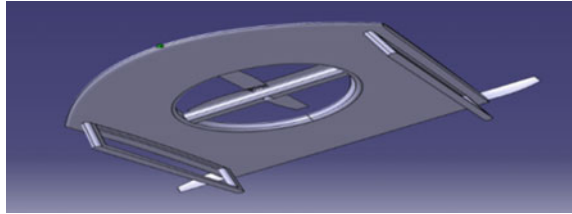


Fig. 3 MAV in streamline shape



2.3 Modification—2 (Inclusion of Aerodynamic Effects)

Aerodynamics plays a vital role in MAV design consideration, which primarily includes flow separation at sharp edges and shear force between fluid and MAV solid surface. Hence, the design of the MAV intentionally modified as curved surface in order to provide smooth flow around the MAV. Figure 3 shows the typical isometric view of MAV.

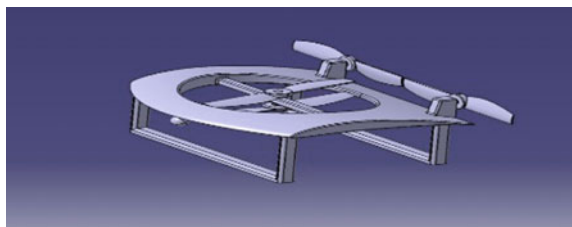
2.4 Modification—3 (Inclusion of Payload Space and Coaxial Propeller)

Surveillance and increment of weightlifting properties are important roles in the UAV. Hence, this modification comprises of implementation of coaxial propellers and suitable location of camera. Implementation of coaxial propellers and camera location provides the effect surveillance with high stability by overcoming the effect of rotational effect due to single main rotor rotation. Figure 4 shows the isometric view of modified MAV.

2.5 Modification—4 (Inclusion of Components)

This modification is based on the components and their location in order to do efficient operation. In this paper, four propellers are used, in which two are for VTOL that is puller configuration and the other two are for forward speed which is pusher configuration. Here, HQ Bullnose prop has been suggested because its

Fig. 4 MAV with camera and coaxial



thrust-producing capability matches with this operation. The more suitable motor for this work is Cobra CM2204 2300 because its KV rate perfectly suits and also it fulfills the forward speed operation [7]. A Tattu 30 A, brushless Bhlheli-2-4S has been suggested for this MAV in order to achieve different MAV maneuvers by having control on the power supply with secured flight [8]. The selection of batteries is depending upon the motors' capability, the amount of weight, and the specification of propellers. The battery suggested for this MAV is lithium battery, which is Tattu 4 S LIPO battery because its specification completely satisfies the basic requirements of MAV. Batteries are the heaviest item on this MAV, so especially separate safe locations are created in the dead center of the MAV in order to achieve more stable operation [9]. The outer design of the MAV is aerofoil shape, which will provide low drag compared to other shapes. Dimensions of the MAV have been shown in Figs. 5, 6 and MAV's parts and also its location have been completely shown in Fig. 7.

Fig. 5 Top view

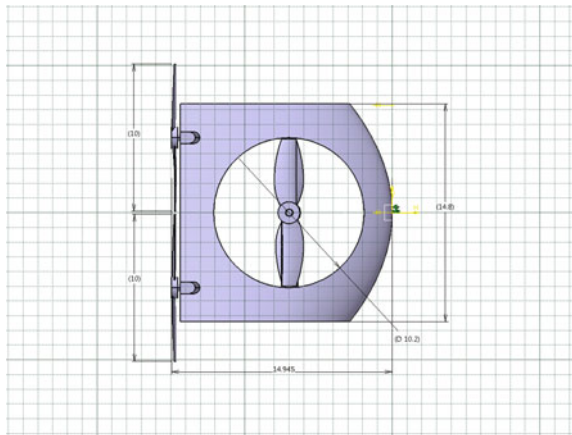


Fig. 6 Side view

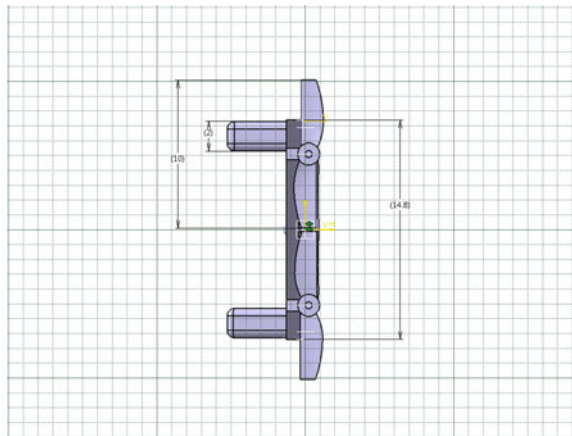
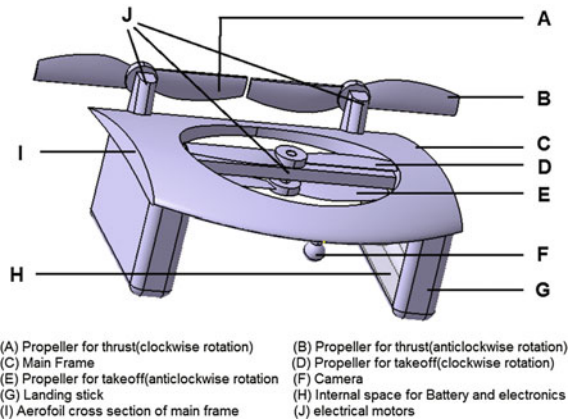


Fig. 7 Location of parts



3 Design Optimization Using FSI—(Modification—5)

Computational simulation is one of the emerging engineering analyses, which is used to predict the engineering parameters on the object. This paper finally undergoes the advanced optimization technique of a MAV, which is inclusion of FSI while it is flying. FSI is the non-stationary coupling between a fluid flowing through the flexible mechanical structure. During the computation of FSI problems, the flexible structure and fluid models are required to interface. The interaction between incompressible fluid flows and immersed structures is nonlinear multi-physics phenomena that have applications to a wide range of scientific and engineering disciplines [10].

3.1 Fluid–Solid Interaction

FSI has been used here because of its effective prediction of the structural parameters, due to fluid impact load while undergoing high-speed operation. The prediction methodology of FSI has been divided into two groups, which are one-way coupling and two-way coupling. In one-way coupling, the fluid analysis has been solved separately as per the given boundary conditions, and thereby, the results are imported in structural analysis as one of the boundary conditions. In two-way coupling, the boundary conditions of the fluid analysis and solid analysis have been given individually; after that, the consolidated settings have been integrated in FSI tool [10]. In this paper, two-way coupling methodologies have been used with the help of Ansys Workbench 16.2. Two-way coupling is a better performer compared to one-way coupling due to its computing structures. In two-way coupling, the boundary conditions play a vital role, which means the results are only generated if and only if the given boundary conditions are correct; hence,

the above conditions are not suitable for one-way coupling. Here, 3D tetrahedral element has been chosen because of MAV geometry criticality [10]. The integrated MAV has been discretized by more than 5 lakhs tetrahedral elements in order to gain accrued results. Optimization of MAV based on two-way coupling FSI analysis is comprised of two cases, which are horizontal takeoff landing (HTOL) and VTOL.

3.2 HTOL Results

In HTOL operation, the pusher-type propellers are the dominant components, which are used to provide forward speed. Other two vertical coaxial propellers are assumed to rotate at a low-level speed. Hence, the boundary conditions are different in HTOL and VTOL operations. In this optimization analysis, the MAV has been assumed as fixed beam; thereby, the fixed support has been separately given in the landing surface of the MAV. Pressure plot is shown in Fig. 8, and thereby, Figs. 9 and 10 show the stress and deformation results of MAV while undergoing HTOL operation.

Fig. 8 Pressure plot

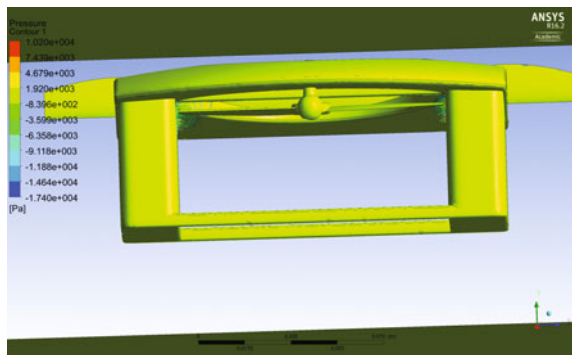


Fig. 9 Deformation plot

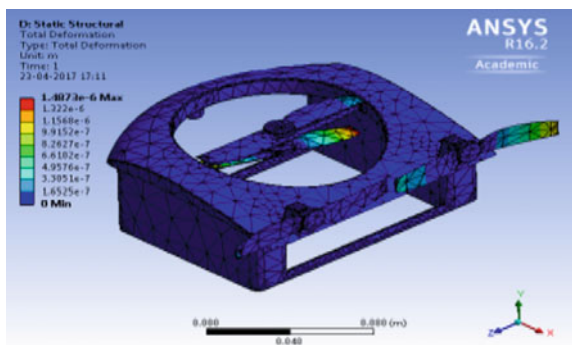


Fig. 10 Stress plot

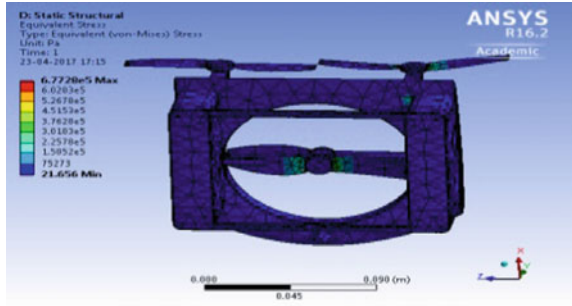
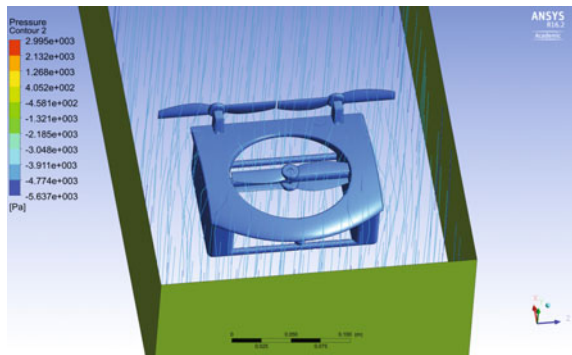


Fig. 11 Pressure plot



3.3 VTOL Results

Here, boundary settings have been given in the separate sections, in which speed of the airspeed, pressure-based solver, turbulence model, turbulence specification method, solution method, solution initialization, and spatial discretization have played a predominant role in the flow analysis. In this case, coaxial propellers for VTOL and its clearance between the propellers play a vital role, which is determined from VTOL FSI analysis. Pressure plot is shown in Fig. 11, and thereby, Figs. 12 and 13 show the stress and deformation results of MAV.

3.4 Final Optimized Design

From the two-way coupling analysis, it is observed that the maximum deformations act on the locations of on the forward speed propellers and coaxial propellers, in which deformation on the forward speed propellers is within an acceptable limit, but in the case of coaxial propellers, internal body interaction is happened due to the impact load. Hence, the clearance between coaxial propellers has been increased by 1.5 cm. Figures 14 and 15 show the updated MAV designs, which have the

Fig. 12 Deformation plot

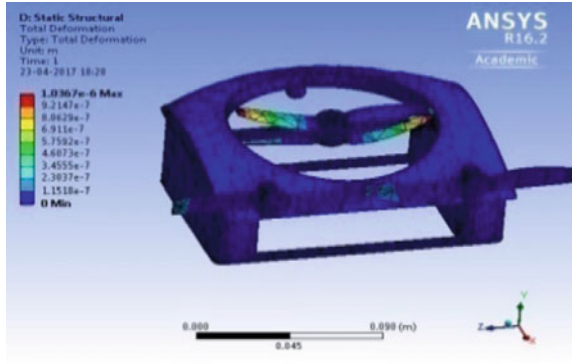


Fig. 13 Stress plot

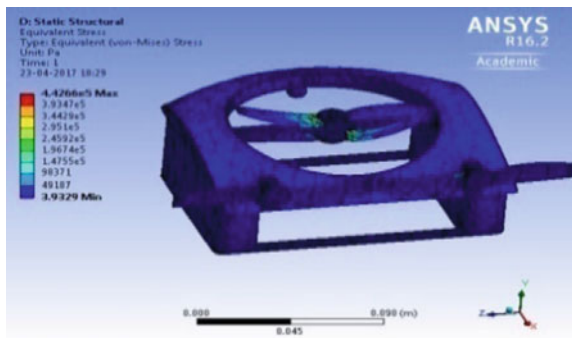


Fig. 14 Updated MAV design

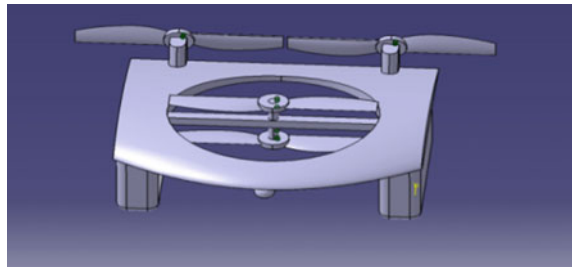
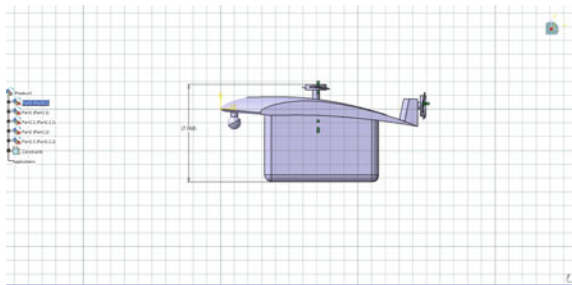


Fig. 15 Modified dimension of MAV



modification based on numerical simulation results. The modifications considered are increase in the clearance of vertical and horizontal propellers.

3.5 Final Optimized Results

Figures 16 and 17 show the HTOL deformation results of optimized MAV for fixed and free beam assumptions, respectively. Similarly, Figs. 18 and 19 show the VTOL deformation results of optimized MAV for fixed and free beam assumptions.

Fig. 16 HTOL—MAV acting as fixed beam

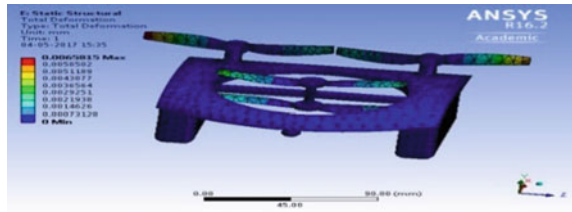


Fig. 17 HTOL—MAV acting as free beam

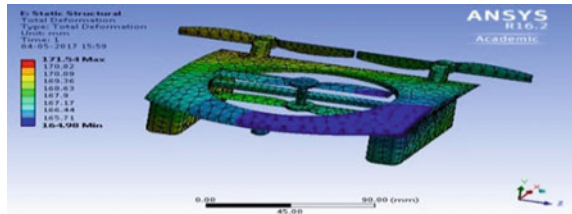


Fig. 18 VTOL—MAV acting as fixed beam

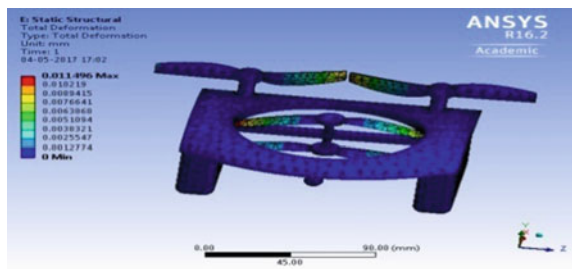
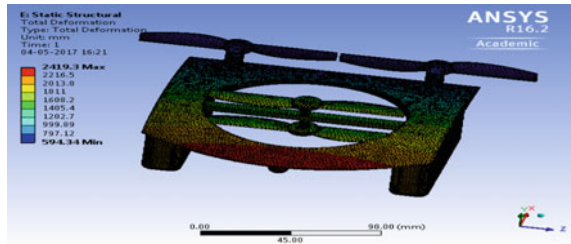


Fig. 19 VTOL—MAV acting as free beam



4 Conclusion

The design of MAV has been modeled by CATIA with dimensions evaluated from theoretical approaches. After that, the optimization has been included; modifications involved in the MAV designs are based on aerodynamic effects, thrust-producing capability, selection of practical components, and fluid–solid interaction results. At the end of all the modifications, the updated MAV model has been optimized with the help of Ansys Workbench 16.2. The numerical simulation has been carried out for optimized MAV model for a forward speed of 20 m/s with Kevlar property. The results are plotted and compared for both cases (static and dynamic) and also for HTOL and VTOL. From the stress and deformation results, it is understood that the values are within limit in the Kevlar MAV for high-speed HTOL operation.



References

1. Vijayanandh, R., et al.: Numerical study on structural health monitoring for unmanned aerial vehicle, special issue on trends and future in engineering. *J. Adv. Res. Dyn. Control Syst.* **9** (Sp-6), 1937–1958 (2017)
2. Raj Kumar, G., et al.: Conceptual design and structural analysis of integrated composite micro aerial vehicle, special issue on special issue on environment, engineering & energy. *J. Adv. Res. Dyn. Control Syst.* **9**(Sp-14), 857–881 (2017)
3. Vijayanandh, R., et al.: Design, fabrication and simulation of hexacopter for forest surveillance. *ARNP J. Eng. Appl. Sci.* **12**(12), 3879–3884 (2017). ISSN 1819-6608
4. Michelson, R.C., et al.: Overview of Micro Air Vehicle System Design and Integration Issues, pp. 1–12. Georgia Tech Research Institute, Georgia Institute of Technology, Atlanta, GA, USA
5. Mishra, S., et al.: Design and analysis of composite structure for development of a flapping wing micro air vehicle. *J. Basic. Appl. Eng. Res.* **1**(4), 90–92 (2014) Print ISSN: 2350-0077; Online ISSN: 2350-0255
6. Shkarayev, S.: Aerodynamic Design of VTOL Micro Air Vehicles. In: 3rd US-European Competition and Workshop on Micro Air Vehicle Systems (MAV07) & European Micro Air Vehicle Conference and Flight Competition (EMAV2007), pp. 4–18, 17–21 Sep 2007, Toulouse, France
7. Sai Kumar, A., et al.: Design and fabrication of 150 mm fixed wing micro aerial vehicle. *Int. J. Sci. Technol.* **3**(3), 4–9 (2013). ISSN (online): 2250-141X, www.ijst.co.in

8. Perel, R., et al.: Design, Analysis and Performance of a Rotary Wing MAV. Johns Hopkins University/Applied Physics Laboratory Laurel, MD 20725, pp. 3–17
9. Hossain, M.A., et al: Development of Design and Manufacturing of a Fixed Wing Radio Controlled Micro Air Vehicle (MAV). MIST Journal: GALAXY (DHAKA) **3**, 4–12 (2011). ISSN 2073-6444
10. Kumar, V., et al.: Opportunities and Challenges with Autonomous Micro Aerial Vehicles, pp. 4–16. GRASP Laboratory, University of Pennsylvania, Philadelphia, PA

Studies on Carbon Materials-Based Antenna for Space Applications



Prasanna Ram , Manoj Aravind Sankar  and N. G. Renganathan

Abstract Printing small antenna structures for space application would be highly challenging, and the materials to be used for the antenna fabrication would have major impact on the performance of the antenna system. Antennas are primarily fabricated using copper as the material. In recent times, various materials are being explored for their applicability, reliability, durability, and scalability with respect to antenna applications. In lieu of the high thermal conductivity of copper, which could lead to thermal expansion on exposure to sun's rays and thus decrease its efficacy as an antenna; graphene has been a better competitor and contender for space antennas. Taking cost of synthesis and capital investment into consideration, this paper aims to give a face-lift to the other allotropic forms of carbon, namely graphite, lampblack, and activated charcoal, which are comparatively far cheaper and extensively available and could be on a par with graphene as far as antenna application is concerned.

Keywords Carbon allotropes · Antenna application · Packaging factor
Electron avalanche · Internal resistance

P. Ram (✉) · M. A. Sankar · N. G. Renganathan
Vel Tech Rangarajan Dr. Sagunthala R&D Institute of Science
and Technology, Avadi, Chennai 600062, Tamil Nadu, India
e-mail: prasannaram88@gmail.com

M. A. Sankar
e-mail: manoj1508.aravind@outlook.com

N. G. Renganathan
e-mail: ngrenganathan@gmail.com

© Springer Nature Singapore Pte Ltd. 2019
U. Chandrasekhar et al. (eds.), *Innovative Design, Analysis and Development Practices in Aerospace and Automotive Engineering (I-DAD 2018)*, Lecture Notes in Mechanical Engineering, https://doi.org/10.1007/978-981-13-2718-6_29

1 Introduction

1.1 Available Forms of Materials

In the antennas such as conventional or smart patches, mostly copper-based fabrication materials are used [1]. Their restrictions are due to temperature coefficient and area occupancy. Losses occur on account of limitations in thickness and varying resistance due to repetitive additive manufacturing mechanism. Apart from copper, the other materials suitable for antenna are silver and graphene [2], both of which are costly to extract and synthesize, respectively. In this Paper suitability of allotropic forms of carbon viz. Graphite, Lamp Black, Graphene and Activated Charcoal for antenna applications has been attempted and the results have been reported.

1.2 Alternate Materials

Due to enormous rise in the resource allocation, it is necessary that the antennas should be replaced to give enhanced efficiency, optimization, and scaling performance [3, 4]. So, carbon-based components [5, 6] and nanosilver [7, 8]-based forms are more popular nowadays. Since there is a demand for low-cost material without performance sacrifice, the other allotropic forms of carbon namely lampblack, graphite [9], and activated charcoal are studied in this paper, for their suitability with respect to antenna applications.

While taking into consideration the allotropes of carbon, diamond and fullerene have not been analyzed in this study. Diamond is expensive, and its distinguishing property of total internal reflection (TIR) is undesirable in space applications. By virtue of TIR, it would internally reflect the radiations falling on it, rather than absorbing wholly, leading to losses. Fullerene, though cheaper than graphene, is a structural material, whose properties are a function of the arrangement of the carbon atoms in the lattice, the prominent structures being C-60 and C-70. Any changes in the structural defects or mutations might be caused by energizing radiations in space which would vary the antenna properties considerably, thus affecting the efficacy.

1.3 Challenges in Materials

Materials that are used for antenna fabrication should possess a limited granule size and resistivity property which are the key factors to determine the S parameters of that particular design. In the recent literature, it is found out that S_{11} should be in the range of -15 dB or above and voltage standing wave ratio (VSWR) tends to be in

the range of 0–1, but practically because of achieving S_{11} [10] between –30 and –90 dB will cause the VSWR driven to 1–5. It significantly deviates the design rules with respect to wavelength and consumes larger material coating to achieve the desired frequency. Due to the resistive, inductive, and capacitive property deviation, graphene, lampblack, graphite, and activated charcoal are the alternate materials tried for antenna material, and the S parameters are expected to have precision deviation compared to conventional materials.

Antennas using alternate materials similar to abovementioned with low gassing effect will be more suitable for terrestrial and extraterrestrial applications. In case of terrestrial application, these materials having the property of working in terahertz frequency and low power consumption nature will be suitable for 5G and more [11, 12]. And in the case of space applications, they are having the ability to replace conventional antennas which are having higher weight, lower frequency, and power consumption issues.

2 Fabrication of Materials

2.1 *New-Gen Materials*

Fabrication methods such as additive manufacturing [13], prototyping using inkjet mechanism [14], screen printing, and doctor blade mechanism are more suitable for alternate materials such as graphene [15] (powder and ink), graphene platelets, and exfoliated graphene particles. Depending upon the usage, the organic mixture will be chosen.

2.2 *Liquidation of Materials*

The materials chosen for the analysis of their inherent antenna properties are the allotropic forms of carbon—crystalline (graphite, graphene [16]), and paracrystalline (lampblack, activated charcoal). These materials will be used in measured proposition with solvents such as THF, DMF, liquid paraffin, water and found out the issues such as surface tension property and insoluble pith formation due to non-bonding toward organic solvents such as water and diluted acids at room temperature. It is forming a good solving proposition with THF and DMF in different levels for the abovementioned allotropes. With the help of ultrasonic pressure, we found out that the bonding between the reagent and the particle increases to increase the liquidation process.

2.3 *Synthesis of Materials*

Lampblack is obtained by the incomplete combustion of Pancha Deepam oil (a mixture of ghee produced from the milk of *Bos taurus* and the oils extracted from *Azadirachta indica*, *Sesamum indicum*, *Ricinus communis*, and *Madhuca longifolia*). The oil is burnt in a brass vessel, and the lampblack particles get deposited on the surface of a copper plate placed about 5 cm from the tip of the flame. Lampblack is then scrapped off. This is the traditional procedure as per the Indian Medical Science—Ayurveda [17] of manufacturing lampblack. Activated charcoal powder chosen for the study is that of medicinal grade [18]. Graphite and graphene are synthesized in laboratory by mechanical grinding and exfoliation method, respectively.

Designs would be prototyped using conventional materials such as laminated paper, flame retardant (FR-4), copper, and polished glass.

2.4 *Issues in Fabrication*

Major issues are due to uniformity, viscosity, and platelet formation due to granule size and solvent bonding. In case of inkjet printing for the fabrication of antenna [19], nozzle problem with respect to centipoise of the particular ink creates clogging and nozzle residue properties, in the case of screen printing, viscosity plays a very important role in uniformity of printing, and in case of gravure printing [20] and doctor blade mechanism, the ionic radii and viscosity forming unsolidified patches due to non-uniformity of absorption cause deviation in the performance. The platelet formation due to repetitive layers will cause non-uniform lattice orientation, and because of this, antenna property will be deviated.

3 Radiative Imaging

3.1 *Sunlight*

The property of the antenna will be directly affected due to the particle of the environment and the light exposure of the particular area. For the experimentation purpose, the sunlight-exposing mechanism was tried to analyze the changes due to sun radiation natural phenomenon [21, 22]. The forward-looking infrared (FLIR) image of the study and the three-dimensional infrared (3D-IR) graph depicting the temperature distribution across the surface of the same are as shown in Figs. 1a, 2a and 1b, 2b, respectively.

From the Graphs its clear that FLIR of polished glass substrate coated with carbon allotropes exposed to sunlight has not produced major distribution difference in temperature, and these substrates will not be a suitable material for antenna

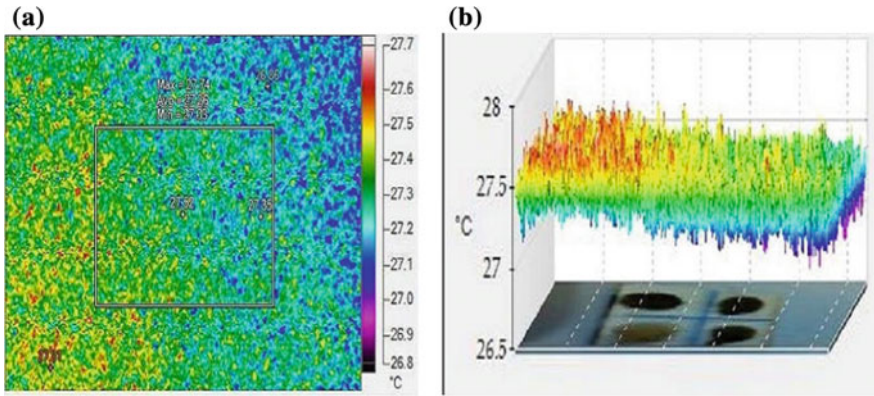


Fig. 1 a FLIR of polished glass substrate coated with carbon allotropes exposed to sunlight (left); b 3D-IR graph (right)

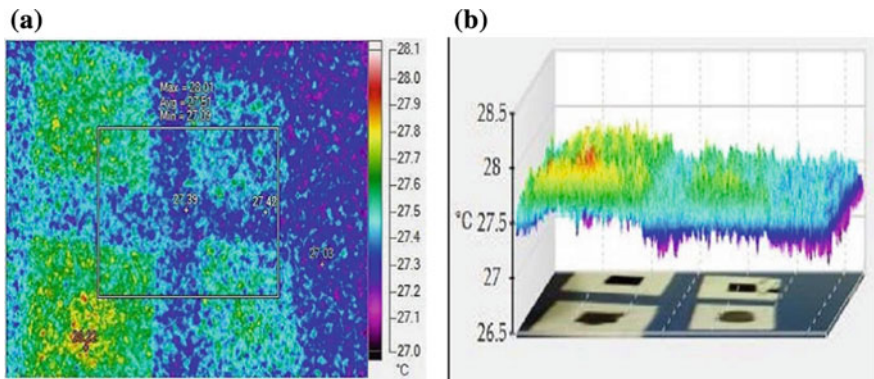


Fig. 2 a FLIR of laminated paper substrate coated with carbon allotropes exposed to sunlight (left); b 3D-IR graph (right)

in view of thermomagnetic potential useful for getting useful power to be tapped during space applications.

3.2 Ultraviolet Source

The samples are exposed to ultraviolet radiations. In this case, heat does not play a major role as in incandescence, since UV is purely associated with light, unlike infrared (IR), as evident in the FLIR images of the coating on various substrates in Figs. 3a, 4a, 5a, and 6a, b and the corresponding 3D-IR graphs in Figs. 3b, 4b, 5b, and 6c, d. Here, the scattering is due to the organic ions which are present by nature

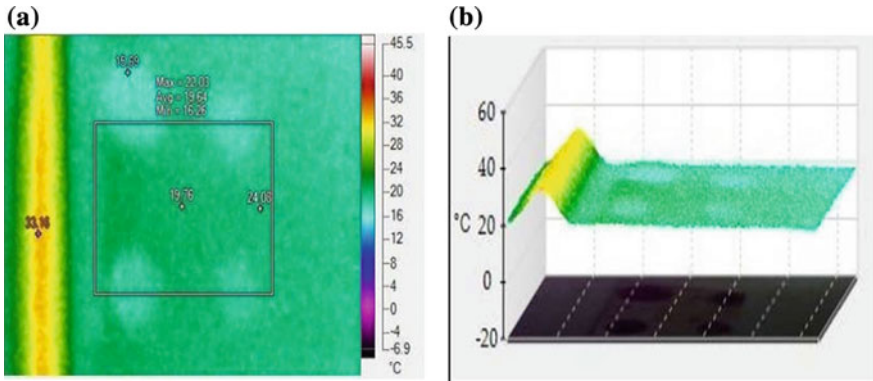


Fig. 3 a FLIR of copper substrate coated with carbon allotropes exposed to ultraviolet source of 8 W (left); b 3D-IR graph (right)

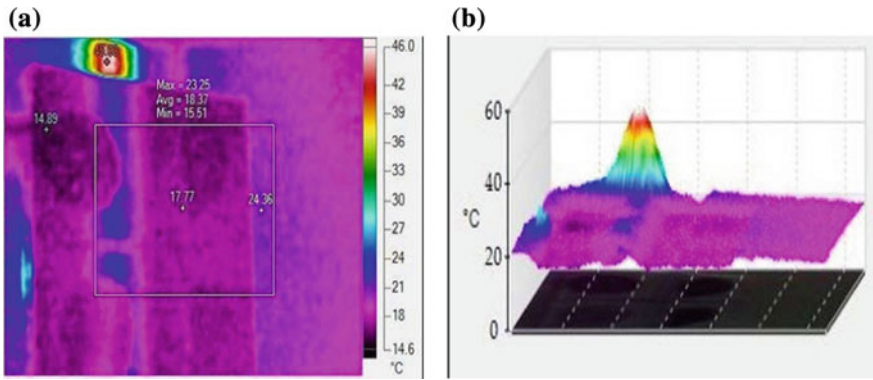


Fig. 4 a FLIR of polished glass substrate coated with carbon allotropes exposed to ultraviolet source of 8 W (left); b 3D-IR graph (right)

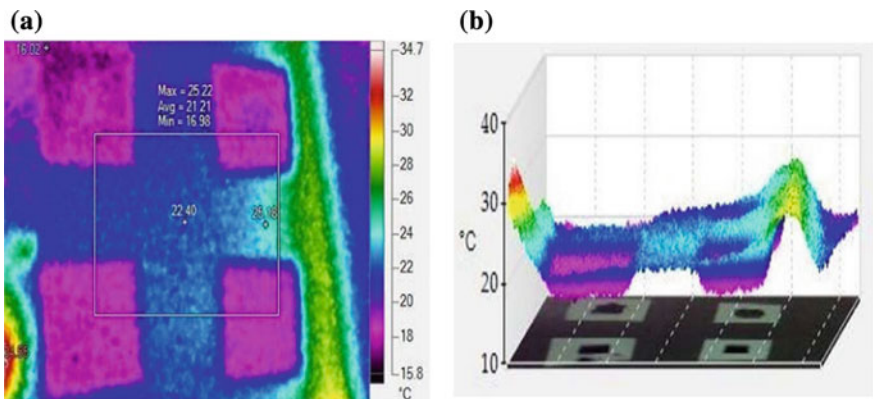


Fig. 5 a FLIR of laminated paper substrate coated with carbon allotropes exposed to ultraviolet source of 8 W (left); b 3D-IR graph (right)

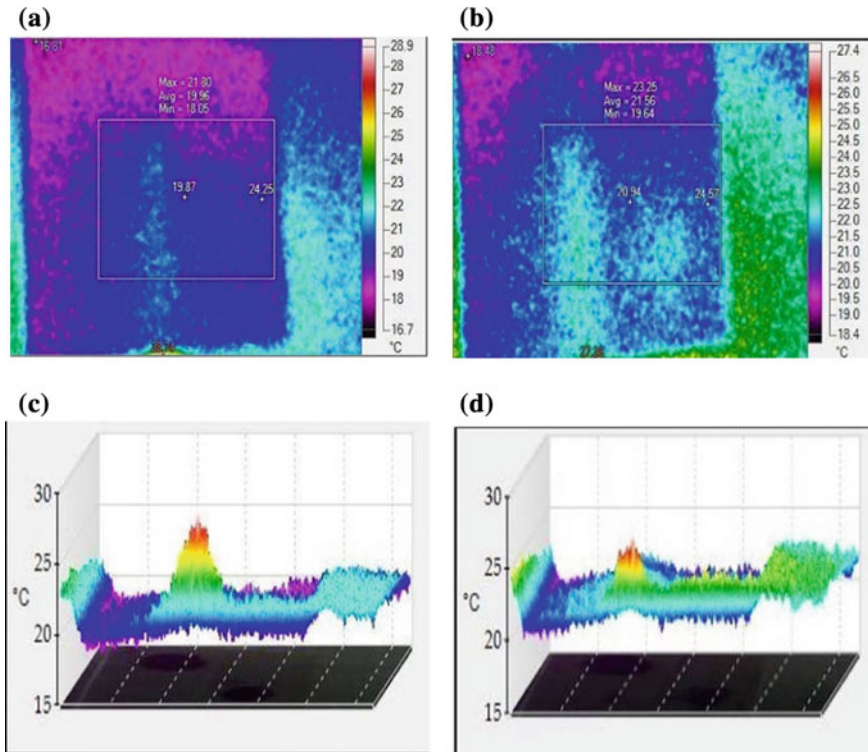


Fig. 6 **a** FLIR of FR4 substrate coated with graphite and activated charcoal exposed to ultraviolet source of 8 W, UV-C region; **c** 3D-IR graph; **b** FLIR of FR4 substrate coated with graphene and lampblack exposed to ultraviolet source of 8 W, UV-C region; **d** 3D-IR graph

in the material. These ions first absorb and then radiate. The difference is in the ionic layers, due to which radius factor is formed. This would show uniformity, but due to mismatching in lattice and porosity, the scattering imaging shows non-uniform structure and this in accordance with results reported in [22, 23].

FLIR of copper substrate coated with carbon allotropes exposed to UV source and FLIR of glass substrate coated with carbon allotropes exposed to UV source indicate the temperature distribution which is reasonably high, and hence, these materials could be considered as suitable materials to be used in antenna materials for getting reasonable power.

FLIR of laminated paper substrate coated with carbon allotropes exposed to UV source indicates the temperature difference which is reasonably high, and these materials can be used as antenna materials for getting useful power; these can be used instead of copper substrate as discussed earlier, if it is to be cost effective.

FLIR of FR4 substrate coated with graphite and activated charcoal exposed to UV source indicates the temperature difference which is very minimal, and these substrates cannot be used as antenna materials for tapping the thermomagnetic potential to tap power.

3.3 Infrared Source

The coated samples are exposed to infrared source, for about 15 minutes. The infrared source used is an incandescent tungsten halogen lamp of 200 W, 2000 lm. The thermal properties of the sample vary based on wavelength absorption. The median carbon material would absorb more light, whereas the outer paper material would scatter all light. The material porosity is responsible for the absorption when a polished substrate is used, and this scatters more waves. Copper, laminated paper, and FR4 have higher reflection, and glass has higher refraction property, which could be inferred from the FLIR images in Figs. 7a and 8a and 3D-IR graphs in Fig. 7b and 8b [22, 24].

FLIR of polished glass substrate coated with carbon allotropes exposed to IR source indicates the temperature difference which is substantial, and these are preferred in antenna applications if the source of heating is IR.

FLIR of laminated paper substrate coated with carbon allotropes exposed to IR source indicates the temperature difference which is substantial to tap power if the source of light is IR.

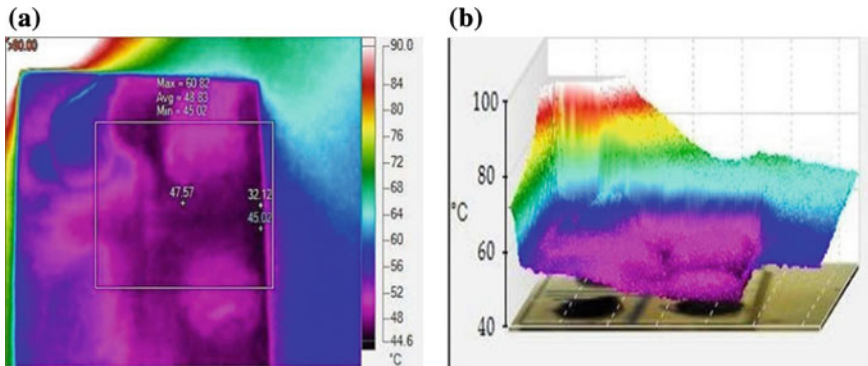


Fig. 7 a FLIR of polished glass substrate coated with carbon allotropes exposed to infrared source of 200 W, 2000 lm (left); b 3D-IR graph (right)

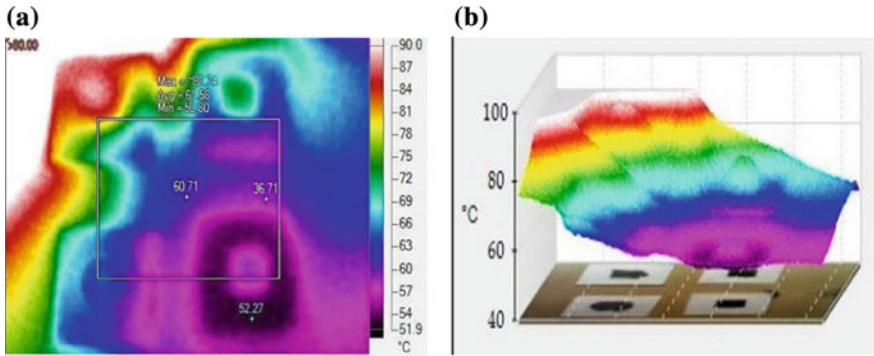


Fig. 8 a FLIR of laminated paper substrate coated with carbon allotropes exposed to infrared source of 200 W, 2000 lm (left); b 3D-IR graph (right)

3.4 Visible Light

The property of light over the prototype was analyzed to understand the nature of the changes caused due to the measured lumens source [25, 22]. The analyses are presented in Figs. 9a, 10a, 9b and 10b.

FLIR of the carbon allotrope-coated copper and FR4 substrates under visible light conditions do not exhibit a significant temperature gradient, the same being 0.60 and 0.80 °C in copper and FR4 substrates, respectively. Thus, antenna behavior could not be expected in this part of electromagnetic spectrum.

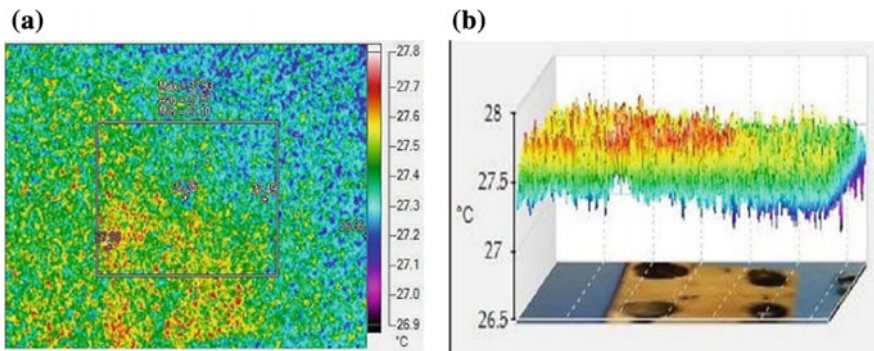


Fig. 9 FLIR of copper substrate coated with carbon allotropes exposed to luminescent source of 0 W (left); 3D-IR graph (right)

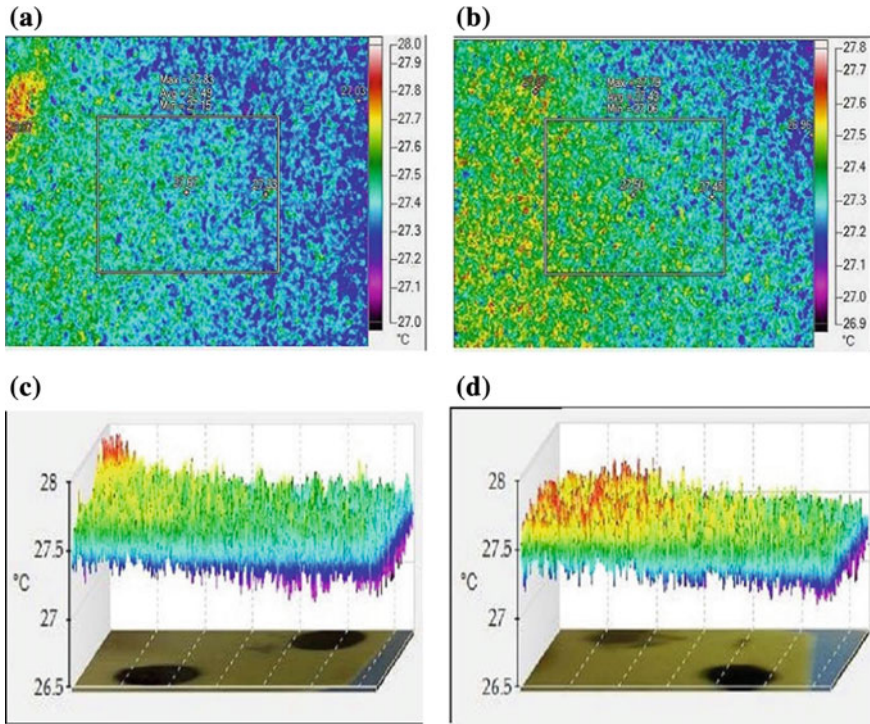


Fig. 10 **a** FLIR of FR4 substrate coated with graphite and activated charcoal exposed to luminescent source of 0 W; **c** 3D-IR graph; **b** FLIR of FR4 substrate coated with graphene and lampblack exposed to luminescent source of 0 W; **d** 3D-IR graph

3.5 Comparison

Even though copper and glass coated with carbon materials show better performance from the temperature distribution shown in Fig. 11 along the principal diagonal of the planar laminar of various carbon allotropes coated substrates which are exposed to different photometric radiations. These materials could not be used as structural material in view of cost and strength. Paper substrate coated with carbon materials can be thought of its application in space, and this has to be improved in view of strength and these are shown in Fig. 11.

3.6 Refrigeration

Refrigeration cooling was carried out at closed cooler facility where the temperature was maintained from 0 to 40 °C to study the property of the antenna materials (carbon allotropes) in that condition. The aspect of aptness of the antennas using

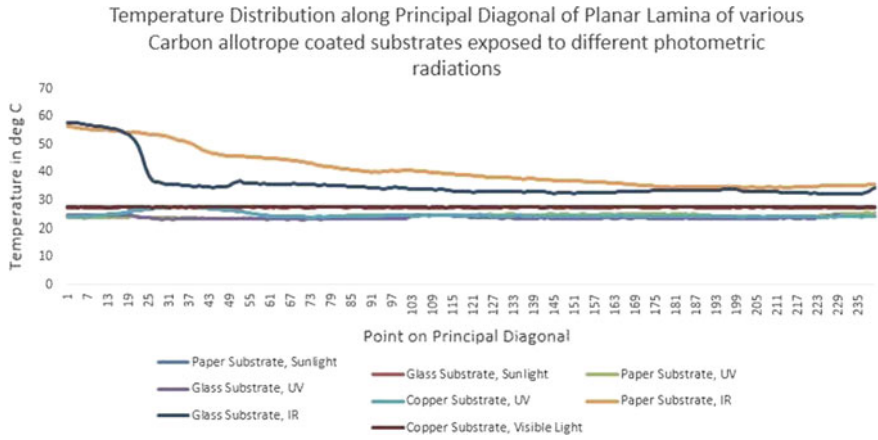


Fig. 11 Temperature distribution along principal diagonal of planar lamina of various carbon allotrope-coated substrates exposed to different photometric radiations. It was trialed and the results are shown in the Fig. 11

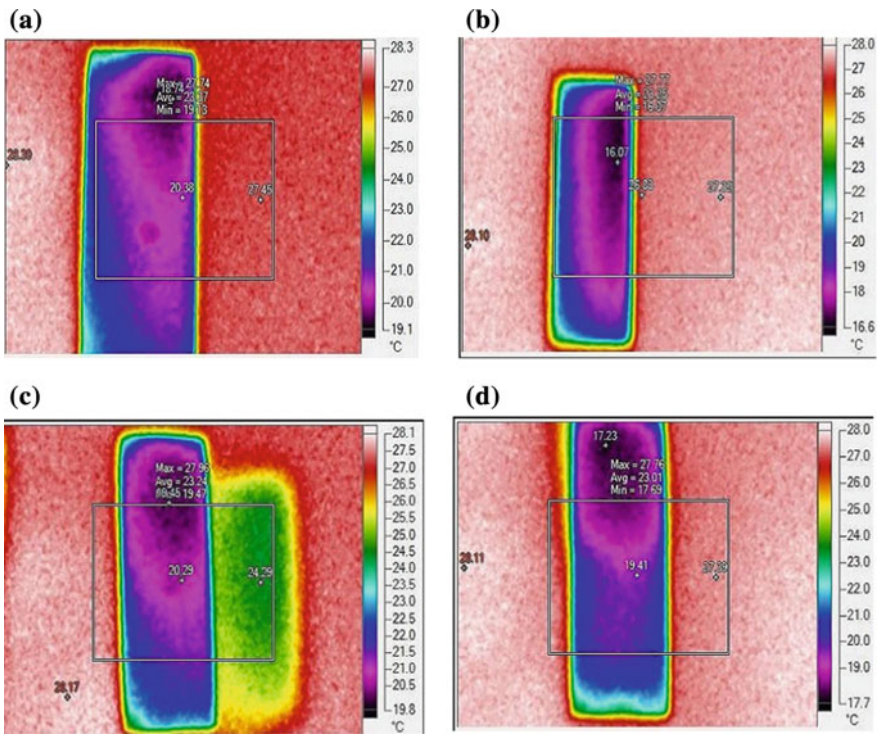


Fig. 12 FLIR of refrigerated microscopic glass slide forced deposited with liquid paraffin dispersed with **a** lampblack, **b** graphite, **c** activated charcoal, **d** graphene

carbon materials in plants which function at sub-zero temperatures in space has been taken into consideration for this study [22, 26–28]. The carbon allotropes dispersed in liquid paraffin, due to the latter's high viscosity, are deposited on microscopic glass slide and then refrigerated for thermal analysis. Figure 12a–d shows the FLIR images of the study. The corresponding 3DIR graphs are shown in Fig. 13a–d.

The graphite and graphene refrigerated samples can be used as antenna materials in view of larger difference in temperature, and these samples will provide better thermo emf if they are cooled to get enough power, and of these samples, graphene is going to serve the purpose as it is evident from Fig. 14 where the temperature distribution of various carbon allotropes subjected to refrigeration is shown and it has got enough strength and is easily amenable for large-scale applications. It was experimented and shown in the Fig. 14.

From the above figures, it is concluded that all the four materials behave in a similar manner. Graphite has got the potentialities to go to temperature of 17.50 °C. On the other hand, all the other materials almost reach 200 °C. Since graphite is not going to be a structural material for space applications in view of cost and strength, graphene will be a preferred material and the other two lampblack and activated charcoal are not amenable as structural materials for space design.

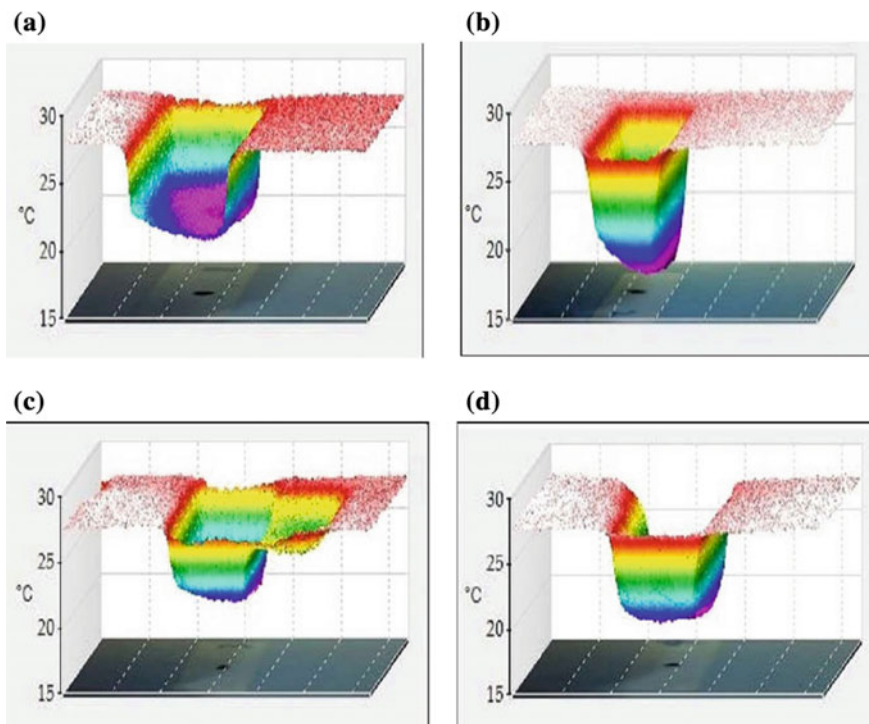


Fig. 13 3DIR graphs of refrigerated microscopic glass slide forced deposited with liquid paraffin dispersed with **a** lampblack, **b** graphite, **c** activated charcoal, **d** graphene

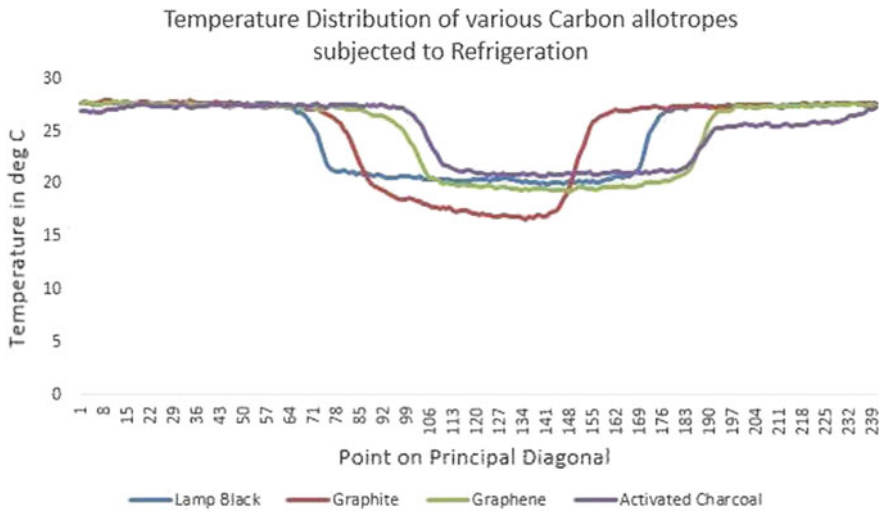


Fig. 14 Temperature distribution of various carbon allotropes subjected to refrigeration

4 Characterization Techniques

4.1 Compound Microscopy

The compound (or) biological microscope is used to analyze the optical properties. Microscope with a resolution of 600–1200× was tried to analyze air gap caused due to surface tension of the solvent in ink mechanism. It is found that surface tension property of ink plays a very important role in antenna fabrication, in the case of using alternate materials [22, 27, 28]. The compound microscopy is shown in Fig. 15a–d.

From the compound microscopic study, it is evident that the surface of graphene is more uniform compared to the other allotropes of carbon. Lampblack has more pores, thus resulting in higher surface area. Graphite, being chemically the repetitive hexagonal layers of graphene held together by van der Waals’ forces, is observed to be the clusters of graphene in a fractal manner. Activated charcoal is more powdery, thus resulting in larger air gap.

4.2 Inverted Metallurgical Microscopy

The single-layer and multilayer printing dye for inkjet printer, gravure printer, and screen printing would result in platelet formation and in non-uniform layering of the component. So, an inverted imaging process of the solutes dispersed in liquid

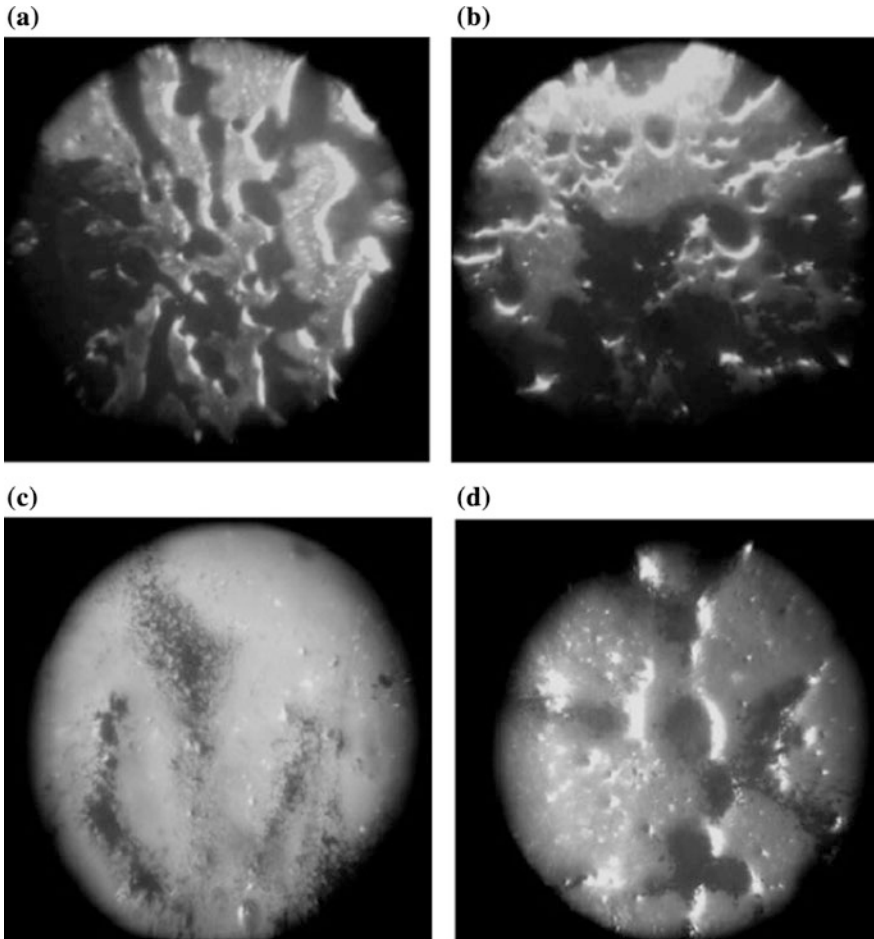


Fig. 15 Compound microscopy of **a** lampblack, **b** graphite, **c** graphene, **d** activated charcoal

paraffin was used to understand the surface porosity and uniformity in the coating of antenna material; the same is depicted in Fig. 16a and 15b–d [29, 22].

From the inverted metallurgical microscopy, it could be inferred that graphite and graphene are multilayered, whereas lampblack and activated charcoal are unilayered.

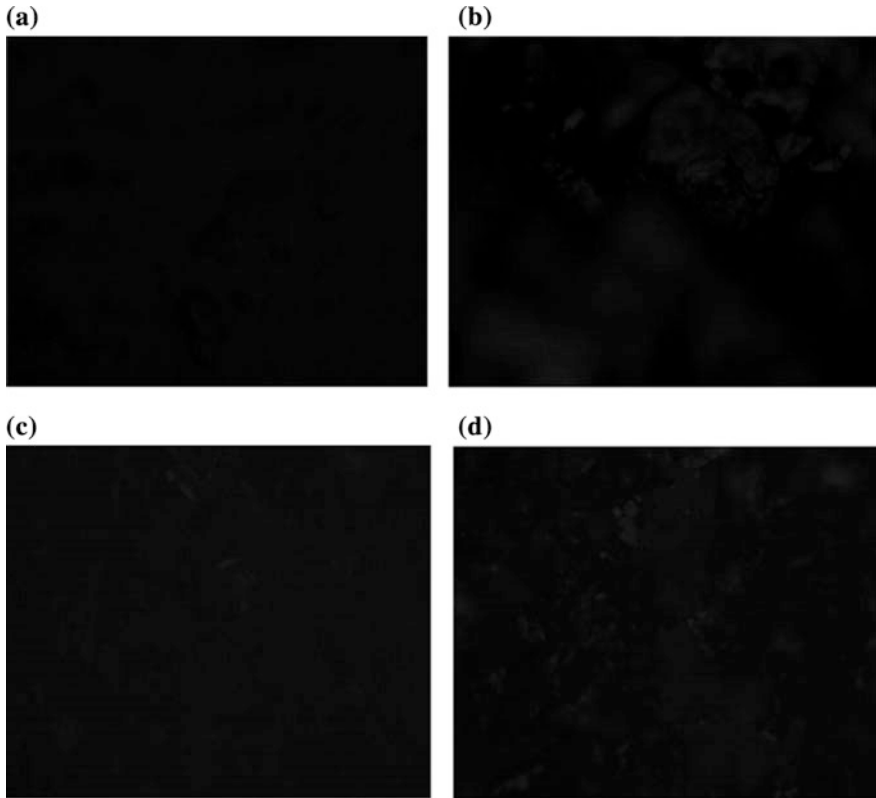


Fig. 16 Inverted metallurgical microscopy of **a** lampblack, **b** graphite, **c** graphene, **d** activated charcoal

4.3 Resistance Measurement

Resistance plays a significant parameter function in surface coating of antenna mechanism and thus, on the uneven thickness of the material air gap in the fabrication and temperature of fabrication. So, the electrical analysis of the liquid paraffin consisting of the dispersion of the carbon allotropes for its resistance due to material is done by four-probe resistance mechanism and is indicated in Table 1 [30, 22]. The area of coating is $10 \text{ mm} \times 10 \text{ mm}$, and the thickness is within 2 mm. The material offering the least electrical resistance would be most suited for applicability in antenna.

From Table 1, it is evident that graphene and graphite, to a considerable extent, are the most suited for antenna applications. Lampblack and activated charcoal are not feasible for antenna, as far as liquid paraffin is the solvent considered.

Table 1 Electrical resistance of carbon allotropes coating

Material	Electrical resistance (Ω)
Lampblack	0.35 M
Graphene	5.6 K
Graphite	11.02 K
Activated charcoal	1.42 M

4.4 Reactive Sampling

Since the solutes (graphene, graphite, lampblack, and activated charcoal) are in the powdered form, a solvent is to be determined for their dissolution [16]. Each allotrope (0.1 g) of carbon is dispersed in 10 ml of selected solvents such as tetrahydrofuran (THF), *N,N*-dimethylformamide (DMF), distilled water, and liquid paraffin, and their solubility studies are done and enumerated in Tables 2, 3, 4, and 5.

Table 2 Solubility of the allotropes of carbon in 99% 1,4-epoxybutane oxacyclopentane [oxolane/THF]

Solute	Inference
Lampblack	Soluble and forms a true solution
Graphene	Soluble and forms a true solution
Graphite	Soluble and forms a true solution
Activated charcoal	Partially soluble and forms a colloid

Table 3 Solubility of the allotropes of Carbon in 99.9% DMF

Solute	Inference
Lampblack	Soluble and forms a true solution
Graphene	Soluble and forms a true solution
Graphite	Partially soluble and forms a colloid; insoluble and forms a suspension upon
Activated charcoal	Digital ultrasonic cleaning for 150 s, forms a colloid

Table 4 Solubility of the allotropes of carbon in oxidane (distilled water)

Solute	Inference
Lampblack	Solute floats on the top of solvent
Graphene	Solute floats on the top of solvent
Graphite	Solute floats on the top of solvent
Activated charcoal	Solute floats on the top of solvent

Table 5 Solubility of the allotropes of carbon in liquid paraffin

Solute	Inference
Lampblack	Insoluble and forms a suspension
Graphene	Insoluble and forms a suspension
Graphite	Insoluble and forms a suspension
Activated charcoal	Insoluble and forms a suspension

5 Conclusion

Glass substrate coated with carbon allotropes will not be a suitable material for antenna in view of low thermomagnetic potential developed during exposure to sunlight. Copper substrate coated with carbon allotropes can be considered as suitable material to be used as antenna material when these are exposed to UV source. Laminated paper substrate coated with carbon allotropes can be considered as suitable material for antenna fabrication if the source of exposure is UV, and these can be used instead of copper substrate since these materials will be cost effective. FR4 substrates coated with graphite and activated charcoal cannot be used as antenna materials for tapping thermomagnetic potential if the source of exposure is UV. Glass substrate coated with carbon allotropes is preferred if the source of exposure is IR. Laminated paper substrate coated with carbon allotropes can be used if the source of exposure is IR. In view of cost and strength, paper substrate coated with carbon materials is preferred to copper or glass coated with carbon materials. Graphite and graphene samples are preferred to the source of cooling is by refrigeration and between these, graphene is better in view of sealing up. Graphene is more uniform compared to other allotropes of carbon. Lampblack is not suitable in view of large porosity. Activated charcoal is more powdery. From the resistance angle, graphene and graphite are suitable materials compared to lampblack and activated charcoal when dispersed in liquid paraffin, and between the former two, graphene is preferred to graphite in view of the lowest resistance. The solvent studies indicate that the solvent must be chosen taking into consideration the nature of the solution needed. The dispersion behavior of the solute in solvent could lead to dissolution and form a true solution or form chunks leading to a colloid or stay in the liquid as a suspension, either floating or sinking based on the relative density.

Acknowledgements The authors would like to acknowledge Dr. Gowthaman Swaminathan—Director R&D, Vel Tech Rangarajan Dr. Sagunthala R&D Institute of Science and Technology; Dr. Radhakrishnan Narayanaswamy—Vel Tech TBI Biowaste Management Laboratory; and Dr. C. Ramesh Kumar—Organic Chemistry Laboratory, for extending their research facilities for prototyping and calibrations.

References

1. Straw, R.D., Severns, R., Beezley, B., Hare, E.: ARRL Antenna Handbook, 18th edn. The American Radio Relay League, Inc., Newington, CT (1998)
2. Llatser, I., et al.: Graphene-based nano-patch antenna for terahertz radiation. *Photon Nanostruct: Fundam. Appl.* (2012). <https://doi.org/10.1016/j.photonics.2012.05.011>
3. Singh, G., Rajni, Marwaha, A.: A review of metamaterials and its applications. *Int. J. Eng. Trends Technol.* **19**(6), 305–310 (2015)
4. Wu, B.-I., Wang, W., Pacheco, J., Chen, X., Grzegorzczuk, T., Kong, J.A.: A study of using metamaterials as antenna substrate to enhance gain. *Prog. Electromagn. Res.* **51**, 295–328 (2005)
5. Hanson, G.W.: Fundamental transmitting properties of carbon nanotube antennas. *IEEE Trans. Antennas Propag.* **53**(11), 3426–3435 (2005)
6. Hao, J., Hanson, G.W.: Infrared and optical properties of carbon nanotube dipole antennas. *IEEE Trans. Nanotechnol.* **5**(6), 766–775 (2006)
7. Song, Lingnan, Myers, Amanda C., Adams, Jacob J., Zhu, Yong: Stretchable and reversibly deformable radio frequency antennas based on silver nanowires. *ACS Appl. Mater. Interfaces* **6**, 4248–4253 (2014)
8. Nikitin, P.V., Lam, S., Rao, K.V.S.: Low cost silver ink RFID tag antennas. In: 2005 IEEE Antennas and Propagation Society International Symposium, IEEE Antennas and Propagation Society International Symposium Digest, vol. 4B, pp. 353–356. IEEE, Washington DC (2005)
9. Boan, B.J., Schwam, M.: Mesh-configured RF antenna formed of Knit graphite fibers. United States Patent, Appl. No.: 46,144, 5 May 1987, Patent Number: 4,812,854, 14 Mar 1989
10. Chen, X., Grzegorzczuk, T.M., Wu, B.-I., Pacheco, J., Jr., Kong, J.A.: Robust method to retrieve the constitutive effective parameters of metamaterials. *Phys. Rev. E* **70**(1), 016608-1–016608-7 (2004)
11. Rappaport, T.S., Sun, S., Mayzus, R., Zhao, H., Azar, Y., Wang, K., Wong, G.N., Schulz, J. K., Samimi, M., Gutierrez, F.: Millimeter wave mobile communications for 5G cellular: it will work! *IEEE Access* **1**, 335–349 (2013)
12. Yilmaz, Turker, Akan, Ozgur B.: On the use of low terahertz band for 5G indoor mobile networks. *Comput. Electr. Eng.* **48**, 164–173 (2015)
13. Nassar, I.T., Weller, T.: An electrically-small, 3-D cube antenna fabricated with additive manufacturing. In: 2013 IEEE Topical Conference on Wireless Sensors and Sensor Networks (WiSNet), IEEE Radio and Wireless Week 2013, pp. 58–60. IEEE, Austin, Texas, USA (2013)
14. Nate, K.A., Hester, J., Isakov, M., Bahr, R., Tentzeris, M.M.: A fully printed multilayer aperture-coupled patch antenna using hybrid 3D/inkjet additive manufacturing technique. In: Proceedings of the 45th European Microwave Conference, 2015 European Microwave Conference (EuMC), 2015 European IEEE, Paris, France (2015)
15. Akbari, M., Khan, M.W.A., Hasani, M., Björninen, T., Sydänheimo, L., Ukkonen, L.: Fabrication and characterization of graphene antenna for low-cost and environmentally friendly RFID tags. *IEEE Antennas Wirel. Propag. Lett.* **15**, 1569–1572 (2015)
16. Paredes, J.I., Villar-Rodil, S., Martínez-Alonso, A., Tascón, J.M.D.: Graphene oxide dispersions in organic solvents. *Langmuir* **24**(19), 10560–10564 (2008)
17. Makeup and Beauty Home. <http://www.makeupandbeautyhome.com/>. Last accessed 2018/01/31
18. Health vit. <https://www.healthvit.com/>. Last accessed 2018/01/29
19. Shaker, G., Safavi-Naeini, S., Sangary, N., Tentzeris, M.M.: Inkjet printing of ultra-wideband (UWB) antennas on paper-based substrates. *IEEE Antennas Wirel. Propag. Lett.* **10**, 111–114 (2011)
20. Zhu, H., Narakathu, B.B., Fang, Z., Aijazi, A.T., Joyce, M., Atashbar, M., Hu, L.: A gravure printed antenna on shape-stable transparent nanopaper. *Nanoscale* **6**, 9110–9115 (2014)

21. Brennan, P.J., Fedor, C., Pausch, G.: Sunlight, UV, & accelerated weathering. *Kunststoffe - German Plastics* **78**(4), 323–327 (1988)
22. Wikipedia. https://en.wikipedia.org/wiki/Main_Page. Last accessed 2018/02/05
23. Pottasch, S.R.: The lower solar corona: interpretation of the ultraviolet spectrum. *Astrophys. J.* **137**, 945–966 (1963)
24. Godbout, S., Guimont, H., Marquis, A., De Foy, C.: A comparison of halogen and incandescent infrared lamps for piglets. *Can. Biosys. Eng.* **45**, 5.15–5.19 (2003)
25. Dexter, D.L.: A theory of sensitized luminescence in solids. *J. Chem. Phys.* **21**(5), 836–850 (1953)
26. Arora, R.C.: Refrigeration and Air Conditioning. PHI Learning Private Limited, New Delhi (2010)
27. Explainthatstuff. <http://www.explainthatstuff.com/>. Last accessed 2018/01/27
28. Howstuffworks. <https://www.howstuffworks.com/>. Last accessed 2018/01/28
29. Chennai Metco. <http://www.chennaietco.com/index.html>. Last accessed 2018/01/02
30. MITOPENCOURSEWARE. <https://ocw.mit.edu/index.htm>. Last accessed 2018/01/30

Progress and Issues Related to Designing and 3D Printing of Endodontic Guide



Ankit Nayak , Prashant K. Jain  and P. K. Kankar 

Abstract In the case of calcified pulp canal, a customized guide is used for the formation of access cavity to remove the infected pulp from pulp chamber; this guided approach of treatment is known as guided endodontic. The accuracy of guided endodontic treatment depends on design and fabrication of the guide. Guide path and support structure are the two essential part of the endodontic guide. The guide path is a hole of specific orientation and diameter, responsible for the orientation of file to follow the pre-decided drilling path during treatment while the support structure of guide will provide grip and placement on the teeth. If there is some deviation between the reference point of guide and teeth, then it will be the cause of the surgical error. So the intent is to fabricate optimally oriented guide path with the detailed negative impression of the tooth crown on the guide, which will be able to perfectly grip and place on the teeth. Cone beam computed tomography (CBCT) of the patient face is used to get anatomical details of the tooth to decide the orientation of guide path. Similarly, the architectural details of teeth captured by intraoral surface scan (SS) data are used to design support structure of guide. CBCT and intraoral SS data are merged to get the combined detail of teeth anatomy and architecture. This combined dataset exported from computational software (CAD software package) to design the endodontic guide. After that the STL model of the designed guide will send for fabrication on additive manufacturing (AM) machine. The endodontic guide comprises of freeform surfaces, negative impression of teeth, and guide path, so it is utterly essential to retain these features after fabrication. However, AM is the prevalent technology for fabrication of customized parts, but due to induced volumetric error, feature loss will occur which may lead drill path deviation and treatment failure. If guide designs for additive manufacturing by keeping some factors (triangulation, slicing, build orientation, nozzle/laser velocity)

A. Nayak (✉) · P. K. Jain · P. K. Kankar
CAD/CAM Lab, Mechanical Engineering Discipline, PDPM Indian Institute
of Information Technology, Design and Manufacturing Jabalpur, Jabalpur,
Madhya Pradesh 482005, India
e-mail: ankitnayak@iiitdmj.ac.in

© Springer Nature Singapore Pte Ltd. 2019
U. Chandrasekhar et al. (eds.), *Innovative Design, Analysis and Development
Practices in Aerospace and Automotive Engineering (I-DAD 2018)*, Lecture Notes
in Mechanical Engineering, https://doi.org/10.1007/978-981-13-2718-6_30

in mind, then feature loss can easily be controlled. The design and fabrication issues for additive manufacturing of endodontic guide along with the recent developments in guided endodontics discussed in this article.

Keywords Additive manufacturing · CAD · Biomedical engineering
Guided endodontics

1 Introduction

Root canal treatment (RCT) is the commonly used dental treatment process to remove the infected pulp. RCT comprises of diagnosis of the infected tooth to know about the infection and anatomy, local anesthesia, opening creation to access root canal, removal of infected tissues, filling and sealing of opening. It has been observed that the RCT is not entirely secure and error-free treatment. Some common types of failures are reported after the treatment [1]. Moreover, treatment will be successful if there will not any type of port treatment abnormality. The success of RCT is based on the different factors, namely comprehensive study of the case [2], selection of proper tool [3–6], filling material and cautious operation [7]. In the same way, failures of treated endodontic depend on the different factors, namely apical percolation, operative error, and error in case selection [1].

The successful RCT is subjected to the selection of correct drilling and filing direction of root canal [2, 3, 8]. Dentists use the radiograph [3] and CBCT [4–7, 9] data to quantify the filing direction for access preparation. In case of calcified root canal [10], it is complicated to find out the optimal file direction, due to the invisibility of the root canal in the radiograph. Risk of root perforation, file fracture, and root fracture are also included in RCT of the calcified root canal.

Deviation of files from the intent axis is one of the causes of clinical accidents [11–13] and post treatment abnormalities. To overcome such type of failure, guided endodontics [10, 14–16] was proposed. For better manual and robotic RCT, it is utterly essential that the file should follow the intended path or axis to avoid root perforation. Researchers working in this area are developing the methodology and technique to design the filing guide for RCT.

Number of researchers [3, 9, 13] concentrated on developing the methodology to design the optimized jigs for RCT to enhance the success rate of treatment. Researchers [10, 14, 15] have also made attempts to design and fabricate their jig for RCT of the calcified tooth, and in order to mechanize RCT, Dong et al. propose the use of the microrobot [17] to enhance the reliability and quality of RCT.

2 Design and Fabrication of Endodontic Guide

Typically four steps are followed for guided endodontics, as shown in Fig. 1.

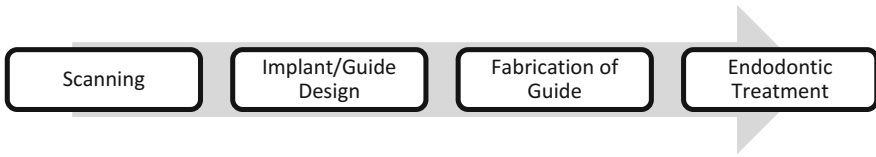


Fig. 1 Typical steps in guided endodontic

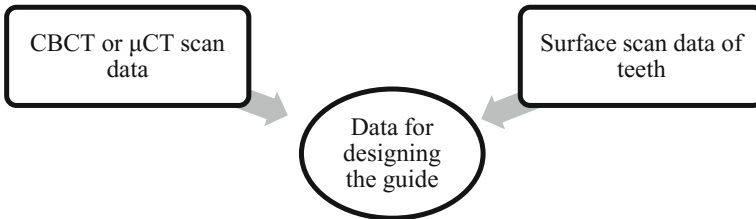


Fig. 2 Data acquisition for guide design

Guided endodontic is all about to move the drill bit and file perfectly on the intent path. Designing of endodontic guide depends on the anatomy of the targeted tooth and the architecture of neighbor tooth. The anatomical detail (CBCT or μ CT) of tooth helps to decide drill path in treatment and is governed by the orientation of guide hole or metal sleeve (in case of customized endodontic guide) [10, 14]. Guide profile was designed with respect to the oral architecture, and it is captured with the help of intraoral surface scanning of mouth [14].

Designing of guide profile and designing of metal sleeve orientation were the two steps for guide design. Designing of guide profile comprises the structural detail of guide so that it can be perfectly fitted on the teeth; while the angular orientation of metal sleeve governed the direction of drilling. CBCT and surface scan data were mutually merged to design the guide as shown in Fig. 2 [10, 14].

Krastl et al. [10] and Zehnder et al. [15] were used implant design tool coDiagnostiXTM for scan matching and design of endodontic guide. The virtual bur was created in coDiagnostiXTM and superimposed on tooth so that it will create the direct access to the apical third of the root canal. Galaxis/Galileos Implant, Sirona Dental Systems software was used by Buchgreitz et al. [14] for designing the drill path and to submerge the surface scan and CBCT data. A virtual sleeve is placed in CBCT data to guide the bur during operation [10, 14, 15]. Merged images create the voxel image of guide along with the bur, and it is exported in the STL format to the 3D printer for fabrication.

Different types of additive manufacturing (AM) process [18] are available for fabrication of endodontic guide. Solid- and liquid-based process like fused deposition modeling (FDM), 3D printing (3DP), selective laser sintering (SLS), laser cladding (LC), laminated object manufacturing (LOM), laser vapor deposition (LVD) were developed. Among these AM processes, stereolithography SL, FDM,

LOM, and SLS are most popular commercially available processes. In FDM process, semi-molten polymeric material is deposited by using extruder head. In 3D printing, parts are manufactured by binding of solid powder particles together. Patterns of different slices are glued together. In SLS, powder material is fused layer by layer and forms a three-dimensional part. In order to develop 3D printed part, generation of geometric model of part is the first step. Then it will convert into tessellated version of the CAD model also called SL format. Tessellation process approximated various surfaces of a CAD model by series of triangular plane surface, and coordinates of vertices of triangles and their surface normal are listed in Standard Tessellation Language (STL) format. In preprocessing step, it is necessary to analyze model for various defects in STL file like flipped triangles, hidden lines, bad edge. In fourth step, the orientation of part deposition will be selected. In fifth step, slicing of tessellated model will be performed, and supports to overhanging features will be provided in step sixth. Slicing of CAD model can be carried out on the tessellated version of the CAD model or directly on a surface of a solid model of the part. In seventh step, path for laser scanning or material deposition are generated. Now the next step is to print the part with very less human intervention. Part fabricated with AM needs post-processing cleaning excess material adheres with the part. Rapid prototyping is subjected to manufacture the prototypes and parts relatively very less time. Krastl et al. [10] and Zehnder et al. [15] used 3D printing (Object Eden 260 V, Material: MED610, Stratasys Ltd., Minneapolis, MN, USA) for fabrication of template and CNC machine for fabrication of sleeve to guide the drill during cavity preparation.

Fabricated endodontic guide was placed on the tooth and check it for reproducibility and correct fitting [15]. The canal was prepared up to the known working length by putting the bur into the metal sleeve. The prepared root canal access was checked with 10-K file under a dental microscope [15].

To check the adequacy of designed guide, postoperative CBCT scan of operated teeth was performed. Pre- and postoperative CBCT scans were superimposed [14, 15] to find out the deviation between planned and performed access cavity. An ex vivo study was also performed on guided endodontic by Buchgreitz et al., and they found that the mean deviation between the drill path and target was significantly lower than 0.7 mm (CI 95%, $P < 0.001$) [14]. Zehnder et al. found that the mean deviation angle between planned and prepared access cavities was 1.81° [15]. The guided access cavity preparation for RCT of calcified pulp canal was performed by Krastl et al., and after 15 months, it found that the patient was clinically asymptomatic [10]. Results of guided endodontic treatment are favorable for the use of the discussed methodology for guide designing, fabrication, and endodontic treatment.

3 Design and Fabrication Issues

The literature reveals typical design issues related to endodontic guide design and fabrication. Compatibility, alignment, and fabrication techniques are important design and fabrication issues which must be considered for designing of endodontic guide.

3.1 Compatibility

The endodontic guide should be compatible with intraoral architecture, and it should be easy to mount on the teeth without affecting the soft tissues of mouth and teeth. The material of guide should not be toxic and should not form the toxic stuff after reacting with saliva and other chemicals used in RCT.

3.2 Alignment

Coronal reference point of guide is the negative impression of coronal reference point of tooth. A minor deviation between the superimposition of coronal reference points will be the cause of RCT failure. In order to prepare root canal access without any deviation, it is proposed to design self-align guide such that the coronal reference point of tooth will automatically be fitted on the coronal reference point of the guide.

3.3 Fabrication Technique

Endodontic guides were fabricated by using additive manufacturing (AM) technique. In AM, the material is deposited layer by layer as per the contour data of respective slice. Slice height (layer thickness) of fabricated part is the machine specific data which affects the surface finish of fabricated part [1], and it is due to the approximation of 3D complex surface data into contour data. Approximated contour data results in the volume deviation in manufactured part, and this induced error is known as volumetric error [8]. Similarly, in the fabrication of endodontic guide, the volumetric error begets feature loss which results in loose grip between teeth and guide shown in Fig. 3.

To visualize the effect of slice height on volumetric error, a guide (cap) of the canine tooth has been designed and fabricated with 0.3 mm slice height on flashforge creator pro FDM machine. It can be analyzed from Fig. 3 that the freeform surfaces of CAD model have been approximated with two-dimensional contours which result in the feature loss in fabricated part.



Fig. 3 a STL model of guide, b image of fabricated guide (FDM) SH = 0.3 mm, c sliced CAD model with slice height = 0.3 mm

The volumetric error can be controlled by fabricating the part using adaptive slicing [19] as shown in Fig. 3. On the other hand, researchers designed and fabricated the endodontic guide with wide support structure [10] to avoid the loose grip between teeth and guide. Post-processing of fabricated guide can also be done in order to achieve the better fit between guide and tooth.

4 Conclusion

From the literature, it is concluded that the guided endodontics approach for the treatment of calcified tooth is safe for clinical practice. Method of guide design is proven by researchers, but still, it is in developing phase. Oral architecture and tooth anatomy were captured in intraoral CBCT scan, but fabrication process and process parameters are also needed to consider to avoid feature loss during guide design. A robust computational method for pulp chamber and root canal allocation is needed to develop for confident guided endodontic treatment.

References

1. Ingle, J.I., Simon, J.H., et al.: Outcome of endodontic treatment and re-treatment. *Ingle's Endod.* **5**, 747–768 (2002)
2. Abou-Rass, M., Frank, A.L., Glick, D.H.: The anticurvature filing method to prepare the curved root canal. *J. Am. Dent. Assoc.* **101**, 792–794 (1980)
3. Oliveira, M.A.V.C., Venâncio, J.F., Raposo, L.H.A., Barbosa Júnior, N., Biffi, J.C.G.: Morphometric evaluation and planning of anticurvature filing in roots of maxillary and mandibular molars. *Braz. Oral Res.* **29**, 1–9 (2015)
4. Nayak, A., Kankar, P.K., Jain, N., Jain, P.K.: Force and vibration correlation analysis in the self-adjusting file during root canal shaping: An in-vitro study. *J. Dental Sci.* (2018). <https://doi.org/10.1016/j.jds.2018.01.002>
5. Garg, H., Grewal, M.S.: Cone-beam computed tomography volumetric analysis and comparison of dentin structure loss after retrieval of separated instrument by using ultrasonic EMS and ProUltra tips. *J. Endod.* **42**, 1693–1698 (2016)

6. Park, P.S., Kim, K.D., Perinpanayagam, H., Lee, J.K., Chang, S.W., Chung, S.H., Kaufman, B., Zhu, Q., Safavi, K.E., Kum, K.Y.: Three-dimensional analysis of root canal curvature and direction of maxillary lateral incisors by using cone-beam computed tomography. *J. Endod.* **39**, 1124–1129 (2013)
7. Estrela, C., Bueno, M.R., Sousa-Neto, M.D., Pécora, J.D.: Method for determination of root curvature radius using cone-beam computed tomography images. *Braz. Dent. J.* **19**, 114–118 (2008)
8. Alharbi, N., Osman, R., Wismeijer, D.: Effects of build direction on the mechanical properties of 3D-printed complete coverage interim dental restorations. *J. Prosthet. Dent.* **115**, 760–767 (2016)
9. Kernen, F., Benic, G.I., Payer, M., Schär, A., Müller-Gerbl, M., Filippi, A., Köhl, S.: Accuracy of three-dimensional printed templates for guided implant placement based on matching a surface scan with CBCT. *Clin. Implant Dent. Relat. Res.* **18**, 762–768 (2016)
10. Krastl, G., Zehnder, M.S., Connert, T., Weiger, R.: Guided endodontics : a novel treatment approach for teeth with pulp canal calcification and apical pathology. *Dental Traumatol.* **32**, 240–246 (2016)
11. González Sánchez, J.A., Duran-Sindreu, F., de Noé, S., Mercadé, M., Roig, M.: Centring ability and apical transportation after overinstrumentation with ProTaper Universal and ProFile Vortex instruments. *Int. Endod. J.* **45**, 542–551 (2012)
12. Yoo, Y.-S., Cho, Y.-B.: A comparison of the shaping ability of reciprocating NiTi instruments in simulated curved canals. *Restor. Dent. Endod.* **37**, 220–227 (2012)
13. Nayak, A., Jain, P.K., Kankar, P.K., Jain, N.: Computer-aided design-based guided endodontic: a novel approach for root canal access cavity preparation. *Proc. Inst. Mech. Eng. Part H J. Eng. Med.* **232**, 787–795 (2018)
14. Buchgreitz, J., Buchgreitz, M., Mortensen, D., Bjørndal, L.: Guided access cavity preparation using cone-beam computed tomography and optical surface scans—an ex vivo study. *Int. Endod. J.* **49**, 790–795 (2016)
15. Zehnder, M.S., Connert, T., Weiger, R., Krastl, G.: Guided endodontics : accuracy of a novel method for guided access cavity preparation and root canal location. *Int. Endod. J.* **47**, 966–972 (2016)
16. Diogenes, A., Ruparel, N.B., Shiloah, Y., Hargreaves, K.M.: Regenerative endodontics: a way forward. *J. Am. Dent. Assoc.* **147**, 372–380 (2016)
17. Dong, J., Ph, D.: WIP: a study on the development of endodontic micro robot. **8**, 26–34 (2006)
18. Taufik, M., Jain, P.K.: Role of build orientation in layered manufacturing: a review. *Int. J. Manuf. Technol. Manag.* **27**, 47–73 (2013)
19. Taufik, M., Jain, P.K.: Volumetric error control in layered manufacturing. In: 19th Design for Manufacturing and the Life Cycle Conference; 8th International Conference on Micro- and Nanosystems, vol. 4, p. V004T06A017. ASME (2014)

Physical and Tribological Behaviour of Dual Particles Reinforced Metal Matrix Composites



V. Mohanavel, K. Rajan, M. Ravichandran, S. Suresh Kumar, M. Balamurugan and C. Jayasekar

Abstract Metal matrix composites (MMCs) have been an active area of research and scientific investigation for past few years, but only in recent times, MMCs have become realistic engineering materials. In the present study, physical and tribological performance of graphite and alumina particulates reinforced AA6351 matrix composites were examined experimentally. These final composites are produced through liquid metallurgy process. To examine the worn surface morphology of the composite was evidently exposed by scanning electron microscope (SEM) technique. The experimental results expose the tribological properties of composites increased with inclusion of filler reinforcements.

Keywords AA6351 alloy · Dual particles · Tribological properties
SEM · Stir casting

V. Mohanavel (✉)

Department of Mechanical Engineering, Kingston Engineering College, Vellore, India
e-mail: mohanavel.phd@gmail.com

K. Rajan

Department of Mechanical Engineering, Dr. MGR Educational and Research Institute University, Chennai, India

M. Ravichandran

Department of Mechanical Engineering, Chendhuran College of Engineering and Technology, Pudukottai, India

S. Suresh Kumar

Faculty of Mechanical Engineering, Panimalar Polytechnic College, Chennai, India

M. Balamurugan

Department of Mechanical Engineering, Anand Institute of Higher Technology, Chennai, Tamil Nadu, India

C. Jayasekar

Department of Mechanical Engineering, Ganadipathy Tulsi's Jain Engineering College, Vellore, India

© Springer Nature Singapore Pte Ltd. 2019

U. Chandrasekhar et al. (eds.), *Innovative Design, Analysis and Development Practices in Aerospace and Automotive Engineering (I-DAD 2018)*, Lecture Notes in Mechanical Engineering, https://doi.org/10.1007/978-981-13-2718-6_31

339

1 Introduction

1.1 Aluminium Matrix Composites and Reinforcements

In recent decades, aluminium-based metal matrix composites (AMCs) are one of the potentially attractive class of materials and are useful for structural, electrical and transportation applications [1]. Particulate reinforced aluminium matrix composites have occupied several sectors such as automobile, aircraft, marine, structural and non-structural applications, and they are commercially viable too. This shows the remarkable combination of mechanical and physical properties of the composite like thermal stability, electric conductivity, low density, wear resistance, high specific strength and stiffness [2, 3].

1.2 Reinforcements Employed in AMCs

The reinforcement material is embedded into a matrix. The reinforcement is generally much stronger and stiffer than the matrix and provides the composite its superior properties.

The following factors must be considered while selecting the reinforcement materials.

- Shape—flake, whisker, fibre, spherical and irregular particulate.
- Size—diameter and aspect ratio.
- Impurities—Si, Na and Ca in sapphire reinforcement.
- Structural defects—voids, occluded material and second phases.
- Inherent properties—strength, modulus and density.

The reinforcements are widely ceramics typically these ceramics being carbides, borides, nitrides and oxides. The reinforcing ingredients in composites offer strength to the composite. The main role of the reinforcement is improving the properties of the composite materials. In addition to strength, they act other additional purposes like corrosion resistance, thermal conduction, resistance to wear, heat resistance as well as rigidity [4, 5]. The reinforcement particles widely used in the forms of particulate, discontinuous fibre and continuous fibre. Several reinforcement contents employed in the composites materials including graphite, carbon and ceramics particulates. Extensively used ceramic particles like borides, nitrides, carbides and oxides. Magnesium, aluminium, silver and copper are the matrix materials employed. Depending on the particular application for the material, the volume percentage of reinforcement in the metal matrix composites varies from 10 to 70.

1.3 Effect on Dual Particles Reinforced AMCs

In the recent decades, most of the researchers have focused mainly on the study of mechanical behaviour of dual particles reinforced hybrid composites. These reinforcements have high elastic modulus, high hardness, high melting points and excellent mechanical properties. Earlier researchers have shown that the addition of lubricating particles in aluminium alloy matrixes in order to enhance its mechanical and tribological characteristics of composites. The dual reinforcing materials have noteworthy influence on the enrichment of the hardness, tensile strength, machinability and wear properties of the produced composites. This dual particles are mainly attributed to the load bearing capacities and pinning effect of the hard ceramic particulates and the solid lubricating effect dominated by selected reinforcement like BN, Gr and Al_2O_3 [6].

Radhika and Subramanian [7] produced $\text{AlSi10Mg}/\text{Al}_2\text{O}_3/\text{Gr}$ AMCs by stir casting route and evaluate the influence of dual particles in the matrix. The hybrid composite consists of AlSi10Mg alloy reinforced with aluminium oxide (3, 6 and 9 wt%) with an constant mass fraction of graphite (3 wt%) particles. The addition of dual particles into aluminium alloy enhanced the mechanical properties and alters the microstructure of the composites. $\text{AlSi10Mg}/9 \text{ wt}\% \text{Al}_2\text{O}_3/3 \text{ wt}\% \text{Gr}$ composite exhibits 25% greater shear strength, 20% higher hardness and 32% superior tensile strength compared to nonreinforced matrix alloy. Wear characteristics of base alloy and proposed composites were evaluated by pin-on disc-test machine. Dry sliding wear behaviour of aluminium alloy reinforced with 9 wt% Al_2O_3 and 3 wt% Gr has maximum wear resistance compared to base matrix alloy.

Alidokht et al. [8] exhibited that the addition of hard silicon carbide particulates to A356 alloy enriched the wear properties of the prepared composites, and the wear resistance of dual particles reinforced composite was further enhanced with the incorporation of MoS_2 as second reinforcement in A356/SiCp composites. The hybrid composites with multiple reinforcements possessed superior tribological properties than base matrix alloy and single reinforced composites.

Veereshkumar et al. [9] stated the experimental results of hardness, compression strength, tensile strength, ductility, yield strength, wear rate and volumetric wear loss of dual particles reinforced hybrid composites. The composites were manufactured through stir casting method, in which 0–4 weight fraction of tungsten carbide (WC) particulates were incorporated into the matrix material in steps of 1 wt% by maintaining the graphite particles to 4 wt% constant. With increasing the amount of WC, the ductility of the composites was decreased and the tensile strength and density were increased. The increase in mechanical properties was noticed with increase in amount of tungsten carbide. Tensile strength of dual particles reinforced composite enhances by an amount of 73% as the content WC particulates increased to 3 wt%.

Umanath et al. [10] made a $\text{AA6061}/\text{Al}_2\text{O}_3/\text{SiC}$ AMC through liquid state process (stir casting) and evaluated the microstructure and wear behaviour of the composite. The effect of volume fraction of dual particles (5 and 15%), applied load

(39.24 and 58.86 N), rotational speed (200 and 400 rpm) and counter face hardness (25 and 35 HRC) on dry sliding wear behaviour of composites examined through pin-on-disc apparatus. The experimental results showed that the wear resistance of the 15% of hybrid composite is superior than that of the 5% composite.

1.4 Stir Casting

The aluminium-based metal matrix composite is the combination of two or more constituents in which one is the reinforcement and the other is the matrix. These materials are extensively prepared through the liquid metallurgy or powder metallurgy techniques. The powder metallurgy technique has its own setbacks, like production cost and size of the components. Therefore, the liquid casting route is the optimum and economical method for production of AMCs. In particular, liquid state stir casting process is the most flexible, simple and economical when compared to other processing methods [11–13].

Baradeswaran and Elaya Perumal [14] manufactured the AA7075/B₄C composites using stir casting technique. K₂TiF₆ (potassium hexafluoro-titanate) inorganic salt added as the flux, to overcome the wetting problem between the matrix and the reinforcement. It was observed from the experimental results that the hardness, tensile strength and compression strength of the final composites increases with increasing B₄C particles, owing to the incorporation of the hard ceramic particles, which serve as the barrier to the motion of dislocation. The flexural strength of the parent alloy and final composite was 349 and 497 MPa, respectively. Wear analysis outcomes exhibit the wear rate is significantly less for the prepared composites compared to nonreinforcement base matrix alloy.

From the above literature survey, it is manifest that very few information is available on dual particles based on hybrid composites. In the present research work, the Al6351 aluminium alloy was reinforced with a different weight fraction of aluminium oxide (4, 8, 12, 16 and 20 wt%) and the constant weight fraction of graphite (3 wt%) to prepare the hybrid composite and compare the physical and tribological properties with unreinforced matrix alloy.

2 Experimental Procedure

Commercially available aluminium AA6351 was selected as the matrix. The calculated weight percentage of 4 wt%Al₂O₃/3 wt%Gr particles was preheated to 400 and 300 °C, respectively. They are then incorporated to the matrix aluminium melt. The matrix-reinforcement melt was stirred continuously at 400 rpm, and it was being continued for 30 min. Then well-mixed melt was poured into the preheated die kept ready for the purpose. The similar procedure is followed to produce the aluminium matrix composites with 8, 12, 16 and 20 wt%Al₂O₃/3 wt%Gr.

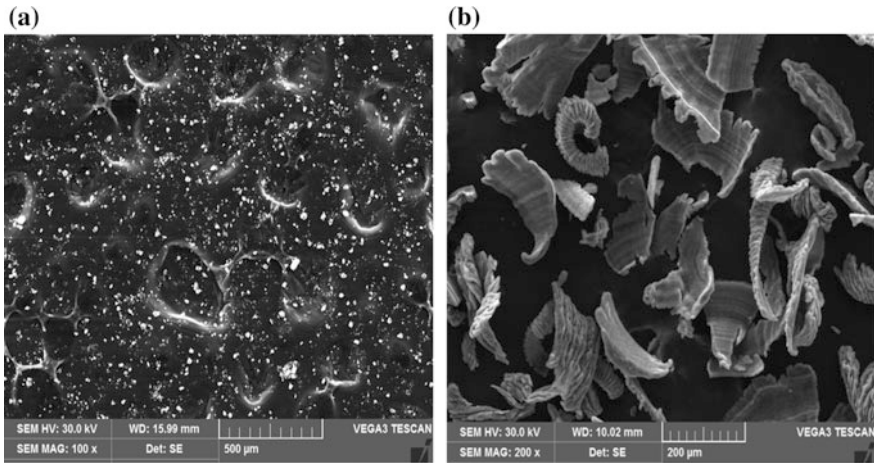


Fig. 1 SEM image of reinforcement particles **a** Al_2O_3 **b** Gr

The SEM micrograph of Al_2O_3 and Gr particles is shown in Fig. 1. The casting facility which was used to manufacture the composite is shown in Fig. 2. The manufactured samples were machined and cut so as to prepare the specimens for different studies. The experimental density of the composite was measured by Archimedeian method by weighing small pieces cut from the produced composites in air and in water. Wear behaviour was analysed using a pin-on-disc wear apparatus. The wear was measured by weight loss, as a difference of weights of the wear pins, before and after wear tests to an accuracy of 0.0001 g. The wear test was conducted at a sliding distance of 1500 m, the normal force of 10, 20 and 30 N and sliding velocity of 1 m/s. The counter disc was made of EN32 steel having a hardness of HRC 60.

3 Results and Discussions

3.1 Density of the Composites

Table 1 shows the density of AA6351/ Al_2O_3 /Gr AMCs. It can be noticed that the density of the composite is lower than the unreinforced matrix alloy. The results showed the decrease in density of the composites from 2.69 to 2.679 gm/cm^3 . The decrease in density may be due to low density of Al_2O_3 (2.71 gm/cm^3) and Gr (2.2 gm/cm^3) than that of AA6351 (2.69 gm/cm^3).



Fig. 2 Stir casting setup

Table 1 Displays the density of AA6351/Al₂O₃/Gr AMCs

Sl. No.	Composition	Density (gm/cm ³)
1	AA6351	2.69
2	AA6351/4%Al ₂ O ₃ /3%Gr	2.6761
3	AA6351/8%Al ₂ O ₃ /3%Gr	2.6769
4	AA6351/12%Al ₂ O ₃ /3%Gr	2.6777
5	AA6351/16%Al ₂ O ₃ /3%Gr	2.6785
6	AA6351/20%Al ₂ O ₃ /3%Gr	2.6793

3.2 Wear Rate of the AA6351/Al₂O₃/Gr AMCs

The influence of weight fraction of dual particles on the wear rate of AA6351/Al₂O₃/Gr composites is shown in Fig. 3. This figure evident that the wear rate of the manufactured composite is linearly decreased with the increase in dual particle addition. The remarkable decrease in wear rate may be due to the superior hardness and good bonding between the matrix and the reinforcement. The AA6351/20% Al₂O₃/3%Gr composites showed the minimum wear rate when compared to the matrix alloy.

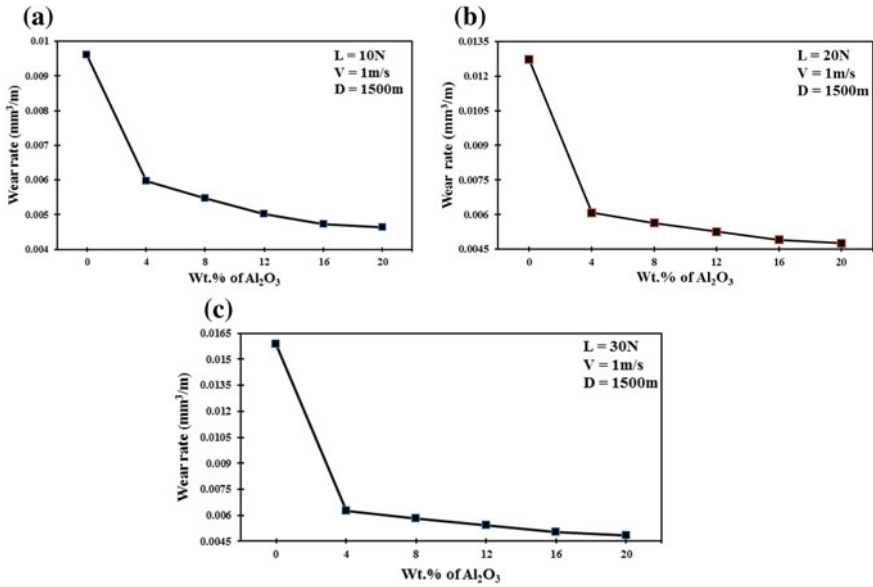


Fig. 3 Wear rate of the AA6351/Al₂O₃/Gr composites

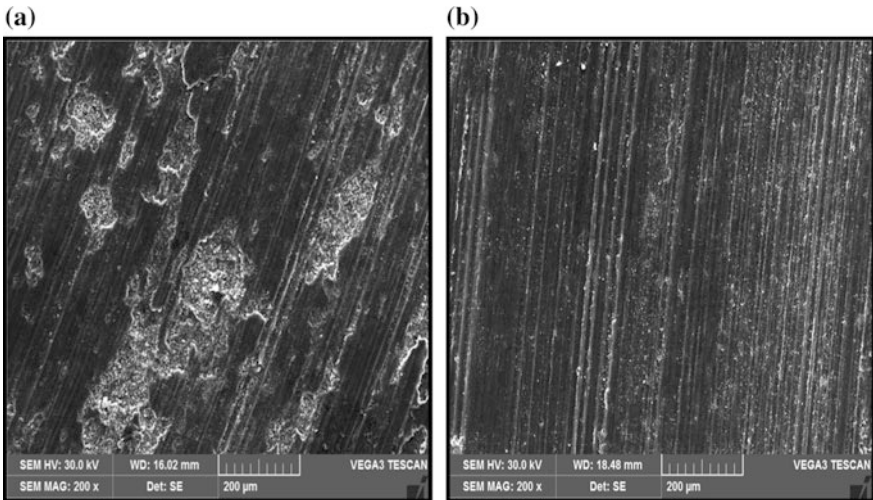


Fig. 4 Worn surface morphology of AA6351 alloy and AA6351/20%Al₂O₃/3%Gr composites

3.3 Worn Surface Morphology of the AA6351/Al₂O₃/Gr AMCs

The SEM micrographs of the worn surface of AA6351 and AA6351/Al₂O₃/Gr composites are depicted in Fig. 4. In Fig. 4a, worn surface of AA6351 alloy shows

the huge amount of plastic flow of material. The worn surface of AA6351/20% Al₂O₃/3%Gr AMCs shows parallel grooves like pattern without the occurrence of plastic flow is depicted in Fig. 4b. It is also noticed that the wear debris is loose in nature and non-adherent with the matrix because of the enhanced hardness of the matrix due to the inclusion of dual particles in the matrix [7, 9].

4 Conclusions

The significant conclusions of the experiment on AA6351/Al₂O₃/Gr composites were as follows: novel AA6351 alloy-based composites containing Al₂O₃/Gr have been efficaciously produced with different mass fraction by stir casting process. The tribological properties of the composites are found superior than that of the base AA6351 matrix alloy. AA6351/20%Al₂O₃/3%Gr AMCs possess the minimum amount of wear when compare to the base alloy.

References

1. Sajjadi, S.A., Ezatpour, H.R., Beygi, H.: Microstructure and mechanical properties of Al-Al₂O₃ micro and nano composites fabricated by stir casting. *Mater. Sci. Eng. A* **528**, 8765–8771 (2011)
2. David Raja Selvam, J., Robinson Smart, D.S., Dinaharan, I.: Microstructure and some mechanical properties of fly ash particulate reinforced AA6061 aluminum alloy composites prepared by compositing. *Mater. Des.* **49**, 28–34 (2013)
3. Mohanavel, V., Rajan, K., Senthil, P.V., Arul, S.: Production, microstructure and mechanical behaviour of AA6351/TiB₂ composite synthesized by direct melt reaction method. *Mater. Today Proc.* **4**(2PA), 3315–3324 (2017)
4. Akbari, M.K., Baharvandi, H.R., Mirzaee, O.: Investigation of particle size and reinforcement content on mechanical properties and fracture behavior of A356-Al₂O₃ composite fabricated by vortex method. *J. Compos. Mater.* **48**(27), 3315–3330 (2014)
5. Kumar, M., Murugan, A.M., Baskaran, V., Hanumanth Ramji, K.S.: Effect of sliding distance on dry sliding tribological behaviour of aluminium hybrid metal matrix composite (AlHMMC): an alternate for automobile brake rotor—a grey relational approach. *Proc. Inst. Mech. Eng. Part J J. Eng. Tribol.* **228**(3), 332–338 (2014)
6. Mohanavel, V., Rajan, K., Arul, S., Senthil, P.V.: Mechanical behaviour of hybrid composite (AA6351 + Al₂O₃ + Gr) fabricated by stir casting method. *Mater. Today Proc.* **4**(2PA), 3093–3101 (2017)
7. Radhika, N., Subramanian, R.: Effect of reinforcement on wear behaviour of aluminium hybrid composites. *Tribology* **7**(1), 36–41 (2013)
8. Alidokht, S.A., Abdollah, Z.A., Soleymani, S., Assadi, H.: Microstructure and tribological performance of an aluminium alloy based hybrid composite produced by friction stir processing. *Mater. Des.* **32**, 2727–2733 (2011)
9. Veereshkumar, G.B., Swamy, A.R.K., Ramesha, A.: Studies on properties of as-cast Al6061-WC-Gr hybrid MMCs. *J. Compos. Mater.* **46**(17), 2111–2122 (2011)
10. Umanath, K., Palanikumar, K., Selvamani, S.T.: Analysis of dry sliding wear behaviour of Al6061/SiC/Al₂O₃ hybrid metal matrix composites. *Compos. B* **53**, 159–168 (2013)

11. Akbari, H.K., Baharvandi, H.R., Shirvanimoghaddam, K.: Tensile and fracture behavior of nano/micron TiB_2 particle reinforced casting A356 aluminum alloy composites. *Mater. Des.* **66**, 150–161 (2015)
12. Ravichandran, M., Dineshkumar, S.: Experimental investigations of Al-TiO₂-Gr hybrid composites fabricated by stir casting. *Mater. Test.* **58**(3), 211–217 (2016)
13. Mohanavel, V., Rajan, K., Ravichandran, M.: Synthesis, characterization and properties of stir cast AA6351-aluminium nitride (AlN) composites. *J. Mater. Res.* **31**(2), 3824–3831 (2016)
14. Baradeswaran, A., Elaya Perumal, A.: Influence of B₄C on the tribological and mechanical properties of Al 7075-B₄C composites. *Compos. B* **54**, 146–152 (2013)

Parametric Optimization of Friction Welding Parameter of Ferritic Stainless Steel and Copper Material Using Taguchi Approach



C. Shanjeevi, S. Velu, J. Thamilarasan and S. Satish Kumar

Abstract Joining of dissimilar materials is increased rapidly in many industry sectors all over the worldwide. Friction welded joint not only gained its property related to mechanical strength but also with absence of defects in weld region. In this study, the weld behavior and its measurement of impact strength is analyzed using friction welding. Friction pressure, upset pressure, and rotational speed are varied using Taguchi's L_9 orthogonal array with constant burn-off length throughout the experiment. The dissimilar materials such as ferritic stainless steel and copper material are welded effectively under each condition. The response made from impact test is ranged from 24 to 46 J/cm². Analysis of variance (ANOVA) showed that the parameter involved under rotational speed is the most influencing factor in determining the impact strength followed by upset and friction pressure. The confirmation test is conducted to validate the optimal parameter and was found to be increase in impact strength with increase in 1.8% than the predicted welding parameter.

Keywords Friction welding · Taguchi · Stainless steel · Copper

C. Shanjeevi (✉) · S. Velu · J. Thamilarasan
Department of Mechanical Engineering, Vel Tech Rangarajan
Dr. Sakunthala R&D Institute of Science and Technology, Chennai, India
e-mail: dr.c.shanjeevi@veltechuniv.edu.in

S. Velu
e-mail: svelu@veltechuniv.edu.in

J. Thamilarasan
e-mail: thamilarasan@veltechuniv.edu.in

S. Satish Kumar
Department of Mechanical Engineering, Velammal Engineering College,
Chennai, India
e-mail: satish_shan@yahoo.com

1 Introduction

Ferritic stainless steels are having high chromium content with less carbon content has good resistance to stress corrosion cracking and greater ductility. Due to this property, ferritic stainless steel has tremendous applications in the field of automotive exhaust system, home appliances, and key components in industries [1, 2]. Moreover, ferritic stainless steel is a cost effective with appropriate candidate for replacing standard grade of austenitic stainless steel. Friction welding is a defect-free welding in the weld interface with less time consumption.

Joining of dissimilar materials such as copper and steel has great importance in applications, although problems exist due to brittle intermetallic compound and high thermal conductivity. Friction welding is taken into account for considering strong welds to minimize this problem [3]. Madhusudan et al. have undergone the experiment on similar and dissimilar weld of stainless steel grades using electron beam and friction welding process [4]. The crack initiation along with the interface of weld region is studied, and impact values are compared with parent material on titanium alloys [5]. The dissimilar joint of stainless steel and copper material is also investigated related to the mechanical properties using optimized parameter [6]. Subsequently, the combination of dissimilar steel material is also analyzed with respect to the properties of microstructure and mechanical behaviors of impact strength and compared to their parent metals [7–9]. The experiment was also investigated to measure the impact properties of dissimilar materials in terms of metallurgical aspects [10].

Based on the study, various researchers have undergone a study on dissimilar combinations. However, the study on impact toughness of ferritic stainless steel and copper joint in particular with finding of optimized parameter is very limited. In this present work, impact study is made with the combination of ferritic stainless steel and copper material by friction welding and its optimal parameters are determined.

2 Experimental Details

The material chosen for welding of ferritic stainless steel and copper is with 24 mm diameter and length 75 mm. The chemical composition of parent materials is listed in Table 1. Friction welding machine is chosen with a maximum speed of 2500 rpm. The flash formations are varied with different welding conditions.

Table 1 Chemical composition of parent materials

Element %	Cr	Ni	Mn	Cu	Fe bal
Ferritic stainless steel	15.79	0.19	1	–	81.44
Copper	–	–	–	99.99	<0.01

Table 2 Experimental factors and their levels

Factors	Levels		
	1	2	3
Friction pressure (MPa)	22	33	43
Upset pressure (MPa)	65	87	108
Rotational speed (rpm)	500	1000	1500

Table 3 Experimental levels and results

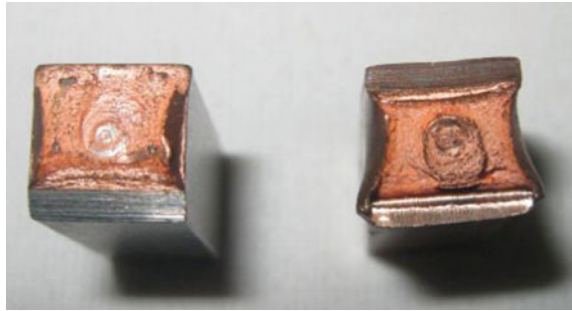
Experimental run	Input parameters			Impact strength (J/cm ²)	S/N ratio value
	Friction pressure (MPa)	Upset pressure (MPa)	Rotational speed (rpm)		
1	22	65	500	42	32.4650
2	22	87	1000	38	31.5957
3	22	108	1500	34	30.6296
4	33	65	1500	36	31.1261
5	33	87	500	37	31.3640
6	33	108	1000	46	33.2552
7	43	65	1000	24	27.6042
8	43	87	1500	40	32.0412
9	43	108	500	39	31.8213



Fig. 1 Physical appearance of welded joint

The friction welding parameters involved are friction pressure, upset pressure, and rotational speed, respectively. The burn-off length of 1.5 mm is kept constant throughout the experiment. Taguchi’s L₉ orthogonal array with three levels and three parameters is chosen for this study is listed in Tables 2 and 3. The physical appearance of joint made through friction welding is shown in Fig. 1, and the fracture made through impact test is shown in Fig. 2.

Fig. 2 Impact tested specimen



3 Results and Discussion

The impact values measured from the friction welded joint were ranged from 24 to 46 J/cm². Based on the measured output, higher the impact value the better the corresponding welding parameter considered. Hence, the impact values are calculated in terms of larger-the-better category under signal-to-noise (*S/N*) ratio in order to determine the optimal parameter which is given in Eq. (1).

Larger the better

$$S/N \text{ ratio}(\eta) = -10 \log_{10} \left(\frac{1}{n} \right) \sum_{i=1}^n \frac{1}{y_{ij}^2} \tag{1}$$

The optimal parameter based on the calculation of response is found with *A*₂, *B*₃, and *C*₁ is listed in Table 4. Based on the mean response, it was noted that with high upset pressure and decrease in rotational speed, the strength made through impact is considered with better the optimal parameter.

The SN ratio based on the main effect plot is shown in Fig. 3, and the predicted value for the effect of impact strength is derived from the following Eq. (2).

$$\hat{\gamma} = \gamma_m + \sum_{i=1}^q (\bar{\gamma}_i - \gamma_m) \tag{2}$$

Table 4 Response table for mean impact strength

Factors	Levels			Max – Min	Rank
	1	2	3		
Friction pressure (<i>A</i>)	38.00	39.67	34.33	5.33	3
Upset pressure (<i>B</i>)	34.00	38.33	39.67	5.67	2
Rotational speed (<i>C</i>)	42.67	37.67	31.67	11.00	1

Larger-the-better is considered for the value of impact strength. Hence the maximum values corresponding to each factor are shown in bold

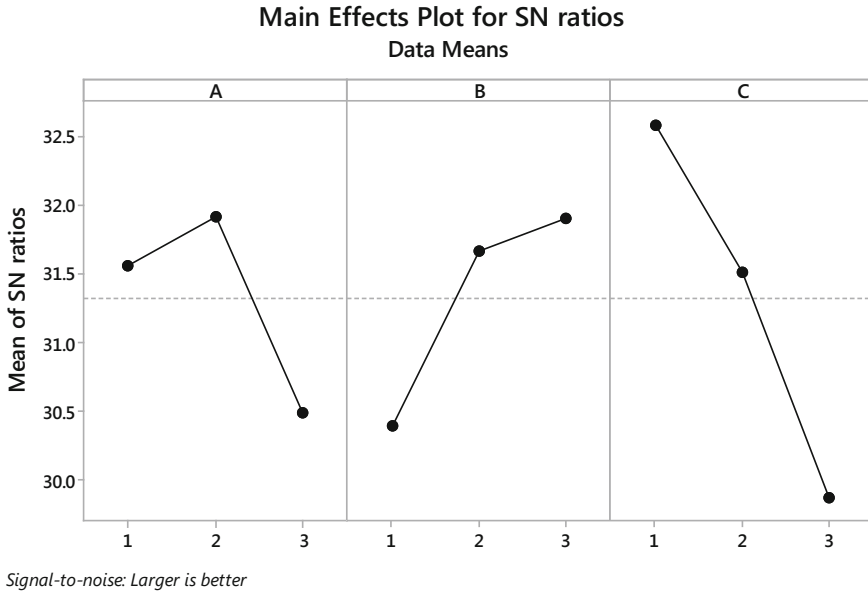


Fig. 3 Main effect plot for S/N ratio

Table 5 Analysis of variance for tensile strength

Welding parameters	DF	SS	MS	F	p-value	% contribution
Friction pressure (A)	2	3.312	1.656	1.93	0.341	16.37
Upset pressure (B)	2	3.925	1.962	2.29	0.304	19.40
Rotational speed (C)	2	11.273	5.636	6.57	0.132	55.73
Error	2	1.716	0.858			8.48
Total	8	20.226				

In order to find the most influencing friction welding parameter, ANOVA test is performed to evaluate the welded joint is listed in Table 5. Based on ANOVA, the most significant parameter affecting friction welding parameter is found with 55.73% of rotational speed followed upset pressure 19.40% and friction pressure 16.37%, respectively. From the *F*-values, it denotes that rotational speed determines the most influenced parameter of welding considered. For the confirmation test, the experiment is conducted with optimal combination of parameters and found to be 48.23 J/cm² as shown in Table 6 with an increase of 1.8% than the predicted mean value observed.

Table 6 Optimal value of welding characteristics

Output characteristic	Optimal parameter	Significant parameters (at 95% confidence level)	Predicted value (J/cm ²)	Experimental value (J/cm ²)
Impact strength	$A_2B_3C_1$	A, B, C	47.35	48.23

4 Conclusions

The combination of ferritic stainless steel and copper material is successfully joined using friction welding. Based on the statistical analysis, impact studies are investigated with the following conclusions.

- Taguchi's L_9 orthogonal array is a predominant method to determine the optimal parameter for identifying the better combination for impact strength.
- The optimal conditions are achieved with maximization of impact strength with a combination of $A_2B_3C_1$. It shows that with decrease in rotational speed and increase in upset pressure, the value of impact strength results to better output.
- The most significant welding parameter is found with rotational speed 55.73% followed by upset pressure 19.40% and friction pressure 16.37%, respectively.

References

1. De Abreu, H., Bruno, A., Tavares, S., Santos, R.P., Carvalho, S.S.: Effect of high temperature annealing on texture and microstructure on an AISI-444 ferritic stainless steel. *Mater. Charact.* **57**, 342–347 (2006)
2. Khorrami, M.S., Mostafaei, M.A., Pouraliakbar, H., Kokabi, A.H.: Study on microstructure and mechanical characteristics of low-carbon steel and ferritic stainless steel joints. *Mater. Sci. Eng. A* **608**, 35–45 (2014)
3. Sahin, M.: Joining of stainless steel and copper materials with friction welding. *Ind. Lubr. Tribol.* **61**(6), 319–324 (2009)
4. Madhusudan Reddy, G., Srinivasa Rao, K.: Microstructure and mechanical properties of similar and dissimilar stainless steel electron beam and friction welds. *Int. J. Adv. Manuf. Technol.* **45**, 875–888 (2009). <https://doi.org/10.1007/s00170-009-2019-6>
5. Ma, T.J., Li, W.Y., Yang, S.Y.: Impact toughness and fracture analysis of linear friction welded Ti–6Al–4V alloy joints. *Mater. Des.* **30**, 2128–2132 (2009)
6. Shanjeevi, C., Satish Kumar, S., Sathiya, P.: Multi-objective optimization of friction welding parameters in AISI 304L austenitic stainless steel and copper joints. *J. Eng. Manuf.* **230**(3), 449–457 (2016)
7. Subhash Chander, G., Madhusudhan Reddy, G., Venugopal Rao, A.: Influence of rotational speed on microstructure and mechanical properties of dissimilar metal AISI 304–AISI 4140 continuous drive friction welds. *J. Iron Steel Res. Int.* **19**(10), 64–73 (2012)

8. Kagaya, C., Kawaguchi, Y., Kato, M.: Impact properties of the weld interface in SCM415/SCM415 friction welded butt joints. *Weld. Int.* **11**(5), 341–345 (1997)
9. Yokoyama, T., Ogawa, K.: Impact tensile properties of 6061 aluminium alloy to SUS 304 stainless steel friction-welded butt joints. *Weld. Int.* **17**(7), 514–523 (2003)
10. Ito, Y., Shindo, T., Ando, H., Udagawa, T.: Improvement of impact strength of friction-welded joints by weld interface shape optimization. *Weld. Int.* **15**(10), 98–804 (2001)

Experimental Investigation on the Thermal Performance of the Light-Emitting Diode (LED) Heat Sinks



A. S. Praveen, Kaipa Sai Chaithanya, R. Jithin and K. Naveen Kumar

Abstract Light-emitting diodes (LEDs) are steadily growing lighting technology due to its reduced energy consumption, high light output and better lifetime as compared to incandescent lighting. However, the heat generated at LED chip during its operation, poses a considerable hurdle in its growth. In LEDs, about 70–85% of total energy is converted as heat, and only remaining 15–30% is harnessed as light energy. Excessive rise in the junction temperature ($>95\text{ }^{\circ}\text{C}$) can cause failure of LEDs. The goal of this study is to experimentally investigate the heat transfer performance of the heat sinks using 16 W LED. The variation of case and junction temperature in LED for different configured heat sinks such as bare and finned heat sink was studied. It was observed that the case temperature (T_c) and junction temperature (T_j) reduced by 37.6 and 28.3%, respectively, for the finned heat sink as compared to the bare heat sink.

Keywords Light-emitting diode (LED) · Heat sink · Thermal resistance
Junction temperature

1 Introduction

Light-emitting diodes (LEDs) are fast growing lighting technology due to its lifetime and energy efficacy. LED is predominantly increasing its origins in the lighting industry. Many of the researchers and governments of various countries are investing a lot in LED technology due to less energy consumption. LED lighting is next generation illumination devices where it has high lifetime when compared to halide lamps and incandescent bulbs. Recently, LED Chip on Board (COB) is commonly used to improve the better optical efficiency. Even though it is having better optical efficiency, there has been an adverse effect of heat produced by this

A. S. Praveen (✉) · K. S. Chaithanya · R. Jithin · K. Naveen Kumar
Department of Mechanical Engineering, Vel Tech Rangarajan Dr. Sagunthala
R&D Institute of Science and Technology, Avadi, Chennai 600 062, India
e-mail: draspraveen@veltech.edu.in

© Springer Nature Singapore Pte Ltd. 2019
U. Chandrasekhar et al. (eds.), *Innovative Design, Analysis and Development
Practices in Aerospace and Automotive Engineering (I-DAD 2018)*, Lecture Notes
in Mechanical Engineering, https://doi.org/10.1007/978-981-13-2718-6_33

semiconductor device at its junction. When the junction temperature increases, there has been a quasi-static increase in its thermal resistance; thereby, it hinders the performance and lifetime of LED. Many researchers reported that 2 °C increment of threshold temperature could cause 10% decrease in its optical illumination efficiency and overall efficiency [1]. In order to counter the effect of rise in its junction temperature, different thermal management solutions such as fins, heat pipes, improved drives, graphite forms, etc., are adopted.

Moon et al. [2] done experimentation with 100 W socket type COB LED lamp to improve the heat dissipation and thermal performance through fixed cooling fin through natural convection with stable operating characteristics. Park et al. [3] prove that large medium (LM) fin type heat sinks show a superior thermal performance. Jang et al. [4] found that the increase in number of fins and length of fins up to some optimistic value increases the heat transfer rate by natural convection. Orientation angles also have a larger effect on heat transfer rate whereas the increases in the angle of orientation cause blockade effect of flow of heat from COB to ambient atmosphere. Lu et al. [5] prove in his research work that high junction temperature leads to low driver voltage, and junction temperature mainly depends on ambient temperature and thermal resistance. Tang et al. [6] observed that the thermal conductivity of conventional heat sink (CHS) much lower than integrated heat sink with vapor chamber (IHSVC). The junction temperature and case temperature are lower than those of CHS at any input current which indicates the cooling capacity of IHSVC is superior to that of CHS. In this paper, the effect of heat transfer in aluminum bare and finned heat sink was studied using 16 W LED package. The variation of case and junction temperature with respect to time was studied.

2 Experimental Procedure

2.1 Material

Aluminum (Al-6063) is taken as a material for heat sinks since it has good thermal conductivity, easily dissipates the heat and economical for LED manufacturing. The bare and finned heat sinks were fabricated using electrical discharge machining (EDM). Figure 1 depicts the dimensions of bare and finned heat sinks in millimeters.

2.2 Experimental Setup

The 16 W LED fixed on the heat sink with the help of thermal interface material (TIM) HT-GY260 which is having thermal conductivity of 1 W/m K. In order to meet the requirements of LED safety and lifetime, different types of heat sinks

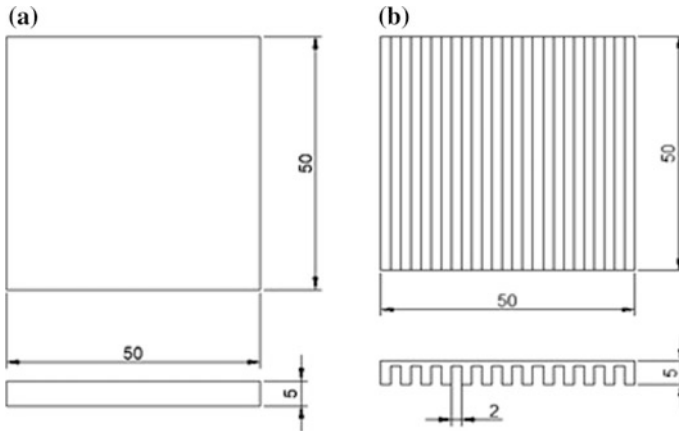


Fig. 1 Dimensions of (a) bare (b) finned heat sinks

have designed, fabricated and studied the temperature variation with respect to case temperature (T_c) which will be noted in the thermocouple. Since junction temperature is a function of case temperature and an internal property of the semiconductor LED, first case temperature values recorded. The experiment was repeated three times, and the average value was reported. The junction temperature can be calculated using Eq. (1) [6].

$$T_j = T_c + (R_{j-c}) \times P_d \tag{1}$$

where T_j is junction temperature, T_c is case temperature, R_{j-c} is thermal resistance between junction of chip and inner heat sink (substrate), and P_d is dissipative power.

Thermal resistance can be calculated by using case temperature, junction temperature and input power using Eq. (2).

$$R = \frac{T_j - T_c(\text{mean})}{Q} \tag{2}$$

where Q is input power, which can be calculated from the product of forward voltage and forward current.

The negative terminal of LED should be connected to the power source/LED driver negative terminal and thermocouple probe to calculate the case temperature (T_c) where this parameter helps us in finding the junction temperature (T_j). Fig. 2 shows the schematic representation of the experimental setup. R_{j-s} is thermal resistance between junction and solder, R_{s-b} is the thermal resistance between the solder and the TIM, R_{b-h} is the thermal resistance between the TIM and heat sink, and R_{h-a} is the thermal resistance between the heat sink and ambient.

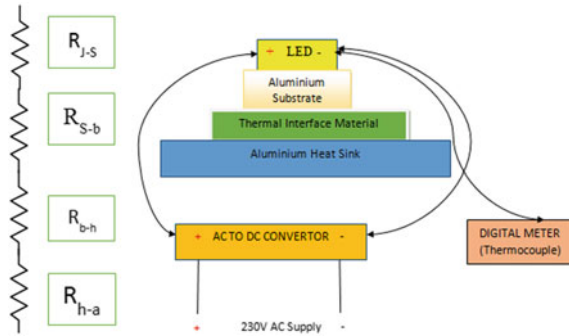


Fig. 2 Schematic representation of experiment setup

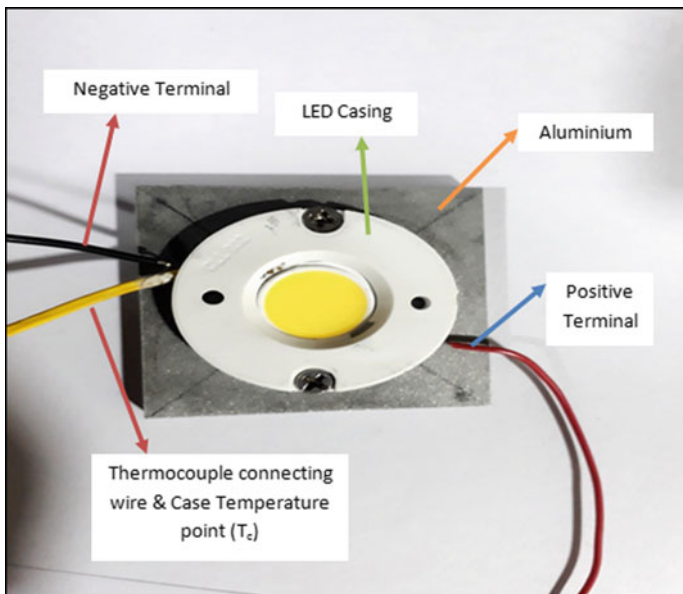


Fig. 3 LED setup in casing with connections to thermocouple

After connecting all the setup case, temperatures will be calculated through thermocouples as shown in Fig. 3. The experiment was conducted for 60 min. The experimentation is done on (a) flat plate of 50 mm × 50 mm × 5 mm thickness and (b) fin type plate of 50 mm × 50 mm and fin thickness of 1 mm and fin height 2 mm and base thickness for 1 mm. In the experiment, a LED driver is used which gives power input of 15.2 W (P_e), forward voltage of 38 V (DC) and forward current of 400 mA. Normally in LED, 75–80% of total energy (DC power supplied) is converting to heat energy due to because of electron accumulation at the junction of semiconductor LED.

3 Results and Discussion

A careful study has been done on LED heat transfer at ambient conditions. The variation of case temperature with time for both the heat sinks was recorded. Figure 4(a) and (b) show the variation of case temperature and junction temperature with time for bare and finned heat sink. It is observed that the case temperatures have been increased for the LED without heat sink with the junction temperature value exceeding the manufacturers threshold point ($T_{j(max)} = 135\text{ }^\circ\text{C}$ —LED manufactures data) which is $180.25\text{ }^\circ\text{C}$ for only 15 s which will inhibits the performance of LED by producing the fumes near the casing. In the case of LED with bare heat sink, case temperatures raised exponentially with respect to time becomes steady state after 30 min reaching temperature of $105\text{ }^\circ\text{C}$ and junction temperature of $135.4\text{ }^\circ\text{C}$ ($>T_{j(max)}$). In the case of finned heat sink, the case temperature has increased up to steady state temperature of $65.5\text{ }^\circ\text{C}$ after 20 min and the corresponding junction temperature is nearly $97\text{ }^\circ\text{C}$ which is less than the threshold limit junction temperature (T_c) of the manufactures LED specifications. Upon doing all these experimental values, thermal images have been taken for heat sink flat plate and heat sink fin type which is shown in Fig. 5(a) and (b). The experimental results show the dependence and importance of free surface area to conduct and dissipate heat. The finned heat sink has more conduction dissipation effect.

In Fig. 5(a) and (b), it is seen that heat distribution along the surfaces has been increasing where it is reaching the surface temperature of $143\text{ }^\circ\text{C}$ maximum which observes the necessity of surface area and optimal design parameters for the LED module. The red indications at the center of LED show the temperature at which at junction of this semiconductor devices starts increasing and overall a time where it will fail the LED module or will reduce the intensity of luminous flux.

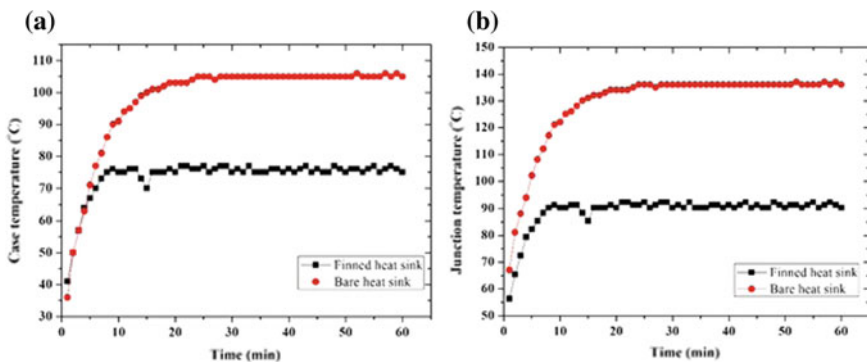


Fig. 4 Variation of (a) case temperature and (b) junction temperature

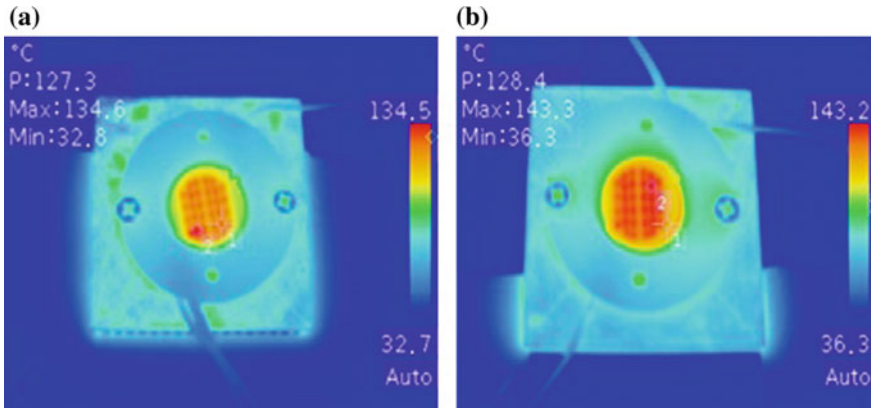


Fig. 5 Infrared image of LED with (a) finned (b) bare heat sink

4 Conclusion

In the present investigation, the effect of heat transfer in LED heat sink was studied using two types heat sinks such as bare heat sink and finned heat sink using 16 W LED. The variation in the case and junction temperature was observed against the time. It is observed that junction temperature of finned was lower as compared with the bare heat sink. This may be due to the increase in surface area for the finned heat sink. This shows the importance of heat sinks designs with optimum parameters and conditions. From the results, it was seen that 37.6% of case temperature and 28.3% junction temperature can be reduced with the usage of finned heat sink as compared to bare heat sink.

References

1. Cho, E.-C., Huang, J.-H., et al.: Graphene based thermoplastic composites and their application for LED thermal management. *Carbon* **102**, 66–73 (2016)
2. Moon, S.-H., Park, Y.-W., Yang, H.-M.: A single unit cooling fins aluminum flat heat pipe for 100 W socket type COB LED lamp. *Appl. Therm. Eng.* **126**, 1164–1169 (2017)
3. Park, D.H., Lee, D.B., et al.: A parametric study on heat dissipation from a LED—lamp. *Appl. Therm. Eng.* **108**, 1261–1267 (2016)
4. Jang, D.S., Yu, S.H., et al.: Optimum design of radial heat sink with a fins with application to LED light bulbs. *Heat Mass Transf.* **71**, 496–502 (2014)
5. Lu, X.-y., Hua, T.-C., et al.: Thermal analysis of high power LED package with heat pipe heat sink. *Microelectron. J.* **42**, 1257–1262 (2011)
6. Tang, Y., Lin, L., Zhang, S., et al.: Thermal management of high power LEDs based on integrated heat sink with vapor chamber. *Energy Convers. Manag.* **151**, 1–10 (2017)

Numerical Modelling of Spiral Cyclone Flow Field and the Impact Analysis of a Vortex Finder



R. Vignesh, D. Balaji, M. Surya, A. Vishnu Pragash and R. Vishnu

Abstract In most industries to remove gas–solid particle separation, cyclone separators are used. Though it plays a major role, the efficiency of the cyclone is not up to mark. In order to fulfil that with the help of CFD platform to investigate the flow field in Stairmand cyclone. For a numerical analysis 3D, grid independent Stairmand cyclone is performed by a Eulerian–Lagrangian model with Reynolds stress model (RSM) is chosen as a turbulence closure model and also grid convergence index study has been carried out. The numerical analysis is carried out with the coupled flow pressure field and two-way coupled particle tracking (stochastic tracking model) which were verified with experimental data. In Stairmand cyclone, the performance is affected by the collision between the circulating gas stream and the gas stream of fresh inlet charge at the junction of inlet duct results in flow short-circuiting (pressure drop). To avoid short-circuiting, spiral inlet is designed for cyclone separator and also study has been extended out numerically for the spiral cyclone separator (SCS) with different vortex finder diameter, length, eccentric position, convergent and divergent type vortex finder.

Keywords GCI · Short-circuiting · Spiral inlet · Vortex finder
RSM

1 Introduction

The Cyclone separators are not new to the industries. This had been using ever since 1800s because of its simplicity. Though its working principle is simple, the mixture of fluid flow moment inside cyclone is turbulent. The analysis of complex turbulent 3D flow with particle-fluid interaction is very difficult either analytically or experimentally. Many researchers tried in past decades, puts great effort to design

R. Vignesh (✉) · D. Balaji · M. Surya · A. Vishnu Pragash · R. Vishnu
Department of Mechanical Engineering, KPR Institute of Engineering and Technology,
Arasur, Coimbatore 641 407, India
e-mail: vignesh.r@kpriet.ac.in

© Springer Nature Singapore Pte Ltd. 2019
U. Chandrasekhar et al. (eds.), *Innovative Design, Analysis and Development Practices in Aerospace and Automotive Engineering (I-DAD 2018)*, Lecture Notes in Mechanical Engineering, https://doi.org/10.1007/978-981-13-2718-6_34

the high efficient cyclone using LDA—Laser Doppler Anemometry and PIV—Particle Image Velocimetry. The complex study of gas–solid flow pattern has been studied experimentally by employing LDA, PDA and Hotwire anemometry, which have not give effective results. Due to rapidly developed computer technologies as in few decades, computational fluid dynamics have great potential to predict the individual fluid–solid flow trajectories, forces on particles and their velocities, which has been proved out successfully by many researchers. Griffiths and Boysan [1] was one of the first, worked on CFD simulation of the cyclone. From their results, it pronounces that $k-\varepsilon$ model is insufficient to simulate swirly flow. To describe the particle diffusion in turbulent flow, Yuu et al. [2] used the both Eulerian and Lagrangian tracking method. The most successful significant particle diffusion tracking is achieved in the stochastic Lagrangian method. Some other various tracking models are Langevin stochastic differential equation model, the stochastic dispersion-width transport model and SPEED model developed by Sommerfeld et al. [3], Litchford and Jeng [4], Chen and Pereria [5]. Wang et al. [6] concluded the reason for short circulating flow is by the collision between inlet gas stream and swirled stream and also states that the collection efficiency mainly depends on particle entering a position. Xiang and Lee [7] and Qian and Zhang [8] numerically investigated the effect of geometric parameters by using RSM turbulence model. Elsayed [9] concludes, between pressure drop and cut-off diameter give the inverse results for an increase in inlet width or height. The cyclone consists of seven geometric parameters which is affecting the efficiency and pressure drop. Many researchers carried out their work in any one of the geometric parameters alone. As of now no literatures available to give the complete geometric analysis of cyclone and also some of the gaps found during the review. In Wang et al. [6] tell about occurring of short circulating flow, in order to rectify this spiral inlet cyclone is designed. In vortex finder, Wang et al. [6] state the geometric centre of cyclone does not coincide with the axis of the output flow so that mixing flow between upward and downward flow occurs which make a region as chaotic flow this leads to the occurrence of pressure drop to resolve this eccentric type vortex finder can be designed and also the effect of convergent and divergent type vortex finder on cyclone performance is not adequate in literatures. This study intended to resolve all the above-stated gaps and needs are fulfilled by CFD simulation.

2 Numerical Setup and Physical Model

The mixture of fluid flow moment inside the cyclone is turbulent; it is very complex to capture the physics of the turbulent flow and also has particle dispersed turbulent flow so it must to study the cyclone with particle-fluid interaction. In FLUENT [10], the dispersed motion of particles is modelled in discrete phase model (DPM). The governing equation [11, 12] involved here are continuity equation $\frac{\partial(\rho u_i)}{\partial x_i} = 0$,

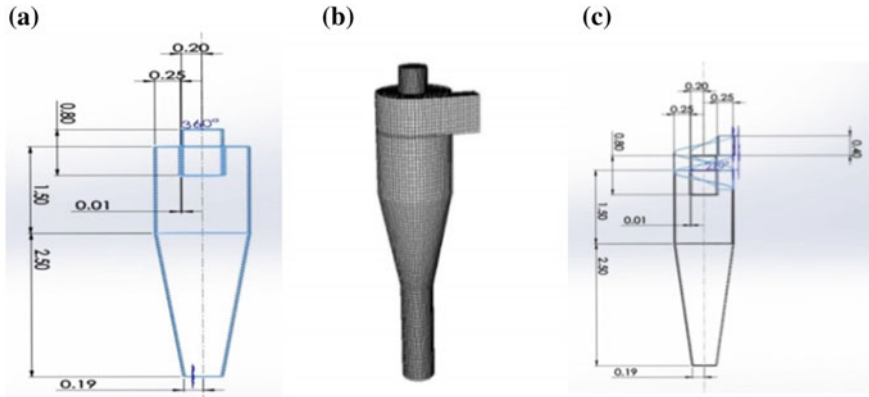


Fig. 1 a Stairmand cyclone schematic diagram; b cyclone with structured hexahedral mesh; c Stairmand cyclone is modified with spiral inlet

Table 1 The geometrical dimensions of the Stairmand cyclone

D	a/D	b/D	D_e/D	S/D	h/D	H/D	B/D
1	0.5	0.2	0.5	0.5	1.5	4	0.375

Momentum conservation equation $\frac{\partial(\rho u_i u_j)}{\partial x_i} = -\frac{\partial p}{\partial x_j} + \frac{\partial}{\partial x_j} \left(\mu_{\text{eff}} \frac{\partial u_i}{\partial x_j} \right) + \frac{\partial}{\partial x_i} \left(\mu_{\text{eff}} \frac{\partial u_j}{\partial x_i} \right) + \rho g_j + F_j$, Governing equations for particle motion $m_i \frac{dV_i}{dt} = F_{D,i} + m_i g + \sum_{j=1}^{n_i} (F_{n,ij} + F_{t,ij})$, Interaction between fluid and solids two-way coupling $\vec{F} = -\sum_{i=1}^n \frac{F_{D,i}}{V_{\text{cell}}}$, $F_D = F_{D0} \alpha^{-(\beta+1)}$, RSM Transport equation $\frac{\partial(\rho u_i' u_j')}{\partial t} + \frac{\partial(\rho u_k u_i' u_j')}{\partial x_k} = B_{ij} + D_{ij} + \Pi_{ij} + E_{ij} + S$. Stress diffusion term (B_{ij}), shear production term (D_{ij}), pressure-strain term (Π_{ij}), dissipation term (E_{ij}). The cyclone taken for simulation is a Stairmand cyclone. The schematic diagram of Stairmand cyclone is displayed in Fig. 1a and their values in Table 1. The Stairmand cyclone is modified with spiral inlet Fig. 1c and also with eccentric vortex, convergent and divergent type vortex finder is displayed in Fig. 2a, b, c. The cyclone fluid domain is discretized with structured hexahedral mesh using ICEM CFD platform Fig. 1b. Three grids are considered coarse 782,673, medium 971,085, finer 1,137,142 cells, respectively.

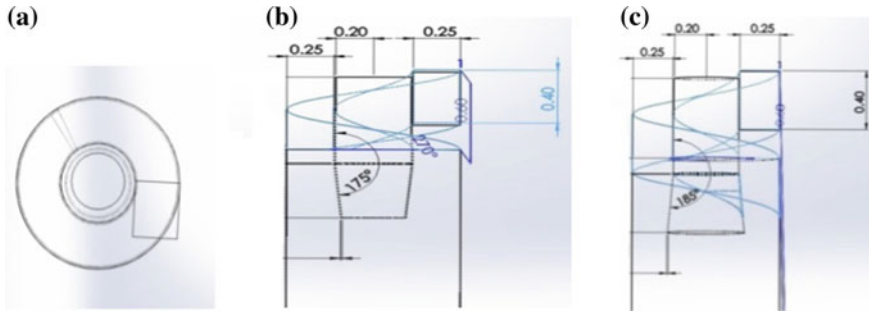


Fig. 2 **a** Stairmand spiral cyclone with eccentricity vortex finder; **b** Stairmand spiral cyclone with convergent vortex finder 5° convergent angle; **c** Stairmand spiral cyclone with divergent vortex finder 5° divergent angle

3 GCI Using Richardson Extrapolation Theory

In the numerical analysis, it is very important to do the grid independence study. Grid independence study has been carried for the cyclone separator so as to find whether the results obtained are independent of the grid. Three grids (coarse, medium, finer) are considered for scrutiny is presented in Table 2.

As seen from computational results, dissimilarity between fine and medium mesh results is less than 5% which is in the range of considerable error occurred during experimentation. However, in order to reduce the uncertainty, spatial error and temporal error obtained for every grid solution. Roache [13] suggests a grid convergence index (GCI) ‘The basic idea is to approximately relate the results from any grid refinement test to the expected results from a grid doubling using a second-order method’. In this study to precisely estimate the order of convergence, three levels of the grid are considered. Table 2 indicates the grid information of Euler number and the cut-off diameter. GCI on the mesh (*m*) is defined as: $g_{12} = \frac{1.25|\sigma_{12}|}{r_{21}^p - 1}$

and $g_{23} = \frac{1.25|\sigma_{23}|}{r_{23}^p - 1}$. Table 3 presents the grid convergence calculation for three grid levels of cyclone using GCI method. From that, results came to know that the monotonic convergence *R*-value is lesser than unity and also the asymptotic range of value is close to unity. If *R* is non-monotonic (*R* > 1) and the asymptotic range is

Table 2 Details of the grid independence study for Stairmand cyclone

Cyclone	<i>N</i>	Eu	<i>X</i> ₅₀
Coarse (a)	782,673	2.89	2.23
Medium (b)	971,085	2.97	2.21
Fine (c)	1,137,142	3.11	2.31
% change (a–c)		8.81%	
% change (b–c)		2.22%	

Table 3 Stairmand cyclone grid convergence calculation using GCI

Model	m_i	N_i	f_i	$r_{i+1,i}$	$\sigma_{i+1,i}$	$e_{i,i+1}$	$g_{i,i+1} \%$	R
Stairmand	Zero grid space (m_0)		3.29					
	Fine mesh (m_1)	1,137,142	3.21	$r_{21} = 1054$	$\sigma_{21} = -0.022$	$e_{12} = -0.070$	$g_{12} \% = 0.509$	0.360
	Medium mesh (m_2)	971,085	3.14	$r_{32} = 1.075$	$\sigma_{32} = -0.061$	$e_{23} = -0.190$	$g_{23} \% = 1.023$	
	Coarse mesh (m_3)	782,673	2.95					

not close to the unity ($\alpha = 1$), the application of Richardson extrapolation method is not appropriate. For this kind of non-monotonic convergence mixed first- and second-order extrapolation technique [14, 15, 16] is used to determine the order of grid convergence error. When the first- and second-order error term are included the GCI written as $g_{12} = \frac{e_{23}(1-r_{21}^2) + e_{12}r_{21}^2(r_{32}^2-1)}{r_{21}(r_{21}-1)(r_{32}-1)(r_{21}r_{32}-1)}$, $g_{23} = \frac{e_{23}(r_{21}-1) - e_{12}r_{21}(r_{32}-1)}{r_{21}(r_{21}-1)(r_{32}-1)(r_{21}r_{32}-1)}$.

The following conclusions have been taken out from the GCI analysis. For the three cyclones, GCI values for the successive grid refinements are in reduced affirm ($GCI_{12} < GCI_{23}$) and monotonic convergence ($R < 1$) is achieved. Hence, this designates that the numerical results for the two variables become independent to cells. Hence, there won't is a much change in solution during the further refinement of the grid. The cyclone is computed with a fine mesh having 1,137,142 cells.

4 Results and Discussion

4.1 Tangential Velocity

To validate the quality of the numerical model, in Fig. 3a comparing its predicted values to the experimental values. In Fig. 3b at the inner or core region, a tangential velocity equal to zero, tangential velocity increases with radius after it reaches the critical point the tangential velocity decreases with radius in the outer region attains zero states at the outer wall this profile called as Rankine type of vortex. From Fig. 4a, another trend noticed here is above the vortex finder, the swirled flow collides with the incoming fresh charges and forms chaotic flow near to the vortex finder which makes to have a sharp decrease in velocity at an entrance region. Hence, it would lead to the cause of short-circuiting flow. To overcome this, spiral shape inlet arrangement is designed for the cyclone as in Fig. 1c. The Fig. 4b results inculcate that creation of short-circuiting flow is avoided. The cons noticed here is due to spiral inlet, the slight decrease in tangential velocity trend is occurring

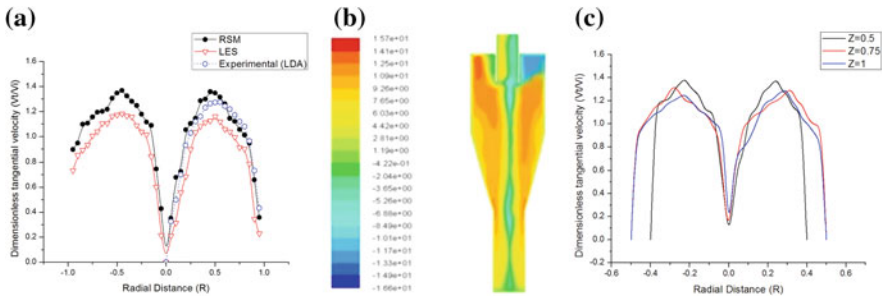


Fig. 3 a Comparison of tangential velocity between LDA experimental results of Boyson [1], LES simulation results of [17] and current RSM simulation results; b contour plot for the time-averaged tangential velocity at 10 m/s for Stairmand cyclone; c radial profile for the time-averaged tangential velocity at different section and inlet velocity 10 m/s

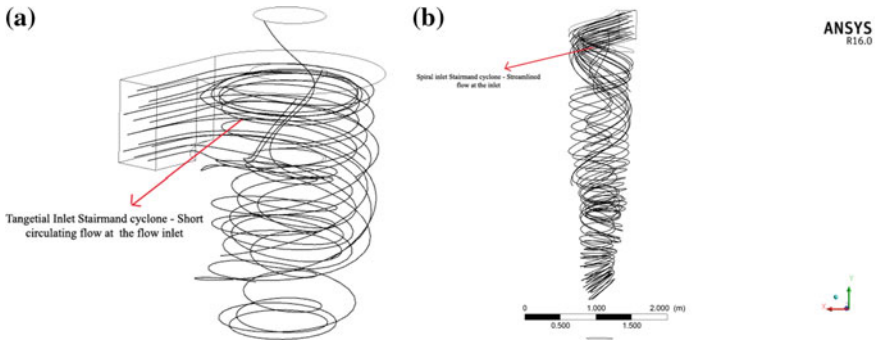


Fig. 4 **a** Trajectories of particle-fluid for tangential inlet Stairmand cyclone and **b** trajectories of particle-fluid spiral inlet Stairmand cyclone

and it increases the radial velocity in the core region of vortex finder which makes the smaller particles are trapped into it. Hence, it ultimately affects our collection efficiency.

4.2 Axial Velocity

From Fig. 5a, the axial velocity plotted over the radial position which pronounces that the axial velocity attains zero at the wall, and it is maximum at the position of maximum tangential velocity. The negative trend of axial velocity is seen in the region above the critical point of tangential velocity (0.25–0.45 position), and the positive trend of axial velocity is seen over the vortex finder due to the more amount of fluid flow on the vortex finder. At the axis of the vortex finder, there is dip in axial velocity gradually reaches to zero and also the geometric centre of

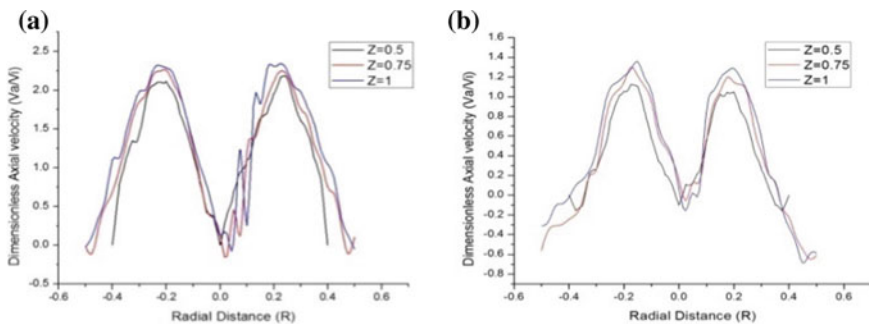


Fig. 5 **a** The time-averaged axial velocity at 20 m/s inlet velocity for spiral Stairmand cyclone and **b** the time-averaged axial velocity at 6% eccentricity vortex finder for spiral Stairmand cyclone

cyclone does not coincide with the axis of the output flow so that mixing flow between upward and downward flow occurs which make a region as chaotic, this is the same scenario occurs in [6] Wang paper. This leads to the occurrence of pressure drop at vortex finder in order to rectify this eccentric type vortex finder arrangement placed in a cyclone.

4.3 Effect of Vortex Finder Diameter and Length

The pressure drop is measured out for a set of different vortex length and vortex diameter. The effect of vortex length (Fig. 6b) and the cyclone with longer S have a reduced turbulent intensity (kinetic energy) level in the inner region; hence, it causes an increase in axial velocity under vortex finder which leads to probability of particles trapped into the vortex finder. The tangential velocity is proportional to centrifugal force which is proportional to the cyclone efficiency, once as an increase in ‘ S ’, the tangential velocity decreases which in turn leads to lower cyclone efficiency. From Fig. 6a, scenario for the effect of vortex finder diameter shows that as a decrease in vortex diameter leads to increase in axial and tangential velocity, the graph trend put into the picture that increases in pressure drop and a decrease in cut-off diameter. From this conclude that pressure drop of cyclone mainly depends on vortex length and vortex diameter, henceforth optimum point is to be selected based on the values obtain as diameter 0.58 m and length in the range of 1.108–1.756 m.

4.4 Effect of Convergent and Divergent Vortex Finder

The cyclone analysis is carried out with three different sizes of convergent, divergent type vortex finder. For a divergent type, the pressure contour plot Fig. 6c

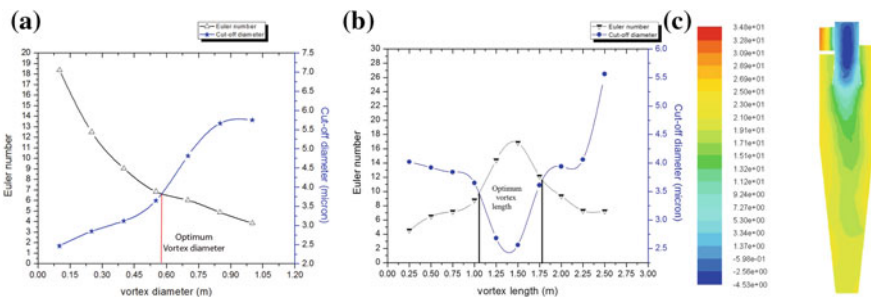


Fig. 6 a Comparison between the effect of vortex finder diameter and b vortex finder height on Eu and cut-off diameter; c contour plot for the time-averaged pressure on spiral Stairmand cyclone with divergent vortex finder for 50 divergent angle

specifies that as increasing the divergence angle at the core region of vortex low-pressure region is formed. This makes the flow to be accumulated in the core region without reaching the bottom of the cyclone due to this more trapping of particles take place and sends out through the vortex outlet. Therefore, it decreases the cyclone collection efficiency. For convergent type, when there is a decrease in convergence angle the low-pressure region occurs at the leading convergent section. Due to the convergent section trapping of a particle in vortex outlet is restricted, this makes an increase in collection efficiency.

5 Conclusion

The identified problem had been addressed with the help of introducing spiral flow to the Stairmand cyclone separator that had been evaluated to ensure the efficiency using numerical analysis. The following outcomes are derived from the analysis are: short-circuiting of flow in the tangential inlet cyclone had been eradicated using a spiral inlet cyclone. Formation of chaotic flow under the vortex finder is being addressed with the offset placement of vortex finder; this leads to dilution of chaotic flow and the optimum eccentricity point that has been identified at 4%. The pressure field study reveals that the increase in gas velocity leads to increase in pressure drop. The geometrical analysis for the spiral cyclone separator is based on vortex diameter and length. So that had been optimized diameter 0.58 m and length in the range of 1.108–1.756 m with respect to Euler's number and cut-off diameter. The flow field study of divergent vortex finder reveals that the decrease in collection efficiency of the cyclone, trend get reversed while using convergent vortex finder.

References

1. Griffiths, W.D., Boysan, F.: Computational fluid dynamics (CFD) and empirical modeling of the performance of a number of cyclone samplers. *J. Aerosol Sci.* **27**(2), 281–304 (1996)
2. Yuu, S., Yasukouchi, N., Hirose, A.: Particle turbulent diffusion in a dust laden round. *AIChE J.* **24**, 509–519 (1978)
3. Sommerfeld, M., Kohnen, G., Ruge, M.: Some open questions and inconsistencies of Lagrangian particle dispersion models. In: Proceedings of Ninth Symposium on Turbulent Shear Flows, Kyoto, Japan, Paper 5.1 (1993)
4. Litchford, R.J., Jeng, S.M.: Efficient statistical transport model for turbulent particle dispersion in sprays. *AIAA J.* **29**, 1443–1451 (1991)
5. Chen, X.Q., Pereria, J.C.F.: Efficient computation of particle dispersion in turbulent flows with a stochastic-probabilistic model. *Int. J. Heat Mass Transf.* **40**(8), 1727–1741 (1997)
6. Wang, B., Xu, D.L., Chu, K.W., Yu, A.B.: Numerical study of gas-solid flow in a cyclone separator. *Appl. Math. Model.* **30**, 1326–1342 (2006)
7. Xiang, R.B., Lee, K.W.: Numerical simulation of flow patterns in cyclones of different cone dimensions. *Part. Syst. Charact.* **22**(3), 212–218 (2005)

8. Qian, F., Zhang, M.: Effects of the inlet section angle on the flow field of a cyclone. *Chem. Eng. Technol.* **30**(11), 15 (2007)
9. Elsayed, K., Lacor, C.: The effect of cyclone inlet dimensions on the flow pattern and performance. *Appl. Math. Model.* **35**, 1952–1968 (2011)
10. Fluent: FLUENT 6.3 user's guide. Fluent Incorporated, Lebanon (2006)
11. Gheshlaghi, M.E., Goharrizi, A.S., Shahrivar, A.A.: Simulation of a semi-industrial pilot plant thickener using CFD approach. *Int. J. Min. Sci. Technol.* **23**(1), 63–68 (2013)
12. Di Felice, R.: The voidage function for fluid-particle interaction systems. *Int. J. Multiph. Flow* **20**, 153–159 (1994)
13. Roache, P.J.: Perspective: a method for uniform reporting of grid refinement studies. *J. Fluids Eng.* **116**(3), 405–413 (1994)
14. NASA: NPARC Alliance verification and Validation, Examining Spatial (Grid) Convergence. <http://www.grc.nasa.gov/WWW/wind/valid/tutorial/spatconv.html>
15. Roy, C.J., McWherter-Payne, M.A., Oberkampf, W.L.: Verification and validation for laminar hypersonic flowfields. AIAA Paper, pp. 200–2550 (2000)
16. Roy, C.J.: Grid convergence error analysis for mixed-order numerical schemes. AIAA Paper, pp. 2001–2606 (2001)
17. Boyson, F., Ewan, B.C.R., Swithenbank, J., Ayers, W.H.: Experimental and theoretical studies of cyclone separator aerodynamics. *ICHEME Symp. Ser.* **69**, 305–320 (1983)

Lattice Boltzmann Simulation of Double-Sided Deep Cavities at Low Reynolds Number



Balashankar Kesana, Vikas V. Shetty and D. Arumuga Perumal

Abstract Lattice Boltzmann method (LBM) has been created as an option computational technique conversely with conventional computational fluid dynamics (CFD) strategies. In the present work, the fluid flow of the two-dimensional low Reynolds number flow in a rectangular cavity with two opposite moving lids and different aspect ratios (depth-to-width ratios) is examined using LBM. The impacts of aspect ratio shifting from 1.2 to 10 on vortex structure in the cavity were watched. The streamline patterns were displayed in detail. As the perspective proportion is steadily expanded from 1.2, the stream structure creates the longitudinal way of the cavity and the quantity of vortices step by step increments with the expanding viewpoint proportion. The advancement of bigger external vortices is from the centre of the cavity and observed stream patterns were symmetric about the cavity centre at various proportion.

Keywords Lattice Boltzmann method · Finite difference method
Aspect ratio · *D2Q9* model

1 Introduction

The Lattice Boltzmann method (LBM) is one of the computationally productive strategies that advanced as a class of CFD procedures utilized for fathoming complex fluid frameworks and warmth exchange issues [1]. LBM has progressively pulled in the light of a legitimate concern for analysts in computational fluid dynamics to take care of testing issues of modern and scholarly significance. Dissimilar to fathoming the customary Navier–Stokes conditions, LBM models the fluid as an accumulation of invented particles and tackles the discrete Boltzmann condition over a discrete grid work [2]. LBM has a few amazing points of interest

B. Kesana · V. V. Shetty · D. Arumuga Perumal (✉)
Department of Mechanical Engineering, National Institute of Technology Karnataka,
Surathkal, Mangalore 575 025, India
e-mail: perumal@nitk.edu.in

© Springer Nature Singapore Pte Ltd. 2019
U. Chandrasekhar et al. (eds.), *Innovative Design, Analysis and Development Practices in Aerospace and Automotive Engineering (I-DAD 2018)*, Lecture Notes in Mechanical Engineering, https://doi.org/10.1007/978-981-13-2718-6_35

over other ordinary CFD systems including, however, not restricted to in managing complex limit conditions and coordinating tiny connections [3].

The stream in a rectangular cavity includes numerous mind-boggling stream wonders, for example, unique composes and sizes of vortices, bifurcation, change and turbulence [4]. This issue of stream development in lid-driven depression fills in as benchmark problem which is generally used to check the adequacy of as good as ever numerical techniques, thus it is a magnificent issue to apply the fundamentals of Lattice Boltzmann strategy that were learnt and furthermore increase clear bits of knowledge into how the cross-sectional Boltzmann technique really works. The two-dimensional enduring stream in a rectangular cavity can be driven by one or a couple of interpreting lids. The cavity stream with a solitary moving top has been contemplated widely.

Examinations about the vortex structure in a two-sided lid-driven rectangular cavity have been directed, yet to a considerably lesser degree [5]. Investigation of feeds stream in a square depression with the tops moving in inverse ways demonstrated that the stream design was symmetric about the centre of the cavity, which is additionally apparent from the streamline plots produced for different Reynolds number and aspect proportions.

2 Methodology and Validation

In the LBM, the first order equation is discretized by finite difference technique. In the present work, the customary single-relation time (SRT) show is utilized. In active hypothesis, it is planned as [1]

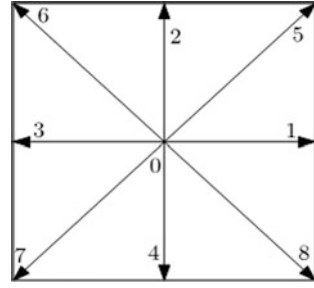
$$f_i(\mathbf{x} + c_i \Delta t, t + \Delta t) - f_i(\mathbf{x}, t) = -\frac{1}{\tau} \{f_i(\mathbf{x}, t) - f_i^{\text{eq}}(\mathbf{x}, t)\} \quad (1)$$

where f_i is the molecule dispersion work, c_i is the molecule speed in the i th direction, $f_i^{\text{eq}}(\mathbf{x}, t)$ is the balance dissemination work at x, t and τ is the unwinding time. In incompressible fluid stream, unwinding time is registered in connection to the consistency of the liquid in the light of the continuum supposition. The cross-sectional show decided for our work is the $D2Q9$ square lattice (Fig. 1) which has nine discrete speeds. In this model, every node has eight neighbours associated with eight connections. The surrounding streaming particles on a node move to the neighbouring cross section along these connections in a period step.

The discrete particle velocities are defined as, [1].

$$c_i = \begin{cases} (0, 0), & \text{if } i = 0 \\ \cos\left(\frac{\pi(i-1)}{4}\right), \sin\left(\frac{\pi(i-1)}{4}\right) & \text{if } i = 1, 2, 3, 4 \\ \sqrt{2} \cos\left(\frac{\pi(i-1)}{4}\right), \sqrt{2} \sin\left(\frac{\pi(i-1)}{4}\right) & \text{if } i = 5, 6, 7, 8 \end{cases} \quad (2)$$

Fig. 1 $D2Q9$ square lattice model



A suitable equilibrium function has been proposed by Mohammad [1] as,

$$f_i^{(eq)} = \rho w_i \left[1 + \frac{3(\mathbf{c}_i \cdot \mathbf{u})}{c^2} + 4.5 \frac{(\mathbf{c}_i \cdot \mathbf{u})^2}{c^4} - 1.5 \frac{(\mathbf{u} \cdot \mathbf{u})}{c^2} \right] \quad (3)$$

The lattice weights are given by $\omega_0 = 4/9, \omega_1 = \omega_2 = \omega_3 = \omega_4 = 1/9, \omega_5 = \omega_6 = \omega_7 = \omega_8 = 1/36$. The naturally visible properties of the fluid, for example, thickness ρ and force $\rho \mathbf{u}$ are characterized as the velocity moments of the distribution function f_i as takes after:

$$\rho = \sum_{i=0}^N f_i, \quad \rho \mathbf{u} = \sum_{i=0}^N f_i \mathbf{c}_i. \quad (4)$$

Boundary conditions assume an extremely key part in any numerical answer for an issue. For instance, think about the association of the fluid with top wall as $f_7 = f_5, f_4 = f_2, f_8 = f_6$. Two-dimensional lid-driven square cavity with sides of length L is considered. The top wall is moving in positive x heading. The cavity is loaded with a Newtonian fluid with consistent thickness ν and steady thickness ρ . The top wall is moving in positive x -axis. The cavity is loaded with a Newtonian fluid with steady thickness ν and consistent thickness ρ . The simulation has been performed numerically utilizing the LBM for Reynolds number of 100 and it has been approved with the observations of Ghia et al. [6]. Lattice estimate utilized for computation is 129×129 , and error convergence criteria are 1×10^{-6} . The speed profiles are approved with standard consequences of Ghia et al. [6] and are plotted as shown in Fig. 2.

3 Results and Discussion

The outcome got for the instance of against parallel top driven cavity with Reynolds number $Re = 10$ and top velocity $u = 0.1$ for top lid and $u = -0.1$ for bottom lid for perspective proportions differing from 1.2 to 10 are delineated (Figs. 3, 4 and 5).

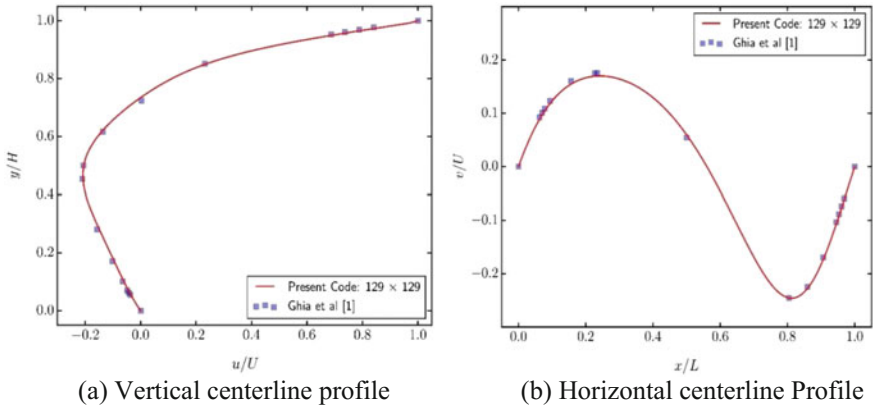


Fig. 2 Validation of the $Re = 100$ centreline profiles against Ghia et al. [6]

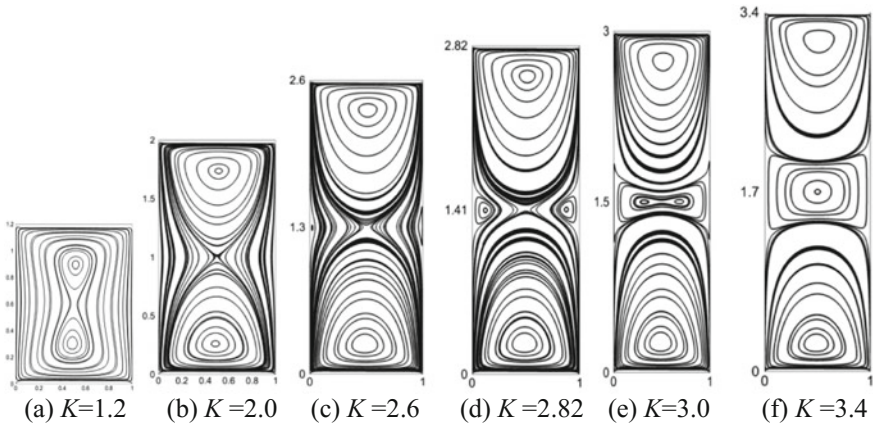


Fig. 3 Streamline pattern for Reynolds number $Re = 10$ for different proportions of aspect ratios. **a** $K = 1.2$, **b** $K = 2.0$, **c** $K = 2.6$, **d** $K = 2.82$, **e** $K = 3.0$, **f** $K = 3.4$

Figure 3a, b separately demonstrate the stream designs where the $K = 1.2$, $K = 2.0$ it can be seen from that the cavity's centre is a saddle point and two sub-eddies are available with their centres situated in the vertical centreline of the cavity. As the perspective proportion K builds, the sub-eddies develop and centres near the cavity's top and bottom walls. At $K = 2.82$ indicates two sub-eddies and formation of two disengaged side eddies. As K value raised, the side eddies develop and approach the central point of the cavity.

At K marginally more prominent than 2.82, two separated side eddies meet with each other at the inside saddle point for this situation the cavity centre and form into a couple of transverse sub-vortices. As K is increased past this esteem, the focuses of transverse sub-vortices approach the central point of depression and the

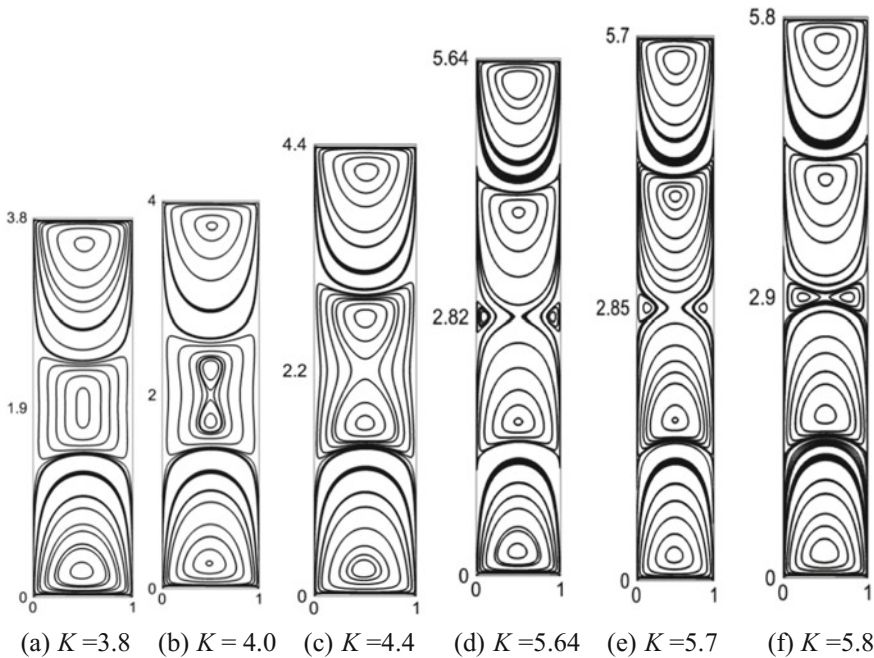


Fig. 4 Streamline pattern for Reynolds number $Re = 10$ for different proportions of aspect ratios. **a** $K = 3.8$, **b** $K = 4.0$, **c** $K = 4.4$, **d** $K = 5.64$, **e** $K = 5.7$, **f** $K = 5.8$

longitudinal sub-vortexes are isolated into two external huge vortexes (Fig. 3e where the $K = 3.0$). As K incremented further, the sub-vortexes fixates lying on the centreline of the cavity approach the central point of cavity and combine to frame a centre (see Fig. 3f). Now the third huge vortex is finished between the other two and there are three vast eddies now involving the cavity. Expanding the aspect value to higher esteems, the large eddy situated in the centre locale of the cavity develops into a couple of sub-vortexes with the centres lying on the vertical centreline of the cavity (Fig. 4b–d). At much more noteworthy estimations of view-point proportions, a couple of new side vortexes shows up again in the centre locale by each side divider (Fig. 4d, e). At marginally higher K , two side eddies touch the cavity’s centre and are transformed into transverse sub-swirls. In this way, the transverse sub-whirlpools isolate the longitudinal sub-vortexes into two external substantial eddies (Fig. 4f). As K is expanded further, the sub-vortexes union and now the streamline design is constituted by five extensive eddies (Fig. 5a, b). As K increments advance a couple of new longitudinal sub-vortexes merge (Fig. 5c, d). Furthermore, with expanding perspective proportion, a couple of new side vortexes is again developed in the centre locale beside each side divider which later approach the cavity focus and are transformed into transverse sub-vortexes. Thusly, the transverse sub-vortexes isolate the longitudinal sub-eddies into two external huge

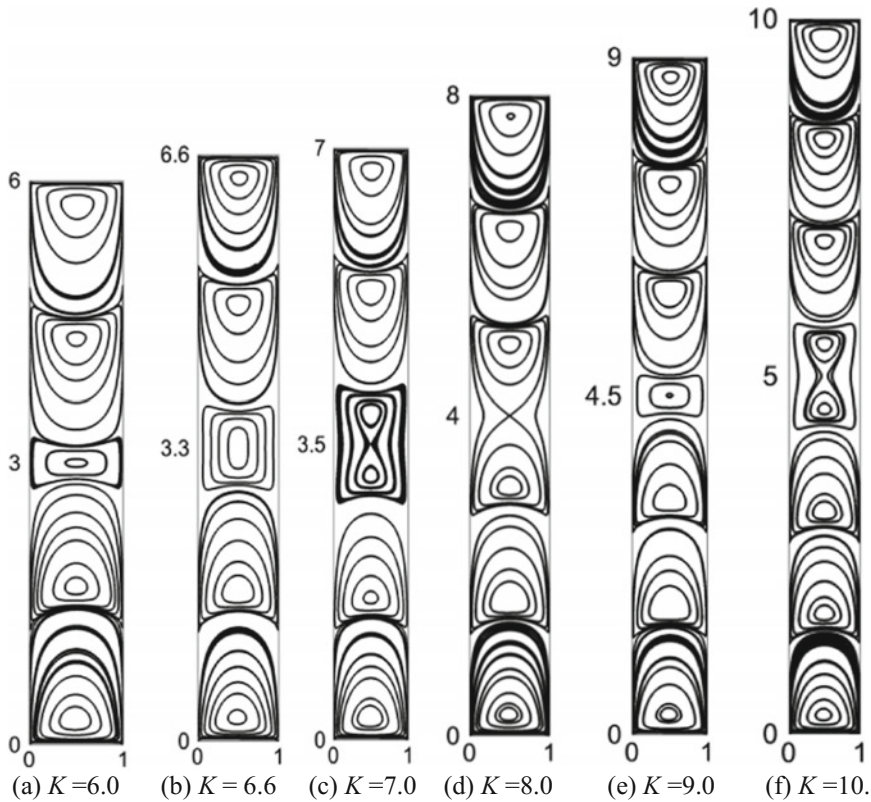


Fig. 5 Streamline pattern for Reynolds number $Re = 10$ for different proportions of aspect ratios. **a** $K = 6.0$, **b** $K = 6.6$, **c** $K = 7.0$, **d** $K = 8.0$, **e** $K = 9.0$, **f** $K = 10$

vortices and now the streamline design is constituted by seven huge vortexes (Fig. 5e). As K increments facilitate a couple of new longitudinal sub-eddies rise (Fig. 5f) and a similar vortexes generated.

4 Conclusion

The development of the vortexes for two-dimensional rectangular cavity for low Reynolds number stream for antiparallel top driven cavity have been examined using Lattice Boltzmann method. In view of the numerical results, directed for various aspect proportions, the accompanying conclusions can be made. For the low Reynolds number stream in a rectangular cavity with two-sided antiparallel lids, the stream designs are symmetric about the central point of the cavity for various aspect proportions. At the point when the perspective proportion is bigger

than 1.2, the stream structure unfurls the longitudinal way of hole and the quantity of vortices continuously increments with the aspect proportion expanding. The advancement of stream design shows the periodicity. In every periodicity, it was watched that the four primary phases of the vortex advancement are comparable at the central point of the depression. As the angle proportion is expanding, the quantity of vortices increments the longitudinal way.

References

1. Mohammad, A.: *Lattice Boltzmann Method: Fundamentals and Engineering Applications with Computer Code*. Springer, London (2011)
2. Perumal, D.A., Dass, A.K.: A Review on the development of lattice Boltzmann computation of macro fluid flows and heat transfer. *Alexandria Eng. J.* **54**, 955–971 (2015)
3. Perumal, D.A., Dass, A.K.: Application of lattice Boltzmann method for incompressible viscous flows. *Appl. Math. Model.* **37**, 4075–4092 (2013)
4. Perumal, D.A., Dass, A.K.: Multiplicity of steady solutions in two-dimensional lid-driven cavity flows by lattice Boltzmann method. *Comput. Math. Appl.* **61**, 3711–3721 (2011)
5. He, S., Wu, L., Xu, T.: Periodicity and self-similarity of vortex evolution in a double lid-driven cavity flow. *Procedia Eng.* **31**, 267–273 (2012)
6. Ghia, U., Ghia, K.N., Shin, C.T.: High-resolutions for incompressible flow using Navier-Stokes equations and a multigrid method. *J. Comput. Phys.* **43**, 387–441 (1982)

A Study of Thermo-structural Behavior of Annular Fin



Rahul Sharma, Lakshman Sondhi, Vivek Kumar Gaba
and Shubhankar Bhowmick

Abstract Adding an annular/radial fin to a heat exchanger increases the surface area in interaction with the surrounding fluid, thus increasing the convective heat transfer between the object and surrounding fluid. Since surface area increases as length from the object increases, an annular fin transfers more heat than a similar pin fin at any given length. The present work involves computation of temperature gradient followed by the determination of thermal stresses in radial and tangential direction, radial displacements, and strains of annular fins and compares the results for different aspect ratio (ratio of the inner radius to outer radius) by varying inner radius of the annular fin. A general second-order non-linear ordinary differential equation has been derived for all the parameters as the governing equation. The performance parameters of the annular fins for different aspect ratio have been calculated and plotted on graphs.

Keywords Annular fin · Aspect ratio · Temperature distribution
Thermal stresses · Isotropic material · Axisymmetric investigation

1 Introduction

Adding an annular fin increases the surface area in contact with the surrounding fluid thus increasing the convective heat transfer between the heat sources and surrounding fluid. An annular fin transfers more heat compared to a similar pin fin of same extruded length due to increased surface area exposed to the surrounding. The temperature gradient throughout the fin depends on the end conditions observed, and there arises thermal stresses in radial and tangential directions of the

R. Sharma · L. Sondhi
Department of Mechanical Engineering, SSTC, Bhilai, India

V. K. Gaba · S. Bhowmick (✉)
Department of Mechanical Engineering, NIT, Raipur, India
e-mail: sbhowmick.mech@nitrr.ac.in

© Springer Nature Singapore Pte Ltd. 2019
U. Chandrasekhar et al. (eds.), *Innovative Design, Analysis and Development Practices in Aerospace and Automotive Engineering (I-DAD 2018)*, Lecture Notes in Mechanical Engineering, https://doi.org/10.1007/978-981-13-2718-6_36

annulus. Furthermore, in practice, the annulus is mechanically fastened on the pipe or other heat source. This may give rise to additional stresses by virtue of pre-stressed mounting.

The literature survey points toward the existence of a few investigations exploring the stress and displacement in isotropic annular fins or disks that are mainly focused on studying the effects of geometry parameters on displacement and stress fields under different boundary conditions. Kim [1] used the theory of two-dimensional uncoupled quasi-static thermoelasticity to obtain the solution for stress field generation by moving point heat source in a circular disk. Yovanovich et al. [2] reported one- and two-dimensional solutions for thermal performance of annular fins having a constant cross section. For an annular fin with periodic heat transfer at boundary and having temperature-dependent thermal conductivity, Chiu and Chen [3] reported the stress field using Adomian's decomposition method. Paul et al. [4] compared thermal stresses in fins of different profile and materials operating at high temperature. In another study, the performance of annulus with different geometrical profiles and subject to variable heat transfer coefficient has been reported by Mokheimer [5]. In a recent work, using modified Durbin's numerical inversion method, Bas and Keles [6] reported the transient thermal stresses in annular fin in the Laplace domain with its base subjected to a decayed exponential heat flux as a function of time. Sudheer et al. [7] reported a finite element solution of the temperature distribution and thermal stresses in a silicon carbide ceramic finned tube. Gencer et al. [8] reported the bending of the fin due to thermal stresses.

The present work involves computation of temperature gradient and thermal stresses and displacement in annular fins and compares the results for different aspect ratio (ratio of the inner radius to outer radius) by varying inner radius of the annular fin. A general second-order ordinary differential equation has been derived for all the parameters. The performance parameters of the annular fins for different aspect ratio have been calculated and plotted on graphs.

2 Mathematical Formulation

In the present study, the fin, with insulated tip, is assumed to be under steady heat flow without internal heat source and effect of external environment is considered negligible on surface convection. The problem is modeled in one dimension; i.e., the temperature gradient and displacement is assumed to exist only along the radial direction and is symmetric with respect to the mid-plane and is under plane stress. The fin material is assumed to be homogeneous and isotropic. The annular fin is fixed to the cylindrical tube, and stresses are reported for both fin without prestress and with prestress at inner boundary.

The second-order differential equation for the heat transfer through the fin is developed to find the temperature profile. For calculating the heat balance, an element of length ' dr ' of the fin (Fig. 1) is considered. Applying thermal energy balance to the element, the differential equation of heat flow is derived as follows:

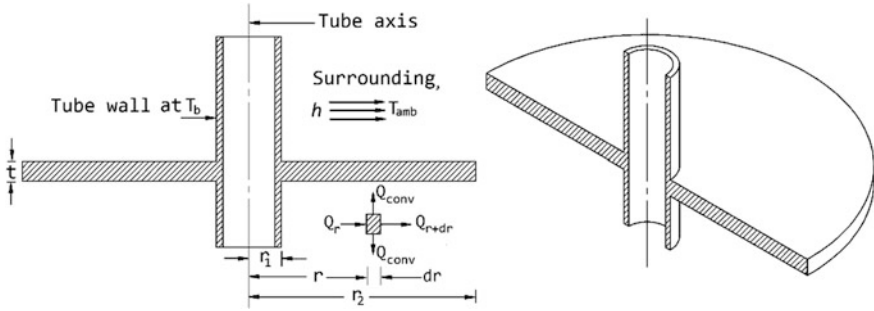


Fig. 1 Fin geometry

$$\frac{d^2\theta}{dr^2} - m^2\theta = 0; \quad m = \sqrt{\frac{hP}{kA_c}} \tag{1}$$

The solution to Eq. (1) is widely available for isotropic materials in reference texts and articles; however, it must be noted at this point that if material grading is introduced with additional complications of non-stationary fins having variable geometry as well, then the solution calls for numerical treatment using *bvp4c* as reported in Gaba et al. [9, 10] and hence is not reproduced here to maintain brevity. The following boundary conditions are used for fin with base temperature and the insulated tip

$$T|_{r=r_1} = T_b; \quad \left. \frac{dT}{dr} \right|_{r=r_2} = 0 \tag{2}$$

Using Eqs. (1) and (2), the temperature distribution is obtained and stored at quadrature points along the fin radius. Since, the changes in temperature in a constrained body cause expansion/contraction, in annular fin, this leads radial displacements depending upon the imposed boundary conditions. The solution of the displacement field is obtained using Galerkin's error minimization, applied over the governing equation obtained using variational principle (Eq. 3a).

$$\delta(U + W) = 0 \tag{3a}$$

$$U = \int_{r_1}^{r_2} (\sigma_r \epsilon_r + \sigma_\theta \epsilon_\theta) \pi r t \, dr \tag{3b}$$

$$W = -P_c (2\pi r_1 t) u|_{r=r_1} \tag{3c}$$

In Eq. (3a), U is the strain energy stored in the annular fin by virtue of thermal field and mounting and W is the work potential due to prestress at inner boundary. The radial and tangential strain in annular fin is given by

$$\varepsilon_r = \frac{du}{dr} = \frac{\sigma_r}{E} - \mu \frac{\sigma_\theta}{E} + \alpha\Delta T; \quad \varepsilon_\theta = \frac{u}{r} = \frac{\sigma_\theta}{E} - \mu \frac{\sigma_r}{E} + \alpha\Delta T \tag{4}$$

Upon substituting Eq. (4) in Eq. (3b),

$$U = \frac{E\pi t}{(1 - \mu^2)} \left[\int_{r_1}^{r_2} \left\{ \frac{u^2}{r} + r \left(\frac{\partial u}{\partial r} \right)^2 + 2\mu u \frac{\partial u}{\partial r} - \alpha r(1 + \mu) \left(\frac{\partial u}{\partial r} + \frac{u}{r} \right) \Delta T \right\} dr \right] \tag{5}$$

Equations (5) and (3c), substituted in Eq. (3a), yield the following equation.

$$\delta \left[\frac{E}{(1 - \mu^2)} \left[\int_{r_1}^{r_2} \left\{ \frac{u^2}{r} + r \left(\frac{\partial u}{\partial r} \right)^2 + 2\mu u \frac{\partial u}{\partial r} \right\} dr \right] - 2P_c r_1 u|_{r=r_1} \right] = 0 \tag{6}$$

To facilitate the numerical computation, Eq. (6) is expressed in normalized coordinate (ξ) and the displacement function u is approximated by a linear combination of sets of orthogonal coordinate functions (Eq. 7).

$$u \cong \sum c_i \phi_i, \quad i = 1, 2, \dots, n_f \tag{7}$$

In Eq. (7), n_f is the number of coordinate functions. The normalized variables used in formulation are

$$\xi = \frac{r - r_1}{r_2 - r_1}; \quad R_f = \frac{r_1}{r_2}; \quad \varphi = \frac{\theta}{\theta_b} = \frac{T - T_\infty}{T_b - T_\infty}$$

Here, ξ is the normalized radius, R_f is the aspect ratio, and φ is the dimensionless temperature. Subsequently, upon substituting the normalized variables, assumed displacement field and replacing the operator ‘ δ ’ by $\delta/\delta c_j$, $j = 1, 2, \dots, n_f$, the governing equation takes the following form:

$$\int_0^1 \left\{ \left(\frac{\Delta}{\Delta\xi + r_1} \right) \phi_i \phi_j + \left(\frac{\Delta\xi + r_1}{\Delta} \right) \phi'_i \phi'_j + \mu (\phi_i \phi'_j + \phi_j \phi'_i) \right\} d\xi - \int_0^1 \alpha(1 + \mu)(\Delta\xi + r_1) \left(\frac{\phi_j}{\Delta\xi + r_1} + \frac{\phi'_j}{\Delta d\xi} \right) \Delta(\Delta T) d\xi = P_c E(1 - \mu^2) r_1 \left\{ \sum c_i \phi_i \Big|_{r=r_1} \right\} \tag{8}$$

3 Results and Discussions

The excess temperature, θ , and consequently the thermal stresses depend on the base radius r_1 , tip radius r_2 , base excess temperature, fin thickness t , thermal conductivity k , and fin parameter m . The results are presented for annular fin having $r_2=20$ cm or 0.2 m, $t=0.01$ m, $\theta_b=100$ °C and convection coefficient $h=25$ W/m² K. The study is carried out for annular fins of three different aspect ratios (R_f) 0.3, 0.4, and 0.5. The fin material is assumed to be isotropic, and for thermal study, thermal conductivity is varied from 100 to 300 W/m K. The displacement and stresses are reported on account of temperature profile obtained for material with conductivity 200 W/m K. The material parameters, thus, correspond to commercially available aluminum ($E=70$ GPa).

The excess temperature distribution of annular fins of different aspect ratios is plotted in Fig. 2a–c. In each plot, the distribution is plotted for different thermal conductivities. It is observed that with increasing conductivity, the tip temperature also increases. The temperature distribution along the fin induces radial displacement and thermal stresses in radial and tangential direction, respectively.

In Fig. 3, the normalized displacement is validated for both mounting end conditions at $R_f=0.3$. Further, under similar end conditions, displacement is plotted for the remaining aspect ratio considered in the study. The effect of prestress on displacement at inner radius is shown in the plot.

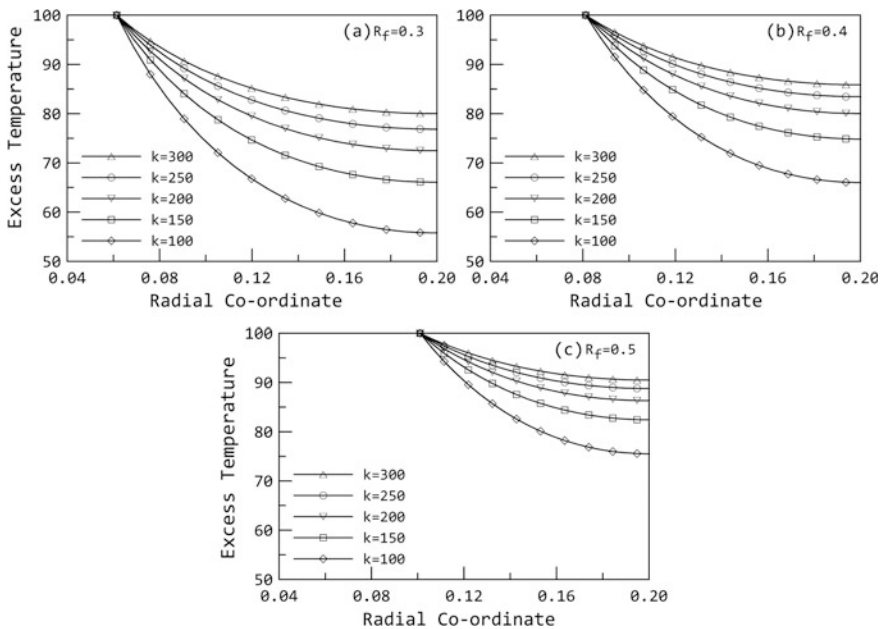


Fig. 2 Excess temperature distribution for $R_f =$ a 0.3, b 0.4, and c 0.5

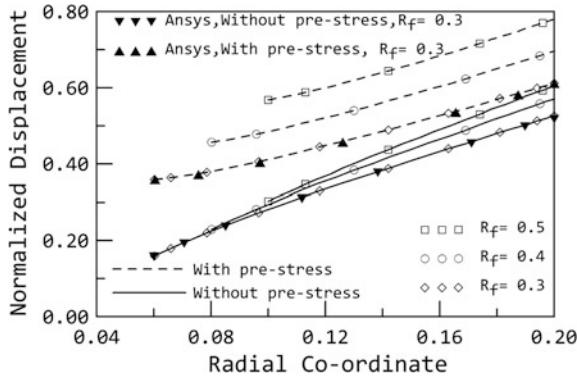


Fig. 3 Normalized displacement in annular fin under thermo-mechanical loading

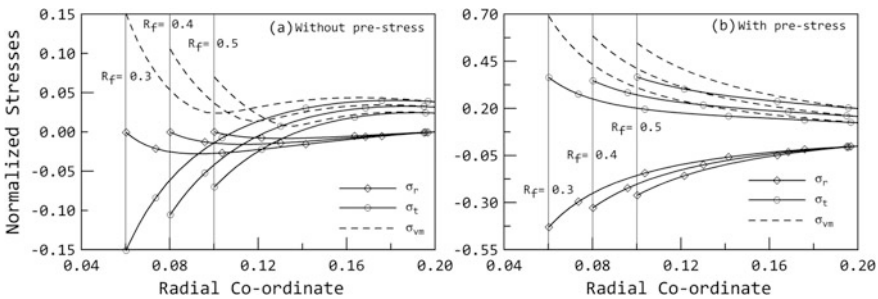


Fig. 4 Normalized stresses in annular fins **a** without prestress and **b** with prestress

The thermal stresses are plotted in Fig. 4a–b for annular fins of different aspect ratios and conductivity 200 W/m K. In Fig. 4a, the stresses are plotted assuming the fin base without prestress. The effect of prestressed mounting on heat source is evident in Fig. 4b wherein the magnitude of stresses under thermo-mechanical loading observed to be much higher than stresses induced in fins without prestress. In Fig. 4a, the radial stresses at base correspond to zero value, indicating simple support at fin base.

4 Conclusions

The excess temperature and resulting thermal stresses and displacement in thin isotropic annular fins of rectangular profile have been reported. The study is carried out for different aspect ratios. The excess temperature for annular fins having insulated tip is reported. The study reveals that the excess temperature increases with the increase in the aspect ratio. Thermo-mechanical study of stresses and

displacement for three different aspect ratios under two different mounting end conditions without prestress and prestressed mounting is also reported. The effect of prestress is evident from the results. Further, the effect of aspect ratio on thermal stresses and displacement is also reported in the plots.

References

1. Kim, T.J.: Quasi-static thermal stress due to a moving heat source in a circular disk. *AIAA J.* **9**, 2078–2079 (1971). <https://doi.org/10.2514/3.6472>
2. Yovanovich, M., Culham, J.R., Lemczyk, T.F.: Simplified solutions to circular annular fins with contact resistance and end cooling. *J. Thermophys. Heat Transf.* **2**, 152–157 (1988). <https://doi.org/10.2514/3.79>
3. Chiu, C.-H., Chen, C.-K.: Thermal stresses in annular fins with temperature dependent conductivity under periodic boundary condition. *J. Therm. Stresses* **25**, 475–492 (2002). <https://doi.org/10.1080/01495730252890195>
4. Paul, P., Sharma, R.C., Bezewada, R., Wakeel, M., Murigendrappa, S.M.: Comparative study of thermal stress distributions in fins operating at high temperature for different profiles and materials. In: *Proceedings of International Conference on Advances in Mechanical Engineering* (2011)
5. Mokheimer, E.M.: Performance of annular fins with different profiles subject to variable heat transfer coefficient. *Int. J. Heat Mass Transf.* **45**, 3631–3642 (2002)
6. Bas, H., Keles, İ.: Novel approach to transient thermal stresses in an annular fin. *J. Thermophys. Heat Transfer* **29**(4), 705–710 (2015). <https://doi.org/10.2514/1.T4535>
7. Sudheer, M., Shanbhag, G.V., Kumar, P., Somayaji, S.: Finite element analysis of thermal characteristics of annular fins with different profiles. *ARPJ. Eng. Appl. Sci.* **7**(6), 750–759 (2012)
8. Gencer, A.H., Tsamados, D., Moroz, V.: Fin bending due to stress and its simulation. In: *International Conference on Simulation of Semiconductor Processes and Devices (SISPAD)* (2013). <https://doi.org/10.1109/sispad.2013.6650586>
9. Gaba, V.K., Tiwari, A.K., Bhowmick, S.: Thermal performance of functionally graded parabolic annular fins having constant weight. *J. Mech. Sci. Technol.* **28**, 4309–4318 (2014). <https://doi.org/10.1007/s12206-014-0945-1>
10. Gaba, V.K., Tiwari, A.K., Bhowmick, S.: A parametric study of functionally graded rotating annular fin. *Procedia Eng.* **127**, 126–132 (2015). <https://doi.org/10.1016/j.proeng.2015.11.436>

A New Design to Achieve Variable Compression Ratio in a Spark Ignition Engine



Aditya Roy, Chetan Mishra, Sarthak Jain and Naveen Solanki

Abstract Spark ignition engines are known to have low part load efficiencies which contribute in increasing fuel consumptions. Compression ratio plays a significant role in deciding the performance of an engine at different load conditions. For this reason, the variable compression ratio (VCR) engine has, since long, been considered as an effective solution to the problems encountered while operating an engine at varying load conditions. There has been a significant amount of effort by researchers as well as OEMs for developing efficient and optimum designs of the VCR engine. The design makes use of a cylinder head which is equipped with a movable ram for varying the clearance volume. Actuators have been used to actuate the movement of the ram which facilitates to vary the compression ratio. The whole system has been designed keeping the potential challenges in mind and means have been sought to negate them. VCR engines give more flexibility to the user and at the same time, improve performance characteristics such as brake power, brake thermal efficiency, and torque while decreasing emissions and lowering specific fuel consumption.

Keywords Variable compression ratio · SI engine · Engine head Actuator · Solidworks

1 Introduction

Challenges are encountered when parameters such as load increase on a given IC engine. Variation in load directly corresponds to variations in power requirements from an engine. During high load conditions, the power required increases. On the other hand, low load conditions can be done away with lower power outputs. The concept of varying the compression ratio of an engine cylinder enables this. In high

A. Roy (✉) · C. Mishra · S. Jain · N. Solanki
Department of Mechanical and Automation Engineering, Maharaja Agrasen
Institute of Technology, Sector 22, Rohini, Delhi 110086, India
e-mail: aditya.roy1510@gmail.com

© Springer Nature Singapore Pte Ltd. 2019
U. Chandrasekhar et al. (eds.), *Innovative Design, Analysis and Development Practices in Aerospace and Automotive Engineering (I-DAD 2018)*, Lecture Notes in Mechanical Engineering, https://doi.org/10.1007/978-981-13-2718-6_37

load conditions, the compression ratio can be decreased to maximize the power output. In low load situations, the compression ratio can be increased in order to maximize efficiency. Under conditions of varying loads, knock susceptibility can be reduced by using compression ratios which adapt with the load demands. Rao et al. [1] performed experiments on a single cylinder four stroke VCR diesel engine to find an optimum compression ratio. Tests were performed on various compression ratios and the optimum compression ratio was found out to be 14.8 at which there was an improvement in performance and significant decrease in emissions.

Tsuchida et al. [2] performed several experiments to develop lower fuel consumption and higher output simultaneously but fuel consumption did not reduce after a certain compression ratio. In this experiment, stroke length was increased to improve fuel economy by suppressing surface-to-volume ratio of the combustion chamber which reduced fuel consumption.

Kadota et al. [3] developed a new design of dual piston VCR in which compression ratio existed between two stages and the reciprocating motion of piston was governed by inertia force and hydraulic pressure. Hidden Markov Model was used to determine the compression ratio switching timing. Ignition timing control system was used to control individual cylinder and simultaneously performed knocking control.

Rabhi et al. [4] performed experiments on MCE-5 VCR engine to reduce fuel consumption and emissions while the power output and torque remain the same. This engine can be used for mass production of rigid and robust low friction engines.

Kommana et al. [5], Channapattana et al. [6] performed an experiment to study the behavior of VCR engine under biodiesel. To replace the conventional fuel, the mixture of palm kernel oil and eucalyptus oil or the blend of biodiesel like B20, B40, B60, and B80 was chosen. Various tests were performed and emissions like carbon monoxide and hydrocarbon were reduced. Komatsu et al. [7] performed an experiment and established an automatic adjustment system for VCR magnetic heads cylinder on a rotating cylinder. This arrangement improves many head positioning errors like setting angle errors and rotational angle error and different head positions were determined using different image processing algorithms.

Performance characteristics such as brake power, brake mean effective pressure, specific fuel consumption, and brake thermal efficiency continuously vary with change in compression ratio. VCR engines also exercise a control over the exhaust gas temperatures, which leads to a reduction in engine component temperatures.

1.1 Benefit of Using VCR

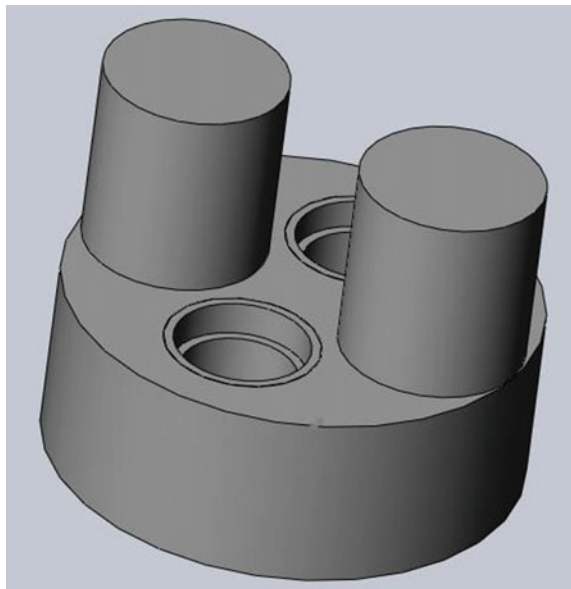
A major factor that limits the performance of an SI engine is the concept of knocking and pre-ignition. A term called highest useful compression ratio (HUCR) is used in case of SI engines. This is the value of compression ratio, which when exceeded, would produce knock in the engine.

Under full load conditions, the throttle sends in more air-fuel mixture. If the CR is high under this situation, the operating temperature would increase rapidly enabling the end mixture to autoignite thus causing knock. On the other hand, under low load conditions, the throttle sends in less amount of air-fuel mixture. Now if the CR is low, the mixture would not reach the required temperature to ignite and effect combustion. Due to these reasons, under full load conditions, the VCR engine utilizes low CR values to maximize power outputs without causing knock and under low load conditions, the VCR engine makes use of high CR values to maximize fuel efficiency.

2 Design Principle

Cylinder dimensions of 84 mm bore diameter and 90 mm stroke length with a displacement of 500 cc have been selected. The cylinder head is equipped with a movable ram which varies the clearance height of the cylinder. Ram is actuated by two actuators. As the actuator is actuated, the ram gets displaced which in turn changes the height of the combustion chamber. As this height is varied, the clearance volume gets changed and hence the compression ratio is varied. A 3D view of the designed assembly is shown in Fig. 1.

Fig. 1 3D view of engine head assembly



2.1 Working

User has to feed the required compression ratio to the ECU using a regulator switch or any suitable arrangement. ECU then sends required signals to actuators. Since push rod is connected to the movable ram, when signals are sent to the actuator from ECU, the push rod gets displaced which further displaces the ram. In this way, the clearance volume is altered. The two actuators used can be of any type like hydraulic, pneumatic, or mechanical, but the necessary condition is that it should be able to produce the required force so that it can displace the ram and make way for the entry of air-fuel mixture and exit of exhaust gases.

When the user wants to gain on efficiency, he/she can turn on the efficiency mode which will send a signal to ECU to increase the compression ratio of the engine using a regulator switch or any suitable arrangement. ECU will then send required signals to actuators which will convert those signals into displacement and force and hence actuate the pushrods outwards.

On the other hand, when driver wants to negotiate a high load along with a good amount of acceleration, or climb a hill without getting prey to knock, he/she can now move the knob to power mode as a result of which, the actuator will displace pushrod in negative direction hence moving the pushrod in backward direction, which in turn increases the combustion chamber volume. The clearance volume is increased thus decreasing the compression ratio. A labeled sectional view is shown in Fig. 2.

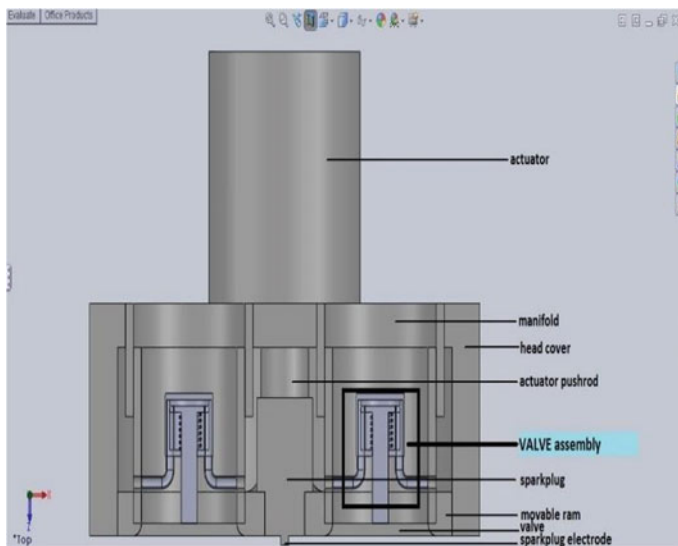


Fig. 2 Labeled half section front view

2.2 Components

- **Ram.** As can be seen in Fig. 3, there is a ram which acts as the head of the combustion chamber. It can be displaced vertically which enables it to change the height of the combustion cylinder and hence the compression ratio. It contains valves, manifolds, spark plug, and actuators. The ram is sealed from its circumference by using several stiff piston rings that will seal it better than the normal piston rings so that the air-fuel mixture does not leak from the gap.
- **Actuator.** The actuator used can be of any type like mechanical, pneumatic, or hydraulic actuators. Work is to be done to calculate the range of forces to be applied by the actuator using required mathematical relations. The designed actuator casing is shown in Fig. 4.
- **Manifolds.** As shown in Fig. 5, they are designed such that they can be elongated or shortened when ram moves in vertical direction. Manifolds are two hollow tubes which are inserted one into the other and thus the larger one slides over the smaller one. They direct the air-fuel mixture to the combustion chamber and the exhaust gases from combustion chamber to atmosphere.
- **Valves.** The valves have been designed very strategically. It consists of a piston-based system actuated by flow of air. There are two ports, namely the inlet and outlet ports. When valve is to be opened, air flows in and pushes the piston downwards. When valve is to be closed, air flows out of the chamber which is further connected to an actuator circuit. In addition, the spring attached helps to facilitate the closing of valve. Figures 6 and 7 show the 3D sectional

Fig. 3 2D view of ram

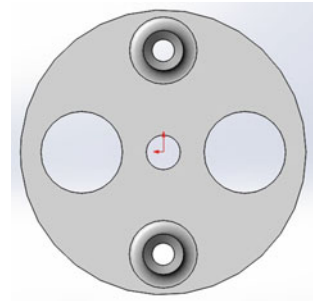
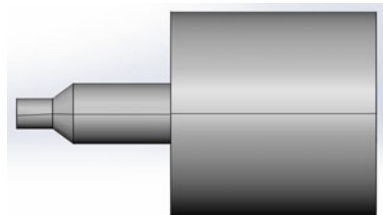


Fig. 4 2D view of actuator casing



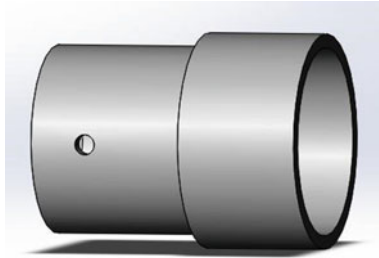


Fig. 5 3D view of manifold

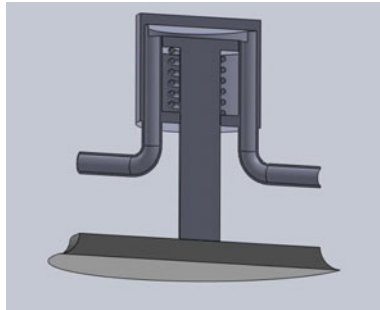


Fig. 6 3D view of valve

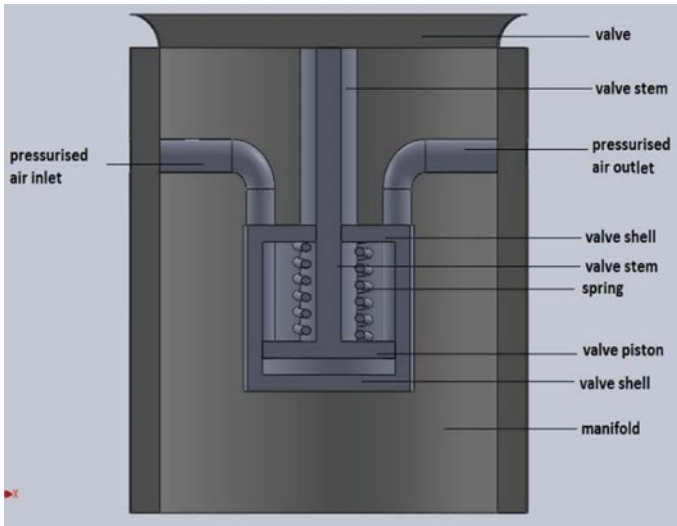


Fig. 7 Sectioned assembly view of valve and manifold

Fig. 8 3D view of head cover



view and sectional front view of the valve, respectively. Such a valve mechanism completely eliminates the camshaft. The valve timing is attained with the help of crankshaft position sensor which sends its signals to the ECU which further controls the air compressor for valve actuation.

- **Head Cover.** As shown in Fig. 8, it is a shell type cylinder and contains all the parts inside. It acts as a protection to all the parts inside it.

3 Conclusion

The arrangement of actuating a ram to achieve variable compression ratio as employed in this design is a very simple and economical approach. This helps the user to get an engine response according to his requirements. Overall efficiency of an engine increases with the help of this concept. The benefits of higher brake power, higher brake thermal efficiency, and more torque can be tapped using this design. At the same time, it promises lower fuel consumption levels for the identical engine displacement values. An important advantage of using this is that it enables the engine to create lesser emissions which is need of the hour keeping in mind the stringent emission norms. Component temperatures can be reduced which would help in lowering the wear and tear further reducing potential costs. The proposed design makes use of an actuator system which actuates a ram within the engine head. This promises a very wide range of compression ratio variation, but the HUCR value needs to be taken into account which is only possible by experimentation. Scope lies in the theoretical analysis of this design to calculate the actual force to be exerted by the actuators for achieving the variation in clearance volume. Force calculation of actuators would further govern their selection.

References

1. Rao, G.V.N.S.R., Raju, R., Rao, M.M.: Optimizing the compression ratio of diesel fueled CI engine. *ARNP J. Eng. Appl. Sci.* **3**(2), (2008)
2. Tsuchida, H., Hiraya, K., Tanaka, D., Shigemoto, S., Aoyama, S., Tomita, M., Sugiyama, T., Hiyoshi, R.: The effect of a longer stroke on improving fuel economy of a multiple-link VCR engine. *SAE Tech. Pap.* (2007)
3. Kadota, M., Ishikawa, S., Yamamoto, K., Kato, M., Kawajiri, S.: Advanced control system of variable compression ratio (VCR) engine with dual piston mechanism. *SAE Int. J. Engines* **2** (1), (2009)
4. Rabhi, V., Beroff, J., Dionnet, F.: Study of a gear-based variable compression ratio engine. *SAE Tech. Pap.* (2004)
5. Kommana, S., Banoth, B.N., Kadavakollu, K.R.: Performance and emission of VCR-CI engine with palm kernel and eucalyptus blends. *Perspect. Sci.* **8**, 195–197 (2016)
6. Channapattana, S.V., Kantharaj, C., Shinde, V.S., Pawar, A.A., Kamble, P.G.: Emissions and performance evaluation of DI CI—VCR engine fuelled with honne oil methyl ester/diesel blends. In: *Energy Procedia, The International Conference on Technologies and Materials for Renewable Energy, Environment and Sustainability*, vol. 74, pp. 281–288, Elsevier (2005)
7. Komatsu, T., Nagashima, S., Tsukada, H.: An automatic adjustment system for VCR magnetic heads on cylinder units. *CIRP Ann. Manufact. Technol.* **38**(1), 9–12 (1989)

Experimental Investigation on Energy Saving due to Bubble Disturbance in Boiling Process



S. Santhosh Kumar and S. Balaguru

Abstract Boiling is the process through which a liquid is brought to a temperature at which it forms bubbles at solid-liquid interface and converts into vapour. The present work focuses on developing a system that involves less energy consumption for boiling of water. A thorough study of boiling process was made. The science behind the boiling curve of water is critically analysed. The four stages of boiling curve of water are studied, and a new theory called bubble disturbance theory is proposed. The transition region of the boiling curve shows decrease in heat flux pertained to poor heat conduction through bubbles formed at interface. A novel idea of disturbance of bubble at this stage to increase heat transfer rate was predicted. Experiments were conducted to observe the boiling of water with and without bubble disturbance. Results have shown that the proposed system with bubble disturbance will save energy up to 20%.

Keywords Boiling · Vapour · Bubble disturbance · Conduction
Heat flux · Transition

1 Introduction

Boiling of water at 1 atm involves four distinct stages. They are free convection, nucleate, transition and film boiling regimes. The curve plotted for excess temperature against heat flux shows that there is a steady increase in heat transfer during the initial two stages, but then the heat transfer decreases during the third stage. The reason behind the decrease is attributed to the formation of bubbles at the interface between solid and liquid, i.e. water container to water interface at the bottom.

S. Santhosh Kumar · S. Balaguru (✉)

Department of Mechanical Engineering, Vel Tech Rangarajan Dr Sagunthala R & D Institute of Science and Technology, Chennai, Tamilnadu, India
e-mail: iitmgu239@gmail.com

© Springer Nature Singapore Pte Ltd. 2019

U. Chandrasekhar et al. (eds.), *Innovative Design, Analysis and Development Practices in Aerospace and Automotive Engineering (I-DAD 2018)*, Lecture Notes in Mechanical Engineering, https://doi.org/10.1007/978-981-13-2718-6_38

397

Many research work related to analysis of boiling of water has been made. The purposes of these researches are to understand the boiling process and suggest certain methods to enhance heat transfer in boiling. The change in physical behaviour of boiling due to addition of small amount of additives was experimentally investigated by Mane et al. [1]. Boiling curves are useful in understanding boiling phenomena. Many studies related to boiling curve measurements have been done. New boiling curve measurement techniques using digital instruments were introduced by Peterson et al. [2]. After the advent of computer, various numerical models regarding different physical phenomena have been developed. Modelling and simulation of flow boiling heat transfer were developed by Krause et al. [3]. Measurement of temperature using K Type thermocouple was discussed by Balaguru et al. [4]. The simulations on heat conduction property of stainless steels were performed by Balaguru et al. [5]. These simulations give better understanding of interaction of various parameters in heat transfer. Various experimental techniques for measurement of boiling curves have been developed. Boiling involves steady state and transient behaviour, to make precise measurements in developing boiling curve is of high importance. One such measurement technique using micro-sensors was developed by Auracher et al. [6].

Although many studies have been done to understand the boiling process, none of them introduced the idea of disturbance of bubble formed during the transition state to increase the heat transfer and hence reduce the energy required to achieve the superheated state. The present study proposes such theory and experimentation to validate the theory.

2 Heat Transfer Process

The process of heat transfer during the boiling of water can be explained as follows. The container will always be in direct contact with the heat source. The heat transfer between heat source and container takes place through convection and radiation, and then the heat is transferred within the container thickness by means of conduction. This heat is then transferred to the water by means of convection. The heat is distributed within the water by means of natural convection due to buoyancy. As the temperature of water that is in direct contact with bottom of the cooking vessel reaches its boiling point, the water becomes water vapour in the form of bubble. As the heating continues, more bubbles are formed at the interface. These bubbles form a layer at the interface. Vapour is poor conductor of heat; it will decrease the heat transfer at this stage. The graph showing change in heat flux against temperature difference also called as boiling curve is shown in Fig. 1.

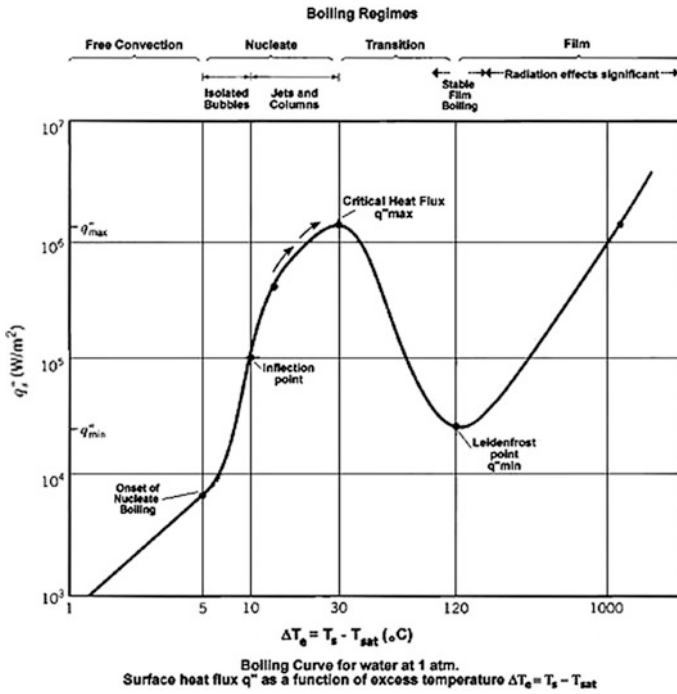


Fig. 1 Boiling curve of water

3 Theoretical Assertions

From the study of this process, it can be understood that the bubble layer is reason for decrease in heat transfer. Considering this, a theory is proposed as, disturbance of bubbles by any means will increase the heat transfer and hence will reduce the power consumption.

One another argument for increase in heat transfer rate can be explained as follows. During bubble disturbance by using external means, there might be an unintended forced convection which may lead to increase in heat transfer.

Yet another argument for the increase in heat transfer due to bubble disturbance can be described as follows. Rate of convection heat transfer depends upon area exposed to heat transfer. Equation for heat transfer rate due to convection is given as,

$$Q = hA\Delta T.$$

where

- Q is heat transfer rate, J/s
- h is heat transfer coefficient, W/(m² K)
- A is Area, m²
- ΔT is temperature difference (K or °C)

When bubble is formed at the interface, the area of water exposed to metal surface is reduced; this can be presumed as reason for reduction in heat transfer rate. Bubble disturbance will increase the exposed surface, and hence, it will increase the heat transfer.

4 Experimental Details

Experiments to validate this theory were conducted with water contained in stainless steel vessel. Experiments were conducted for two cases, namely temperature measurement without bubble disturbance and temperature measurement with bubble disturbance. To measure temperature, a waterproof thermometer was used. A level of 2 cm was marked in the thermometer, and it is dipped in the water at this level for measuring the temperature at constant depth in both cases of experiment.

The image and specification of the thermometer are shown below (Fig. 2).

Specification:

- Automatic power off after 10 min.
- Measurement range: -50 to $+300$ °C
- Accuracy: ± 1
- Waterproof
- Probe length 20 cm
- Units Celsius and Fahrenheit.

Water contained in the container is placed over the heat source. The heat source is maintained at constant temperature by the position of adjustment knob. Also, the quantity of water placed in the container is noted. Now water is allowed to boil. The experiment is conducted without disturbing the bubble till the temperature reaches



Fig. 2 Water proof digital thermometer



Fig. 3 Bubble formation at bottom of vessel

120 °C. Here, the temperature rise above 100 °C is observed because of superheated vapour (Fig. 3).

Digital clock is used to measure the time taken for constant increase in temperature of 5 °C each. The observed values are tabulated (Table 1).

A graph is plotted for time against temperature. The graph shows non-linear increase in temperature with time (Graph 1).

The experiment is repeated under similar conditions but with bubble disturbance. A metal stick was used to disturb the bubbles formed at the interface.

The observed values are tabulated, and a graph is drawn from the observed values (Table 2).

A graph is plotted for time against temperature. The graph shows non-linear increase in temperature with time (Graph 2).

5 Comparison of Results

The results show that the increase in temperature is non-linear, this is because of complex phenomena of bubble formation and buoyancy effects.

The graph shows that temperature increases rapidly initially, and then the rate of increase is decreased. This is because of the reduction in heat flux due to bubble formation.

The comparison between two experiment shows that the time taken for the water to reach the temperature of 120 °C is 100 min without bubble disturbance, and under similar conditions, the time taken by the water to reach a temperature 120 °C is 80 min with bubble disturbance.

Table 1 Time taken for increase in temperature without bubble disturbance

Temperature (in °C)	Time (in minutes)
40	3.07
45	5.11
50	7.14
55	9.21
60	12.12
65	15.10
70	17.32
75	21.09
80	25.25
85	31.22
90	38.27
95	47.38
100	57.54
105	66.53
110	77.54
115	87.32
120	98.42

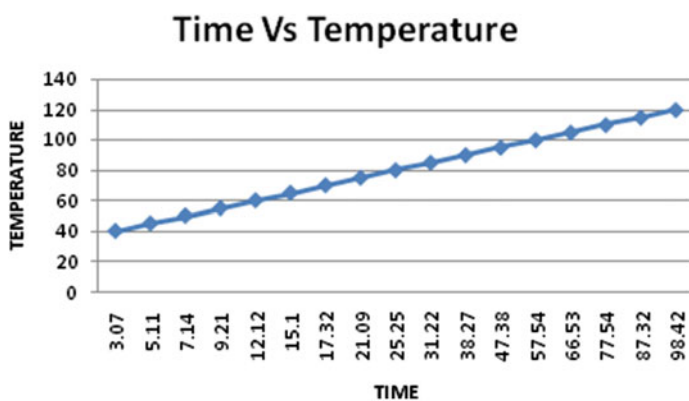
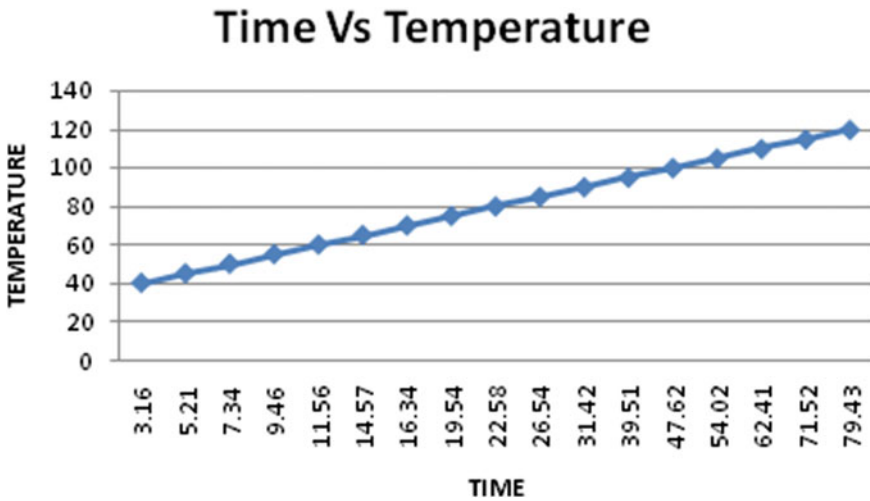
**Graph 1** Temperature versus time graph without bubble disturbance

Table 2 Time taken for increase in temperature with bubble disturbance

Temperature (in °C)	Time (in minutes)
40	3.16
45	5.21
50	7.34
55	9.46
60	11.56
65	14.57
70	16.34
75	19.54
80	22.58
85	26.54
90	31.42
95	39.51
100	47.62
105	54.02
110	62.41
115	71.52
120	79.43



Graph 2 Temperature versus time graph with bubble disturbance

6 Conclusions

From the theory predicted and experiment conducted to validate the theory, the following can be concluded.

- (1) The theory is proposed as ‘*The disturbance of bubble during film boiling phase will increase heat transfer rate*’.
- (2) There is a saving of 20% of energy due to bubble disturbance in boiling water in stainless steel vessel to a superheated temperature of 120 °C.
- (3) The phenomenon of increase in temperature with time is a non-linear process.

If suitable disturbance method is developed, this theory can be applied to many applications of boiling such as power plant, refrigeration and food processing industries.

References

1. Sanjay, M., Ravindra, Y.: Experimental analysis of boiling and measurement of contact angle of drop on surface. *Inter. Res. J. Eng. Technol.* 56–57 (2015). e-ISSN: 2395-0056 02(02)
2. Peterson, W.C., Zaalouk, M.G.: Boiling-curve measurements from a controlled heat-transfer process. *J. Heat Transf.* **93**(4), 408–412 (2010)
3. Krause, F., Schüttenberg, S., Fritsching, U.: Modelling and simulation of flow boiling heat transfer. *Int. J. Numer. Method Heat Fluid Flow* **20**(3), 312–331 (2010)
4. Balaguru, S., Murali, V., Chellapandi, P.: Effects of different operating temperatures on the tensile properties of the grid plate hardfaced with colmonoy in a pool type sodium-cooled fast reactor. *Sci. Technol. Nucl. Install.* **2017**, 1–9 (2017)
5. Balaguru, S., Kumar, S., Murali, V., Chellapandi, P.: Thermo mechanical analysis of SS304 circular grid plate hardfaced with colmonoy. *Appl. Mech. Mater.* **229–231**, 710–717 (2012)
6. Auracher, H., Buchholz, M.: Experiments on the fundamental mechanisms of boiling heat transfer. *J. Braz. Soc. Mech. Sci. Eng.* **27**(1) (2005)

Highway Traffic Scenario-Based Lane Change Strategy for Autonomous Vehicle



Gourish Hiremath, Kiran Wani and Sanjay Patil

Abstract In recent years, autonomous or unmanned ground vehicles (UGV) have become the prima focus of research in automotive industry and even in academic institutions. Advanced driver assistance systems technologies like lane keeping system (LKS), obstacle or collision avoidance system, lane departure warning system (LDW), automatic parking system have been thoroughly researched and are being practically implemented in most of the modern-day vehicles. According to recent report by Ministry of Road Transport and Highways (MoRTH), India, the number of accidents due to improper overtaking and jumping/changing lanes is a major concern, with manoeuvrability of the driver being the sole attribute. This paper focuses on control logic for safe navigation of vehicle before lane change manoeuvre is initiated in traffic environment. The simulations have been carried out to simulate the control logic and of subject vehicle merging into two vehicles (lead and lag) for a single lane change manoeuvre. The parameters such as position, speed and gap distance between the vehicles in the current and target lane are taken into consideration for controlling the vehicle manoeuvre to avoid collisions.

Keywords Autonomous systems · Autonomous vehicle · Lane change manoeuver

G. Hiremath (✉)
College of Engineering, Pune, Maharashtra, India
e-mail: gourishh28@gmail.com

K. Wani · S. Patil
ARAI Academy, Pune, India
e-mail: wani.pga@araiindia.com

S. Patil
e-mail: sapatil.pga@araiindia.com

1 Introduction

In 2016, India witnessed reports of 480,652 road accidents that injured 494,624 individuals and claimed 1,500,785 lives. This translates to average of 1317 accidents and 413 accident deaths taking place on Indian roads each day, according to data released by the Ministry of Road Transport & Highways (MoRTH) [1]. The data highlights that driver fault remains the single most important factor responsible for road accidents in the country accounting almost 84%, killing 80.3% and injuring almost 83.9% on all roads in the country. Out of all the factors in driver's fault, jumping/changing lanes accounted for 8513 (2.1%) accidents, claiming 2795 (2.3%) lives and injuring 8177 (2.0%) individuals. Overtaking accounted for 7.3% accidents, 7.8% lives and injuring 7.0% individuals [1].

1.1 Automated Vehicle Technologies

In recent years, research and development of autonomous vehicle also or 'Self Driving car' have added a great significance so as to provide complete safety for commutation of humans. These vehicles can monitor its environment using various techniques like laser light, radar, odometer (use of data from motion sensors to estimate change in position), GPS, computer vision and navigate it from one place to another without any human intervention. Only human input will be given the start and end destinations [2].

Some of the automated vehicle technologies like lane keep assist system, parking assistance system, adaptive/active cruise control, automatic braking, trailer backup assist, blind spot detection, obstacle/collision avoidance system are now available in most of the vehicles. They require human intervention at the steering wheel to take control of the vehicle at a moment's notice. These technologies have helped in providing improved safety for the vehicle and have made provision to come nearer to the fully automated vehicle stage [3].

Jaswal and Rajashekhar [3] and der Automobil Industry [4] the lane change manoeuvre has been a challenging problem for road automation during the last two decades. This system uses a combination of techniques viz. Obstacle avoidance, blind spot detection and/or lane assist system to move the vehicle change from one lane to another or in overtaking process. This system is being tested successfully at low speeds where the control becomes easier and the sensors are good in response. But at high speeds of around 60 kmph, with the fast-moving vehicles the sensor response becomes critical and controlling parameter using the combination of other assisting systems becomes important. The driver needs a complete monitoring of the vehicle.

This paper proposes algorithm to get the desired safe gap distance for a host (autonomous) vehicle in a five-vehicle traffic scenario before it initiates the steering

control for a safe lane change manoeuvre. The manoeuvre is for a single lane change and lane change model [5] referred explains about the steps involved for carrying out the process.

2 Proposed Lane Change Scenario

The lane change manoeuvring control for the autonomous vehicle involves the subject vehicle merging in between two vehicles in the target lane. Here, the vehicle parameters of the lead and lag vehicles are considered to have safe manoeuvring. The deceleration or acceleration required by the subject vehicle to avoid collision will be main aspect. But the project work assumes the vehicle to change lane at constant speed and thus the safe distance criteria or the gap distance will be a key factor over here.

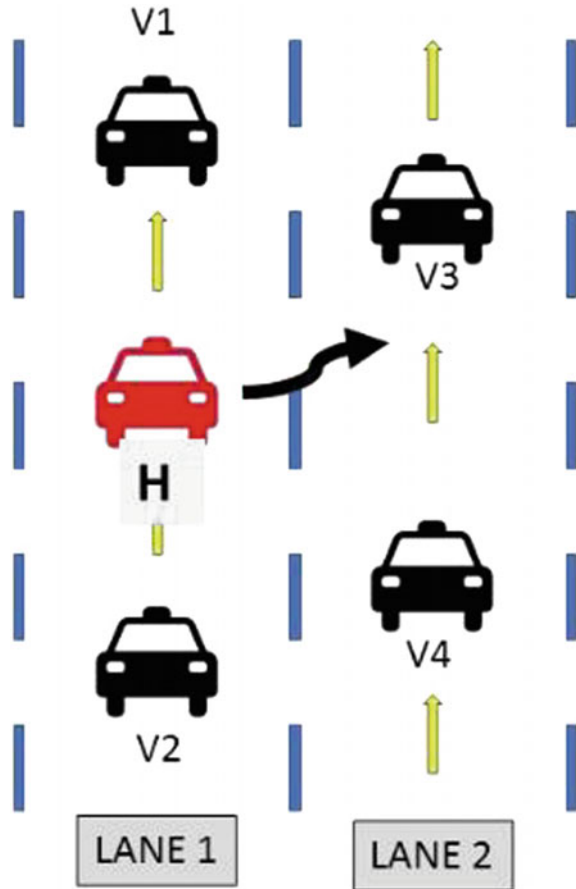
This project work proposes of developing a steering control strategy for lane changing purpose. The control strategy is to be developed for single lane change manoeuvrability with five vehicles in consideration. The five vehicles will include a host vehicle in which the control strategy for the said purpose is input. The host vehicle is in between two vehicles say vehicle 1 ahead of it and vehicle 2 behind it. These three vehicles are on one lane say Lane 1. The host vehicle needs to manoeuvre from one lane i.e. Lane 1 to another lane say Lane 2 safely. The remaining two vehicles say vehicle 3 and vehicle 4 are in Lane 2. The final output of the lane changing process of host vehicle will be to safely merge between these two vehicles and maintain the necessary speed and distance after completing the required manoeuvre. Figure 1 below shows the prerequisite of this manoeuvrability.

2.1 Lane Change Model

In the basic lane change model, the vehicle in the current lane tries to change its direction to either left or right only if the gap in the selected lane is acceptable or else it will remain in the same lane. Two types of lane change exist, namely Mandatory Lane Change (MLC) and Discretionary Lane Change (DLC), based on the execution of lane change [5].

$$a_{(n+1)} = \frac{av^m \Delta v}{\Delta x^l} \tag{1}$$

Fig. 1 Proposed lane change scenario



H = Host Vehicle
Vi = Vehicle no.
i = 1, 2, 3, 4

2.2 Lane Changing Process

There isn't any mathematical model, analytic relationship or a generalized process which can completely explain the lane changing process. As explained in [5], several decision-making steps can be considered. These steps are (a) Desire to change lane. Lane changes may be performed due to several factors such as reduced speed in the current lane, queuing, forced deceleration because of the lead vehicle. The desire to change the lane becomes stronger when the driver also perceives a higher utility in the target lane in terms of higher speed or higher acceleration or a

better position in the queue. If the vehicle has to decelerate due to lead vehicle comparatively moving at a lesser speed and the driver wishes to have better speed and queue position, then the driver desires to change lane. The deceleration or acceleration of the host vehicle in our case is given by Eq. 1 shown above

If $a_{n+1} < 0$, then the driver has to decelerate the vehicle which is not desired and therefore in this case the driver desires to change the lane. Otherwise, the vehicle needs to be continued in the same lane. (b) Selection of target lane. When there is a desire to change the lane, the driver then targets a lane to shift. A simpler way of modelling target lane selection is based on the concept of utility maximization. In this approach, one assumes that the driver will select a lane that maximizes his perceived utility. Utility of i th lane U_i can be taken as a function of several parameters such as velocity, gap between vehicles, acceleration. In this chapter, for ease in analysis, we assume the utility is same as the acceleration. Given utility of i th lane as U_i , then the probability of choosing the i th lane can be given by

$$p(i) = \frac{e^{U_i}}{\sum_{i=1}^N e^{U_i}} \tag{2}$$

where N is the number of lanes. It is assumed that the driver will choose the lane that has the maximum probability as his target lane. (c) Ensuring feasible lane change. The deceleration required for the lag vehicle in the target lane can be computed using car following model as

$$a_{n+1} = \frac{\alpha v^m \Delta v}{\Delta x^l} \tag{3}$$

If a_{n+1} is less than the critical deceleration, it is feasible to change the lane to the selected target lane. Otherwise, the vehicle will continue in the current lane. (d) Decision to change lane based on gap acceptance. The lead gap is the gap between the subject vehicle and the vehicle ahead of it in the lane it is changing to. The lag gap is defined in the same way relative to the vehicle behind in that lane. For merging into an adjacent lane, a gap is acceptable only when both lead and lag gap are acceptable. Probability that the gap is accepted is the product of the probability that the lead gap is accepted and the probability that the lag gap is accepted, given by

$$p(t_{lead}, t_{lag}) = p(t_{lead}) \times p(t_{lag}) \tag{4}$$

where

$$p(t) = \begin{cases} 1 - e^{-\gamma(t-T)} & \text{if } t > T \\ 0 & \text{otherwise } t = \frac{g}{v_{n+1}} \end{cases} \tag{5}$$

For a successful lane change of the vehicle, all the four steps condition should be satisfied and if any one doesn't satisfy the lane change process will be averted.

Control Algorithm Accordingly, with the above lane change model, a control algorithm for the host vehicle to manoeuvre in the proposed scenario is developed. The procedure followed to verify conditional approach to initiate a safe lane change manoeuvre is explained as follows and for consideration with autonomous vehicle, we assume that the vehicle is equipped with radar sensors for measuring the respective distance gap.

Procedure:

- The lane changing control needs to be activated. The ECU and the sensors will be active.
- The sensors on the host vehicle will detect the vehicles in its current lane and in the desired lane where it needs to be shifted. Suppose vehicles detected are as $V1$ and $V2$ in Lane 1 and $V3$ and $V4$ in Lane 2. If none of the vehicles is detected and the host vehicle desires to change the lanes due to mandatory condition, the lane change process will take place in the same speed of the vehicle.
- A radar sensor will detect and give the distance gap between the host vehicle and its entire respective surrounding vehicle be it from the front, rear or side. The values of the gap will be denoted as D_i where $i = 1, 2, 3, 4$ as explained before. This measured gap will be given to ECU as input. The distances measured are as $D1, D2, D3$ and $D4$ for vehicles $V1, V2, V3$ and $V4$ respectively.
- The ECU will analyse this ' D_i ' value and compare it with the set distance ' S '. The first conditional parameter will now come into picture wherein D_i should be greater than ' S '. This condition needs to be satisfied with respect to all vehicles. The condition which will be given in our case will be $D1 > S, D2 > S, D3 > S$ and $D4 > S$. Pertaining to this condition being satisfied, the signal to change lanes will be given to ECU and the desired output will be in process. The lane change operation will be averted if any of the distance gap D_i is not greater than ' S '.
- While changing lanes, Lane 1 to Lane 2 in our case, the vehicles $V3$ and $V4$ will come into consideration for conditional parameter 2. The host vehicle condition to either accelerate or decelerate will be decided from this parameter 2. Suppose D_c is the difference between the distance gap $D3$ and $D4$ and the set distance gap is SC . If $DC > SC$ then the host vehicle will accelerate and if $DC < SC$, then it will decelerate in Lane 2. If there is no vehicle in Lane 2 or the difference is too large, then the vehicle will do the required in constant speed same as in its previous lane.
- If any of this condition of this parameter is not satisfied, then the lane changing operation will be averted and the lane change assist system will be deactivated. The vehicle will be in manual control now and the driver needs to decide further process.
- The conditional parameter S and SC will be calculated from referring the lane changing models explained in the previous section.

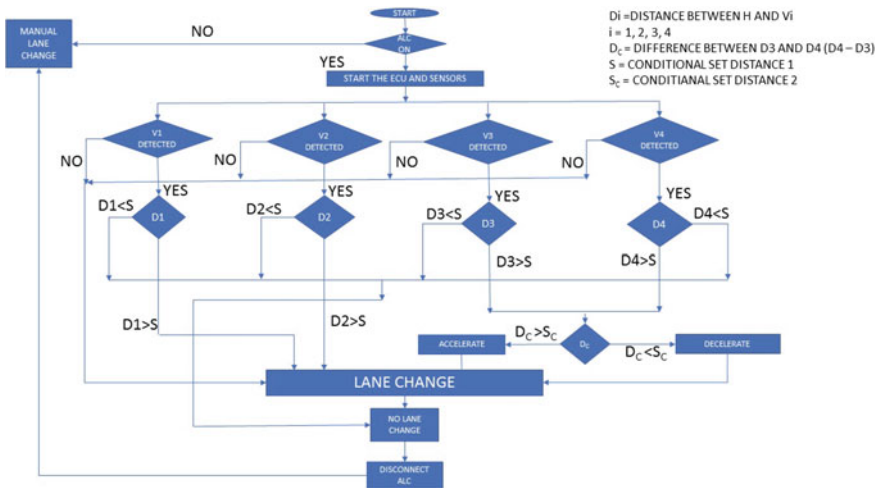


Fig. 2 Algorithm for lane change model

The flowchart for the above four step if-then-else algorithm is shown below (Fig. 2).

2.3 MATLAB Simulink Model

Simulink is used to verify the proposed algorithm and get the safe distance gap between the vehicles to avoid collisions while manoeuvring.

Since the paper proposes for a lane change manoeuvre in a highway scenario, acceleration and deceleration rate parameter is an important prospect to carry out any simulation so that the manoeuvring is safe. In the five vehicles scenario shown in Fig. 1 and considering the lane change feasibility explained in the lane changing process, critical deceleration condition parameter which if not in limits can avert the lane change process. This deceleration rate parameter is not any constant value but is variable not only with different speed of vehicle but also with the type of vehicle considered and also with different highway regions. For a typical highway patch, the critical deceleration rates for different speeds and different vehicle types like car, buses, trucks are calculated by researchers through experimentation and have been put forth in various highway and transport conferences. One such research study work was done at the Nagpur–Mumbai highway on a two-lane 1.5 km stretch [6]. From this study experiment, the mean (critical) deceleration rate was measured to be 2.42 m/s^2 for a petrol engine car and it is assumed same for this paperwork.

This critical deceleration rate comes into picture to ensure that the lane change manoeuvre is feasible wherein the deceleration of the lag vehicle in the target lane should be less than the critical deceleration for safe manoeuvre.

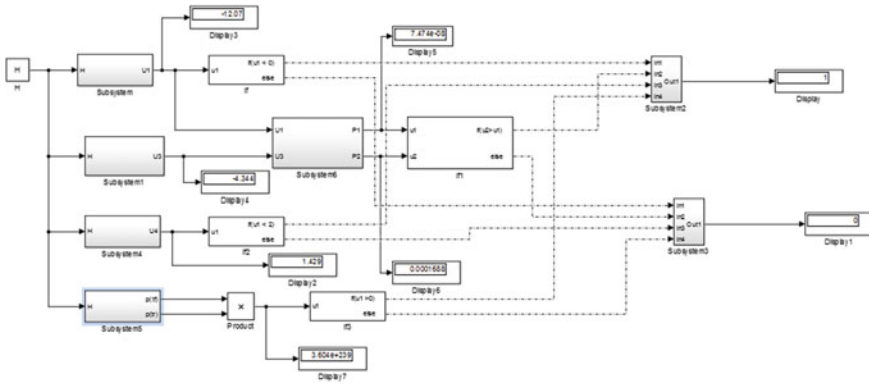


Fig. 3 Simulink model for working on the logic proposed

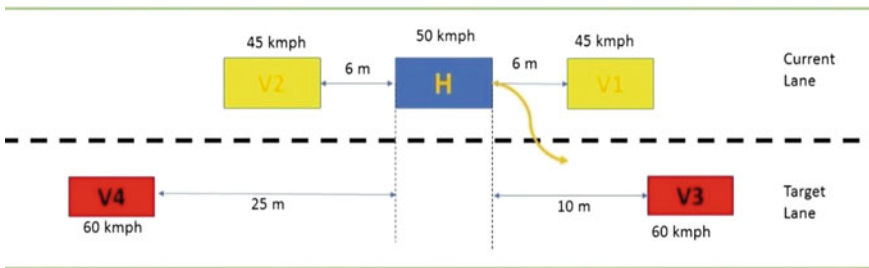


Fig. 4 Pictorial representation of safe distance gap before initiating lane change

$$a_{n+1} = \frac{\alpha v^m \Delta v}{\Delta x^l} < 2.42$$

From the lane change model considered and some literature survey, there isn't any experimentation done to give specific value of sensitivity coefficient (α), speed exponent (m) and distance headway exponent (l). Thus, for simulation purpose the above values are assumed to have value 1 i.e. $\alpha = m = l = 1$. The Simulink model shown below is developed to simulate the logic aspect (Fig. 3).

Simulation Result. The simulation was carried out on trial and error basis by keeping the host vehicle speed $H = 50$ kmph, $V1 = V2 = 45$ kmph and $V3 = V4 = 60$ kmph but varying the distance gap Δx value in each condition. From this trial method, the safe distance gap for safe manoeuvring for processed and it is as shown in the Fig. 4.

3 Conclusion

For the proposed lane change scenario and by considering the lane change model, it is evident that the logic applied to get the safe distance gap between the host vehicle and lead/lag vehicle can be successfully carried out. This value can be very useful for motion planning of the autonomous vehicle to generate a safe path for lane change manoeuvre. Though for the paperwork, the speed limits were assumed but this model can be applied to any speed data for the said manoeuvring condition.

References

1. Autocar Pro News Desk, 1,317 Accidents and 413 deaths on Indian roads each day in 2016, AutoCar Professional, 06 Sept 2017
2. Bagloee, S. et al.: Autonomous vehicles: challenges, opportunities, and future implications for transportation policies. *JMT* **V24**(4), 284–303 (2016)
3. Rajasekhar, M., Jaswal, A.: Autonomous Vehicle: The Future of Automobiles, 2015 IEEE International Transportation Electrification Conference (ITEC), Chennai, pp. 1–6 (2015)
4. Bajpayee, D., Mathur, P.: A Comparative study about Autonomous Vehicle, 2nd International Conference on Innovations in Information Embedded and Communication Systems ICII ECS '15 (2015)
5. Mathew, T.: Lane changing models, Lecture notes in Transportation System Engineering, IIT Bombay, Sep 2017
6. Bokare, P., Maurya, A.: Acceleration-deceleration behavior of various vehicle types. *Trans. Res. Procedia* **25**, 4733–4749 (2017)

Friction and Wear Analysis of PTFE Composite Materials



Sachin Salunkhe and Pavan Chandankar

Abstract Polytetrafluoroethylene (PTFE) is a very important polymer-based engineering material. The PTFE material has many applications such as in aerospace, food and beverage industry, pharmaceuticals and telecoms. In this paper, investigate the effect of sliding distance, varying load, filler content in PTFE, sliding velocity experimentally by using a pin on disc test rig. A relative analysis of three different composites usually (PTFE + 30% carbon, PTFE + 30% bronze, and PTFE + 30% glass) are presented. Commercially, pure PTFE has high wear rate in order to reduce this wear rate the experimental investigation is carried out by using pin on disc test rig under constant sliding speed and constant time of 15 min. The results revealed that pure PTFE has high wear rate than the composite PTFE materials.

Keywords PTFE composite · Pin on disc · Wear rate

1 Introduction

PTFE (polytetrafluoroethylene) is the highly useful plastic materials which were registered by name Teflon. PTFE is one branch of plastics, known as fluoropolymers [1]. A polymer is a compound type material. Compound is formed by a chemical reaction in which particles are combined into a group of repeating large molecules. Polyester and nylon are polymers which are commonly used as a synthetic fibres. PTFE is the polymerized form of tetrafluoroethylene. PTFE has a very high melting point and is also stable at very low temperatures. It has many unique properties, which make it valuable in scores of applications [2]. It is a supreme bearing material which has heavy and light load pressures with medium and low surface speeds required since it recorded as a low coefficient of friction when

S. Salunkhe (✉) · P. Chandankar

Department of Mechanical Engineering, Vel Tech Rangarajan Dr. Sagunthala R&D Institute of Science and Technology, Avadi, Chennai, India
e-mail: drsalunkhesachin@veltech.edu.in

© Springer Nature Singapore Pte Ltd. 2019

U. Chandrasekhar et al. (eds.), *Innovative Design, Analysis and Development Practices in Aerospace and Automotive Engineering (I-DAD 2018)*, Lecture Notes in Mechanical Engineering, https://doi.org/10.1007/978-981-13-2718-6_40

415

rubbed against metallic engineering surfaces. PTFE has fulfilled all qualities of bearing alloys such as embedded ability, conformability, load capacity, corrosion resistance, fatigue strength, compatibility and hardness. In this paper, the characterization of PTFE materials are calibrated with low coefficient of friction. The low coefficient of friction is developed from the ability of its information extended linear molecules to low shear strength films and counter-faces during sliding. It is a crystalline solid with good stability from -454 to $+500$ °F (-270 to $+260$ °C) and is chemically inert to known reagents and solvents except molten alkaline metals and gaseous fluorine under pressure. Its relative softness and poor heat conductivity are responsible for the competency as a bearing material to applications involving low speeds and low unit pressures. PTFE is technically superior and economically cheaper friction material as compared to conventional bearing materials. Recently, many researchers have worked on PTFE composite materials such as Khedkar et al. [3] investigated the tribological behaviour of PTFE filled with carbon, graphite, MoS₂, E-glass fibres and poly-p-phenylene terephthalamide (PPDT) fibres. Unal et al. [4] studied and analysed the effect of test speed and load values on the friction and wear behaviour of pure PTFE, and PTFE filled with glass fibre reinforced (GFR), bronze and carbon (C). Bajaj et al. [5] investigated the tribological behaviour of PTFE filled with glass fibres, carbon, bronze, graphite. Friction and wear are very important surface phenomenon. Yuan and Yang [6] investigated the tribological characteristics of polytetrafluoroethylene (PTFE) coatings by using ball-on-disc wear tester under vacuum conditions. Kapsiz et al. [7] explored the friction and wear characteristics of cylinder liner (CL)/piston ring (PR) pair. Conte and Igartua [8] explored the comparative study of frictional energy analysis of PTFE composites. They used soft and hard phase in a polymer matrix enhances for improving the tribological properties of the PTFE. Prabu et al. [9] described and studied the influence on banana fibre-reinforced unsaturated polyester composites filled with red mud on wear responses. Sudheer et al. [10] evaluated the tribological performance of potassium-titanate-whiskers (PTW)-reinforced epoxy composites of independent parameters such as sliding velocity, normal load, filler content and sliding distance. Sahin and Mirzayev [11] investigated dry wear of PTFE composites, bronze-filled composites (B60), glass-filled composites (G15) and carbon-filled composites (C25), under different sliding conditions. From the available literature, it is found that the worldwide researchers have applied effort to investigate of behaviour of various composite materials. Few of the researchers have attempted in the area of PTFE by the addition of filler materials with specified weight percentage. Therefore, there is a need to investigate the influence of filler addition on wear and friction behaviour of PTFE composite materials. The present paper investigated the effects of varying load, sliding distance, sliding velocity and filler content in PTFE by experimentally using a pin on disc tribometer. The objective of the present research is relating the influence of sliding speed, load, sliding distance and percentage of carbon, glass and bronze addition to the PTFE with dry sliding wear of the PTFE.

2 Experimentation

A round-shaped specimen is fitted and pressed into contact of the disc by means of lever which is loaded by lever arm and dead weights as shown in Fig. 1. The pin is inserted into the pin holder which mounted on flat. The pin is mounted for free slide at the right angle to the axis for the disc is rotates. The tangential force applied by the disc on the pin is measured by the beam type load cell connected to the indicator. These types of procedure need not be any interface between normal pressing force and the tangential force arising from friction. Electric motor with a belt and pulley is used for rotating the disc with a required speed.

2.1 Procedure

The specimen was cleaned and dried before actual testing and prior to measuring. The specimen should free from all dirt and foreign matter. The specimen was cleaned by using non-chlorinated, non-film-forming cleaning agents and solvents. The dry materials with open grains were used to remove all traces of the cleaning

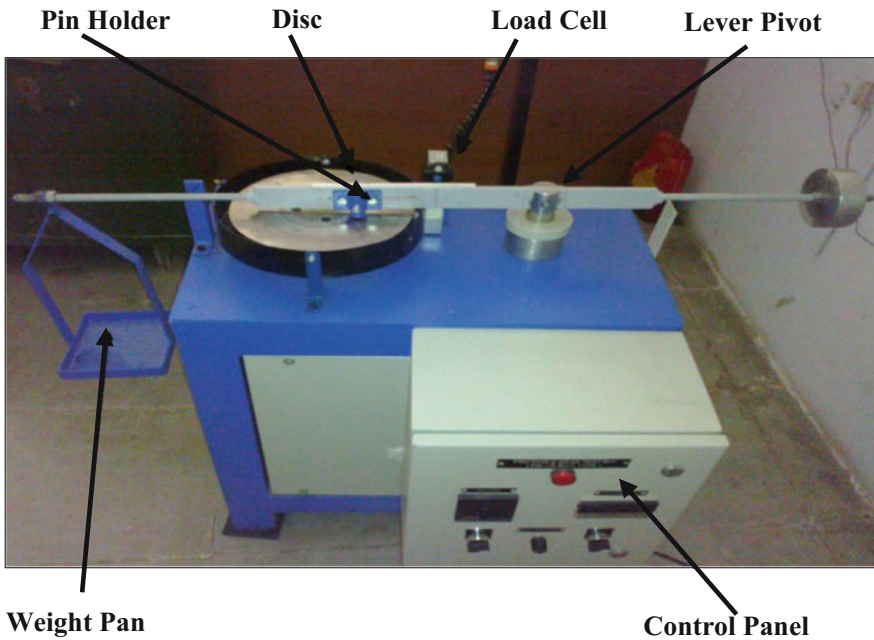


Fig. 1 Experimental set up of pin on disc

fluids that may be entrapped in the material. The dimensions and weight of the specimens are $\pm 2.5 \mu\text{m}$ and $\pm 0.0001 \text{ g}$ were used. The disc is inserted on locating device and perpendicular to the axis. The pin is inserted in specimen holder and, if necessary, in order to maintain the necessary contact conditions between disc and the specimen adjustment were required that the specimen is perpendicular (61°) to the disc surface. After pin is inserted on specimen, the require mass is added into the lever and develop the selected force for pressing the pin against the disc. The speeds of the motor were adjusted according to the desired value while to stop the motor hold the pin specimen out of contact with the disc. Revolution counters (or equivalent) are set to the desired number of revolutions. The tests were carried out till revolutions achieved. Tests have not be interrupted or restarted. Wear Test: The wear testing is carried out in accordance with American society for testing and materials (ASTM) standard. The tests are conducted under a dry-lubricating condition by considering various parameters such as contact on load is 10 N, spindle speed is 0.1 m/s and sliding distance is 500 m. The specimens were removed and cleaned off all loose wear debris such as existence of features on or near the wear scar such as protrusions, displaced metal, discoloration, microcracking or spotting. The dimensions of the specimens were remeasured to the nearest $\pm 2.5 \mu\text{m}$ or reweigh the specimens were to the nearest $\pm 0.0001 \text{ gm}$.

3 Preparation of Material

3.1 Materials

The specimen should not be fail during testing without affecting the size and stresses. The materials are tested and described by dimensions, surface finish, material type, form, composition, microstructure and indentation hardness in this paper.

3.2 Test Specimens

The standard pin specimen having cylindrical or spherical in shape have a diameters range from 2 to 10 mm. The diameter of disc is from 30 to 100 mm with about 2–10 mm thickness. Figure 2 shows the PTFE and its three different composite materials. From right-hand side, figure indicates pure PTFE, second is PTFE filled 30% carbon named as composite A, third shows PTFE filled 30% bronze name composite C, extreme left-hand side indicates the PTFE filled 30% glass named composite B which is in white colour.

Fig. 2 Wear specimens

3.3 Surface Finish

The present paper considers a $0.8 \mu\text{m}$ roughness of a ground surface. At the time of surface preparation avoid subsurface damages that alters the material significantly. Some surface preparation may be applicable for some test programs. The standard rod of virgin PTFE and its composite with fillers such as 30% carbon, 30% bronze and 30% glass is used. The sample pieces were prepared by using necessary turning and facing operations on the respective sample rods. The dimensions of specimen $12 \times 70 \text{ mm}$ were used. The specimen of pins is fitted into the pin holder, and observations are as shown in Table 1. The tribological behaviour of PTFE filled with 30% carbon, 30% glass and 30% bronze are performed on a pin on disc wear tester (Model TR 20-LE) under room conditions. In this paper, the tribological behaviour of the composites materials with the three different variables are used, Taguchi approach the design of experiments. In the design of experiment, full factorial method sliding tests with four parameters and three levels ($3^4 = 81$) tests are required. But in this paper, however, only nine experiments are performed of each composite material with the use of the simplified orthogonal arrays designed by Taguchi. The variables are sliding speed; load and filler proportions in PTFE.

Table 1 The general and mechanical properties of three test materials at room temperature

Materials	Density (gm/cc)	Tensile strength	Elongation (%)	Hardness	Heat resistance
30% C filler PTFE	2.12	130 g/cm^2	122	70 shore D	-250 to +260 $^{\circ}\text{C}$
30% G filler PTFE	2.24	145 kg/cm^2	210	70 shore D	-250 to +260 $^{\circ}\text{C}$
30% Br filler PTFE	3.1	126 kg/cm^2	111	70 shore D	-250 to +260 $^{\circ}\text{C}$

Table 2 L9 (27) orthogonal arrays designed by Taguchi method

No. of test runs	Load	Velocity (m/s)	C:SD (km)
1	3	0.9424	0.8
2	3	1.2566	1.13
3	3	1.5707	1.4
4	4	1.2566	1.13
5	4	1.5707	1.4
6	4	0.9424	0.8
7	5	1.5707	1.4
8	5	0.9424	0.8
9	5	1.2566	1.13

The parameters values and the experimental setup by Taguchi's orthogonal arrays are shown in Table 2.

4 Results and Discussion

The experimental results of combinations of various parameters are shown in Figs. 3, 4, 5, 6, 7 and 8. The wear of the PTFE composites filled 30% carbon, 30% glass and 30% bronze which are shown graphically in Figs. 3, 4, and 5, respectively. The wear rate of the PTFE composites filled 30% carbon, 30% glass and 30% bronze are 5, 14, 23 in μm , respectively, at constant time for 15 min for constant sliding speed 300 rpm at room temperature. In Fig. 3, the wear rate is increased with increasing time steadily as shown in figure. From the below graph, it is revealed that wear of PTFE filled with wt%30 C has low wear rate as compared to PTFE filled with wt%30 Gl and wt%30 Br. The increasing order of wear rate PTFE filled wt%30 C > wt%30 Br > wt%30 Gl.

The coefficients of friction of the PTFE composites filled 30% carbon, 30% glass and 30% bronze are shown in Figs. 6, 7, and 8, respectively. The smooth shape along the wear track is a characteristic of PTFE systems. Carbon-filled PTFE, glass-filled PTFE and bronze-filled PTFE are average friction coefficients of $\bar{\mu} = 0.240$ and $\bar{\mu} = 0.351$, and $\bar{\mu} = 0.348$, respectively. 30% Carbon wt. PTFE composite has steady frictional behaviour with an average friction coefficient of $\bar{\mu} = 0.348$. The 30% carbon wt PTFE composite has increased in the initial condition then it is decreased at time $t = 150$ s and again it increased in steady mode frictional behaviour with an average friction coefficient of $\bar{\mu} = 0.348$. Similarly, in the case of glass-filled PTFE composite materials. In the case of bronze-filled PTFE composite, it obtained a steady behaviour as shown in Fig. 8.

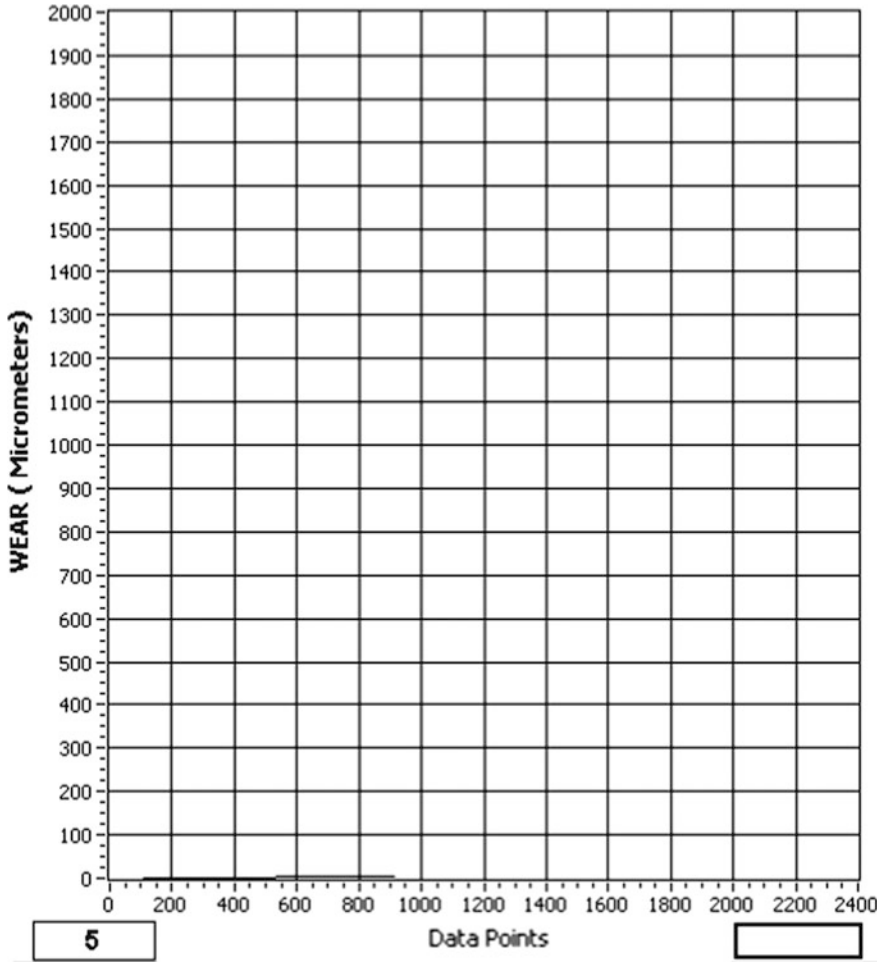


Fig. 3 Coefficients of friction versus time for a composite sample PTFE to filler wt%30 C

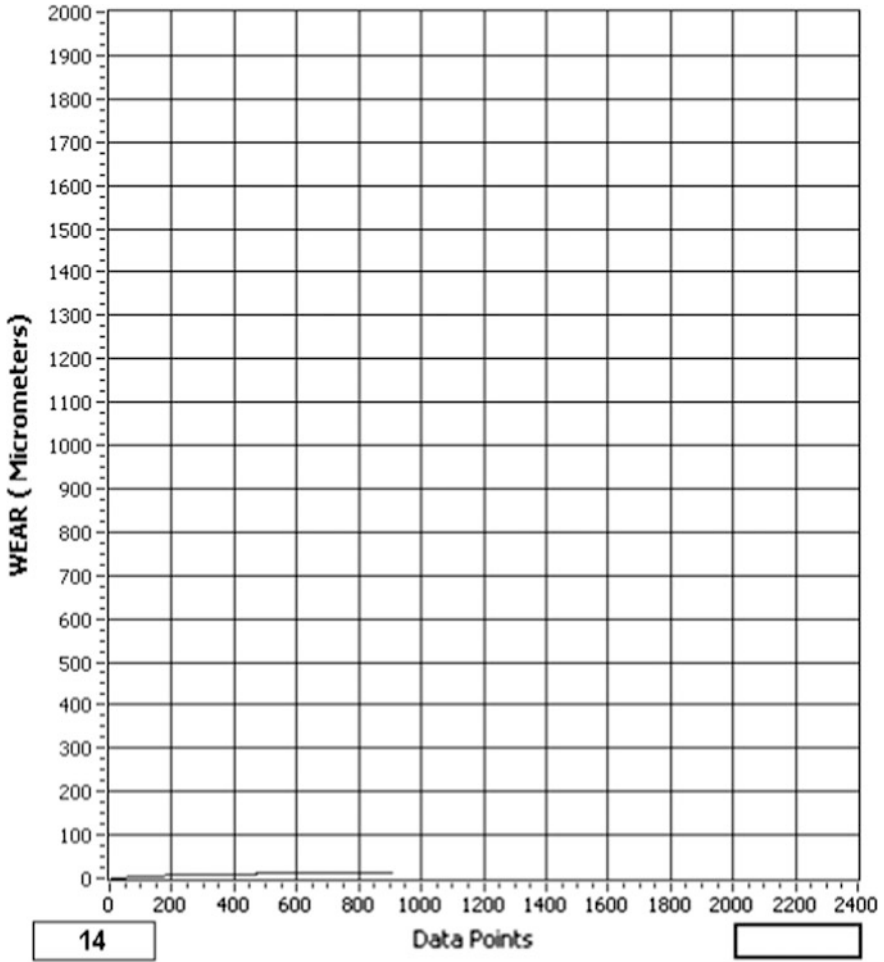


Fig. 4 Wear rate versus time for composite sample PTFE to filler wt%30 Br

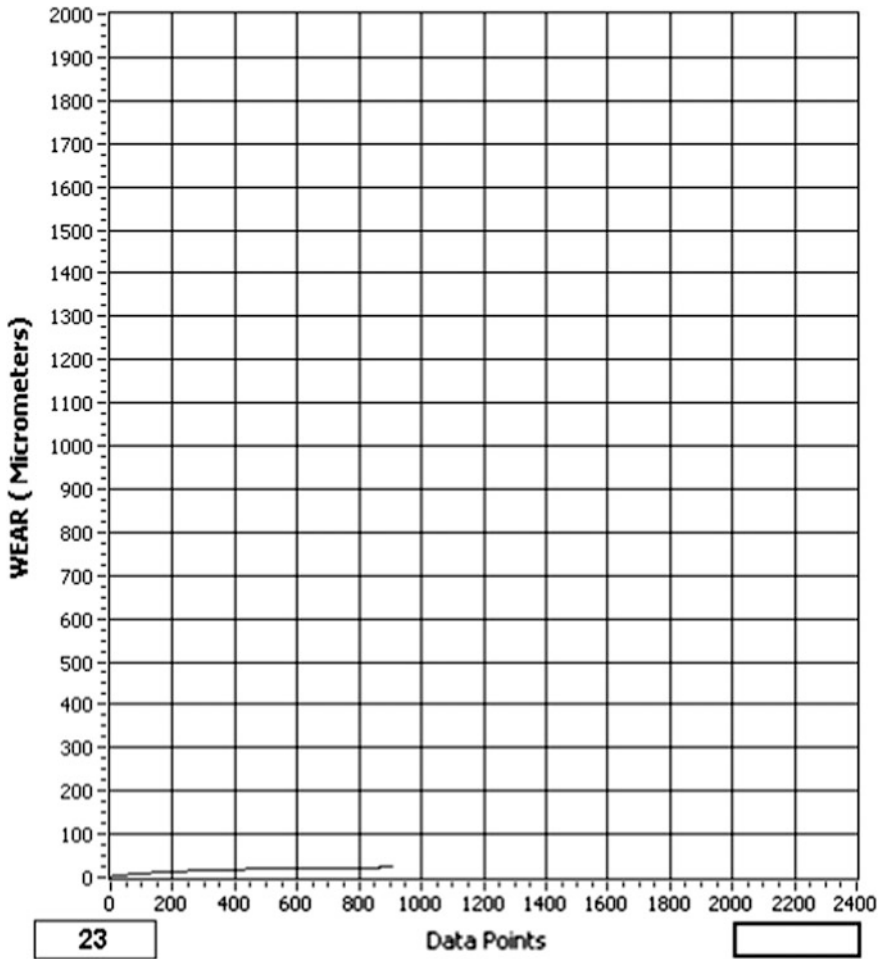


Fig. 5 Wear rate versus time for a composite sample PTFE to filler wt%30 GI

5 Conclusions

Based on the present investigation on solid PTFE, three different composites at various parameter settings of sliding velocity, loading and sliding distance are presented. Solid wear behaviour of these composites materials is successfully analysed using pin on disc test rig. Taguchi method is a simple, systematic and efficient method for the identification and optimization of the control factors and their interactions to get the optimum results of the processes. The results indicate that sliding velocity, loading and sliding distance and filler materials are the important factors in affecting the wear rate. Despite the effect of sliding velocity is

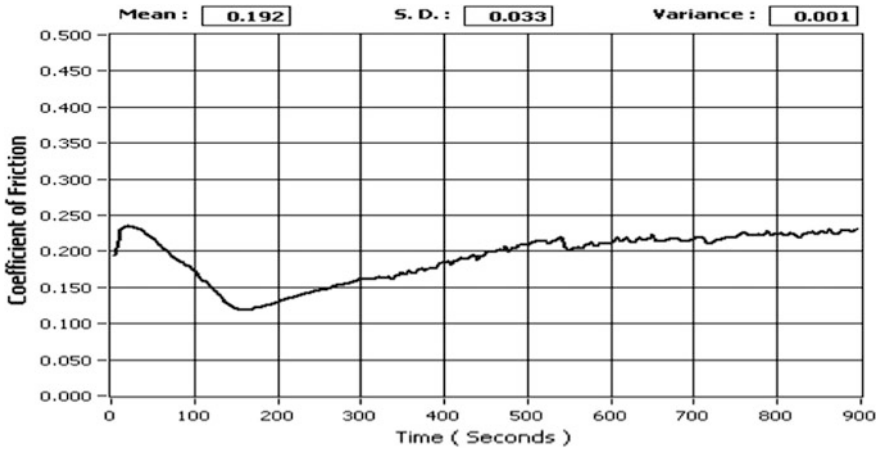


Fig. 6 Coefficients of friction versus time for a composite Sample PTFE to filler wt%30 C

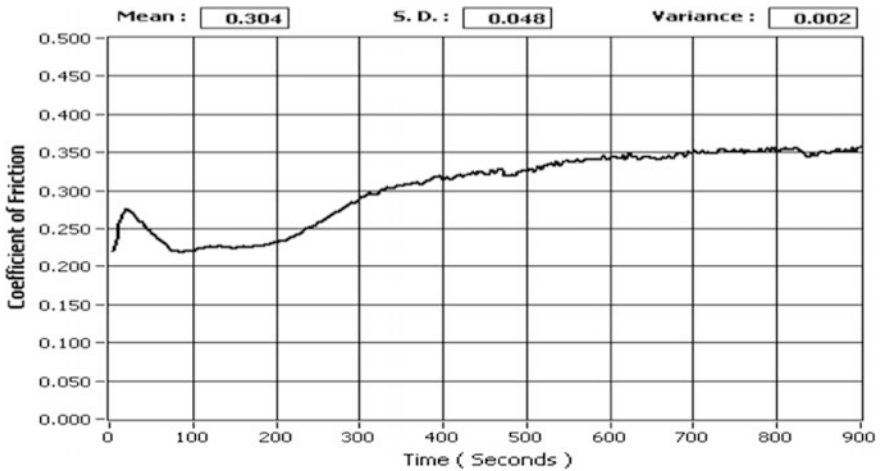


Fig. 7 Coefficients of friction versus time for a composite sample PTFE to filler wt%30 GI

less compared to other factors, it cannot be ignored because it revealed significant interaction with sliding distance, loading and filler materials. The wear life of the pure PTFE is very short because PTFE cannot form durable transfer film on the steel counter-face. PTFE has been developed to form big flakes and left the contacting region during the friction process. PTFE composite material could carry out obvious back-transfer to the composite, which effectively reduced wear of the pure PTFE.

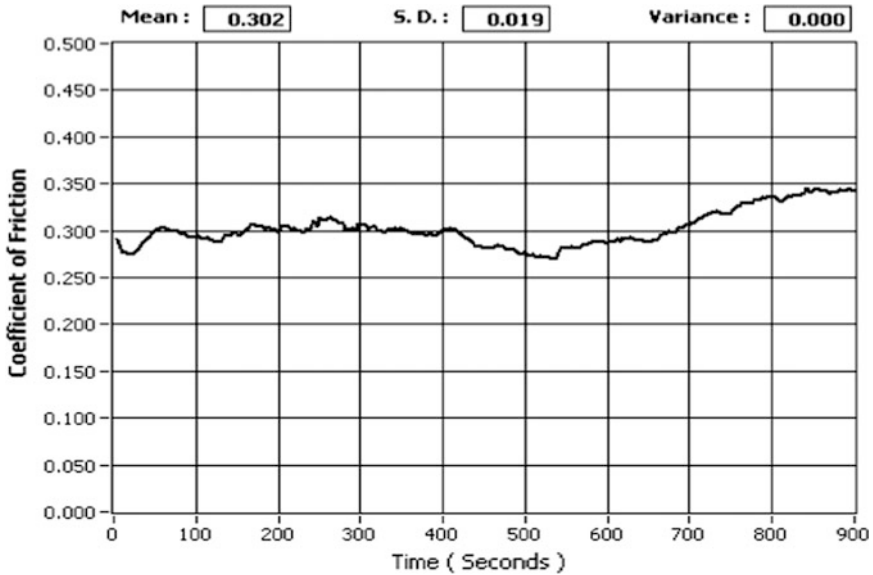


Fig. 8 Coefficients of friction versus time for a composite sample PTFE to filler wt%30 Br

References

1. Biswas, S.K., Vijayan, K.: Friction and wear of PTFE—a review. *Wear* **158**, 193–213 (1992)
2. Sawyer, W.G., Freudenberg, K.D., Bhimaraj, P., Schadler, L.S.: A study on the friction and wear behavior of PTFE filled with alumina nanoparticles. *Wear* **254**, 573–580 (2003)
3. Khedkar, J., Negulescu, I., Meletis, E.I.: Sliding wear behavior of PTFE composites. *Wear* **252**, 361–369 (2002)
4. Unal, H., Mimaroglu, A., Kadioglu, U., Ekiz, H.: Sliding friction and wear behaviour of polytetrafluoroethylene and its composites under dry conditions. *Mater. Des.* **25**, 239–245 (2004)
5. Bajaj, D.S., Vikhe, G.J., Kharde, Y.R.: An investigation of tribological behavior of PTFE + glass fiber against variable surface roughness of counter surface. *Indian J. Tribol* **3**, 47–54 (2008)
6. Yuan, X.D., Yang, X.J.: A Study on friction and wear properties of PTFE coatings under vacuum conditions. *Wear* **269**, 291–297 (2010)
7. Kapsiz, M., Durat, M., Ficici, F.: Friction and wear studies between cylinder liner and piston ring pair using Taguchi design method. *Adv. Eng. Softw.* **42**, 595–603 (2011)
8. Conte, M., Igartua, A.: Study of PTFE composites tribological behavior. *Wear* **296**, 568–574 (2012)
9. Prabu, V.A., Manikandan, M., Uthayakumar, M.: Friction and dry sliding wear behavior of red mud filled banana fibre reinforced unsaturated polyester composites using Taguchi approach. *Mat. Phys. Mech.* **15**, 34–45 (2012)
10. Sudheer, M., Prabhu, R., Raju, K., Bhat, T.: Optimization of dry sliding wear performance of ceramic whisker filled epoxy composites using Taguchi approach. *Adv. Tribol.* (2012). <https://doi.org/10.1155/2012/431903>
11. Sahin, Y., Mirzayev, H.: Wear characteristics of polymer—based composites. *Mech. Compos. Mater.* **51**(5), 543–554 (2015)

Flow Analysis of Catalytic Converter—LCV BS III Applications for Optimising Pressure Drop



C. P. Om Ariara Guhan  and G. Arthanareeswaran 

Abstract Recently, Indian government enforces stringent control standards for automotive emissions in order to minimise pollution and keep the environment green. To confirm these emission norms, new advanced technologies have been developed in the automotive emissions after treatment systems market. Diesel oxidation catalyst is one of the important contraptions which play a major role in reducing CO and unburned HC emissions. By employing CFD software, the flow properties of catalytic converter can be analysed. This helps to optimise the surface area of DOC, and the effective reaction area is utilised for oxidising the unburned hydrocarbon and carbon monoxide of engine exhaust gases. In the present work, 0.8-litre DOC has been modelled in CATIA V5 software, and CFD analysis was executed by ANSYS CFX software. The pressure drop has been compared by varying the cell density and wall thickness. Finally, the results are compared and the parameters of substrate which give optimum pressure drop are established and concluded. The novelty of the present work is that wall thickness of the porous media substrate, which is in mill inch, has been considered to find out the pressure drop. Calculated pressure drop is verified with engine test bed pressure drop experimental data, before concluding the results.

Keywords Catalytic converter · Diesel oxidation catalyst · Pressure drop

C. P. Om Ariara Guhan
Hinduja Tech Ltd, Chennai 600032, Tamil Nadu, India

G. Arthanareeswaran (✉)
Department of Chemical Engineering, National Institute of Technology,
Tiruchirappalli 620015, India
e-mail: arthanaree10@yahoo.com

© Springer Nature Singapore Pte Ltd. 2019
U. Chandrasekhar et al. (eds.), *Innovative Design, Analysis and Development Practices in Aerospace and Automotive Engineering (I-DAD 2018)*, Lecture Notes in Mechanical Engineering, https://doi.org/10.1007/978-981-13-2718-6_41

1 Introduction

Pressure drop optimisation is one of the most important activities in catalytic converter design. Normally during internal combustion engine working process, there will be work loss due to admitting fresh charge into cylinder and removing exhaust gas from the cylinder. Because of this energy loss, the volumetric efficiency of engine is being affected. This loss leads to reduce the performance of engine also. IC engine net output is having linear relationship with back pressure [1]. Catalytic converter can be modelled in two ways. One is single channel model and the other is entire convertor model [2]. Single channel models [3] usually have the process of modelling solid and fluid phase separately, then available physical space is considered as solution domain. For 2D and 3D, this would be a time-consuming process. To overcome this time-consuming problem, volume average process is used, and the model is treated as continuous porous medium [4]. The main disadvantage of volume average process is information loss at microlevel. To overcome this issue, the representative channel method is used in the industry. In this methodology, minimum number of channels are modelled and then assembled with macromodel. To find out the result, the interpolation is made between them [5, 6]. Jeong and Kim [7] proved that to optimise the monolith design, compromise should be made between uniformity index and pressure drop. They used variable cell density concept as radially. Ramanathan et al. [8] used transient 1D simulation model for calculating light-off criteria and estimated the cold-start emissions for nonuniform precious materiel-loaded monolith. Weilenmann [9] explained two important points of catalyst simulation. He executed the analysis by modifying the exhaust gas mass flow rate and temperature according to load and speed changes in real driving scenario. Gundlapally and Balakotaiah [10] compared cold-start emissions of a catalytic converter with ceramic [1 W/(m K)] and metallic [50 W/(m K)] substrates with intermediate conductivity. In the present work, we studied the effect of pressure drop, maximum space velocity variation and residence time for varying cell density as well as varying wall thickness of a DOC. Based on this study, we can conclude the optimised cell density and wall thickness for improved pressure drop. In this analysis, the designs of catalytic converter substrates were modelled in CATIA V5 software. By using CFX software, the system was optimised with CFD methodology.

2 Theory

The ceramic honeycomb-structured substrate was assumed as continuous porous medium when CFX was employed [6]. The flow is assumed as fully developed laminar flow [11]. The porous medium was modelled by adding source term to the momentum equation. The source term S_i was given by:

$$s_i = \frac{\partial p}{\partial x_i} = - \left(\sum_{j=1}^3 D_{ij} \mu v_j + \sum_{j=1}^3 C_{ij} \frac{1}{2} \rho |v_j| v_j \right) \tag{1}$$

where the subscript i is the direction of Cartesian coordinate system. The pressure drop was calculated empirically by [12]:

$$\Delta p = \left(\frac{28.4 \mu v L}{d_h^2} \right) + \left(\frac{0.5 \rho v^2}{2} \right)$$

3 Experimental Work

3.1 Design

DOC catalytic converter has been designed with the help of CATIA V5 for pressure drop optimisation analysis. 0.8-litre close coupled CATCON has been designed with an overall length of 192.5 mm and 103 mm outer diameter. CATCON consists of three major design areas as front cone, body and rear cone. The front cone area was designed with 51.1 mm cone diameter at inlet and 31.3 mm cone length. The body area was designed with 103 mm diameter and 132.1 mm length. The rear cone area was designed with 51.1 mm cone diameter at the exit and 22.5 mm cone length. The three-dimensional view of catalytic converter model is shown in Fig. 1. The geometrical parameters of the converter are listed in Table 1. Four ceramic

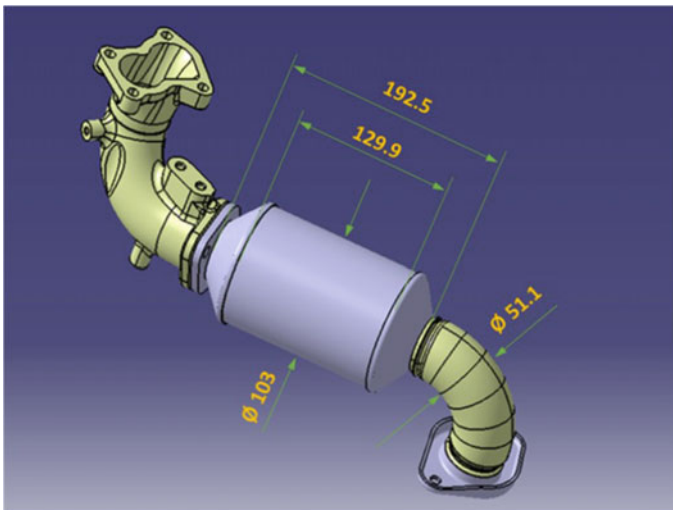


Fig. 1 Catalytic converter

Table 1 Parameters of substrate

Parameters	Values (mm)
Diameter of monolith	90.7
Length of the monolith	126
Insulation thickness	5
Inlet and outlet cone length	24.6
Diameter of inlet and outlet pipes	51.1

Table 2 Substrate properties

Cell density (cps)	Wall thickness (mil)	Dh of cell channel (mm)	OFA (%)	GSA (m ² /m ³)
400	4.5	1.106	75.8	2742.139
400	6.5	1.055	69	2616.155
600	4.3	0.877	71.6	3265.162
600	3.5	0.8981	75	3340.752

substrates have been modelled with various cell densities for flow analysis. The geometrical properties of the ceramic substrates simulated in this work are summarised in Table 2.

3.2 Computational Modelling and Grid Generation

The STEP file of 0.8-litre CATIA V5 3D model of close coupled CATCON was imported inside the meshing tool ICFM CFD. The geometry has been cleaned up, and the fluid domain was extracted. Tetrahedral mesh elements were used to complete the mesh generation. A total number of meshing elements were about 956672. The aspect ratio has been checked for 0.2.

3.3 Boundary Conditions of the Model

In the present work, k -epsilon ($k - \epsilon$) model used for simulating the turbulence model, working fluid is exhaust gas. Properties of exhaust gas are defined as density = 0.55 kg/m³, viscosity = 3.81e⁻⁵ Pa s. Executed the CFD analysis for mass flow rate of 195 kg/h, 546 °C has been considered as inlet condition. Open to atmosphere (0 Pa) has been considered as outlet condition. Porous media properties are summarised in Table 3.

Table 3 Porous media properties

	400 cpsi/ 4.5 mil	400 cpsi/ 6.5 mil	600 cpsi/ 4.3 mil	600 cpsi/ 3.5 mil
Inertial coefficient ($/m$)	15.885	19.173	17.779	16.224
Viscous coefficient ($1/m^2$)	$3.236e^{07}$	$3.907e^{07}$	$5.435e^{07}$	$4.959e^{07}$

4 Results and Discussion

4.1 Pressure Drop Analysis with Varying Mass Flow Rate

The kinetic energy of mean flow has been dissipated as heat. This is simulated in pressure drop analysis. Due to the heat dissipation, the pressure energy has been reduced. The total pressure drop of catalytic converter which is having 400 cpsi, 4.5 mil and 0.025 mm wash coat thickness is about 2.47 kPa. It is clear from Fig. 2 that when the mass flow rate increases, the pressure drop also increases. The flow rate varied from 180 to 210 kg/h, and the resultant pressure drop profile variation was observed. Figure 3 explains pressure distribution.

4.2 Pressure Drop Analysis with Varying Flow Rate with Varying Wall Thickness and Constant Cell Density (400 cpsi)

Figure 4 explains that pressure drop increases if we keep cell density as constant and with varying wall thickness. This is due to reduction in exposed area. When

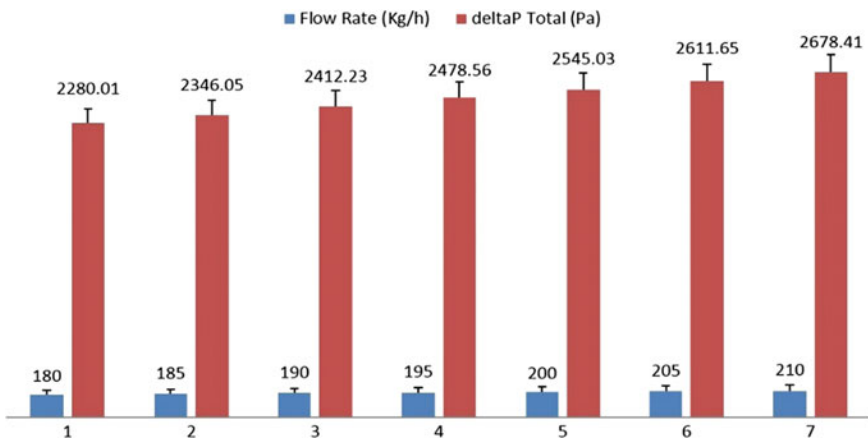


Fig. 2 Pressure drop with varying flow rate

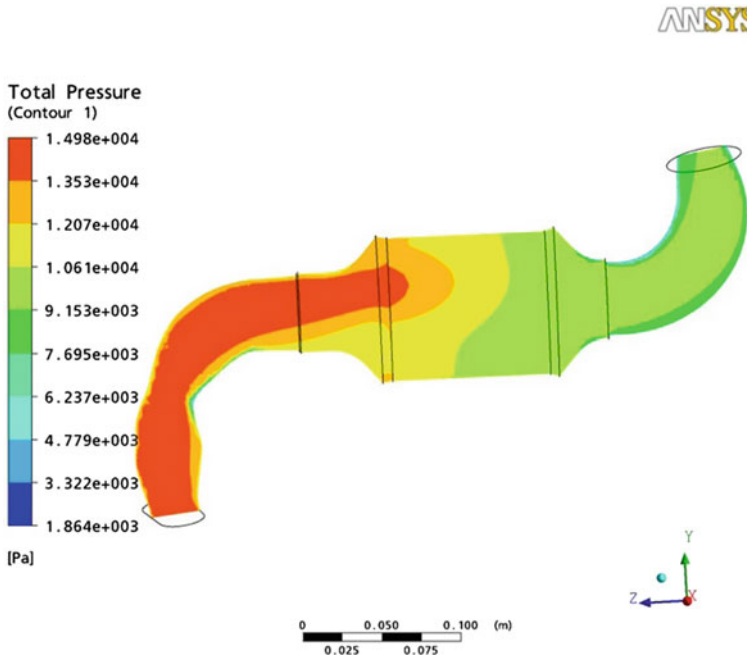


Fig. 3 Pressure distribution

wall thickness increases, the resistance also increases for the exhaust flow in substrate. CFD analysis clearly shows that the pressure drop increases when the wall thickness increased from 4.5 to 6.5 mil. The analysis has been carried out by changing mass flow rate for the same boundary conditions, and the results are analysed in Fig. 5 that explains the velocity distribution of catalytic converter.

4.3 Experimental Validation

Pressure drop obtained by CFD results of the 400 cpsi 4.5-mil substrate with 0.025 mm wash coat thickness is compared with engine test bed pressure drop experimental data for the verification of the accuracy of simulation results. Engine test bed data has been measured at 3300 rpm and 195 kg/h inlet mass flow rate which is explained in Fig. 6. The pressure drop obtained by CFD result is 2545.03 Pa. Engine test bed experimental pressure drop value is 2392.3 Pa.

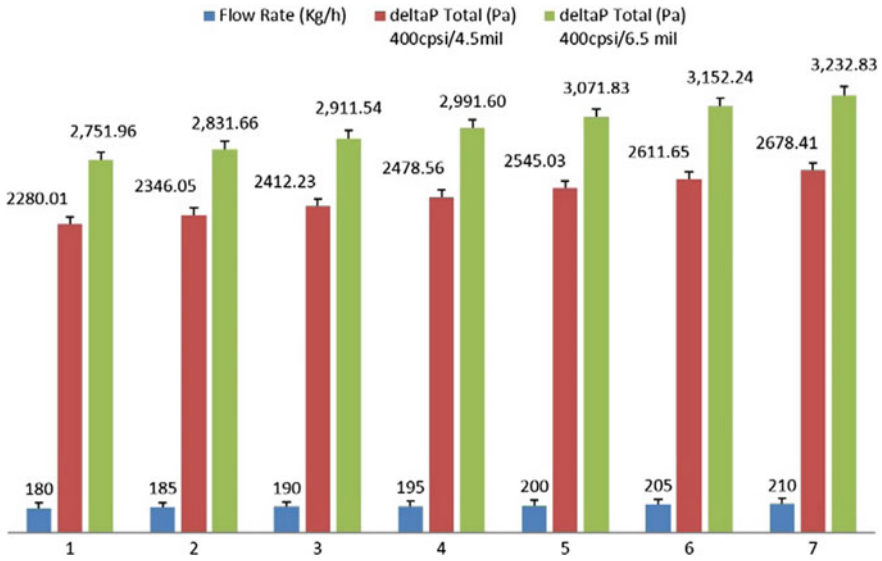


Fig. 4 Varying wall thickness and constant cell density

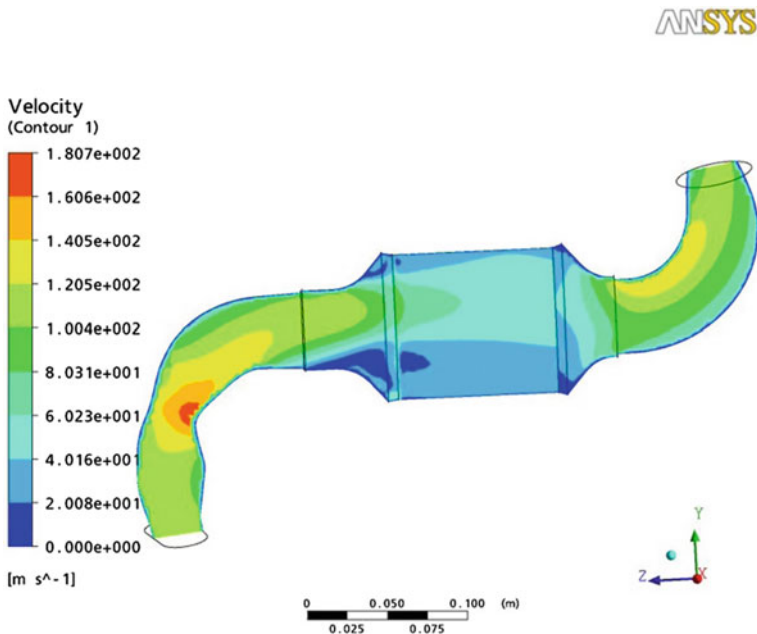


Fig. 5 Velocity distribution of CATCON



Fig. 6 Test bed set-up

5 Conclusion

This present work investigated the pressure drop variations with reference to the change in cell density and wall thickness. The computational tool CFX was used to study the fluid flow characteristics. As the mass flow rate increases, pressure drop also increases.

- Pressure drop was more desirable in 400 cpsi 4.5-mil substrate with 0.025 mm wash coat thickness after comparing with other proposed substrates.
- Velocity profile was more uniform in 400 cpsi 4.5-mil substrate with 0.025 mm wash coat thickness when compared to other proposed substrates.
- Residence time is reduced when mass flow rate of exhaust fluid increased, and there is not much variation was observed due to wall thickness variation of the substrate, when volume of substrate was kept constant.
- With reference to the above analysis, 400 cpsi 4.5-mil substrate with 0.025 mm wash coat thickness is optimal for this particular application.
- Pressure drop obtained by CFD results for 400 cpsi 4.5-mil substrate with 0.025 mm wash coat thickness was compared with engine test bed pressure drop experimental data. The percentage of error is 6%.

References

1. Kamble, P.R., Ingle, S.S.: Copper plate catalytic converter: an emission control technique. SAE Technical Paper 2008-28-0104 (2008)
2. Hayes, R.E., Fadic, A., Mmbaga, J., Najafi, A.: CFD modelling of the automotive catalytic converter. *Catal. Today* **188**(1), 94–105 (2012)
3. Hayes, R.E., Kolaczowski, S.T., Thomas, W.J.: A finite element model for a catalytic monolith reactor. *Comput. Chem. Eng.* **16**(7), 645–657 (1992)
4. Zygorakis, K.: Transient operation of monolith catalytic converters: a two-dimensional reactor model and the effects of radially nonuniform flow distributions. *Chem. Eng. Sci.* **44** (9), 2075–2086 (1989)

5. Tischer, S., Deutschmann, O.: Recent advances in numerical modeling of catalytic monolith reactors. *Catal. Today* **105**(3–4), 407–413 (2005)
6. Braun, J., Hauber, T., Tobben, H., Windmann, J., Zacke, P., Chatterjee, D., Correa, C., Deutschmann, O., Maier, L., Tischer, S., Warnatz, J.: Three-dimensional simulation of the transient behavior of a three-way catalytic converter. SAE Technical Paper 2002-01-0065 (2002)
7. Jeong, S., Kim, W.: A study on the optimal monolith combination for improving flow uniformity and warm-up performance of an auto-catalyst. *Chem. Eng. Process.* **42**(11), 879–895 (2003)
8. Ramanathan, K., West, D.H., Balakotaiah, V.: Optimal design of catalytic converters for minimizing cold-start emissions. *Catal. Today* **98**(3), 357–373 (2004)
9. Weilenmann, M.: Aspects of highly transient catalyst simulation. *Catal. Today* **188**(1), 121–134 (2012)
10. Gundlapally, S.R., Balakotaiah, V.: Analysis of the effect of substrate material on the steady-state and transient performance of monolith reactors. *Chem. Eng. Sci.* **92**, 198–210 (2013)
11. Jeong, S., Kim, T.: CFD investigation of the 3-dimensional unsteady flow in the catalytic converter. SAE Technical Paper 971025 (1997)
12. Ekstrom, F., Andersson, B.: Pressure drop of monolithic catalytic converters experiments and modeling. SAE Technical Paper 2002-01-1010 (2002)

Step Toward Computer-Aided Integration of Sheet Metal Applications



Ravi Kumar Gupta, H. M. A. Hussein, S. S. Salunkhe, Mukur Gupta
and S. Kumar

Abstract Integration of sheet metal product design, simplification, and fabrication applications is one of the major titles in the sheet metal industry. The integration of sheet metal product design and production in a computer-aided environment is a challenge due to its complicated shapes and the possibility of applications which it needs. In this paper, step toward computer-aided integration of sheet metal applications based on central repository and information management is explained by describing the development of a generic architecture and basic operations required to build the central repository. This architecture is elaborated upon for the integration of sheet metal part model (design) with sheet metal applications in which sheet process planning is one of them. The architecture and the integrations are demonstrated using a case study.

Keywords Sheet metal product development · Applications · CAD
Process planning

R. K. Gupta (✉)

Mechanical Engineering Department, Manipal University Jaipur, Jaipur, India
e-mail: rkgiisc@gmail.com; ravikumar.gupta@jaipur.manipal.edu

H. M. A. Hussein

Mechanical Engineering Department, Faculty of Engineering, Helwan University,
Cairo 11792, Egypt
e-mail: hmahuss@hotmail.com

S. S. Salunkhe

Veltech Dr. RR & Dr. SR University, Chennai, India
e-mail: drsalunkhesachin@veltechuniv.edu.in

M. Gupta

Vivekananda Institute of Technology, Jaipur, India

S. Kumar

Mechanical Engineering Department, S.V. National Institute of Technology Surat,
Surat, India

© Springer Nature Singapore Pte Ltd. 2019

U. Chandrasekhar et al. (eds.), *Innovative Design, Analysis and Development
Practices in Aerospace and Automotive Engineering (I-DAD 2018)*, Lecture Notes
in Mechanical Engineering, https://doi.org/10.1007/978-981-13-2718-6_42

1 Introduction

Sheet metal is one of the important products in the industry. Many products in our daily life are manufactured from sheet metal. The usages of sheet metal in product development are increasing day by day due to several regions such as durability, easy in creating different shapes, use in miniature to giant products, light in weight are some of them. Sheet metal is irreplaceable component in automotive, airplanes, domestic appliances, and many other applications.

There is also a big variety of sheet metal applications such as data extraction, feature recognition, process planning, nesting, sheet metal folding and unfolding, strip layout design, strip balancing, design for stamping or stampability, die block design, part comparison, check manufacturability, cost and time estimation for sheet metal parts, die type selection, sheet metal parts indexing and retrieving, punch shape recognition, punch arrangement, die cost estimation, and sheet metal die design. For each application, there is a need for inputs, which may be inserted manually or automatically from a database. The inputs for every application differ from one to other, but there is still shared sheet metal data between the different applications. Researchers in this branch made their programs to serve one or maybe two of these applications. For this reason, most of them don't use database for sheet metal parts or focus to make a robust solution for all applications in sheet metal.

This paper summarizes the achieved work done for the integrated system in sheet metal applications. The integrated system serves many sheet metal applications such as indexing and retrieving [1–3], check sheet metal part manufacturability [4, 5], die type selection [6], parts comparison and simplification [7–9], 2D blanking die design [10], 3D modeling and expert system in blanking die design [11], feature recognition and process planning [12–15], and cost estimation [16].

The work in this paper is focusing on development of generic architecture for computer-aided integration of product development based on central repository.

2 Architecture for Computer-Aided Integration for Sheet Metal Product Development

The present study aims at exchanging shape information in a product model across PLM applications. The proposed architecture for computer-aided integration for sheet metal product development is presented in Fig. 1. B-rep of the sheet metal product model is considered for processing the shape information. The process first extracts feature information that is required to represent shape feature as application independent and unambiguous representation which is then used for mapping feature label and representation [8, 15] in the database for construction the product model repository. The mapped information (the product model repository) is used for constructing/representing the product model being exchanged in target application. Additional information required in a target application may be computed

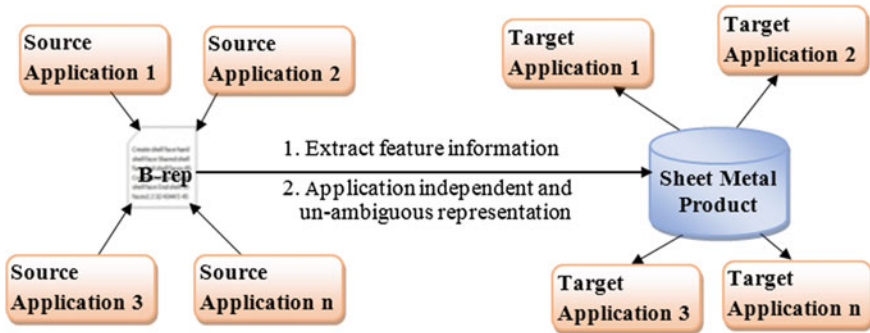


Fig. 1 Architecture for computer-aided integration for sheet metal product development

using the product model repository. The proposed architecture includes computation procedures to build product information which is received from a source application, computation procedures to provide product information required for a target application. The database in this architecture provides information required for construction of product information as and when required or come across the application for a function or procedure in the application.

Source application is a CAD modeling such as AutoCAD, CATIA, and SolidWorks where a sheet metal product model is created and then the boundary representation along with the construction procedures are used to build product model database which is then used for exchange of product information to target application as shown in Fig. 1. A target application may be a sheet model making and stamping, nesting, process planning etc. Building database using a source application: i.e., AutoCAD is explained in the following section.

3 Sheet Metal Part Database

The proposed integrated system includes a database for sheet metal parts, with all related (design, geometrical, and documentation data). The tested example of sheet metal parts is real workpieces data taken from industry. The sequence of feeding the parts database with the new part data is described herewith in Fig. 2. Figure 2a shows the main menu of the proposed program. The part data icon is non-activated icon in this stage. In Fig. 2b, the program calls the part text file data. The part must be drawn first on AutoCAD, and then converted into text file using AutoLISP code. In Fig. 2c, the program converts the text file into the part geometrical shape. The part data icon converts to be active icon. Figure 2d shows the parts documentation data window. All the necessary part data which could not extract from the part shape must be added in this menu. Figure 2e shows the parts design data menu. The material type, the factor of safety, the strip thickness, the degree of accuracy, and the quantity information could be added in this menu. From Fig. 2f to i, the data

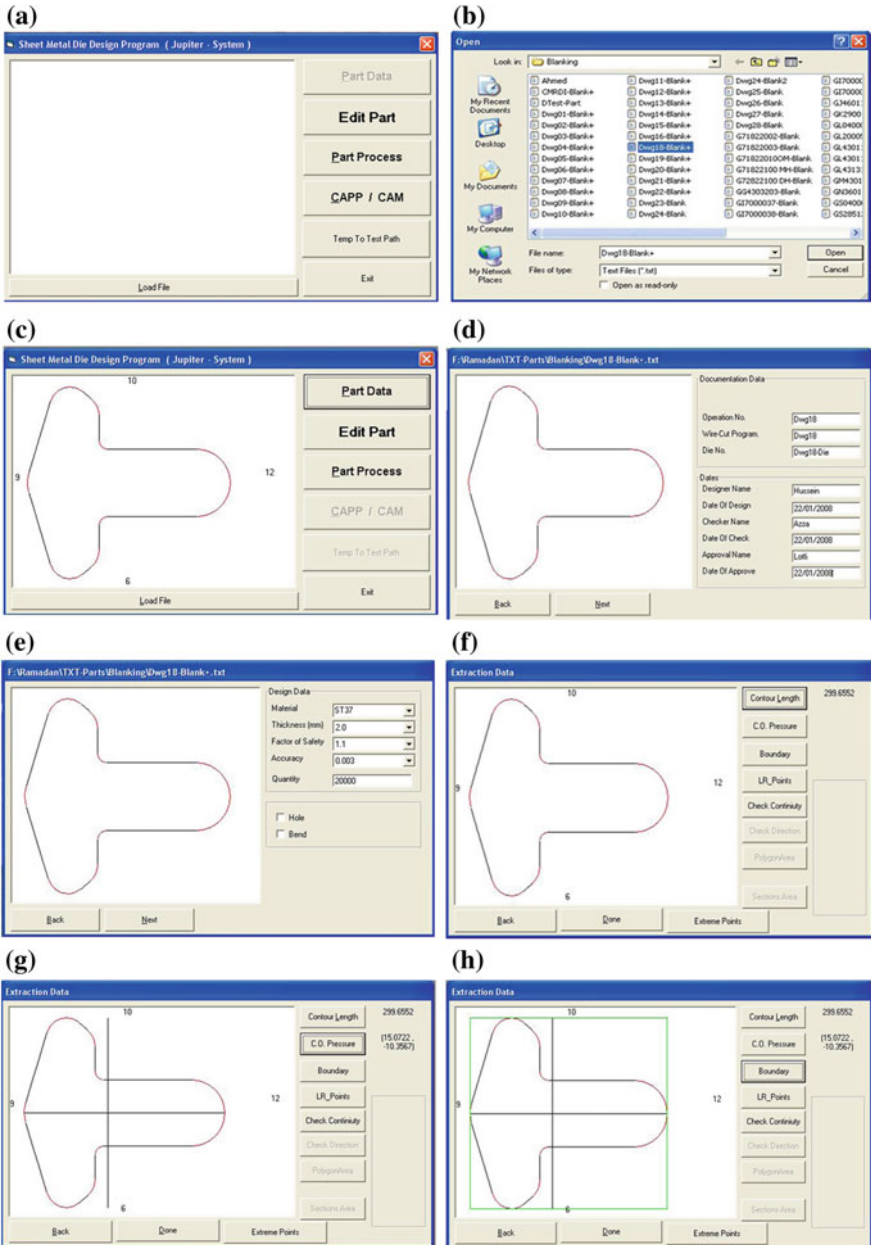


Fig. 2 Main program menus for the case study part: construction of central repository for an example part

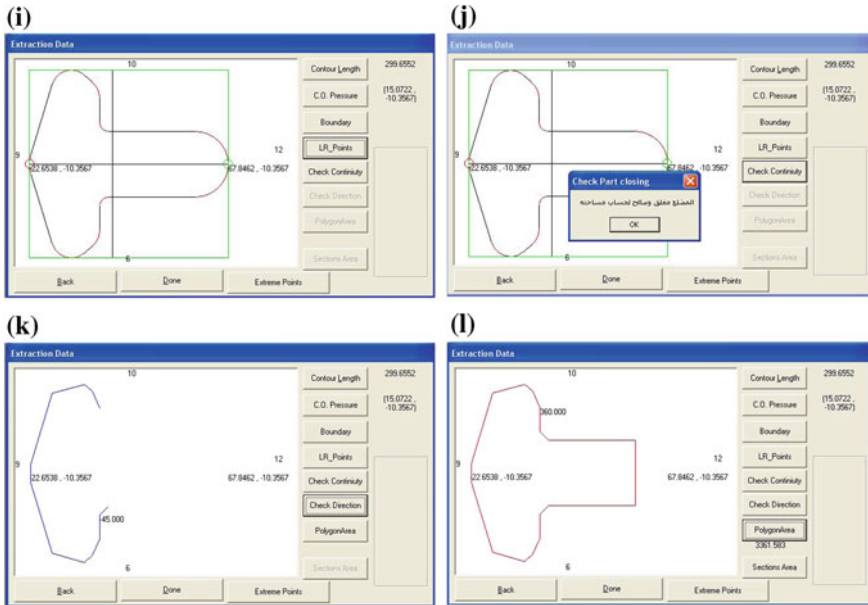


Fig. 2 (continued)

extraction modules are shown for the geometrical part. Figure 2f shows the extracting of the contour length. Figure 2g shows the module of extracting of the center of pressure. Figure 2h shows the module of determining the boundary surrounding the part shape.

Figure 2i shows the module of determination of the intersection point between part shape and the horizontal line passing from the center of pressure. This module is important in automated design the blanking die in two dimensions. Figure 2j shows the check of continuity module which checks the part closing items. Figure 2k shows the module of re-arranging part items direction. This step is very important in determining the part area. Figure 2l shows the module for calculation of polygon area. The second step after successfully entering the part data is the part process step. This icon is the gate to the most common sheet metal applications. Blanking die design is one of those applications modules. The system introduces the designing of blanking dies in two dimensions and in three dimensions.

4 Time and Cost Estimation Module for a Target Application

The proposed code is constructed using Visual Basic 6 program, the code divided into four main menus, punching, nipping, bending, and plasma cutting operations. Every menu concern with the time and cost parameters for every sheet metal

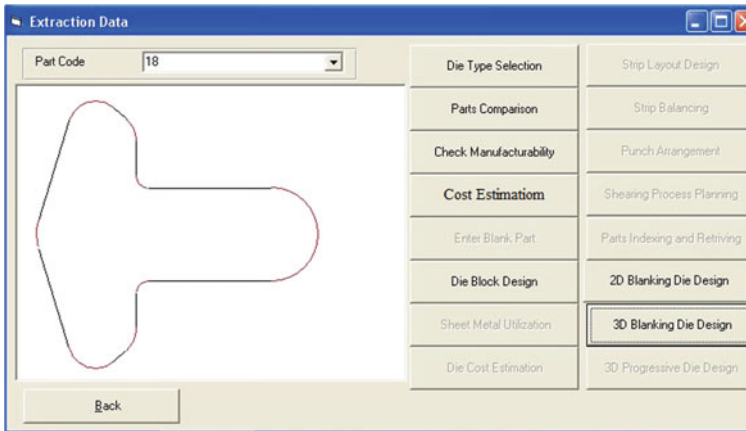


Fig. 3 Time and cost estimation module: example of construction of product information for a target application

operation. The selected sheet metal operations are the most popular sheet metal machining operation in the field. The system is user friendly, in which the user time data parameters in its required box, in the prepared machining operation pages. The program code accumulated the user time and cost results from each page and showed in the operation result. The time and cost module is added as application in a sheet metal program as shown in Fig. 3.

5 Discussion

Product database can be referred as intelligent product information repository which includes shape information, procedures to infer/extract information required for source application. Source application considered as CAD modeling tool. Target application considered as process planning, manufacturing, inspection, marketing, collecting customer feedback, and redesign etc. The proposed architecture for exchange of product information and inferring information ensures design intent, integrity, and consistency of product information.

6 Conclusion

In this paper, generic architecture for computer-aided integration of sheet metal applications based on central repository and information management is presented. Product architecture and basic operations required to build the central repository for a sheet metal product is presented using a case study. This architecture is elaborated

upon for the integration of sheet metal part model (from a source application as AutoCAD) with sheet metal applications module (time and cost estimation) for a target application. The architecture is presented with simple part geometry in laboratory environment which can be extended to real (from industry parts) and complex problems in product design and development in sheet metal industry.

References

1. Tor, S.B., Britton, G.A., Zhang, W.Y.: Indexing and retrieval in metal stamping die design using case-based reasoning. *J. Comput. Inf. Sci. Eng.* **3**(4), 353–362 (2003)
2. Jagirdar, R., Jain, V.K., Batra, J.L.: Characterization and identification of forming features for 3-D sheet metal components. *Int. J. Mach. Tools Manuf.* **41**(9), 1295–1322 (2001)
3. Hussein, H.M.A., Barakat, A.F.: Indexing and retrieving in 2D sheet metal part, F_ThB3–6. In: International Conference on Technology of Plasticity, ICTP 2008, Korea, 7–11 Sept 2008, pp. 2038–2043
4. Hussein, H.M.A., Kumar S.: Computer aided check on manufacturability of sheet metal parts. In: International Conference on Advances in Mechanical Engineering, ICAME 2008, SVNIT Surat, Gujarat State, India, 15–17 Dec 2008, pp. 736–741
5. Wang, C.H., Borne, D.A.: Design and Manufacturing of Sheet Metal Parts: Using Features to Aid Process Planning and Resolve Manufacturability Problems. Carnegie Mellon University, Research Showcase@CMU (1997)
6. Hussein, H.M.A., Kumar, S.: Computer assist stamping processes selection. In: International Conference on Production Engineering Design and Control, PEDAC09, Alexandria, Egypt (2009)
7. Hussein, H.M.A., Kumar, S.: A computerized retrieval system for sheet metal parts. *AIJSTP Asian Int. J. Sci. Technol. Prod. Manuf.* **1**(2), 31–40 (2008)
8. Kulkarni, Y., Gupta, R.K., Sahasrabudhe, A., Kale, M., Bernard, A.: Leveraging feature information for defeaturing sheet metal feature-based CAD part model. *Comput. Aided Des. Appl.* **3**(6), 156–169, Taylor & Francis (2016)
9. Gupta, R.K., Zhang, Y., Bernard, A., Gurumoorthy, B.: Generic classification and representation of shape features in sheet-metal parts. In: Hussein, H.M.A., Kumar, S. (eds.) *AI Applications in Sheet Metal Forming*. TMMME Book Series, Ch. 2, pp. 15–39. Springer (2017)
10. Hussein, H.M.A.: A CAD System in Sheet Metal Blanking Dies in 2D. In: First International and 22th All Indian Manufacturing Technology Design and Research Conference (22th AIMTDR), IIT-Roorke, India, 21–23 Dec 2006, pp. 253–258
11. Hussein, H.M.A., Abdeltif, L.A., Etman, M.I., Barakat A.F.: An approach to construct an intelligent system in sheet metal cutting die design. In: 9th Cairo University International Conference on Mechanical Design & Production (MDP-9), Cairo, Egypt, 8–10 Jan 2008, pp. 61–70
12. Kannan, T.R., Shunmugam, M.S.: Processing of 3D sheet metal components in STEP AP-203 format. Part I: feature recognition system. *Int. J. Prod. Res.* **47**(4), 941–964 (2009)
13. Kannan, T.R., Shunmugam, M.S.: Processing of 3D sheet metal components in STEP AP-203 format. Part II: feature reasoning system. *Int. J. Prod. Res.* **47**(5), 1287–1308 (2009)
14. Gupta, R.K., Gurumoorthy, B.: Classification, representation, and automatic extraction of deformation features in sheet metal parts. *Comput. Aided Des.* **45**(11), 1469–1484, Elsevier (2013)

15. Gupta, R.K., Gurumoorthy, B.: Unified taxonomy for reference ontology of shape features in product model. In: Bernard, A., Rivest, L., Dutta, D. (eds.) *Product Lifecycle Management for Society*, IFIP AICT, 409(30), pp. 295–307. Springer (2013)
16. Verlinden, B., Duflou, J.R., Collin, P., Cattrysse, D.: Cost estimation for sheet metal parts using multiple regression and artificial neural networks: a case study. *Int. J. Prod. Econ.* **111** (2), 484–492 (2008)

Thermodynamic Analysis of Diesel Engine Fuelled with Aqueous Nanofluid Blends



S. P. Venkatesan and P. N. Kadiresh

Abstract Thermodynamic analyses are performed on diesel engine with different types of nanofluid blend operations. Three best blends, i.e., D + 50ZN, D + 50AN, D + 50CN are chosen for exergy analysis. The effects of nanofluid on diesel are examined from the second law perspective. Availability equations are applied to both diesel and nanofluid blend modes at varying engine loads, and exergy terms such as brake work availability, exhaust gas availability, cooling water availability, and irreversibility are calculated and compared. There is an increase in exergy efficiency with an increase in load for all fuel blends tested. The nanofluid blend operations are favored thermodynamically at all loads. For diesel at full load, 26.88% of the fuel exergy is converted to brake power. At same load, nanofluid blend modes have resulted higher exergy efficiency of 28.22, 28.78, 29.16% for D + 50ZN, D + 50AN, D + 50CN, respectively, due to the higher brake work availability and decreased destruction availability.

Keywords Aqueous zinc oxide (ZN) · Aqueous aluminum oxide (AN) · Aqueous cerium oxide (CN) · Diesel engine · Exergy efficiency

1 Introduction

In order to reduce greenhouse gases from diesel engines, aqueous nanofluids mixed diesel blends have been employed as an alternative fuel. The experimental investigations of nanofluid blends operations reveal increase in performance than diesel fuel. From the nanofluid blends mode aspect, it is very necessary to learn where-

S. P. Venkatesan (✉)

Department of Mechanical Engineering, Sathyabama Institute of Science and Technology, Chennai, India
e-mail: spvsathyabama@gmail.com

P. N. Kadiresh

Department of Aerospace Engineering, BSA Crescent Institute of Science and Technology, Chennai, India

© Springer Nature Singapore Pte Ltd. 2019

U. Chandrasekhar et al. (eds.), *Innovative Design, Analysis and Development Practices in Aerospace and Automotive Engineering (I-DAD 2018)*, Lecture Notes in Mechanical Engineering, https://doi.org/10.1007/978-981-13-2718-6_43

445

about the available fuel energy during engine operations [1, 2]. Further, obtaining the maximum possible performance of engine fuelled with nanofluid blends modes is crucial which can furnish an essential comparison parameter with diesel engine. System (engine) losses due to the impact of process changes like load and blends are also to be estimated, and these will help to improve the engine performance and reduce the energy destroyed. Through these, the thermal and exergy efficiency of the diesel and nanofluid blends are to be discussed. Engine operations are theoretically treated by the first and second law of thermodynamics [3, 4]. This work is applied the thermomechanical availability investigation by retrieving data of the nanofluid blends experiments. It provides thermodynamics aspects and performance calculations of the engine operation. In this work, with second law perspective, the effects of nanofluid type, on nanofluid blends operations are examined. Finally, the thermomechanical availability analysis outcomes of the nanofluid blends and diesel are compared. Particularly, the influence of nanofluid on the availability terms such as work output, heat losses by cooling water and exhaust gas, second law efficiency, and energy destruction are studied by combining the first and second laws of thermodynamics.

2 Methodology and Experimentation

From the literature survey, the metal oxides which can be used in form of aqueous phase in diesel are identified [5–7]. Metal oxides for engine testing are scrutinized and narrowed down to three, namely zinc oxide, aluminum oxide, and cerium oxide, based on their physical and chemical properties and its influence on combustion behavior of diesel after an elaborate literature survey [8–11]. Metal oxides nanoparticles are synthesized as noted in the literature, and they are characterized through XRD, EDS, and SEM. After the synthesization and characterization of these three metal oxide nanoparticles, three nanofluids, (metal oxide nanoparticle aqueous 5 wt% suspension), namely aqueous zinc oxide, aqueous aluminum oxide, and aqueous cerium oxide, are prepared by chemical synthesis. Four different concentrations (30, 40, 50, and 60 cc) of each nanofluid are selected and mixed with one liter of diesel. Similarly for three nanofluids, totally 12 blends are prepared. Fuel properties such as calorific value, density, viscosity, flash, and fire point are determined for each blend using ASTM standard test methods. Detailed experimental load tests on engine fuelled with diesel and blends are carried out to evaluate the effects of nanofluid and its dose level on combustion performance and emissions parameters. In order to avoid experimentation error, each test is repeated thrice. The test results of blends are validated with that of diesel under same test conditions.

In the end of the engine tests, it is concluded that the D + 50ZN, D + 50AN, and D + 50CN blends have shown a better performance and emission reduction compare to their other aqueous blends and diesel.

Exergy analysis is the most effective method to find the energy resource utilization of the system (engine) [12–14]. In this work, the exergy analysis of diesel engine fuelled by D + 50ZN, D + 50AN, D + 50CN, and diesel are done with available experimental results data of blends.

3 Availability Analysis

The study of energy balance on engine helps to learn “how the fuel energy available is lost” and guides in finding ideas to curtail the same and increase the engine performance in terms of power output and efficiency [15]. It also provides the knowledge to optimize engine settings. According to the application, it is very essential to have the knowledge of an engine running time period and its loading condition for efficient operation of an engine. In this work, the impact of variations of engine load and nanofluid type on energy and exergy balance of nanofluid blends are determined and discussed with diesel. The experimental observation data are used for the first and second law analyses purpose as per Eqs. (1)–(13) [16].

3.1 Energy Analysis

First law of thermodynamics analysis of the amount of fuel energy converted into shaft work, heat carried away by the cooling water, heat carried away by the exhaust gas, and unaccounted heat loss are calculated as per Eqs. (1)–(6).

$$\text{Heat input (diesel), } Q_{\text{in}} = [(m_d/3600) \times \text{LHV}_d], \text{ kW} \quad (1)$$

$$\text{Heat input (nanofluid blend), } Q_{\text{in}} = [(m_n/3600) \times \text{LHV}_n], \text{ kW} \quad (2)$$

$$\text{Shaft work, } P_{\text{shaft}} = \text{Brake power output, kW} \quad (3)$$

$$\begin{aligned} \text{Heat carried away by the cooling water, } Q_{\text{cw}} \\ = [(m_w/3600) \times C_{\text{Pw}} \times (T_2 - T_1)], \text{ kW} \end{aligned} \quad (4)$$

$$\text{Heat carried away by the exhaust gas, } Q_{\text{eg}} = [(m_{\text{eg}}/3600) \times C_{\text{Peg}} \times (T_5 - T_6)], \text{ kW} \quad (5)$$

$$\text{Unaccounted heat losses, } Q_{\text{unaccounted}} = [Q_{\text{in}} - (P_{\text{shaft}} + Q_{\text{cw}} + Q_{\text{eg}})], \text{ kW} \quad (6)$$

3.2 Exergy Analysis

Second law of thermodynamics analysis of the fuel availability converted into shaft availability, cooling water availability, exhaust gas availability, destroyed availability, and exergy efficiency are calculated as per Eqs. (7)–(13).

$$\text{Input availability of diesel, } (A_{\text{in}})_{\text{Diesel}} = [\varphi \times (m_d/3600) \times \text{LHV}_d], \text{ kW} \quad (7)$$

$$\text{Input availability of nanofluid, } (A_{\text{in}})_{\text{nano}} = [\varphi \times (m_n/3600) \times \text{LHV}_n], \text{ kW} \quad (8)$$

The chemical exergy factor (φ) for liquid fuels can be determined by

$$\Phi = 1.0401 + (0.1728(h/c)) + (0.0432(o/c)) + (0.2169(\alpha/c)(1 - 2.0628(h/c))$$

where h , c , o , and α are the mass fractions of H, C, O, and S, respectively,

$$\text{Shaft availability, } A_{\text{shaft}} = \text{Brake power output, kW} \quad (9)$$

Cooling water availability

$$A_{\text{cw}} = Q_{\text{cw}} - [(m_w/3600) \times C_{\text{Pw}} \times T_0 \times \ln(T_2/T_1)], \text{ kW} \quad (10)$$

Exhaust gas availability

$$A_{\text{eg}} = Q_{\text{eg}} + [(m_{\text{eg}}/3600) \times T_0 \times (C_{\text{Peg}} \ln\{T_0/T_5\} - R_{\text{eg}} \ln\{P_0/P_{\text{eg}}\})], \text{ kW} \quad (11)$$

The gas constant of the exhaust gas (R_{eg}) is determined by exhaust gas calorimeter energy balance

$$\text{Destroyed availability, } A_{\text{destroyed}} = [A_{\text{in}} - (A_{\text{shaft}} + A_{\text{cw}} + A_{\text{eg}})], \text{ kW} \quad (12)$$

$$\begin{aligned} \text{Exergy efficiency } (\eta_{\text{II}}) &= (\text{Availability recovered}/\text{Availability input}) \\ &= 1 - (A_{\text{destroyed}}/A_{\text{in}}) \end{aligned} \quad (13)$$

4 Results and Discussion

The typical variations of the exergy terms during various tested fuel modes are shown individually in Figs. 1, 2, 3, and 4.

During an engine test, as load increases, the richer fuel increase the combustion temperature which in turn causes increase in available work and decrease in heat transfer losses availability. Availability, thereby increases exergetic efficiency for all naofluid blends at higher loads. When compared to diesel, the exergetic

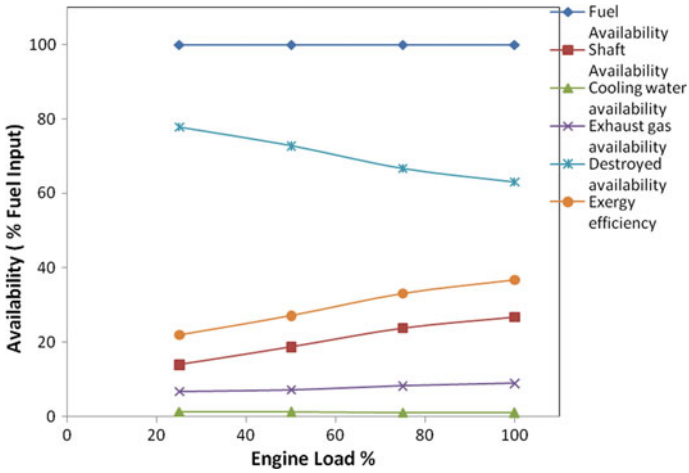


Fig. 1 Availability distribution of diesel fuel with load

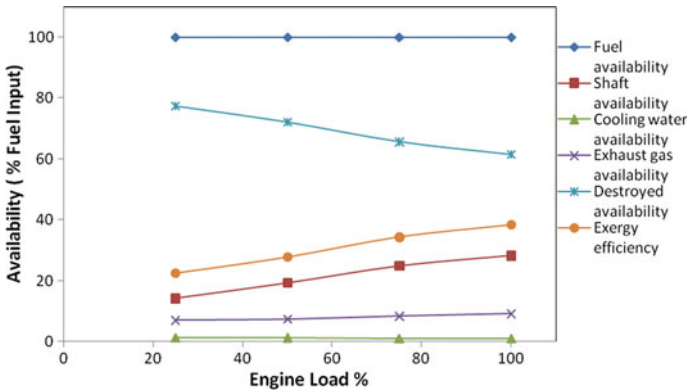


Fig. 2 Availability distribution of D + 50ZN blend with load

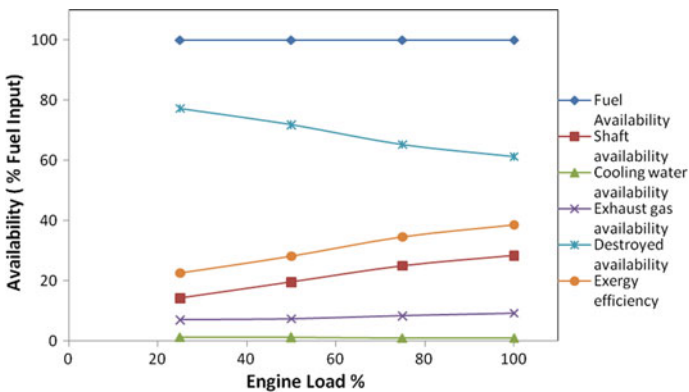


Fig. 3 Availability distribution of D + 50AN blend with load

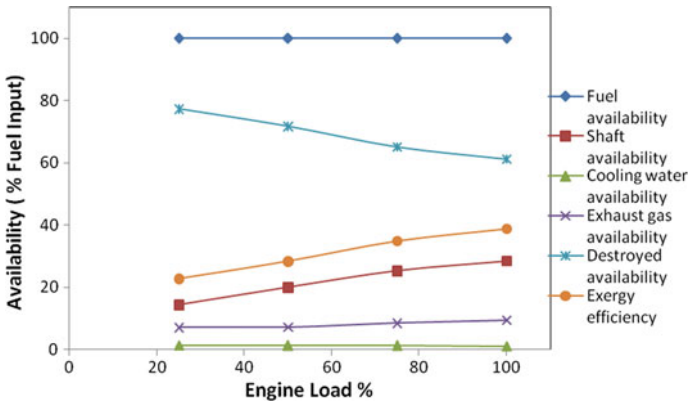


Fig. 4 Availability distribution of D + 50CN blend with load

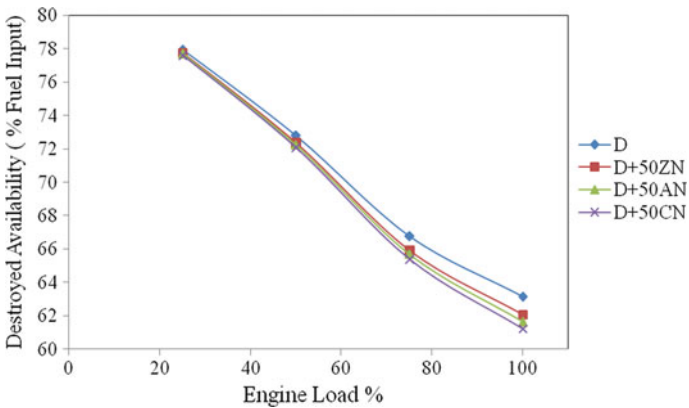


Fig. 5 Destroyed availability of fuel blends and diesel at various load

efficiencies of nanofluid blends are marginally increased and favored thermodynamically at all loads. Due to the better combustion of nanofluid blends, shaft availability and exergy efficiency are higher at all loads.

Destroyed availabilities for blends at different loads are shown in Fig. 5. The destroyed availabilities for blends decrease as the load increases. Increasing combustion temperatures, decreasing the duration of combustion and decreasing entropy production are the reasons for the decreasing destroyed availabilities of blends compared to diesel at higher loads [17].

At low loads, poor combustion causes low exhaust gas and cooling water availabilities, i.e., high destruction availability. At maximum efficiency condition (100% load), the minimum destroyed availability is found as 61.58, 61.31, and 61.12% for D + 50ZN, D + 50AN, and D + 50CN, respectively. While at the same condition, this value is found as 63.14% for diesel mode. Due to presence of

aqueous nanofluid in diesel, the combustion temperatures of nanofluid blends increased. This causes an increase work availability of the nanofluid blends. It causes the increase of exergy efficiency and a decrease in destroyed availability.

Figure 6 shows the fuel availability of the nanofluid blends and diesel. The results show that at minimum loads, the fuel availability decreases as the fuel consumed by the engine decrease. When load increases, to develop higher work output for the corresponding loads, more quantity of fuel is consumed by the engine which causes increase fuel availability at higher loads. For an equal shaft work as of diesel, nanofluid blends require lower fuel availability than diesel due to high energetic and better combustion of nanofluid blends.

Figures 7 and 8 show the cooling water availability and exhaust gas availability versus load, respectively, for various modes of operation. The exhaust gas temperature of nanofluid blends operations is lower than diesel fuel for the entire range

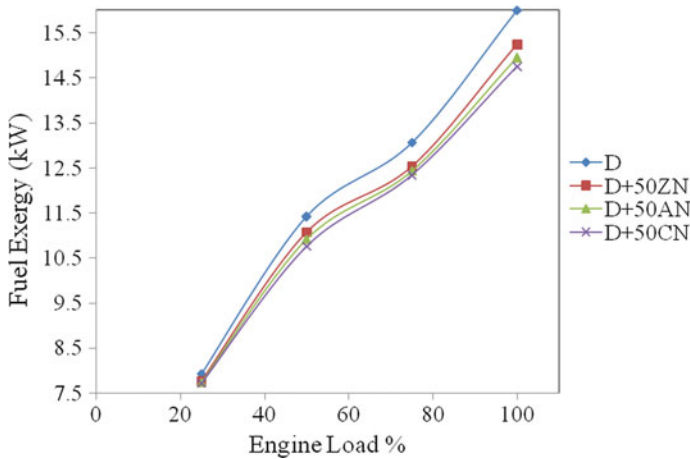


Fig. 6 Fuel exergy at different loads

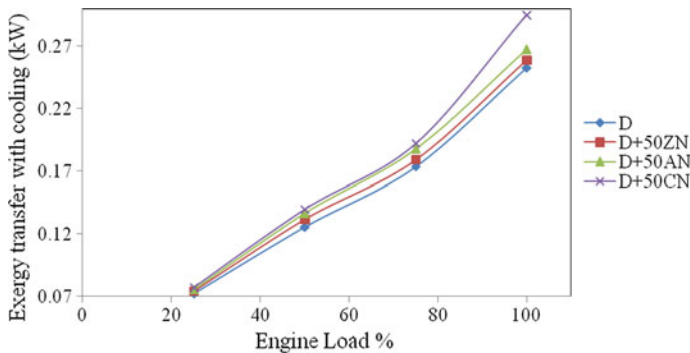


Fig. 7 Availability transfer by cooling water versus load

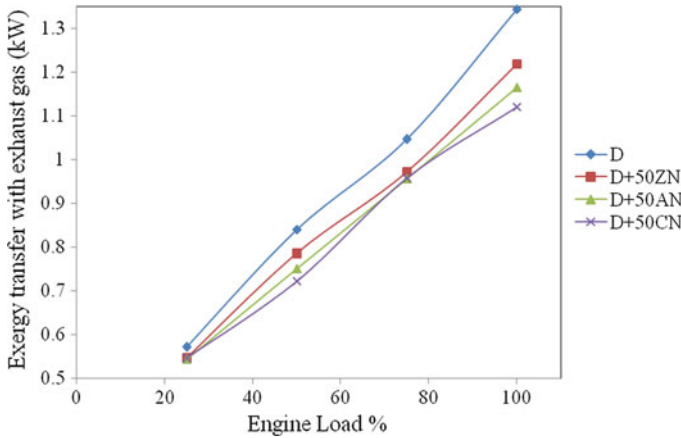


Fig. 8 Availability transfer by exhaust gas versus load

of load. This leads to lower exhaust gas availability for nanofluid blends. The minimum exhaust gas availability is obtained for D + 50CN blend. At 100% load, the exhaust gas availability is found as 1.121 kW for D + 50CN mode as compared to that of 1.343 kW of diesel. At full load, this value is 1.165 and 1.22 kW for D + 50AN and D + 50ZN mode. The cooling availability of nanofluid blends operations is more due to the improved convective heat transfer coefficient with cooling water. The maximum cooling availability accessible is 0.295, 0.267, 0.259, and 0.2527 kW for D + 50CN, D + 50AN, D + 50ZN, and D, respectively, at full load. At lower loads, poor combustion causes less exergy transfer with exhaust gas and cooling water, and hence, resulted in higher destroyed availability.

Figures 9 and 10 show the shaft availability and cumulative work availability accessible from both cooling water and exhaust gas losses for different loads. When load increases, the work availability increases. This is because of increasing the fuel energy input and decreasing the combustion duration during higher load operation. Also when load increases, all tested fuel generates more increment in cumulative cooling water and exhaust gas availabilities [18]. This allows the more availability converted to work availability. The nanofluid blends modes produced little lower accessible work availability (about 0.62–1.42 kW) when compared to diesel (about 0.64–1.6 kW).

Figure 11 shows the second law efficiency versus load for diesel and nanofluid blends modes. As the load increases, the cumulative work, cooling water, and exhaust gas availabilities are increased which in turn increase the gross work availability and second law efficiency. The highest exergy efficiency of 38.76% is observed for D + 50CN blend at 100% load. At higher loads, fuel energy input to the engine increases which results in improvement in combustion, increasing the cumulative work availability, and decreasing the combustion irreversibilities. The lower is the irreversibility, the higher is the exergy efficiency and vice versa. There is a marginal difference in exergy efficiency between the nanofluid blends modes.

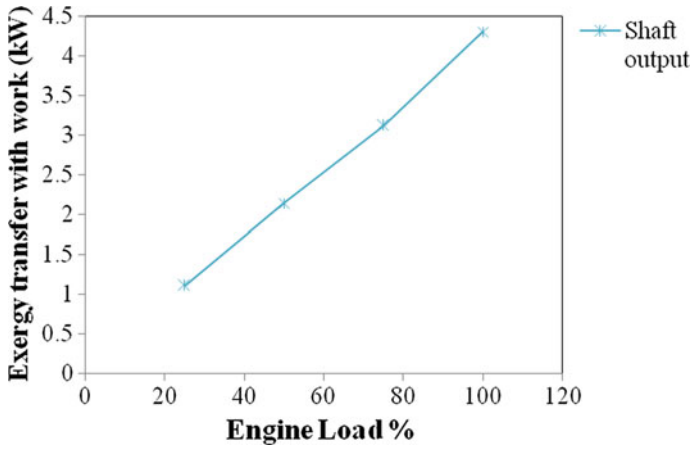


Fig. 9 Shaft availability versus load

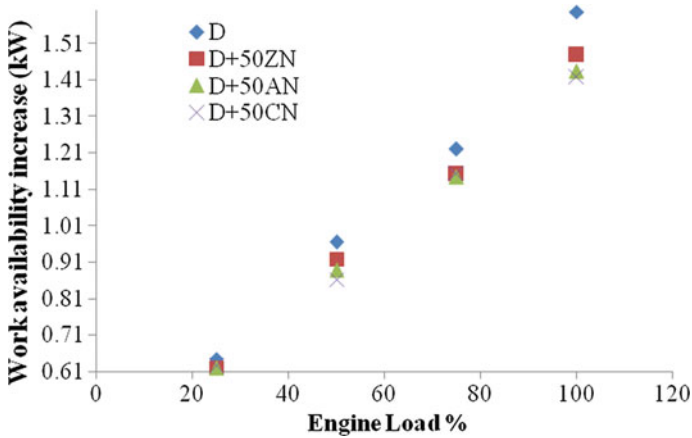


Fig. 10 Cumulative work availability accessible from both cooling water and exhaust gas

The comparison of energy and exergy efficiency of tested fuel modes is shown in Fig. 12. It can be noticed that the maximum exergy efficiency of nanofluid blends modes (about 38%) are higher than the energy efficiency of base diesel engine (about 29%). This suggests that less amount fuel availability input and more percentage of fuel availability input that is converted into work availability are the reasons for higher exergy efficiency in nanofluid blends than diesel.

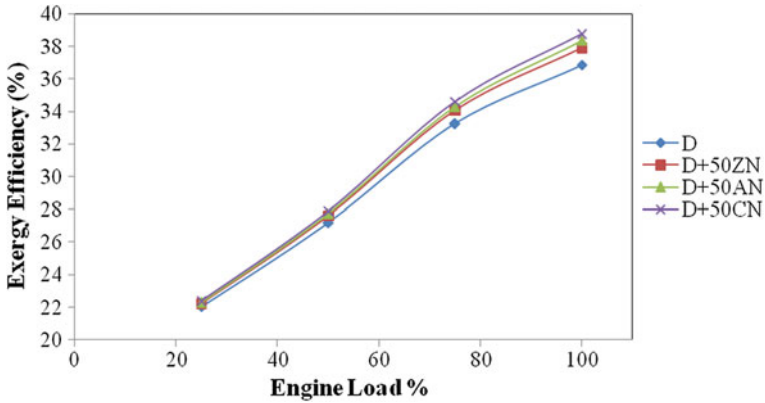


Fig. 11 Second law efficiency with load

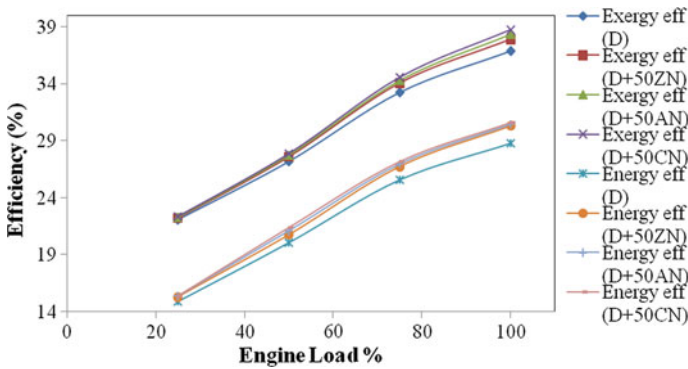


Fig. 12 Comparison of energy and exergy efficiency versus load

5 Conclusions

A thermodynamic investigation is performed on a diesel engine. The engine is tested under nanofluid blends operations. Availability equations are applied to both diesel and nanofluid blends modes at varying engine loads. The exergy terms such as brake work, exhaust gas, cooling water, and irreversibility are compared and discussed. There is an increase in exergy efficiency with an increase in load for all fuel modes, and due to the higher work output, nanofluid blends modes have resulted higher exergy efficiency.

The results suggest that due to a significant increase in exergy efficiency, nanofluid blends can be an effective substitute to the fossil diesel. Due to better fuel-air mixture combustion and higher energy content of nanofluid, nanofluid blends modes require marginally lower fuel chemical exergy than that of diesel

mode. This analysis confirmed that the nanofluid in the blend influences for more conversion of fuel availability input into work availability. The D + 50CN blend has shown better exergy efficiency than other blends. At full load, 29.16% of the fuel exergy is converted into brake power, 1.6% is lost through heat transfer, 8% is expelled by the exhaust gases, and 61.24% is lost by exergy destruction for D + 50CN blend, and these parameters are 26.88, 1.58, 8.4, 63.14%, respectively, for diesel.

References

1. Reddy, A.V., Kumar, T.S., Kumar, D.K.T., Dinesh, B., Santosh, Y.V.S.S.: Energy and exergy analysis of I.C. engines. *Int. J. Eng. Sci.* **3**(5), 07–26 (2014)
2. Tosun, E.: Energy and exergy analysis of a diesel engine. MSc Thesis, Cukurova University, Institute of Natural and Applied Sciences, Adana (2013)
3. Islam, M.M., Rahman, M.A., Abedin, M.Z.: First law analysis of a DI diesel engine running on straight vegetable oil. *Int. J. Mech. Mech. Eng.* **11**(3), 1–5 (2011)
4. Zheng, J., Caton, J.A.: Second law analysis of a low temperature combustion diesel engine: effect of injection timing and exhaust gas recirculation. *Energy* **38**(1), 78–84 (2012)
5. Wong, K.V., Leon, O.D.: Applications of nanofluids: current and future. *Adv. Mech. Eng.* 1–11 (2010). <https://doi.org/10.1155/2010/519659>
6. Mehta, R.N., Chakraborty, M., Parikh, P.A.: Nanofuels: combustion, engine performance and emissions. *Fuel* **120**, 91–97 (2014)
7. Kao, M.-J., Ting, C.-C., Lin, B.-F., Tsung, T.-T.: Aqueous aluminum nanofluid combustion in diesel fuel. *J. Test. Eval.* **36**(2), 1–5 (2007)
8. Yetter, R.A., Risha, G.A., Son, S.F.: Metal particle combustion and nanotechnology. *Proc. Combust. Inst.* **32**(2), 1819–1838 (2009)
9. Selvaganapathy, A., Sundar, A., Kumaragurubaran, B., Gopal, P.: An experimental investigation to study the effects of various nanoparticles with diesel on DI diesel engine. *ARPN J. Sci. Technol.* **3**(1), 112–115 (2013)
10. Sadhik Basha, J., Anand, R.B.: Role of nanoadditive blended biodiesel emulsion fuel on the working characteristics of a diesel engine. *J. Renew. Sustain. Energy* **3**(2), 1–17 (2011)
11. Mirzajanzadeh, M., Tabatabaei, M., Ardjmand, M., Rashidi, A., Ghobadian, B., Barkhi, M., Pazouki, M.: A novel soluble nano-catalysts in diesel-biodiesel fuel blends to improve diesel engines performance and reduce exhaust emissions. *Fuel* **139**, 374–382 (2015)
12. Harilal, S.S., Hitesh, J.Y.: Energy analyses to a CI-engine using diesel and bio gas dual fuel: a review study. *Int. J. Adv. Eng. Res. Stud.* **1**(2), 212–217 (2012)
13. Thibordin, S., Kasama, S., Supachai, W.: The analysis of exergy in a single cylinder diesel engine fuelled by diesel and biodiesel. *J. Sci. Technol. MSU* **3**, 556–562 (2012)
14. Ozkan, M., Ozkan, D.B., Ozener, O., Yilmaz, H.: Experimental study on energy and exergy analyses of a diesel engine performed with multiple injection strategies: effect of pre-injection timing. *Appl. Therm. Eng.* **53**, 21–30 (2013)

15. Kopac, M., Kokturk, L.: Determination of optimum speed of an internal combustion engine by exergy analysis. *Int. J. Exergy* **2**(1), 40–54 (2005)
16. Rosen, M.A.: Using exergy to correlate energy research investments and efficiencies: concept and case studies. *Entropy* **15**, 262–286 (2013)
17. Debnath, B.K., Sahoo, N., Saha, U.K.: Thermodynamic analysis of a variable compression ratio diesel engine running with palm oil methyl ester. *Energy Convers. Manag.* **65**, 147–154 (2013)
18. Ghazikhani, M., Hatami, M., Ganji, D.D., Gorji-Bandpy, M., Behravan, A., Shahi, G.: Exergy recovery from the exhaust cooling in a DI diesel engine for BSFC reduction purposes. *Energy* **65**, 44–51 (2014)

Investigation of Twin Cylinder Direct Injection CI Engine Characteristics Using Calophyllum Inophyllum Biodiesel Blends



Pathikrit Bhowmick, Dhruv Malhotra, Pranjal Agarwal,
Aatmesh Jain and K. C. Vora

Abstract In the contemporary world, human consumption of energy in the form of fossil fuels is growing at an alarming rate and is a major concern for scientists as well as economists. In order to counter these phenomena, the study of biodiesel fuels is carried out by most researchers as an alternative to the conventional fossil fuels. In this present study, the effects of Calophyllum Inophyllum biodiesel blends on the engine performance, combustion, and emission characteristics were investigated. An experimental study was done on a twin cylinder diesel engine of direct injection type at a constant speed of 1500 rpm with Calophyllum Inophyllum methyl ester (CIME) biodiesel blends B5, B10, B20, and B100 by volume. Results showed that CIME blend B5 produced 3.28% lower BSFC and 4.8% higher BTE compared to pure diesel. Comparable combustion characteristics were observed for all biodiesel blends among which B5 showed the best results. B5 CIME blend depicted lower emission results with 12.29% and 9.57% decrease in HC and CO, respectively, as compared to conventional diesel. However, NO_x emissions were found to be higher for all blend concentrations with respect to conventional diesel.

Keywords Calophyllum Inophyllum · Combustion · Emissions
Biodiesel blends

1 Introduction

The persistent rise in the demand for fossil fuels is increasing at a startling rate. The world's proven natural gas resources are on the verge of eradication which is severely impacting global economy. The inability of fossil fuels to satisfy the thirst for high energy demand has become an important area of concern for various

P. Bhowmick (✉) · D. Malhotra · P. Agarwal · A. Jain · K. C. Vora
ARAI Academy, The Automotive Research Association of India, Pune, India
e-mail: bhowmick.pathikrit@gmail.com

© Springer Nature Singapore Pte Ltd. 2019
U. Chandrasekhar et al. (eds.), *Innovative Design, Analysis and Development Practices in Aerospace and Automotive Engineering (I-DAD 2018)*, Lecture Notes in Mechanical Engineering, https://doi.org/10.1007/978-981-13-2718-6_44

researchers across the globe [1]. Like other countries, India being a home to over 1.3 billion people is also facing deficiency of crude oil to meet its energy requirements. Being an oil importing country, India spends a great amount of its revenue on purchasing petroleum products which influences its dependency on oil-rich countries [2]. Therefore, in order to prevent the further up-rise in its economy, India needs to address potential alternative fuels with lower overall emissions which can be treated as a substitute to the prevailing fossil-derived fuels [3]. Hence, biodiesel and ethanol are considered to be prospective substitutes to petro-diesel in the country.

Biodiesel is believed to be a serious contender to diesel fuel due to its cleaner combustion, eco-friendly nature, and less harmful exhaust emissions [4]. Among the non-edible sources of biodiesel, *Calophyllum Inophyllum* oil popularly known as “honne oil” or “beauty leaf” originates along the coastal regions of Indian and Pacific oceans and are known for many benefits like high oil content, high survival vigor in environment and remains fertile up to the age of 50 years [5–7]. Ong et al. [8] selected *Calophyllum Inophyllum* oil with high FFA content and have optimized the production of biodiesel. Various blends of *Calophyllum Inophyllum*, being a fuel with high energy content, have given satisfactory results by showing a rise in brake thermal efficiency and depletion in fuel consumption, also comparatively producing less smoke and CO emissions. Monirul et al. [9] made a comparison of performance and emission between the diesel-biodiesel blends of Palm oil, *Calophyllum Inophyllum* and *Jatropha* which were then compared to pure diesel. With the increasing blend ratio from 10% to 20%, the BSFC increased from 7.96% to 10.16% for all the three types of biodiesel. Smoke was found least for *Jatropha* B10 blend, which came out to be 31.09% less than diesel fuel. However, lowest NO_x emissions were emitted by pure diesel fuel only. Ong et al. [10] have done similar work by comparing *Calophyllum Inophyllum*, *Jatropha Curcus*, and *Ceiba Pentrandra* biodiesel at full throttle for 10%, 20%, 30%, and 50% blending by volume. Optimized engine performance due to complete combustion was observed for 10% blends thus reducing fuel consumption. However, NO_x emissions were found to have increased compared to pure diesel. Rahman et al. [11] carried out performance and emission testing of palm and *Calophyllum Inophyllum* biodiesel blends at high idling conditions, and it was noted that brake specific energy consumption was better for *Calophyllum Inophyllum* biodiesel due to a higher heating value. Increasing blend percentage resulted in lower CO and HC emissions; however, NO_x was only significant for Palm B20 and *Calophyllum* B20 blend.

From the above comprehensive literature review, it can be inferred that *Calophyllum Inophyllum* biodiesel poses to be a serious alternative to conventional diesel fuel and its feedstock is abundantly available in India. However, very limited work has been carried out by the Indian researchers in extraction of *Calophyllum Inophyllum* biodiesel and understanding the engine characteristics using blend concentrations up to B20 as per national biofuels policy framed by the country in the year 2015. Therefore, this present study focuses on production of *Calophyllum Inophyllum* biodiesel and investigation of the performance, combustion, and emission characteristics of biodiesel fuel when run inside a two-cylinder direct

injection diesel engine with various blend concentrations like B5, B10, and B20 without any modifications and finally comparing with the results of conventional petro-diesel.

2 Fuel Preparation

In this study, a double stage transesterification process was used to extract biodiesel from *Calophyllum Inophyllum* oil. Since *Calophyllum Inophyllum* oil consists of high amount of free fatty acid, i.e., about 23% and also contains high density and viscosity, therefore a single-stage transesterification was not feasible for biodiesel extraction and to prevent saponification [13].

In the first stage of transesterification, a 16:1 molar ratio of alcohol (methanol) to *Calophyllum Inophyllum* oil was selected and 1% by weight of concentrated sulfuric acid was mixed to it. This mixture was then constantly stirred at 60 °C for about 90 min. In the subsequent stage, a 6:1 molar ratio of methanol to *Calophyllum Inophyllum* oil was mixed with 1% by weight of potassium hydroxide and stirred constantly at 60 °C for about 90 min. The sample was allowed to settle for 24 h, and two different layers were obtained, i.e., biodiesel in the above layer and glycerol in the lower layer and separation of *Calophyllum Inophyllum* methyl ester (CIME) from glycerol is done. Lastly, the purification of oil was carried out which involved a typical wash to eliminate residual alcohol and glycerol from the obtained biodiesel.

3 Experimental Setup

The investigational study was done on a 4-stroke two-cylinder DI engine generally used for agricultural tractor applications (refer Table 1). This engine developed an utmost power output of 21 kW at an invariable speed of 2000 rpm. The engine loading and torque quantification were carried out using an air cooled eddy current

Table 1 Technical details of engine specifications

Make and model	Simpsons make, S 217	Compression ratio	18.5:1
Type/ configuration	Twin cylinder, 4-stroke, NA, vertical in-line diesel engine	Combustion chamber	Direct injection, hemispherical shape
Rated power	21 kW @ 2000 rpm	Fuel system	MICO Bosch in-line pump
Bore × stroke	91.44 mm × 127 mm	Fuel injection pressure	220 bar
Displacement	1670 cc		

Table 2 Different properties of biodiesel and its blend concentrations [12]

Properties	Diesel	B100	ASTM testing method
Density	815	865	D4052
Flash point	53	160	D93
Fire point	65	178	D93
Kinematic viscosity	2.3	5.58	D445
Calorific value	42.5	39.8	D270

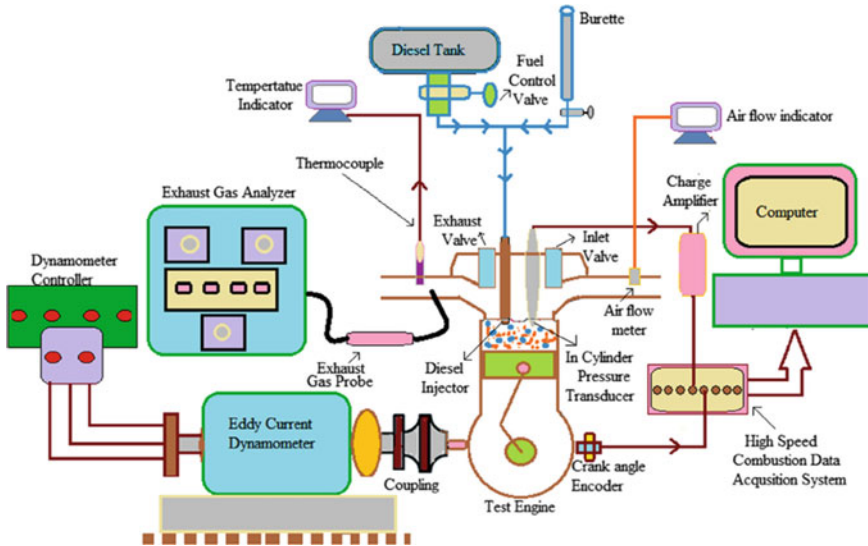


Fig. 1 Schematic diagram of experimental setup

dynamometer capable of producing 75 kW power output which was coupled to the engine. A Mass Air Flow (MAF) sensor was utilized for measurement of flow rate of air inside the cylinders while the fuel consumption rate was calculated manually using a burette apparatus and a digital stopwatch. Kistler made pressure sensor was placed inside the cylinder head for investigation of in-cylinder pressure which was further linked to a combustion analyzer. For engine emissions measurement, AVL DiGas 444 exhaust gas analyzer was employed for measuring CO, HC, and NO_x emissions whereas AVL 415 smoke meter was used for recording the exhaust smoke. The present research highlights the performance, combustion, and emission characteristics of an unmodified tractor diesel engine fueled with CIME blends like B5, B10, B20, and B100. All the experiments were conducted at a constant speed of 1500 rpm and at a consistent fuel injection pressure of 220 bar. The sample standard deviation was analyzed for obtaining exact results after repeating all tests for three times. (Please refer Table 2 for properties of various CIME blends and Fig. 1 for experimental engine setup).

4 Results and Discussions

4.1 Brake Specific Fuel Consumption

The effect of biodiesel blends on the brake specific fuel consumption (BSFC) compared to pure diesel fuel are shown in Fig. 2(a). It was perceived that B5 blend produced a BSFC of 0.2136 kg/kWh which was 3.28% lower compared to the BSFC of pure diesel at maximum load whereas other biodiesel blends showed higher BSFC than B5 blend and pure diesel at full load condition. This result may be ascribed by lower heating value, high viscosity and density of CIME blends which cause the fuel injection rate to increase for attaining equal engine power output. Ashok et al. [12] mentioned that lower calorific value of Calophyllum Inophyllum biodiesel acts as a trade-off to BSFC by increasing the fuel injection rate. However, B5 biodiesel blend despite having slightly higher viscosity and density than pure diesel yielded the lowest BSFC which may be attributed to its better physical and chemical properties enhancing the fuel atomization rate and promoting better combustion characteristics.

4.2 Brake Thermal Efficiency

The variation of brake thermal efficiency (BTE) with respect to the brake mean effective pressure (BMEP) was studied as shown in Fig. 2(b). It was perceived that as the engine load increased, the BMEP increased, which in turn increased the thermal conversion efficiency for all the test samples. As per the results, diesel fuel showed comparatively higher BTE at every loading condition than all the biodiesel blends except B5 blend. The lower heating value and high rate of fuel consumption of biodiesel and its blends are said to have caused a decrease in the BTE at all loads.

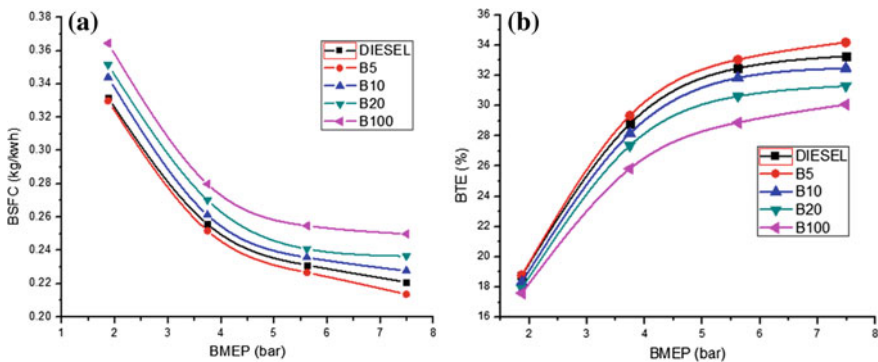


Fig. 2 (a) Brake specific fuel consumption versus brake mean effective pressure at various loads and (b) brake thermal efficiency versus brake mean effective pressure at various loads

But in case of B5 blend, the BTE was found to be always higher than pure diesel throughout the loading condition with a maximum of 34.1% which was 4.8% higher than diesel at full load condition. This increase in BTE for B5 blend may be due to slightly higher oxygen content which may have triggered better fuel atomization and complete combustion which was found concordant to previous studies [9].

4.3 In-Cylinder Pressure

The variation of in-cylinder pressure was monitored at various crank angles for all the test samples as shown in Fig. 3. It was noticed that B5 blend produced the maximum peak pressure of 74.016 ± 0.5 bar, whereas the peak pressure for pure diesel, B10, B20, and B100 blends were witnessed to be 73.81 ± 0.35 , 72.7 ± 0.4 , 72.27 ± 0.23 and 69.95 ± 0.28 bar at full load condition, respectively. In case of pure diesel, the ignition delay of the fuel proved to be very pivotal for attaining peak in-cylinder gas pressure. Previous studies showed that as the oxygen content increases for higher blend concentrations, the cetane number of the fuel increased and the ignition delay reduced which prompted the fuel to atomize and vaporize immediately after injection inside the combustion chamber and ignited it rapidly [13]. Even then, the peak in-cylinder pressures for all biodiesel blends were noted to be lower than conventional diesel due to higher heating value except B5.

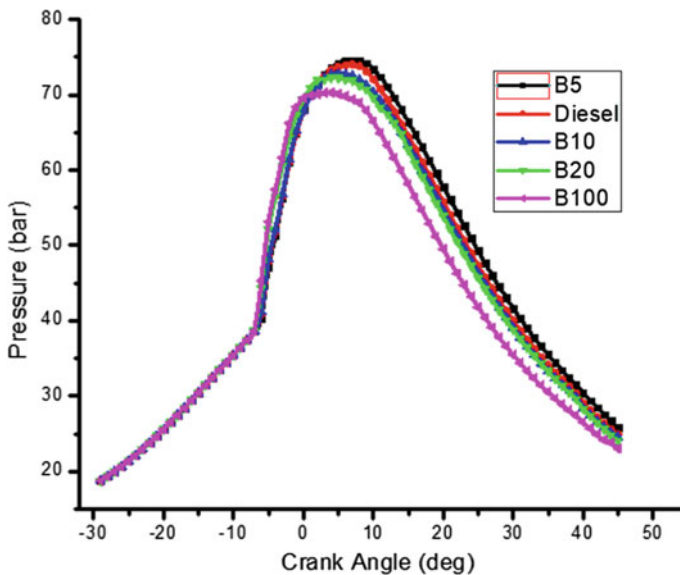


Fig. 3 Variation of in-cylinder combustion pressure for all test samples at 100% load

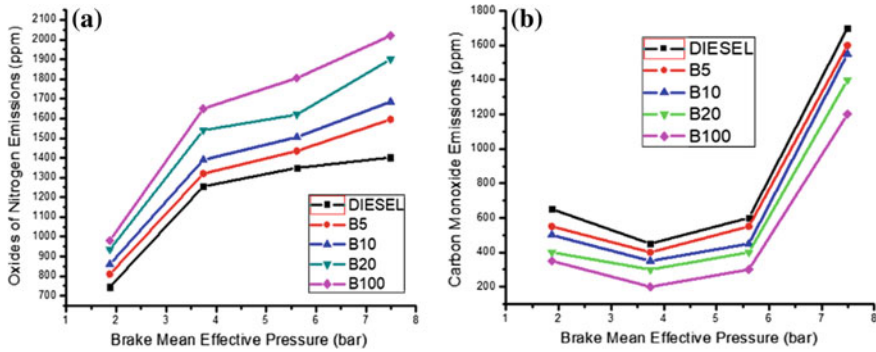


Fig. 4 (a) Variation of oxides of nitrogen and (b) carbon monoxide emissions for various loading conditions

4.4 Oxides of Nitrogen Emissions

Oxides of nitrogen emissions (NO_x) are very much predominant in diesel engines and are mainly formed because of higher availability of oxygen, high cycle temperatures, and ample reaction time. The variations of NO_x emissions for different BMEP are depicted in Fig. 4(a). It was noted that all the biodiesel blends produced higher NO_x emissions with respect to conventional diesel at all loads. As the BMEP increased, diesel fuel showed 9.08%, 14.77%, 25.76%, and 38.63% lower average NO_x emissions than B5, B10, B20, and B100 blends, respectively. Among all the blends, B5 showed the lowest NO_x emissions at all loads. This may be caused due to high oxygen content and higher combustion temperatures in the local zones of combustion chamber, at all loading conditions. Muthukumaran et al. [13] have suggested that even if combustion for biodiesel blends starts in advance, still it doesn't favor the diffusion combustion phase which seldom decreases the NO_x emissions.

4.5 Carbon Monoxide Emissions

Carbon monoxide (CO) emissions are formed due to in-homogeneity of fuel distribution with fuel-rich mixture. CO is oxidized into CO_2 at higher cycle temperatures when oxygen is available adequately. From the results as seen in Fig. 4(b), it was noticed that all the CIME blends produced lower CO emissions compared to pure diesel at all loads. Diesel fuel produced 9.57%, 18.68%, 30.26%, and 43.36% higher average CO emissions than B5, B10, B20, and B100 blends, respectively. This may be due to the fact that with the rise in biodiesel blend concentrations, the increase in cetane number and extra oxygen content leads to lower formations of rich fuel pockets and promotes complete combustion. This result was found to be agreeable with previous studies [14].

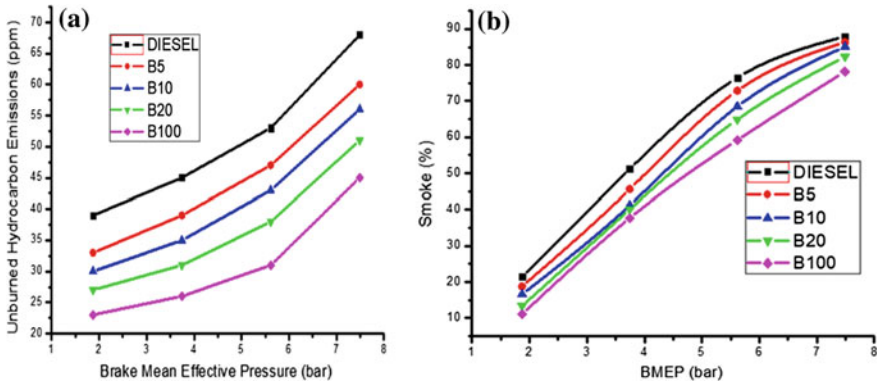


Fig. 5 (a) Variation of unburned hydrocarbon and (b) smoke emissions for various loading conditions

4.6 Unburned Hydrocarbon Emissions

The amount of unburned hydrocarbon (UBHC) emissions mainly depends on certain factors like properties of fuel and its spray characteristics, injection timing, fuel atomization rate, and piston displacement volume. Figure 5(a) shows the variation of unburned hydrocarbon emissions for various loading conditions. The UBHC emissions were noticed to be highest for pure diesel and started reducing as the biodiesel blend concentrations increased. Conventional diesel fuel produced 12.29%, 19.58%, 28.84%, and 40.78% higher average UBHC emissions than B5, B10, B20, and B100 blends, respectively. This may be because of the simultaneous effect of higher cetane number and higher oxygen content of CIME blends that promoted better fuel combustion and lowered the UBHC emissions which was found similar to previous research [12].

4.7 Smoke

CI engines are one of the largest emitters of smoke which are dependent on the amount of sulfur content and aromatic compounds in the fuel, cycle temperature, and availability of oxygen inside the combustion chamber. The smoke emissions for various test samples are shown in Fig. 5(b). It was noted that diesel produced higher amount of average smoke emissions that were found to be 2.12%, 3.88%, 8.53%, and 20.21% higher than B5, B10, B20, and B100 blends, respectively. At high load, smoke opacity observed by B100 was found to be least as compared to all other test samples, diesel being the maximum. Smoke opacity reduced as biodiesel concentration increases in the fuel. Mosarof et al. [15] inferred that biodiesel blends

contain higher oxygen content, aromatic compounds, and almost no sulfur compared to diesel which helped in reducing smoke emissions at all loading conditions.

5 Conclusions

The present research highlights the performance, combustion, and emission characteristics of an unmodified tractor diesel engine fueled with CIME blends. The following conclusions were drawn from the experimental results:

- CIME B5 blend produced 3.28% lower BSFC and 4.8% higher BTE compared to diesel fuel.
- CIME B5 blend produced the best combustion characteristics compared to all biodiesel blends with 0.28% increase in peak pressure compared to diesel at full load.
- Emissions results for all biodiesel blends were observed to be lower than base diesel. However, B5 blend showed 12.29%, 2.12% and 9.57% decrease in average HC, smoke and CO emissions, respectively compared to conventional diesel. However, the NO_x emissions were found to be higher for all blend concentrations than pure diesel.

A final conclusion can be drawn stating that 5% blend of CIME can be used directly in a diesel engine without any major alterations. Thus, CIME can be used as a potential alternative for diesel in India to enhance the performance and emission characteristics of an engine.

References

1. Jeshvaghani, H.S., Fallahipanah, M., Gahruei, M.H., Chen, L.: Performance analysis of diesel engines fueled by biodiesel blends via thermodynamic situation of an air standard diesel cycle. *Int. J. Environ. Sci. Technol.* <https://doi.org/10.1007/s13762-013-0274-4>
2. Yogish, H., Chandarshekar, K., Pramod, M.R.: A study of performance and emission characteristics of computerized CI engine with composite biodiesel blends as fuel at various injection pressures. *Heat Mass Transf.* **49**, 1345–1355 (2013). <https://doi.org/10.1007/s00231-013-1181-4>
3. Borugadda, V.B., Paul, A.K., Chaudhari, A.J., Kulkarni, V., Sahoo, N., Vaibhav, V.: Influence of waste cooking oil methyl ester biodiesel blends on the performance and emissions of a diesel engine. *Waste Biomass Valor.* <https://doi.org/10.1007/s12649-016-9749-0>
4. Venkanna, B.K., Reddy, C.V.: Biodiesel production and optimization from Calophyllum Inophyllum linn oil (honne oil)—a three stage method. *Biores. Technol.* **100**, 5122–5125 (2009). <https://doi.org/10.1016/j.biortech.2009.05.023>
5. Ong, H.C., Mahlia, T.H.L., Masjuki, H.H., Norhasyima, R.S.: Comparison of palm oil, Jatropha Curcas and Calophyllum Inophyllum for biodiesel: a review. *Renew. Sustain. Energy Rev.* **15**, 3501–3515 (2011). <https://doi.org/10.1016/j.rser.2011.05.005>

6. Atabani, A.E., Cesar, A.S.: Calophyllum Inophyllum L.—a prospective non-edible biodiesel feedstock. Study of biodiesel production, properties, fatty acid composition, blending and engine performance. *Renew. Sustain. Energy Rev.* **37**, 644–655 (2014)
7. Sanjid, A., Masjuki, H.H., Kalam, M.A., Ashrafur, R.S.M., Abedin, M.J., Palash, S.M.: Impact of palm, mustard, waste cooking oil and Calophyllum Inophyllum biofuels on performance and emission of CI engine. *Renew. Sustain. Energy Rev.* **27**, 664–682 (2013). <https://doi.org/10.1016/j.rser.2013.07.059>
8. Ong, H.C., Masjuki, H.H., Mahlia, T.M.I., Silitonga, A.S., Chong, W.T., Leong, K.Y.: Optimization of biodiesel production and engine performance from high free fatty acid Calophyllum Inophyllum oil in CI diesel engine. *Energy Convers. Manag.* **81**, 30–40 (2014). <https://doi.org/10.1016/j.enconman.2014.01.065>
9. Monirul, I.M., Masjuki, H.H., Kalam, M.A., Mosarof, M.H., Zulkifli, N.W.M., Teoh, Y.H., How, H.G.: Assessment of performance, emission and combustion characteristics of palm, jatropha and Calophyllum Inophyllum biodiesel blends. *Fuel* (2016). <https://doi.org/10.1016/j.fuel.2016.05.010>
10. Ong, H.C., Masjuki, H.H., Mahlia, T.M.I., Silitonga, A.S., Chong, W.T., Yusaf, T.: Engine performance and emissions using Jatropha Curcas, Ceiba Pentandra and Calophyllum Inophyllum biodiesel in a CI diesel engine. *Energy* **69**, 427–445 (2014). <https://doi.org/10.1016/j.energy.2014.03.035>
11. Rahman, S.M.A., Masjuki, H.H., Kalam, M.A., Abedin, M.J., Sanjid, A., Sajjad, H.: Production of palm and Calophyllum Inophyllum based biodiesel and investigation of blend performance and exhaust emission in an unmodified diesel engine at high idling conditions. *Energy Convers. Manage.* **76**, 362–367 (2013). <https://doi.org/10.1016/j.enconman.2013.07.061>
12. Ashok, B., Nanthagopal, K., Jeevanantham, A.K., Bhowmick, P., Malhotra, D., Agarwal, P.: An assessment of Calophyllum Inophyllum biodiesel fuelled diesel engine characteristics using novel antioxidant additives. *Energy Convers. Manage.* **148**, 935–943 (2017). <https://doi.org/10.1016/j.enconman.2017.06.049>
13. Muthukumar, N., Saravanan, C.G., Yadav, S.P.R., Vedharaj, V.S., Roberts, W.L.: Synthesis of cracked Calophyllum Inophyllum oil using fly ash catalyst for diesel engine application. *Fuel* **155**, 68–76 (2015). <https://doi.org/10.1016/j.fuel.2015.04.014>
14. Palash, S.M., Kalam, M.A., Masjuki, H.H., Masum, B.M., Fattah, I.M.R., Mofijur, M.: Impacts of biodiesel combustion on NO_x emissions and their reduction approaches. *Renew. Sustain. Energy Rev.* **23**, 473–490 (2013). <https://doi.org/10.1016/j.rser.2013.03.003>
15. Mosarof, M.H., Kalam, M.A., Masjuki, H.H., Alabdulkarem, A., Ashrafur, A.M., Arslan, A., Rashedul, H.K., Monirul, I.M.: Optimization of performance, emission, friction and wear characteristics of palm and Calophyllum Inophyllum biodiesel blends. *Energy Convers. Manag.* **118**, 119–134 (2016). <https://doi.org/10.1016/j.enconman.2016.03.081>

A Novel Beetle-Inspired Fuel Injection System for Improved Combustion Efficiency



R. Kuppuraj and S. A. Pasupathy

Abstract Flash evaporation technique inspired from bombardier beetle was investigated for diesel fuel injection system to improve the burning efficiency. The effect of flash evaporation on spray cone angle and spray penetration was investigated for two injection pressures with pintle type injector. Both the parameters were measured using a camera at a speed of 120 frames per second. The results of our pilot study suggest that wider cone angle and moderate penetration can be achieved even at low injection pressures which will eventually help to improve the combustion process and fuel efficiency and reduces carbon emission.

Keywords Flash evaporation · Bombardier beetle · Fuel injection system
Carbon emission · Biomimetics · Spray and atomization

1 Introduction

A typical fuel injection system produces fine atomized spray with extremely small-sized droplets to achieve proper mixing of fuel with oxidizer [1, 2]. Burning efficiency of fuel and pollutant formation is greatly influenced by spray formation and its penetration inside the combustion chamber of heterogeneous systems like diesel engines [3]. Most of these systems use high-pressure injection mechanism to produce spray of desired droplet size and is limited to certain extent [4, 5]. However, the penetration is directly proportional to the injection pressure with no limits on penetration [1, 3]. Since the increase in injection pressure increases the penetration velocity, it also produces undesired effects like fuel impingement on the wall surface which may often affect the system [6]. Moreover, this will result in

R. Kuppuraj
Indian Institute of Science, Bangalore, India

S. A. Pasupathy (✉)
Department of Electronics and Communication Engineering,
Kumaraguru College of Technology, Coimbatore 641049, Tamil Nadu, India
e-mail: pasupathy.sa.mce@kct.ac.in

poor burning of fuel and high amount of emission. To overcome these problems, researchers are concentrating to produce finer droplets at low injection pressures [7]. Flash boiling atomization is one of the most powerful alternate methods of producing fine spray under the low injection pressures [8]. Flash evaporation is a process of rapid fuel evaporation when the fuel is exposed to a medium having pressure lower than the vapor pressure of the fuel. Although majority of the fuels are having low vapor pressure, the flash evaporation of these fuels can be achieved by preheating the fuel [9]. Despite the fact that the flash evaporation technique was effectively investigated for gasoline fuel injection system [10], it is yet to be investigated for diesel fuels. Since the diesel fuel has low vapor pressure, achieving flash evaporation in diesel fuel is proving very difficult [11]. Natural spray mechanism found in bombardier beetle utilizes preheating principle to achieve flash boiling in its explosion chamber, and it ejects fine spray to escape from predators [12]. This natural flash boiling concept can be a good source of inspiration to mitigate the problems associated with flash evaporation of diesel fuel. Hence, in this work, we adopted the preheating mechanism to diesel fuel and investigated the effect of spray formation for two different injection pressures with different preheating temperatures.

1.1 Bombardier Beetle—Spray Mechanism of Nature

To escape from the predators, bombardier beetles eject a very hot noxious fluid from the tip starting at the end of the abdomen as shown in Fig. 1. The ejection velocity varies between 3.25 and 19.5 m/s with a fluid temperature around 100 °C [13]. The ejection is enabled by the chemical reaction between two fluids (hydroquinone and hydrogen peroxide) which takes place inside the reaction chamber of the beetle as shown in Fig. 2. This ejection mechanism is very similar to the pulse combustion process takes place in common engineering systems. As vapor pressure of the fluid is directly proportional to the temperature, the chemical reaction increases the temperature inside the chamber which induces flash boiling in the beetle. This preheating concept is called superheating. However, the pressure inside the chamber is yet to be measured. In this work, the flash boiling and spray pattern of diesel was investigated by superheating the fluid as in bombardier beetle. Since the vapor pressure of diesel is lower than the ambient pressure, the flash boiling of diesel was achieved by superheating.

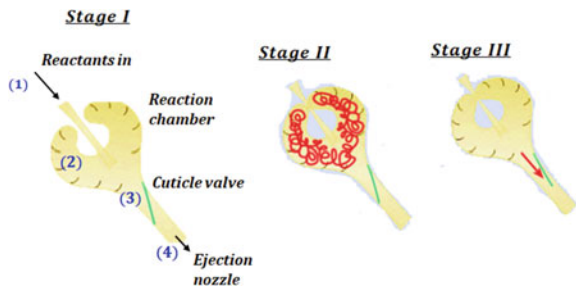
2 Materials and Methods

Achieving flash evaporation at the ambient temperature and at the standard fuel injection pressure is difficult due to low vapor pressure of the diesel. In order to accomplish the flash evaporation for diesel fuel, the regular fuel injection system

Fig. 1 Photograph of bombardier beetle’s ejection shows that noxious liquid is discharged from the small tip starting from the abdomen. Figure reproduced from [14]



Fig. 2 Under the normal condition, pressure inside reaction chamber (2) is low, so the inlet passage (1) is open and exit valve (2) is in a closed condition. Due to low pressure, the fluid from the reservoir will be injected through (1) [15]



was modified as shown in Fig. 3 so as to mimic the bombardier beetle. The fuel from the reservoir was pumped through a fuel rail to the spring operated nozzle (pintle type). The fuel rail was wound with a heating coil, and the temperature of the fuel passing through the rail was controlled by varying the voltage supplied to the coil using an autotransformer. Arbitrarily chosen three different temperature ($T_f = 30, 1000, \text{ and } 1700 \text{ }^\circ\text{C}$) were tested in this work for two different injection pressure (200 and 100 bar). The injection pressure was adjusted by changing the spring tension of the nozzle, and the pressure was measured using a gauge as shown in Fig. 3. The fuel jet from the nozzle ejected to the free environment was recorded by a standard video camera. The image quality was improved by using a focus lamp illuminated on the spray. The images of ejection were retrieved from the video footage, and they were analyzed using ImageJ software. The images were analyzed for cone angle and spray penetration distance. At each temperature, the measurement was repeated for three times, and the standard deviation of these three reading are shown as error bars in the results section. To compute the cone angle and penetration depth, it is necessary to have viscosity values for the temperature we had tested. Hence, the viscosity of the fuel at chosen temperatures was measured using Saybolt viscometer, which has a temperature range of 20–270 °C with measurement error of 0.2%. The viscosity measurements were conducted as per ASTM D-88, and the standard deviation of three measurements is shown as error bars in Fig. 4 (Table 1).

Fig. 3 When reactants (hydro quinine and hydrogen peroxide) starts entering through (1), reaction chamber (2) which is a flexible membrane acts like a bourdon tube and expands as the pressure increases inside the chamber and closes the inlet (1) [15]



Fig. 4 Due to chemical reaction between reactants, the temperature increases and makes the fluid boiling which increase the pressure inside the chamber (2). After reaching certain level of pressure, the exit valve (4) opens to eject the fluid [15]



3 Results

The primary and secondary breakup of droplets and the spray pattern are the common parameters usually investigated in spray studies [16]. The breakup of droplets is characterized by three nondimensional numbers: (1) Weber number, (2) Reynolds number, and (3) Ohnesorge number. Due to experimental limitations, in this work, only spray pattern was investigated, which includes cone angle and penetration depth. Since the fuel is preheated, it is essential to measure the viscosity of the fuel for these temperatures, and the same is shown in Fig. 4.

Table 1 Experimental conditions

Parameters	Specifications
Fuel used	Diesel oil (ASTM D975-13/grade no. 1-D S15)
Injector type	Single point plain atomizer (pintle type)
Injection pressure	200 and 100 bar
Ambient air pressure and density	1 bar and 1 kg/m ³
Fuel temperature	30–1700 °C
Heating coil	Fiber Te on coated aluminum coil
Spray imaging camera	Video camera (8.9 megapixels) which records 120 frames per second
Viscosity measurement	Saybolt viscometer (ASTM D-88 standard)

3.1 Spray Pattern

The effect of preheating of fuel on spray pattern for two different injection pressures is depicted in Figs. 5 and 6. The cone angle (θ) was measured from these images using the software, ImageJ. Due to the use of low-speed camera, the penetration depth could not be measured. As stated in Sect. 1, it is believed that the flash boiling was achieved due to preheating of diesel close to its boiling point. However, for low preheating temperatures, there was no variation in spray pattern was observed (Fig. 8).

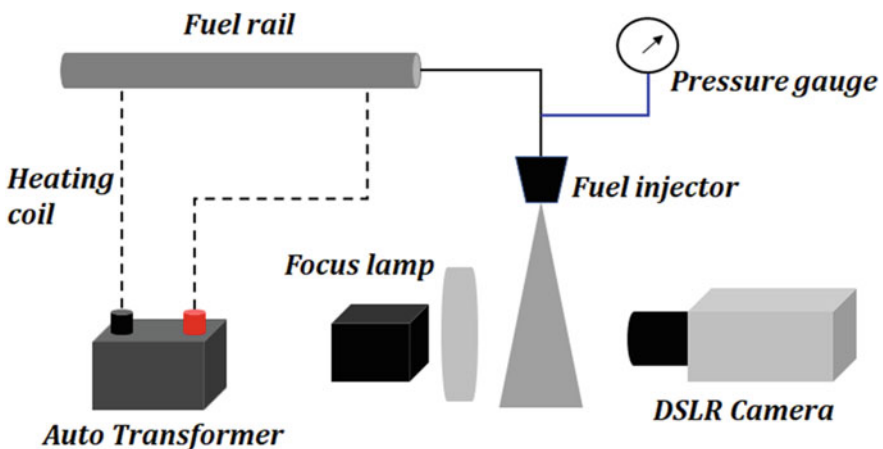


Fig. 5 Schematic of experimental setup

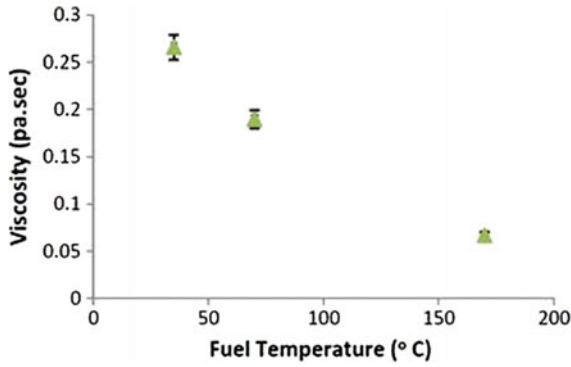


Fig. 6 The effect of temperature on viscosity of diesel fuel

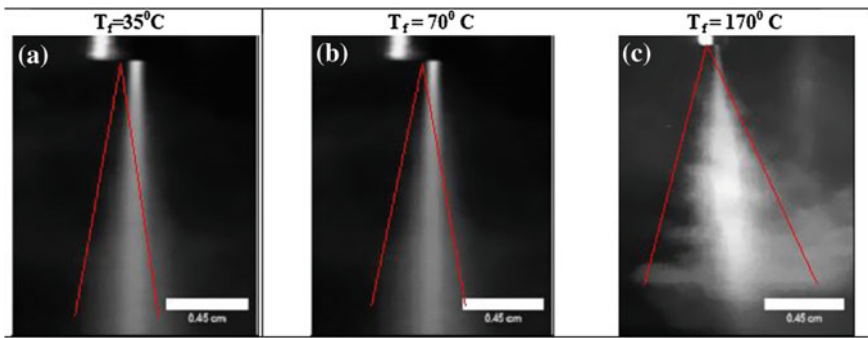


Fig. 7 Photographic image shows spray pattern under different fuel temperatures @ 200 bar injection pressure

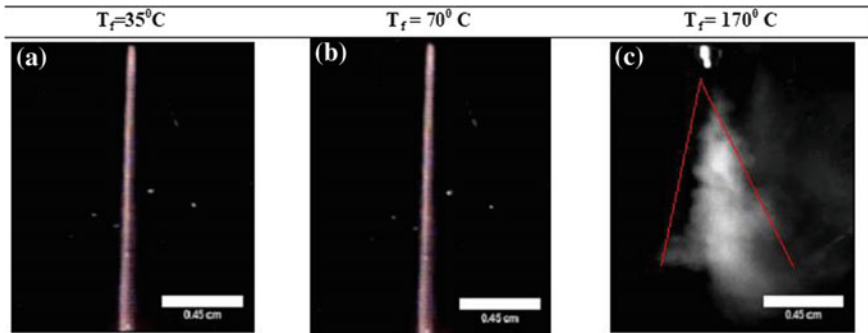


Fig. 8 Photographic image shows spray pattern under different fuel temperatures @ 100 bar injection pressure

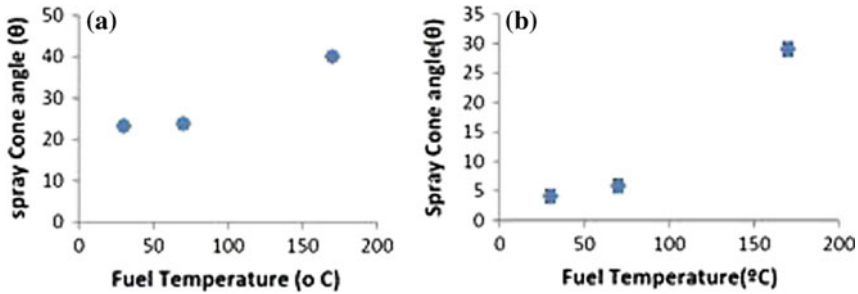


Fig. 9 Cone angle for varying temperatures at two different pressures: plot **a** at 200 bar injection pressure, **b** at 100 bar injection pressure

3.2 Spray Cone Angle

Effect of temperature on cone angle: The measured cone angle for increasing temperature at two different injection pressures is shown in Fig. 7 and 8. For each temperature, the experiment was conducted for three times, and the mean value was used in the graph, and the standard deviations of this experiment were shown as error bar (Fig. 9). The reason for the formation of large cone angle is due to the reduction in viscosity of the fuel. Since the viscosity is in inverse relation with temperature, the large cone angle was formed for higher preheating temperatures. This was also in accordance with [17], who investigated the spray cone angle for various fuels having different viscosity under constant injection pressure.

Effect of injection pressure on cone angle: Even at low preheating temperature, the cone was formed for high injection pressure (200 bar). Whereas, when the pressure was dropped to 100 bar, the cone was not formed at low preheating temperatures, but a wide cone was formed for the temperatures close to the boiling point (see Fig. 8C). It was learned that the flash evaporation by preheating has the potential to form a cone angle even at low injection pressure (Fig. 9).

3.3 Spray Penetration

Effect of injection pressure on spray penetration: Due to experimental limitations, spray penetration after injection was not measured in this pilot study. However, it can be understood from physical meaning that the spray tip penetration is having a linear relationship with injection pressure. Hence, the penetration depth will be reduced for the reduction of injection pressure.

Effect of fuel temperature on spray penetration: Few literatures [11, 18, 19] reported the effect of fuel temperature on spray formation due to flash boiling.

Their results indicate that high fuel temperature increases the cone angle and decreases the penetration depth. The same effect was also observed in our study that wide cone angle was formed for high temperature with low injection pressure (100 bar) as shown in Fig. 8C. This wide cone angle reduces the penetration depth as compared with low temperature. Since the fuel is heated near to the boiling point, the fuel may start changing its phase as observed in the bombardier beetle. This change of phase may reduce the momentum of the fluid causing it to disperse rapidly and forming wider cone angle while reducing the penetration depth.

4 Discussion

To achieve an effective combustion, an injection system should produce spray with wide cone angle, moderate penetration, droplets with extremely small size, quick evaporation, and rapid mixing with ambient fluid [2, 7]. As reported in our results Sects. 3.1 and 3.2, the concept of preheating inspired by bombardier beetle produces wider cone angle and medium spray tip penetration. However, this system provides an opportunity to investigate the occurrence of flash evaporation during the preheating process. Although other parameters are needed to be investigated, the initial results suggest that bio-inspired system will have the potential to produce efficient fuel injection systems. The major limitation of this technique is that it requires external power source to preheat the fuel. However, the waste heat recovered from the exhaust can be used to preheat the fuel so as to reduce the power consumption. Since it also produces wider cone angle at low injection pressures, the cost and power required for high-pressure system can be substantially reduced. Moreover, this system can be effectively used for stationary IC engines used in power production applications, mixing enhancement in supersonic combustors and reducing the over penetration problems commonly occurred in homogeneous charge compression ignition engines (HCCI). If this system is implemented in real time, it is anticipated that it will not only improve the combustion process but eventually reduces the harmful emissions. Our pilot study opens a new avenue to investigate the biomimetic flash evaporation technique for fuels similar to diesel. The various spray parameters such as droplet size, evaporation, mixing with air, combustion, and emission are needed to be further investigated in real-time systems with enhanced instrumentation. Nevertheless, bombardier beetle ejects the noxious fluid in a pulsed manner (500 pulses/s); it may also be a good resource to develop a multiple fuel injection system.

Acknowledgements The authors would like to thank Indian Institute of Technology, Delhi (IITD), India, for permitting the first author to carry out this work as a summer research fellow and also appreciate Professor M. R. Ravi of IITD for providing valuable suggestions during this work.

References

1. Heywood, J.B.: *Internal Combustion Engine Fundamentals*, vol. 930. McGraw-Hill, New York (1988)
2. Sirignano, W.A.: *Fluid Dynamics and Transport of Droplets and Sprays*. Cambridge University Press (2010)
3. Van Basshuysen, R., Schfer, F.: *Internal Combustion Engine Handbook—Basics, Components, Systems and Perspectives*, vol. 345 (2004)
4. Crowley, P.J., Hilsbos, R.L., Wieland, H.L., Straub, R.D., Teerman, R.F., Timmer, R.C.: Common rail fuel injection system. Google Patents, 1992
5. Fort, L.N., Albert, A.F., Darragh, E.P.: High constant pressure, electronically controlled diesel fuel injection system. Google Patents, 1980
6. Rajkumar, S., Bakshi, S., Mehta, P.S.: Predicting mixing rates in multiple injection CRDI engines (2009)
7. Lefebvre, A.H.: *Atomization and Sprays*, vol. 1040. CRC Press (1989)
8. Sher, E., Bar-Kohany, T., Rashkovan, A.: Flash-boiling atomization. *Prog. Energy Combust. Sci.* **34**(4), 417–439 (2008)
9. Parrish, S.E., Zink, R.J.: Spray characteristics of multi-hole injectors under flash boiling conditions. In: 21st Annual Conference on Liquid Atomization and Spray Systems (2008)
10. Kawano, D., Ishii, H., Suzuki, H., Goto, Y., Odaka, M., Senda, J.: Numerical study on flash-boiling spray of multicomponent fuel. *Heat Transf. Asian Res.* **35**(5), 369–385 (2006)
11. She, J.: Experimental Study on Improvement of Diesel Combustion and Emissions Using Flash Boiling Injection. SAE International, Warrendale, PA, SAE Technical Paper 2010-01-0341 (2010)
12. Strahs, G.: Biochemistry at 100 °C: explosive secretory discharge of bombardier beetles (*Brachinus*). *Science* **165**, 61–63 (1969)
13. Eisner, T., Aneshansley, D.J.: Spray aiming in the bombardier beetle: photographic evidence. *Proc. Natl. Acad. Sci.* **96**(17), 9705–9709 (1999)
14. Beheshti, N., McIntosh, A.C.: The bombardier beetle and its use of a pressure relief valve system to deliver a periodic pulsed spray. *Bioinspir. Biomim.* **2**(4), 57 (2007)
15. McIntosh, A., Beheshti, N.: Insect inspiration. *Phys. World* **21**, 29–31 (2008)
16. Huh, K.Y., Lee, E., Koo, J.: Diesel spray atomization model considering nozzle exit turbulence conditions. *At. Sprays* **8**(4) (1998)
17. Su, T.F., Kozma, J.M., Warrick, C.B., Farrell, P.V.: Effects of fuel viscosity and ambient temperature on spray characteristics from multi-hole nozzle injectors. *Int. J. Fluid Mech. Res.* **24**(1–3) (1997)
18. Neroorkar, K., Gopalakrishnan, S., Grover, J., Schmidt, D.P.: Simulation of flash boiling in pressure swirl injectors. *At. Sprays* **21**(2), 179–188 (2011)
19. Xu, M., Zhang, Y., Zeng, W., Zhang, G., Zhang, M.: Flash Boiling: Easy and Better Way to Generate Ideal Sprays than the High Injection Pressure. SAE International, Warrendale, PA, SAE Technical Paper 2013-01-1614 (2013)

Effect of Friction Stir Processing on the Dry Sliding Wear Behaviour of AA6082-5TiB₂ Composite



Sreehari Peddavarapu and S. Raghuraman

Abstract AA6082 alloy reinforced with TiB₂ particles was synthesized through stir casting method to yield the AA6082-5(wt%)TiB₂ metal matrix composite. Dry sliding wear behaviour was studied to understand the effect of friction stir processing (FSP) on the composite with the design of experiment software, which was used to plan the experiments and was conducted at 15–50 N applied load and 300–1200 rpm rotational speed. It was compared with the same set experiments performed on the sample without FSP. Experiments were conducted by preparing the samples according to specific dimensions on pin-on-disc tribometer at room temperature. Effect of applied load and rotational speed on the wear or mass loss was plotted. It was observed that the mass loss on both the composites is found to be different. Optical microscopy studies were conducted. Abrasive and adhesive wear mechanisms were observed due to the presence of hard TiB₂ reinforcement particles.

Keywords Alloy · Composite · Wear · Stir casting · Coefficient of friction Reinforcements

1 Introduction

6XXX series aluminium alloys are having high demand in defence, aerospace, ship building—marine and automotive industries due to their high strength to weight ratio and made them suitable for a variety of applications [1]. They have been introduced in the automotive components such as connecting rods, piston, brake rotors, cylinder liners, push rods by the world-reputed companies and proven to be successful to a certain extent [1–3]. Constant effort has been put up to improve the strength and wear properties of Al alloys in order to meet the ever-increasing need. These Al alloys are not suitable for high-temperature applications [2]. To overcome

S. Peddavarapu (✉) · S. Raghuraman
School of Mechanical Engineering, SASTRA University, Thanjavur 613401, India
e-mail: sreehari@mech.sastra.edu

© Springer Nature Singapore Pte Ltd. 2019
U. Chandrasekhar et al. (eds.), *Innovative Design, Analysis and Development Practices in Aerospace and Automotive Engineering (I-DAD 2018)*, Lecture Notes in Mechanical Engineering, https://doi.org/10.1007/978-981-13-2718-6_46

the poor elevated temperature and tribological properties, the hard particulate or whisker-type reinforcement ceramics such as oxides, borides and carbides are introduced into the Al-based matrix to enhance stiffness, specific strength, wear and fatigue properties at elevated temperature. Various methods are reported in the literature to produce aluminium matrix composites (AMCs) [1–3]. However, stir casting process is a cost-effective method for the bulk manufacturing. Production of stir-casted composites required considerable attention due to the factors such as the difficulty in achieving a uniform distribution of the reinforcement material, wettability between the two main substances, porosity in the cast metal matrix composites and the chemical reactions between the reinforcement material and the matrix alloy.

Titanium diboride (TiB_2) has some unique properties like high hardness (3400 HV), high Young's modulus (345–409 GPa), low density and high wear resistance [4]. It is also noted that TiB_2 does not react with the molten aluminium matrix, leads to no reaction product at interface, and TiB_2 is also known to be the hardest material that can be reinforced with an alloy matrix [1, 4]. The porosity levels need to be minimized, and chemical reactions between the reinforcement materials and the matrix alloy must be avoided.

Nevertheless, the strength of the composite depends on the aforementioned factors which demand the further processing like friction stir processing (FSP) to achieve the uniform distribution of the reinforcement material. Friction stir processing adopts the principle of friction stir welding in which the dynamic plastic deformation occurs in a solid state, produces the homogenous fine and equiaxed grains, replacing the coarse reinforcements as well the grains and thus development of superplastic properties.

AMCs are successfully attempted and have been made to examine the effect of applied load and sliding velocity on the wear behaviour of aluminium alloy and its composites. The strong interaction between load and sliding velocity to cause wear of a material has been clearly demonstrated by several investigators [5]. Comprehensive reviews have been done on the abrasive wear behaviour of AMCs with a variety of reinforcements under different test conditions [4, 6]. It was noted that the study on the effect of TiB_2 particles on the AA6082 alloy before and after FSP is necessary to know the effect of FSP as well as the wear parameters on wear behaviour.

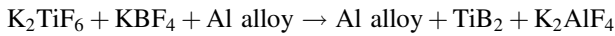
In the present study, the ceramic particles TiB_2 were chosen as reinforcements in the AA6082 matrix to produce AA6082-5% TiB_2 by stir casting method and FSP is performed on the stir-casted composite. Wear behaviour was examined to understand the effect of FSP on the in situ stir-casted composite. Effect of the applied load and sliding velocity on wear mass loss in as-cast condition and FSP were tested by pin on disc tribometer at room temperature. Wear maps were plotted with the help of design of experiment software to understand the mode of wear with the assistance of optical microscopy.

2 Experimental Procedure

2.1 A6082-5%TiB₂ Composite Preparation

AA6082-5%TiB₂ composite was synthesized through an exothermic in situ reaction between K₂TiF₆ (109 g) and KBF₄ (114 g) salts to yield titanium diboride (TiB₂) dispersoids in the molten AA6082 alloy by stir casting route. This procedure was adopted from our earlier research work [1].

In situ TiB₂ particles were formed inside the molten aluminium alloy through the following reaction.



The K₂AlF₄ floats up as a dross which was removed subsequently. The melt was then stir-casted by top pouring into cast iron mould which was preheated to about 200 °C. See Peddavarapu et al. [1] for further detail preparation of AA6082-5% TiB₂ composite.

2.2 Friction Stir Processing

On a converted vertical milling machine with a non-consumable cylindrical tool, FSP was carried out on AA6082-5(wt%)TiB₂ metal matrix composite, synthesized through the stir casting method. From our previous experience [1], 40 mm/min feed at the tool rotation of 560 rpm produced the defect-free quality weld. Hence, the same set of feed and tool rotation has been selected for the current work.

FSP process starts with plunging of a non-consumable cylindrical tool (Fig. 1b), which is brought into contact with the workpiece while it is rotating at the desired speed, until the shoulder of the tool touches the surface. After the tool makes contact, it is made to travel along a straight path. As the tool is continuously rotating, there is a large amount of heat that is generated due to the intense severe plastic deformation and the friction between the tool and the workpiece which in turn increases the temperature of the workpiece. The tool forges the material at the wake side as the tool moves forward and thus, a refined equiaxed grain structure is formed.

2.3 Dry Sliding Wear Study

The cast sample (Sample1) and the FSP sample (Sample2) were cut to square cross section from both the composites to dimensions of 50 mm × 6 mm × 6 mm to conduct the wear test on pin on disc setup, and subsequently, they were mechanically

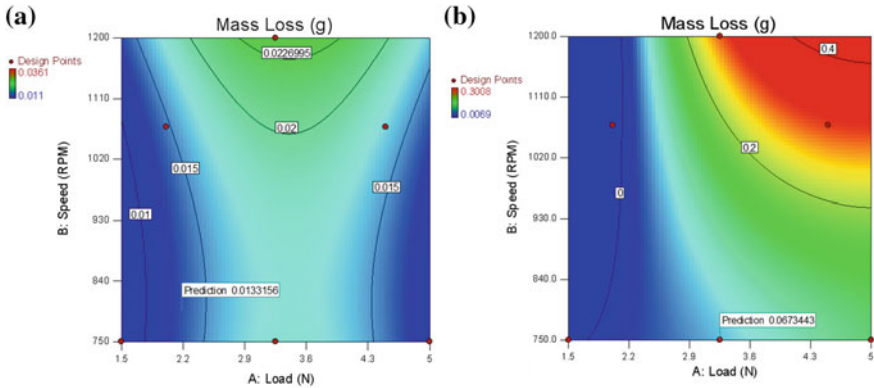


Fig. 1 Mass loss maps for **a** Sample1; **b** Sample2

polished and etched with Keller’s reagent (1% HF, 1.5% HCl, 2.5% HNO₃ and remaining water) for microstructural observations on optical microscopy. The design of experiment software was used to plan the experiments and conducted at 10–50 N applied load for 200–1400 rpm rotational speed for 15 min each to analyse the experimental results. Samples were polished on disc polishing before subjected to wear test. The initial weight of the samples was measured after cleaning with acetone followed by drying using an electronic weighing balance of 0.01 mg accuracy. Computer pin on disc tribometer was used to conduct the dry sliding wear tests against a counterface of EN31 steel disc of HRC 60. The disc was cleaned with acetone before and after the commencement of each test to get the precise values.

3 Result and Discussion

The loss of mass due to wear in the mating parts leads to appreciable dimensional changes and in turn leads to catastrophic failure of parts. Therefore, it is essential to keep the mass loss within tolerance limits for a productive functional life period of mating parts in machinery. Thus, mass loss is considered as an important parameter in wear studies. Mass loss of the square pin specimens for each experiment was accurately calculated using a four decimal Shimadzu Digital Balance and correlated with load and speed. Totally, each nine experiments were conducted for Sample1 and Sample2 based on L9 orthogonal array as listed in the Table 1.

Based on the experimental values for the mass loss obtained from the pin on disc test, results are plotted using the design of experiment software for both the specimens as shown in Fig. 1.

Unlike FSP sample, the wear behaviour is substantially influenced by the porosity of cast sample (Sample1). Initial removal of metal called debris occupies

Table 1 Mass loss values for stir-casted sample and FSP sample

Experiment no.	Load (N)	Speed (RPM)	Mass loss (g) (without FSP) (Sample1)	Mass loss (g) (with FSP) (Sample2)
1	1.5	750	0.0111	0.0141
2	2.01	431.8	0.011	0.0079
3	2.01	1068.1	0.0135	0.0079
4	3.25	300	0.0361	0.0069
5	3.25	750	0.0175	0.0126
6	3.25	1200	0.0239	0.3008
7	4.5	431.8	0.0123	0.0175
8	4.5	1068	0.0149	0.2225
9	5	750	0.0152	0.0167

the pores on the worn surface, which in turn affects further wear behaviour of the material result in different wear maps (Fig. 1a, b) for Sample1 and Sample2, respectively. From the Table 1, the maximum mass loss is observed for the Sample2 which is due to the FSP that produces the fine grains along with the broken reinforcements as a result of dynamic recrystallization (DRX). This DRX decreases hardness of the specimen which in turn lowers the wear resistance.

The general trend observed in the alloys is that the mass loss increases with increase in load at any speed. This is in conformity with the general principle of wear. The reason for this trend is the delamination of oxide layer forming on the contact surface of the specimen, which subsequently increases the wear rates [7–9]. This trend was observed in Sample2, whereas in Sample1 wear behaviour is different due to the porosity from the casting. However, beyond a threshold load, the trend is reversed which may be due to oxidative wear. It is reported in the literature [9–12] that at higher loads with the nominal speeds, heat generation is predominant due to friction result in oxidative layers which prevent further wear. The same is reported even for the high speeds at moderate load.

Figure 2a illustrates the typical dendritic microstructure and the reinforcements of the AA6082-5%TiB₂ as-cast composite. Figure 2b depicts the microstructure of completely recrystallized fine grains and reinforcements due to FSP.

Optical microscope images in Fig. 3a, b exhibit the maximum worn surfaces of the cast sample and the FSP sample, respectively. Worn surface analysis of pin samples indicates parallel grooves, craters, and partial irregular pits were observed in both the composites, which indicate adhesive wear. The plastic flow of the material on the pin was due to abrasion and the wear tracks clearly show the traces of micro-cutting and micro-ploughing effect which suggest abrasive wear mechanism [5]. Thus, both abrasive and adhesive wear mechanisms are observed with abrasive wear mechanism being predominant in nature. It can be expected that hard ceramic reinforcements reduced the deformation by hindering the plastic flow of the matrix material (AA 6082) during the abrasive action of ceramic grit [11].

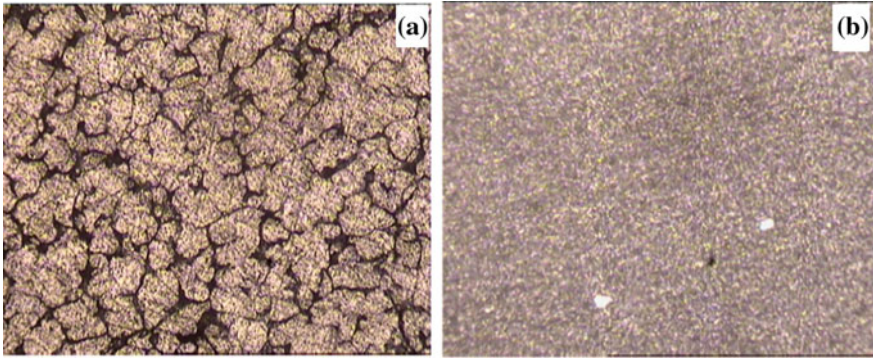


Fig. 2 Optical microscopic images at 100X of **a** Sample1; **b** Sample2

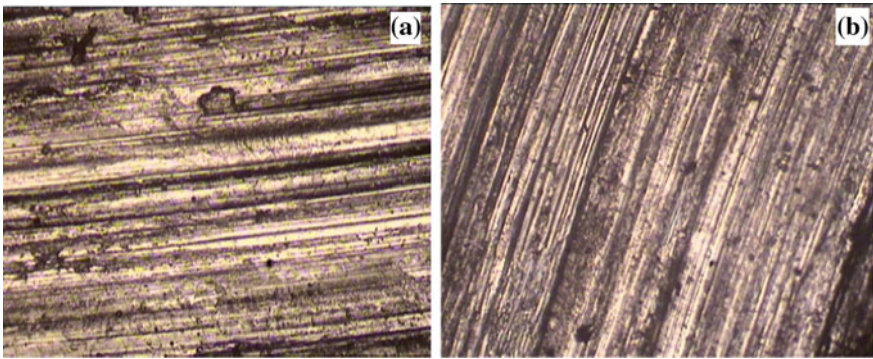


Fig. 3 Optical microscope images of the maximum worn surface at 100X of **a** Sample1; **b** Sample2

4 Conclusion

Dry sliding wear behaviour of cast sample and the FSP sample was studied by understanding the wear mechanisms for the different sliding speeds and applied loads. The response of both the samples are studied with respect to a mass loss for an almost identical set of experimental conditions and found to be different and found the following conclusions:

1. For relatively moderate applied load at higher speed, wear mechanism map pertaining to cast sample shows maximum wear, whereas FSP sample shows to have maximum wear at relatively higher load and at speed.
2. Wear modes were studied for both the composites which indicate the abrasive and adhesive wear mechanisms with abrasive wear mechanism being predominant in nature.

References

1. Peddavarapu, S., Raghuraman, S., Bharathi, R.J., et al.: Micro structural investigation on friction stir welded Al–4.5 Cu–5TiB₂ Composite. *Trans. Indian Inst. Met.* **70**, 703–708 (2017)
2. Kalaiselvan, K., Murugan, N.: Role of friction stir welding parameters on tensile strength of AA6061–B4C composite joints. *Trans. Nonferrous Met. Soc. China* **23**, 616 (2013)
3. Ashish, B., Saini, J.S., Sharma, B.: A review of tool wear prediction during friction stir welding of aluminium matrix composite. *Trans. Nonferrous Met. Soc. China* **26**, 2003 (2016)
4. Tee, K.L., Lu, L., Lai, M.O.: Wear performance of in-situ Al–TiB₂ composite. *Wear* **240**, 59 (2000)
5. Poria, S., Sahoo, P., Sutradhar, G.: Tribological characterization of stir-cast aluminium-TiB₂ metal matrix composites. *Silicon* **8**, 591 (2016)
6. Suresh, S., Moorthi, N.S.V., Vettivel, S.C., Selvakumar, N.: Mechanical behaviour and wear prediction of stir cast Al–TiB₂ composites using response surface methodology. *Mater. Des.* **59**, 383 (2014)
7. Akbari, M.K., Baharvandi, H.R., Shirvanimoghaddam, K.: Tensile and fracture behaviour of nano/micro TiB₂ particle reinforced casting A356 aluminium alloy composites. *Mater. Des.* **66**, 150 (2015)
8. Sivaprasad, K., Kumaresh Babu, S.P., Natarajana, S., et al.: Study on abrasive and erosive wear behaviour of Al 6063/TiB₂ in situ composites. *Mater. Sci. Eng A* **498**, 495 (2008)
9. Kandavel, T.K., Chandramouli, R., Manoj, M., et al.: Influence of copper and molybdenum on dry sliding wear behaviour of sintered plain carbon steel. *Mater. Des.* **50**, 728 (2013)
10. Kaushik, NCh., Rao, R.N.: Effect of applied load and grit size on wear coefficients of Al 6082–SiC–Gr hybrid composites under two body abrasion. *Tribol. Int.* **103**, 298 (2016)
11. Kumar, N., Rao, P.N., Jayaganthan, R., et al.: Effect of cryorolling and annealing on recovery, recrystallisation, grain growth and their influence on mechanical and corrosion behaviour of 6082 Al alloy. *Mater. Chem. Phys.* **165**, 177 (2015)
12. Kaushik, NCh., Rao, R.N.: Effect of grit size on two body abrasive wear of Al 6082 hybrid composites produced by stir casting method. *Tribol. Int.* **102**, 52 (2016)

Optimization of Sliding Wear Performance of Ti Metal Powder Reinforced Al 7075 Alloy Composite Using Taguchi Method



A. Kumar, A. Patnaik and I. K. Bhat

Abstract Al 7075 matrix composite reinforced with titanium metal powder was fabricated by stir casting method. Microstructure and wear properties of matrix alloy and developed composites have been evaluated. The composites with varying filler content from 0 to 2 wt% Ti were fabricated using high vacuum casting machine technique. Dry sliding friction and wear tests were performed on multi-specimen tribotester machine over a normal load range of 20–80 N and sliding velocities of range 0.25–1.25 m/s. The experiments were carried out using Taguchi's L_{25} orthogonal array, and the influence of working factors on wear rate was examined using ANOVA techniques. Results revealed that Al 7075 Ti alloy composite exhibited lower coefficient of friction and wear rate increased. Wear rate of composites increased with increased in load and sliding velocity. It is observed that the 2 wt.%Ti filled 7075 aluminium alloy composite is demonstrated minimum specific wear rate. Morphological studies on worn surface were examined using scanning electron microscope (SEM).

Keywords Al 7075 alloy · Wear · Titanium metal powder · Field emission scanning electron microscopy (FESEM)

1 Introduction

High strength 7075 alloy matrix composites have drawn considerable interest in aerospace, automotive, chemical, biochemical and other advanced structural applications due to outstanding mechanical properties, like the lightweight, high

A. Kumar (✉)

Mechanical Engineering Department, FGIET, Raebareli 229316, Uttar Pradesh, India
e-mail: ashi15031985@gmail.com

A. Patnaik

Mechanical Engineering Department, M.N.I.T, Jaipur 302017, India

I. K. Bhat

Applied Mechanics Department, M.N.N.I.T, Allahabad 211004, Uttar Pradesh, India

© Springer Nature Singapore Pte Ltd. 2019

U. Chandrasekhar et al. (eds.), *Innovative Design, Analysis and Development Practices in Aerospace and Automotive Engineering (I-DAD 2018)*, Lecture Notes in Mechanical Engineering, https://doi.org/10.1007/978-981-13-2718-6_47

485

strength, high stiffness, and good wear resistance [1]. Baradeswaran et al. [2] have studied the mechanical behaviour, modelling and optimization of wear parameters of B_4C and graphite reinforced aluminium hybrid composites and have reported that the hardness and wear resistance of composites increase with increase in particulate filler content in base matrix. Wang and Song [3] have reported the sliding wear behaviour of Al_2O_3 fibre/SiC particle filled aluminium alloy matrix and fabricated by using squeeze casting techniques. They have observed that wear resistance decreases with increase in the filler content (SiC) at room temperature while the temperature increases with decrease in the wear resistance of composites. Many researcher have been reported by Kumar et al. [4] have observed that the wear resistance and microhardness increased with increase in TiO_2 Content and have investigated that the micro structures of worn surface is analysed by scanning electron microscopy (SEM) and Phase analysed by XRD Techniques. Thakur et al. [5] have studied the influence of changing wt% amount of Ti particulate filled aluminium alloy composites and have reported that the mechanical properties such as yield strength, ultimate tensile strength and elastic modulus increase with increase in filler content while ductility decrease with the addition Ti reinforced in alloy matrix. Mobasherpour et al. [6] have investigated the influence of nanosize Al_2O_3 reinforcement on the mechanical behaviour of synthesis 7075 aluminium alloys composites and have observed that hardness tensile strength and density increase with increase in filler content, and then the worn surface of composites was analysed by using SEM, and peak are identified by XRD. Toptan et al. [7] have studied the influence of B_4C volume fraction, sliding velocity, applied load and sliding distance on reciprocal dry wear behaviour of composites and have reported that the coefficient friction and specific wear rate increase with increase in filler content, and worn surface of specimen is determined by SEM.

In the light of above, the present investigation focuses on friction and wear behaviour of Ti metal powder reinforced 7075 aluminium alloy composites using Taguchi's DOE.

2 Experimental Details

2.1 Preparation of the Specimens

The aluminium alloy (Al 7075) was used as the base material, with Ti metal powder as the filler content. The Al 7075 alloy composites were fabricated by high vacuum casting machine and then the various wt% of titanium filler (0–2 wt% at step of 0.5%) content.

The fine particle size of titanium metal powder was used as filler material. The chemical composition of Al 7075 was determine and listed in Table 1. The base material (Al 7075) was melted in a graphite crucible 700 °C using vacuum furnace. Temperature control instrument for the molten metal was kept ,with thermo couple put into melts section then it is measured to melts section temperature.

Table 1 The chemical composition of Al 7075 alloy (wt%)

Element	Si	Fe	Cu	Mn	Mg	Cr	Zn	Ti	Al
Content	0.4	0.5	1.6	0.3	2.5	0.15	5.5	0.2	Bal.

The preparation of Ti particulate filled Al 7075 alloy composites takes place in a high-temperature vertical vacuum furnace which is the assembly of one heating unit that include one graphite crucible, plunger through a narrow 8 mm diameter tip and temperature measuring instrument (infrared temperature measuring sensor). Then mixture of 2 wt% magnesium was added that improves wet ability of the composites. Hence, the molten material with addition of reinforcement was poured directly into cast iron mould (140 × 90 × 10 mm) via opened plunger followed by its solidification. The fabricated alloy composites cools at room temperature, and then the composite material specimens were prepared for mechanical characterization and wear behaviour of composites.

2.2 Tribological Testing

The tribological behaviour of the specimens was performed using multi-specimen tester equipment, manufactured by Ducom Engineers, Bangalore, as per ASTM G 99. Tribotester was used to simulate the specific wear rate as per ASTM G 99 standard at ambient environmental conditions. The experimental data are listed in Table 2, using EN-31 hardened steel disc (60–70 HRC). The specimens of 10 mm diameter and 13 mm height pins were prepared from the composites and then polished at different grade size paper for wear test. The tests were performed at room temperature (30 °C) at a sliding speed of 0.25 m/s, under 20, 35, 50, 65 and 80 N applied load, using wear track diameter 40 mm with sliding velocity 0.25 m/s and sliding distance of 250 m. The steady-state experiments were conducted at room temperature (30 °C) at applied normal 20 N under sliding speed of 0.25–1.25 m/s, using wear track diameter 40 mm with sliding distance of 250 m. The specimens were cleaned with acetone, dried, and their weight was computed for find out the weight loss by using an electronic weighing machining with accuracy of ±0.001 mg.

Table 2 Working range of selected parameters

Control	Level					
	I	II	III	V	IV	units
Normal load	20	35	50	65	80	N
Filler content	0	0.5	1	1.5	2	%
Sliding velocity	0.25	0.50	0.75	1	1.25	m/s
Sliding distance	250	500	700	1000	1250	m

The specific wear rate (W_s ; mm³/N-m) of alloy composites is evaluated using below expression [8]

$$W_s = \frac{\Delta m}{\rho \times v_s \times t \times f_n} \quad (1)$$

where Δm represents mass loss of samples (g), ρ is the sample density (g/cc), v_s is the sliding velocity (m/s), t is the test duration (s) and f_n is the normal load (N).

2.3 Experimental Design

Taguchi optimization technique minimizes the experimental run without considerable data loss and was an effective method to solve the complex problem. Here, the performance characteristic was represented by S/N ratio for the lower the better (LB) approach. The input control factors and their values are listed in Table 2. Here, we made use of L_{25} orthogonal array design for one output parameter, i.e. wear rate.

The S/N ratio with a LB characteristic is given by [8].

$$\frac{S}{N} = -10 \log \frac{1}{N} \sum Y^2 \quad (2)$$

where N = number of observation and Y = observed data. Finally, the significant factor setting and optimal performance are analysed via analysis of variance (ANOVA) was evaluated.

2.4 Surface Morphology Studies

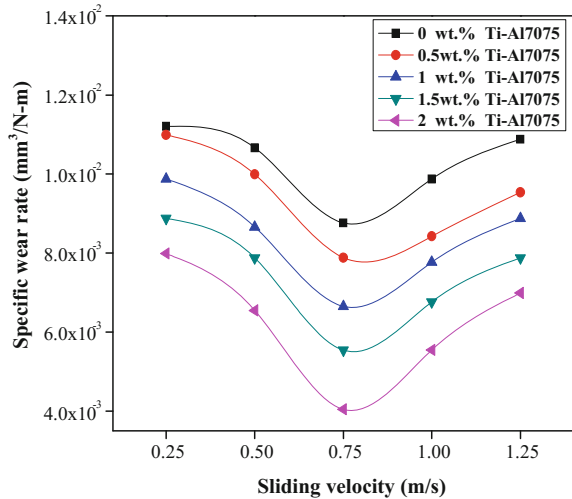
The surface morphology behaviour of Ti metal powder filled Al 6061 alloy composites was examined below area emission scanning electron microscope (FEI Nova Nano SEM 450, USA).

3 Results and Discussion

3.1 Effect of the Sliding Velocity on Specific Wear Rate of Ti Metal Powder Filled Al 7075 Alloy Composites

The variation of the sliding velocity on specific wear rate of Ti metal powder filled Al 7075 alloy composites are shown in Fig. 1. The constant normal load and sliding

Fig. 1 Effect of sliding velocity on specific wear rate of Ti metal powder filled Al 7075 alloy composites

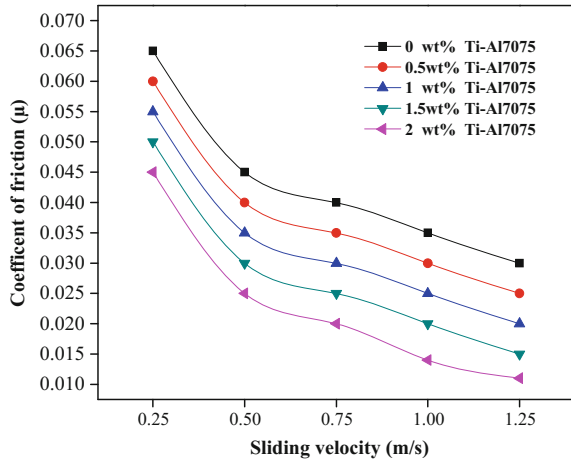


distance are taken as 20 N and 250 m. It is observed that the wear rate of composite are shown higher (0.01088 mm³/N-m) at higher load 80N, while the increased in filler content, the wear rate is decreased. It is noted that wear rate of all composites shows the continuous linearly decrease, after that the wear rate is hastily increased. The decreased in wear rate at 0.75 m/s sliding velocity, after that wear rate of composite is increased from 0.75 to 1.25 m/s. In general, the wear rate of fabricated composites decreases due to better interfacial bonding reinforcement and matrix and more hardness of composite. The wear rate of composite material increases due to poor bonding between matrix and reinforcement. The decrement in wear rate due to the debris particles reaches on counter surface and then wear rate is minimised along with sliding speed [8]. It is observed that the wear rate increased due to the friction heat increases with the increase of the sliding velocity, the oxidation reaction on the tribo-surface and increasing the formation rate of oxidation protective films [9].

3.2 Effect of Sliding Velocity on Coefficient of Friction of Ti Metal Powder Filled Al 7075 Alloy Composites

Figure 2 shows the variation of sliding velocity on coefficient of friction of Ti metal powder filled Al 7075 alloy composites. The results noticed that with the increase in sliding velocity the specific wear rate of unfilled and particulate filled alloy composites continuously decreases irrespective of different filler content. The friction of coefficient value is maximized at 0.25 m/s sliding velocity, while the minimized value of coefficient friction at 0.5 m/s sliding velocity. It is mainly attributed that the coefficient of friction value decreases with increase in sliding velocity while the

Fig. 2 Effect of sliding velocity on coefficient of friction of Ti metal powder filled Al 7075 alloy composites



coefficient of friction decreases with increase in filler content. The coefficients of friction of fabricate alloy composites decreases due to the sliding action takes place between disc and pin surface, inhibiting metal to metal contact of the sliding surfaces [10]. Thus, coefficient of friction decreases slowly. It is another reason that the coefficient of friction decrease due to increase the temperature between pins and disc surface. And the coefficient of friction decrease with increasing sliding velocity [11].

3.2.1 Effect of Normal Load on Specific Wear Rate of Ti Metal Powder Filled Al 7075 Alloy Composites

Figure 3 depicts that the variation of normal load on specific wear rate of Ti metal powder filled Al 7075 alloy composites. It is observed that the specific wear rate of unfilled Al 7075 alloy composites are maximum specific wear rate as compared to filler filled Al 7075 aluminium alloy composites. The higher specific wear rates of all wt% of composites are occurred in between 65 and 80 N Normal loading condition. It is mainly attributed to the specific wear rate increased because of the particle size, homogeneous mixture, hardness of the reinforcement and matrix alloy, respectively. It is observed that the specific wear rate of 2 wt% titanium particulate shows the lower wear rate in comparison to neat alloy composites. It is observed that the order of specific wear rate is 0 wt% > 0.5 wt% > 1.0 wt% > 1.5 wt% > 2 wt%. The specific wear rate increases due to plastic deformation of material. The reason that the specific wear rate increases due to the high temperature, plastic deformation of disc surface generated increasing to the adhesion of pin surface on to the disc [12]. Similar result are report by A. K. Mondal obtained that the specific wear rate of composites increases with increasing load while the specific wear rate decreases with increase in the filler content [13].

Fig. 3 Effect of normal load on specific wear rate of Ti metal powder filled Al 7075 alloy composites

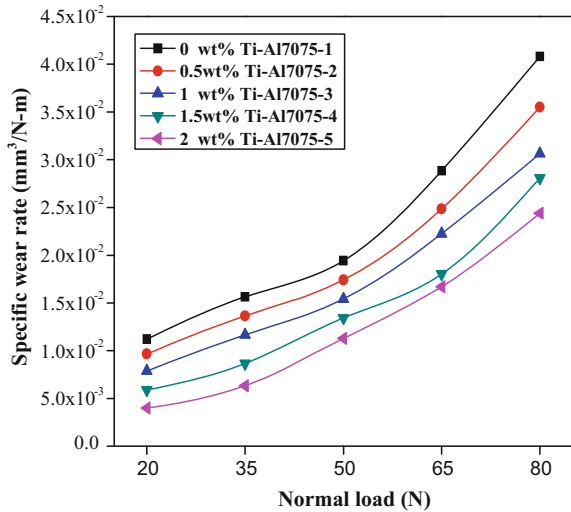
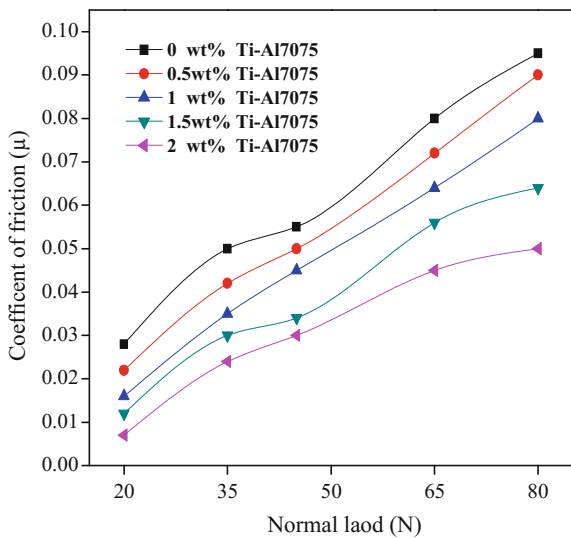


Fig. 4 Effect of normal load on coefficient of friction of Ti metal powder filled Al 7075 alloy composites



3.2.2 Effect of Normal Load on Coefficient of Friction of Ti Metal Powder Filled Al 7075 Alloy Composites

Figure 4 depicts the variation of coefficient of friction under various normal loads (keeping other factors is constant: sliding velocity; 0.25 m/s, sliding distance; 250 m) for base and particulate filled 7075 Al alloy composites. It is evident from the figure that the coefficient of friction increases with the increase in normal load for various wt% of titanium metal powder particulate filled 7075 Al alloy

composites; it can be occurred due to hard reinforced particles may be remove during rubbing process and get pin between surface that lead maximum coefficient of friction [14]. The higher value of coefficient of friction, i.e. in between 0.075 and 0.090 is observed for 0 wt% of titanium metal powder particulate filled 7075 Al alloy composites [15]. The coefficient of friction increases with increase in filler content, normal load and sliding distance. Thus, the coefficient of friction increases with increase in load whereas coefficient of friction decrease with increase in filler content.

3.3 Taguchi Design Experimental Analyses

The test results are also determined by using the Taguchi technique, and significant factors affecting material loss are identified. The Taguchi analysis results are given in Table 3; the overall mean for S/N ratio of the wear rate is obtained to be 30.002 dB. Figure 5 depicts graphically the influence of the three control parameters on specific wear rate. These results are analysed by using the MINITAB 16, famous software particularly used for design of experiment applications. The S/N ratio response is presented in Table 4. It depicts the determined S/N ratios for every level of control factors. The delta value shows that for each control factor have significant influence. The delta value equals the difference between higher and lower S/N ratios for a particular factor. The maximum value of delta, the higher influence, is control factor. It is evident from the figure that the sliding distance is the higher significant factor followed by sliding velocity and normal load while the reinforcement has the less or almost no significance on wear rate of the titanium metal powder filled alloy composite. Finally, The control parameter trends show the sliding distance, sliding velocity, reinforcement and normal load. The results observed that the specific wear shows minimum at various condition (i.e normal load, sliding distance, filler content etc.) [16, 17].

3.4 ANOVA and Effect of Factor

The aim of the statistical analysis of variance (ANOVA) is to examine which design factor mainly affects the wear rate. The optimal combination of the process factors is predicted by using the ANOVA techniques. These results are carried out for level of significance of 5% (i.e. the level of confidence 95%). From the ANOVA Table, It is observed that the specific wear rate trend is Sliding velocity > Normal Load > Reinforcement > Sliding distance. Table 5 shows the analysis of variance for S/N ratios of the wear rate. From the Table 5, It noticed that the value of R-Sq (64.20), Normal load (23.68%), Filler content (18.85%) and sliding distance (2.37%). The influence of sliding distance and reinforcement on the wear rate is obtained to be insignificant with very less percentage contributions.

Table 3 Experimental layout of L_{25} orthogonal array

Expt. no.	Normal load (N)	Filler Content (wt%)	Sliding velocity (m/s)	Sliding distance (m)	Specific wear rate ($\text{mm}^3/\text{N}\cdot\text{m}$)	S/N ratio (dB)
1	20	0	0.25	250	0.006667	43.5218
2	20	0.5	0.50	500	0.006954	43.1552
3	20	1.0	0.75	750	0.025035	32.0291
4	20	1.5	1.0	1000	0.002782	51.1140
5	20	2.0	1.25	1250	0.017385	35.1964
6	35	0	1.0	250	0.003042	50.3356
7	35	0.5	1.25	750	0.016064	35.8829
8	35	1.0	0.25	1000	0.087622	21.1478
9	35	1.5	0.50	1250	0.133866	17.4666
10	35	2.0	0.75	250	0.010131	39.8867
11	50	0	0.50	750	0.010431	39.6334
12	50	0.5	0.75	1000	0.027809	31.1161
13	50	1.0	1.0	1250	0.131041	17.6518
14	50	1.5	1.25	250	0.009736	40.2326
15	50	2.0	0.25	500	0.086926	21.2170
16	65	0	1.25	1000	0.016273	35.7709
17	65	0.5	0.25	1250	0.113004	18.9381
18	65	1.0	0.5	250	0.020341	33.8327
19	65	1.5	0.75	500	0.090313	20.8850
20	65	2.0	1.00	750	0.042377	27.4575
21	80	0	0.75	1250	0.027805	31.1175
22	80	0.5	1.0	250	0.005563	45.0934
23	80	1.0	1.25	500	0.010014	39.9879
24	80	1.5	0.25	750	0.267038	11.4686
25	80	2.0	0.5	1000	0.333797	9.5304

3.5 Surface Morphology of Ti Metal Powder Filled Al 7075 Alloy Composite

The studies of SEM photographs for titanium metal powder filled with aluminium alloy composites materials Taguchi design experimental test runs are illustrated in Fig. 6. The SEM image in Fig. 6 has the maximum SWR for fabricated composite materials under L_{25} Taguchi design of experimental test runs (Table 3). Figure 6a shows the SEM image for the first run (i.e. Experiment run 4, Table 3). It observed that the worn surface of composite specimen shows the lowest wear rate ($0.002782 \text{ mm}^3/\text{N}\cdot\text{m}$) for 1.5 wt% of particulate titanium metal powder filled metal alloy composites at lower load (20 N) and less sliding velocity (0.25 m/s). Figure 6a shows debris particle and sliding direction. The debris particles are

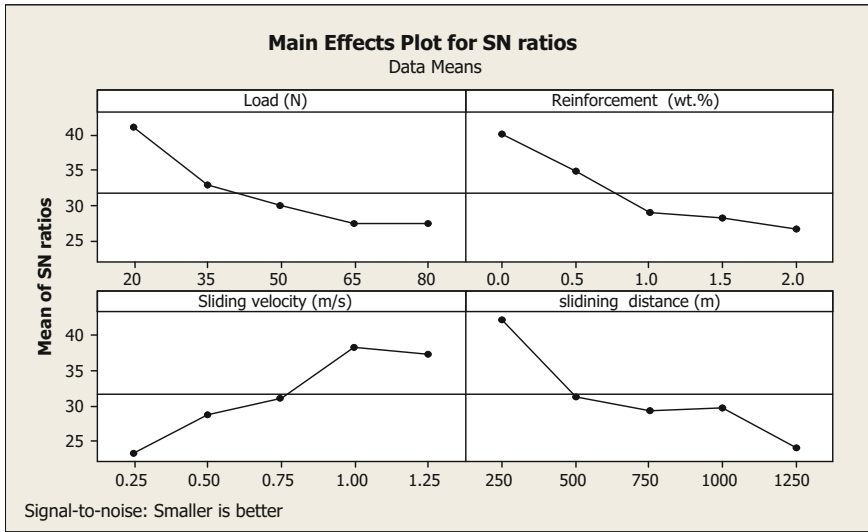


Fig. 5 Effect of control factors on wear rate of Ti filled Al 7075 alloy composites

Table 4 Response Table for Signal to Noise Ratios Smaller is Better

Level	Normal load (N)	Reinforcement (wt%)	Sliding velocity (m/s)	Sliding distance (m)
1	41.00	40.08	23.26	42.15
2	32.94	34.84	28.72	31.31
3	29.97	28.93	31.01	29.29
4	27.38	28.23	38.33	24.07
5	27.44	13.42	37.41	18.08
Delta	13.63	13.42	15.07	18.08
Rank	3	4	2	1

Table 5 Analysis of variance for SNRA1 using adjusted SS for tests

Source	DF	Seq SS	Adj SS	Adj MS	F	P	P (%)
Normal load	4	639.6	639.6	159.9	1.08	0.428	19.28
Filler content	4	625.5	625.5	156.4	1.05	0.438	18.85
Sliding velocity	4	785.7	785.7	196.4	1.32	0.340	23.68
Sliding distance	4	78.9	78.9	19.7	0.13	0.966	2.37
Error	8	1187.7	1187.7	148.5			35.80
Total	24	3317.4					100

S = 12.1843, R-Sq = 64.20%, R-Sq (adj) = 0.00%

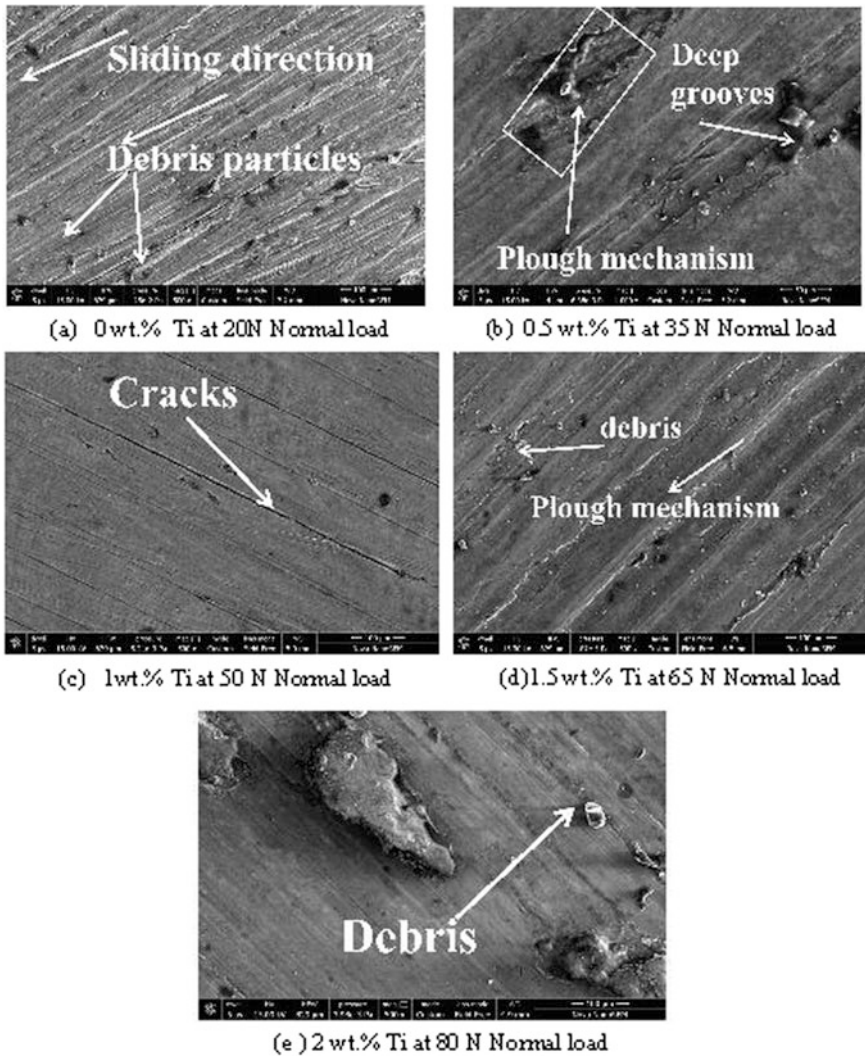


Fig. 6 Micrographs of the highest SWR of the composite materials under L_{25} Taguchi design of experimental test runs

generated by plastic deformation. An increased in load on counter surface of disk and pin sample, then wear rate is also increased. It is noticed that the sliding direction occurred due to high material loss of sample in parallel groove direction. The micrograph (Fig. 6b) for 0.5 wt% of particulate filled with aluminium alloy composites shows the maximum wear rate (Experiment run 9, Table 3) at 0.50 m/s sliding velocity, applied normal load (35 N) and sliding distance (1250 m). Figure 6b shows the deep grooves and plough mechanism. The deep grooves occurred due to the increase in applied load and plastic deformation of material,

i.e. high content of mass loss. The plough mechanism occurs due to large plastic deformation and wear debris particles. [18]. Figure 6c depicts the photographs for 1 wt% Ti particulate filled Al 7075 aluminium alloy composite which shows the higher specific wear rate (Experiment run 13, Table 3) under sliding condition at sliding velocity (0.25 m/s), normal load (50 N) and the sliding distance (1250 m). The cracks may be due to increase of the normal load leads to enhancing of the temperature of sliding surfaces [19]. Figure 6d depicts the SEM photographs for 1.5 wt% Ti particulate filled aluminium alloy composites which depicts the maximum specific wear rate [Experiment run 17, Table 3 via sliding condition such as sliding velocity (0.25 m/s) normal load (65 N), sliding distance (1250 m)]. From the graph, it is clear that plough mechanism and debris occur due to increasing of applied load, filler content and formation of pits [20]. The SEM micrograph depicted in Fig. 6e for 2 wt% Ti metal powder filled Al 7075 alloy composite against (Experiment run 22, Table 3) for a sliding velocity of 0.5 m/s load 80 minimum wear rate. From the graph, it is clearly observed that the wear debris due to higher load and deformation of material.

4 Conclusions

From the study on friction and tribological properties of titanium metal powder filled 7075 aluminium alloy composites, the following inference are derived.

- The wear resistance is better due to filler content, hence could be potential new developed composites materials for gear applications.
- The specific wear rate of fabricated alloy composites decreases with increase in sliding velocity (0.25–1.25 m/s) under steady-state conditions. The wear rate order is: 0 wt% Ti > 0.5 wt% Ti > 1 wt% Ti > 1.5 wt% Ti > 2 wt% Ti while the COF order is: 0 wt% Ti > 0.5 wt% Ti > 1 wt% Ti > 1.5 wt% Ti > 2 wt% Ti order, respectively.
- The specific wear rate of said alloy composites increases with normal load (20–80 N) under steady-state conditions. The order of wear rate is: 0 wt% Ti > 0.5 wt% Ti > 1 wt% Ti > 1.5 wt% Ti > 2 wt% Ti irrespective of the normal load condition while COF order is 0 wt% Ti > 0.5 wt% Ti > 1 wt% Ti > 1.5 wt% Ti > 2 wt% Ti, respectively.
- The experimental analysis via Taguchi approach highlights minimum specific wear rate for 0 wt% Ti particulates filled alloy composites at normal load of 35 N; sliding velocity of 1 m/s; sliding distance of 1000 m. The ANOVA analysis order is sliding distance < sliding velocity < normal load < filler content.
- The worn surface morphology of specimens indicates the associated wear mechanism responsible for wear rates of such alloy composites under experimental parameters at laboratory environment. The alloy composites with 2 wt% Ti particulate filler content shows minimum specific wear rate hence, deemed fit for gear applications.

References

1. Hongqiang, D., Yuanfei, H., Lu, W., Liqiang, W., Jianwei, M., Zhang, D.: Configuration design and fabrication of laminated titanium matrix composites. *Mater. Des.* **99**, 219–224 (2016)
2. Baradeswaran, A., Vettivel, S.C., Perumal, A.E.: Experimental investigation on mechanical behavior, modeling and optimization of wear parameters of B4C and graphite reinforced aluminum hybrid composites. *Mater. Des.* **63**, 620–663 (2014)
3. Wang, Y.Q., Song, J.: Dry sliding wear behavior of Al₂O₃ fiber and SiC particle reinforced aluminum based MMCs fabricated by squeeze casting method. *Tans. Nonferrous Met. Soc. China* **21**, 1441–1448 (2011)
4. Kumar, A.V., Rajadurai, S.J.: Influence of rutile (TiO₂) content on wear and micro-hardness characteristics of aluminum-based hybrid composites synthesized by powder metallurgy. *Trans. Nonferrous Met. Soc. China* **26**, 63–73 (2016)
5. Thakur, S.K., Gupta, M.: Improving mechanical performance of Al by using Ti as reinforcement. *Compos. A* **38**, 1010–1018 (2007)
6. Mobasherpour, I., Tofigh, A.A., Ebrahimi, M.: Effect of nano-size Al₂O₃ reinforcement on the mechanical behavior of synthesis 7075 aluminum alloy composites by mechanical alloying. *Mater. Chem. Phys.* **138**, 535–541 (2013)
7. Toptan, F., Kerti, I., Rocha, L.A.: Reciprocal dry sliding wear behavior of B4Cp reinforced aluminium alloy matrix composites. *Wear* **291**, 74–85 (2012)
8. Kumara, A., Patnaika, A., Bhat, I.K.: Investigation of nickel metal powder on tribological and mechanical properties of Al-7075 alloy composites for gear materials. *Powder Metall.* (2017). <https://doi.org/10.1080/00325899.2017.1318481>
9. Rao, R.N., Das, S.: Effect of matrix alloy and influence of SiC particle on the sliding wear characteristics of aluminium alloy composites. *Mater. Des.* **32**, 1066–1071 (2011)
10. Kumar, A.B., Murugan, N., Dinaharan, I.: Dry sliding wear behavior of stir cast AA6061-T6/AlNp composite. *Trans. Nonferrous Met. Soc. China* 2785–2795 (2014)
11. Prabhakar, S., Radhika, N., Raghu, N.R.: Analysis of tribological behavior of aluminium/B4C composite under dry sliding motion. *Proc. Eng.* **97**, 994–1003 (2014)
12. Mondal, A.K., Kumar, S.: Dry sliding wear behaviour of magnesium alloy based hybrid composites in the longitudinal direction. *Wear* **267**, 458–466 (2009)
13. Niranjana, K., Lakshminarayanan, P.R.: Dry sliding wear behavior of in situ Al-TiB₂ composites. *Mat. Des.* **47**, 167–173 (2013)
14. Mukunda, D., Prasanna, K., Kanakuppi, S., Gundenahalli, P.P., Satyappa, B.: Dry sliding wear behaviour of garnet particles reinforced zinc-aluminum alloy metal matrix composites. *Mater. Sci.* **12**(3), 1392–1320 (2006)
15. Dinaharan, I., Murugan, N.: Dry sliding wear behavior of AA6061/ZrB₂ in-situ composite. *Trans. Nonferrous Met. Soc. China* **22**, 810–818 (2012)
16. Alidokhta, S.A., Abdollah-zadeh, A., Assadi, H.: Effect of applied load on the dry sliding wear behaviour and the subsurface deformation on hybrid metal matrix composite. *Wear* **305**, 291–298 (2013)
17. Renukappa, N.M., Suresha, B., Devarajaiah, R.M., Shivakumar, K.N.: Dry sliding wear behaviour of organo-modified montmorillonite filled epoxy nano-composites using Taguchi's techniques. *Mater. Des.* **32**, 4528–4536 (2011)
18. Koksai, S., Fici, F., Kayici, R., Savas, O.: Experimental optimization of dry sliding wear behavior of in situ AlB₂/Al composite based on Taguchi's method. *Mater. Des.* **42**, 124–130 (2012)

19. Antony, C., Kumar, V., Selwin Rajadurai, J.: Influence of rutile (TiO₂) content on wear and micro-hardness characteristics of aluminum-based hybrid composites synthesized by powder metallurgy. *Trans. Nonferrous Met. Soc. China* **26**, 63–73 (2016)
20. Mirazimi, J., Abachi, P., Purazrang, K.: Micro structural characterization and dry sliding wear behavior of spark plasma sintered Cu – YSZ composites. *Trans. Nonferrous Met. Soc. China* **26**, 1745–1754 (2016)

A Comparative Study on Mechanical and Dry Sliding Wear Behaviour of Al 7075-T6 Welded Joints Fabricated by FSW, TIG and MIG



Lalta Prasad, Lalit Mohan, Himanshu Prasad Raturi
and Virendra Kumar

Abstract The development of the welding process has provided an alternative improved way of satisfactorily producing aluminium joints, in a faster and reliable manner. The aim of the present work is focused on the comparative study on the mechanical and dry sliding wear (tribological property) behaviour of welding joint fabricated by friction stir welding (FSW), tungsten inert gas (TIG) and metal inert gas (MIG) on 6 mm thick aluminium alloy 7075 T6. The samples were fabricated, and their testing was carried out as per the ASTM standards. The maximum tensile strength (242.3 MPa) and impact strength (12 J) and joint efficiency (44%) were obtained for FSW joints, whereas these properties for TIG and MIG welded joints were on the lower side. The elongation at the break was found to be higher for FSW joint as compared to that of TIG and MIG joints. The minimum specific wear rate was obtained for FSW joint as compared to that of TIG and MIG joints. Microstructure results show that the smaller grain sizes were obtained in the weld centre of FSW, whereas grain growth was observed in TIG and MIG welds. FSW joints were better than TIG and MIG joints.

Keywords Friction stir welding · TIG · MIG · Dry sliding wear

L. Prasad (✉)

Department of Mechanical Engineering, National Institute of Technology Uttarakhand, Srinagar(Garhwal), Uttarakhand 246174, India
e-mail: laltagbpec@gmail.com

L. Mohan · H. P. Raturi

Department of Mechanical Engineering, G.B. Pant Institute of Engineering & Technology, Ghurdauri, Pauri Garhwal, Uttarakhand 246194, India

V. Kumar

Department of Mechanical Engineering, K.R. Mangalam University, Gurgaon 122103, Haryana, India

© Springer Nature Singapore Pte Ltd. 2019

U. Chandrasekhar et al. (eds.), *Innovative Design, Analysis and Development Practices in Aerospace and Automotive Engineering (I-DAD 2018)*, Lecture Notes in Mechanical Engineering, https://doi.org/10.1007/978-981-13-2718-6_48

1 Introduction

Friction stir welding (FSW) is a relatively new joining process, developed at The Welding Institute (TWI) in 1991 for aluminium alloys and is presently attracting considerable interest [1–4]. Friction stir welding has been initially developed for welding aluminium alloys, but several recent studies show that it should also be successfully applied to other materials, such as particles reinforced aluminium-based composites [5–7]. FSW is an energy efficient process that requires no filler material and the use of a shielding gas [8]. The process of FSW depends on various input parameters like tool rotation speed, welding speed, plunge depth, tilt angle, sideways tilt angle, shoulder geometry, shoulder scrolls and probe geometry [9]. A study on FSW was carried out with an extrusion process. In this study, the tracer experiments with steel shot in 6061-T6 and 7075-T6 alloy butt joints [10]. The tensile strength of the FSW joint on AA6061/B₄C AMC was investigated by Kalaiselvan et al. [11]. They reported that the joint efficiency of the joint was 93.4%, and the joint was failed at heat affected zone. The fracture surface of AA6061/B₄C AMC shows a network of dimples whose size is smaller compared to the matrix alloy [11]. Friction stir welding of dissimilar AA2024 and AA7075 aluminium alloys was reported by Khodir and Shibayanagi [12]. They found that the maximum tensile strength of the joint was achieved for the joint produced at a welding speed of 1.67 mm/s when 2024 Al alloy was located on the advancing side. Microstructure and failure mechanisms of refill friction stir spot welded 7075-T6 aluminium alloy joints was investigated by Shen et al. [13]. They reported that the mechanical properties of the joint were affected by void and the alclad between the upper and lower sheets.

In the present work, a comparative study on mechanical and dry sliding wear behaviour of Al 7075-T6 welded joints fabricated by FSW, TIG and MIG.

2 Experimental Setup Methodology

Aluminium alloy 7075-T6 was used in the present work because it is strong, with a strength comparable to many steels, good fatigue strength, average machinability and lower resistance to corrosion than many other Al alloys. The mild steel rod tool was selected for friction stir welding (FSW) process. The FSW tool was prepared on the lathe. The tool used for welding was a concave shoulder (diameter 21 mm) cylindrical pin (diameter 6 mm) tool having no threads on its periphery for FSW, and pin length (length 4.5 mm) has chosen slightly smaller than the plate thickness. Many factors must be taken into consideration when a filler metal is selected for a specific application. The welding wire for TIG was chosen as SFA/AWS A5.28 ER 80S. The parameters selected in the FSW process were shoulder diameter to pin diameter ratio (D/d) = 3.22, tool rotations speed = 1400 rpm, tool traverse speed = 56 mm/min. The dimensions of AA7075-T6 aluminium alloys plate was

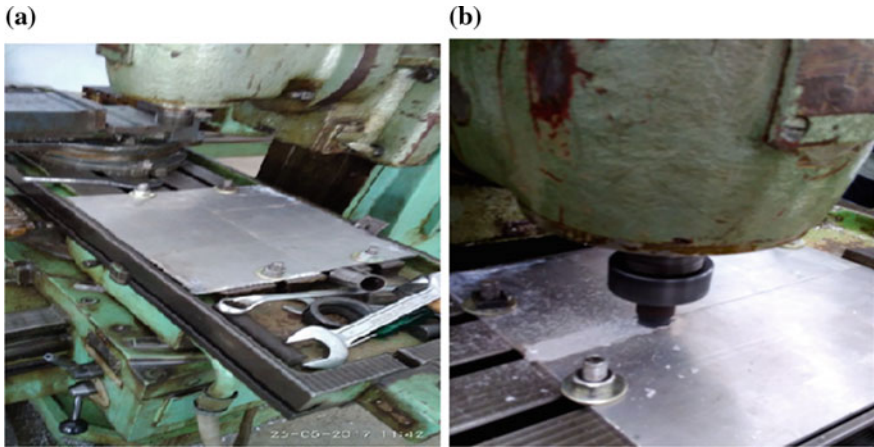


Fig. 1 Details of FSW process, **a** fixture designed to transform a conventional milling machine, **b** welding operation during FSW

length 300 mm, width 150 mm and thickness 6 mm. Figure 1 shows the details of fixture designed to transform a conventional milling machine into a friction stir welding process and welding operation during FSW process. Tensile samples are prepared along the traverse direction of joint. The test samples were prepared in the traverse direction of the joint according to the ASTM E-08. The impact tests were performed according to the ASTM E23 standard.

3 Results and Discussion

3.1 Comparison of the Tensile Strength of Weld Joints

Tensile testing of the composite laminates was carried out according to ASTM B557 M-15. The tests were conducted on a tensile testing machine (HEICO—HL-590, New Delhi, India). Each value reported was the average of three specimen tests. The extension rate was kept constant at a rate of 10 mm/min during the test. Figure 2 shows the tensile strength of the joints prepared by three processes (namely FSW, TIG and MIG). All the samples were failing from the joint section. In FSW specimens, fracture of the specimen has occurred in the HAZ region, which was the weakest region in the weld area in terms of hardness. The fracture path has followed the weakest region where it can propagate easily. In MIG and TIG welded specimens, the fracture has occurred in the weld centre. The highest joint efficiency in terms of ultimate tensile strength has been obtained in FSW as 44%; for TIG welding, it was 31%, and the lowest joint efficiency was obtained in MIG welding as 33%. It has been observed that the joint efficiency of FSW was higher compared to another welding process.

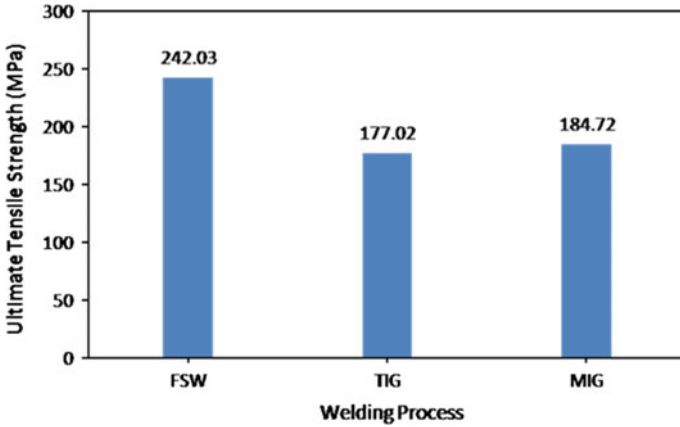


Fig. 2 Comparison of the tensile strength of weld joints

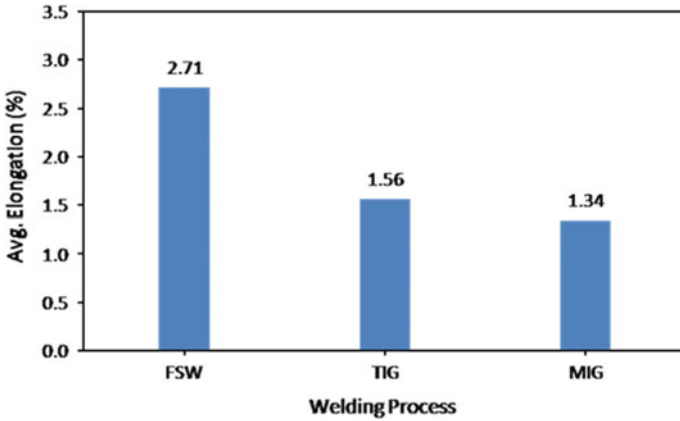


Fig. 3 Comparison of average elongation (%) of weld joints

Figure 3 shows the average elongation of welded joints. The elongation in FSW specimen was higher than that of TIG and MIG joint. The reason for higher elongation in FSW was due to the high tensile strength of the joint.

3.2 Comparison of Impact Strength of Weld Joints

The notched Charpy impact testing was conducted on the impact tester according to ASTM E23 standard. The impact tester (Fine Testing Machines, Pune, India) has

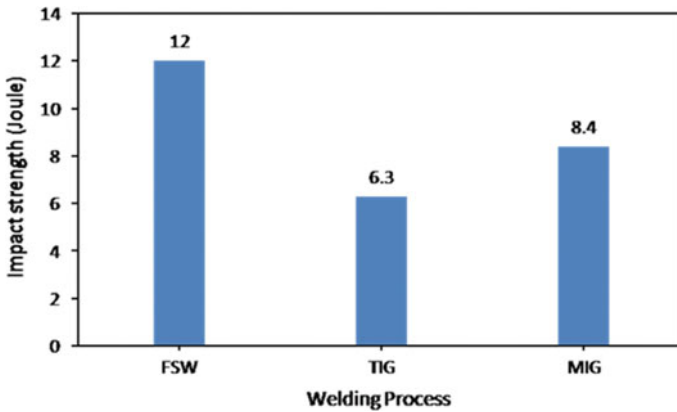


Fig. 4 Comparison of impact strength of weld joints

maximum impact energy of 300 J with the weight of pendulum 20 kg and striking velocity 5.346 m/s. Three samples of each joint were tested. The amount of impact energy absorbed by the specimen before yielding was read off on the calibrated scale attached to the machine as a measure of impact strength in joules. The FSW joint shows the highest value of impact strength as compared to that of TIG and MIG samples as shown in Fig. 4.

3.3 Comparison of Three-Body Wear Rate of Weld Joints

Abrasive tests were conducted on dry sand abrasive tester according to ASTM G 65. The dry sand abrasive tester (TR 50 Model) was supplied by Ducom instruments Pvt. Ltd., Bangalore, India. In the present study, the dry silica sand (grain size 100 μm) was used as abrasive particle. The specific wear rate (W_s) of the specimen is calculated by using Eq. (1) as given below:

$$W_s = \left[\frac{\Delta V}{F_n \times S_s} \right] \quad (1)$$

where ΔV = Volume loss (mm^3), S_s = Sliding distance (m), F_n = Normal load (N).

It has been seen from Fig. 5 that the wear rate of samples prepared by FSW was very low as compared to that of the other samples (TIG and MIG). The possible reason for low wear rate of FSW sample was high impact strength as shown in Fig. 4.

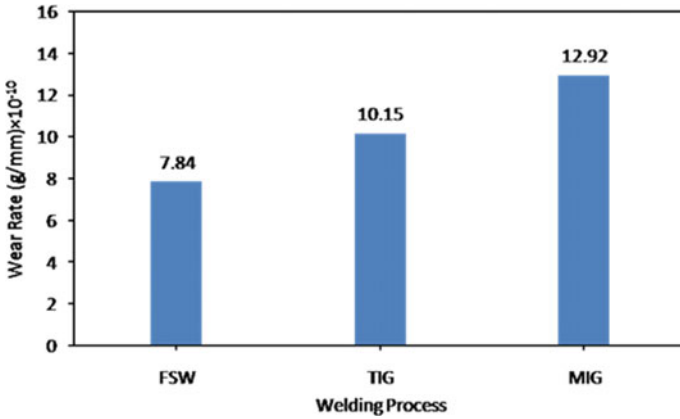


Fig. 5 Comparison of specific wear rate of weld joints

3.4 Comparison of Vickers Hardness Test of Weld Joints

The hardness tests were conducted according to the ISO standards. The Vickers hardness tester BV-250 (SSS Instruments, Kolhapur, India) was used to find the hardness of the specimens. Figure 6 shows the variation of the Vickers hardness of welded joints at the various zone of the specimen. The lowest hardness was found in the HAZ region for all the samples. The Vicker hardness of the samples in various zones (e.g. nugget zone, mechanically affected zone and advancing & rereating side) were measured and these values are shown in the Fig. 6. The maximum hardness was found for joint prepared by TIG welding.

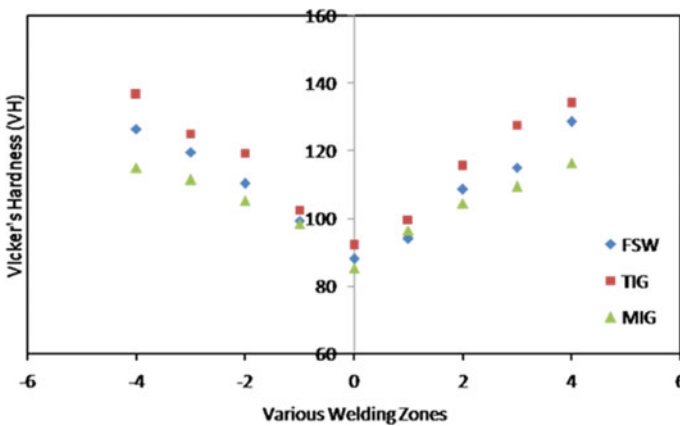


Fig. 6 Comparison of Vickers hardness of weld joints

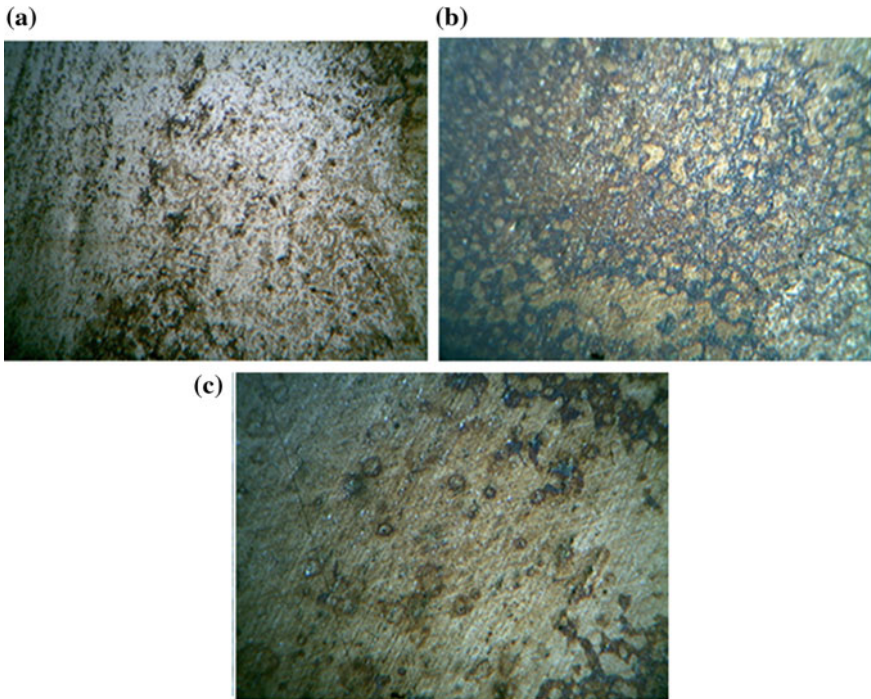


Fig. 7 Comparison of microstructure images of weld joint. **a** FSW, **b** TIG, **c** MIG process

3.5 Comparison of Microstructure Images of Weld Joints

The microstructure images of the joints are shown in Fig. 7. In microstructure analysis conducted on an optical microscope, TMAZ exhibits highly elongated grains of Al alloy in FSW due to stirring, but it does not have a recrystallized microstructure. The depth of microscopic voids in FSW is lower compared to TIG and MIG welding process. The grain size and general microstructural texture were investigated through optical microscopy of cold-mounted 7075-T6. The microstructure images of welded joints(FSW, TIG and MIG) were compared in the Fig. 7. It may be observed from the Fig. 7 that the FSW joint has more structured inclusions whereas the TIG joint has random distribution of inclusions.

4 Conclusions

The experimental study was carried out on mechanical properties and wear behaviour of Al 7075-T6 welded joints fabricated by FSW, TIG and MIG. From the investigations, the following major conclusions were drawn:

- The highest joint efficiency (44%) in terms of ultimate tensile strength has been obtained in FSW as compared to the TIG and MIG.
- Vickers hardness value in various regions of the weld was measured, and the highest value of hardness was observed in weld nugget zone region adjacent to the advancing side in TIG joints.
- The impact strength was highest for FSW joints, and wear rate was also on the lower side for the FSW joint.
- In friction stir welding, the energy input and distortion are significantly lower than in fusion welding technique, thus improve the welding properties, and the resulting joints offers less distortion, less residual stresses, fewer weld defects than another joining process like TIG and MIG.

References

1. Miles, M.P., Decker, B.J., Nelson, T.W.: Formability and strength of friction-stir-welded aluminum sheets. *Metall. Mater. Trans. A* **35A**, 3461–3468 (2004)
2. Thomas, W.M., Nicholas, E.D., Needham, J.C., Murch, M.G., Temple-Smith, P., Dawes, C.J.: International Patent Application PCT/GB92/02203 and GB Patent Application 9125978.8, UK Patent Office, London, 6 Dec 1991
3. Dawes, C., Thomas, W.: Friction stir joining of aluminium alloys. *TWI. Bull* **6**, 124 (1995)
4. Ellis, M., Stangwood, M.: Properties of friction stir welded 7075 T651 aluminium. *TWI. Bull.* **6**, 138 (1995)
5. Mishra, R.S., Ma, Z.Y.: Friction stir welding and processing. *Mater. Sci. Eng., R* **50**, 1–78 (2005)
6. Marzoli, L.M., Strombeck, A.V., Dos Santos, J.F., Gambaro, C., Volpone, L.M.: Friction stir welding of an AA6061/Al₂O₃/20p reinforced alloy. *Compos. Sci. Technol* **66**(2), 363–371 (2006)
7. Fernandez, G.J., Murr, L.E.: Characterization of tool wear and weld optimization in the friction-stir welding of cast aluminum 359 + 20% SiC metal-matrix composite. *Mater. Charact.* **52**, 65–75 (2004)
8. Gibson, B.T., Lammlein, D.H., Prater, T.J., Longhurst, W.R., Cox, C.D., Ballun, M.C., Dharmaraj, K.J., Cook, G.E., Strauss, A.M.: Friction stir welding: process, automation, and control. *J. Manuf. Processes* **16**(1), 56–73 (2014)
9. Threadgill, P.L.: Terminology in friction stir welding. *Sci. Technol. Weld. Joining* **12**(4), 357–360 (2007)
10. Colligan, K.: Material flow behavior during friction welding of aluminum. *Weld. J* **75**(7), 229–237 (1999)
11. Kalaiselvan, K., Dinaharan, I., Murugan, N.: Characterization of friction stir welded boron carbide particulate reinforced AA6061 aluminum alloy stir cast composite. *Mater. Des.* **55**, 176–182 (2014)
12. Khodir, S.A., Shibayanagi, T.: Friction stir welding of dissimilar AA2024 and AA7075 aluminum alloys. *Mater. Sci. Eng., B* **148**, 82–87 (2008)
13. Shen, Z., Yang, X., Zhang, Z., Cui, L., Li, T.: Microstructure and failure mechanisms of refill friction stir spot welded 7075-T6 aluminum alloy joints. *Mater. Des.* **44**, 476–486 (2013)

Overview of Cryogenics Production and Automation in Cryo-distribution at TIFR, Mumbai



K. V. Srinivasan, A. Manimaran, K. A. Jaison and Vijay A. Arolkar

Abstract Low temperature facility (LTF) of Tata Institute of Fundamental Research, (TIFR) Mumbai, India has been operating and maintaining helium liquefiers, nitrogen generators for more than five decades. LTF is one of the largest cryogenic facilities in India under the R&D Sectors. Cryogenics being produced and dispensed to about 45 research laboratories within TIFR including some critical cryogen-using setups, magnetometer facility, homemade setups, various departments such as Nuclear and Atomic Physics, Chemical Sciences, Biological Sciences too use cryogenics in a large quantities. In order to fulfill the above large cryogenics demand and to maintain the supply in an uninterrupted manner, LTF implemented various automation in terms of cryogen distribution, Dewar tracking, reporting, etc. The paper will present our experience, architecture, methodology adopted, and automation implemented in the cryo-distribution at TIFR along with the proposed work.

Keywords Cryogenics · Dispensation · Dewars · Automation

1 Introduction

Cryogenics (Low Temperature) facility at TIFR, Mumbai, provides the support of liquid helium, liquid nitrogen, and other cryogenic support services to the users of the institute for the past five decades.

K. V. Srinivasan (✉) · K. A. Jaison · V. A. Arolkar
Low Temperature Facility, Tata Institute of Fundamental Research, Mumbai, India
e-mail: kvsrini@tifr.res.in

A. Manimaran
School of Mechanical Engineering, Veltech Dr. RR & Dr. SR Technical University, Chennai, India

© Springer Nature Singapore Pte Ltd. 2019
U. Chandrasekhar et al. (eds.), *Innovative Design, Analysis and Development Practices in Aerospace and Automotive Engineering (I-DAD 2018)*, Lecture Notes in Mechanical Engineering, https://doi.org/10.1007/978-981-13-2718-6_49

1.1 About Liquid Helium Plants at TIFR

In the year 1962, the facility at TIFR, Mumbai, was started with helium liquefier of M/s Arthur D Little Inc., USA, with a liquefaction capacity of 3–5 liters per hour. The installation of this ADL Collins helium liquefier was started on January 10, 1962, and the commissioning was formally announced on February 22, 1962. Later with model KOCH-1410 liquefier was installed in the year 1976 and it was replaced by PSI-1610 helium liquefier in the year 1991. The year 2012 was the golden jubilee year for the helium liquefaction and the low temperature research at TIFR, Mumbai. Currently, the facility operates and maintains the Linde make, L280 Helium Liquefier, since 2008, which can liquefy to a rate 70–150 liters per hour in various combinations. The helium liquefiers which were in operation till 2008 and the helium liquefier which is currently in operation at TIFR are shown in Fig. 1.

1.2 About Liquid Nitrogen Plants at TIFR

Similarly, liquid nitrogen production was started in the year 1968 with Philips make PLN430 liquid nitrogen plant working with air separation column. The second unit of PLN430 was added in the year 1976 to meet the growing liquid nitrogen demands. These plants were kept operational till the year 2004. During the year 1989, Sulzer make, turbine-based liquid nitrogen plant, model: LINIT-25 was installed which was kept operational till the year 2010. Presently, the Stirling make, STIRLIN-8 liquid nitrogen plant is in operation, since 2010. The liquid nitrogen produced with the Stirling Cryogenics, Netherlands, makes two units of STIRLIN-4 system which was installed in the year 2010. The cooling power of this nitrogen plant is about 8 kW at 80 K. The plant liquefaction capacity is about 110 liters per hour at an elevated pressure of 2 bar and also capable of increasing up to 4 bar, if required. The photograph of the above liquid nitrogen plants and the currently operated liquid nitrogen plant at LTF is given as Fig. 2.

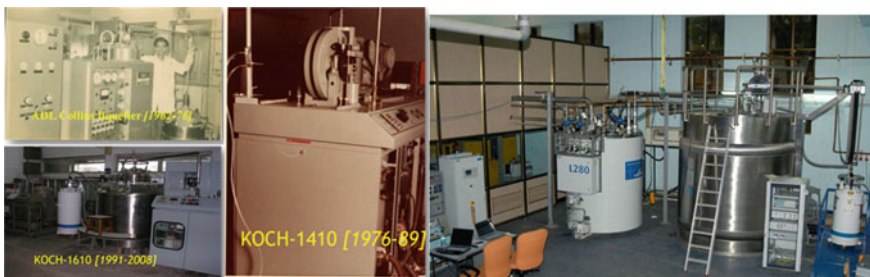


Fig. 1 Helium liquefiers at TIFR until 2008 and the current helium liquefier



Fig. 2 Liquid nitrogen plant at TIFR past and the present

2 Cryogenics Production and Dispensation

2.1 Cryogenics Users at TIFR

Low Temperature Facility caters the cryogen needs to the various facilities and laboratories of the institute such as Condensed Matter Physics and Materials Science (DCMP and MS), Nuclear and Atomic Physics (DNAP), Biological Sciences (DBS), Astronomy and Astrophysics (DAA), and Chemical Sciences (DCS). The LTF facility meets the cryogen demands of more than 40 users, under various research facilities such as NMR spectrometers of 500/600/700 and 800 MHz (which is also the national facility of India), SQUID magnetometers, Physical Property Measurement systems, Vibrating Sample Magnetometer, Micro-Kelvin refrigerator, Dilution milli-Kelvin refrigerator, Adiabatic de-magnetization Milli-Kelvin refrigerator, Nano-electronics, Scanning Tunneling Spectroscopy, Point Contact Spectroscopy, Photoelectron Spectroscopy, Mossbauer along with 12 other local setups [1].

2.2 Liquid Helium and Liquid Nitrogen Production

The average annual liquid helium consumption is about 125,000 L, which is one of the largest consumption by similar research facilities in India. Presently, Low Temperature Facility provides liquid helium and liquid nitrogen and related cryogenic support services to various facilities and laboratories of the institute. LTF improved the user's service from the uninterrupted supply of cryogenics "On Demand" to "Any Time Availability" basis. LTF works round the clock in shifts and mostly in unattended operation mode. The various users of the institute consume close to 300,000 L of liquid nitrogen annually, of which the Pelletron LINAC Facility (PLF) of TIFR utilizes the majority supply of liquid nitrogen. The annual consumption of liquid helium along with the growth rate and annual liquid nitrogen consumption by the various users of TIFR including the PLF is shown in Fig. 3.

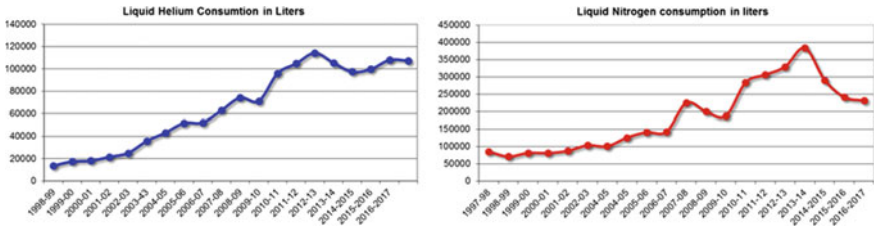


Fig. 3 Annual liquid helium and liquid nitrogen consumption at TIFR

2.3 Liquid Helium and Liquid Nitrogen Dispensation

To cater the helium dispensation to the users, LTF operates more than 30 liquid helium dewars of various sizes and capacities. LTF manages a fleet of liquid helium dewars includes 100 L capacity lightweight aluminum alloy helium dewar (about 15 dewars), 200 L capacity aluminum alloy dewars(6 dewars), and 60 L capacity steel dewars (about 5 numbers). LTF handles about 50 liquid nitrogen dewars of various capacities ranging from 85 liters to 250 liters which are in regular service to facilitate the users within the institute. Typically, LTF dispenses more than 640 liquid nitrogen dewars every year. In addition to the above, large and bulk requirements of liquid nitrogen to the Pelletron Accelerator Facility (PLF) and for the beam hall (INGA) experiments are met from the 5000 L vertical liquid nitrogen storage vessel and through the 310 m long, dedicated vacuum-jacketed liquid nitrogen pipeline. Figure 4 shows the liquid helium dewars and the liquid nitrogen dewars maintained by LTF [2].



Fig. 4 Liquid helium and liquid nitrogen dewars

3 Automation in Cryogenics Dispensation

LTF initiated automation in cryogen dispensation in the year 2004 with the implementation of online-based cryogen request form (both liquid helium and liquid nitrogen) through TIFR intranet system “TIFR Datanet”. It was strengthened further by adding online Mass Spectrometer Leak Detector (MSLD) service in 2005. The current form of online liquid helium and liquid nitrogen dispensation software was modified in 2008 using simple interactive software. For secured operation, this facility of online access is restricted only for those who have registered with TIFR Datanet. It is fully secured, and all transaction are recorded and stored in TIFR Datanet servers. The system generates email upon all transactions, i.e., both during the dewar issue and its return.

3.1 Web-Based Dispensation System–Liquid Nitrogen

The Web-based dispensation system was developed and maintained by Information Systems Development Group (ISDG) of TIFR, Mumbai [3]. For the operational convenience, the request for liquid nitrogen is made online directly by the users from the TIFR Datanet account. The navigation link for the online LTF request is provided in the home page of TIFR Datanet. The system generates the request tag which will be communicated to the users confirming their successful request and an intimation to the LTF. Based on the type of request and availability, LTF allocates liquid nitrogen dewars from the list of available filled dewars to the users. The email about the dewar allocation sent to the users for tracking their allotted dewars. The various screenshots of the nitrogen dispensation software controlled and administered by the LTF as shown in Fig. 5.

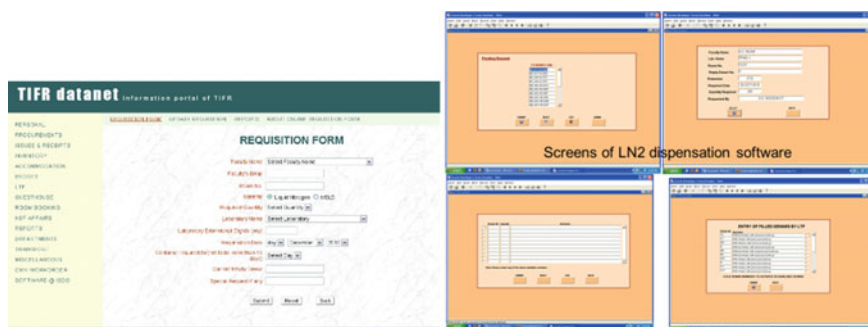


Fig. 5 Screenshot of liquid nitrogen online request form and dispensation software

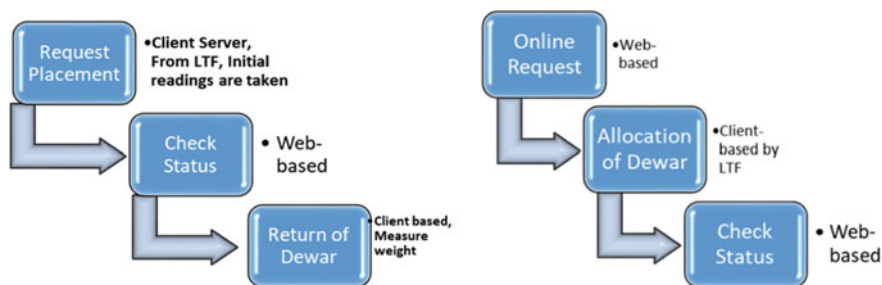


Fig. 6 Web distribution flow chart for liquid helium and liquid nitrogen

3.2 Web-Based Dispensation System-Liquid Helium [3]

The basic architecture and distribution flow chart of the Web-based liquid nitrogen dispensation software explained in Fig. 6.

For operational convenience and safety precaution, the helium users will directly interact with the LTF personnel for the dewar dispensation and dewar return after their usage. To assist that, a special software “Helium Request” is loaded on a PC which is devoted as “User Service Station”. After successful login to the “Helium Request” and using simple navigation screens users make a request and based on their request and dewar availability, users will have then an access to the screen showing the available dewars. User selects the required dewar from the available list of dewars, and the quantity of liquid helium issued is measured on the basis of weight. An ultra-low profile (40 mm), high accuracy (50 g), wide platform (900 by 900 mm) weighing scale is used for this application. The system generates email to the users, upon successful dewar allocation. The total helium gas accounting for every dewar is carried out by the system upon every return of helium dewar, with the few and minimal data entered by the users. The various screens of the helium dewar dispensation software are shown in Fig. 7.

3.3 Reporting

The report generation is the integral part of the cryogen dispensation software and also powerful tool in analyzing and interpreting the data. The above automation invokes voluminous quantum of data in terms of enormous transactions involved in the cryo-distribution system like us. It is now possible to have a library of all dewar distribution data right from November 2004. The data is stored in the TIFR Datanet central database system. Separate navigation for Reporting and Requisition Summary is provided within the Datanet page of LTF. With this, users can view or download the all the transaction details with many options like cryogen wise, month wise, laboratory wise, room wise, dewar wise. The screenshot showing the liquid

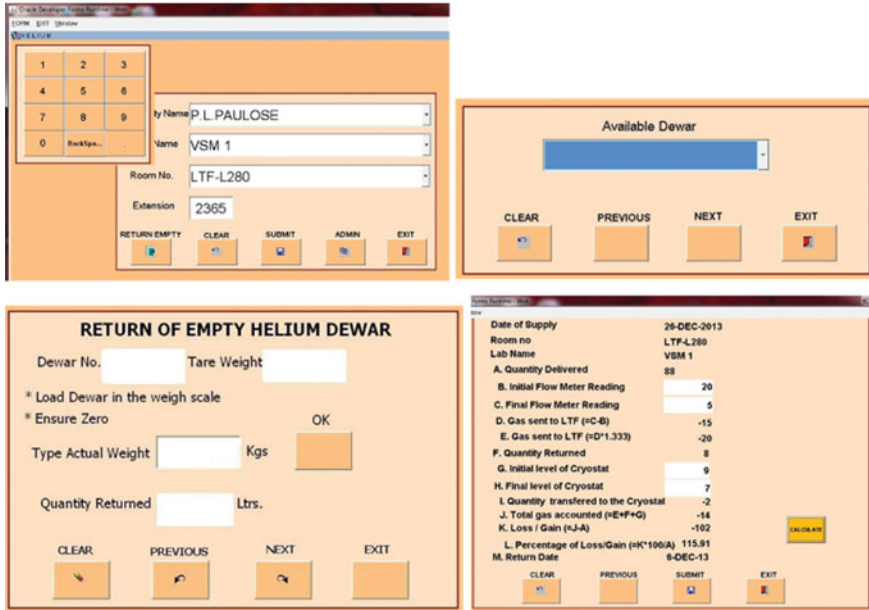


Fig. 7 Screenshot of liquid helium dispensation software

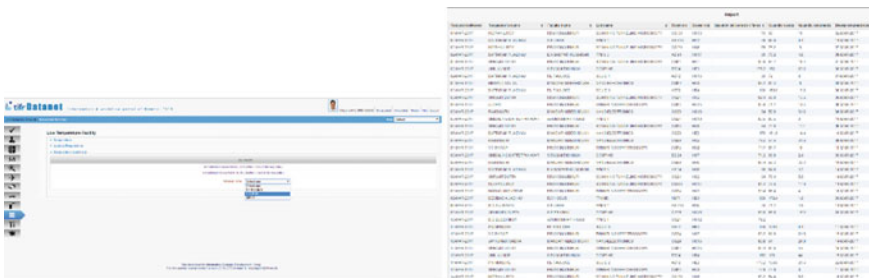


Fig. 8 The screenshot of liquid helium requisition summary page and list of liquid helium dewars issued

helium requisition summary page and the list of liquid helium dewars issued to all the laboratories in the month of March 2016 is shown in Fig. 8.

3.4 Automation in Helium Gas Accounting

Boil-off helium gas from the various laboratories is being collected at LTF section. The quantity of boil-off gas from each laboratory is monitored using a gas flow

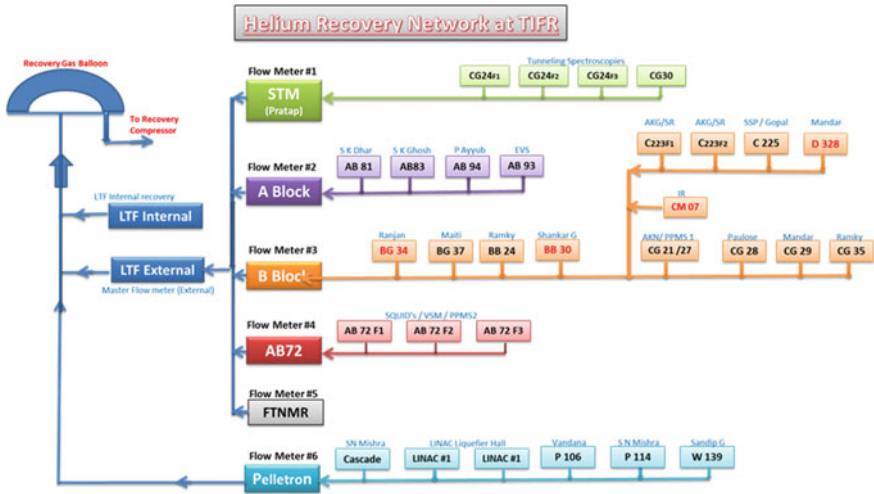


Fig. 9 Helium gas recovery network at TIFR

integrator and also at an intermediate cluster level at five locations before monitored finally at LTF end. The schematic of the helium gas recovery network at TIFR is mentioned in Fig. 9. There are about 45 flow meters which need to be monitored and analyzed the quantity of gas collection for the reporting purpose. These activities are currently being done manually and proposed to be automated using a custom-made software. Based on the manual entry of flowmeter reading, this software will show the online gas accounting, develop plots and graphs, trend showing the gas collection gas loss, percentage, etc.

3.5 Web-Based Reporting System for Helium Gas Management

LTF uses Elster made, diaphragm type, gas flow meters and few of the meters fitted with a retro-fittable low-frequency (LF) pulser [4]. These pulse transmitter works on the principle that a pulse magnet in the first moving drum of the index meters activates a reed switch in the pulse transmitter. These low-frequency pulse generator generates output as a digital pulse for every rotation of the meter, which directly corresponds to the gas quantity. Figure 10 shows the cross-sectional view of the diaphragm gas meter fitted with LF pulser along with the technical data of the LF pulser including the wiring diagram. Currently, the work is focused toward the transporting the digital pulse to a remote monitoring PC by Ethernet-based or by GSM-based modem.

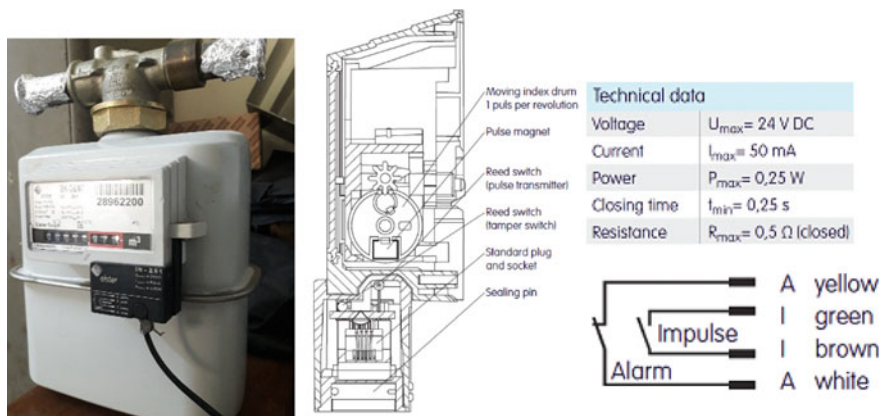


Fig. 10 Helium gas flow meter with LF pulser along with its wiring diagram

4 Summary

With the effective implementation, custom-made automation software and reporting system are now possible to manage such a network of research facilities and laboratories in a much more effective manner. This also provides maximum flexibility to the users in terms of simple and effective user-friendly software and allows the effective control on dewars. With the current experience, a similar software can be established for any cryogenic facility for its effective operation and control.

Acknowledgements The author expresses sincere thanks to Dr. Nihita Goel, Head Information Systems Development Group (ISDG—TIFR, Mumbai), Ms. Sushma Patel (ISDG, TIFR, Mumbai), Ms. Sarita Rane (ISDG, TIFR, Mumbai) and the staff at LTF of TIFR, for their support and cooperation.

References

1. Srinivasan, K.V.: Operation of cryogenic facility in e-way at Tata Institute of Fundamental Research, Mumbai, India. *J. Phys.: Conf. Ser.* **400**, 052008 (2012). <http://iopscience.iop.org/1742-6596/400/5/052008/>
2. Srinivasan, K.V., et al.: Liquid nitrogen distribution for Pelletron Linac Facility, Mumbai. *J. Cryog. IJC* **39** (2014). <http://dx.doi.org/10.5958/2349-2120.2014.00808.5>
3. Goel, N.: Automation of cryo-distribution and tracking system implemented at TIFR. Orla presentation at DAE-BRNS Workshop on Cryogenic Facility Management, TIFR, Mumbai, 9 Jan 2014
4. Data Sheet of ElsterI retro-fittable Low Frequency (LF) pulser for Elster-Instromet diaphragm gas meters. <https://docuthek.kromschroeder.com/documents/download.php?lang=de&doc=37899>

5. Frederick, L., Labbe, G., Ihas, G.G.: Tracking Liquid Helium Production, Distribution, and Consumption by Networked Computer. Center for UltraLow Temperature Research and Department of Physics, University of Florida, Gainesville, FL 32611 USA (2000)
6. Srinivasan, K.V.: Cryogens production and distribution at TIFR, Mumbai, INDIA. In: Poster at 26th International Conference on Low Temperature Physics LT26, Beijing, China (2011)
7. Srinivasan, K.V.: Oral presentation. Overview of cryogens production and automation in cryo-distribution at TIFR, Mumbai. In: National Conference on Advances in refrigeration and Cryogenics—NCARC-2016 held in MGM's College of Engineering and Technology, Navi Mumbai on 11th June 2016
8. Panda, U.: Control system of cryogenic plant for superconducting cyclotron at VECC, VECC, Kolkatta. In: India Proceedings of Cyclotrons, Lanzhou, China MOPCP008 (2010)
9. Frederick, L., Labbe, G., et al.: Tracking Liquid Helium Production, Distribution, and Consumption by Networked Computer. Center for Ultra Low Temperature Research and Department of Physics, University of Florida, Gainesville, FL 32611 USA. [http://dx.doi.org/10.1016/S0921-4526\(99\)02817-3](http://dx.doi.org/10.1016/S0921-4526(99)02817-3)
10. Siemens. Modular PLC controllers SIMATIC S7. <http://www.automation.siemens.com/mcms/programmable-logic-controller/en/simatic-s7-controller/>
11. Panda, U., et al.: Process control migration of 50 LPH helium liquefier. In: IOP Conference Series: Materials Science and Engineering, vol. 171. <http://iopscience.iop.org/article/10.1088/1757-899X/171/1/012005/pdf>

Analysis of Recast Layer, Wear Rate and Taper Angle in Micro-electrical Discharge Machining Over Ti-6Al-4V



S. Rajamanickam and J. Prasanna

Abstract In this paper, micro-electrical discharge machining of thin titanium alloy foil sheet (Ti-6Al-4V) is performed using 100- μ m tungsten rod to study the output parameters such as recast layer thickness at entry and exit surfaces, material removal rate, linear wear rate and taper angle. The electrical input parameters considered in this research work are, namely, pulse on-time, current, pulse off-time and voltage. Further, SEM analysis reported is highly useful in calculating the output parameters originality for all input parameters combinations and additional value to the experimental observations. Grey relational analysis is employed to find the optimum machining parameter among the various combinations of electrical input parameters in micro-electrical discharge machining. The smaller hole is highly useful in fabrication of micro-products.

Keywords Ti-6Al-4V · Electric discharge machining · Regression analysis

1 Introduction

Micro-machining is also called micro-processing used to build μ -holes or μ -parts or μ -structures. It can be created by EDM, LBM, ECM and USM. The EDM is best suited for creating micro-holes in hard materials and even suited for nano-machining [1]. Ti-6Al-4V is one of the hard materials come under the categories of difficult for machine materials [2]. It can be easily machined by electric discharge machining [3]. In EDM, the workpiece materials are machined by standard sparking methods [4]. At present, Ti-6Al-4V is broadly used in aerospace,

S. Rajamanickam (✉)

Department of Mechanical Engineering, Vel Tech High Tech
Dr. Rangarajan Dr. Sakunthala Engineering College, Avadi, Chennai, India
e-mail: manic1327@gmail.com

S. Rajamanickam · J. Prasanna
College of Engineering, Guindy, Chennai, India
e-mail: prasanna@annauniv.edu

mould and dye-making industries, automotive, biomedical and other main industries because of their unique properties [5, 6].

Pure tungsten electrode of 200- and 300- μm electrode is employed in electrical discharge machining of tungsten carbide of Grade MG18 having 100- μm thickness [7]. The micro-holes and micro-slots were performed in conventional CNC EDM machine using tungsten carbide tool of 50- μm diameter and 100- μm -square cross sections in copper plate of thickness 0.1 mm [8].

The authors successfully used grey relational analysis optimizations method for electric discharge machining of EN-24 alloy steel [9]. The authors performed Taguchi grey relational analysis optimizations method to improve wire-cut electrical discharge machining process parameter while machining Inconel 825 with considerations of multi-response parameters [10]. Grey relational analysis optimization technique is exercised to improve multi-response characteristics in drilling process [11]. Grey relational analysis and fuzzy-based Taguchi method multi-objective optimization of electrical discharge machining of SKD 11 alloy steel are performed using pure copper electrode of diameter 8 mm in KT-200 experimental machine [12].

The Al-10% SiC_p composites are drilled in electrical discharge machining process using a brass electrode of diameter 2.7 mm. The process is optimized with high quality at low cost by adopting grey relational analysis methods [13]. The diameter 200–500 μm holes found more useful in the following applications, namely printed circuit boards, fuel injection nozzle, high pressure orifices, pneumatic sensors and manipulators, guides for wire bonders and spinning nozzles [8].

In this work, investigations of micro-electrical discharge machining of Ti–6Al–4V using pure tungsten electrode of 100 μm are conducted to obtain micro-holes with higher material removal rate and lower recast layer thickness, wear rate and taper angle. The analysis is performed for different combinations of electrical parameters and their levels as mentioned in Table 1.

2 Experimentation

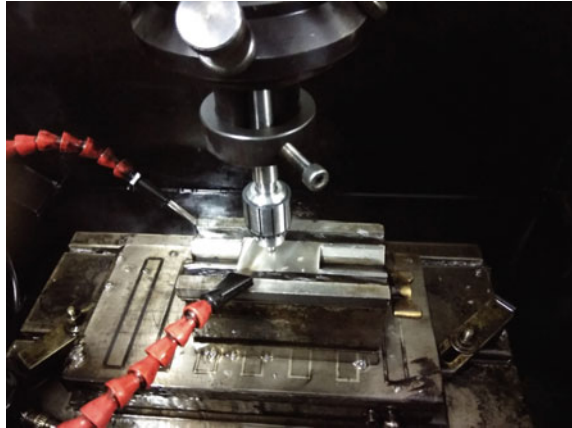
2.1 Experimental Set-up

The workpiece material used in this study was 0.1-mm-thin foil sheet of Ti–6Al–4V. The electrode material used in this study was a commercially available pure

Table 1 Different input parameters with their levels

Factors 'symbol' (units)	Levels			
	Level 1	Level 2	Level 3	Level 4
On-time ' T_{on} ' (μs)	5	10	15	20
Current ' I ' (A)	0.5	1	1.5	2
Off-time ' T_{off} ' (μs)	5	10	15	20
Voltage ' V ' (μs)	35	40	45	50

Fig. 1 Working zone of EDM



tungsten rod of 100- μm diameter. The dielectric fluid used was commercial EDM oil with high dielectric properties and flash point. The sparking machine model “SRP EDM-DIGISOFT 40” is employed in the research work. The working zone of EDM is shown in Fig. 1.

2.2 *Experimental Procedure*

The negative polarity of machining is employed for all combinations of input settings. In this study, through hole was drilled in Ti-6Al-4V thin foil sheet of 100 μm . After drilling through holes in a workpiece, it is cleaned manually using piece of cloths. The time taken for making through hole was noted, and linear wear is also observed. Now, the workpiece is taken for SEM micro-analysis for getting image of the machined hole at both entrance and exit surfaces to find output parameters such as recast layer, material removal rate and taper angle. The experimental plan and calculated values of output parameters are found in this research work as given in Table 2.

2.3 *Measurement*

By using ImageJ software, the recast layer thickness at entry and exit surfaces taken at eight different positions and average is taken for analysis. The wear rate and taper angle are calculated using the formulae hinted in Eq. 1–3.

Table 2 Experimental plan and output parameter values

Run	On-time	Current	Off-time	Voltage	Recast layer		Linear wear rate	Material removal rate	Taper angle
					Entry	Exit			
1	5	0.5	15	40	18.4250	12.6750	0.42372	0.01232	14.7618
2	10	0.5	15	40	20.8250	18.9875	3.33333	0.02359	11.6401
3	15	0.5	15	40	29.0125	17.6750	27.7777	0.13079	22.9283
4	20	0.5	15	40	20.6500	12.7250	0.45248	0.02167	26.6909
5	15	1	15	40	21.7625	15.9500	18.5185	0.03426	18.2499
6	15	1.5	15	40	24.8375	20.3875	23.3644	0.03821	11.4613
7	15	2	15	40	20.0625	13.8875	33.3333	0.01996	14.2652
8	15	0.5	10	40	07.0875	07.4125	5.76923	0.01795	20.1405
9	15	0.5	5	40	18.3250	16.6000	88.8888	0.08019	13.6987
10	15	0.5	20	40	19.7875	12.5250	78.4313	0.01642	17.9263
11	15	0.5	15	45	19.5250	14.1875	65.2173	0.01895	8.30649
12	15	0.5	15	35	19.2666	14.6000	01.7543	0.04528	19.2006
13	15	0.5	15	50	20.1500	21.4250	34.3137	0.03232	17.2365

$$\text{LWR} = \frac{\text{LW}}{t} \quad (1)$$

$$\text{MRR} = \frac{\pi H(D^2 + d^2 + Dd)}{12t} \quad (2)$$

$$\text{TA} = \tan \left| \frac{(D-d)}{2 * H} \right| \quad (3)$$

where LWR indicates linear wear rate of the electrode measured in mm/min, MRR is material removal rate measured in mm³/min, TA is taper angle measured in degree, D and d is the diameter of the machined hole at entrance surface and exit surface, t is machining time, and H is the thickness of workpiece materials.

3 Optimization Using Grey Relational Analysis

In 1982, Deng developed the grey relational analysis techniques for determining appropriate solutions for the real-world problems. The steps involved in the grey relational analysis are:

3.1 Step 1: Grey Relational Normalization

The material removal rate of output parameter is normalized using Eq. 4. It is used for Higher is the Better characteristics.

$$x_{ij} = \frac{y_{ij} - \min_{ij} y_{ij}}{\max_{ij} y_{ij} - \min_{ij} y_{ij}} \quad (4)$$

The recast layer at entry and exit surfaces, linear wear rate and taper angle is normalized using Eq. 5, where $i = 1-13$ and $j = 1-5$. It is used for Lower is the Better characteristics.

$$x_{ij} = \frac{\max_{ij} y_{ij} - y_{ij}}{\max_{ij} y_{ij} - \min_{ij} y_{ij}} \quad (5)$$

3.2 Step 2: Grey Relational Coefficient

The grey relational coefficient can be found after knowing the required characteristics by employing Eq. 6.

$$\zeta_{ij} = \frac{\Delta_{\min} - k\Delta_{\max}}{\Delta x_{ij} - k\Delta_{\max}} \quad (6)$$

Distinguishing coefficient (k) is normally in between 0 and 1. We have taken as $k = 0.5$. Where $\Delta_{\min} = 0$, $\Delta_{\max} = 1$, and $\Delta x_{ij} = (\text{maximum } x_{ij} - x_{ij})$.

3.3 Step 3: Grey Relational Grade

Finally, the grey relational grade is arrived by taking an average of grey relational coefficient using Eq. 7. It is ranked in order to know the optimum input parameter combinations among the available. The results of grey relational normalization, grey coefficient values are presented in Table 3.

$$\gamma_i = \frac{1}{n} \sum_{j=1}^n \zeta_{ij}, \quad \text{where, } n \text{ is number of output parameter} \quad (7)$$

4 Results and Discussions

The grey relation grade and rank for the particular run are calculated. The maximum grey relational grade is coined in run number 8. It is declared as the optimum setting. The corresponding input setting shows on-time 15 μs , current 0.5 A, off-time 10 μs and voltage 40 V. The run versus grey relational grade is plotted in Fig. 2.

The SEM image of micro-holes of the machined surface at entrance and exit for the optimum input setting is expressed in Fig. 3a, b. Particularly in this setting, the recast layer at both entrance and exit surfaces is very low compared to all other input combinations for making through holes in Ti-6Al-4V of thickness 100 μm . It is also keenly explored that the machined holes fail to produce the circular shape. Figure 3c, d indicates the machined surface SEM images at entrance and exit surfaces for the least optimum input setting. In this setting, it is recorded a noticeable amount of recast layer compared to all other combinations of input parameters.

Table 3 Results of grey relational normalization, coefficient values

Run	Grey relational normalization				Grey relational coefficient					
	Recast layer		Linear wear rate	Material removal rate	Taper angle	Recast layer		Linear wear rate	Material removal rate	Taper angle
	Entry	Exit				Entry	Exit			
1	0.4830	0.6244	1.0000	0.0000	0.6489	0.4916	0.5711	1.0000	0.3333	0.5875
2	0.3735	0.1740	0.9671	0.0952	0.8187	0.4439	0.3771	0.9383	0.3559	0.7339
3	0.0001	0.2676	0.6908	1.0000	0.2047	0.3334	0.4057	0.6179	1.0000	0.3860
4	0.3815	0.6209	0.9997	0.0789	0.0000	0.4470	0.5687	0.9994	0.3518	0.3333
5	0.3307	0.3907	0.7955	0.1852	0.4591	0.4276	0.4507	0.7097	0.3803	0.4804
6	0.1905	0.0740	0.7407	0.2186	0.8284	0.3818	0.3506	0.6585	0.3902	0.7445
7	0.4083	0.5379	0.6280	0.0645	0.6759	0.4580	0.5197	0.5734	0.3483	0.6067
8	1.0000	1.0000	0.9396	0.0475	0.3563	1.0000	1.0000	0.8922	0.3442	0.4372
9	0.4875	0.3443	0.0000	0.5729	0.7067	0.4938	0.4327	0.3333	0.5393	0.6303
10	0.4208	0.6351	0.1182	0.0346	0.4767	0.4633	0.5781	0.3618	0.3412	0.4886
11	0.4328	0.5165	0.2676	0.0560	1.0000	0.4685	0.5084	0.4057	0.3463	1.0000
12	0.4446	0.4871	0.9850	0.2782	0.4074	0.4737	0.4936	0.9708	0.4092	0.4576
13	0.4043	0.0000	0.6169	0.1688	0.5143	0.4563	0.3333	0.5662	0.3756	0.5072

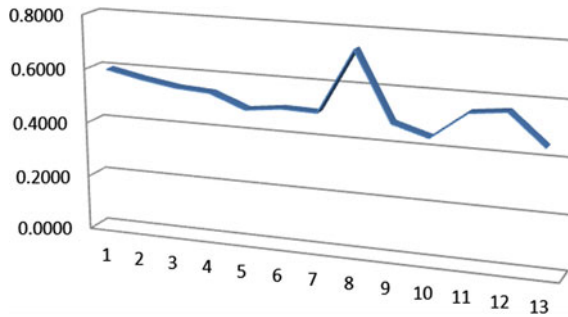


Fig. 2 Run versus grey relational grade

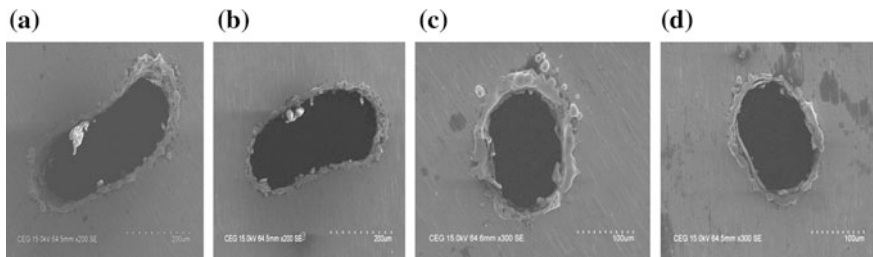


Fig. 3 Machined hole at entrance and exit surfaces for best and worst settings

5 Conclusion

Analysis of micro-holes drilling in EDM of Ti–6Al–4V to obtain the better output parameters using 100- μm -pure tungsten electrodes has been conducted with various combinations of electrical parameters. Based on the experimental investigations, the following conclusions are drawn:

- The optimum input setting for higher material removal rate and lower recast layer thickness, wear rate and taper angle was found using grey relational analysis. The optimum input parameters obtained have on-time 15 μs , current 0.5 A, off-time 10 μs and voltage 40 V.
- The run number 8 gives the minimum values of recast layer thickness at both entrance and exit surfaces. The lowest linear wear rate is declared for the run number 1. The very low taper angle is presented at the run number 11. The highest value of material removal rate is calculated for the run number 3.

Acknowledgements The authors wish to thank the persons from College of Engineering, Anna University, Chennai, Tamil Nadu, India, for their contribution and Vel Tech High Tech Dr. Rangarajan Dr. Sakunthala Engineering College, Chennai, Tamil Nadu, India, for their support and strong motivation.

References

1. Egashira, K., Morita, Y., Hattori, Y.: Electrical discharge machining of submicron holes using ultrasmall-diameter electrodes. *Precis. Eng.* **34**, 139–144 (2010)
2. Fonda, P., Wang, Z., Yamazaki, K., Akutsu, Y.: A fundamental study on Ti–6Al–4V's thermal and electrical properties and their relation to EDM productivity. *J. Mater. Process. Technol.* **202**, 583–589 (2008)
3. Ho, K.H., Newman, S.T.: State of the art electrical discharge machining (EDM). *Int. J. Mach. Tools Manuf.* **43**, 1287–1300 (2003)
4. Marafona, J., Chousal, J.A.G.: A finite element model of EDM based on the Joule effect. *Int. J. Mach. Tools Manuf.* **46**, 595–602 (2006)
5. Kibria, G., Sarkar, B.R., Pradhan, B.B., Bhattacharyya, B.: Comparative study of different dielectrics for micro-EDM performance during microhole machining of Ti–6Al–4V alloy. *Int. J. Adv. Manuf. Technol.* **48**, 557–570 (2010)
6. Shabgard, M., Khosrozadeh, B.: Investigation of carbon nanotube added dielectric on the surface characteristics and machining performance of Ti–6Al–4V alloy in EDM. *J. Manuf. Processes* **25**, 212–219 (2017)
7. Jahan, M.P., Wong, Y.S., Rahman, M.: A study on the quality micro-hole machining of tungsten carbide by micro-EDM process using transistor and RC-type pulse generator. *J. Mater. Process. Technol.* **209**, 1706–1716 (2009)
8. Masuzawa, T.: State of the art of micromachining. *Ann. CIRP* **49**, 473–488 (2000)
9. Mishra, B.P., Routara, B.C.: An experimental investigation and optimisation of performance characteristics in EDM of EN-24 alloy steel using Taguchi Method and Grey Relational Analysis. *Mater. Today: Proc.* **4**, 7438–7447 (2017)
10. Rajyalakshmi, G., Venkata Ramaiah, P.: Multiple process parameter optimization of wire electrical discharge machining on Inconel 825 using Taguchi grey relational analysis. *Int. J. Adv. Manuf. Technol.* 1–14 (2013)
11. Tosun, N.: Determination of optimum parameters for multi-performance characteristics in drilling by using grey relational analysis. *Int. J. Adv. Manuf. Technol.* **28**, 450–455 (2006)
12. Lin, C.L., Lin, J.L., Ko, T.C.: Optimisation of the EDM process based on the orthogonal array with fuzzy logic and grey relational analysis method. *Int. J. Adv. Manuf. Technol.* **19**, 271–277 (2002)
13. Narender Singh, P., Raghukandan, K., Pai, B.C.: Optimization by grey relational analysis of EDM parameters on machining Al–10%SiCP composites. *J. Mater. Process. Technol.* **155–156**, 1658–1661 (2004)

Evaluation of Critical Speed for Aluminum–Boron Carbide Metal Matrix Composite Shaft



Arun C. Dixit , B. K. Sridhara and M. V. Achutha

Abstract This work deals with finding an alternative lightweight material over conventional materials for manufacturing drive shafts. Drive shafts are a key component for transmitting power from one end to the other. However, the conventional materials used for producing drive shafts pose several disadvantages especially concerning with their weight. Conventional drive shafts are susceptible to large vibration during high-speed traversing because of truncated strength-to-weight ratio. The work aims at improving the critical speed of the specimen by proposing a new composite material made of aluminum matrix reinforced with boron carbide (B_4C) particles. Specimens with weight percentage 0, 3, 6, 9, 12% of reinforcement were manufactured through stir casting technique. The work has established a new lightweight material with enhanced critical speed which can be used for various high-speed applications. Other important mechanical properties like hardness and tensile strength were also analyzed. Modal analysis was carried on the specimens using ANSYS 15 Workbench.

Keywords Drive shaft · Critical speed · Strength-to-weight ratio
Boron carbide · Aluminum LM6

A. C. Dixit (✉)

Department of Mechanical Engineering, Vidyavardhaka College of Engineering,
Mysore, India

e-mail: arundixitu@gmail.com

B. K. Sridhara · M. V. Achutha

Department of Mechanical Engineering, National Institute of Engineering,
Mysore, India

© Springer Nature Singapore Pte Ltd. 2019

U. Chandrasekhar et al. (eds.), *Innovative Design, Analysis and Development Practices in Aerospace and Automotive Engineering (I-DAD 2018)*, Lecture Notes in Mechanical Engineering, https://doi.org/10.1007/978-981-13-2718-6_51

527

1 Introduction

1.1 Drive Shafts

A drive shaft is a mechanical component for transmitting torque and rotation, usually used to connect other components of a drive train that cannot be connected directly because of distance or the need to allow for relative movement between them [1].

As torque carriers, drive shafts are subject to torsion and shear stress, equivalent to the difference between the input torque and the load [2]. They must therefore be strong enough to bear the stress, while avoiding too much additional weight as that would in turn increase their inertia. Steel and aluminum are the two most commonly used materials for manufacturing drive shafts [3]. However, steel shafts are too heavy thus truncating the performance, and aluminum does not possess the strength of the steel. The new trend is the use of composite materials as they possess high strength-to-weight ratio [4].

1.2 Critical Speed

All rotating shafts, even in the absence of external load, will deflect during rotation. The unbalanced mass of the rotating object causes deflection that will create resonant vibration at certain speeds, known as the critical speeds. This phenomenon or condition will become more apparent at higher rotational velocities. However, there is a point or rotational velocity where the vibrations and amplitude increase significantly. The rotational velocity at which the vibration increases dramatically is called the critical speed of the rotating mass.

Typically, the designed operating speed of a machine is less than the critical speed. This is done to prevent a machine from ever achieving the undesired critical speed vibration and possible resulting failure.

1.3 Metal Matrix Composites

Metal matrix composites (MMCs) are the ones in which metals are used as the base of the composition for a composite material, for example, titanium, aluminum, and iron. The work aims at developing a metal matrix composite [particulate composite] by combining a lightweight metal with hard particles. Various weight percentages of the reinforcement are chosen based on the literature review, and the best weight percentage reinforcement is proposed based on the results obtained (Table 1).

Table 1 Details of the specimens manufactured

Specimen name	Base alloy	wt% of B ₄ C
A0	Al LM6	0
A1	Al LM6	3
A2	Al LM6	6
A3	Al LM6	9
A4	Al LM6	12

2 Materials and Experimental Procedure

2.1 Aluminum LM6

LM6 is a corrosion-resistant aluminum casting alloy with average durability and strength, with high impact strength and ductility which possess excellent casting properties. Wrought alloys are heat-treated post casting which possess superior properties when compared to casted alloys. Out of the two available forms of aluminum, the work aims at improving the properties of casted aluminum since the forged aluminum already offers superior properties. Out of the series [LM2–LM24], LM6 exhibits lesser strength when compared to other alloys and hence a suitable choice for reinforcing.

2.2 Boron Carbide

Boron carbide (B₄C) is a crystalline compound of boron and carbon [5]. It is an extremely hard, synthetically produced material that is used in abrasive and wear-resistant products. It is odorless, insoluble in water, and has a melting point of 2763 °C and density of 2.52 g/cm³ which is less compared to density of aluminum (2.79 g/cm³) [6, 7]. Boron carbide ceramic particles are one of the hardest materials second only to diamond. The addition of boron carbide into any other matrix boosts the properties of the composites thus developed. The B₄C reinforced aluminum metal matrix composites exhibits best properties at 8% weight reinforcement [8]. Thus, to strike a balance, 2 percentage compositions above and below 8% is selected.

3 Results and Discussions

3.1 Tensile Test Results

From Table 2, it is noted that there is an increase in the values of ultimate tensile strength of the composites when compared to the base alloy. However, this increase

Table 2 Tensile test results

wt% of B ₄ C	Peak load (N)	Tensile strength (N/mm ²)	Young's modulus (10 ³ × N/mm ²)
0	12695.00	102.953	70.081
3	13137.1	108.434	73.73
6	13330.6	109.326	74.34
9	11084.36	92.986	63.22
12	10704.8	90.828	61.763

Fig. 1 Tensile strength versus wt%

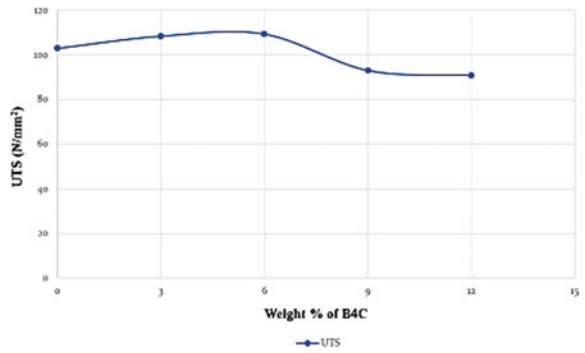
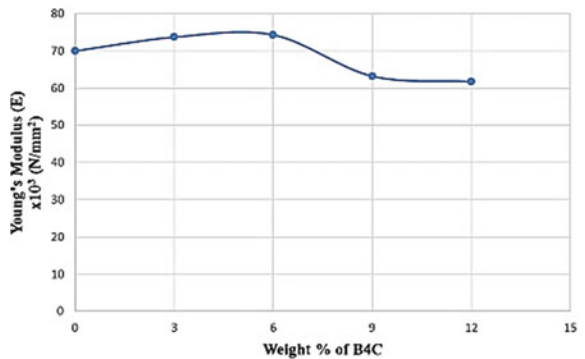


Fig. 2 Young's modulus versus wt%



is not persistent. The value of tensile strength of the composites showed growth for 3% and then peaked at 6% reinforcement. With further increase in percentage reinforcement, the tensile strength started to truncate, even falling below the base alloy. The behavior of tensile strength and yield strength wrt percentage reinforcement can be clearly realized from Figs. 1 and 2.

Table 3 Hardness test results

wt% of B ₄ C	Vickers hardness	Brinell hardness
0	70	53
3	82	64
6	100	83
9	125	110
12	132	116

3.2 Hardness Test

From Table 3, it is evident that with every 3% increase in the weight percentage of boron carbide particles, there is an increase in the hardness value. This behavior is due to the fact that ceramic particles like boron carbide being hard materials increase the hardness when added to a matrix.

3.3 Critical Speed Results

Numerical values were found by modal analysis in ANSYS 15 Workbench (Fig. 3). Analytical values are the ones based on the formulae.

- a = Model frequency for each shaft = $\sqrt{\frac{E \times I}{M}}$
 where E is Young’s modulus, I is moment of inertia, and M is mass per length of shaft.
- ω , Angular speed = $\frac{22 \times a}{L^2}$
 where L is length of the shaft.
- N_C is critical speed = $\frac{60 \times \omega}{2\pi}$

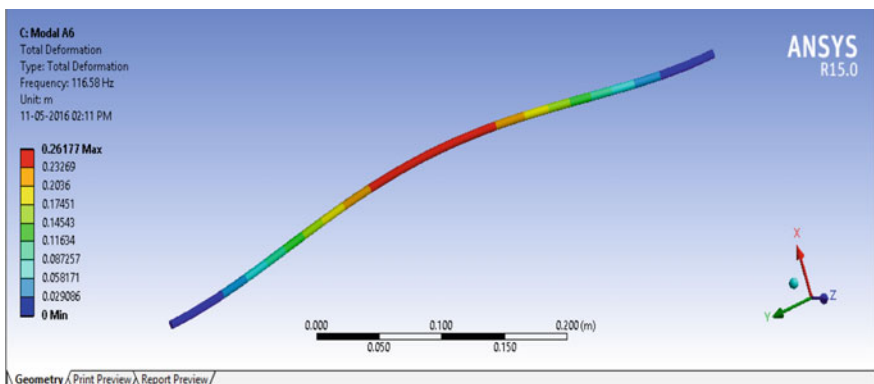


Fig. 3 Natural frequency of first mode of vibration of A6 specimen

Table 4 Consolidated results of critical speed tests

Specimen name	Weight %	Mass (g)	Numerical values (RPM)	Theoretical values (RPM)	Experimental values (RPM)
Mild steel	–	107.6	6650.2	6706.83	6383
A0	0	35.4	6777	6667.62	5762
A3	3	35.1	6960.6	6846.52	6531
A6	6	34.6	6994.8	6880.22	6759
A9	9	34.3	6455.4	6349.44	6361
A12	12	33.9	6384.6	6283.97	5530

Experimental values were determined by test specimen which was gripped rigidly at both ends (fixed–fixed type) and rotated in standard apparatus where the speed was slowly increased until the composite started to whirl (a loop is formed). The first sign of appearance of the loop is the indication to stop further increasing the rotational speed of the shafts (Table 4).

The pure matrix alloy exhibited a critical speed of 5762 rpm. As boron carbide is used to reinforce the matrix (97% Al + 3% B₄C), the critical speed increased to 6531 rpm. On further increase in percentage of boron carbide (94% Al + 6% B₄C), the critical speed escalated to 6759 rpm. After this point, addition of boron carbide (3% increment) at each trial came at the cost of reduction in critical speed of the composite. When the speed of each specimen reached its critical point, appearance of deflection was evident. This deflection caused the composite to showcase a loop. The matrix alloy displayed deflection prior to all other composites, owing to its low strength.

A mild steel specimen of same dimensions as that of the developed composites was taken and tested for its critical speed just to obtain the effectiveness of the newly conceptualized shafts. The steel specimen weighed a hefty 107.6 g in comparison to the composites which weighed a maximum of 35.8 g. Furthermore, the steel shaft was only able to handle a speed of 6383 rpm which is remarkably lesser than that of the A6 specimen, which could handle speeds up to 6759 rpm. The main objective of reducing the weight of a drive shaft is thus achieved.

4 Scanning Electron Microscopy (SEM)

Figure 4 shows the SEM of aluminum LM6 alloy. The bright matrix is clearly visible with no reinforcements, and also there are no signs of voids in the casted product.

Figure 5 shows SEM of 6% B₄C reinforced aluminum metal matrix composite at 1000 μ m magnification in which the granules of boron carbide particles are clearly visible. From this, it can be concluded that the particles of B₄C were uniformly

Fig. 4 SEM of aluminum LM6 base alloy

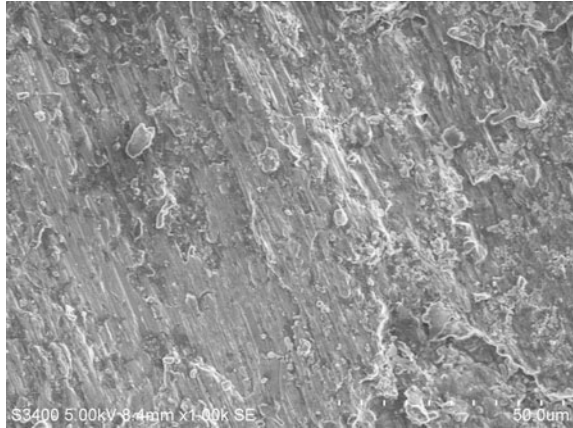
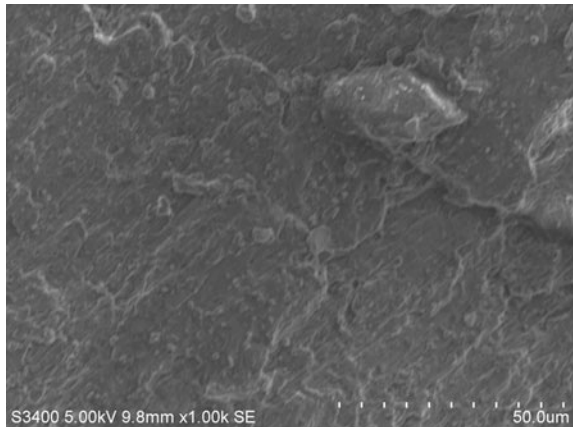


Fig. 5 SEM of 6% B₄C reinforced composite



mixed with the aluminum matrix during the stir casting process. The image is darker when compared to the base alloy image which shows the uniform distribution of B₄C particles. Furthermore, the image depicts no voids in the casting.

5 Conclusion

1. Tensile strength increased from 0 to 6% and started to decline through 9–12%
2. Hardness of the specimen showed consistent growth with the increase in percentage reinforcement
3. Mass of the composites decreased with the increase in percentage reinforcement

4. Maximum speed was observed on the specimen with 6% reinforcement (6759 rpm) which bettered mild steel (6383 rpm). This shows an increase in critical speed by 6%. Also, with respect to base alloy, there was an increase by 17%.
5. The aluminum boron carbide composites weigh of 34.6 g while a steel shaft of same dimensions weighs 107.6 g (68% reduction in weight). In comparison base alloy weighs 35.4 g (3% reduction in weight).

The newly contrived composite weighs only a fraction of the traditional metals used in drive shafts while flaunting significant increase in critical speed and strength. This allows the top speed to be increased far beyond the safe operating speeds of a standard aluminum or steel driveshaft. The main failure mode of the shaft is fatigue. The durability/fatigue studies of the proposed composite need to be analyzed in order to propose their application.

References

1. Suryawanshi, B.K., Damle, P.G.: Review of design of hybrid aluminum/composite drive shaft for automobile. *Int. J. Innov. Technol. Explor. Eng.* **2** (2013)
2. Parshuram, D., Mangsetty, S.: Design and analysis of composite/hybrid drive shaft for automobiles. In: *Int. J. Eng. Sci.* **2** (2013)
3. Sino, R., Baranger, T.N., Chatelet, E., Jacquet, G.: Dynamic analysis of a rotating composite shaft. *Compos. Sci. Technol.* (2009)
4. Gomez, L.: Analysis of boron carbide aluminum matrix composites. *J. Compos. Mater.* **43** (2009)
5. Nie, C.-Z., Gu, J.-J., Liu, J.-L., Zhang, D.: Production of boron carbide reinforced 2024 aluminum matrix composites by mechanical alloying. *Mater. Trans.* **48** (2007)
6. Pyzik, A.J.: Processing of boron carbide-aluminum composites. *J. Am. Ceram. Soc.* **72** (1989)
7. Thirumalai, T.: Production and characterization of hybrid aluminum matrix composites reinforced with boron carbide (B₄C) and graphite. *J. Sci. Ind. Res.* **73** (2014)
8. Rama Rao, S., Padmanabhan, G.: Fabrication and mechanical properties of aluminum–boron carbide composites. *Int. J. Mater. Biomater. Appl.* ISSN 2249–9679 (2012)
9. Ibrahim, M.F., Ammar, H.R., Samuel, A.M., Soliman, M.S.: Metallurgical parameters controlling matrix/B₄C particulate interaction in Aluminum–Boron carbide metal matrix composites. *Int. J. Cast Metals Res.* **26** (2013)
10. Gopal Krishna, U.B., Sreenivas Rao, K.V., Vasudeva, B.: Effect of particulate size on the tensile property of boron carbide reinforced aluminum matrix composites. In: *International Conference on Challenges and Opportunities in Mechanical Engineering* (2012)

Smart System for Feature Recognition of Sheet Metal Parts: A Review



Sachin Salunkhe, Soham Teraiya, H. M. A. Hussein
and Shailendra Kumar

Abstract Sheet metal is one of the most frequently used primary manufacturing methods to produce different variety (shape and size) of components. The production of these sheet metal parts with a product (design) features is a major task in the sheet metal industries. Feature recognition is a primary activity for design of dies. Usually, this task is performed by experienced process planner in industries. The present review gives an overview of computer-aided smart system for feature recognition of sheet metal parts. The proposed system is capable to extract/recognize all design features of sheet metal parts automatically from 3D CAD model. The system has been implemented in AutoCAD using AutoLISP programming language.

Keywords Sheet metal · Die design · Feature recognition · Stamping industries

S. Salunkhe (✉)

Department of Mechanical Engineering, Vel Tech Rangarajan Dr. Sagunthala R & D Institute of Science and Technology, Avadi, Chennai, India
e-mail: kashid32@gmail.com

S. Teraiya

Department of Mechanical Engineering, Dr. S. & S. S. Ghandhy College of Engineering and Technology, Surat, India
e-mail: sohamteraiya@gmail.com

H. M. A. Hussein

Department of Mechanical Engineering, Faculty of Engineering, Helwan University, Cairo, Egypt
e-mail: hmahuss@hotmail.com

S. Kumar

Department of Mechanical Engineering, Sardar Vallabhbhai National Institute of Technology, Ichchhanath, Surat, India
e-mail: skbudhwar@med.svnit.ac.in

© Springer Nature Singapore Pte Ltd. 2019

U. Chandrasekhar et al. (eds.), *Innovative Design, Analysis and Development Practices in Aerospace and Automotive Engineering (I-DAD 2018)*, Lecture Notes in Mechanical Engineering, https://doi.org/10.1007/978-981-13-2718-6_52

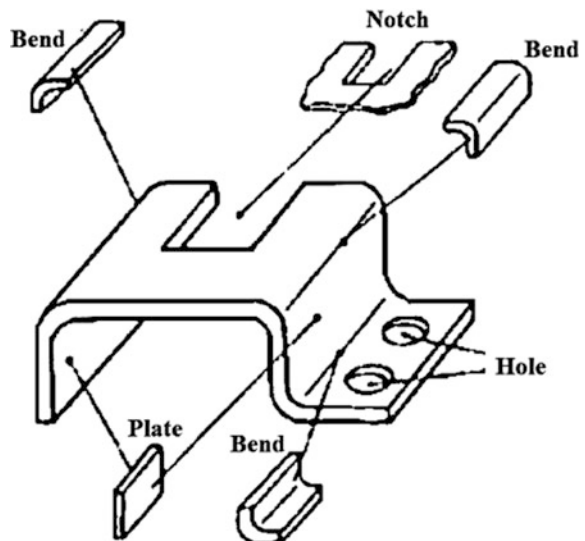
535

1 Introduction

Sheet metals are playing an important role in our day-to-day life. It is broadly used in automotive sector, aviation industry, medical tables and equipments, building constructions, etc. Stamping industries demand that sheet metal parts should be produced to accurate shape or near accurate shape with following functional characteristics [1]: (1) adequate dimensional accuracy, (2) surface finish, (3) adequate structural integrity and (4) reduction in material wastage. In stamping industries, die design is an important activity according to product features. Feature recognition is a primary activity of die design in sheet metal industries. Product features such as shape and size of parts and design information are used in reasoning for manufacture of part [2]. The feature mainly includes two types of information. The first is engineering information which includes design and manufacturing process, for example, diameter and depth of hole. The second is geometric information which describes the shape and topology of the features. Some of the typical design features of sheet metal parts are shown in Fig. 1. Present scenario in sheet metal industry needs to complete automation from design stage (feature recognition) to manufacturing final product. Commercial CAD systems available for automation in sheet metal industries, but the cost of such software is very high that cannot be affordable by small-scale stamping industries.

After studying these CAD systems, it has been found that these can perform only simple calculations and drafting, and not capable to automatically recognize type and size of an object. To overcome the above problems, there is stern need to developing a smart system for automatic feature recognition of sheet metal parts. Feature recognition is the process of extraction of design information from the CAD

Fig. 1 Sheet metal design features by Wierda [3]



model and identifying the features to be manufactured on a product without human intervention. The feature recognition process involves recognizing higher level features, for example, a hole, from the lower level geometrical entities represented within the part, for example, straight lines or circular curves. Feature recognition is typically thought as a process that is performed on a geometric model of a finished part. Constructive solid geometry (CSG) and boundary representation (B-rep) [4] are the methods for feature recognition.

2 Literature Review

Automatic feature recognition has been an active research area for more than last two decades. The reevaluation being started of feature recognition in the late 1980s. Several researchers from worldwide have successfully attempted on feature recognition of sheet metal parts such as Cser et al. [5] proposed case-based learning and feature recognition system for manufacturing sheet metal products. Nnaji et al. [6] developed feature extraction, recognition and reasoning of sheet metal parts which created in CAD model. IGES file type is used for automatic feature extraction. Meeran and Pratt [7] developed automatic feature recognition for simple prismatic part. The input parameter of feature recognition is 2D drawing of prismatic part in a DXF format. The coding is written in PROLOG language. Lentz and Sowerby [8] proposed feature recognition system for concave and convex regions of a sheet metal component. The B-rep model has been used for extraction of features. Streppel et al. [9] developed feature extraction module for sheet metal bending lines or flat pattern parts. STEP or neutral file format of CAD is used for exchange product model. Mantripragada et al. [10] proposed feature-based technique for box-type sheet metal parts. Computer-aided engineering (CAE) system is used to design box-type sheet metal parts. Jagirdar et al. [11] proposed feature recognition method for shearing operations for 2D sheet metal components created by a wireframe model. 'C' language is used as a programming language, and geometric data are obtained from AutoCAD DXF output file. Ceglarek [12] developed multivariate analysis and evaluation of adaptive sheet metal assembly systems. The system is capable to measure part information. Gao et al. [13] developed system for extract design features of a part from 3D CAD model. A feature library is developed for feature detection and stored in a plain ASCII file format. Xie et al. [14] presented an integration of CAD/CAPP/CAM for compound sheet metal cutting and punching. Object-oriented method and STEP file are used for feature automatic recognition of parts. Wang et al. [15] developed smart technique for assess geometrical information on wrinkling on deep-drawn forming parts. Lutters et al. [16] proposed feature recognition system to identify sheet metal features.

Rigopoulos and Arkun [17] developed a new online assess technique to assess profile of sheet metal-forming process. Ge et al. [18] developed smart system for automatic online monitoring of sheet metal parts. The developed system is capable

to identify the behaviour of high-frequency vibration during pressing operation. Shunmugam and Kannan [19] proposed the design features automatically from the orthographic projections and generate 3D wireframe model. Attributed adjacency graph method is used to generate 3D wireframe model flat pattern of sheet metal. Holland et al. [20] described CAD system for selection of metal-forming process and feature recognition. STEP AP203 file format is used for feature recognition. C++ programming language is used for search STEP text file. Pal et al. [21] introduced a concept of genetic algorithm for feature recognition from large CAD database. The proposed system has mainly been developed for meeting the growing complexity of product across all manufacturing domain. Zhao and Shah [22] developed feature recognition and rules associated system for manufacturability analysis of sheet metal parts. Ferreira and Vivian [23] presented the recognition of features in cylindrical parts created with the ACIS solid modelling (2D) kernel through the Internet. Ciurana et al. [24] presented computer-aided process planning and feature-based system for choosing the manufacturing route and characteristics in sheet metal processes. Huang et al. [25] developed smart system to assess part features such as flange, punch and bend. Cicek and Gulesin [26] developed automatic recognition system of 3D CAD models of sheet metal parts. The output of the developed system informs of face adjacency relations and attributes. Klingenberg and Boer [27] used condition-based maintenance (CBM) to assess design information for blanking of sheet metal parts. Developed smart system is able to assess product and design information such as tool wear and causing product quality. Zhang et al. [28] proposed feature recognition for both isolated and intersecting geometric features of free form surface models. Kannan and Shunmugam [29] used 3D model data in STEP AP—203 for various features with similar manufacturing attribute are identified using a set of rules based on topology, geometry and Boolean logic. Oh et al. [30] developed new methods of feature evaluation of sheet metal formability. Strain is measured from the extracted 3D image of sheet metal blank. Gupta and Gurumoorthy [31] presented a new algorithm to extract free-form surface features (FFSFs) from surface model. Concept of separating curve has been proposed in case of formed feature on the surface. Behera et al. [32] developed advanced algorithm for automatic feature detection of formed sheet metal parts by single-point incremental forming (SPIF). Stereolithography (STL) model format is used for detection of features such as geometry, curvature, location, orientation and process parameters. Hussein and Mousa [33] have developed generative feature recognition system for solid model based on STEP-AP203 format. The system is designed using Visual Basic 2008, MS Access and EW Draw module. Gupta et al. [34] proposed extract process parameters from sheet metal parts using (B-rep). Khan et al. [35] used CAPP with a conjunction of 3D CAD model for extraction of part information and process planning of die components. Neugebauer et al. [36] presented automatic feature extraction, recognition and interpretation sheet metal-forming features. Medial axis transformation (MAT) model is used to extract the features.

Pishyar and Emadi [37] developed automatic surface inspection system to investigate defective parts by comparing the user requirements and the generated

images to minimize the wastes led to the product rejection to be delivered steel with better quality to the customer. Khan et al. [38] present a methodology for automatic extraction of some common 2D internal sheet metal features. Tao et al. [39] presented computer-aided product with a conjunction of life-cycle assessment (LCA) for assessment of design features of parts. The proposed system is categories in two section of feature recognition as product feature (PF) and operation feature (OF). Eriyeti et al. [40] developed a framework of Web-based feature recognition system (FRS) for feature recognition of bending structure on a reconfigurable bending press machine (RBPM). Ubhayaratne et al. [41] developed semi-blind signal extraction technique for analysis of tool wear monitoring of sheet metal parts.

In an evaluation of current set of sheet metal scenario at worldwide, it reveals that most of the researchers have applied efforts for feature recognition of simple part geometry. No literature is available in the area of development of a smart system for automatic feature recognition/extraction of non-symmetric sheet metal parts. In addition, these systems require high-performance computers for processing of algorithm and extraction of features. This type of system will provide a great help to the process planners and die designers working in sheet metal industries. As a result, the productivity of stamping industries will improve a lot and eventually, the cost of sheet metal products will also be reduced. This paper describes a smart system for automatic feature recognition system developed on AutoCAD software. The logic for feature recognition is written in AutoLISP programming language. Based on the literature review, the salient features of major research work in the area of smart system in feature recognition of sheet metal part is summarized in Table 1.

Table 1 Summary of major research work in the area of expert system to die design

Ref. No.	Authors	System details	Remarks
[5]	Cser et al. (1991)	Case-based learning is used for recognition of sheet metal products	Developed for specific applications
[7]	Meeran and Pratt (1993)	Automatic feature recognition technique is used for simple prismatic part sheet metal parts	Deals with only prismatic parts
[8]	Lentz and Sowerby (1993)	Feature extraction methodology is used for hole on sheet metal components	Deals with only simple feature
[11]	Jagirdar (1995)	Feature recognition method is used for 2D sheet metal components	Limited to specific application
[42]	Greska et al. (1997)	Automatic feature recognition technique is used for bend and deep-drawn sheet metal parts	Developed specifically for bend and deep-drawn parts

(continued)

Table 1 (continued)

Ref. No.	Authors	System details	Remarks
[19]	Shunmugam and Kannan (2002)	Automatic feature extraction technique is used for sheet metal parts	Deals with only 3D wireframe models
[43]	Ismail et al. (2005)	Feature recognition technique is used for cylindrical-based and conical-based features of sheet metal parts	Developed specially solid and void 'sides' of a boundary entity of parts only
[44]	Zhou et al. (2007)	Integration of CAD and CAPP system is used for feature recognition of sheet metal parts	System is capable only extract design features related to process planning of sheet metal parts
[26]	Cicek and Gulesin (2007)	Used feature recognition system for sheet metal parts	Limited to specific application
[45]	Sunil and Pande (2008)	CAD system is used for automatic feature recognition of 3D CAD model of sheet metal parts	Limited to specific application
[50]	Farsi and Arezoo (2009)	Smart feature recognition system is used for sheet metal parts	Deals with only bend parts
[30]	Oh et al. (2011)	Feature recognition technique is used for feature evaluation of sheet metal formability	Limited to specific application
[32]	Behera et al. (2012)	Used advanced algorithm system for automatic feature detection of formed sheet metal parts	Developed single-point incremental forming (SPIF) only
[46]	Hussein and Aseel (2013)	Smart system is used for automatic feature recognition of 3D prismatic sheet metal parts	Deals with only prismatic sheet metal parts
[31]	Gupta and Gurumoorthy (2013)	Feature extraction system is used for sheet metal parts from CAD model	Considered only bend parts
[34]	Gupta et al. (2014)	Feature extraction technique is used for extract process parameters from sheet metal parts	Limited to specific application
[36]	Neugebauer et al. (2015)	Automatic feature extraction, recognition and interpretation system is used for sheet metal forming. Medial axis transformation (MAT) model is used to extract the features.	Deals with only symmetric sheet metal parts
[37]	Pishyar and Emadi (2016)	Feature extraction system is used for automatic surface inspection of sheet metal parts	Considered only simple part geometry
[38]	Khan et al. (2016)	Automatic extraction technique is used for 2D internal sheet metal parts	Limited to specific application

(continued)

Table 1 (continued)

Ref. No.	Authors	System details	Remarks
[40]	Eriyeti (2017)	Web-based feature recognition system (FRS) is used for feature recognition of bending parts	Limited to specific application
[41]	Ubhayaratne et al. (2017)	Semi-blind signal extraction technique is used for analysis of tool wear monitoring of sheet metal parts	Developed specifically for tool wear only

3 Description of Proposed System for Feature Recognition

Feature extraction is typically thought as a process that is performed on a geometric model of a finished part. In the proposed smart system, B-rep technique with 3D solid primitives is used for automatic feature extraction of sheet metal parts. B-rep contains the set of information about parts such as faces, edges and vertices of a part. The classification of feature extraction methods is depicted in Fig. 2.

In the present system, AutoCAD software is used for modelling of sheet metal part. CAD software uses B-rep approach for CAD modelling [49]. The B-rep of any CAD part model contains two types of information topological and geometric. The topological information contains connectivity, associativity and neighbourhood information. In addition, topological information deal with high-level attribute of the product design. Geometric information usually deals with intelligent decision on the types of entities necessary to use in a particular model to meet certain geometric requirements such as slopes and/or curvatures. General topology of B-rep is shown in Fig. 3. The data structure of a CAD model contains the connectivity of edges since object is made up of faces and faces are made up of edges and vertices. Initially, the proposed system identifies regions of CAD model of part. On identifying the regions, adjacency between them is constructed. This adjacency is further used to recognize features. Geometrical and topological conditions of the identified regions are used to recognize features. The system extracts features based on the parent–child relationship between them. Proposed smart system has been coded in AutoLISP language.

Figure 4 shows the execution of the proposed smart system. Initially, the system invites the user to enter input in form of 3D CAD drawing of sheet metal part in AutoCAD software. The proposed system extracts design features in two stages—(i) pre-feature extraction and (ii) feature extraction. In pre-feature extraction stage, faces of the 3-D CAD drawing file of sheet metal part are exploded. Features of sheet metal part such as sheet thickness, hole(s) (number of holes, shape and size of holes), distance between holes, distance between edge of hole to the edge of part, notch(es) (type and size of notch), corner radius, size of sheet metal part are extracted automatically by the proposed system. FE.DAT. These extracted features

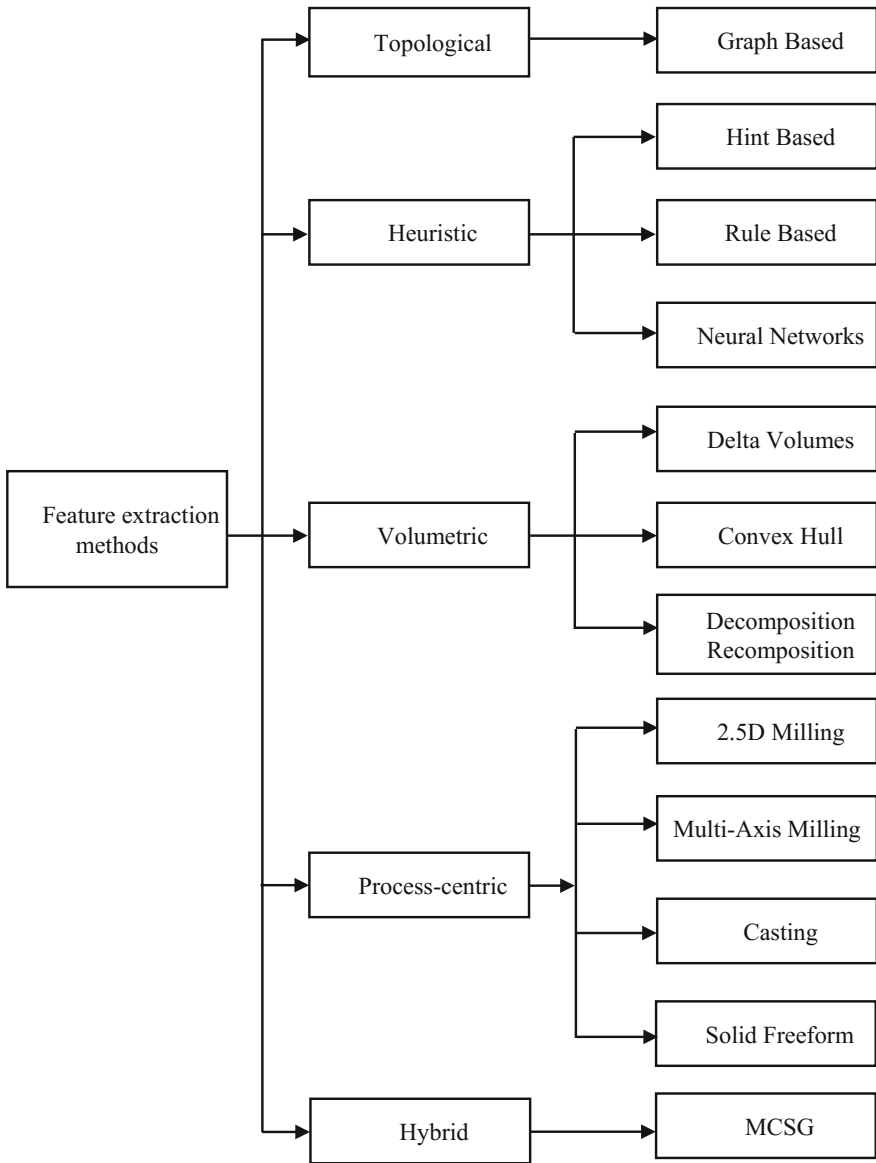
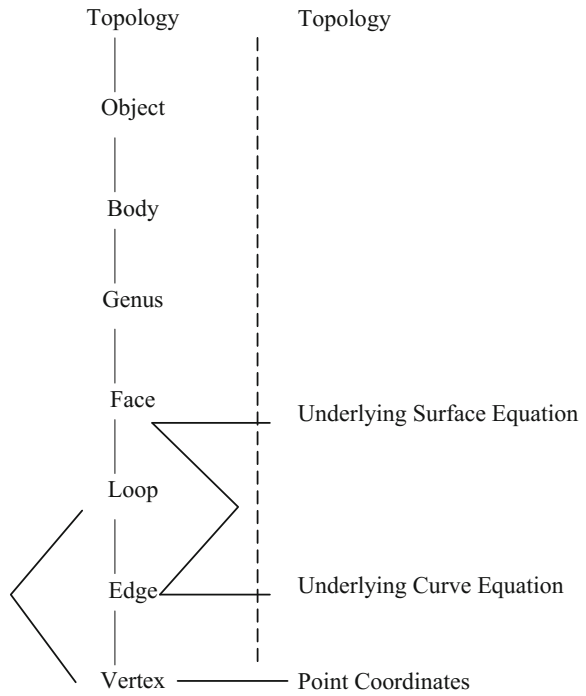


Fig. 2 Classification of feature extraction methods [47]

Fig. 3 General topology of B-rep [48]



are displayed to the user and stored automatically in a data file labelled as FE.DAT. The output data file FE.DAT acts as an input to the downstream applications related to die design process. The proposed smart system has been tested successfully for a wide variety of sheet metal parts to extract design features automatically from 3D CAD files. A sample run of the system for one example parts (Figs. 5 and 7) is shown in Figs. 6 and 8. The detail of features extracted by the system is found exactly similar to that of domain experts in the industry namely M/s Panchmahal Dies and Tools Pvt. Ltd., Vadodara, India, and D D Engineering Pvt. Ltd., Pune, India, for said example parts.

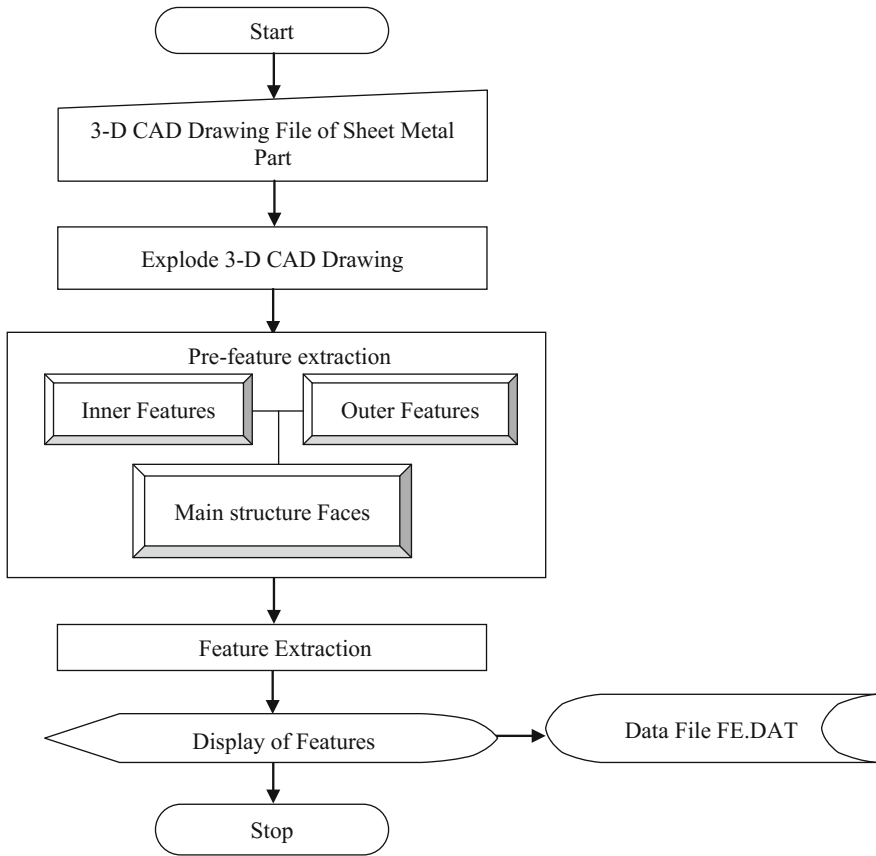


Fig. 4 Execution of system

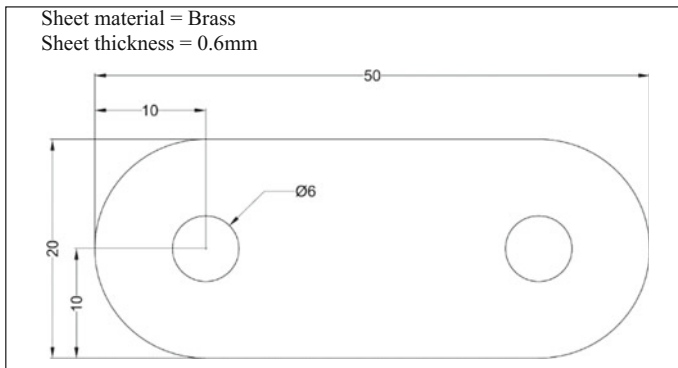


Fig. 5 Example part (all dimensions are in mm) (M/s Panchmahal Dies and Tools Pvt. Ltd., Vadodara, India)

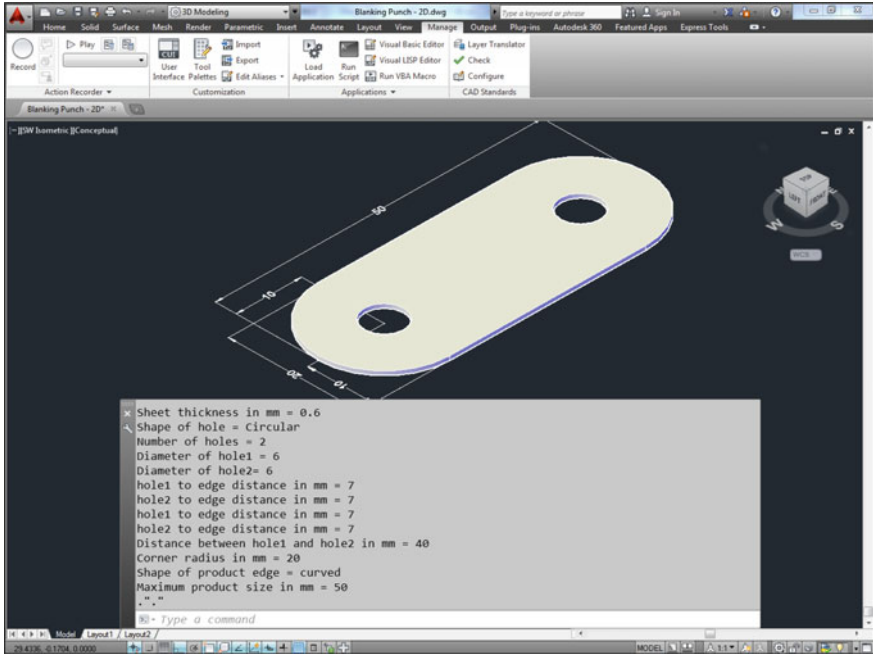


Fig. 6 Output of the proposed system for example part

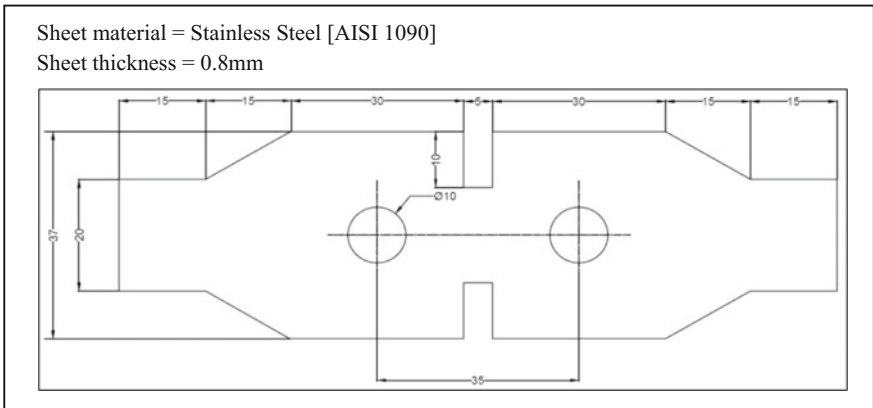


Fig. 7 Example part (all dimensions are in mm) (M/s D. D. Engineering Pvt. Ltd., Pune, India)

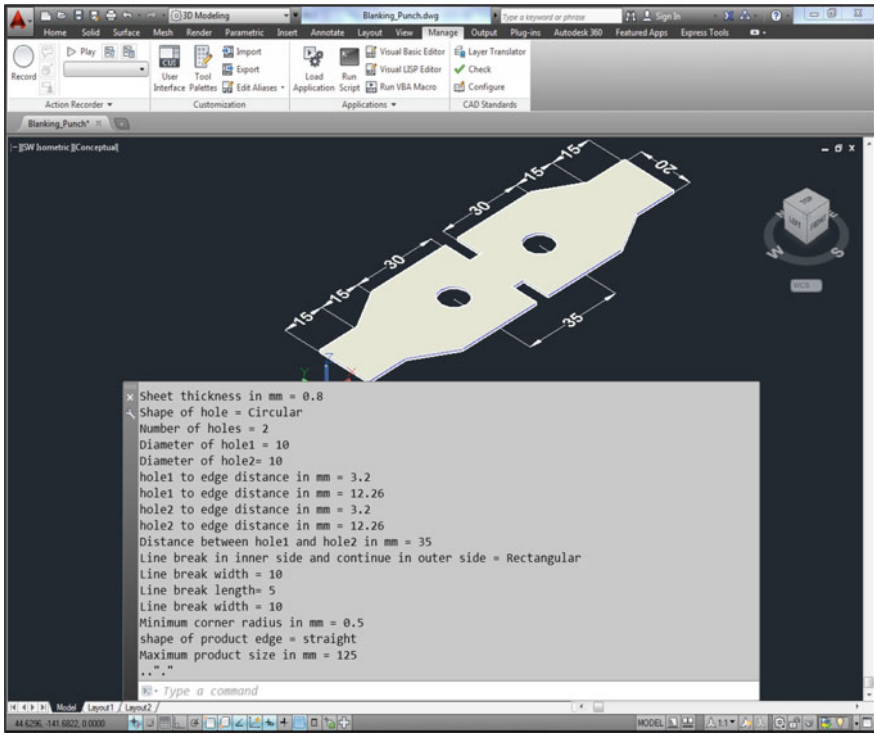


Fig. 8 Output of the proposed system for example part

4 Conclusion

A computer-aided smart system has been developed to assess 3D model features on sheet metal parts. Developed feature recognition system focused on smart solutions to identified design features on sheet metal parts for design of dies. New smart technique (using AutoLISP language) and extraction algorithms (using B-rep technique) for identification of design features on part have been developed. Developed smart technique has classified into design feature based on the characteristics of sheet metal parts. The developed smart system has been constructed using AutoLISP programming language. The smart system is accomplished tedious task of feature extraction such as size of holes, slots, corner radius, sheet thickness, distance between two holes, distance between hole and edge, maximum corner radius and notch in a short period of time. The smart system is useful to die designer and process planner working in sheet metal industries, especially small- and medium-sized stamping industries. Further work is required to strengthen the capability of proposed system to extract features of bending and deep-drawn parts.

References

1. Hwang, B.C., Han, S.M., Bae, W.B., Kim, C.: Development of an automated progressive design system with multiple processes (piercing, bending, and deep drawing) for manufacturing products. *Int. J. Adv. Manuf. Technol.* **43**, 644–653 (2009)
2. Shah, J., Mantyla, M.: *Parametric and Feature Based. CAD/CAM*. Wiley, New Jersey (1995)
3. Wierda, L.S.: Linking design, process planning and cost information by feature-based modelling. *J. Eng. Des.* **2**(1), 3–19 (1991)
4. Srinivasakumar, S.M., Lin, L.: Ruled based automatic part feature extraction and recognition from CAD data. *Comput. Ind. Eng.* **22**(1), 49–62 (1992)
5. Cser, L., Geiger, M., Greska, W., Hoffmann, M.: Three kinds of case-based learning in sheet metal manufacturing. *Comput. Ind.* **17**, 195–206 (1991)
6. Nnaji, B., Kang, T., Yeh, S., Chen, J.: Feature reasoning for sheet metal components. *Int. J. Prod. Res.* **29**(9), 1867–1896 (1991)
7. Meeran, S., Pratt, M.J.: Automated feature recognition from 2D drawings. *Comput. Aided Des.* **25**, 7–17 (1993)
8. Lentz, D.H., Sowerby, R.: Feature extraction of concave and convex regions and their intersections. *Comput. Aided Des.* **25**(7), 421–437 (1993)
9. Streppel, A.H., Vin, L.J., Brinkman, J., Kals, H.J.J.: Suitability of sheet bending modelling techniques in CAPP applications. *J. Mater. Process. Technol.* **36**, 339–356 (1993)
10. Mantripragada, R., Kinzel, G., Altan, T.: A computer-aided engineering system for feature-based design of box-type sheet metal parts. *J. Mater. Process. Technol.* **57**, 241–248 (1996)
11. Jagirdar, R., Jain, V.K., Batra, J.L., Dhande, S.G.: Feature recognition methodology for shearing operations for sheet metal components. *Comput. Integr. Manuf. Syst.* **8**(1), 51–62 (1995)
12. Ceglarek, D.: Multivariate analysis and evaluation of adaptive sheet metal assembly system. *Ann. CIRP* **47**(1), 17–22 (1998)
13. Gao, J.X., Tang, Y.S., Sharma, R.: A feature model editor and process planning system for sheet metal products. *J. Mater. Process. Technol.* **107**, 88–95 (2000)
14. Xie, S.Q., Tu, Y.L., Zhou, Z.D.: An integrated CAD/CAPP/CAM system for compound sheet metal cutting and punching. In: *Automated Systems Based on Human Skill*, Aachen, Germany, pp. 49–54 (2000)
15. Wang, J., Wu, X., Thomson, P.F., Flitman, A.: A neural networks approach to investigating the geometrical influence on wrinkling in sheet metal forming. *J. Mater. Process. Technol.* **105**, 215–220 (2000)
16. Lutters, D., Brinke, E., Streppel, A.H., Kals, H.J.J.: Computer aided process planning for sheet metal based on information management. *J. Mater. Process. Technol.* **103**, 120–127 (2000)
17. Rigopoulos, A., Arkun, Y.: KLE-(V)AR: a new identification technique for reduced order disturbance models with application to sheet forming processes. *J. Process Control* **11**, 679–698 (2001)
18. Ge, M., Zhang, G.C., Du, R., Xu, Y.: Feature extraction from energy distribution of stamping processes using wavelet transform. *J. Vibr. Control* **8**, 1023–1032 (2002)
19. Shunmugam, M.S., Kannan, T.R.: Automatic flat pattern development of sheet metal components from orthographic projections. *Int. J. Mach. Tools Manuf.* **42**, 1415–1425 (2002)
20. Holland, P., Standring, P.M., Long, H., Mynors, D.J.: Feature extraction from STEP (ISO 10303) CAD drawing files for metal forming process selection in an integrated design system. *J. Mater. Process. Technol.* **125–126**, 446–455 (2002)
21. Pal, P., Tigga, A., Kumar, A.: Feature extraction from large CAD databases using genetic algorithm. *Comput. Aided Des.* **37**, 545–558 (2005)
22. Zhao, Z., Shah, J.J.: Domain independent shell for DFM and its application to sheet metal forming and injection molding. *Comput. Aided Des.* **37**, 881–898 (2005)

23. Ferreira, J., Vivian, D.: Feature recognition in axi-symmetrical parts modeled by solids in an Internet-oriented CAD/CAM system. *J. Mater. Process. Technol.* **179**, 260–267 (2006)
24. Ciurana, J., Ferrer, I., Gao, J.X.: Activity model and computer aided system for defining sheet metal process planning. *J. Mater. Process. Technol.* **173**, 213–222 (2006)
25. Huang, Z., Xie, B., Ma, L., Wei, X.: Feature conversion based on decomposition and combination of swept volumes. *Comput. Aided Des.* **38**, 857–873 (2006)
26. Cicek, A., Gulesin, M.: A part recognition based computer aided assembly system. *Comput. Ind.* **58**, 733–746 (2007)
27. Klingenberg, W., Boer, T.W.: Condition-based maintenance in punching/blanking of sheet metal. *Int. J. Mach. Tools Manuf.* **48**, 589–598 (2008)
28. Zhang, C., Zhou, X., Li, C.: Automatic recognition of intersecting features of freeform sheet metal parts. *J. Zhejiang Univ. Sci.* **10**, 1439–1449 (2009)
29. Kannan, T., Shunmugam, M.: Processing of 3D sheet metal components in STEP AP-203 format. Part I: feature recognition system. *Int. J. Prod. Res.* **47**, 941–964 (2009)
30. Oh, K.S., Oh, K.H., Janga, J.H., Kim, D.J., Han, K.S.: Design and analysis of new test method for evaluation of sheet metal formability. *J. Mater. Process. Technol.* **211**, 695–707 (2011)
31. Gupta, R., Gurumoorthy, B.: Automatic extraction of free-form surface features (FFSFs). *Comput. Aided Des.* **44**, 99–112 (2012)
32. Behera, A.K., Lauwers, B., Duflou, J.R.: Advanced feature detection algorithms for incrementally formed sheet metal parts. *Trans. Nonferr. Metals Soc. China* **22**, 315–322 (2012)
33. Hussein, H.M.A., Mousa, H.M.: Computer aided feature recognition in free form parts. *Green Des. Mater. Manuf. Processes* 239–244 (2013)
34. Gupta, R.K., Sreenu, P., Bernard, A., Laroche, F.: Process information model for sheet metal operations. In: 11th International Conference on Product Lifecycle Management, Yokohama, Japan (2014)
35. Khan, A.A., Hussein, H.M.A., Emad, A., Ahmari, A.: Computer-aided process planning in prismatic shape die components based on standard for the exchange of product model data. *Adv. Mech. Eng.* **7**(11), 1–11 (2015)
36. Neugebauer, R., Werner, M., Pröhl, M., Brunnett, G., Kühnert, T.: New feature extraction and processing methods for the advanced knowledge based process planning of forming operations. *Procedia CIRP* **28**, 16–21 (2015)
37. Pishyar, E., Emadi, M.: Investigation of different algorithms for surface defects of steel sheet for quality. *Int. J. Comput. Appl.* **149**(6), 33–37 (2016)
38. Khan, A.A., Emad, A., Hussein, H.M.A., Ahmari, A.: An automatic feature extraction technique for 2D punch shapes. *Int. J. Comput. Electr. Autom. Control Inf. Eng.* **10**(5), 884–888 (2016)
39. Tao, J., Chen, Z., Yu, S., Liu, Z.: Integration of life cycle assessment with computer-aided product development by a feature-based approach. *J. Clean. Prod.* **143**, 1144–1164 (2017)
40. Eriyeti, M., Mpofo, K., Trimble, J., Gwangwava, N.: Model for developing a feature recognition system for a reconfigurable bending press machine. *Procedia CIRP* **63**, 533–538 (2017)
41. Ubhayaratne, I., Pereira, M.P., Xiang, Y., Rolfe, B.F.: Audio signal analysis for tool wear monitoring in sheet metal stamping. *Mech. Syst. Signal Process.* **85**, 809–826 (2017)
42. Greska, W., Franke, V., Geiger, M.: Classification problems in manufacturing of sheet metal parts. *Comput. Ind.* **33**, 17–30 (1997)
43. Ismail, N., Abu Bakar, N., Juri, A.: Recognition of cylindrical and conical features using edge boundary classification. *Int. J. Mach. Tools Manuf* **45**, 649–655 (2005)
44. Zhou, X., Qiu, Y., Hua, G., Wang, H., Ruan, X.: A feasible approach to the integration of CAD and CAPP. *Comput. Aided Des.* **39**, 324–338 (2007)
45. Sunil, V., Pande, S.: Automatic recognition of features from freeform surface CAD models. *Comput. Aided Des.* **40**, 502–517 (2008)

46. Hussein, S., Aseel, J.: STEP-based assembly feature recognition using attribute adjacency graph for prismatic parts. *Eng. Tech. J.* **31**, 1929–1948 (2013)
47. Jones, T.J., Reidsema, C., Smith, A.: Automated feature recognition system for supporting conceptual engineering design. *Int. J. Knowl. Based Intell. Eng. Syst.* **10**(6), 477–492 (2016)
48. Zeid, I.: *CAD/CAM Theory and Practices*. Tata McGraw-Hill Inc., Singapore (1991)
49. Babic, B.: Development of an intelligent CAD-CAPP interface. In: *Proceedings of the International Conference on Intelligent Technologies in Human-Related Sciences*, pp. 351–357 (1996)
50. Farsi, M., Arezoo, B.: Feature recognition and design advisory system for sheet metal components. In: *5th International Advanced Technologies Symposium Karabuk, Turkey*, pp. 1–5 (2009)

Author Index

A

Achutha, M.V., 527
Agarwal, Pranjali, 457
Anand Kumar, S., 79
Anand, Nishchay, 97
Apoorva, S., 11
Arolkar, Vijay A., 507
Arthanareeswaran, G., 427
Arumuga Perumal, D., 373
Arunkumar, P., 1
Arunvinthan, S., 217
Asokan, R., 131

B

Balaguru, S., 397
Balaji, D., 363
Balamurugan, M., 339
Balasubramanian, E., 1
Bhat, I.K., 21, 485
Bhattacharya, S.S., 241
Bhatt, Akash, 257
Bhowmick, Pathikrit, 457
Bhowmick, Shubhankar, 381
Bhuvaneshwaran, G., 1
Boominathan, Elumalai, 41
Bupesh Raja, V.K., 29

C

Chaithanya, Kaipa Sai, 357
Chandankar, Pavan, 415
Chandramohan, Sujatha, 145
Chandramohan, V. P., 267
Chetehouna, Khaled, 277

D

Devendiran, S., 179, 199
Dhileep, Karthick, 217
Dinesh, M., 131
Dixit, Arun C., 527

E

El-Tabach, Eddy, 277

F

Falempin, François, 277

G

Gaba, Vivek Kumar, 381
Gascoin, Nicolas, 277
Giridharan, K., 47
Goswami, Abhinav Giri, 225
Goswami, Chandramani, 21
Gowri, S., 41
Gupta, Mukur, 437
Gupta, Ravi Kumar, 437

H

Hiremath, Gourish, 405
Hussein, H.M.A., 437, 535

J

Jaiganesh, V., 47
Jain, Aatmesh, 153, 163, 457
Jain, Sarthak, 389
Jain, Prashant K., 331
Jaison, K.A., 507
Jayanth, K., 153

Jayasekar, C., 339
Jithin, R., 357

K

Kadiresh, P. N., 445
Kankar, P. K., 331
Karthikeyan, S., 113
Kesana, Balashankar, 373
Khadambari, B., 241
Khandai, Suresh Chandra, 11
Kumar, A., 485
Kumarasamy, A., 285
Kumar, Shailendra, 437, 535
Kumar, Virendra, 499
Kuppuraj, R., 467

L

Logesh, K., 29

M

Madhyastha, Deepak, 107
Malhotra, Dhruv, 457
Manimaran, A., 507
Manivannan, R., 1
Mathew, Arun Tom, 179, 199
Mishra, Chetan, 389
Mohanavel, V., 339
Mohan, Lalit, 499

N

Nadaraja Pillai, S., 217
Najmi, Hussain, 277
Narahari, H.K., 107
Naranje, Anand, 65
Naranje, Vishal, 65, 249
Narayan, Yeole Shivraj, 79
Narendiranath Babu, T., 225, 257
Naveen Kumar, K., 299, 357
Naveen Kumar, R., 299
Nayak, Ankit, 331

O

Om Ariara Guhan, C. P., 427

P

Padmanabhan, S., 47
Pasupathy, S.A., 467
Patel, Dhavalkumar, 257
Patil, Sanjay, 405
Patnaik, Amar, 21, 121, 485

Peddavarapu, Sreehari, 477
Prasad, Lalta, 499
Prasanna, J., 517
Praveen, A. S., 357
Prince Jeya Lal, L., 55
Puli, Ravi Kumar, 267

R

Raghuraman, S., 477
Rajamanickam, S., 517
Rajamani, D., 1
Rajan, K., 339
Rajesh, S., 131
Raj Kumar, G., 299
Ramachandra Rao, M.S., 241
Raman, Ritwik, 153
Ramesh, S., 55
Ram, Prasanna, 311
Rana, Hitesh Kumar, 29
Raturi, Himanshu Prasad, 499
Ravichandra, D., 267
Ravichandran, M., 339
Renganathan, N.G., 311
Roy, Aditya, 389
Rubanrajasekar, B., 131

S

Salunkhe, Sachin, 65, 249, 415, 535
Salunkhe, S.S., 437
Sankaram, M.V.N., 249
Sankar, Manoj Aravind, 311
Santhosh Kumar, S., 397
Sarasavadiya, Hardik, 163
Sarkar, Indranil, 153, 163
Satish Kumar, S., 349
Seid, Solomon, 145
Senthil Kumar, M., 299
Senthilkumar, S., 113
Shah, Manthan J., 163
Shanjeevi, C., 349
Sharma, Rahul, 381
Shetty, Vikas V., 373
Silambarasan, M., 1
Singh, Jasjeev, 249
Singh, Tej, 21
Sivakumar, P., 285
Sivarajan, S., 97
Solanki, Naveen, 389
Sondhi, Lakshman, 381
Soni, Aman, 121

Sridhara, B.K., [527](#)
Srinivasan, K.V., [507](#)
Srivastava, Animesh, [225](#)
Subhankar, Ghosh, [113](#)
Sujatha, S., [145](#)
Suresh Chandra Khandai, [11](#)
Suresh Kumar, S., [339](#)
Surya, M., [363](#)

T

Teraiya, Soham, [535](#)
Thamilarasan, J., [349](#)
Tharnari, Devansh, [257](#)
Tiwari, Rishabh Kumar, [225](#)

V

Velu, S., [349](#)
Venkatasudhahar, M., [29](#)
Venkatesan, K., [179](#), [199](#)
Venkatesan, S.P., [445](#)
Vetri Velmurugan, K., [179](#), [199](#)
Vignesh, R., [363](#)
Vignesh, S., [131](#)
Vijayanandh, R., [299](#)
Vishnu, R., [363](#)
Vishnu Pragash, A., [363](#)
Viswanath, Hari, [285](#)
Vora, K.C., [153](#), [457](#)

W

Wani, Kiran, [405](#)